

**The University of Sheffield**



**Novel Modular Dual 3-phase Permanent Magnet  
Machines for Wind Power Application**

**Yanxin Li**

A thesis submitted for the degree of Doctor of Philosophy

Department of Electronic and Electrical Engineering

The University of Sheffield

Mappin Street, Sheffield, S1 3JD, UK

**March 2018**

# Abstract

This thesis focuses on the investigation of novel modular dual 3-phase permanent magnet (PM) machines with redundant 2-pole machine for wind power application by finite element analyses and experiments.

The process of obtaining the novel modular machines is systematically introduced. In essence, it is equivalent to the combination of a conventional modular machine and a simple redundant one for modularity purpose. A 42-slot/32-pole (42S/32P) electrical machine is chosen as the example to present the features of this novel modular machine. Compared with its counterpart conventional modular machine (36S/30P) this novel modular machine shows comparable electromagnetic performance, while the redundant teeth contributed by the 6S/2P PM machine make it easier to adopt a modular structure. The coils located at the end slots of each segment can be protected effectively by these redundant teeth during the transportation and assembly process. Then, the available slot and pole number combinations for constructing this type of novel modular machine are summarised. The four prototype machines with 39S/32P, 39S/44P, 42S/32P and 42S/44P are used to demonstrate the influence of slot and pole number combinations on electromagnetic performance. Subsequently, the comparative study between the 42S/32P novel modular machine and the conventional modular machines with overlapping windings is performed. Since the dual 3-phase winding of this type of novel modular machine can adopt either thirty or zero degree phase shift between two sets of windings, they are compared with the 192S/32P and 96S/32P PM machines, respectively. Both normal operation with two sets of windings and faulty operation with only one set of winding are investigated. The merit of good fault-tolerant capability can be seen for the novel modular machines. Finally, the influence of different magnetic slot wedges (symmetrical magnetic slot wedges, two kinds of asymmetric magnetic slot wedges, fully closed slots and fully open slots) is investigated. It provides the guidance on how to select the appropriate magnetic slot wedges for electromagnetic performance improvement in different aspects.

## **Acknowledgements**

It is the greatest honour for me to express my sincere thanks to all of the people who provided the help and encouragement during my PhD study.

Firstly, I would like to thank my PhD primary academic supervisor-Professor Zi-Qiang Zhu who is the global pioneer in electrical machine research. During the PhD study, he not only provided high quality supervision on my PhD study, but shared previous personal experience with me as well. Besides, the valuable discussions with my second academic supervisor-Dr. Guang-Jin Li also gave me a lot of inspiration.

Then, I would like to thank the University of Sheffield and Sheffield Siemens Wind Power Research Centre which does the world leading renewable energy research. Because of the financial sponsorship for both university registration fee and living bursary, I could finish my PhD without any hesitation. The special thank would like to give to Dr. Arwyn S. Thomas who often discussed research details with me, Dr. Zhan-Yuan Wu and Mr. Xi-Meng Wu that helped me obtain experimental results.

Finally, I would like to show my thanks to all of the friends and relatives. Thanks very much for all of your companion, support and love. I expect to achieve greater success in the future.

To my motherland, China

# Contents

<b>Abstract</b> .....	<b>I</b>
<b>Acknowledgements</b> .....	<b>II</b>
<b>Contents</b> .....	<b>III</b>
<b>Nomenclatures</b> .....	<b>VI</b>
<b>Chapter 1 General Introduction</b> .....	<b>1</b>
1.1 Background Introduction .....	1
1.1.1 Development and Application of PM Materials.....	1
1.1.2 Development of Radial Flux PM Machines .....	6
1.2 Fractional-slot Non-overlapping Windings.....	13
1.2.1 All and Alternate Teeth Wound Windings .....	14
1.2.2 Multi-layer Windings .....	22
1.3 Dual 3-phase Permanent Magnet Machines.....	24
1.3.1 Zero Degree Phase Shift .....	25
1.3.2 Thirty Degree Phase Shift.....	30
1.3.3 Other Degree Phase Shift .....	33
1.4 Development of Modular Stator Techniques in Electrical Machines .....	35
1.4.1 Physical Coupling.....	36
1.4.2 Physical Partial Decoupling.....	42
1.4.3 Physical Fully Decoupling.....	45
1.5 Scope and Contributions of Thesis.....	49
1.5.1 Research Scope.....	49
1.5.2 Major Contributions .....	52
<b>Chapter 2 Analytical Modelling of Rotor Eccentricity by Superposition Method</b> .....	<b>55</b>
2.1 Prototype Machines.....	55
2.2 Employment Process of the Proposed Superposition Method .....	56
2.2.1 Establishment of Different Concentric Machine Models .....	57
2.2.2 Air-gap Flux Densities of Concentric Machines Prediction by Subdomain Method.....	59
2.2.3 Air-gap Flux Density Synthesis of the Original Eccentric Machine .....	63
2.2.4 Summary of the Proposed Method .....	65
2.3 Cogging Torque.....	66
2.3.1 Prediction Principle .....	66
2.3.2 Finite Element Validation.....	69
2.4 Unbalanced Magnetic Force.....	75
2.4.1 Prediction Principle .....	76
2.4.2 Finite Element Validation.....	81
2.5 Extension of the Method to Axial-varying Eccentricity .....	89
2.6 Conclusion.....	97
<b>Chapter 3 Development of Modular Double-layer Dual 3-phase PM Machine Topologies with Redundant Teeth</b> .....	<b>98</b>
3.1 Construction of Proposed Modular Machines.....	99
3.1.1. Rotor of Proposed Machine .....	101
3.1.2. Stator Core of Proposed Machine.....	102
3.1.3. Stator Winding of Proposed Machine .....	104
3.2 Electromagnetic Performance Analysis .....	107
3.2.1 Field Distribution.....	107
3.2.2 Open-circuit Flux-linkage and Back-EMF .....	111

3.2.3 Torque Characteristics .....	113
3.2.4 Iron Losses.....	118
3.2.5 Demagnetisation .....	121
3.3 Influence of Angle between Two Sets of Windings .....	127
3.3.1 Winding Connection.....	127
3.3.2 Field Distribution.....	128
3.3.3 Open-circuit Back-EMF and Cogging Torque .....	132
3.3.4 On-load Torque.....	134
3.3.5 Iron Losses.....	138
3.3.6 Demagnetisation .....	139
3.4 Experimental Validation .....	143
3.5 Conclusion.....	147
<b>Chapter 4 Investigation of Slot and Pole Number Combinations in Novel Modular Machines .....</b>	<b>148</b>
4.1 Summary of Available Slot and Pole Number Combinations.....	148
4.1.1 Structure of Proposed Modular Machines .....	148
4.1.2 Conditions for Balanced Two Sets of Windings .....	149
4.2 Prototype Machines.....	154
4.3 Electromagnetic Performance Comparison of Prototype Machines .....	158
4.3.1 Field Distribution.....	158
4.3.2 Open-circuit Performance.....	163
4.3.3 On-load Performance.....	165
4.3.4 Iron Losses.....	169
4.3.5 Unbalanced Magnetic Force .....	171
4.3.6 Demagnetisation .....	174
4.4 Conclusion.....	177
<b>Chapter 5 Comparative Study of Modular Dual 3-phase PM Machines with Overlapping/Non-overlapping Windings .....</b>	<b>179</b>
5.1 Prototype Machines.....	180
5.2 Performance Comparison under Normal Operation.....	183
5.2.1 Field Distribution.....	183
5.2.2 Open-circuit Performance.....	187
5.2.3 On-load Performance.....	190
5.2.4 Iron Losses.....	194
5.2.5 Demagnetisation .....	196
5.3 Performance Comparison under Faulty Operation.....	197
5.3.1 Open-circuit Fault.....	199
5.3.2 Short-circuit Fault.....	207
5.4 Experimental Validation .....	213
5.5 Conclusion.....	215
<b>Chapter 6 Investigation of Fault-tolerant Modular Dual 3-phase PM machines with Different Winding Topologies .....</b>	<b>216</b>
6.1 Prototype Machines.....	217
6.2 Performance Comparison with Two Sets of Winding Operation .....	221
6.2.1 Field Distribution.....	221
6.2.2 Open-circuit Performance.....	225
6.2.3 On-load Performance.....	227
6.2.4 Iron Losses.....	230
6.2.5 Demagnetisation .....	232
6.3 Performance Comparison with One Set of Winding Operation.....	234

6.3.1 One Set of Winding Open-circuit .....	236
6.3.2 One Set of Winding Short-circuit .....	242
6.4 Experimental Validation .....	250
6.5 Conclusion.....	254
<b>Chapter 7 Influence of Magnetic Sot Wedges on Novel Dual 3-phase Modular Machines .....</b>	<b>256</b>
7.1 Prototype Machines.....	257
7.2 Influence of Magnetic Slot Wedges on Performances .....	259
7.2.1 Field Distribution.....	259
7.2.2 Open-circuit Performance.....	263
7.2.3 On-load Performance.....	268
7.2.4 Iron Losses.....	277
7.2.5 Demagnetisation .....	280
7.3 Conclusion.....	283
<b>Chapter 8 General Conclusions and Future Work.....</b>	<b>285</b>
8.1 General Conclusions .....	285
8.1.1 Novel Modular PM Machine Topologies .....	285
8.1.2 Slot and Pole Number Combinations of Novel Modular Machines .....	286
8.1.3 Comparison of Different Modular Machines .....	288
8.1.4 Influence of Magnetic Slot Wedges .....	294
8.2 Future Work .....	295
<b>References.....</b>	<b>297</b>
<b>Appendix A Determination of Overload Current Value.....</b>	<b>316</b>
<b>Appendix B Frozen Permeability Method.....</b>	<b>323</b>
<b>Appendix C CAD Diagrams and Materials of Prototyped Machines.....</b>	<b>325</b>

## Nomenclatures

### Variables

Symbol	Meaning	Unit
$A_{DP}$	Area of irreversible demagnetisation for PM	$m^2$
$A_e$	Electric loading	kA/m
$A_{PM}$	PM area	$m^2$
$b_{soe}$	Slot opening between effective teeth	mm
$B_{knee}$	Knee point of N35UH PM under 180 °C	T
$B_m$	Magnitude of flux density	T
$B_r$	Radial component of air-gap flux density	T
$B_{PMi//}$	Flux density in magnetisation parallel direction of the $i^{th}$ PM	T
$B_{PMi\perp}$	Flux density in magnetisation perpendicular direction of the $i^{th}$ PM	T
$B_{PMix}$	X-components of the $i^{th}$ PM flux density	T
$B_{PMiy}$	Y-component of the $i^{th}$ PM flux density	T
$B_{PMix//}$	$B_{PMix}$ projection of the $i^{th}$ PM flux density in parallel magnetisation direction	T
$B_{PMix\perp}$	$B_{PMix}$ projection of the $i^{th}$ PM flux density in perpendicular magnetisation direction	T
$B_{PMiy//}$	$B_{PMiy}$ projection of the $i^{th}$ PM flux density in parallel magnetisation direction	T
$B_{PMiy\perp}$	$B_{PMiy}$ projection of the $i^{th}$ PM flux density in perpendicular magnetisation direction	T
$B_{r1m}$	Fundamental component of radial flux density	T
$B_\alpha$	Circumferential component of air-gap flux density	T
$B_{\delta l}$	Peak value of fundamental air-gap flux density	T
$D_{so}$	Stator outer diameter	mm
$e_{bi}$	Induced phase back-EMF of phase $i$	V
$E_{1m}$	Amplitude of the fundamental phase back-EMF	V
$E_{im}$	Amplitude of higher order harmonics of phase back-EMF	V
$f$	Frequency	Hz
$F_{ed}$	Any exact divisor of a number	-

$F_x$	X-component of UMF	N
$F_y$	Y-component of UMF	N
$i_i$	Current of phase $i$	A
$i_j$	Current of phase $j$	A
$i_{j1}$	Current of the first set of winding	A
$i_{j2}$	Current of the second set of winding	A
$I_d$	D-axis current	A
$I_{ph}$	Phase current	A
$I_q$	Q-axis current	A
$I_{rat}$	Rated phase current	A
$J_{ry}$	Current density of the rotor yoke	A/m <sup>2</sup>
$J_{PMi}$	Current density of the $i^{\text{th}}$ PM	A/m <sup>2</sup>
$k_c$	Carter factor	-
$k_e$	Eddy current loss coefficient of stator lamination	-
$k_h$	Hysteresis loss coefficient of stator lamination	-
$k_w$	Winding factor of fundamental component	-
$K_{f1}$	Hysteresis loss material property quadratic term coefficient	-
$K_{f2}$	Hysteresis loss material property linear term coefficient	-
$K_{f3}$	Hysteresis loss material property constant term coefficient	-
$K_{wc}$	Winding factor	-
$L_{ij}$	Inductance between two phases	H
$L_{AIj1}$	Inductance within the first set of winding	H
$L_{AIj2}$	Inductance between two sets of windings	H
$L_{A1A2}$	Mutual inductance between phase-A1 and -A2	H
$L_{B1B2}$	Mutual inductance between phase-B1 and -B2	H
$L_{C1C2}$	Mutual inductance between phase-C1 and -C2	H
$m$	Phase number	-
$n_r$	Rotor speed	rpm
$N_{cog}$	Cogging torque periodicity number over one mechanical revolution	-
$N_{cogpp}$	Cogging torque periods within one pole pair range	-
$N_p$	Rotor pole number	-



$N_{pc}$	Rotor pole number of the conventional modular machine	-
$N_{pc0}$	Pole number corresponding to the basic electrical machine unit of the conventional modular machines	-
$N_{ph}$	Number of turns per phase	-
$N_{pp}$	Rotor pole number of the proposed modular machine	-
$N_{pr}$	Rotor pole number of the redundant machine	-
$N_s$	Stator slot number of the electrical machine	-
$N_{s0}$	Stator slot number of the basic electrical machine units	-
$N_{sc}$	Stator slot number of the conventional modular machine	-
$N_{sc0}$	Slot number corresponding to the basic electrical machine unit of the conventional modular machines	-
$N_{seg}$	Stator segment number	-
$N_{sLOP}$	Stator slot number of the modular machines with OLP windings	-
$N_{sp}$	Stator slot number of the proposed modular machine	-
$N_{sr}$	Stator slot number of the redundant machine	-
$N_{trNOLP}$	Redundant tooth number of the modular machines with NOLP windings	-
$p$	Rotor pole pair number	-
$p_0$	Rotor pole pair number of the basic electrical machine unit	-
$P_{cop}$	Stator copper loss	W
$P_{Fe}$	Stator iron loss	W
$P_{PM}$	PM eddy current loss	W
$P_{ry}$	Rotor yoke eddy current loss	W
$r_{gap}$	Radius of air-gap centre	m
$R_{ph}$	Phase resistance	$\Omega$
$S_{PMi}$	Area of the $i^{\text{th}}$ PM	$\text{m}^2$
$S_{ry}$	Area of the rotor yoke	$\text{m}^2$
$t$	GCD of the stator slot and rotor pole pair numbers	-
$t_c$	Number of basic electrical machine unit	-
$T_{avg}$	Average torque	Nm
$T_{cogPP}$	Peak-to-peak torque ripple of cogging torque	Nm
$T_{PP}$	Peak-to-peak torque ripple of on-load torque	Nm

$v_i$	Terminal voltage of phase $i$	V
$v_{indA1}$	Induced voltage of phase-A1	V
$y_c$	Coil pitch of the conventional modular machine	mechanical degree
$\Theta_{arm}$	Current MMF over one pole pitch	A turns
$\Theta_{PM}$	PM MMF over one pole pitch	A turns
$\Phi_{1m}$	Magnitude of fundamental flux	Wb
$\Omega_r$	Rotor mechanical angular speed	rad/s
$\alpha$	Stator angular position	mechanical degree
$\alpha_e$	Phase shift between adjacent coils within each segment	electrical degree
$\alpha_i$	Phase shift between any two adjacent coils	electrical degree
$\alpha_p$	PM pole arc to pole pitch ratio	-
$\alpha_{pe}$	Phase shift between two adjacent effective teeth	electrical degree
$\alpha_{ph}$	Phase shift among each phase within one set of winding	electrical degree
$\alpha_{pr}$	Phase shift between the last and the first effective teeth of two adjacent stator segments	electrical degree
$\alpha_{PMi}$	Instant position of the $i^{\text{th}}$ PM	mechanical degree
$\alpha_{PMi0}$	Initial position of the $i^{\text{th}}$ PM	mechanical degree
$\alpha_r$	Phase shift between two adjacent end coils	electrical degree
$\alpha_{set}$	Phase shift between two sets of windings	electrical degree
$\mu_0$	Air permeability	H/m
$\sigma_{PM}$	PM conductivity	S m
$\sigma_{ry}$	Rotor yoke conductivity	S m
$\tau_p$	PM pole pitch	m or rad
$\tau_{pc}$	Pole pitch of the conventional modular machine	mechanical degree

$\tau_{ps}$	Pole pitch expressed by slot number	-
$\tau_s$	Tooth pitch	m or rad
$\tau_{se}$	Tooth pitch of the proposed modular machine between adjacent effective teeth	m
$\tau_{sp}$	Tooth pitch of the proposed modular machine between adjacent effective teeth	electrical degree
$\tau_{sc}$	Tooth pitch of the conventional modular machine	electrical degree
$\eta$	Efficiency	-
$\psi_{1m}$	Peak value of fundamental phase flux-linkage	Wb
$\psi_i$	Flux-linkage of phase $i$	Wb
$\psi_{A1}$	Phase-A1 flux-linkage	Wb
$\psi_{dPM}$	D-axis PM flux-linkage	Wb
$\psi_{PMA1}$	PM component of phase-A1 flux-linkage	Wb
$\omega_e$	Electrical angular frequency	rad/s
$\omega_r$	Rotor electrical angular speed	rad/s

### Abbreviation

ASYM	Asymmetric
BLAC	Brushless alternating current
BLDC	Brushless direct current
D 3p	Dual 3-phase
DP	Demagnetisation percent
DSPM	Doubly salient permanent magnet
EMF	Electromotive force
FCS	Fully closed slots
FEA	Finite element analysis
FOS	Fully open slots
FP	Frozen permeability
FRPM	Flux-reversal permanent magnet
GCD	Greatest common divisor
IRPM	Interior radially magnetised permanent magnet

ICPM	Interior circumferentially magnetised permanent magnet
LCM	Least common multiple
N	Normal
N/A	Not available
NOLP	Non-overlapping
IPM	Interior permanent magnet
MEA	More electric aircraft
MMF	Magnetomotive force
OC	Open-circuit
OLP	Overlapping
PM	Permanent magnet
PP	Peak-to-peak
PSPM	Partitioned stator permanent magnet
S 3p	Single 3-phase
SC	Short-circuit
SFPM	Switched-flux permanent magnet
SIPM	Surface-inset permanent magnet
SMPM	Surface-mounted permanent magnet
SRM	Switched reluctance machine
SVPWM	Space vector pulse width modulation
SPM	Surface-mounted/inset permanent magnet
SYM	Symmetrical
THD	Total harmonic distortion
UMF	Unbalanced magnetic force

# Chapter 1 General Introduction

## 1.1 Background Introduction

### 1.1.1 Development and Application of PM Materials

The applications of permanent magnets (PMs) to electrical machines can be dated back to the 19<sup>th</sup> century when there were only low energy density PM materials, such as magnetite ( $\text{Fe}_3\text{O}_4$ ), being used [BOW75].

Due to the poor quality of natural magnets, the PM machines were not obviously developed until the AlNiCo type PM material was invented around 1930. This kind of PM material has quite large remanence but the coercivity is relatively low. In order to apply AlNiCo in PM machines, the thickness in magnetisation direction was usually quite long to avoid irreversible demagnetisation in early years [KEN85]. However, the property of easy demagnetisation and magnetisation has been applied to flux modulated PM machines recently, especially in memory machines [OST03]. There was another drawback for AlNiCo PM material, viz. nonlinear demagnetisation property in second quadrant of B-H plane. When the field intensity pushes the working point of PMs to a lower flux density, the corresponding recoil line leads to a lower remanence compared with the initial value. Therefore, the performance will be worse if the electrical machines with AlNiCo experience overload condition [GIE10]. The application of AlNiCo material is preferred in high temperature operation because of the quite strong high temperature resistant capability.

Since the ferrite was introduced in 1950s, this kind of PM material fast occupied the market and is still widely applied nowadays due to its much lower price compared with other kinds of PMs. There are two major types of ferrites. One of them has Strontium element, while the other uses Barium element. Although the remanence is much lower for this PM material, the coercivity has been improved. The demagnetisation property is practically linear as well except for low temperature situations. This kind of PM material has positive temperature coefficient, which is different from other PM materials. Therefore, the irreversible demagnetisation must be checked under low temperature operation. Another prominent advantage, viz. high resistivity, can also be seen for this kind of material. Thus, the eddy current loss will be lower [PYR13].

The emergence of rare earth PM material-SmCo brought the enormous development in PM machines. Two kinds of SmCo PMs ( $\text{SmCo}_5$  and  $\text{Sm}_2\text{Co}_{17}$ , respectively) were successively invented. Both remanence and coercivity of this material are evidently improved compared with ferrite. Furthermore, this kind of PM material can keep linear demagnetisation property even if the working temperature is high [FUR01]. Since it is also corrosion resistant, no coating is needed. The issue for this PM material is the high price. It is much more expensive than other kinds of PMs. Therefore, only the applications requiring higher energy density within a small volume and high temperature stability will adopt this kind of PM. Up to now, the latest kind of rare earth PM material-NdFeB, has the largest energy density and its price is much lower than SmCo PM [GIE08]. The sintered NdFeB PM can have comparable or even larger remanence than AlNiCo material, while the coercivity is proportionally large as well. The demagnetisation line is also linear for this kind of PM material except for high temperature situations, which is one of the drawbacks for this kind material. The coating is necessary for this material owing to the susceptibility to corrosion. The approximate demagnetisation properties of major PM materials are shown in Fig. 1.1 for clarity [PEL16], where  $B_{rem}$  is the PM remanence and  $H_c$  is the coercivity.

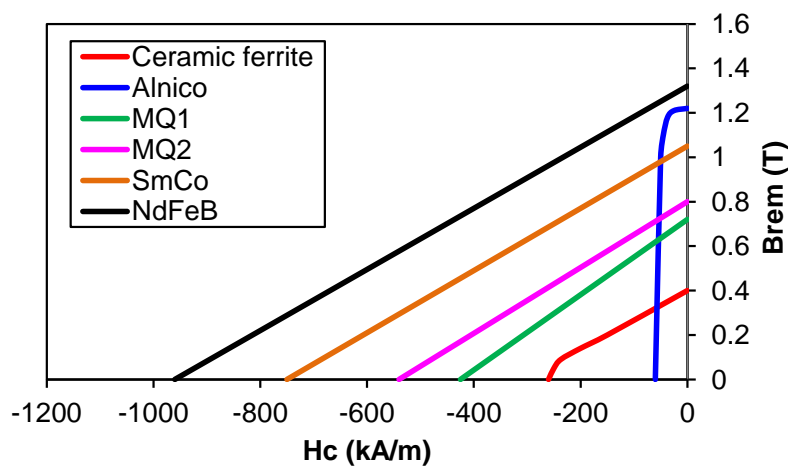
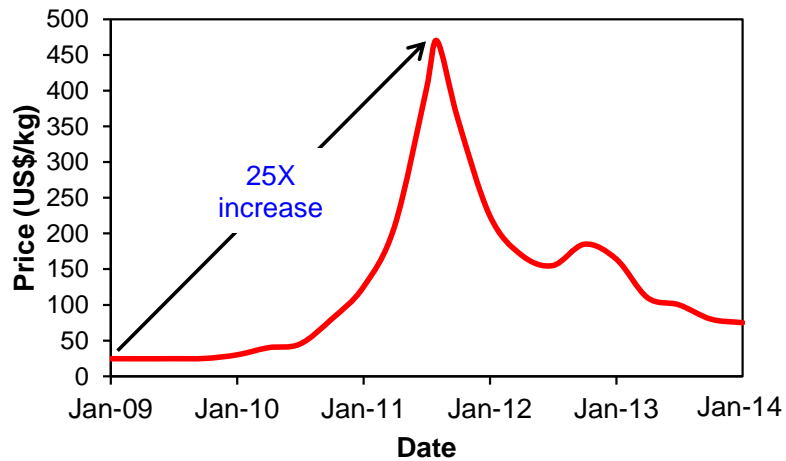


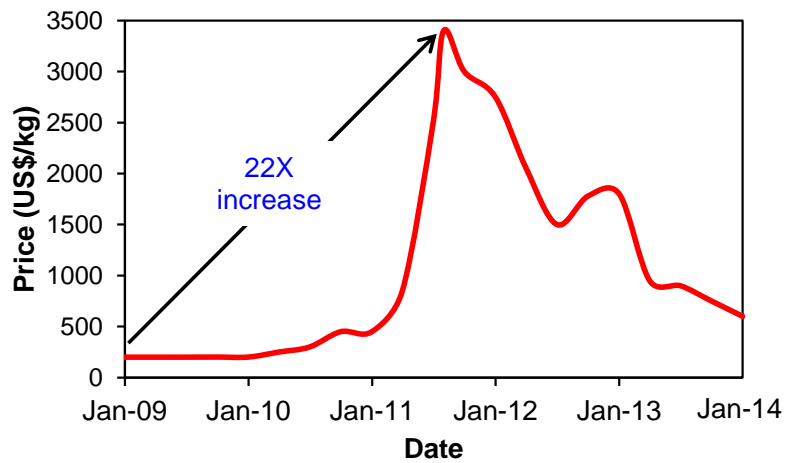
Fig. 1.1. Comparison of demagnetisation characteristics of different PM materials [PEL16].

For the PM materials shown in Fig. 1.1, NdFeB has experienced a huge price fluctuation over the past few years, which leaves deep influence on the development of PM materials and machines. The price variations of two most important elements

manufacturing this kind of PM are shown in Fig. 1.2. Neodymium is the major component determining magnetic energy and Dysprosium is closely related to demagnetisation withstand capability under high temperature. Fig. 1.2 shows that the price of Dysprosium is almost 5~7 times higher than that of Neodymium during all of the time. The price of two elements had a sharp increase in 2011, viz. 20 times expensive than before. How to reduce the amount of these rare earth elements and develop other kinds of new PM materials are increasingly concerned from that time.



(a) Neodymium



(b) Dysprosium

Fig. 1.2. Variation of rare earth metal price [PEL16].

Because of the development of PM material, the corresponding PM machines have been fast developing for recent decades as well. The use of PM machines mainly has following advantages [HEN10]:

(1) PM brushless machines have simple structure and the reliability will be much higher compared with those electrical machines having brushes and commutator, such as electrically excited synchronous machines and universal machines.

(2) Since there are no extra field excitation systems, the excitation loss can be eliminated. Therefore, the efficiency will be higher.

(3) Because of the adoption of high energy density PMs, the electrical machines can be made in smaller volumes if the same torque are achieved compared with the conventional electrical machines without PMs. This means PM machines have higher torque density. Furthermore, the smaller rotor will improve the dynamic performance of the electrical machines as well.

(4) Higher power factor can be obtained, which reduces the converter capacity and reduces the total cost of the whole electrical machine drive system.

PM machines have been widely investigated and applied in a vast number of fields accounting for these merits [GIE10]:

- (1) Industry applications: servo drives; machine tools; intelligent robotics, etc.
- (2) Domestic appliances: air-conditioner (compressor); washing machine; hair dryer; vacuum cleaner; bladeless fan, etc.
- (3) Automobile: integrated starter/generator; electric vehicle; auxiliary systems, etc.
- (4) Aerospace: more electric aircraft, rockets, satellites, etc.
- (5) Transportation: high speed railway, ship propulsion, escalators and elevators, etc.
- (6) Renewable generation: wind power generation; tidal power generation.

Although PM machines have been widely applied in industry and domestic appliances due to the advantages of simple structure, high torque density, high efficiency, low torque ripple, etc. [CRO02], [BIA06d], [ELR10], their electromagnetic performance may be significantly affected by parasitic issues, such as rotor eccentricities due to unavoidable manufacture tolerance [DOR10], [MIC14], [DI15].

For the influence of rotor eccentricity on electromagnetic performance, there are two kinds of rotor eccentricities being considered [EBR09]. The machine shown in



Fig. 1.3 is used to define them. One kind is the static eccentricity. The rotor geometry centre ( $O_r$ ) has an offset referring to the stator geometry centre ( $O_s$ ), which is called eccentricity magnitude ( $\varepsilon$ ). The rotor will rotate in its own axis under such condition, as the thin anticlockwise circular path shown in Fig. 13. The other kind is the rotating eccentricity, which is also called as dynamic eccentricity. Under this condition, the rotor centre will rotate based on the stator geometry centre with the offset, as the thick anticlockwise circular path shown in Fig. 1.3.

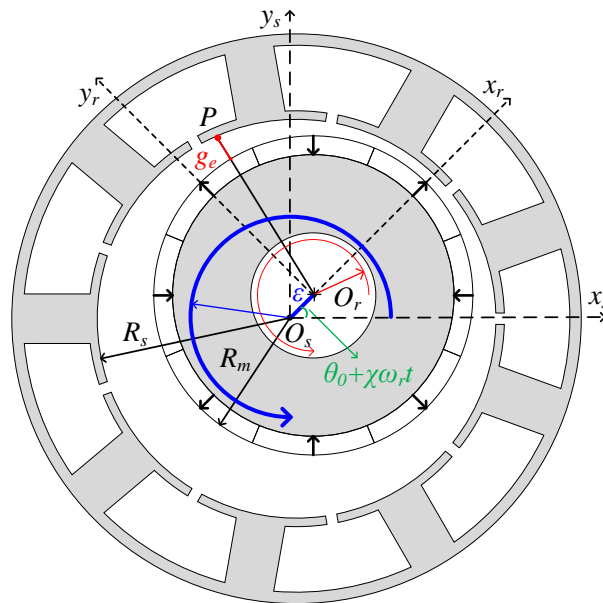


Fig. 1.3. Rotor eccentricity illustration.

Usually, there are three kinds of methods being used to analyse the machine performances with rotor eccentricity. Finite element analysis (FEA) is powerful enough to predict the electromagnetic performance of PM machines. However, the full model is necessary for FEA under either static or rotating eccentricity situations, since the model cannot be simplified by applying periodic boundary condition any more. It has been used to investigate the influence of slot/pole number combinations on cogging torque [ZHU14b]. However, it is problematic when slot/pole numbers are high, for instance, the applications in low speed wind power generators and hydraulic turbines [CHE05]. Under such conditions, the meshing requirement in air-gap region will be high, which is sensitive to cogging torque prediction [HOW92]. Besides, FEA is time-consuming for analysing the machines with rotor eccentricity due to the necessity of building up the full machine model. To simplify the problem, equivalent magnetic circuit (EMC) method is adopted by some researchers [WAN99b],

[ZHA13b]. Although [WAN99b] has some conclusions, it lacks the verification of the method and the process of employing the method is vague. In [ZHA13b], though the establishment of the MEC was stated in detail, the effectiveness of the method is not fully judged. Furthermore, it is complicated to build up the EMC model for the whole machine, especially for the rotating eccentricity. Compared with FEA and the EMC method, the analytical method can fast and accurately predict machine performance and provide more insight on machines. The analytical method was used by some researchers [DOR96], [DOR97], [KIM98a], [KIM98b], [FU12]. [DOR96], [DOR97] adopted 1D permeance function to consider the influence of rotor eccentricity on machine performances, which is quite simple and useful to qualitatively explain some phenomena, whereas they are not accurate enough to predict the electromagnetic performance, such as UMF. In order to improve the accuracy of the analytical model, [KIM98a], [KIM98b] tried to solve the field governing partial differential equations by perturbation method, which is a huge progress on rotor eccentricity research. Paper [FU12] extends the perturbation method by incorporating it into the subdomain model which can accurately consider the slotting effect [ZHU10]. The drawback of adopting scalar potential in [KIM98a], [KIM98b], [FU12], [ZHU10] is evident, viz. hard to show the influence of the armature field, which is crucial to electrical machine operation. What is more, the two methods are too complex and they are only used to predict the air-gap flux density without further investigating the influence of rotor eccentricity on machine performance.

### **1.1.2 Development of Radial Flux PM Machines**

Since the demand of PM machines is increasingly high and the power electronic techniques, control strategies and material science corresponding rapidly grow, machine topologies have being developed as well. For the most commonly used radial flux PM machines, a brief classification of some typical topologies based on the PM arrangement patterns can be seen in Fig. 1.4.

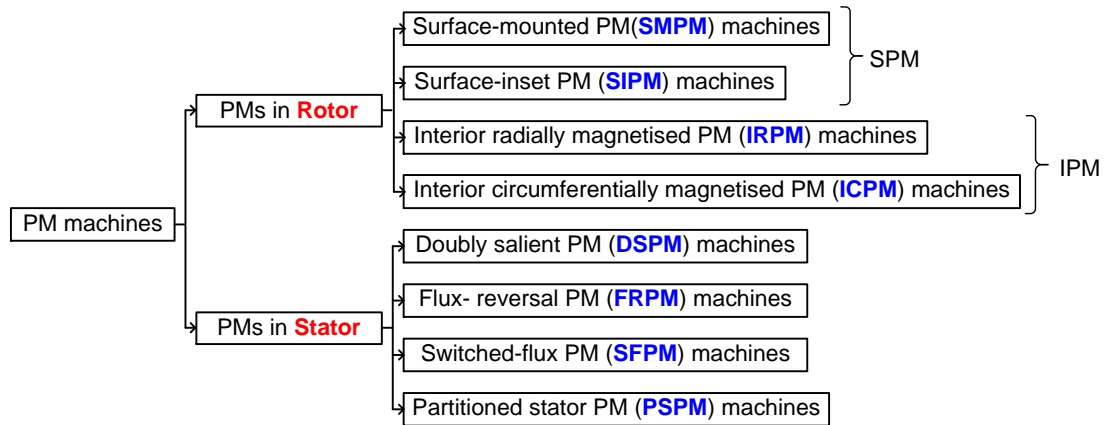


Fig. 1.4. Classification of radial flux PM machines.

Fig. 1.4 shows that there are four typical arrangement patterns when the PMs are located in rotors. The cross-sections of four examples are shown in Fig. 1.5. The winding configurations could be various even if the slot and pole number combination is the same. Therefore, the stator windings are not shown in the figure for simplicity. Each kind of rotor shown in Fig. 1.5 has its own features. There hardly exists  $d$ - and  $q$ -axis inductance difference for the electrical machines with surface-mounted PMs (SMPMs) shown in Fig. 1.5(a), for the practically same reluctances along these two axes. Since this kind of PM machine has quite simple structure and the PM shape can be easily adjusted to optimise the air-gap flux density, they are adopted in quite a few applications [CHE00a], [BIA06b], [BOA14]. When the PM inter-regions are also occupied with ferromagnetic materials, the surface-inset PM (SIPM) machines can be obtained, as shown in Fig. 1.5(b). Since the  $q$ -axis reluctance is largely reduced, the reluctance torque will exist for this kind of PM machine. However, the magnetic field will sharply change around the intersection part between PMs and rotor core, the torque ripple and stator iron loss will be large [SEB87], [ZHU02], [CHA04], [BAR13]. Both PM machines shown in Fig. 1.5(c) and (d) belong to interior PM type, while the former has radially magnetised PMs (IRPM) and the later uses PMs with circumferential magnetisation (ICPM) pattern. For radially magnetised PM machines, not only do they have reluctance torque, the robust rotor core structures make them suitable for high speed operation as well. Moreover, the PMs are protected by the rotor core and away from air-gap. That is why the irreversible demagnetisation capability can be improved [ZHU07a], [DOR12], [REN16]. If the rotors adopt circumferentially magnetised PMs, the flux focusing effect will lead to a much higher air-gap flux density, which is the major advantage for this kind of PM machine

[ZHU14a], [ZHA15], [YAN17]. In real application, the rotor topologies can be according modified to satisfy the specific requirements.

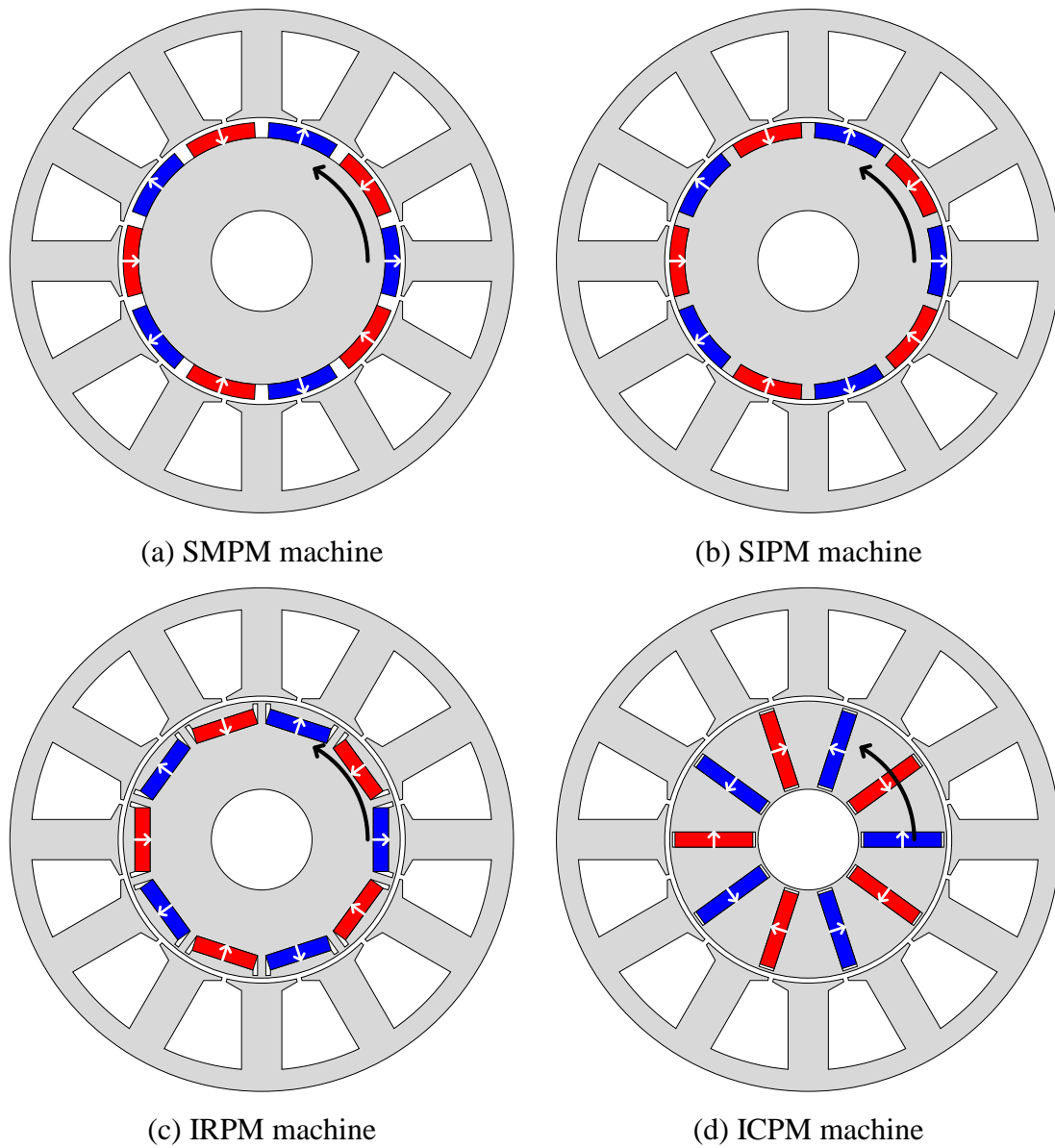
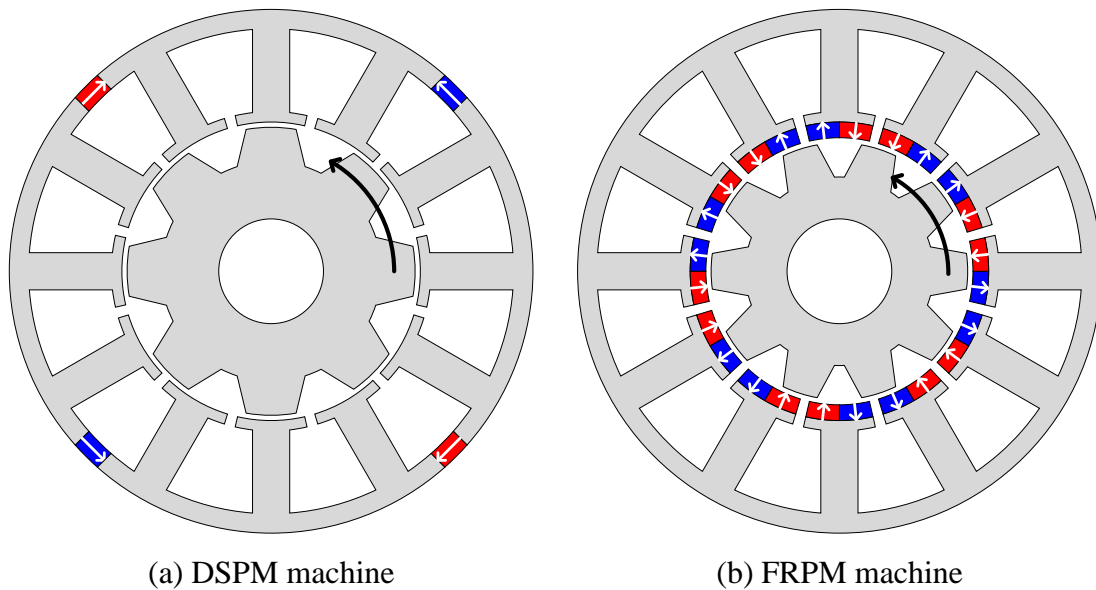


Fig. 1.5. Rotor PM machines with different configurations.

The stator PM machines mainly contain four typical topologies as well according to Fig. 1.4. The cross-sections of the representative PM machines are shown in Fig. 1.6, respectively. The research of these PM machines is one of the topics of high interest in recent years and their major features are briefly summarised as follows. The doubly salient PM (DSPM) machine shown in Fig. 1.6(a) has the advantage of low PM volume and simple rotor structure. The unipolar flux-linkage could be the disadvantage of this PM machine [LIA95], [YAN06], [CHE11]. Therefore, the torque

density could be low. When the PMs are mounted on tooth surface, the flux-reversal PM (FRPM) machine can be obtained [WAN99], as shown in Fig. 1.6(b). Although the flux-linkage of this PM machine is bipolar, the PMs are directly exposed to air. Thus, PMs are vulnerable to be irreversibly demagnetised [KIM05], [MOR10]. The switched PM (SFPM) machine shown in Fig. 1.6(c) uses much larger amount of PMs, its torque density is much higher than previous two kinds of stator PM machines due to flux focusing effect. Due to heavy saturation in stator core, the iron loss is the issue for this kind of PM machine [CHE10a], [CHE10b], [ZHU11]. By utilising the gearing effect concept into this kind of PM machine, a novel topology with partitioned stator (PSPM) was proposed and it shows more advantages as well. Fig. 1.6(d) shows that this kind of PM machine fully utilises the space and keeps the advantages of both rotor and stator PM machines, viz. large slot area and stationary PMs [ZHU14c], [ZHU15], [WU15b]. The complicated rotor structure and two air-gaps could be the demerit for this kind of PM machine. The selection of PM machine topology is also concerned when it comes to the specific applications.



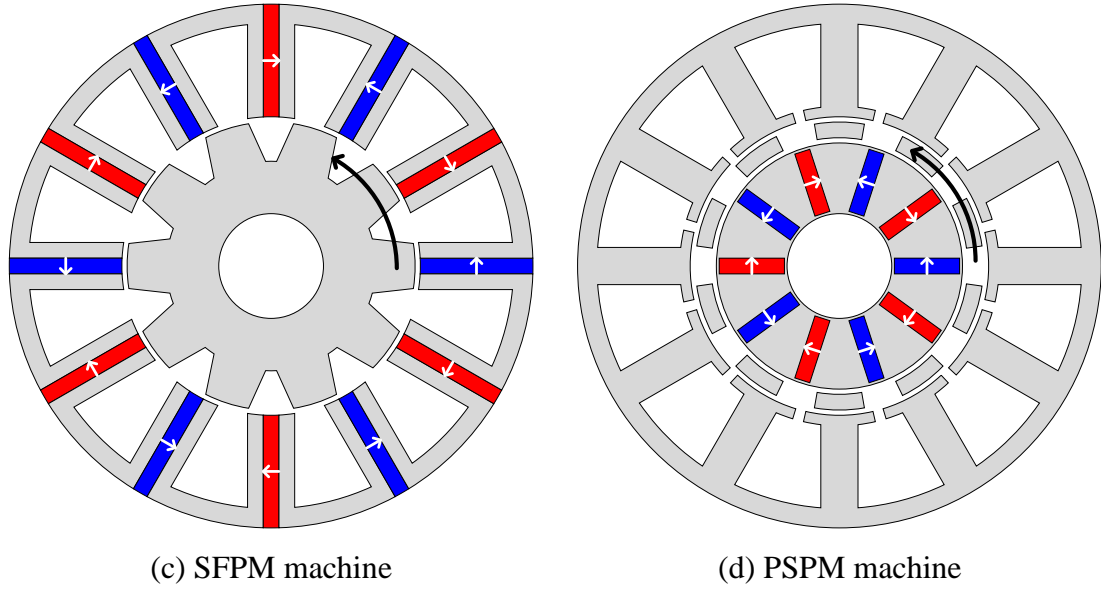
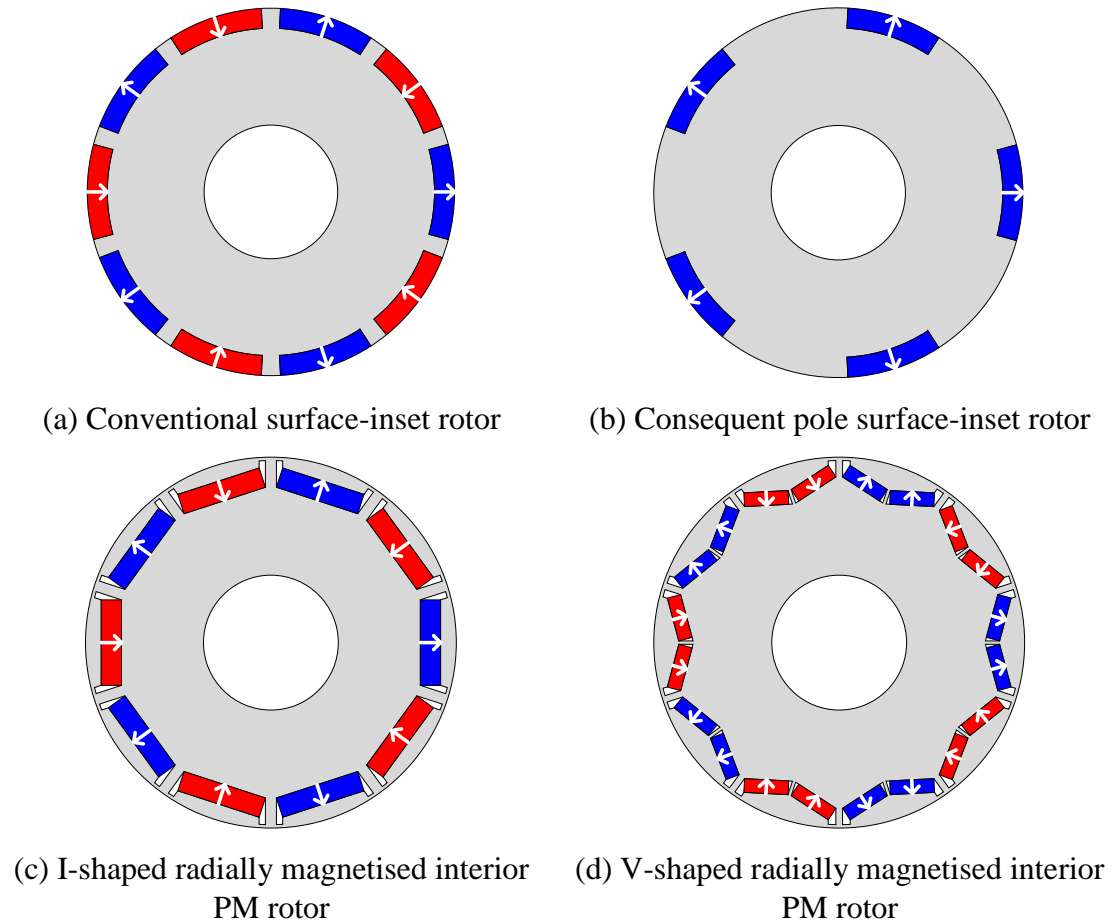
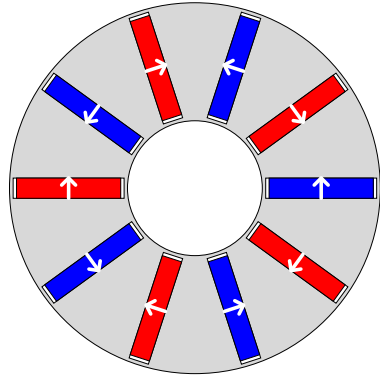


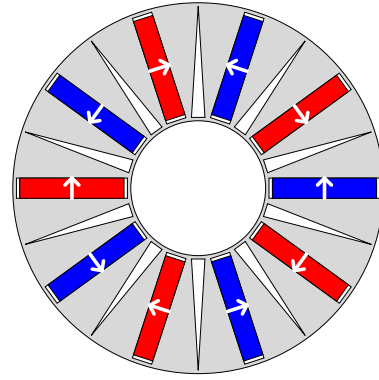
Fig. 1.6. Stator PM machines with different configurations.

It is worth noting that the SPM rotors in all modular machines may be replaced by IPM rotors. Alternate rotor topologies are shown in Fig. 1.7 for completion [ZHU14a].





(e) Conventional circumferentially magnetised PM rotor



(f) Circumferentially magnetised PM rotor with flux barriers

Fig. 1.7. Available rotors for replacing surfaced-mounted ones (10 poles).

Accounting for the advantages of different kinds of PM machines, the manufacturability and the cost, both internal and external rotor surface-mounted PM machines have been widely used for wind power application [CHE00b], [CHE05], [POL06], [LIS11], [POT12], [TAP13]. Many researchers have reviewed the important challenges and opportunities for wind power applications [HAN02], [LI08], [CHE09], [LIS11], [ZHU12a], [ZHU12b], [BOL14], [CHE14b]. Based on the rotor speed, wind power generation systems can be classified into three types: fixed speed, limited variable speed and variable speed.

For fixed speed type system [HAN02], [LI08], it adopts squirrel cage induction machine (SCIM). The stator is directly connected to the grid to deliver power, while the rotor is linked with wind turbine hub by multi-stage gear box. Since the SCIM itself is highly reliable, the maintenance cost is low in terms of generators. However, several issues are obvious. First of all, the gear box is mechanically complicated, requires high manufacture accuracy and will increase system cost. Because of its complexity, the system reliability will be affected. Furthermore, the wind speed will be unstable in real wind farm. Thus, the vibration will be transmitted via gearbox to SCIMs, which reduces system reliability as well. Gear box failure occupies the biggest portion in wind power system faults. When it comes to generators, the SCIM performs relatively poor in power factor. Additional reactive power is needed, which is usually provided by large additional capacitors. The existence of these capacitors will increase system cost and could bring reliability problem. Lastly, the rotor copper

loss is unavoidable in SCIMs due to the requirement of slip for operation. Therefore, the generator efficiency is low.

In order to overcome the disadvantages of fixed speed wind power system, the variable speed type is put forward. In the early stage of variable speed power generation, only limited speed can be adjusted. The SCIMs are replaced by wound rotor induction machines (WRIMs) [CHE09], [LIS11]. Since the rotor winding can be connected with external circuit by slip rings and brushes, the rotor circuit can be adjusted. However, if only resistors are in series with the rotor winding, the speed can be regulated below the synchronous speed. Besides, the energy is still wasted.

For the most applicable variable speed wind power systems, doubly fed induction machines (DFIMs) with multi stage gear box [ZHU12b] and direct drive PM synchronous machines (PMSMs) [CHE14b] are mostly adopted. DFIMs regulate both stator and rotor circuits with the help of power converters. Since the limit of slip is eliminated, the generators can operate in high efficiency situation. DFIM wind power generation system also has quite good fault tolerant capability since the regulation of stator and rotor circuits is relatively independent. The issue caused by gear box still exists in this kind of system, while the power converter cost is high as well. If the gear box is totally eliminated, viz. the generators direct driven by wind, the system will have quite high reliability due to the simple structure. Because of the advantages mentioned above, direct drive PMSMs have been developed very fast over the past few decades. Since the PMs with large energy product are used, the power density of generators is high. The high power factor is also beneficial to lower converter capacity.

The problem for direct drive PMSMs is the large size, which is owing to the low speed. With the increase of generator capacity, the machine size will be further larger. Therefore, the electrical machine stators need to be segmented for easing manufacture and transportation. Besides, with the increasingly deep understanding of winding theory and comprehensive application of power converters, the non-overlapping fractional-slot windings with multi-phase supply are also widely used. Combining these three advanced techniques together, a novel PM machine will be put forward. The three closely related aspects, viz. fractional-slot non-overlapping windings, dual 3-phase windings and modularity techniques, will be respectively reviewed firstly as follows.



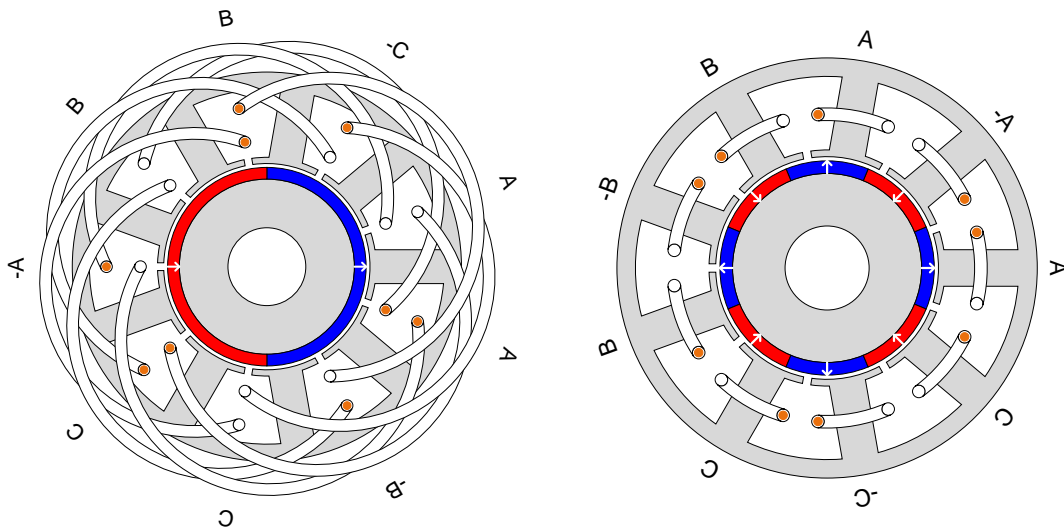
## 1.2 Fractional-slot Non-overlapping Windings

The electrical machine windings are grouped into two categories based on the concept of slot number per pole per phase ( $q$ ) which is defined as follows [LIW61]:

$$q = \frac{N_s}{2pm} \quad (1.1)$$

where  $N_s$  is the stator slot number;  $p$  is the rotor pole pair number and  $m$  is the phase number. When  $q$  is an integer number, the winding is defined as the “integer slot” type and the “fractional slot” winding is defined if  $q$  is a fractional number.

The fractional-slot winding can be further categorized into two types: winding end overlapping and non-overlapping. Taking 3-phase 9-slot PM machine as an example, the two available PM machines with these two kinds of windings are shown in Fig. 1.8. The one with 9-slots/2-poles (9S/2P) combination is overlapping type, while the non-overlapping winding is used for 9S/8P PM machine.



(a) Overlapping winding (9S/2P)

(b) Non-overlapping winding (9S/8P)

Fig. 1.8. Illustration of overlapping and non-overlapping windings.

The drawback of overlapping winding can be clearly seen from Fig. 1.8. The 9S/2P PM machine shown in Fig. 1.8(a) has much longer end part for each coil since each of them spans four teeth. The longer end part will increase the machine axial length, while the phase resistance and the copper loss will accordingly increase. Besides, the slot filling factor will be reduced due to the complicated coil shape except for the

performed windings. In contrast, the 9S/8P with non-overlapping winding has quite simple shape in winding end part. Therefore, the end winding length will be much shorter and consequently the machine axial length is reduced. Meanwhile, the copper loss will be lower and more slot space can be used to accommodate conductors. A higher torque density and efficiency could be achieved. Since the non-overlapping windings have such advantages, a vast number of publications have been discussing this promising kind of winding [KEN85], [CRO02], [ISH05b], [ISH05c], [ISH06], [ELR05], [ELR06a], [ELR06b], [ELR06c], [ELR08a], [ELR08b], [ELR10], [BIA06a], [BIA06c], [BIA08], [DOR11b], [CHE14], [WAN15b], [BEK16], [CHE17], [RAZ17]. The constitution of this kind promising winding will be summarised.

### 1.2.1 All and Alternate Teeth Wound Windings

In order to easily discuss magnetomotive force (MMF), the whole mechanical circumference is chosen as the fundamental period [HEL77]. Thus, the harmonic having the rotor pole pair number is defined as the working one. There are two kinds of non-overlapping windings being comprehensively investigated over the past few decades, viz. all and alternate teeth wound [CRO02], [ISH05c], [WAN08], [TAN12], [PRI15]. Taking the 6S/4P PM machines in [ELR06c] as an example, the cross-sections are shown in Fig. 1.9.

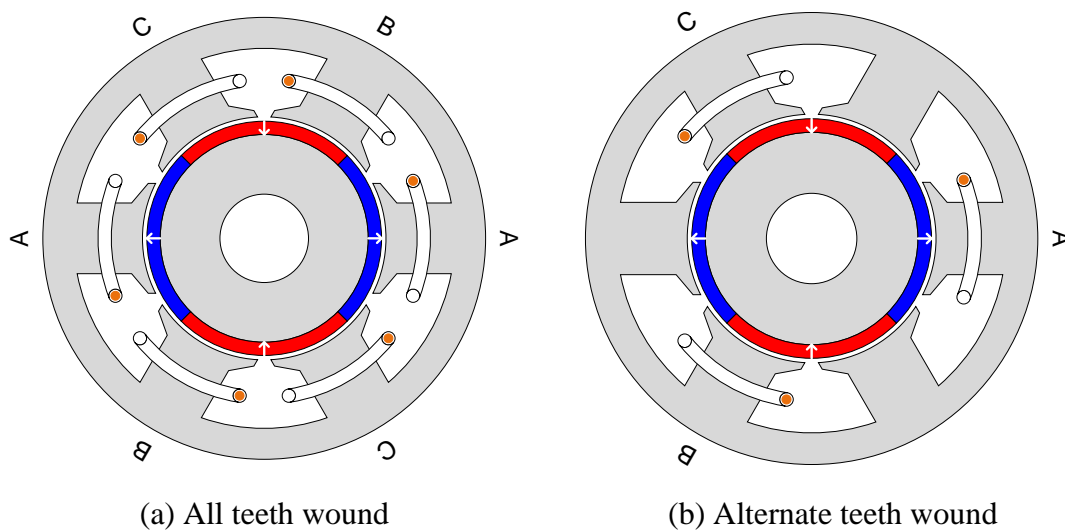


Fig. 1.9. Illustration of all and alternate teeth wound windings.

The requirements in the design of balanced fractional-slot non-overlapping windings are listed here.

(a) The whole  $m$ -phase system must be balanced and the waveforms of back-electromotive force (back-EMF) must have the same shape and be uniformly shifted in space. This will constrain the slot and pole number combinations of PM machines with all teeth wound windings as follows [SMI16], [HUT05], [PYR13]:

$$\begin{aligned}\frac{N_s}{p} &= \frac{tN_{s0}}{tp_0} = \frac{N_{s0}}{p_0} \\ t &= GCD(N_s, p) \\ N_{s0} &= km, \quad k = 1, 2, 3... \\ p_0 &\neq nm, \quad n = 1, 2, 3...\end{aligned}\tag{1.2}$$

where  $N_{s0}$  and  $p_0$  are the stator slot and rotor pole pair numbers of the basic electrical machine unit, respectively;  $t$  is the repetition number of the basic electrical machine unit and  $GCD$  is the greatest common divisor of two numbers.

The first two equations in (1.2) mean the original electrical machine consists of  $t$  basic electrical machine units with  $N_{s0}$  slots and  $p_0$  pole pairs. Then, the analysis on one basic electrical machine is enough. To guarantee each phase having the same slot numbers, the third equation in (1.2) is necessary. However, the  $p_0$  must not be divided by phase number, since the combination of  $N_{s0}$  and  $p_0$  has already been the simplest one. That is why the fourth equation in (1.2) should be highlighted. Similarly, the limitations on the slot and pole number combinations of PM machines with alternate teeth wound windings can be given in (1.3) [BIA06a], [BIA06c].

$$\begin{aligned}\frac{N_s/2}{p} &= \frac{tN_{s0}/2}{tp_0} = \frac{N_{s0}/2}{p_0} \\ t &= GCD(N_s/2, p) \\ N_{s0} &= \begin{cases} km, & t \text{ is even} \\ 2km, & t \text{ is odd} \end{cases}, \quad k = 1, 2, 3... \\ p_0 &\neq nm, \quad n = 1, 2, 3...\end{aligned}\tag{1.3}$$

For PM machines with this kind of winding, the slot number with coils are halved compared with the ones with all teeth wound windings. Thus, the basic electrical machine unit and its repetition number should be obtained according to the first two equations in (1.3). The constraint on the slot number of the basic electrical machine unit needs to be separated into two kinds. When  $t$  is even, the original PM machine

can always use alternate teeth wound winding if the phases of basic electrical machine unit are balanced. However, more stringent condition is needed if  $t$  is an odd number. Only when the basic electrical machine unit itself can adopt alternate teeth wound winding, the original PM machine can use this kind of winding. This is summarised as the third equation in (1.3). The last condition in (1.3) is required for alternate teeth wound winding as well for the requirement of basic electrical machine unit.

(b) The winding factor of the working harmonic should be as large as possible, since it will determine the amplitude of the flux-linkage. The higher flux-linkage could generate a higher on-load torque [CRO02], [LIB04]. Therefore, the constraints need to be further strengthened:

$$\left. \begin{array}{l} y_c = \tau_s = \frac{2\pi}{N_s} \\ \tau_p = \frac{2\pi}{2p} = \frac{\pi}{p} \\ \frac{2}{3}\tau_p \leq y_c \leq \frac{4}{3}\tau_p \end{array} \right\} \Rightarrow \frac{1}{3}N_s \leq p \leq \frac{2}{3}N_s \quad (1.4)$$

where  $y_c$  is the coil pitch;  $\tau_s$  and  $\tau_p$  are the slot and pole pitch, respectively.

For the non-overlapping windings, the coil pitch should be equal to the slot pitch, as shown in the first equation within the parenthesis of (1.4). Moreover, the coil pitch should be within a specific range, which makes sure the angle between two coil side back-EMF vectors is not too large. That is why the relationship between the coil pitch and the pole pitch should be limited by the last equation within the parenthesis of (1.4). Based on these limitations, the slot and pole number combinations will be selected within a specific range, as shown in the derived equation in (1.4). The winding factor of the working harmonic ( $k_w$ ) can be simply predicted as follows [LIW43], [LIW61], [SKA06], [YOK16]:

$$\begin{aligned}
k_p &= \sin\left(\frac{\tau_s}{\tau_p} \frac{\pi}{2}\right) \\
k_d &= \left\{ \begin{array}{l} \frac{\sin(\pi/2m)}{(N_{s0}/2m) \sin(\pi/N_{s0})}, \quad N_{s0} \text{ is even} \\ \frac{\sin(\pi/2m)}{(N_{s0}/m) \sin(\pi/2N_{s0})}, \quad N_{s0} \text{ is odd} \end{array} \right\} \text{All teeth wound} \\
&\left\{ \begin{array}{l} \frac{\sin(\pi/2m)}{(N_{s0}/4m) \sin(2\pi/N_{s0})}, \quad N_{s0} \text{ is even and } \frac{N_{s0}}{2} \text{ is even} \\ \frac{\sin(\pi/2m)}{(N_{s0}/2m) \sin(\pi/N_{s0})}, \quad N_{s0} \text{ is even and } \frac{N_{s0}}{2} \text{ is odd} \\ \frac{\sin(\pi/2m)}{(N_{s0}/m) \sin(\pi/2N_{s0})}, \quad N_{s0} \text{ is odd} \end{array} \right\} \text{Alternate} \\
&\hspace{15em} \text{teeth} \\
&\hspace{15em} \text{wound} \\
k_w &= k_p \cdot k_d
\end{aligned} \tag{1.5}$$

where  $k_p$  is the pitch factor and  $k_d$  is the distribution factor.

(c) Apart from the working harmonic, other lower and higher order harmonics should be as small as possible. They will deteriorate the PM machine performance, such as increasing torque ripple [POP08], [CHE10a], causing rotor eddy current loss [BIA09], [BIA10], [CHU12], generating noise and vibration [WAN06], [ZHU09b], [YAN14] etc. In general, the harmonic order (HO) can be determined according to [HAN17].

$$\text{HO} = \left\{ \begin{array}{l} t(p_0 \pm mk), \quad N_{s0} \text{ is odd} \\ t(p_0 \pm 2mk), \quad N_{s0} \text{ is even} \end{array} \right\} \text{All teeth wound} \\
\left\{ \begin{array}{l} t(p_0 \pm 2mk), \quad N_{s0}/2 \text{ is even and } N_{s0} \text{ is even} \\ t(p_0 \pm mk), \quad N_{s0}/2 \text{ is odd and } N_{s0} \text{ is even} \\ t(p_0 \pm mk), \quad N_{s0} \text{ is odd} \end{array} \right\} \begin{array}{l} \text{Alternate, } k = 0, 1, 2.. \\ \text{teeth} \\ \text{wound} \end{array} \tag{1.6}$$

From (1.6), it can be seen that all teeth wound windings will contain lower harmonics if the phase number is higher. Besides, the basic electrical machine unit with even slot number is preferable, since it can further reduce harmonics [WAN14]. This has been validated in some PM machines [CHE14], [CHE16].

Based on the conditions listed above, the available slot and pole number combinations of single 3-phase PM machines with non-overlapping windings are listed in TABLE 1.1 [MAG03], [MIT04], [WU15a].

TABLE 1.1 AVAILABLE SLOT AND POLE NUMBER COMBINATIONS FOR SINGLE 3-PHASE NON-OVERLAPPING WINDINGS

$N_s$	$N_p=2p$	$K_w$		$t$		Harmonics	
		All	Alternate	All	Alternate	All	Alternate
3	2	0.866	N/A <sup>a</sup>	1	N/A	$1 \pm 3k$	N/A
	4	0.866		1		$2 \pm 3k$	
6	4	0.866	0.866	2	1	$2(1 \pm 3k)$	$1 \pm 3k$
	8	0.866	0.866	2	1	$2(2 \pm 3k)$	$2 \pm 3k$
9	6	0.866		3		$3(1 \pm 3k)$	
	<b>8▲</b>	<b>0.945</b>	N/A	<b>1</b>	N/A	<b><math>4 \pm 3k</math></b>	N/A
	10	0.945		1		$5 \pm 3k$	
	12	0.866		3		$3(2 \pm 3k)$	
12	8	0.866	0.866	4	2	$4(1 \pm 3k)$	$2(1 \pm 3k)$
	<b>10■</b>	<b>0.933</b>	<b>0.966</b>	<b>1</b>	<b>1</b>	<b><math>5 \pm 6k</math></b>	<b><math>5 \pm 6k</math></b>
	14	0.933	0.966	1	1	$7 \pm 6k$	$7 \pm 6k$
	16	0.866	0.866	4	2	$4(2 \pm 3k)$	$2(2 \pm 3k)$
15	10	0.866		5		$5(1 \pm 3k)$	
	14	0.951	N/A	1	N/A	$7 \pm 3k$	N/A
	16	0.951		1		$8 \pm 3k$	
	20	0.866		5		$5(2 \pm 3k)$	
18	12	0.866	0.866	6	3	$6(1 \pm 3k)$	$3(1 \pm 3k)$
	<b>14●</b>	<b>0.902</b>	<b>0.902</b>	<b>1</b>	<b>1</b>	<b><math>7 \pm 6k</math></b>	<b><math>7 \pm 3k</math></b>
	<b>16▲</b>	<b>0.945</b>	<b>0.945</b>	<b>2</b>	<b>1</b>	<b><math>2(4 \pm 3k)</math></b>	<b><math>4 \pm 3k</math></b>
	20	0.945	0.945	2	1	$2(5 \pm 3k)$	$5 \pm 3k$
	22	0.902	0.902	1	1	$11 \pm 6k$	$11 \pm 3k$
	24	0.866	0.866	6	3	$6(2 \pm 3k)$	$3(2 \pm 3k)$
21	14	0.866		7		$7(1 \pm 3k)$	
	16	0.890		1		$8 \pm 3k$	
	20	0.953	N/A	1	N/A	$10 \pm 3k$	N/A
	22	0.953		1		$11 \pm 3k$	
	26	0.890		1		$13 \pm 3k$	
	28	0.866		7		$7(2 \pm 3k)$	
24	16	0.866	0.866	8	4	$8(1 \pm 3k)$	$4(1 \pm 3k)$
	<b>20■</b>	<b>0.933</b>	<b>0.966</b>	<b>2</b>	<b>2</b>	<b><math>2(5 \pm 6k)</math></b>	<b><math>2(5 \pm 6k)</math></b>
	22	0.950	0.958	1	1	$11 \pm 6k$	$11 \pm 6k$
	26	0.950	0.958	1	1	$13 \pm 6k$	$13 \pm 6k$
	28	0.933	0.966	2	2	$2(7 \pm 6k)$	$2(7 \pm 6k)$
	32	0.866	0.866	8	4	$8(2 \pm 3k)$	$4(2 \pm 3k)$

<sup>a</sup> N/A means not available.

Quite a few researchers have focused on the specific PM machines with different slot and pole number combinations based on TABLE 1.1. The PM machines with some representative slot/pole number combinations are used to give a clearer demonstration. The two combinations with mark ▲ are shown in Fig. 1.10 [BI96],

[PON14], where the 9S/8P PM machine itself is a basic electrical machine unit and it can only adopt all teeth wound winding. The combinations of such two units generates the 18S/16P PM machine which can adopt alternate teeth winding. It can be seen from TABLE 1.1 that more harmonics will appear for this kind of winding compared with the all teeth wound counterpart.

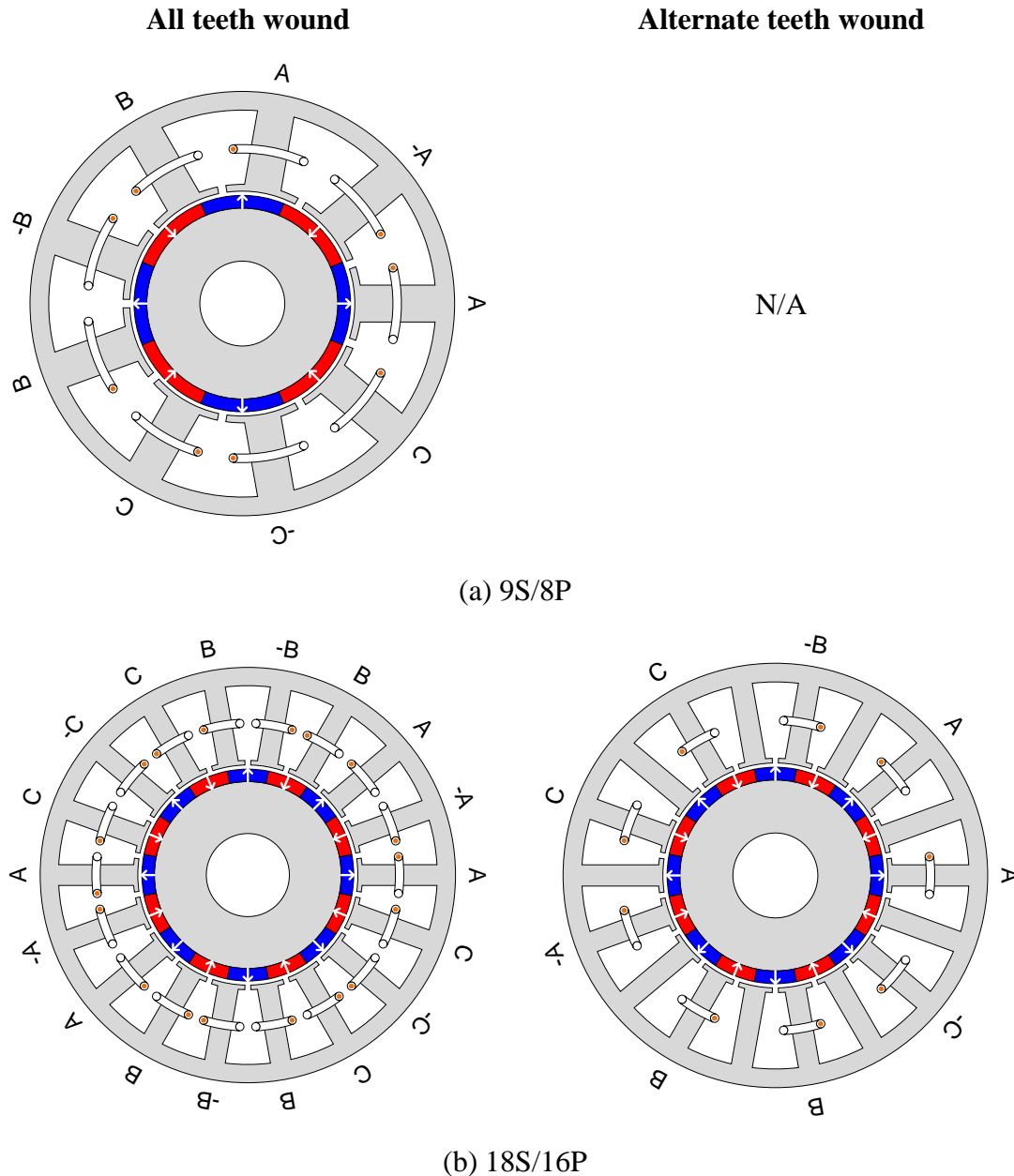


Fig. 1.10. PM machines with 9S/8P and 18S/16P combinations.

For the two combinations addressed with ■, the basic electrical machine unit (12S/10P PM machine) can adopt both all and alternate teeth wound windings. Therefore, no matter how many repetitions exist, the corresponding PM machine can

always use two kinds of windings. The 24S/20P PM machine is used to validate this point and two PM machines are shown in Fig. 1.11 [SAL04], [CHU16]. TABLE 1.1 also shows that the adoption of alternate teeth wound winding will not increase harmonics. However, the magnitudes of harmonics will increase.

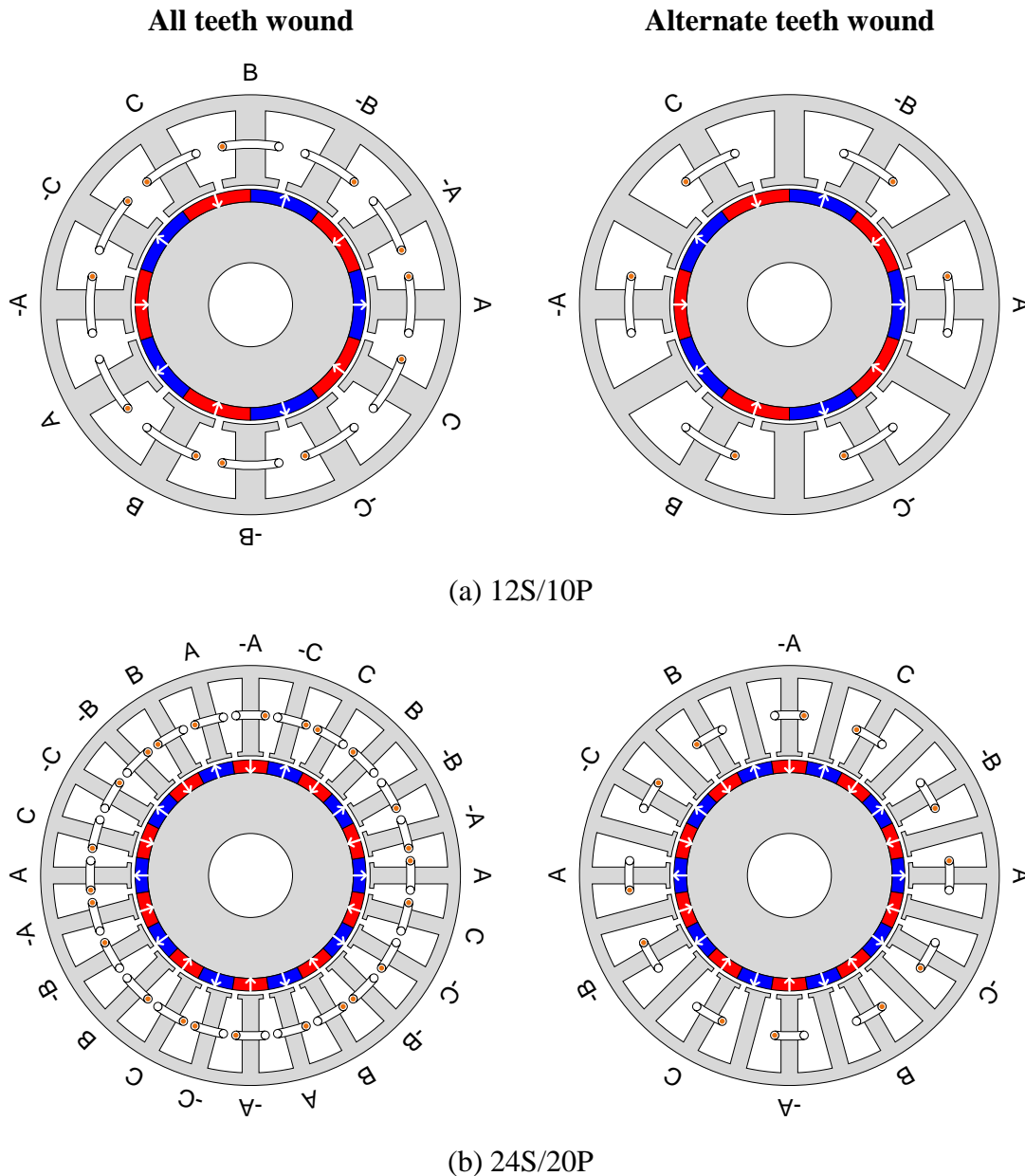


Fig. 1.11. PM machines with 12S/10P and 24S/20P combinations.

The last special slot and pole number combination is 18S/14P [DUT13], as shown in TABLE 1.1 with ● mark. Usually, this combination is hardly adopted, since the winding factor is low. Besides, the use of alternate teeth wound winding will produce new harmonics. The cross-sections with two kinds of winding are shown in Fig. 1.12.



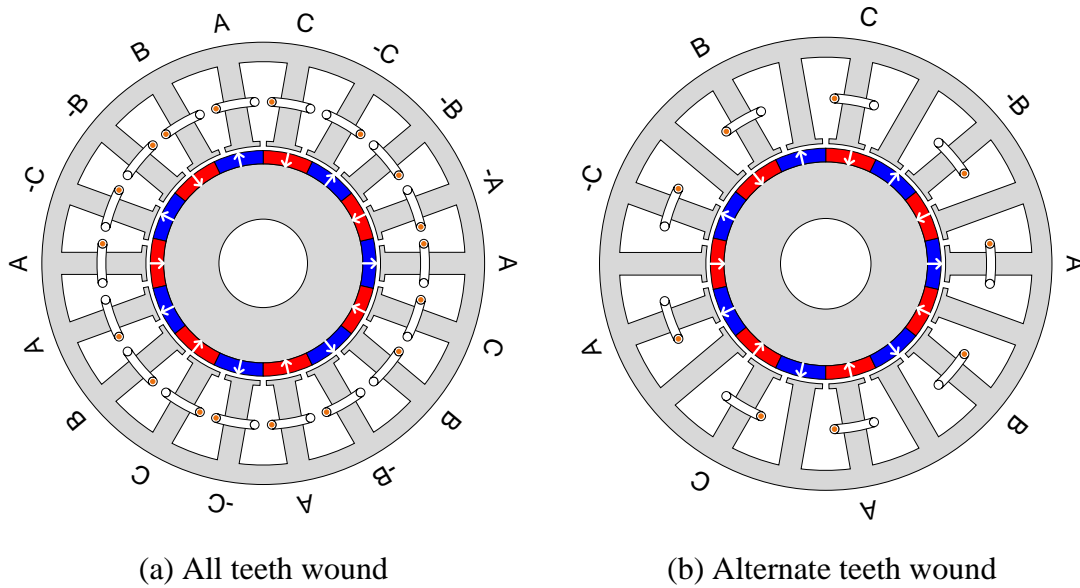


Fig. 1.12. PM machines with 18S/14P.

The major properties of two kinds of windings are compared in TABLE 1.2 [MAG07]. It can be seen that the determination of windings must account for specific requirements.

TABLE 1.2 COMPARISON OF ALL AND ALTERNATE TEETH WOUND WINDINGS

Item	All teeth wound	Alternate teeth wound
$N_s/N_p$	More combinations	Less combinations
Windings	Lower winding factor of the working harmonic; Less MMF harmonics; Lower harmonic magnitude	Higher winding factor of the working harmonic; More MMF harmonics; Higher harmonic magnitude
Back-EMF	More sinusoidal; Lower fundamental component	Less sinusoidal; High fundamental component
Average torque	Lower for low current; Higher for high current	Higher for low current; Lower for high current
Torque ripple	Lower	Higher
Rotor eddy current loss	Lower	Higher
Inductances	Smaller self-inductances; Higher/lower mutual inductances; Better power factor	Larger self-inductances; Lower mutual inductances; Better flux-weakening capability; Better fault-tolerant capability
Noise and vibration	Higher vibration mode; Lower noise radiation	Lower vibration mode; Higher noise radiation

### 1.2.2 Multi-layer Windings

For the all and alternate teeth wound windings discussed above, the number of coil sides in one slot are two and one, respectively. Thus, they are also called as double- and single-layer (DL and SL) windings [BIA06a], [ELR08a]. In fact, the coil sides can be increased to a higher number and the winding end part is still kept non-overlapping. Such kind of winding is defined as multi-layer type and the major purpose of using multi-layer windings is to reduce the harmonics, which has been addressed in [ALB13]. Among all of the multi-layer windings, the four layer one attracts the most attention [GER05], [KIM14], [RED15], [WAN15b], [TES16], [ABD16a]. The slot and pole combinations listed in TABLE 1.1 can adopt four layer winding if another condition is taken into account [ALB13]:

$$N_{s0} > m \quad (1.7)$$

According to (1.7), the two combinations located in the first and last lines corresponding to each slot number should be avoided, since the adoption of four layer winding will not have any benefit. What is more, transferring the alternate teeth wound winding into four layer type is also not preferable, which is equivalent to changing the winding into its all teeth wound counterpart. In essence, the four layer winding can be thought of as the combination of shifted two sets of windings with the half coil turns of the original winding and need to be antiphase arranged after each circumferential shift. Although harmonics need to be reduced, the fundamental component should be kept as high as possible at the same time, which means the shift angle should not be too large. Taking 9S/8P and 12S/10P PM machines as examples, the cross-sections of two electrical machines with four-layer windings are shown in Fig. 1.13, together with the original non-shifted ones [ALB13], [PRI15].

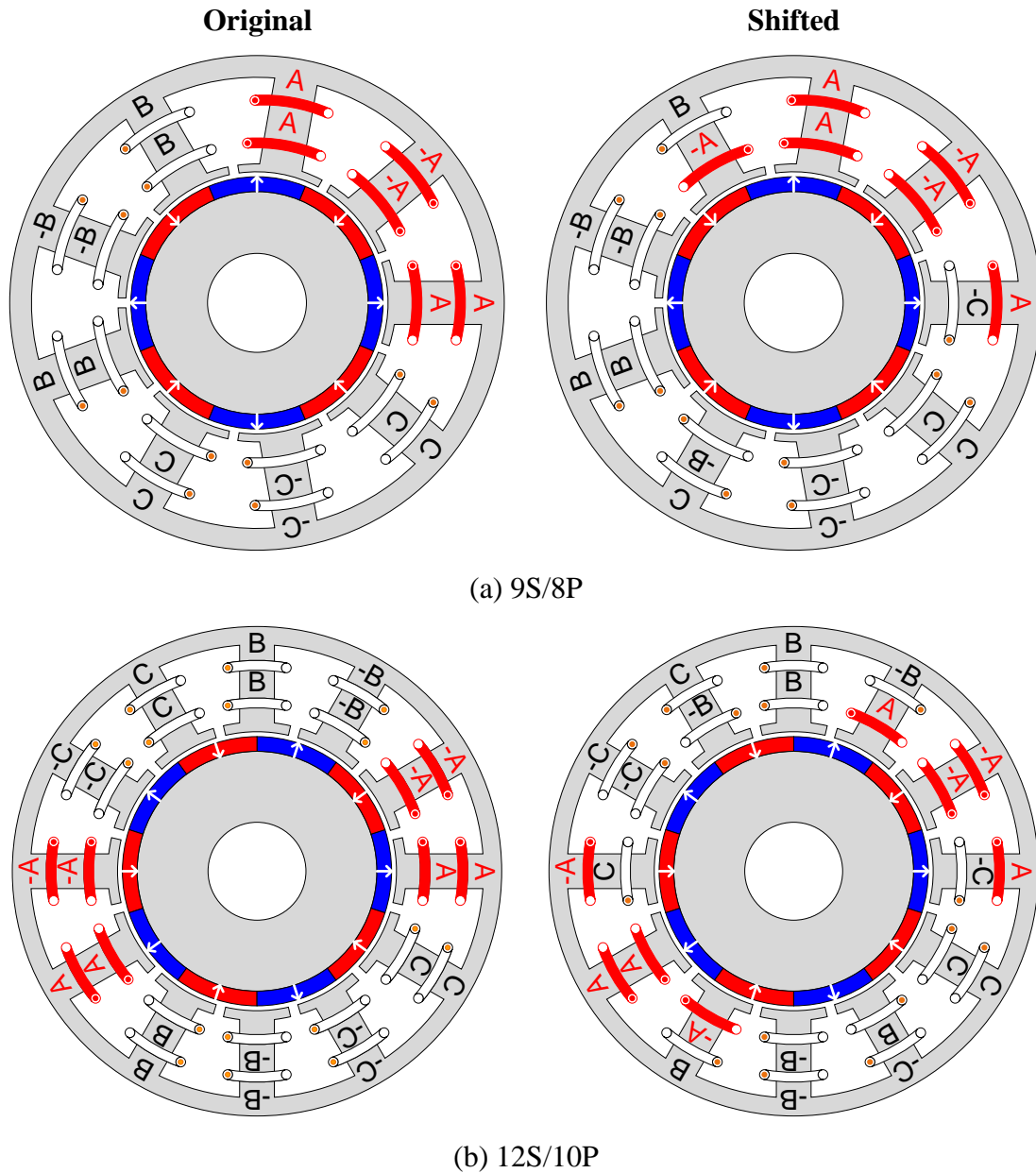


Fig. 1.13. PM machines with four layer windings.

The PM machines with other multi-layer windings were also investigated by some researchers. The three layer winding was proposed in [CIS10a], [CIS10b]. However, the winding topologies are too complicated, which is inappropriate for production. The even higher winding layer number, such as six layer winding [LI14a], can be arranged as well. However, the use of over complex windings may be impossible in the real applications.

From the introduction in this subsection, it can be found that the investigation of fractional-slot windings is still in progress. More promising non-overlapping winding configurations are expected to occur in the future.

### 1.3 Dual 3-phase Permanent Magnet Machines

With the development of power electronics technique, the multi-phase drive can be easily implemented. Compared with the conventional single 3-phase system, multi-phase electrical machines have following advantages [JAH80], [LEV07], [LEV08], [TON14], [BAR16], [DUR16]:

(1) The average torque will be high since the winding factor could be larger and the saturation could be lower. The torque is smoother as well because of the harmonic cancellation effect.

(2) More phases will improve the system reliability since the fault-tolerant capability is enhanced. The post-faulty operation could more easily maintain the system stability.

(3) There are more phases being adopted; and therefore the requirement of power device capacity will be lower, which could further make the system more stable and reduce the cost.

(4) The higher phase number could increase the control flexibility. A multitude of pulse width modulation (PWM) strategies can be implemented

(5) The lower harmonics will be beneficial to the loss reduction. The electrical machines will have higher efficiency.

Among multi-phase electrical machines, those with dual 3-phase windings have been investigated for a long time [ALG30], [HOL70], [NEL74], [ABB84], [GOP93], [ZHA95], [HAD04], [HAD06], [CHA07], [AND09], [KAL13], [KAT14], [HU14], [HU17]. The two sets of same 3-phase windings displaced with fixed angle ( $\alpha_{set}$ ) can construct such kind of the winding, as illustrated in Fig. 1.14.

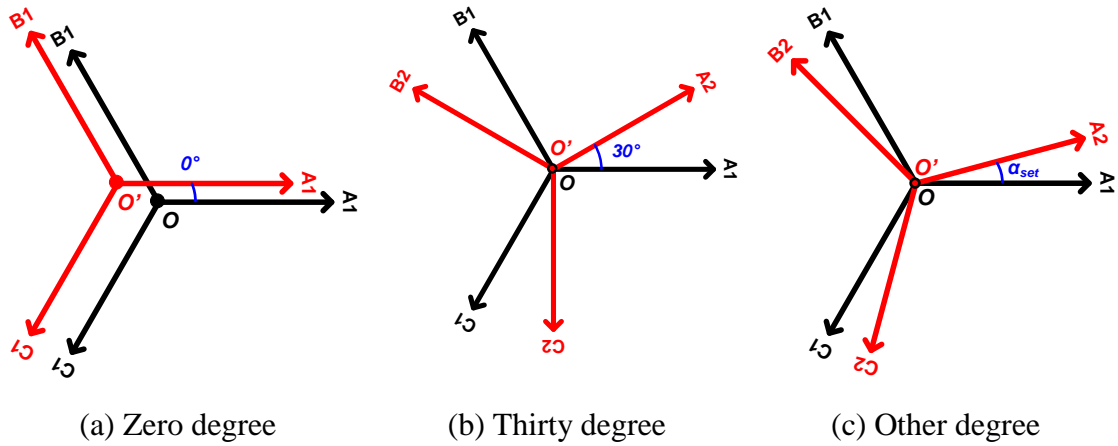


Fig. 1.14. Illustration of dual 3-phase system.

Based on Fig. 1.14, dual 3-phase winding can be classified into different groups according to the phase shift between two sets of windings.

### 1.3.1 Zero Degree Phase Shift

For Zero dual 3-phase windings shown in Fig. 1.14(a), they can be considered as the split of the original single 3-phase windings into two set exactly the same ones [JAC96], [MEC96]. The two sets of windings are aligned with each other in space. In terms of the electrical machine performance, there are no differences between the electrical machines with the original single 3-phase and Zero type dual 3-phase windings when two sets of windings work together. Similar to (1.2)-(1.4), the constraints on slot and pole number combinations for constructing this kind of dual 3-phase winding are given as follows [MIT04]. Both DL and SL windings are taken into account. The all and alternate teeth wound windings also belong to these two general categories [BIA06a].

$$\begin{aligned}
N_{s0} = & \left\{ \begin{array}{l} N_s/t \text{ and } t=\text{GCD}(N_s, p) \\ 6k \text{ and } t \text{ is odd} \\ 3k \text{ and } t \text{ is even} \end{array} \right\} \text{DL} \\
& \left\{ \begin{array}{l} N_s/t \text{ and } t=\text{GCD}(N_s/2, p) \\ 12k \text{ and } t \text{ is odd} \\ 6k \text{ and } t \text{ is even} \end{array} \right\} \text{SL} \\
& p_0 = p/t \neq 3n, \quad n=1,2,3\dots
\end{aligned} \quad , \quad k=1,2,3\dots \quad (1.8)$$

$$\tau_{ps} = \frac{N_s}{2p} \left\{ \begin{array}{l} \notin \text{integer} \Rightarrow y_c = \text{Int}[\tau_p] \left\{ \begin{array}{l} \geq 1, \quad \text{DL} \\ \geq 1 \text{ and } y_c \text{ is odd}, \quad \text{SL} \end{array} \right. \\ \in \text{integer} \Rightarrow y_c = \tau_p \left\{ \begin{array}{l} \geq 1, \quad \text{DL} \\ \geq 1 \text{ and } t \text{ is even}, \quad \text{SL} \end{array} \right. \end{array} \right.$$

$$\frac{2}{3}\tau_{ps} \leq y_c \leq \frac{4}{3}\tau_{ps}$$

where  $\tau_{ps}$  is the pole pitch expressed by slot number;  $\text{Int}[\ ]$  means rounding the number to the nearest integer.

The first two equations in (1.8) give the limitation on the slot and pole pair numbers according to the number of coils sides in one slot and the basic electrical machine unit. Since the coil pitch could span more than one slot, the third equation in (1.8) is a more general definition of coil pitch. The reason for selecting a short pitched coil span is reducing useless winding end connections. The last constraint in (1.8) again guarantees a high pitch factor. The winding factors and the corresponding harmonics can still be predicted by (1.5) and (1.6) by substituting  $m=3$  [SKA06], respectively. TABLE 1.3 lists some available slot and pole number combinations. OLP and NOLP mean the winding end part is overlapping and non-overlapping, respectively.

TABLE 1.3 AVAILABLE SLOT AND POLE NUMBER COMBINATIONS FOR ZERO TYPE DUAL 3-PHASE WINDINGS

$N_s$	$N_p=2p$	$q$	$y_c$	Winding end	$K_w$		$t$		Harmonics	
					DL	SL	DL	SL	DL	SL
<b>6</b>	<b>2▲</b>	<b>1</b>	<b>3</b>	<b>OLP</b>	<b>1</b>		<b>1</b>		<b>1±6k</b>	
	4	1/2	1	NOLP	0.866	N/A	2	N/A	2(1±3k)	N/A
	8	1/4	1	NOLP	0.866		2		2(2±3k)	
<b>12</b>	2	2	6	OLP	0.966	N/A	1	N/A	1±6k	N/A
	<b>4▲</b>	<b>1</b>	<b>3</b>	<b>OLP</b>	<b>1</b>	<b>1</b>	<b>2</b>	<b>2</b>	<b>2(1±6k)</b>	<b>2(1±6k)</b>
	8	1/2	1	NOLP	0.866	0.866	4	2	4(1±3k)	2(1±3k)
	<b>10■</b>	<b>2/5</b>	<b>1</b>	<b>NOLP</b>	<b>0.933</b>	<b>0.966</b>	<b>1</b>	<b>1</b>	<b>5±6k</b>	<b>5±6k</b>
	14	2/7	1	NOLP	0.933	0.966	1	1	7±6k	7±6k
	16	1/4	1	NOLP	0.866	0.866	4	2	4(2±3k)	2(2±3k)
<b>18</b>	2	3	9	OLP	0.960	N/A	1	N/A	1±6k	N/A
	4	3/2	4	OLP	0.966	N/A	2	N/A	2(1±6k)	N/A
	6	1	3	OLP	1	N/A	3	N/A	3(1±6k)	N/A
	8	3/4	2	OLP	0.945	N/A	2	N/A	2(2±3k)	N/A
	10	3/5	2	OLP	0.945	N/A	1	N/A	5±6k	N/A
	12	1/2	1	NOLP	0.866	0.866	6	3	6(1±3k)	3(1±3k)
	14	3/7	1	NOLP	0.902	N/A	1	N/A	7±6k	N/A
	16	3/8	1	NOLP	0.945	N/A	2	N/A	2(4±3k)	N/A
	20	3/10	1	NOLP	0.945	N/A	2	N/A	2(5±3k)	N/A
	22	3/11	1	NOLP	0.902	N/A	1	N/A	11±6k	N/A
	24	1/4	1	NOLP	0.866	0.866	6	3	6(2±3k)	3(2±3k)
<b>24</b>	2	4	12	OLP	0.958	N/A	1	N/A	1±6k	N/A
	4	2	6	OLP	0.966	1	2	2	2(1±6k)	2(1±6k)
	8	1	3	OLP	1	1	4	4	4(1±6k)	4(1±6k)
	10	4/5	2	OLP	0.925	N/A	1	N/A	5±6k	N/A
	14	4/7	2	OLP	0.925	N/A	1	N/A	7±6k	N/A
	16	1/2	1	NOLP	0.866	0.866	8	4	8(1±3k)	4(1±3k)
	<b>20■</b>	<b>2/5</b>	<b>1</b>	<b>NOLP</b>	<b>0.933</b>	<b>0.966</b>	<b>2</b>	<b>2</b>	<b>2(5±6k)</b>	<b>2(5±6k)</b>
	22	4/11	1	NOLP	0.950	0.958	1	1	11±6k	11±6k
	26	4/13	1	NOLP	0.950	0.958	1	1	13±6k	13±6k
	28	2/7	1	NOLP	0.933	0.966	2	2	2(7±6k)	2(7±6k)
32	1/4	1	NOLP	0.866	0.866	8	4	8(2±3k)	4(2±3k)	

Comparing TABLES 1.3 and 1.1, it shows that the requirement of slot and pole number combinations is higher for the Zero type dual 3-phase winding. The two combinations with mark ▲ construct overlapping windings, while the 12S/4P combination contains the two 6S/2P basic electrical machine units [CHU13b]. The cross-sections of PM machines with these two combinations are shown in Fig. 1.15.

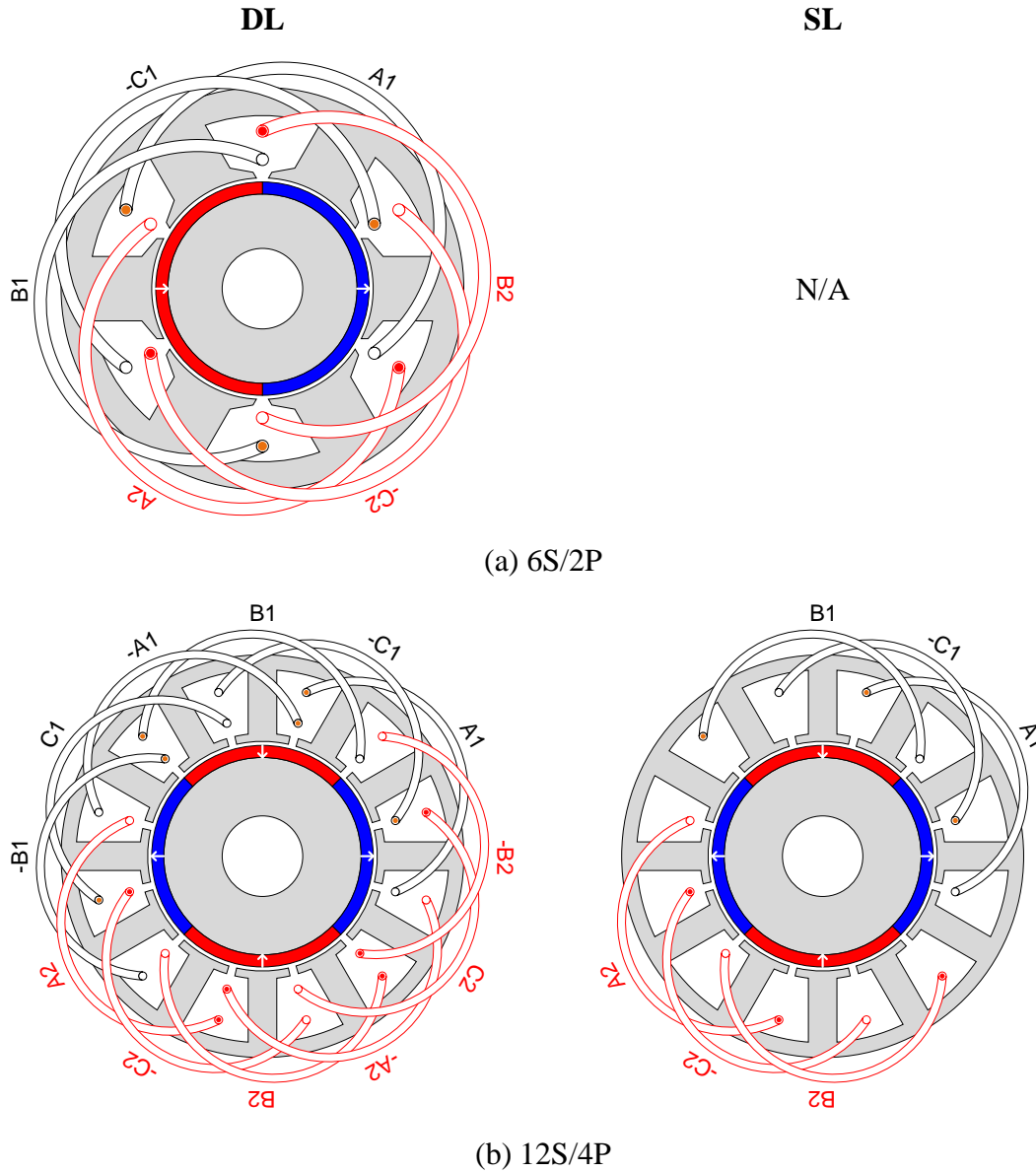


Fig. 1.15. PM machines with overlapping Zero type dual 3-phase windings.

For the PM machines with DL windings shown in the left column of Fig. 1.15, there are no differences in aspect of performance if their winding can be connected into SL windings. The difference only exists in end connections, as shown in Fig. 1.15(b). However, if the short pitched DL winding is adopted, the DL and SL windings will be different from each other [LIW43]. The PM machines with non-overlapping windings are also chosen from TABLE 1.3 to show the configurations of Zero type dual 3-phase windings. The two combinations with mark ■ have 24S/20P and 12S/10P, respectively [BAR11b], [CHU16]. Their cross-sections are shown in Fig. 1.16.



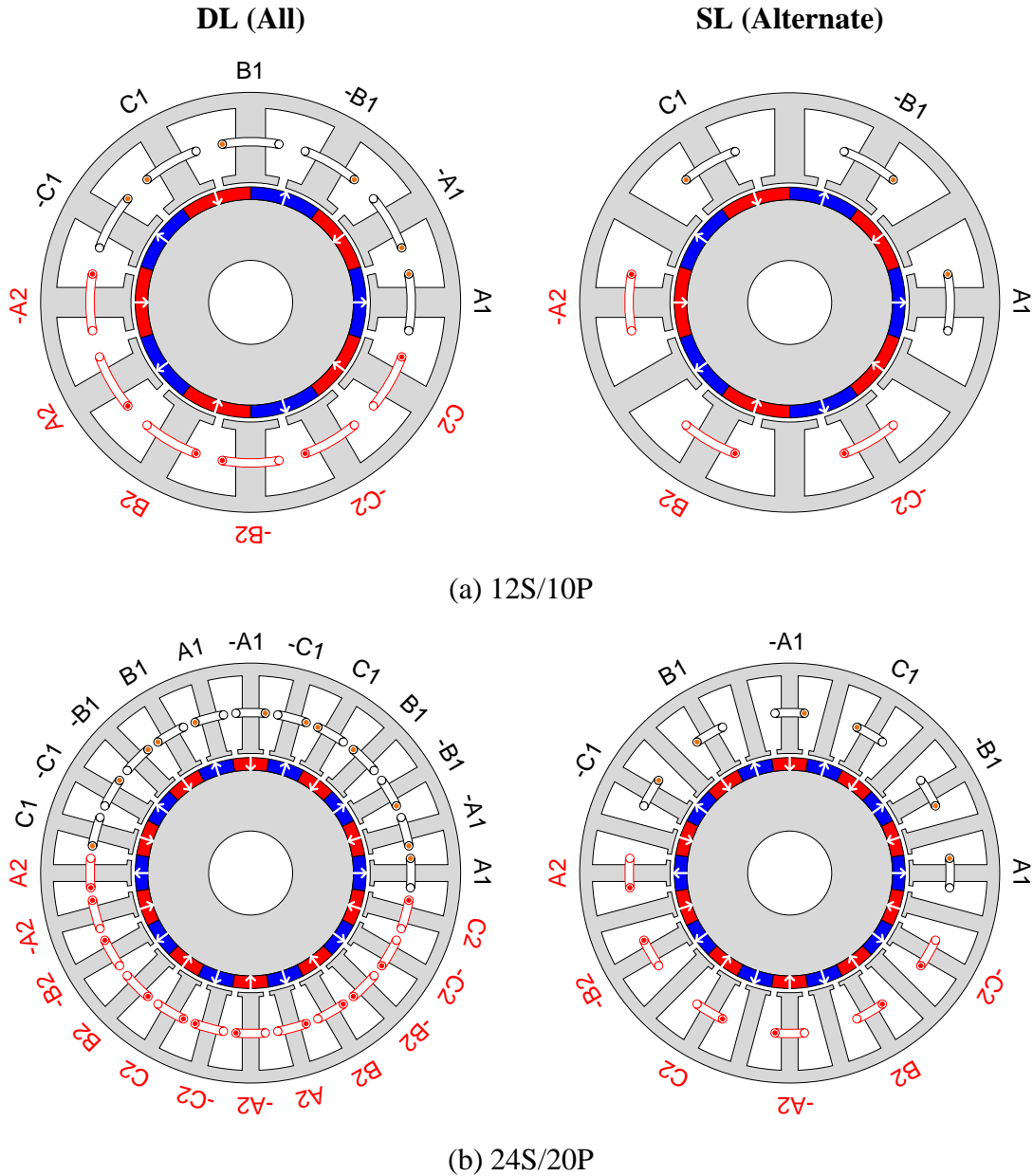


Fig. 1.16. PM machines with non-overlapping Zero type dual 3-phase windings.

Fig. 1.16 shows that the physical coupling between phases due to coil side touching each other has been eliminated in the winding end part. Furthermore, the PM machines with SL windings can further eliminate the physical coupling between adjacent coils. Therefore, the fault-tolerant capability is good and suitable for the operations requiring high reliability [MEC96], [ATK06], [BIA06c], [CAO12b].

### 1.3.2 Thirty Degree Phase Shift

The most common applied dual 3-phase winding has two sets of windings shifted 30 degrees in space, as shown in Fig. 1.14(b). This kind of winding is also called half 12-phase winding, asymmetric 6-phase winding, split phase winding and duplex 3-phase winding [GOP93], [BAR09], [CHE10b], [ZHE12], [POP13]. Since it is inherently a 12-phase winding, the merits of multi-phase machines can be clearly seen, as mentioned above. However, the slot and pole number combinations suitable for this kind of winding need to satisfy more conditions compared with the Zero type dual 3-phase winding [BAR09], [BAR10], [BAR11a], [BAR11b]:

$$\begin{aligned}
 N_{s0} &= \begin{cases} \left. \begin{array}{l} N_s/t \text{ and } t=\text{GCD}(N_s, p) \\ 12k \end{array} \right\} \text{DL} \\ \left. \begin{array}{l} N_s/2t \text{ and } t=\text{GCD}(N_s/2, p) \\ 24k \end{array} \right\} \text{SL} \end{cases}, \quad k = 1, 2, 3\dots \\
 p_0 &= p/t \neq 6n, \quad n = 1, 2, 3\dots \\
 \tau_{ps} &= \frac{N_s}{2p} \begin{cases} \notin \text{integer} \Rightarrow y_c = \text{Int}[\tau_p] \begin{cases} \geq 1, & \text{DL} \\ \geq 1 \text{ and } y_c \text{ is odd}, & \text{SL} \end{cases} \\ \in \text{integer} \Rightarrow y_c \geq 1, \text{ both DL and SL} \end{cases} \\
 &\quad \frac{2}{3}\tau_{ps} \leq y_c \leq \frac{4}{3}\tau_{ps}
 \end{aligned} \tag{1.9}$$

According to the first two equations in (1.9), the slot and pole numbers of the basic electrical machine unit should construct Thirty type dual 3-phase winding itself. The SL winding needs double slots compared with the DL one and the phase number equals 6 ( $m=6$ ). The requirement for the coil pitch must be separately given based on full or short pitch winding, as shown in the third equation in (1.9). The last equation is the same for all of electrical machines. The winding factors and harmonic orders generated by winding arrangement are still predicted by (1.5) and (1.6). TABLE 1.4 lists some available slot and pole number combinations [BAR10], [BAR11b].

TABLE 1.4 AVAILABLE SLOT AND POLE NUMBER COMBINATIONS FOR THIRTY TYPE DUAL 3-PHASE WINDINGS

$N_s$	$N_p=2p$	$q$	$y_c$	Winding end	$K_w$		$t$		Harmonics	
					DL	SL	DL	SL	DL	SL
12	<b>2▲</b>	<b>1</b>	<b>6</b>	<b>OLP</b>	<b>1</b>	<b>1</b>	<b>1</b>	<b>1</b>	<b>1±12k</b>	<b>1±12k</b>
	<b>10■</b>	<b>1/5</b>	<b>1</b>	<b>NOLP</b>	<b>0.966</b>	N/A	<b>1</b>	N/A	<b>5±12k</b>	N/A
	14	1/7	1	NOLP	0.966	N/A	1	N/A	7±12k	N/A
24	2	2	12	OLP	0.991	0.991	1	1	1±12k	1±12k
	<b>4▲</b>	<b>1</b>	<b>6</b>	<b>OLP</b>	<b>1</b>	<b>1</b>	<b>2</b>	<b>2</b>	<b>2(1±12k)</b>	<b>2(1±12k)</b>
	10	2/5	2	OLP	0.958	N/A	1	N/A	5±12k	N/A
	14	2/7	2	OLP	0.958	N/A	1	N/A	7±12k	N/A
	20	1/5	1	NOLP	0.966	N/A	2	N/A	2(5±12k)	N/A
	<b>22■</b>	<b>2/11</b>	<b>1</b>	<b>NOLP</b>	<b>0.983</b>	<b>0.991</b>	<b>1</b>	<b>1</b>	<b>11±12k</b>	<b>11±12k</b>
	26	2/13	1	NOLP	0.983	0.991	1	1	13±12k	13±12k
28	1/7	1	NOLP	0.966	N/A	2	N/A	2(7±12k)	N/A	
36	2	3	18	OLP	0.991	0.991	1	1	1±12k	1±12k
	6	1	6	OLP	0.990	0.90	3	3	3(1±12k)	3(1±12k)
	10	3/5	4	OLP	0.975	N/A	1	N/A	5±12k	N/A
	14	3/7	3	OLP	0.956	N/A	1	N/A	7±12k	N/A
	22	3/11	2	OLP	0.930	N/A	1	N/A	11±12k	N/A
	26	3/13	1	NOLP	0.897	N/A	1	N/A	13±12k	N/A
	34	3/17	1	NOLP	0.986	N/A	1	N/A	17±12k	N/A
	38	3/19	1	NOLP	0.986	N/A	1	N/A	19±12k	N/A
46	3/23	1	NOLP	0.897	N/A	1	N/A	23±12k	N/A	

Comparing TABLES 1.4 and 1.3, the construction of Thirty type dual 3-phase winding is much harder in terms of slot and pole number combinations. The major advantages can be clearly seen by comparing the two kinds of dual 3-phase windings with the same slot and pole number combinations. For PM machines with Thirty type dual 3-phase windings, a higher winding factor for the working harmonic and less harmonics can be obtained. Several examples with overlapping and non-overlapping windings are also shown for clarity. Both PM machines with 12S/2P and 24S/4P combinations in TABLE 1.4 with mark ▲ have overlapping windings and their cross-sections are shown in Fig. 1.17 [ALG30], [HOL70].

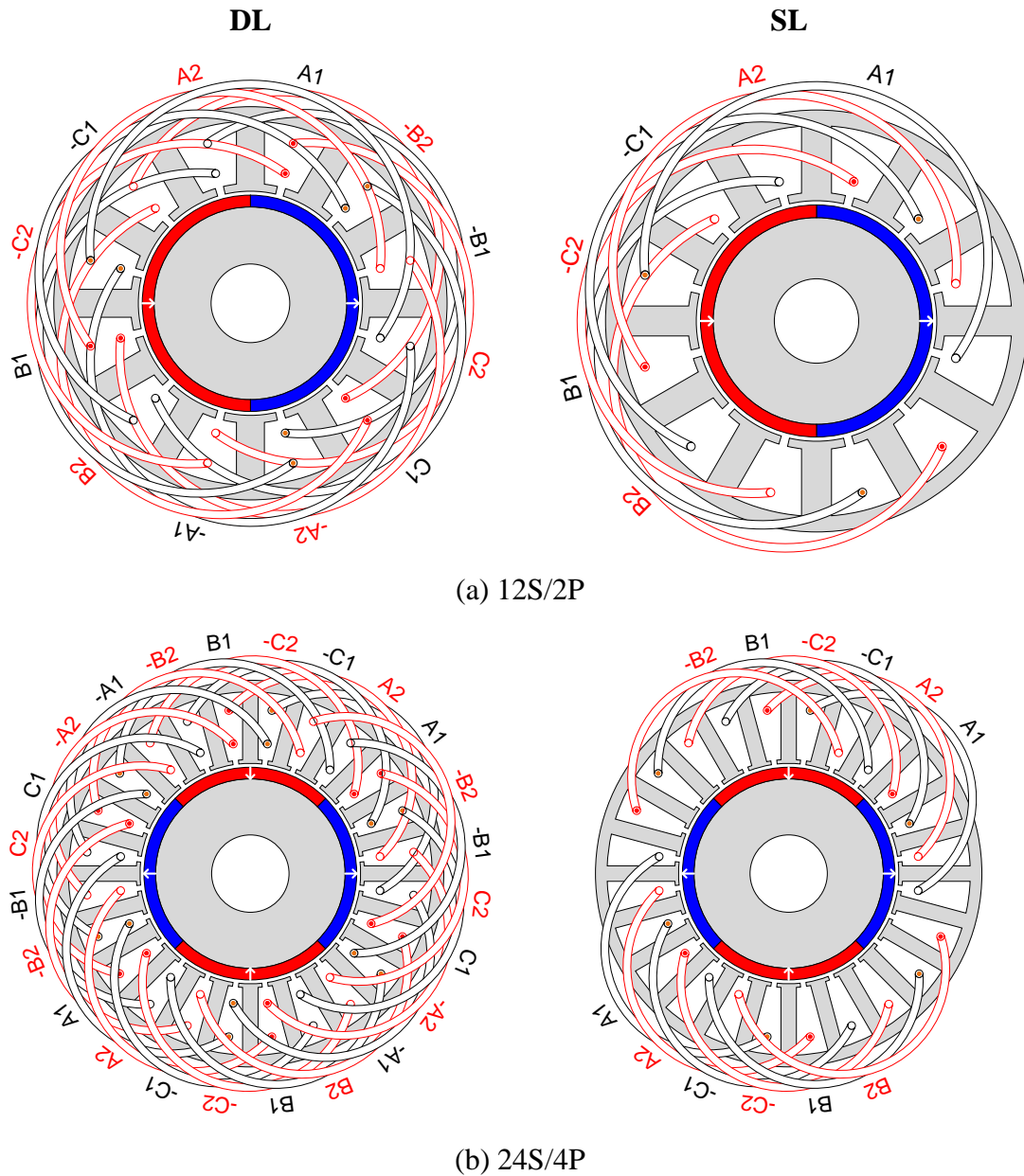


Fig. 1.17. PM machines with overlapping Thirty type dual 3-phase windings.

Fig. 1.17 shows that both overlapping and non-overlapping windings can be adopted for full pitch integer slot machines. The winding harmonics of two kinds of windings will be the same as well referring to TABLE 1.4. The drawback for this kind of winding is the close coupling among six phases, which can be largely restrained by adopting non-overlapping windings. The PM machines with 12S/10P and 24S/22P combinations in TABLE 1.4 with mark ■ are used, as shown in Fig. 1.18 [ALB12], [BAR12], [WAN15c].

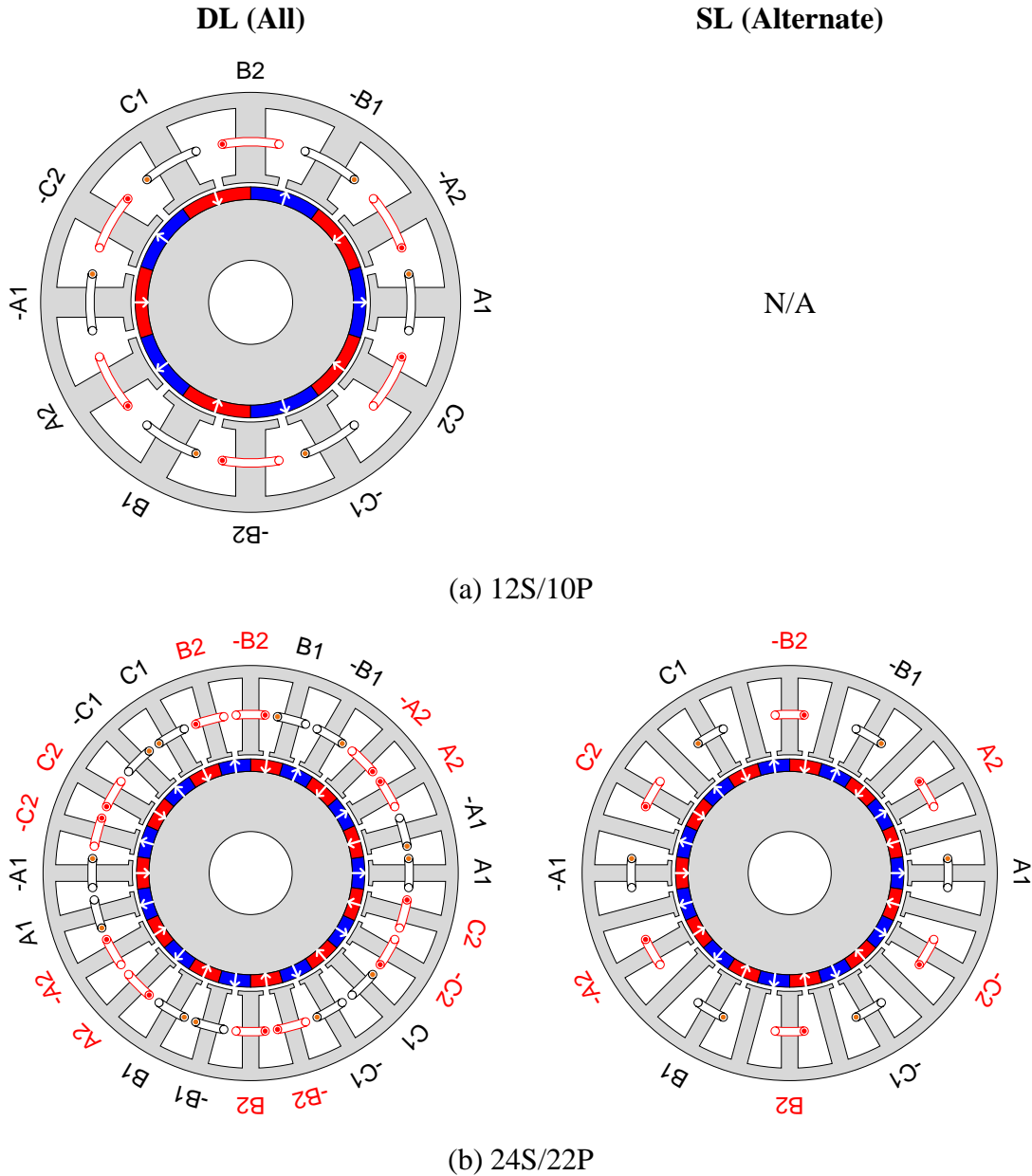


Fig. 1.18. PM machines with non-overlapping Thirty type dual 3-phase windings.

The coupling of winding end part has been evidently reduced, as shown in Fig. 1.18. Compared with the counterpart Zero type dual 3-phase windings, more harmonics have been eliminated, which is quite important when using fractional-slot windings [MAG07], [ZHU07b], [BIA09], [URR13], [ROK17].

### 1.3.3 Other Degree Phase Shift

Besides the above two type dual 3-phase windings, the other kinds of dual 3-phase winding with different shift angles between two sets of windings can be obtained as

well. The relationship between two sets of winding can be expressed by a general fixed offset angle, viz.  $\alpha_{set}$ , as shown in Fig. 1.14(c). The PM machines with 18S/10P combination have been investigated in detail by authors from [WAN14], [PAT14], [PAT15]. The proposed dual 3-phase windings for this slot and pole number combinations can be 20/40 degrees, as shown in Fig. 1.19.

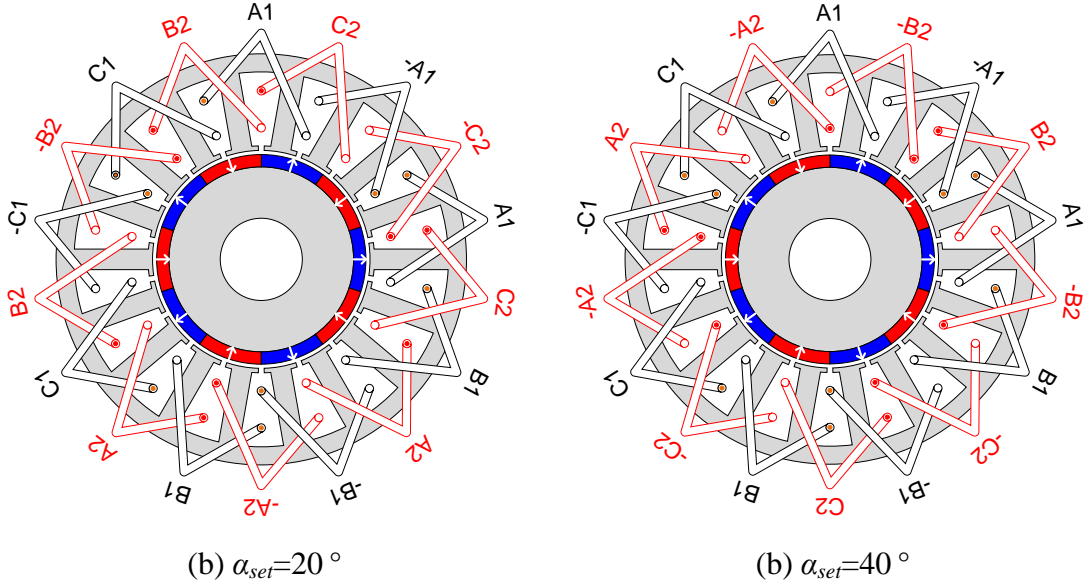


Fig. 1.19. Dual 3-phase PM machines with 18S/10P combination.

Fig. 1.19 shows that the winding end part is overlapped, while the two available winding layouts are still fractional-slot type. Since the dual 3-phase winding is adopted, the winding harmonics are lower than the counterpart single 3-phase machines [PAT14], [CHE14]. However, it can be seen that the coupling among phases will exist since the winding end part is overlapped. A more general determination of shift angle between two sets of windings have been summarised in [SHA15] and [XU17] for different slot and pole number combinations. The merit of these different connections could fulfil the requirement of the specific applications, such as the 15 degree phase shift between two sets of windings in 24S/10P PM machine. For this combination, it can be connected in Thirty type dual 3-phase winding as well according to TABLE 1.4. Both winding layouts are shown in Fig. 1.20.

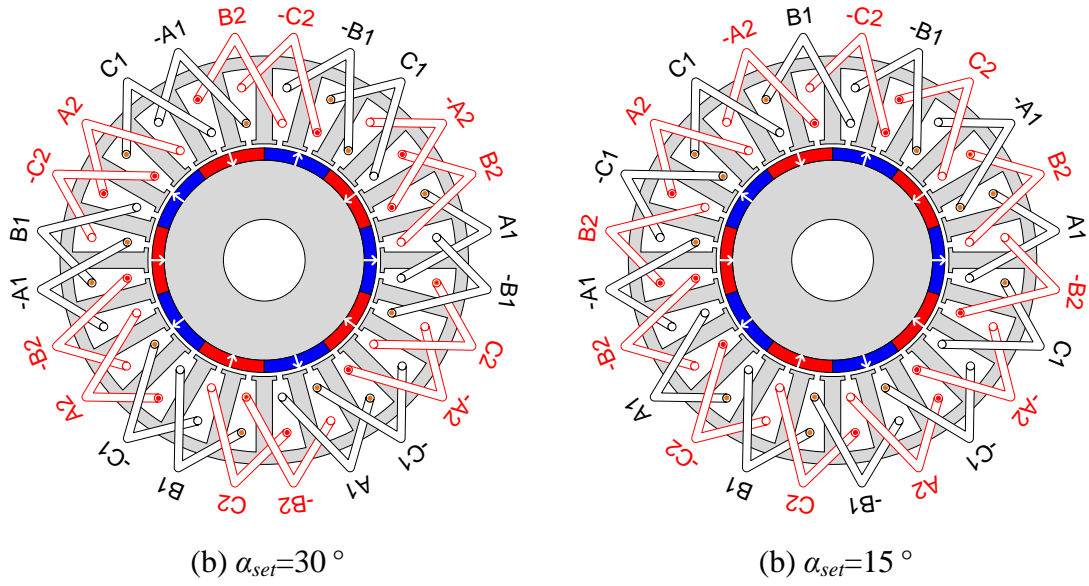


Fig. 1.20. Dual 3-phase PM machines with 24S/10P combination.

The discussion on the merits of Thirty type connection has been published in [DAJ11], [ZHE12], [ABD16b]. The much lower harmonics can be obtained compared with the 12S/10P PM machine, while the end part has some coupling. According to [XU17], the special 15 degree phase shift between two sets of windings lead to a better faulty operation performance.

The dual 3-phase windings are still under development and more and more topologies will be proposed and each will have its own specialities and suitable applications.

#### 1.4 Development of Modular Stator Techniques in Electrical Machines

Because of the huge size and the limitation on mechanical manufacture and transportation, the stators of large size electrical machines need to be segmented. This technique has been widely used in hydroelectric alternators for a long time [FIT03]. With the evolution of electrical machine technology over the past few decades, quite a few electrical machine topologies have been put forward [CRO02], [BIA05], [FOR13], [ZHU11], [CAO12a], [DAJ11], [DAJ12a], [DAJ12b], [DAJ13], [ZHE12]. The modularity technique simultaneously develops and can be employed to the stator manufacture of these electrical machines. The advantages of adopting modular stators mainly include the following aspects [MEC96], [HEI15], [SHI16]:

(1) The requirement of stator machining will be lower, since only the small portions need to be manufactured instead of the whole stator. Therefore, the production efficiency is high.

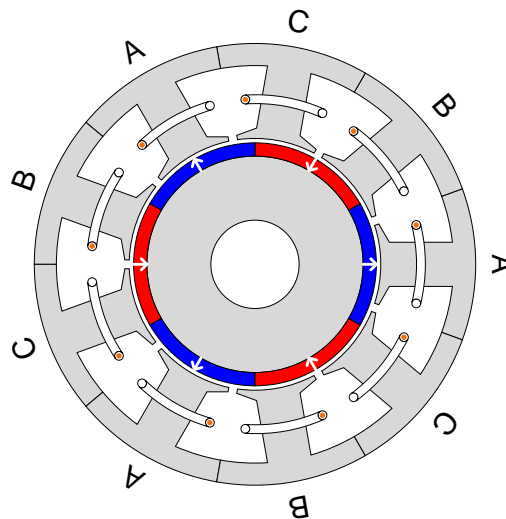
(2) The transportation of small stator segments will be much easier for large size electrical machines and the cost will be accordingly reduced. The windings are easier to be accommodated in the stator slots. Thus, the slot filling factor will increase, which is beneficial to improving electrical machine performance.

(3) The fault tolerant capability of electrical machines will be better since the physical, electric, magnetic and thermal isolation among coils could be fulfilled.

Based on the physical isolation level between adjacent coils, the modular stators can be classified into three kinds.

### 1.4.1 Physical Coupling

When all teeth wound winding is adopted, the end part of adjacent coils will be non-overlapping. Thus, the stators can be made of several segments and the coils can be wound around the teeth of each segment before assembly. However, the adjacent coils still touch each other in slots. An ingenious method in manufacturing the segmented stators can be seen in Fig. 1.21.



(a) Modular 9S/6P PM machine



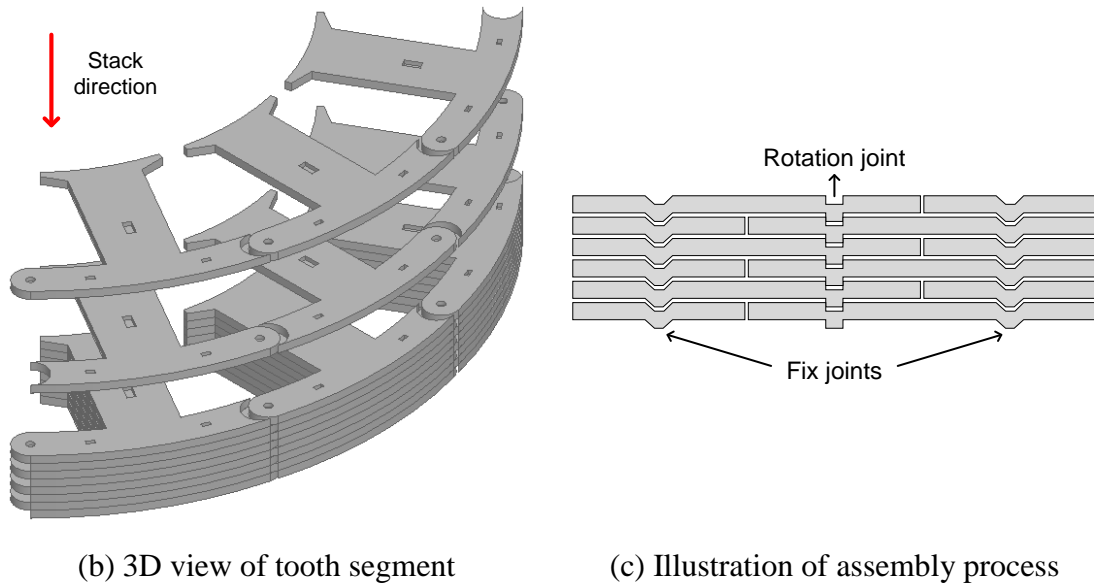
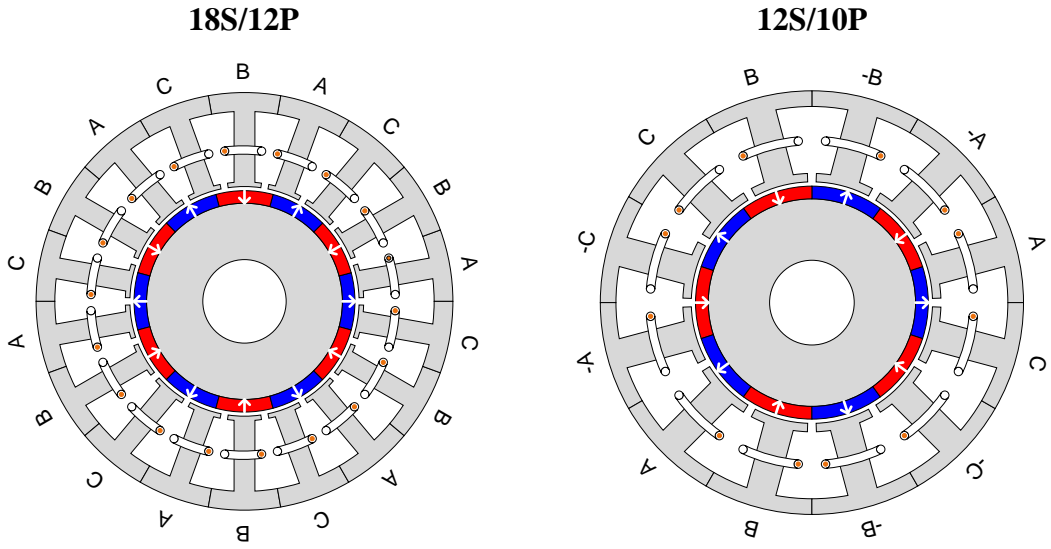


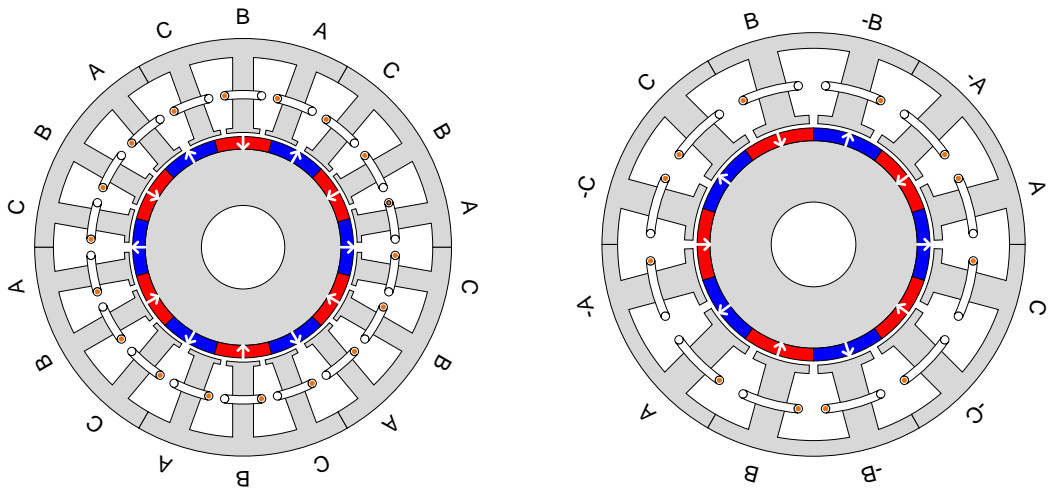
Fig. 1.21. Illustration of a modular method in stator manufacture [AKI03], [LIB06].

Fig. 1.21(a) shows that the stator core of 9S/6P PM machine consists of segments with single tooth, while Fig. 1.21(b) and (c) illustrate the mechanical assembly principle of this stator. Since each segment can easily rotate in rotation joints and be fixed by alternately arranged fix joints in lamination stack direction, the whole stator will be easily constructed. The production efficiency is quite high.

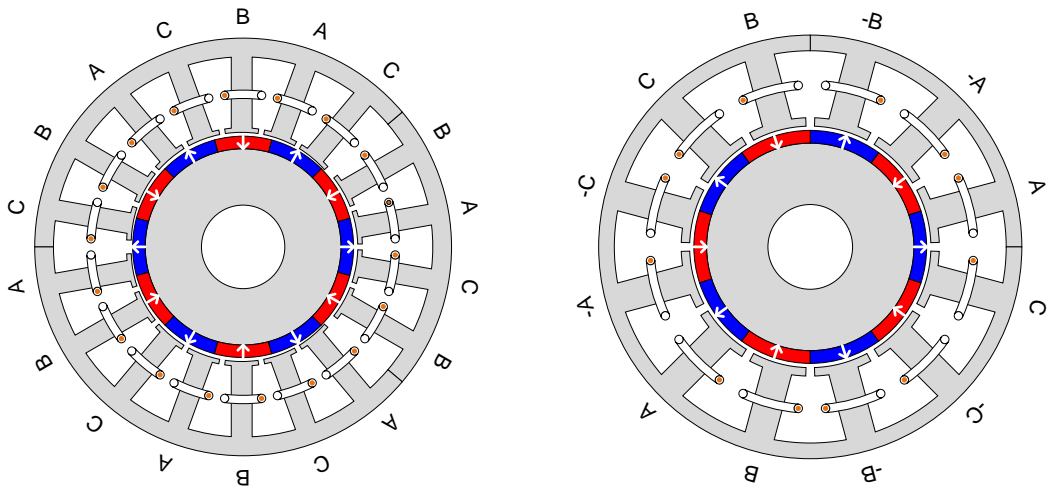
Besides segmenting single tooth, other segmentation approaches on stator cores can be adopted as well. Two PM machines with 18S/12P and 12S/10P combinations were used to investigate the different stator segmentation patterns in [YUA14], [SHE16], as shown in Fig. 1.222. Furthermore, the joint connections between segments can adopt different shapes, as shown in Fig. 1.23. The segmentation method adopted in Fig. 1.22(a) is the same as the one shown in Fig 1.21. The drawback of using this method is the high precision manufacture requirements for the sake of accurate assembly. Therefore, the stators can be cut into segments with several teeth to reduce the manufacture tolerance, as shown in Fig. 1.22(b) and (c). If the stators are symmetrically cut, each segment can be based on basic electrical machine unit with 3 slots in 18S/12P modular machine. Similarity, the PM machine with 12S/10P can be cut based on the coils belonging to the same phase. For the stator segmentations exhibited in Fig. 1. 22(c), though they need less segments, the stator asymmetry will lose the merit of uniformity and increase production cost.



(a) Segmentation for single tooth



(b) Symmetrical group segmentation



(c) Asymmetric group segmentation

Fig. 1. 22. Modular machines with different stator segmentation patterns.

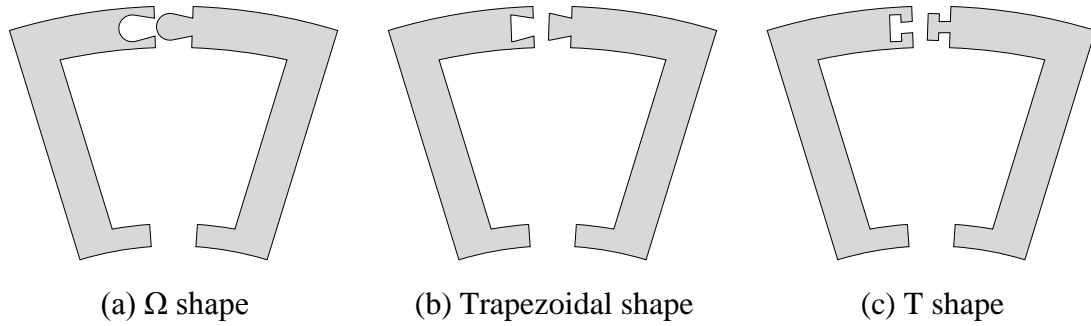


Fig. 1. 23. Different tongues and grooves adopted for joints.

The authors in [SHE11] also proposed another method to manufacture modular stators, as shown in Fig. 1.24. The original PM machine shown in Fig. 1.24(a) adopts the integral laminated stator. For the sake of modularity, each stator tooth can be inserted into a complete solid stator yoke in Fig. 1.24(b). However, the solid stator yoke will generate large eddy current loss during the operation. In order to tackle with this issue, two proposed modular stators are proposed in Fig. 1.24(c) and (d). The stator yoke part of the main flux path is practically kept the same as that in the original PM machine. The additional joints are added to make sure that the stator tooth segments can be incorporated into the complete solid iron. The higher manufacture requirement for tooth segments and support yoke are the major demerit.

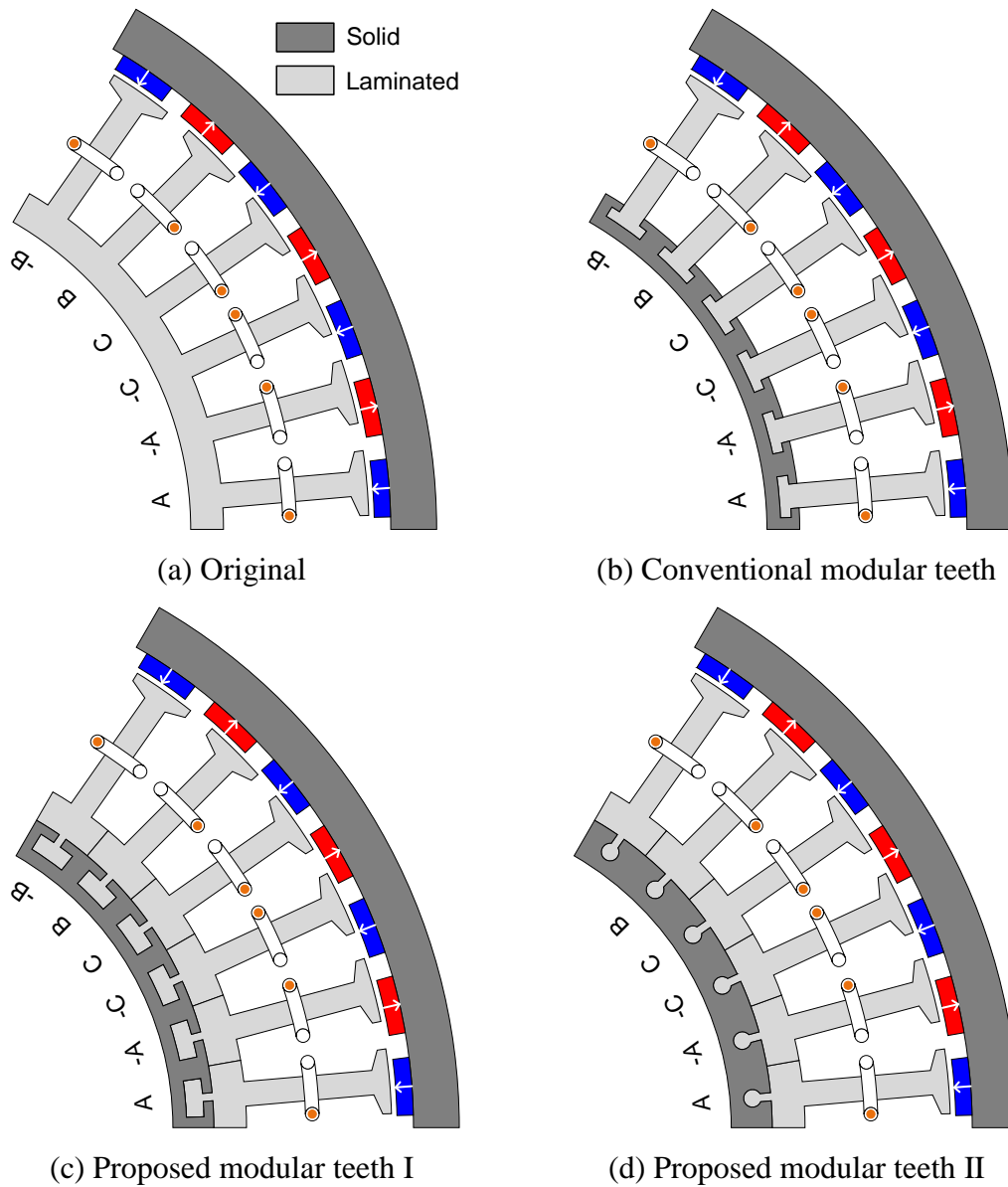
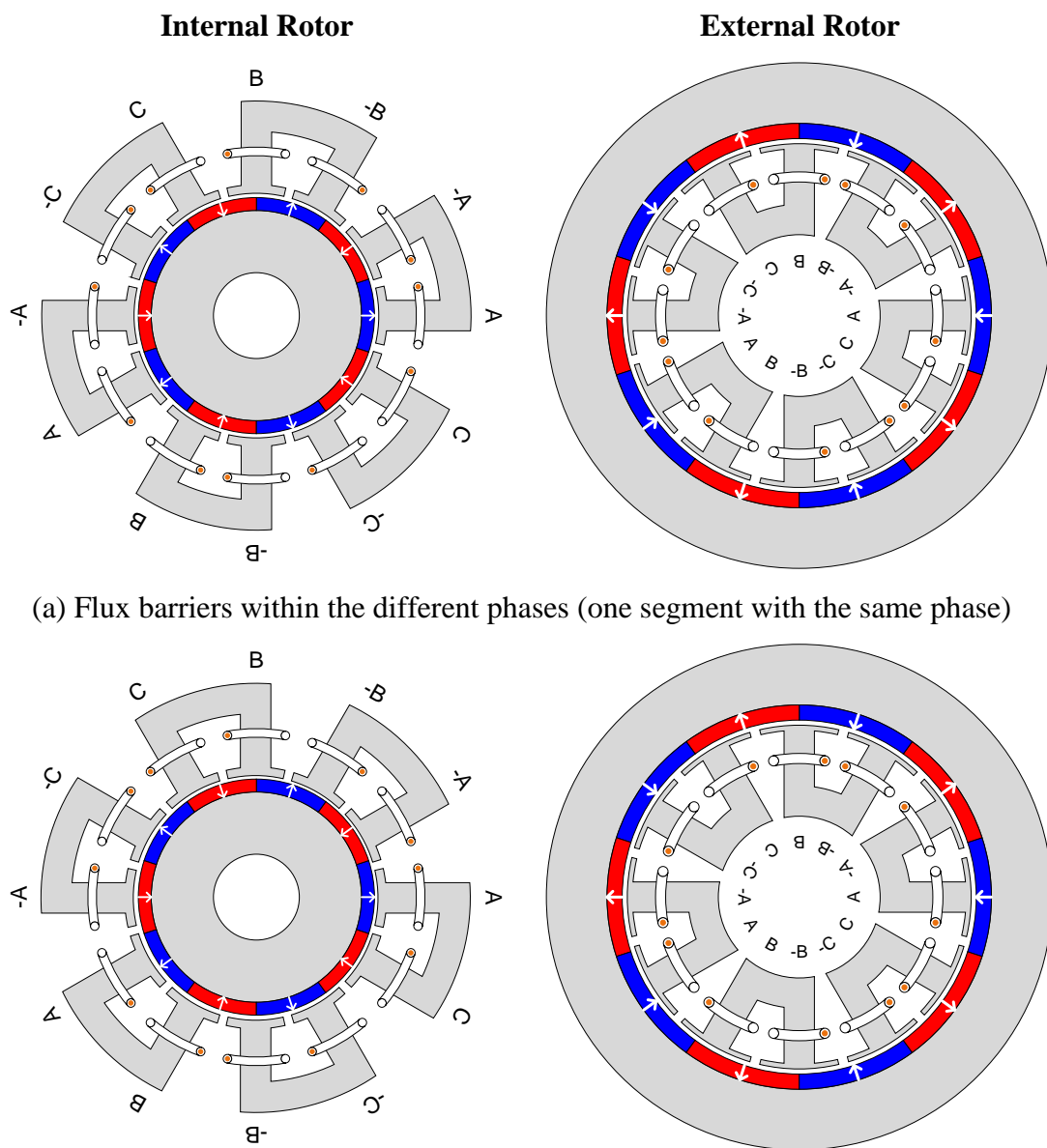


Fig. 1.24. Different stator segmentations for 1/6 of 36S/42P PM machines.

The modular stators in [ISH05a], [DAJ14], [HEI15] alternately add flux barriers in stator yokes, as shown in Fig. 1.25. For the PM machine shown in Fig. 1.25(a), the flux barriers are located between different phases. Thus, each U-core segment contains the coils belonging to the same phase and the whole stator consists of several U-core pieces. The coils are anti-direction wound in the two teeth of the same U-cores. The magnetic decoupling between phases can be enhanced. If the barriers are added within the same phase, viz. each U-core segment containing the coils of different phases, the magnetic circuit of armature field will be changed. The purpose of adopting such structure is to reduce some harmful harmonics [DAJ14]. This modular

structure is shown in Fig. 1.25(b). However, there are some disadvantages using this modular method. On one hand, the existence of additional flux barriers in stator yoke will increase magnetic circuit reluctance and the average torque will be reduced. On the other hand, the stator yoke thickness must increase to the same as tooth width to avoid over saturation. This will lead to a larger volume if the internal rotor structure is adopted, as shown in the left column of Fig. 1.25. In contrast, this side effect will not increase machine outer diameter if the external rotor structure is adopted. The machine topologies in the right column of Fig. 1.25 can clearly show this, which means this kind of modularity technique can be applied in some special occasions.



(a) Flux barriers within the different phases (one segment with the same phase)

(b) Flux barriers within the same phase (one segment with different phases)

Fig. 1.25. Different flux barrier positions in modular machines (12S/10P).

### 1.4.2 Physical Partial Decoupling

When the stator windings or cores are specially designed, some parts of adjacent coils will be isolated by stator teeth. In one hand, it can satisfy the requirement of constructing modular stators. On the other hand, the segment numbers could be limited into a relatively small value. The assembly process and the transportation will be easier in large size electrical machine production process. When integer slot fully pitched single layer winding is adopted, the stators can be automatically separated into segments based on the basic electrical machine unit. An external rotor PM machine was shown in Fig. 1.26 [CHE00b]. Although the stator winding end parts are overlapped among phases within each pole pair, there is no physical coupling between adjacent basic electrical machine units (6S/2P). Therefore, the stator can be cut into a few segments and the coils located at the end part can be protected by stator tooth as well.

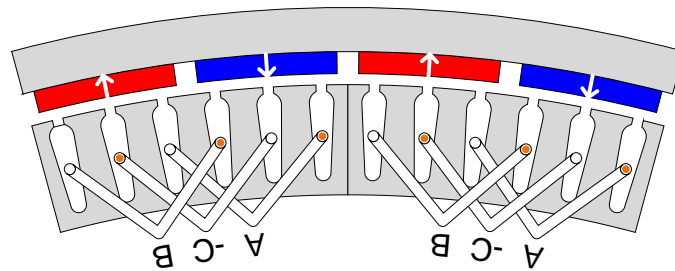


Fig. 1.26. An external rotor wind power generator (144S/48P).

The similar idea can be employed to the commercial Prius 2010 PM machine [BUR11], as shown in Fig. 1.27. This 48S/8P PM machine contains four 12S/2P basic electrical machine units and the single layer fully pitched winding was adopted. The real product shown in Fig. 1.27(a) still adopts overlapping windings, whereas the winding connection shown in Fig. 1.27(b) can be adopted as well. The electromagnetic performance of two cases will be the same, while the later one can adopt modular stators. However, the careful design is necessary to reduce the large torque ripples in integer slot PM machines.

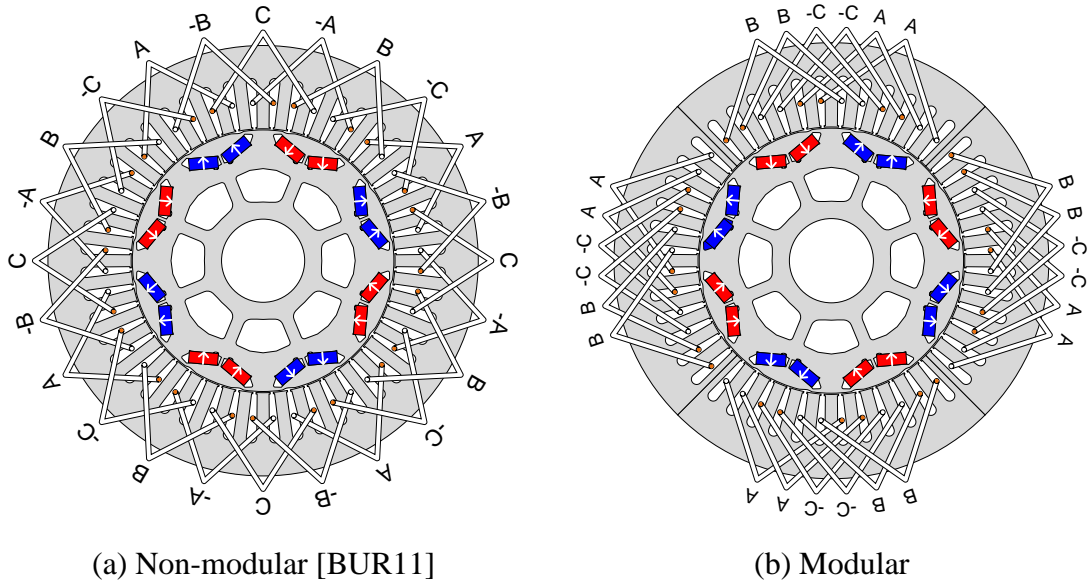
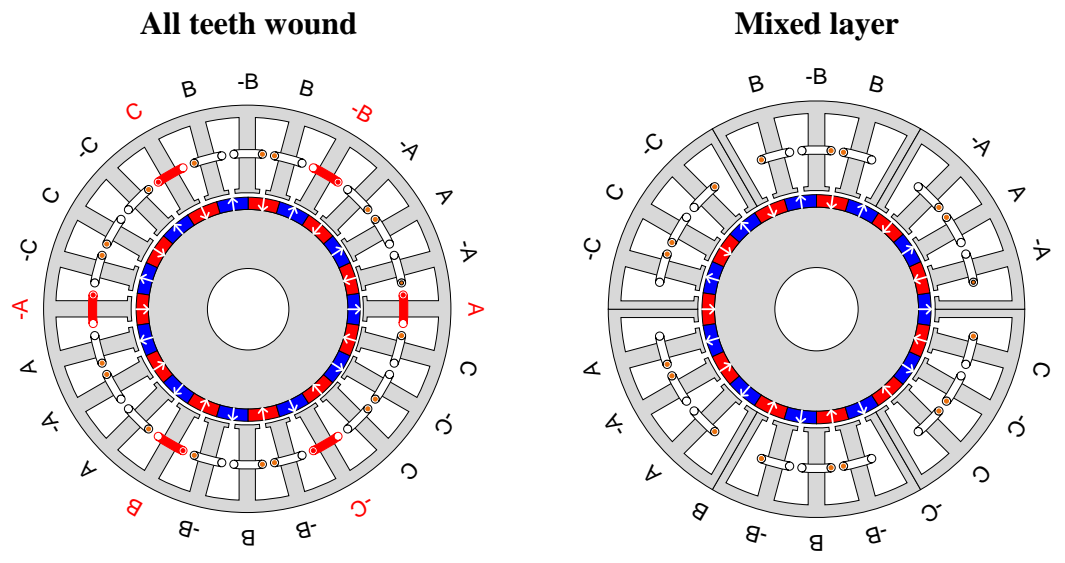
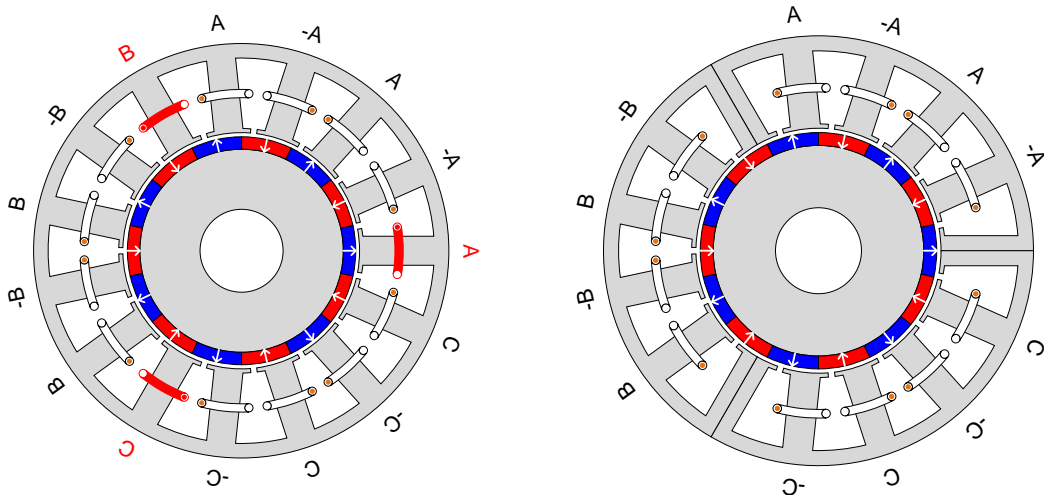


Fig. 1.27. Prius 2010 PM machine (48S/40P).

The authors in [FOR13] removed some coils of all teeth wound windings to provide the unbound teeth for modularity. The removed coils must be able to construct a balanced 3-phase system to keep the proposed modular machine still balanced. The two PM machines representing  $2p=N_s \pm 2$  and  $2p=2p=N_s \pm 1$  slot and pole number combinations are shown in Fig. 1.28. It clearly shows that more coils need to be removed for 24S/22P PM machine, since it has two complementary winding groups for each phase. However, 3 coils need to be removed for 15S/14P PM machine. Abundant harmonics are the major issue for this method.



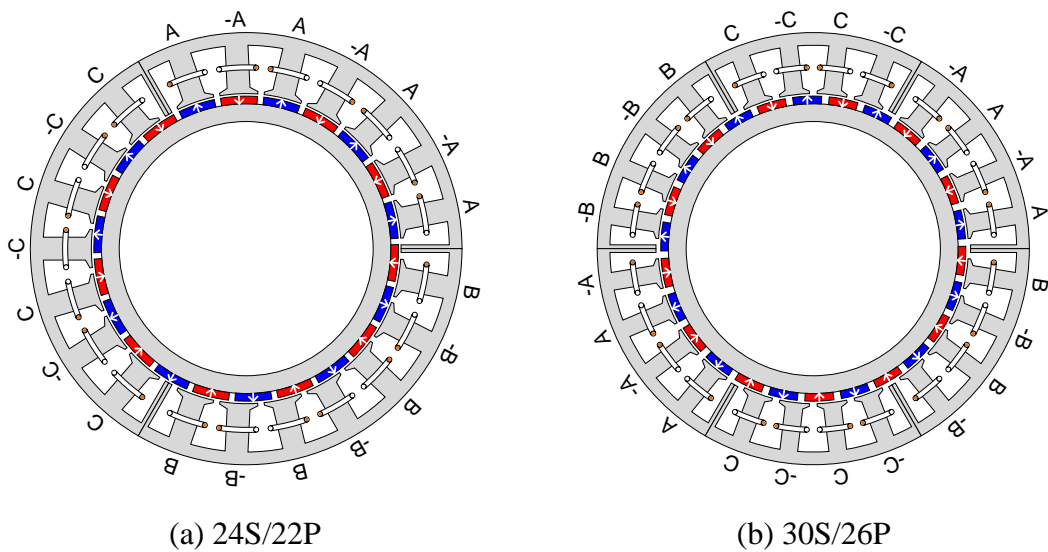
(a) 24S/22P



(b) 15S/14P

Fig. 1.28. Modular machines with removed coils.

If some space is left between segments on purpose, the coils on the teeth of some positions can be removed to leave unwound teeth for stator core modularity. This method was proposed in [CHE08]. The two modular machines obtained by this method are shown in Fig. 1.29. Each segment only has coils belonging to one phase and the coil pitch is assigned the same as the pole pitch to obtain unity winding factor. The reason for using the topology in Fig. 1.29(b) is to get rid of undesirable unbalanced magnetic force, which exists in the PM machine with rotating asymmetric winding layout [ZHU13] shown in Fig. 1.29(a). The large on-load torque ripple restricts the interest of this method.



(a) 24S/22P

(b) 30S/26P

Fig. 1. 29. Modular machines with redundant teeth.



A similar method was proposed by authors in [BAK18], where each segment has complete 3-phase winding, as shown in Fig. 1.30. Fig. 1.30(a) shows that the original 18S/12P PM machine has all teeth wound winding. In order to add some redundant teeth to ease modularity, another pole pair is added and used for redundant teeth arrangement. The four redundant teeth are inserted to construct complementary segments. Since the three phases are unbalanced and the torque ripple is also large, this kind of modularity was not widely applied.

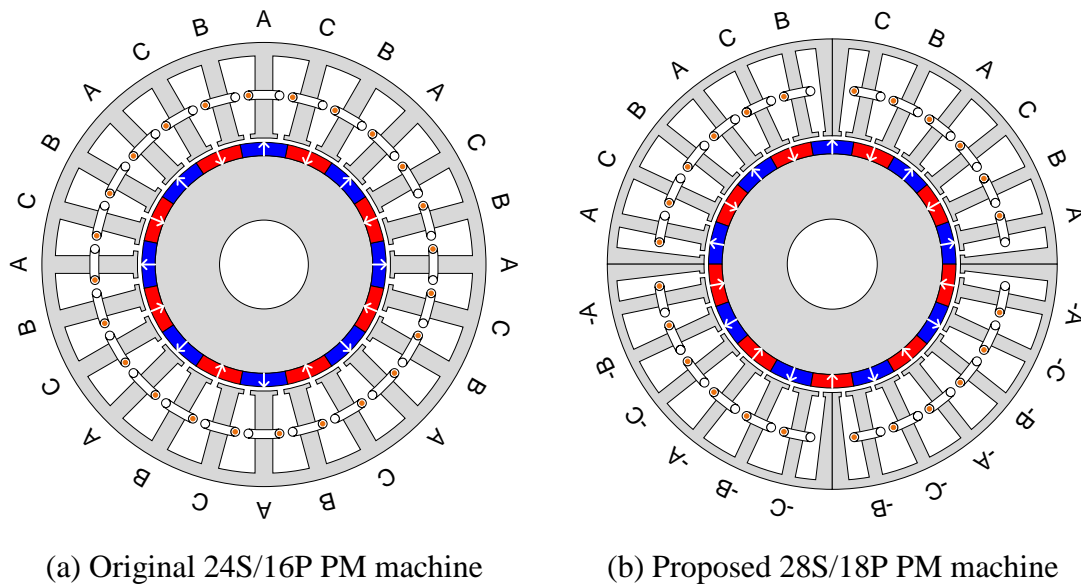


Fig. 1.30. Modular machines with complete winding for each segment.

### 1.4.3 Physical Fully Decoupling

When any two adjacent coils do not touch each other, there is no physical coupling among coils. This kind of winding is suitable for the applications requiring high reliability. A wind power generator stator with E-core segments was put forward in [SPO94] and systematically analysed in [CHE95], [SPO96], [SPO98], as shown in Fig. 1.31. Both stator and rotor cores are segmented to make the fully modular machine. Since there are large slot and pole numbers, the mechanical support of this electrical machine is complicated. This could constrain the use of such structure in real applications. Besides, too much stator space has been wasted and the output torque will be reduced compared with the conventional non-modular machines.

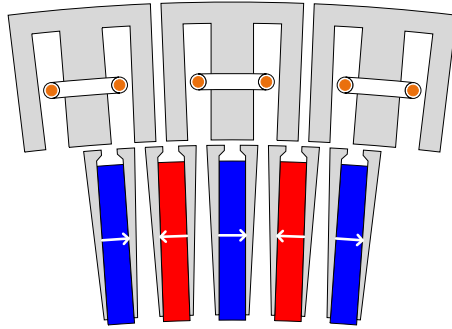


Fig. 1.31. E-core modular wind power generator.

The PM machines with alternate teeth wound winding can inherently adopt such kind of modular stators and the high fault-tolerant capability is the obvious advantage. A 6-phase 12S/8P modular machine was shown in Fig. 1.32 and it was investigated by the authors in [MEC96], [HAY99] for aerospace application.

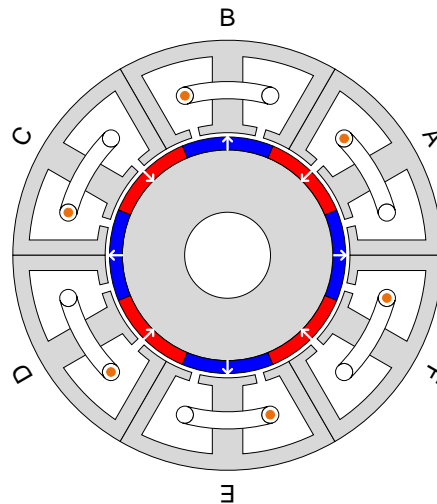


Fig. 1.32. PM modular machine for aerospace application (12S/8P).

The alternate teeth wound winding has been investigated for quite a long time [CRO02], [ISH05c], [WAN05], [WAN06], [WAN08], [OWE10], [WRO10], [VIL12], [PRI15]. It is also extended to PM machines with other phase numbers [ATA03], [CHA07], as shown in Fig. 1.33 for 2-, 3-, 4- and 5-phase cases.

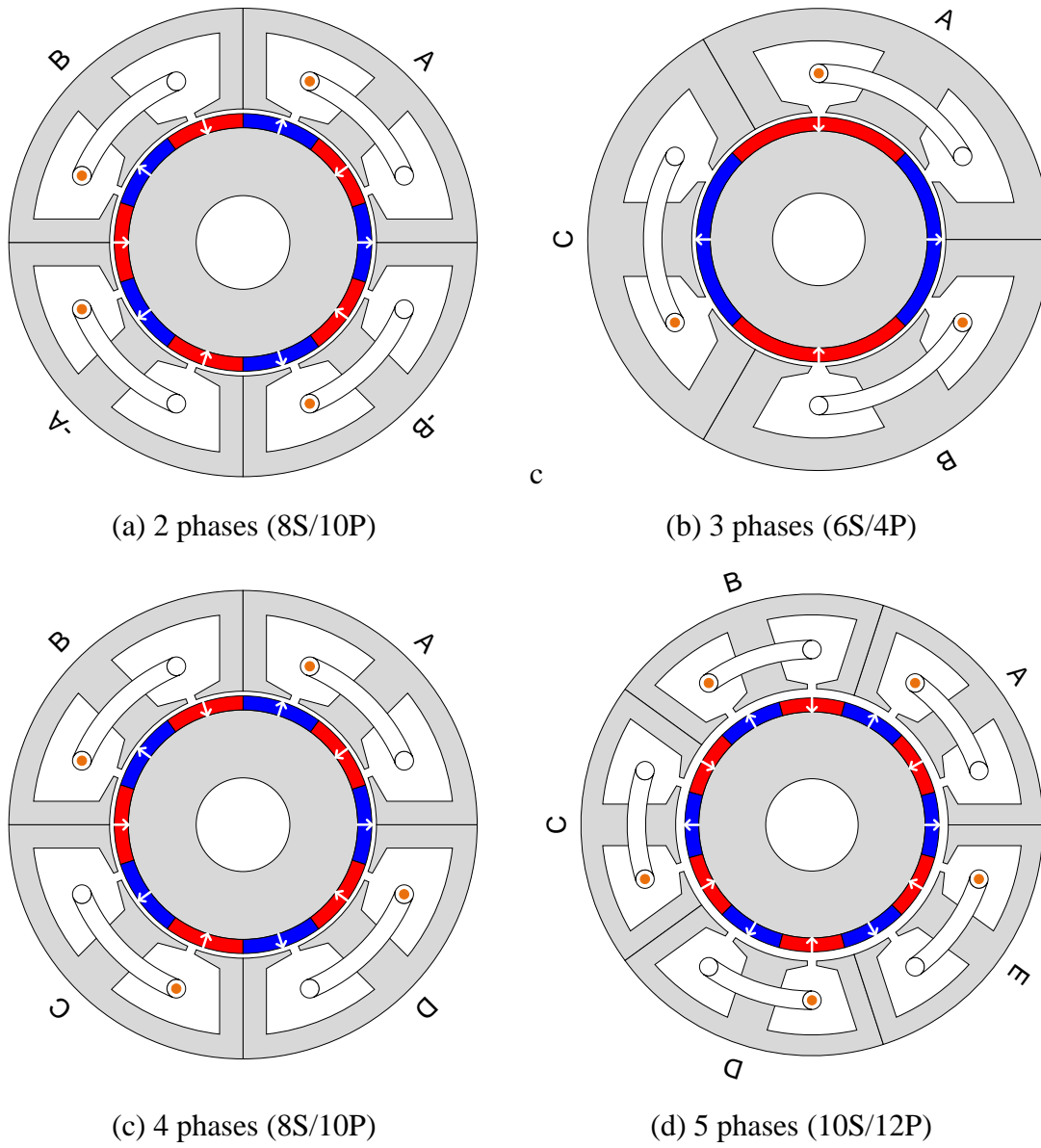


Fig. 1.33. PM machines with alternate teeth wound windings.

When the alternate teeth wound winding is adopted, the stator tooth width can be accordingly adjusted to increase winding factors [CRO02], [ISH05c]. Then, the modular machine has unequal tooth width and the output torque could be higher compared with its equal tooth width counterpart, as shown in Fig. 1.34. The issue for using unequal tooth width stator is large torque ripple, which is owing to heavier local saturation [LI16].

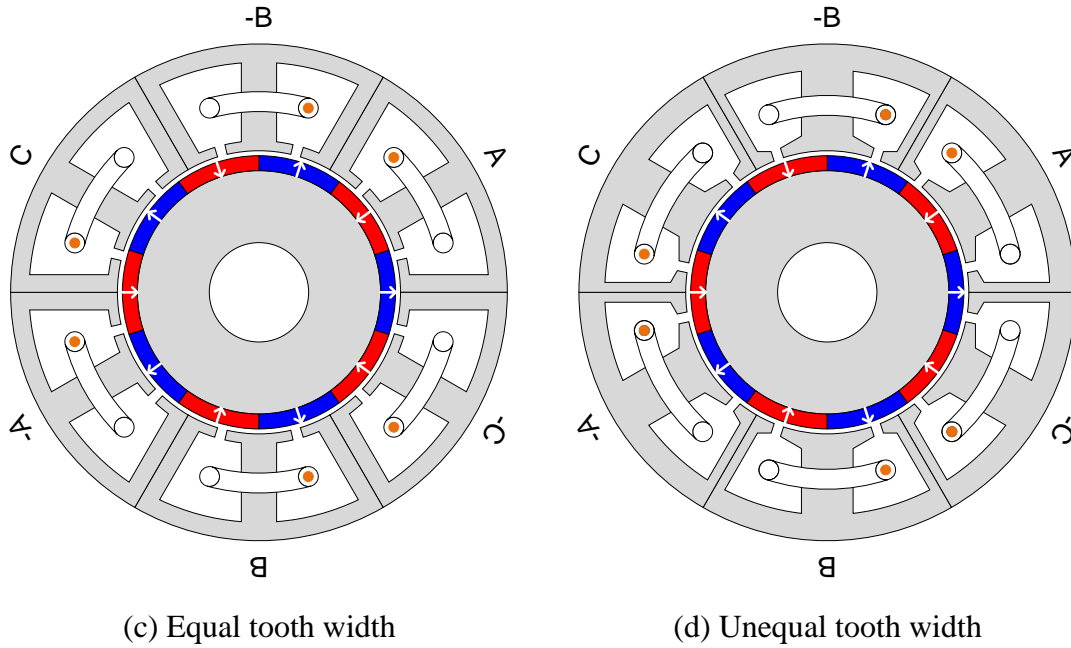


Fig. 1.34. PM machines with unequal teeth (12S/10P).

Since half of the stator teeth are not wound, the stator cores can also have other modular structures. The previous mentioned U-core stator [HEI15] is shown in Fig. 1.35(a) for alternate teeth wound winding. Careful protection is needed for this structure because of the exposed coil sides. The additional flux barriers can be inserted into stator teeth [DAJ13], [NOL14], [LI14b], [LI14c], [LI15a], [LI15b] as shown in Fig. 1.35(b). When the PM pole number is larger than slot number, such kind of topology can have higher torque compared with its counterpart modular machine without barriers [LI14a]. The U-core stator can also be adopted in this electrical machine [DAJ13], as shown in Fig. 1.35(c) and (d). For the later one, the stator U-core is made from axially-laminated technique. The lower power factor due to large inductance and larger torque ripple are the major disadvantages by using these modular stators with alternate teeth wound windings.

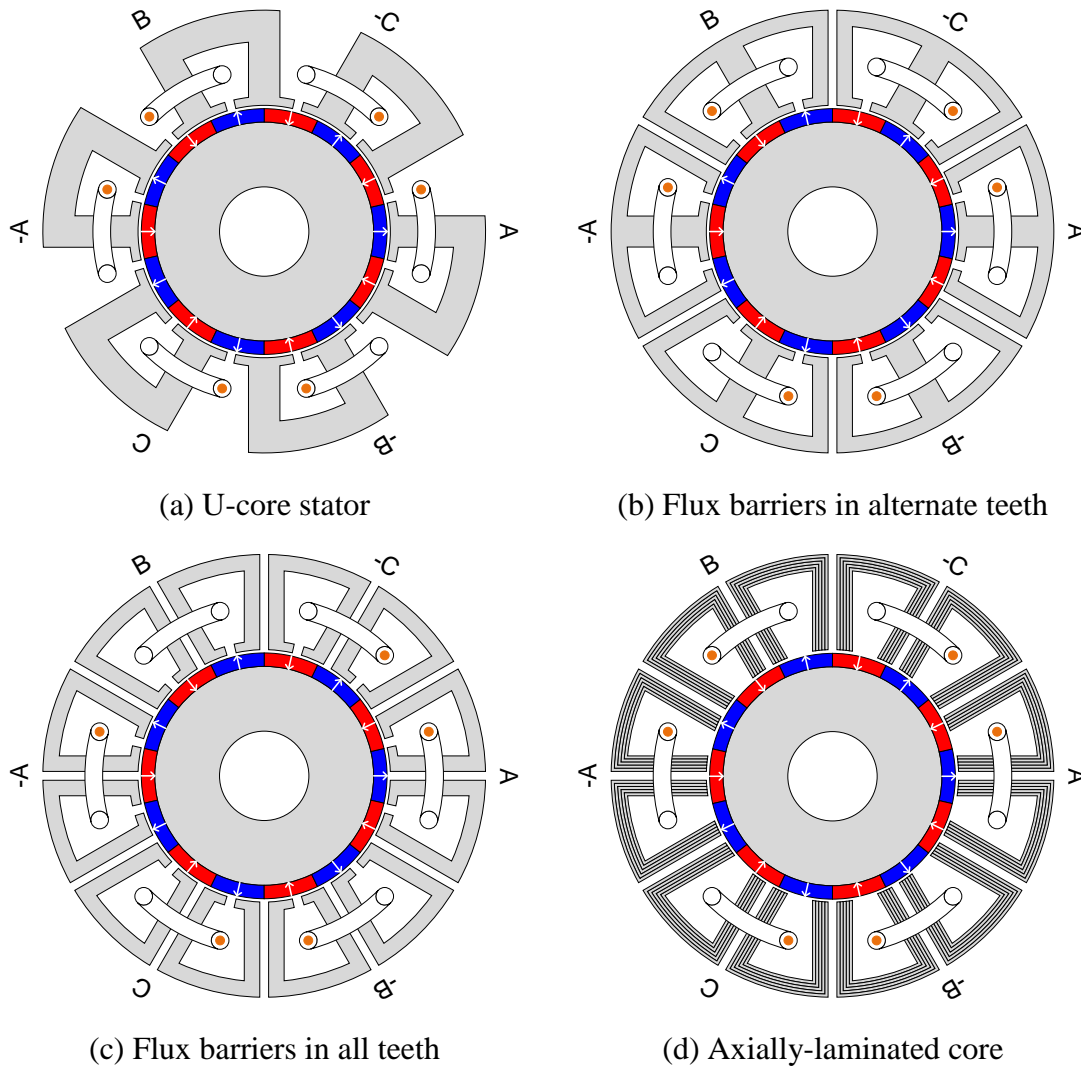


Fig. 1.35. Cross-sections of modular machines with flux barriers (12S/14P).

From the stator modularity techniques described above, it can be found that the appropriate stator core and winding design will ease the manufacture process of electrical machines. The suitable modular machine should be designed based on the specific requirements.

## 1.5 Scope and Contributions of Thesis

### 1.5.1 Research Scope

The novel modular PM machine with redundant 2 pole machine and double layer non-overlapping dual 3-phase winding is the research object in this thesis. The whole thesis structure is shown in Fig. 1.36. The major topic of each chapter has been

highlighted. The concepts related with the novel modular machine in Chapter 1 are all addressed by blue colour. Then, each chapter from 2 to 7 tackles with one theme and the corresponding work is identified by the circle-cross symbol. Based on the analyses, some general conclusions are drawn.

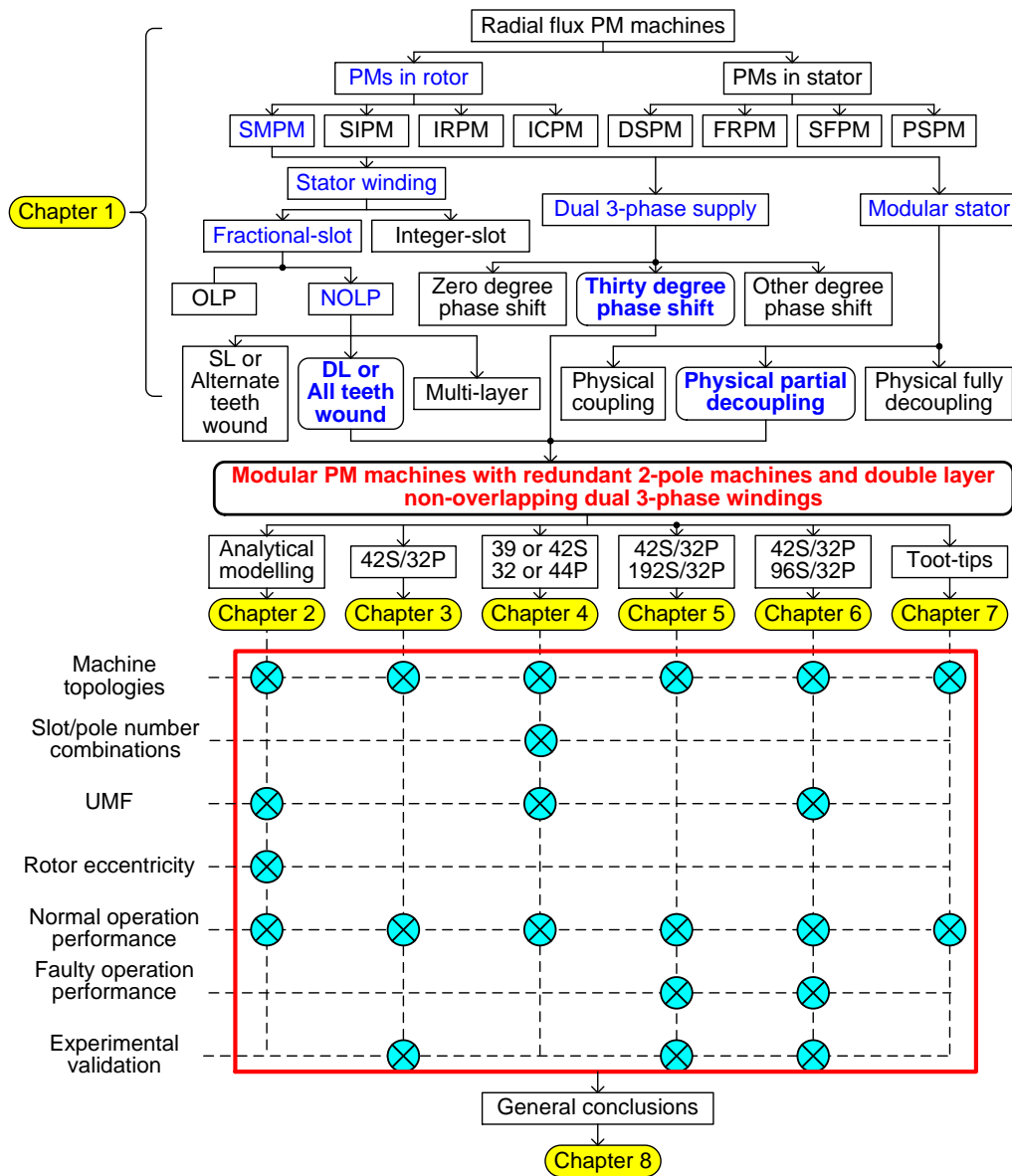


Fig. 1.36. Structure of the thesis.

The content arrangement is briefly explained as follows.

**Chapter 1.** Three important aspects related to the research object in this thesis are overviewed, together with the research background introduction. Starting from the simple classification of radial flux PM machines, the widely investigated fractional-slot non-overlapping windings are summarised. The state-of-art on dual 3-phase

machines is followed by. From the real application point of view, the modularity technique in PM machine manufacture is reviewed finally.

**Chapter 2.** Analytical modelling of rotor eccentricity by superposition method is presented. Both 2D axial-uniform and 3D axial-varying situations are considered, especially in aspects of cogging torque and unbalanced magnetic force.

**Chapter 3.** The construction process of the novel modular machine is introduced in detail. Based on the conventional all teeth wound modular machine, another PM machine with small slot and pole numbers is incorporated for modularity use. Then, a novel modular machine with redundant teeth is obtained. The comparison between this novel modular machine and its original counterpart one has been shown. The experiments on the prototyped machine validate the correctness of the analysis.

**Chapter 4.** The available slot and pole number combinations on constructing the novel modular machines are summarised in this chapter. The modular machine structure is extended in terms of segment number and the four example machines are used as representatives to show the influence of slot and pole number combinations on electrical machine performance.

**Chapter 5.** The operation of novel dual 3-phase modular PM machine in Thirty type mode is compared with the PM machine with overlapping windings. The difference in electrical machine structure is addressed and the electrical machine performance is compared under both normal and faulty operations. The experiments under faulty operation are used to verify the efficacy of the analysis.

**Chapter 6.** The comparative study between the novel modular machine and the conventional modular machine with overlapping winding is shown in this chapter when two sets of windings have zero phase shift. Not only is the two sets of winding operation considered, but the one set of winding operation is analysed as well. The tests on the prototyped conventional modular machine are the validation on analysis.

**Chapter 7.** The influence of magnetic slot wedges on the electrical machine performance of novel modular machines is investigated. The configurations of typical magnetic slot wedges are shown firstly. After this, the electromagnetic performance is compared based on the five representative prototype machines.

**Chapter 8.** The general conclusions based on the analysis in previous chapters are drawn. Some possible future work is mentioned.

**Appendix A.** The determination of overload current value is shown based on the requirement of air-gap length, magnetic loading and electric loading.

**Appendix B.** Frozen permeability method is briefly introduced.

**Appendix C.** CAD diagrams of two prototyped modular machines and material properties are given.

### 1.5.2 Major Contributions

(1) A novel modular machine which adopts all teeth wound dual 3-phase winding and has redundant teeth for stator segmentation is put forward and the influence of different magnetic slot wedges on electrical performance is analysed.

(2) The slot and pole number combinations for constructing the novel modular machines are summarised, together with the emphasis of the available stator segment number.

(3) The electromagnetic performance between the novel modular machines and conventional modular machines with overlapping windings are compared to show the advantages of this novel electrical machine.

(4) List of publications during PhD study:

#### Journal papers:

- [J1] **Y. X. Li**, and Z. Q. Zhu, “Cogging torque and unbalanced magnetic force prediction in PM machines with axial-varying eccentricity by superposition method,” *IEEE Trans. Magn.*, vol. 53, no. 11, pp. 1-4, Nov. 2017.
- [J2] **Y. X. Li**, Q. F. Lu, and Z. Q. Zhu, “Unbalanced magnetic force prediction in permanent magnet machines with rotor eccentricity by improved superposition method,” *IET Proc. -Electr. Power Appl.*, vol. 11, no. 6, pp. 1095-1104, July 2017.
- [J3] **Y. X. Li**, Q. F. Lu, Z. Q. Zhu, D. Wu, and G. J. Li, “Superposition method for cogging torque prediction in permanent magnet machines with rotor eccentricity,” *IEEE Trans. Magn.*, vol. 52, no. 6, pp. 1-10, June 2016.
- [J4] **Y. X. Li**, Q. F. Lu, Z. Q. Zhu, L. J. Wu, G. J. Li, and D. Wu, “Analytical synthesis of air-gap field distribution in permanent magnet machines with rotor eccentricity by superposition method,” *IEEE Trans. Magn.*, vol. 51, no. 11, pp. 1-4, Nov. 2015.
- [J5] Q. F. Lu, **Y. X. Li**, Y. Y. Ye, J. T. Chen, and Z. Q. Zhu, “Novel linear switched-flux PM machine with 9/10 primary/secondary pole number



combination,” *COMPEL - The international journal for computation and mathematics in electrical and electronic engineering*, vol. 34, no. 6, pp. 1656-1672, 2015.

- [J6] G. J. Li, B. Ren, Z. Q. Zhu, **Y. X. Li**, and J. Ma, “Cogging torque mitigation of modular permanent magnet machines,” *IEEE Trans. Magn.*, vol. 52, no. 1, pp. 1-10, Jan. 2016.
- [J7] H. L. Zhan, Z. Q. Zhu, M. Odavic, and **Y. X. Li**, “A novel zero-sequence model-based sensorless method for open-winding PMSM with common DC bus,” *IEEE Trans. Ind. Electron.*, vol. 63, no. 11, pp. 6777-6789, Nov. 2016.
- [J8] **Y. X. Li**, Z. Q. Zhu, and G. J. Li, “Influence of stator topologies on average torque and torque ripple of fractional-slot PM machines with closed-slots,” submitted to *IEEE Trans. Ind. Appl. Revised*.
- [J9] **Y. X. Li**, Z. Q. Zhu, A. S. Thomas, and X. M. Wu, “A novel dual 3-phase fractional-slot modular permanent magnet machine with redundant teeth,” submitted to *IEEE Trans. on Energy Conversion*.
- [J10] **Y. X. Li**, Z. Q. Zhu, A. S. Thomas, and X. M. Wu, “Influence of slot and pole number combinations on modular dual 3-phase PM machines with redundant teeth,” submitted to *IEEE Trans. on Industrial Electronics*.
- [J11] **Y. X. Li**, Z. Q. Zhu, A. S. Thomas, and X. M. Wu, “Comparison of dual 3-phase modular PM machines with overlapping/non-overlapping windings,” submitted to *IEEE Trans. on Magnetics*.
- [J12] **Y. X. Li**, Z. Q. Zhu, A. S. Thomas, and X. M. Wu, “Comparative study of fault-tolerant dual 3-phase modular PM machines with different winding configurations,” submitted to *IEEE Trans. on Industrial Electronics*.
- [J13] **Y. X. Li**, Z. Q. Zhu, A. S. Thomas, and X. M. Wu, “Influence of tooth-tips on dual 3-phase modular PM machines with redundant teeth,” to be submitted to *IEEE Trans. on Energy Conversion*.

#### **Conference papers:**

- [C1] **Y. X. Li**, and Z. Q. Zhu, “Cogging torque prediction in permanent magnet machines with axial-varying rotor eccentricity by superposition method,” in IEEE Magnetics Conference (*INTERMAG 2017*), April 24-28, 2017, pp. 1-1.
- [C2] **Y. X. Li**, Z. Q. Zhu, and G. J. Li, “Comparative study of voltage distortion in fractional-slot PM machines having different winding and stator configurations,” in Eleventh International Conference on Ecological Vehicles and Renewable Energies (*EVER 2016*), April 6-8, 2016, pp. 1-9.
- [C3] **Y. X. Li**, Z. Q. Zhu, and G. J. Li, “Torque investigation of fractional-slot permanent magnet machines with different winding topology and stator structures,” in Eleventh International Conference on Ecological Vehicles and Renewable Energies (*EVER 2016*), April 6-8, 2016, pp. 1-8.
- [C4] **Y. X. Li**, Z. Q. Zhu, G. J. Li, and D. Wu, “Analytical synthesis of air-gap field in permanent magnet machines with rotor eccentricity by

superposition method,” in IEEE Magnetics Conference (*INTERMAG 2015*), May 11-15, 2015, pp. 1-1.

- [C5] Q. F. Lu, **Y. X. Li**, Y. Y. Ye, J. T. Chen, and Z. Q. Zhu, “A linear switched-flux PM machine with 9/10 primary/secondary pole number,” in Ninth International Conference on Ecological Vehicles and Renewable Energies (*EVER 2014*), March 25-27, 2014, pp. 1-7.

## Chapter 2 Analytical Modelling of Rotor Eccentricity by Superposition Method

This chapter proposes an analytical method which combines the superposition and the subdomain methods to predict the electromagnetic performance of permanent magnet (PM) machines with rotor eccentricity. The original machine with rotor eccentricity is divided into a number of air-gap sections along the circumferential direction. For each air-gap section, a concentric model is employed by adopting an equivalent air-gap length to predict the air-gap field by using the subdomain method. The air-gap field distribution of the original model can then be synthesised from these concentric models. Consequently, the electromagnetic performance can be predicted accordingly, such as cogging torque and unbalanced magnetic force (UMF). Finally, direct finite element analysis (FEA) is used to validate the efficacy of the proposed method. The proposed analytical method is also extended to 3D axial-varying eccentricity analysis here and other electrical machines with different slot/pole number combinations can be investigated by this method as well.

### 2.1 Prototype Machines

Two conventional fractional slot PM machines are chosen as examples. One is 9-slots/8-poles (9S/9P) PM machine, which has rotating asymmetric winding. For this machine, there exists the UMF even though the machine is perfectly manufactured. Thus, this kind of UMF is intrinsic. In contrast, another machine which has 12S/10P combination possesses the extrinsic UMF and the winding is rotating symmetrical [ZHU14b]. This kind of machine will not have the UMF unless there are manufacture imperfections, such as rotor eccentricity. The major parameters of two machines are listed in Table 2.1 and the corresponding cross-sections with winding configurations are shown in Fig. 2.1(a) and (b). The rotor eccentricity pointing to a specific direction (positive  $x$ -axis) are highlighted as well.

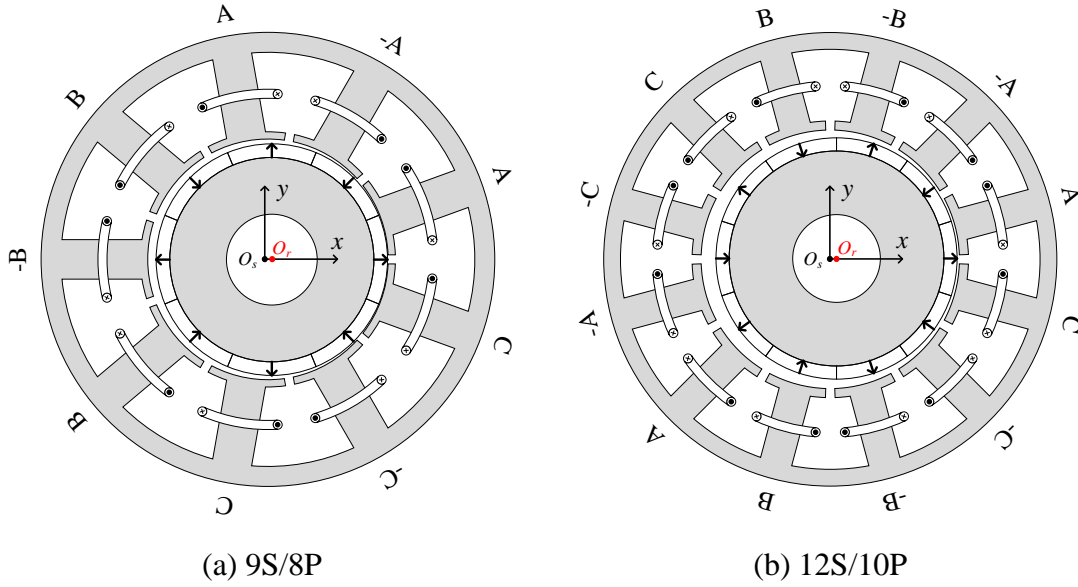


Fig. 2.1. Prototype machines.

TABLE 2.1 PROTOTYPE MACHINE PARAMETERS

Machines ( $N_s/2p$ )	9/8	12/10
Axial length (mm)		50
Stator outer diameter (mm)		100
Slot opening (mm)		2
Nominal air-gap length (mm)		1
PM thickness (mm)		3
PM remanence (T)		1.2
PM relative permeability		1.05
Pole arc to pole pitch ratio		1
PM magnetisation		parallel
Rated current (A)		7.07
Turns per phase	126	132
Stator bore diameter (mm)	53	57
Tooth body width (mm)	8.7	7.1
Stator yoke height (mm)	4.4	3.7

## 2.2 Employment Process of the Proposed Superposition Method

The use of the proposed superposition method is made up of several important steps. The following subsections will illustrate it in detail.

### 2.2.1 Establishment of Different Concentric Machine Models

In order to easily explain the process of employing the proposed method, a 9-slot/8-pole PM machine is chosen as example. To start with, the original eccentric machine will be split into a number of equal spread range sections along the air-gap circumference. The reference point is fixed at the rotor geometry centre under such condition, as shown in Fig. 2.2(a). The section number ( $N$ ) is crucial to the accuracy of the results for this method, since it affects the expression of air-gap eccentricity effect. The detailed investigation of the section number influence on the cogging torque and UMF will be shown later and it is the same as the slot number here for easy understanding, which could guarantee the accurate consideration of the slotting effect. For each section shown in Fig. 2.2(a), the equivalent air-gap length ( $g_{ei}$ ) can be calculated by equation (2.1). The sample points which are used to determine the equivalent air-gap length are set at the centre of the slot opening for simplicity. Considering the structure parameters shown in Fig. 1.3 and the machine model shown in Fig. 2.2(a),  $g_{ei}$  can be expressed as follows:

$$g_{ei} = \sqrt{R_s^2 + \varepsilon^2 - 2R_s\varepsilon \cos(\alpha_i - \chi\omega_r t - \theta_0)} - R_m \quad (2.1)$$

$$i = 1, 2, \dots, N_s$$

where  $R_s$  is the stator inner radius;  $R_m$  is the rotor outer radius;  $\alpha_i$  is the  $i^{\text{th}}$  slot opening centre angular position;  $\omega_r$  is the rotor angular speed;  $\theta_0$  is the rotor initial position and  $\chi$  represents the type of eccentricity. When  $\chi$  equals zero, it means this is static eccentricity. If  $\chi$  is one, it is the rotating eccentricity situation. It can be judged from the equation (2.1) that the equivalent air-gap length of each section with static eccentricity will be constant and they will vary with the rotor position for rotating eccentricity case. Besides the equivalent air-gap length of each section, the slot opening angular position needs modifying under rotor reference frame due to the eccentricity influence. It is clear that the distribution of slots is not uniform any more under rotor eccentricity condition. The angular position of each slot opening ( $\varphi_i$ ) under rotor reference can be calculated by the equation (2.2).

$$\varphi_i = \arctan\left(\frac{R_s \sin \alpha_i - \varepsilon \sin(\chi\omega_r t + \theta_0)}{R_s \cos \alpha_i - \varepsilon \cos(\chi\omega_r t + \theta_0)}\right) \quad (2.2)$$

Equation (2.2) also shows that the slot opening angular positions will be fixed under static eccentricity, while they will change with the time for rotating eccentricity

situation. Other stator structure parameters, such as slot opening width, tooth tip height, slot region width and slot region depth, as well as the whole rotor are kept the same as the original eccentric machine. According to Fig. 2.2(a), three highlighted sections are used to show the establishment of the corresponding concentric machine models which are given in Figs. 2.2(b), (c) and (d). It can be clearly seen that these concentric machine models have different air-gap lengths. Each section performance of the original eccentric machine is approximately considered to be the same as the corresponding sections in concentric machines, as the dashed lines plotted in Fig. 2.2.

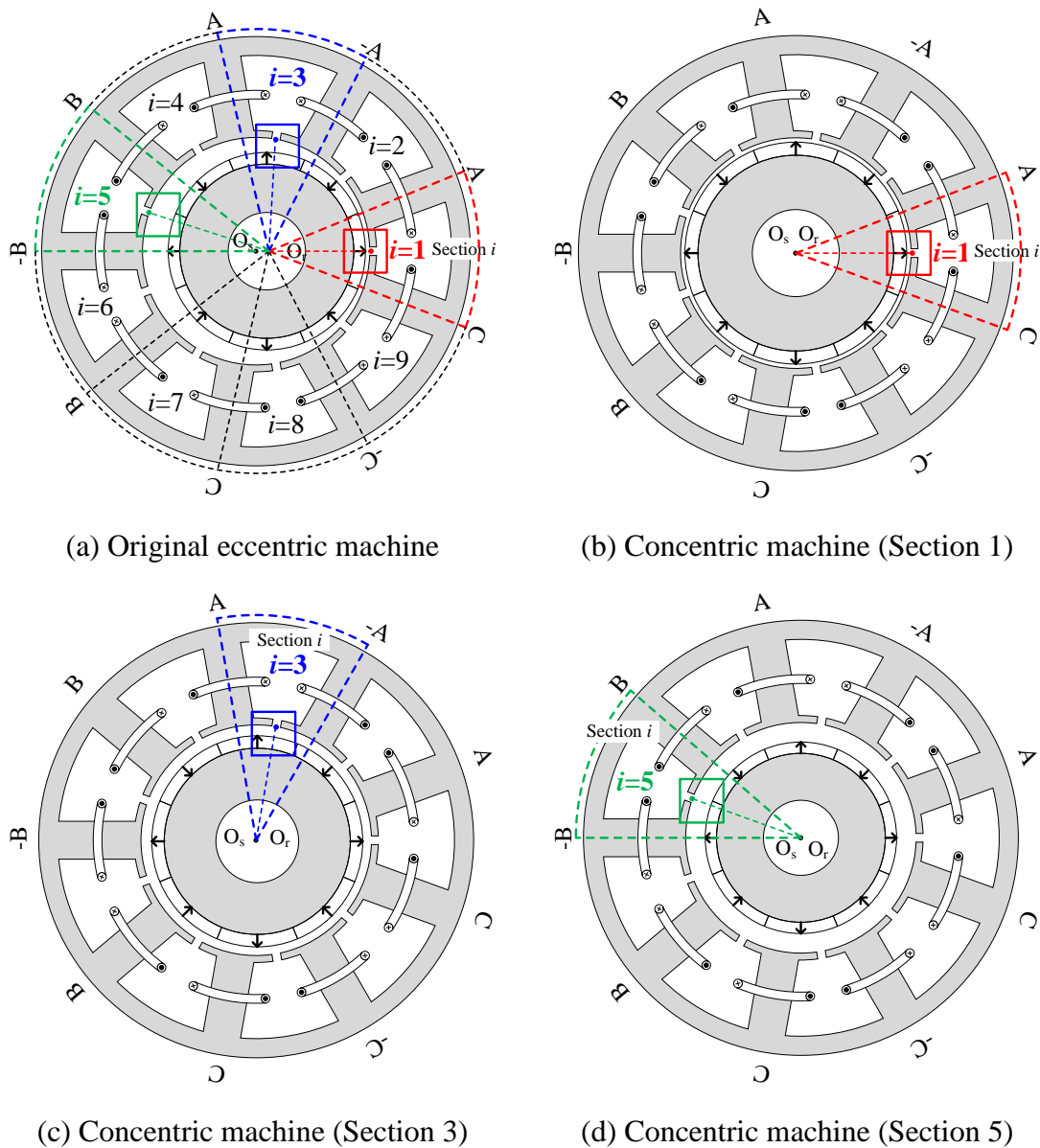


Fig. 2.2. Establishment of different concentric machine models.

## 2.2.2 Air-gap Flux Densities of Concentric Machines Prediction by Subdomain Method

When a series of concentric machine models are build up, their electromagnetic performance can be predicted by subdomain method. Both PM and armature fields must be considered. Therefore, the current density distribution in each slot should be incorporated into the analytical model. The cross-section of 9-slot/8-pole PM machine used for magnetic field calculation under on-load condition is shown in Fig. 2.3.

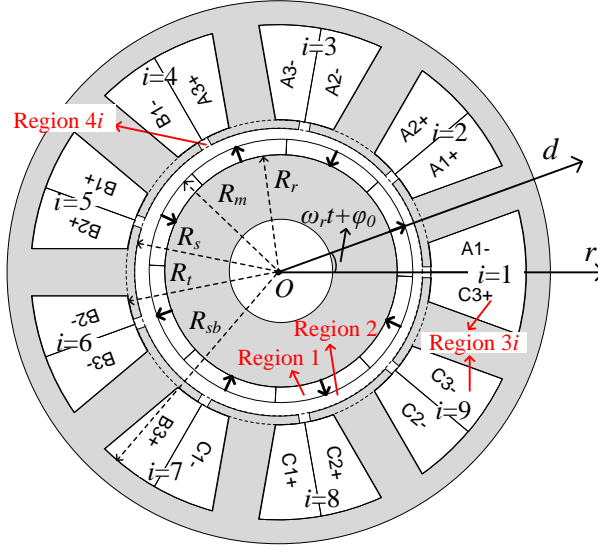


Fig. 2.3. Subdomain model for 9-slot/8-pole PM machine.

The machine model consists of four subdomains, viz. PM, air-gap, slot opening and slot body regions, respectively. The complete subdomain model accounting for slotting and on-load effect can be found in [WU11]. The content which is closely related to the proposed method in this chapter is briefly summarised. Before applying the subdomain method, several assumptions need to be addressed: (1) The permeability of all iron core parts is infinite, viz. neglecting saturation effect; (2) The demagnetisation curve of PM is linear; (3) The influence of PM reaction field due to eddy current is ignored. According to the basic electromagnetic field equations in cylinder reference frame and the assumptions mentioned above, the vector potential of PM region ( $A_{z1}$ ) fulfils the following formula:

$$\frac{\partial^2 A_{z1}}{\partial r^2} + \frac{1}{r} \frac{\partial A_{z1}}{\partial r} + \frac{1}{r^2} \frac{\partial^2 A_{z1}}{\partial \alpha^2} = -\frac{\mu_0}{r} (M_\alpha - \frac{\partial M_r}{\partial \alpha}) \quad (2.3)$$

where  $r$  and  $\alpha$  are the radial and circumferential coordinates, respectively;  $\mu_0$  is the permeability of air;  $M_r$  and  $M_\alpha$  are the radial and circumferential components of PM magnetisation, respectively.

$$M_r = \sum_{k=1,3,5,\dots} M_{rck} \cos k\alpha + M_{rsk} \sin k\alpha \quad (2.4)$$

$$M_\alpha = \sum_{k=1,3,5,\dots} M_{ack} \cos k\alpha + M_{ask} \sin k\alpha \quad (2.5)$$

$$M_{rck} = M_{rk} \cos(k\omega_r t + k\alpha_0) \quad (2.6)$$

$$M_{rsk} = M_{rk} \sin(k\omega_r t + k\alpha_0) \quad (2.7)$$

$$M_{ack} = -M_{ak} \sin(k\omega_r t + k\alpha_0) \quad (2.8)$$

$$M_{ask} = M_{ak} \cos(k\omega_r t + k\alpha_0) \quad (2.9)$$

For parallel magnetisation pattern:

$$M_{rk} = (B_{rem}/\mu_0)\alpha_p (A_{1k} + A_{2k}) \quad k/p = 1, 3, 5, \dots \quad (2.10)$$

$$M_{ak} = (B_{rem}/\mu_0)\alpha_p (A_{1k} - A_{2k}) \quad k/p = 1, 3, 5, \dots \quad (2.11)$$

$$A_{1k} = \frac{\sin[(k+1)\alpha_p(\pi/2/p)]}{(k+1)\alpha_p(\pi/2/p)} \quad (2.12)$$

$$A_{2k} = \frac{\sin[(k-1)\alpha_p(\pi/2/p)]}{(k-1)\alpha_p(\pi/2/p)} \quad (2.13)$$

where  $\alpha_0$  is the rotor initial position;  $B_{rem}$  is the PM remanence and  $\alpha_p$  is the pole-are to pole-pitch ratio. Considering that the tangential component of field intensity at rotor core outer radius is zero, the general solution of  $A_{z1}$  is:

$$A_{z1} = \sum_k [C_{1k} A_1 + C_{2k} M_{ack} - C_{3k} M_{rsk}] \cos(k\alpha) + \sum_k [C_{1k} C_1 + C_{2k} M_{ask} + C_{3k} M_{rck}] \sin(k\alpha) \quad (2.14)$$

$$C_{1k} = \left[ \left( \frac{r}{R_m} \right)^k + G_1 \left( \frac{r}{R_r} \right)^{-k} \right] \quad (2.15)$$

$$C_{2k} = \frac{\mu_0}{k^2 - 1} \left[ R_r k \left( \frac{r}{R_r} \right)^{-k} + r \right] \quad (2.16)$$

$$C_{3k} = \frac{\mu_0}{k^2 - 1} \left[ R_r \left( \frac{r}{R_r} \right)^{-k} + kr \right] \quad (2.17)$$



$$G_1 = (R_r/R_m)^k \quad (2.18)$$

where  $A_1, C_1$  are the coefficients to be determined;  $R_r$  is the rotor core outer radius and  $R_m$  is the rotor PM outer radius. For air-gap region, the vector potential  $A_{z2}$  satisfies:

$$\frac{\partial^2 A_{z2}}{\partial r^2} + \frac{1}{r} \frac{\partial A_{z2}}{\partial r} + \frac{1}{r^2} \frac{\partial^2 A_{z2}}{\partial \alpha^2} = 0 \quad (2.19)$$

The general solution of  $A_{z2}$  can be given:

$$\begin{aligned} A_{z2} = & \sum_k \left[ A_2 \left( \frac{r}{R_s} \right)^k + B_2 \left( \frac{r}{R_m} \right)^{-k} \right] \cos(k\alpha) \\ & + \sum_k \left[ C_2 \left( \frac{r}{R_s} \right)^k + D_2 \left( \frac{r}{R_m} \right)^{-k} \right] \sin(k\alpha) \end{aligned} \quad (2.20)$$

where  $A_2, B_2, C_2, D_2$  are the coefficients to be determined. For the  $i^{\text{th}}$  slot body region, the vector potential  $A_{z3i}$  satisfies:

$$\frac{\partial^2 A_{z3i}}{\partial r^2} + \frac{1}{r} \frac{\partial A_{z3i}}{\partial r} + \frac{1}{r^2} \frac{\partial^2 A_{z3i}}{\partial \alpha^2} = -\mu_0 J \quad (2.21)$$

where  $J$  represents the current density distribution of the  $i^{\text{th}}$  slot region. Since non-overlapping all stator tooth wound winding is adopted for 9-slot/8-pole PM machine, a general current density distribution for the  $i^{\text{th}}$  slot is shown in Fig. 2.4.

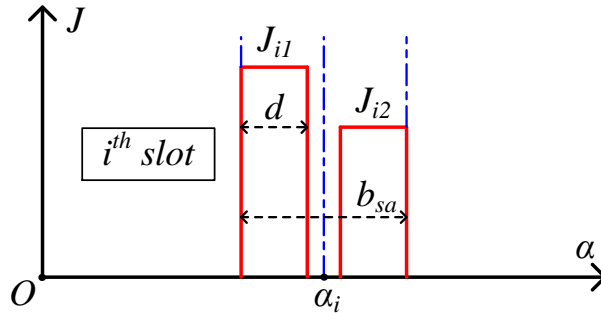


Fig. 2.4. Current density distribution of the  $i^{\text{th}}$  slot.

In Fig. 2.4,  $d$  is the equivalent winding width of one coil;  $b_{sa}$  is the slot region width;  $\alpha_i$  is the  $i^{\text{th}}$  slot angular position and  $J_{i1}, J_{i2}$  are the current density of two coils in one slot region, respectively.  $J$  can be expanded into Fourier series in the range of the slot region width:

$$J = J_{i0} + \sum_n J_{in} \cos[E_n(\alpha + b_{sa}/2 - \alpha_i)] \quad \text{for} \quad \alpha_i - b_{sa}/2 < \alpha < \alpha_i + b_{sa}/2 \quad (2.22)$$

$$J_{i0} = (J_{i1} + J_{i2})d/b_{sa} \quad (2.23)$$

$$J_{in} = \frac{2}{n\pi} (J_{i1} + J_{i2} \cos n\pi) \sin(n\pi d/b_{sa}) \quad (2.24)$$

$$E_n = n\pi/b_{sa} \quad (2.25)$$

Considering the boundary condition that the tangential field intensity of the slot bottom and both sides of the slot region are zero, the general solution of  $A_{z3i}$  can be expressed as:

$$A_{z3i} = A_0 + \sum_n A_n \cos[E_n (\alpha + b_{sa}/2 - \alpha_i)] \quad (2.26)$$

$$A_0 = \mu_0 J_{i0} (2R_{sb}^2 \ln r - r^2) / 4 + Q_{3i} \quad (2.27)$$

$$A_n = D_{3i} \left[ G_3 \left( \frac{r}{R_{sb}} \right)^{E_n} + \left( \frac{R_{sb}}{r} \right)^{E_n} \right] + \mu_0 \frac{J_{in}}{E_n^2 - 4} \left[ r^2 - \frac{2}{E_n} R_{sb}^2 \left( \frac{r}{R_{sb}} \right)^{E_n} \right] \quad (2.28)$$

$$G_3 = (R_t/R_{sb})^{E_n} \quad (2.29)$$

where  $Q_{3i}$  and  $D_{3i}$  are the coefficients to be determined;  $R_{sb}$  is the slot bottom radius and  $R_t$  is the tooth tip radius. For the  $i^{\text{th}}$  slot opening region, the vector potential  $A_{z4i}$  satisfies:

$$\frac{\partial^2 A_{z4i}}{\partial r^2} + \frac{1}{r} \frac{\partial A_{z4i}}{\partial r} + \frac{1}{r^2} \frac{\partial^2 A_{z4i}}{\partial \alpha^2} = 0 \quad (2.30)$$

Accounting for the boundary condition that the field intensity of both slot opening sides equals zero, the general solution of  $A_{z4i}$  can be expressed as:

$$A_{z4i} = D \ln r + Q_{4i} + \sum_m \left[ C_{4i} \left( \frac{r}{R_t} \right)^{F_m} + D_{4i} \left( \frac{r}{R_s} \right)^{-F_m} \right] \cos[F_m (\alpha + b_{oa}/2 - \alpha_i)] \quad (2.31)$$

$$F_m = m\pi/b_{oa} \quad (2.32)$$

where  $D$ ,  $Q_{4i}$ ,  $C_{4i}$  and  $D_{4i}$  are the coefficients to be determined;  $b_{oa}$  is the slot opening width. In order to determine the coefficients in above equations, the interface conditions between any two regions I and II should be considered:

$$A_I = A_{II} \quad \text{and} \quad B_{I\alpha} = B_{II\alpha} \quad (2.33)$$

Combining the equations from (2.3) to (2.33) and incorporating all of the equations with the coefficients to be determined into a matrix, then all of the unknown coefficients can be easily obtained and the vector potential of each subdomain will be acquired. The flux density can be predicted based on:

$$B_r = \frac{1}{r} \frac{\partial A_z}{\partial \alpha} \quad \text{and} \quad B_\alpha = -\frac{\partial A_z}{\partial r} \quad (2.34)$$

where  $B_r$  and  $B_\alpha$  are the radial and circumferential air-gap flux densities of the corresponding region, respectively. Since the air-gap flux density is crucial to electromagnetic performance prediction, only its two components are shown as follows:

$$B_{2r} = -\sum_k \left[ \frac{A_2}{R_s} \left( \frac{r}{R_s} \right)^{k-1} + \frac{B_2}{R_m} \left( \frac{r}{R_m} \right)^{-k-1} \right] \sin(k\alpha) \\ + \sum_k k \left[ \frac{C_2}{R_s} \left( \frac{r}{R_s} \right)^{k-1} + \frac{D_2}{R_m} \left( \frac{r}{R_m} \right)^{-k-1} \right] \cos(k\alpha) \quad (2.35)$$

$$B_{2\alpha} = -\sum_k \left[ \frac{A_2}{R_s} \left( \frac{r}{R_s} \right)^{k-1} - \frac{B_2}{R_m} \left( \frac{r}{R_m} \right)^{-k-1} \right] \cos(k\alpha) \\ - \sum_k k \left[ \frac{C_2}{R_s} \left( \frac{r}{R_s} \right)^{k-1} - \frac{D_2}{R_m} \left( \frac{r}{R_m} \right)^{-k-1} \right] \sin(k\alpha) \quad (2.36)$$

### 2.2.3 Air-gap Flux Density Synthesis of the Original Eccentric Machine

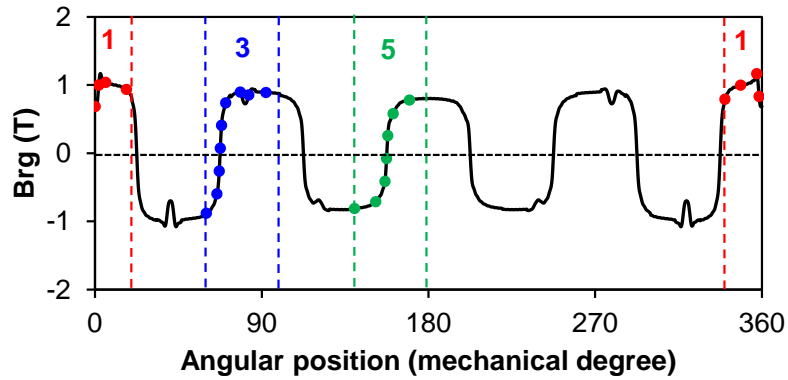
The air-gap flux density of the original eccentric machine can be synthesised from these obtained air-gap flux densities of each concentric machine:

$$B_{rg} = B_{2ri}, \quad \alpha_{is} < \alpha < \alpha_{ie} \quad (2.37)$$

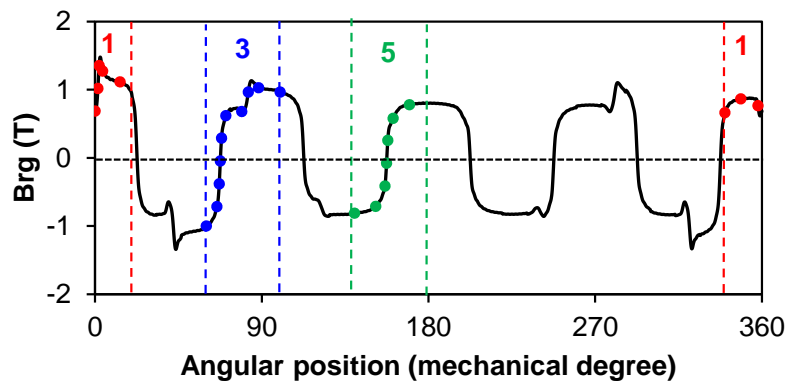
$$B_{\alpha g} = B_{2ai}, \quad \alpha_{is} < \alpha < \alpha_{ie} \quad (2.38)$$

where  $B_{rg}$ ,  $B_{\alpha g}$  are the radial and tangential components of the air-gap flux density corresponding to the original eccentric machine, respectively;  $B_{2ri}$ ,  $B_{2ai}$  are the radial and tangential air-gap flux densities corresponding to the  $i^{\text{th}}$  eccentric machine, respectively;  $\alpha_{is}$ ,  $\alpha_{ie}$  are the start and end angular position of the  $i^{\text{th}}$  section, respectively. Since the current density can be zero for equation (2.21), it means both open-circuit and on-load magnetic field can be obtained by the same model. The waveforms of air-gap flux densities under both open-circuit and on-load conditions are shown in Fig. 2.5. The eccentricity ratio ( $ER$ ), which is used to indicate the extent of eccentricity, is defined as the ratio of the eccentricity magnitude to the rated air-gap length and could change from zero to one. In Fig. 2.5, the solid line is the synthesised air-gap flux density and those dots represent the contribution of three sample sections,

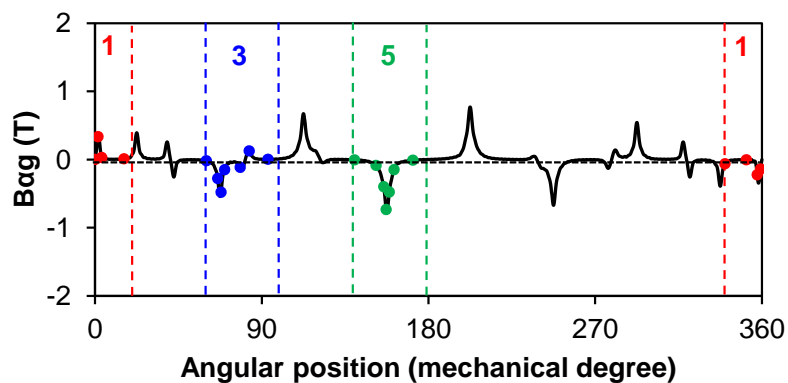
while the numbers represent the corresponding sections. Based on Fig. 2.2(a), it can be seen that each section occupies 40 degree range along the circumference. The section 1 spreads form -20 to 20 degree. Since the machine has mechanical periodic property per 360 degrees, the air-gap flux density of section 1 is divided into two parts in Fig. 2.5, viz. from 0 to 20 degree combining with 340 to 360 degree.



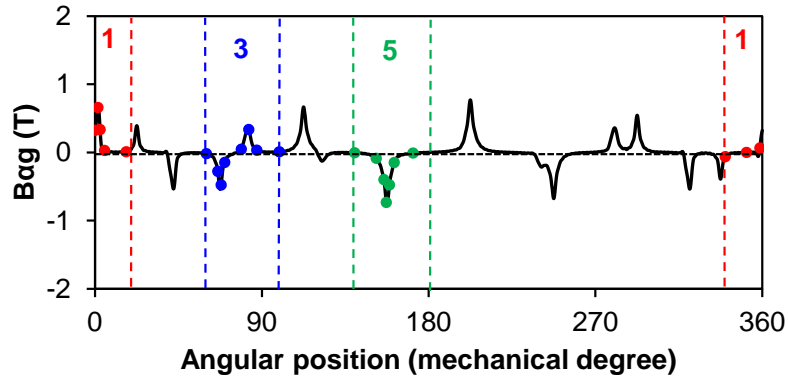
(a)  $B_{rg}$  (Open-circuit with 0.5 eccentricity ratio)



(b)  $B_{rg}$  (On-load with 0.5 eccentricity ratio)



(c)  $B_{ag}$  (Open-circuit with 0.5 eccentricity ratio)



(d)  $B_{ag}$  (On-load with 0.5 eccentricity ratio)

Fig. 2.5. Synthesised air-gap flux density for different load conditions (9-slot/8-pole PM machine).

Figs. 2.5(a) and (c) show that the radial component of air-gap flux density is distorted due to rotor eccentricity, with the magnitude decreasing from the minimum air-gap length to the maximum value. The influence of different load conditions can be observed by comparing Figs. 2.5(a) and (c) for radial component and Figs. 2.5(b) and (d) for circumferential component. An evident difference can be seen, which could lead to different performance.

## 2.2.4 Summary of the Proposed Method

Based on the above description, the process of employing the proposed superposition method to predict the air-gap field of PM machines with rotor eccentricity is summarised in Fig. 2.6 for further clarity.

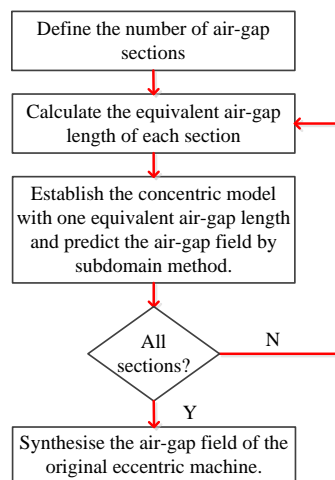


Fig. 2.6. Procedure of employing the proposed superposition method.

## 2.3 Cogging Torque

Cogging torque is one of the most important issues in permanent magnet (PM) machines since it may cause undesirable torque ripple and generate noise and vibration [ACK92], [JAH96]. Although there are potential unbalanced magnetic forces, the cogging torque of PM machines having slot/pole numbers differed by one are negligible theoretically [ZHU09a]. However, it is impossible to eliminate the influence of manufacture tolerance in real applications. All of the non-ideal factors, such as magnet property variation [ISL04], machine dimension and assembly position shift [GAS09], [GAS13], rotor eccentricities [HWA01], [KIM05a], [YOO05], [HSI13], etc., may cause the obvious increase of cogging torque. The employment of the proposed superposition method will be shown in this subsection.

### 2.3.1 Prediction Principle

The cogging torque can be predicted by the integral of Maxwell stress tensor based on the air-gap flux density [ZHA13b]:

$$T_{cogg} = \frac{l_a r^2}{\mu_0} \int_0^{2\pi} B_{rg} B_{\alpha g} d\alpha \quad (2.39)$$

where  $B_{rg}$  and  $B_{\alpha g}$  are the radial and tangential components of the air-gap flux density, respectively;  $l_a$  is the axial length of the machine and  $r$  is the radius applying integral operation. For the proposed superposition method stated in this chapter, the equation (2.39) needs to be modified accordingly since the air-gap flux density of the original eccentric machine is composed of  $N$  sections.

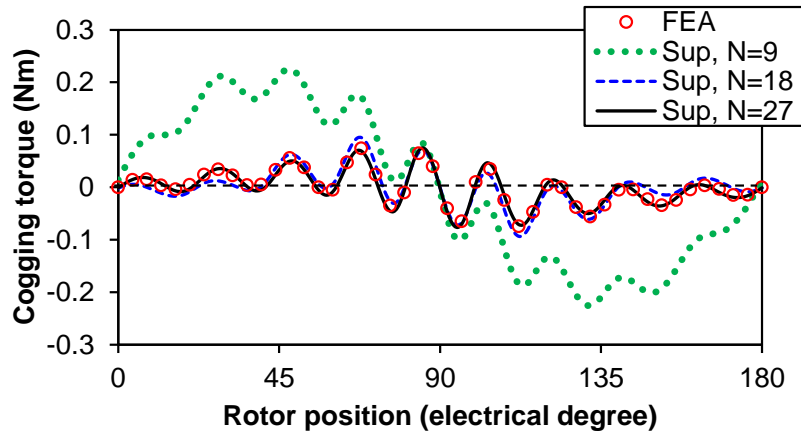
$$T_{cogg} = \frac{l_a r^2}{\mu_0} \sum_{i=1}^N \int_{\alpha_{si}}^{\alpha_{ei}} B_{ri} B_{\alpha i} d\alpha \quad (2.40)$$

In order to clearly show the difference between the results obtained by two methods (the proposed method and FEA), only the cogging torque in one period will be given. According to the existing paper [GAS09], the cogging torque periods for static and rotating eccentricities ( $\theta_{cogse}$  and  $\theta_{cogre}$  respectively) are:

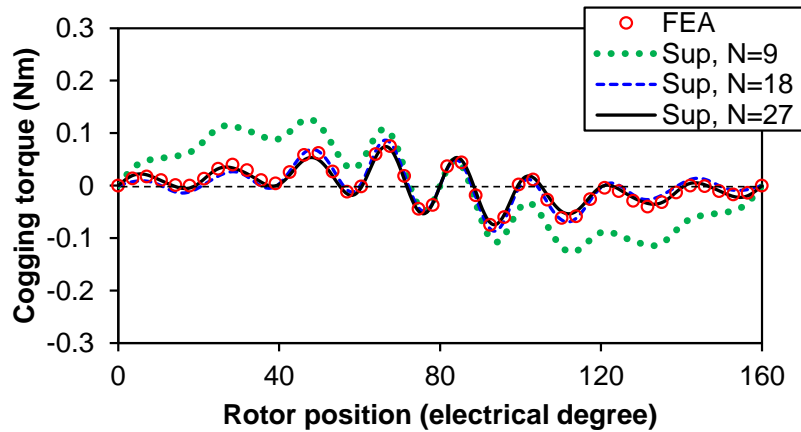
$$\theta_{cogse} = 360/2p \quad (2.41)$$

$$N_{cogre} = 360/N_s \quad (2.42)$$

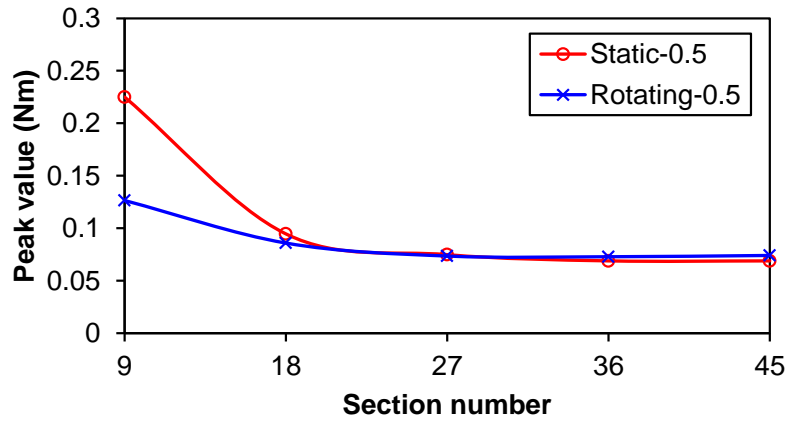
Figs. 2.7(a) and (b) show the cogging torque waveforms obtained from 9 sections for static and rotating eccentricities by the proposed method (legend ‘Sup’), respectively. By comparing them with FEA results (legend ‘FEA’), it is clear that this section number is inappropriate. It is necessary to investigate the influence of section number on cogging torque prediction under static and rotating eccentricity conditions, which has been mentioned in the former analysis. Figs. 2.7 and 2.8 show the section number influence on 9-slot/8-pole and 12-slot/10-pole PM machines, respectively.



(a) Waveforms for static eccentricity with 0.5 eccentricity ratio

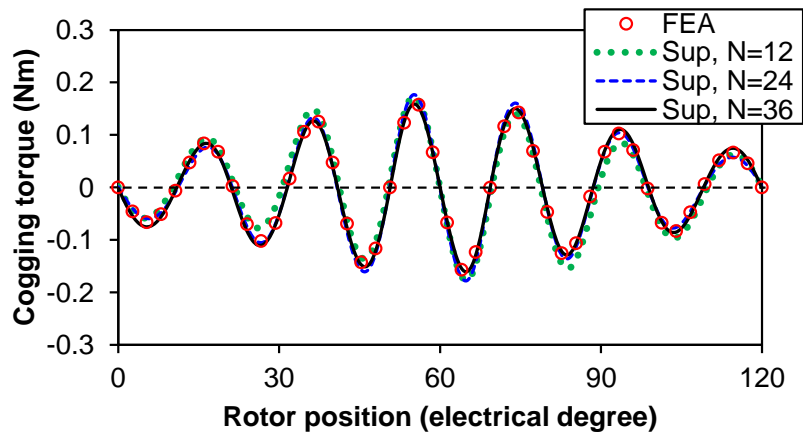


(b) Waveforms for rotating eccentricity with 0.5 eccentricity ratio

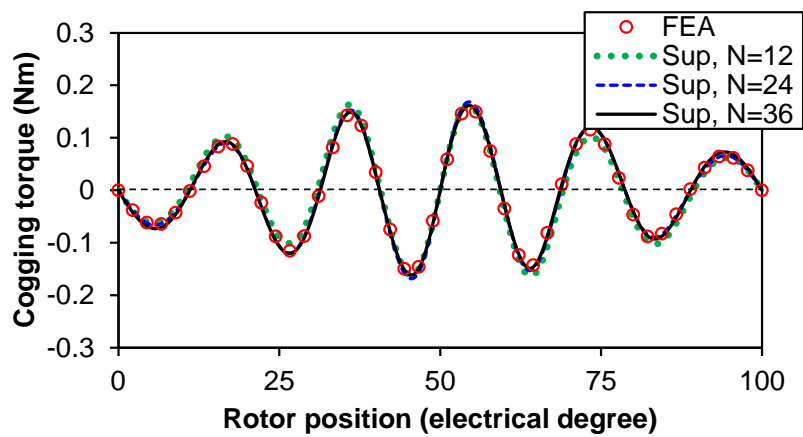


(c) Influence of section number

Fig. 2.7. Influence of section number on 9-slot/8-pole PM machine.

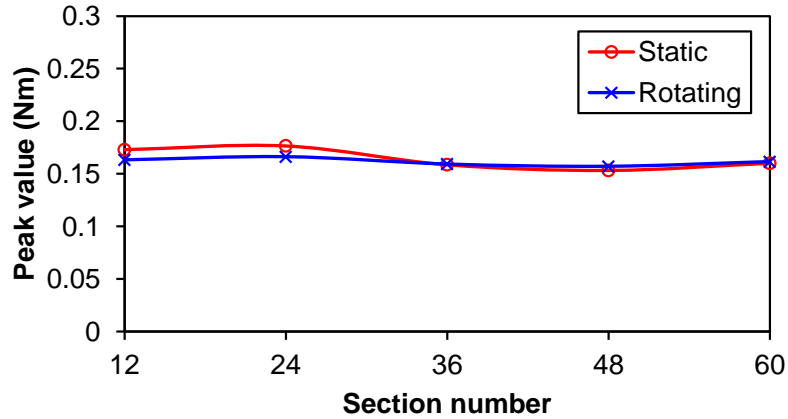


(a) Waveforms for static eccentricity with 0.5 eccentricity ratio



(b) Waveforms for rotating eccentricity with 0.5 eccentricity ratio





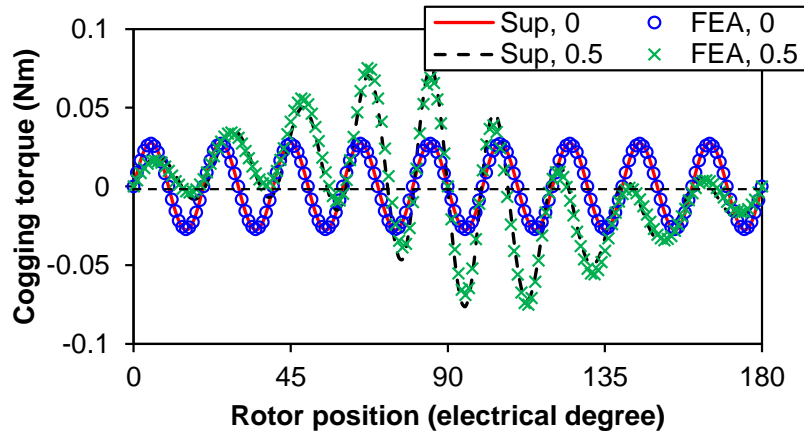
(c) Influence of section number

Fig. 2.8. Influence of section number on 12-slot/10-pole PM machine.

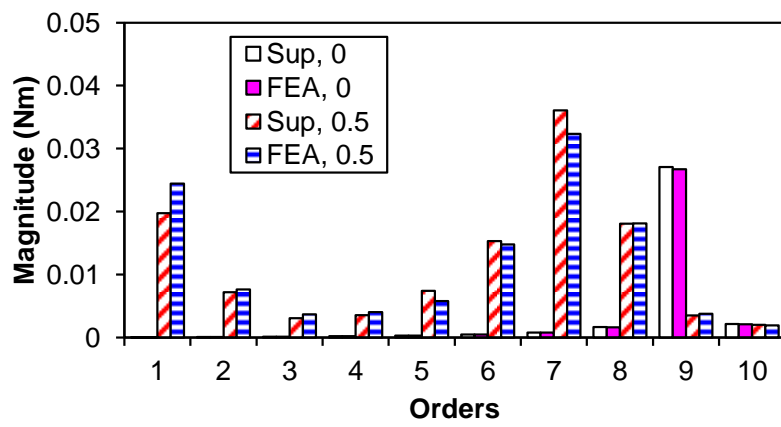
Both Figs. 2.7(a) and (b) show that when the section number is three times of the slot number, the waveforms predicted by two different methods could match well for 9-slot/8-pole PM machine. To be much clearer, Fig. 2.7(c) plots the variation of the cogging torque peak value with the section number. It is clear that the cogging torque peak value will hardly vary if the section number is bigger than 27 (three times of the slot number) for this machine. By contrast, Figs. 2.8(a) and (b) demonstrate that the results could be acceptable when the section number is chosen as the slot number for 12-slot/10-pole PM machine if the tolerance is not very strict. This is an advantage for this machine. Fig. 2.8(c) also shows the change of the cogging torque peak value with the section number under static and rotating eccentricity conditions. It almost does not change when the section number equals three times of the slot number as well. By comparing Figs. 2.7 and 2.8, it can be found that the section number used for predicting the cogging torque by the proposed method could be lower if the cyclic symmetry number, which is the highest common divisor between slot and pole numbers, is higher.

### 2.3.2 Finite Element Validation

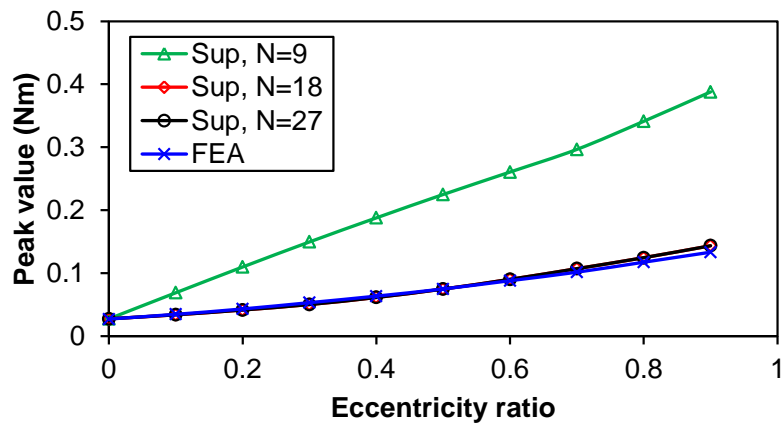
Figs. 2.9 and 2.10 show the cogging torque of 9-slot/8-pole PM machine with static and rotating eccentricities, respectively.



(a) Waveforms (N=27)

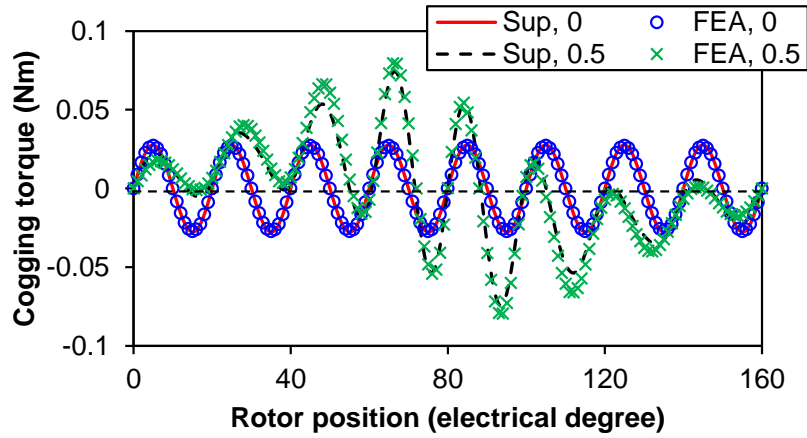


(b) Harmonics (N=27)

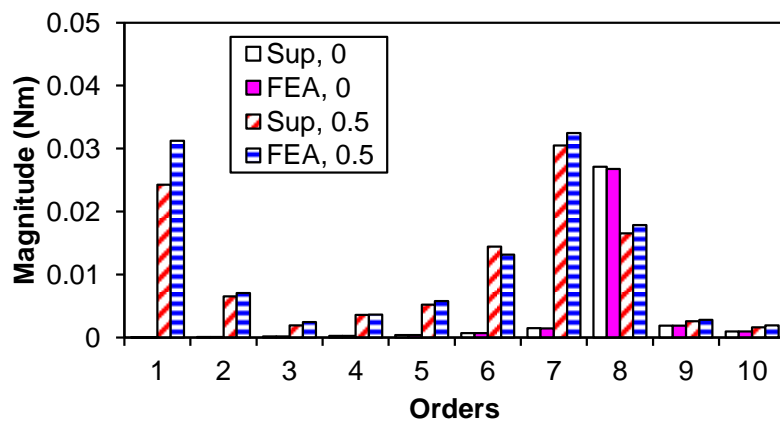


(c) Influence of eccentricity ratio

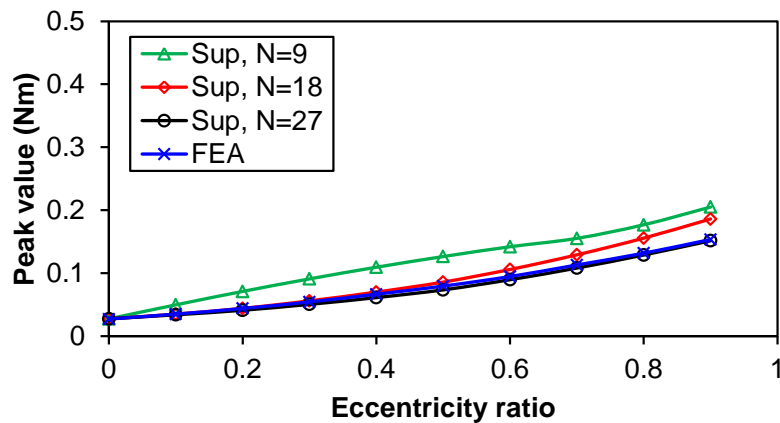
Fig. 2.9. 9-slot/8-pole PM machine with static eccentricity.



(a) Waveforms (N=27)



(b) Harmonics (N=27)



(c) Influence of eccentricity ratio

Fig. 2.10. 9-slot/8-pole PM machine with rotating eccentricity.

The good match of waveforms shown in Figs. 2.9(a) and 2.11(a) validates the effectiveness of the proposed method and the reasonable selection of section number. When the eccentricity ratio of the machine is zero, it could be thought of as a special

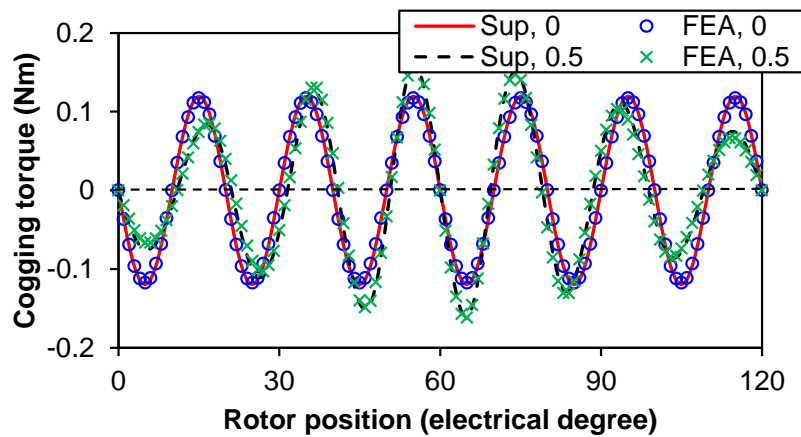
case for rotor eccentricity. The corresponding harmonics shown in Figs. 2.9(b) and 2.10(b) could more clearly show the components change due to the eccentricity effect. If the machine is concentric, the cogging torque period ( $\theta_{cog}$ ) is [ZHU09a]:

$$\theta_{cog} = 360 / LCM(2p, N_s) \quad (2.43)$$

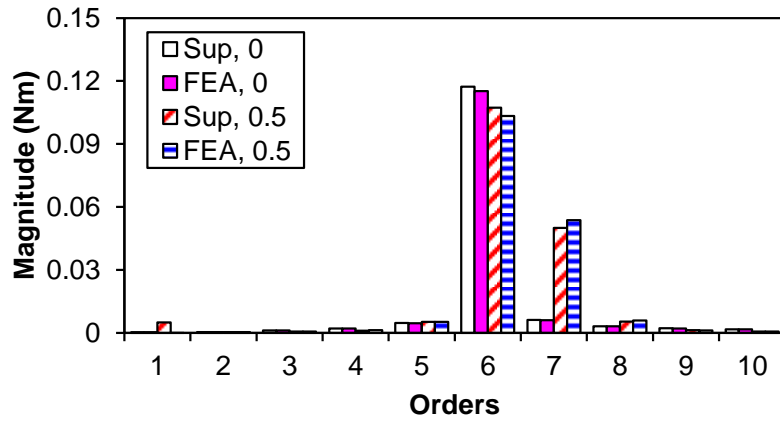
where  $LCM$  means least common multiple. Therefore, the 9<sup>th</sup> harmonic cogging torque is the fundamental component for 9-slot/8-pole PM machine over one pole pitch in this scenario. However, the fundament component will be the 1<sup>st</sup> for static eccentricity. Other harmonic cogging torque components will appear and they will obviously change the waveform of the cogging torque. Similarly, the 8<sup>th</sup> harmonic cogging torque is the fundamental component over one slot pitch for concentric machine, whereas it is the 1<sup>st</sup> component that becomes the fundamental one for rotating eccentricity, as shown in Fig. 2.10(b). The rotating eccentricity will cause more harmonics as well. The generation mechanism of additional harmonic cogging torque components due to rotor eccentricity can be found in [ZHU14b]. Besides, it can be seen that the difference between two methods for 0.5 eccentricity ratio is larger than that for zero eccentricity ratio. This is owing to the approximation of the method. When the eccentricity ratio is zero, the method will be independent with the section number since it has degraded into the conventional subdomain method used for predicting concentric machine performance. However, if there is rotor eccentricity, the finite section number will not fully reconstruct the machine performance of the original eccentric machine, which results in a relative big computation error. Nevertheless, the accuracy of the proposed method could be acceptable. In order to be more convincing, Figs. 2.9(c) and 2.10(c) show the cogging torque peak value variations for both types of rotor eccentricities with different eccentricity ratios and three sections numbers, respectively. Since the machine cannot normally work if the eccentricity ratio reaches one, only the values between zero and 0.9 range are plotted. It is clear that the section number will affect the accuracy of the method if the machine has different eccentricity ratios. According the good agreement for the results obtained by two methods, it not only further verifies the efficacy of the proposed method, but also gives a guidance for selecting the section number to make sure the proposed method accurate (three times of the slot number).

Figs. 2.11 and 2.12 show the cogging torque of 12-slot/10-pole PM machine with static and rotating eccentricities, respectively. The waveforms shown in Figs. 2.11(a)

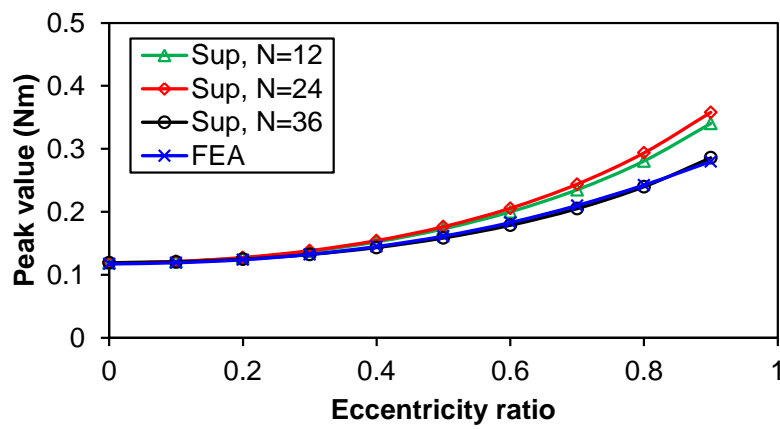
and 2.12(a) show that the influence of rotor eccentricity on cogging torque for this machine is not as obvious as that for 9-slot/8-pole PM machine. This is due to the additional harmonic components of cogging torque for this machine with two kinds of rotor eccentricities do not evidently increase like those for 9-slot/8-pole PM machine, as the corresponding FFT results shown in Figs. 2.11(b) and 2.12(b). This phenomenon can also be explained by the aforementioned concept-cyclic symmetry number. Since the cyclic symmetry number of 12-slot/10-pole PM machine is 2, it is more tolerant to the negative effect caused by rotor eccentricity. As has been known, if the cyclic symmetry is large enough, the rotor eccentricity will hardly affect the cogging torque. Both the results shown in Figs. 2.11(c) and 2.12(c) as well as those in Figs. 2.9(c) and 2.10(c) demonstrate that the cogging torque peak values for both static and rotating eccentricities are almost the same in the two machines no matter how big the eccentricity ratio is. Although the rotor eccentricity could lead to a larger cogging torque for PM machines, the cogging torque peak value for 9-slot/8-pole PM machine is always lower than that of 12-slot/10-pole PM machine when they have the same eccentricity ratio. Again, it can conclude that the three times of the slot number being chosen for the section number is more convincing for the application of the proposed method.



(a) Waveforms (N=36)

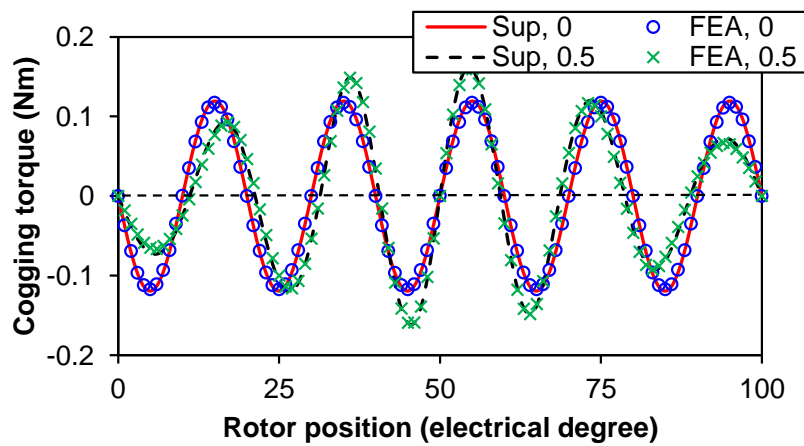


(b) Harmonics (N=36)

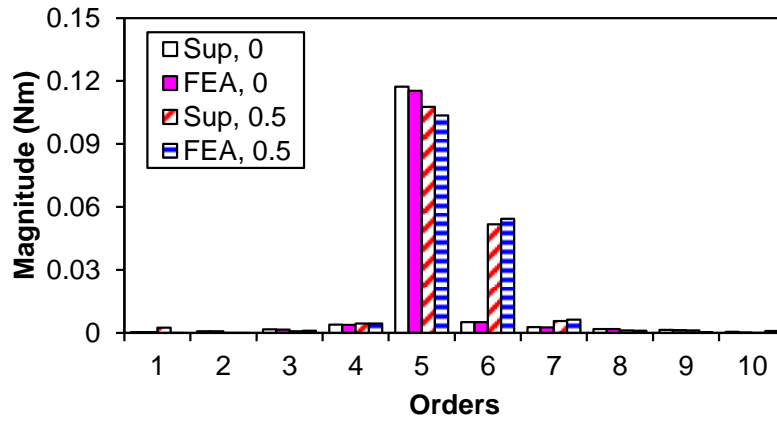


(c) Influence of eccentricity ratio

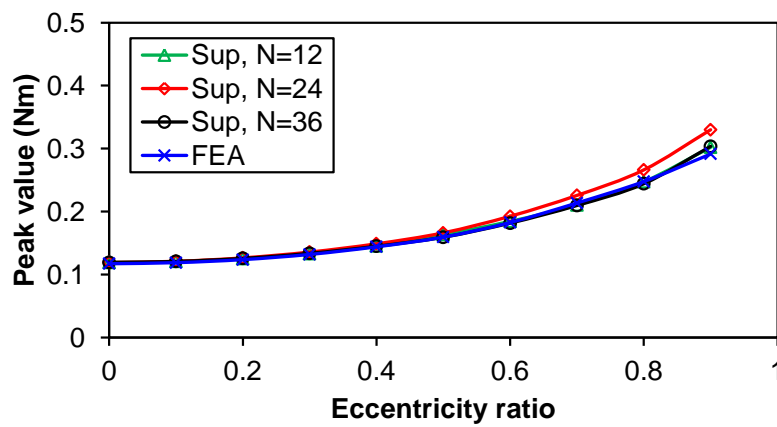
Fig. 2.11. 12-slot/10-pole PM machine with static eccentricity.



(a) Waveforms (N=36)



(b) Harmonics (N=36)



(c) Influence of eccentricity ratio

Fig. 2.12. 12-slot/10-pole PM machine with rotating eccentricity.

Overall, the proposed superposition method is effective and can be used to investigate the influence of rotor eccentricity on cogging torque, which is especially useful for PM machines having large slot/pole numbers, such as in low speed direct drive PM wind power generator application.

## 2.4 Unbalanced Magnetic Force

Unbalanced magnetic force (UMF) is one of the most important issues in permanent magnet (PM) machines with rotating asymmetric winding configurations, where the UMF is intrinsic [BI97], [JAN96]. When the rotating asymmetric machines with static/dynamic eccentricity, the UMF will evidently increase, which will decrease the machine performances and short bearing life [ZHU14b], [BI09]. Besides, the extrinsic UMF will appear in rotating symmetrical machines, if rotor eccentricity

exists. For these machines, there is ideally no UMF if the stator and rotor are concentric, whereas rotor eccentricity leads to the UMF for these machines and consequently deteriorate machine performances.

There are a vast number of papers investigating the UMF. The authors in [BI96] drew a useful conclusion on UMF generation mechanism that only two field harmonics differed by one can produce the UMF. The UMF of switched reluctance machines was analysed in [HUS00], where the influence of saturation and winding connections on UMF were addressed. The UMF of surface-mounted PM (SPM) machine was compared with that of interior PM (IPM) machine in [KIM01] and it found that IPM machine could suffer the higher UMF, especially under rotor eccentricity condition. The PM machine with Halbach array was analysed in [JAN03] and it verified that this kind of machine performs better on UMF even if it is with rotor eccentricity. In [KIM05a], 2D analytical model was adopted to predict the UMF, whereas it lacks validating armature field influence. The 2D permeance function obtained by conformal mapping was used in [LI07] to account for rotor eccentricity effect. However, the details are not clear. Paper [DOR10] emphasised that the demerit of consequent pole PM machine with rotor eccentricity (the much higher UMF than conventional PM machines). The authors in [DPR11a] did a comparison among PM machines having different slot/pole number combinations with static/dynamic eccentricity but some contents need more systematic explanations. An approximate analytical method was presented in [MIC14] to predict the UMF of a slotless PM machine. The effectiveness of this method used for machines with slots should be assessed.

The proposed superposition method is used to predict the UMF of PM machines with rotor eccentricities.

#### **2.4.1 Prediction Principle**

After obtaining the air-gap flux density, predicting the UMF of the original eccentric machine can be executed according to the following equations [BI97]:

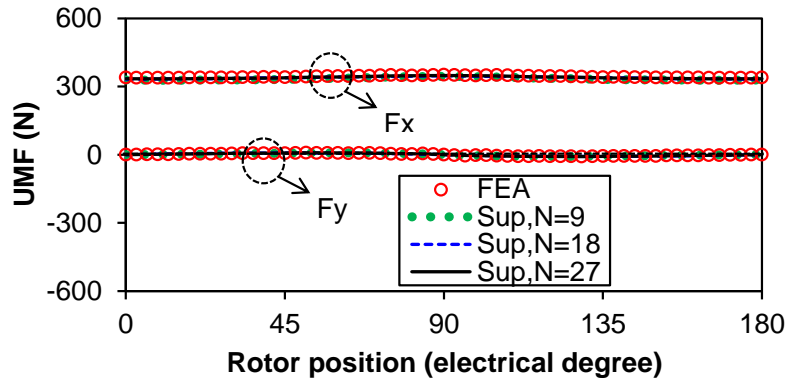


$$\begin{aligned}
F_x &= \frac{1}{2\mu_0} \int_0^{2\pi} [(B_{rg}^2 - B_{tg}^2) \cos \alpha - 2B_{rg} B_{tg} \sin \alpha] r_g d\alpha \\
F_y &= \frac{1}{2\mu_0} \int_0^{2\pi} [(B_{rg}^2 - B_{tg}^2) \sin \alpha + 2B_{rg} B_{tg} \cos \alpha] r_g d\alpha
\end{aligned} \tag{2.44}$$

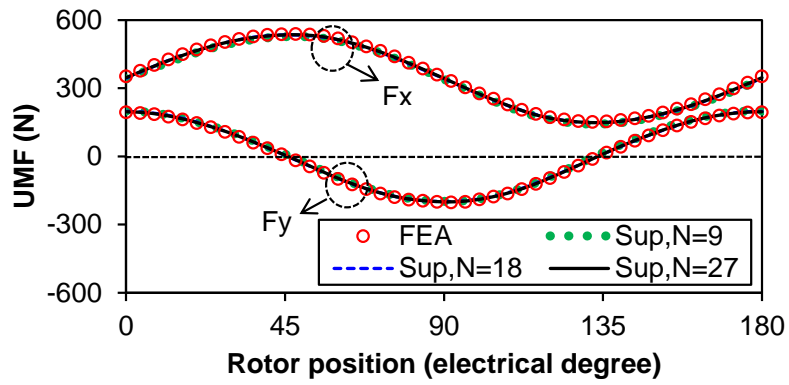
where  $F_x$ ,  $F_y$  are the  $x$  and  $y$  force components, respectively;  $l_a$  is the machine axial length and  $r_g$  is the integral radius for UMF, which is chosen at the centre of the air-gap. Since the air-gap flux density is synthesised from a number of sections, the equation needs to be discretised into the following form:

$$\begin{aligned}
F_x &= \frac{1}{2\mu_0} \sum_{i=1}^N \int_{\alpha_{is}}^{\alpha_{ie}} [(B_{rg}^2 - B_{tg}^2) \cos \alpha - 2B_{rg} B_{tg} \sin \alpha] r_g d\alpha \\
F_y &= \frac{1}{2\mu_0} \sum_{i=1}^N \int_{\alpha_{is}}^{\alpha_{ie}} [(B_{rg}^2 - B_{tg}^2) \sin \alpha + 2B_{rg} B_{tg} \cos \alpha] r_g d\alpha
\end{aligned} \tag{2.45}$$

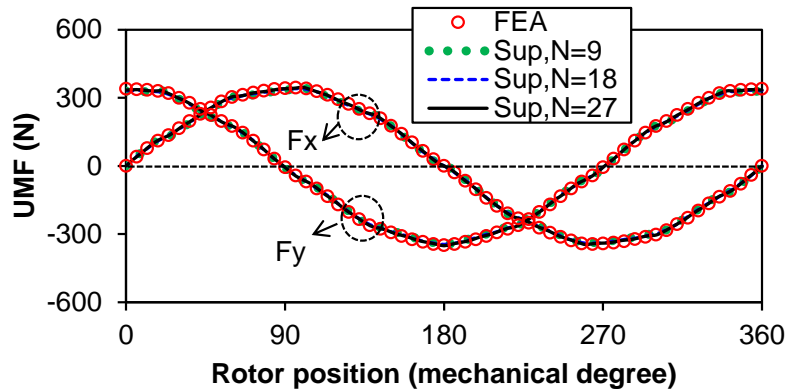
Equation (2.45) means that the UMF of the original eccentric machine is synthesised from the contribution of each concentric machine, which is the core part of the superposition method. Based on the equation (2.45), the results of UMF can be obtained. Since the section number can affect the cogging torque prediction accuracy, it will affect the accuracy of UMF calculation as well and its influence should be investigated. Theoretically, the section number can be chosen as any positive integer number, whereas it could be much better if a general guidance can be found. For the 9S/10P PM machine, it has the UMF even if it is under open-circuit condition. According to the analysis in [JAN96], this UMF comes from the interaction of PM magnetic field and the modulation of slotting effect, thus the slotting effect needs to be precisely considered for the sake of more accurate results. For simplicity, the section number can be chosen based on the slot number, which means it can be chosen as the integer times of the slot number. Fig. 2.13 shows the UMF waveform variation with the section number referring to the FEA result. Both static and dynamic eccentricity under either open-circuit or on-load condition are considered. The UMF under static and dynamic eccentricity will repeat per 360 electrical and mechanical degrees, respectively.



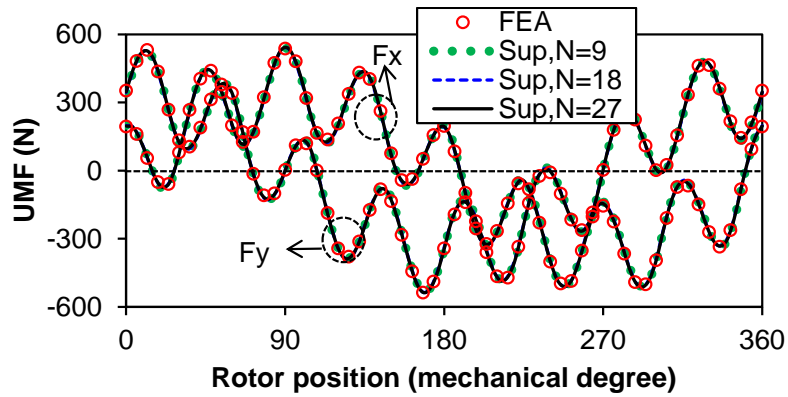
(a) Static eccentricity with 0.5 eccentricity ratio (Open-circuit)



(b) Static eccentricity with 0.5 eccentricity ratio (On-load)



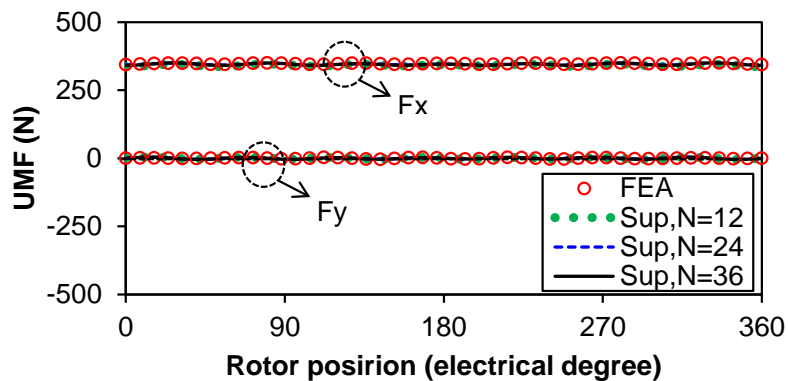
(c) Rotating eccentricity with 0.5 eccentricity ratio (Open-circuit)



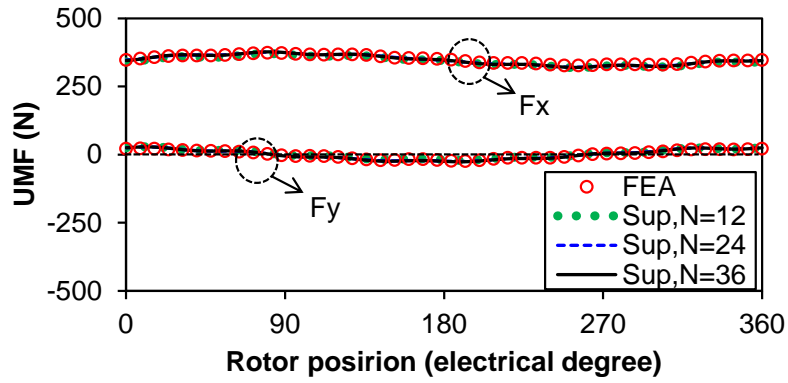
(d) Rotating eccentricity with 0.5 eccentricity ratio (On-load)

Fig. 2.13. Influence of section number on UMF waveforms (9-slot/8-pole PM machine).

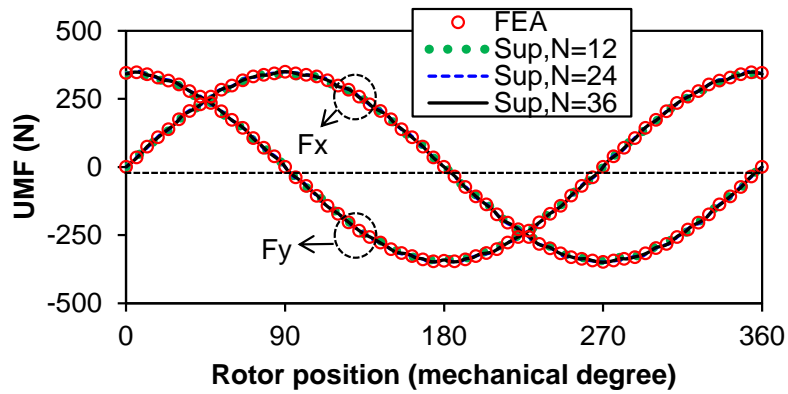
Fig. 2.13 shows that the UMF predicted by the improved superposition method compared with the FEA result is accurate enough, even if the section number equals the slot number. With the increase of the section number, the UMF waveforms will hardly change, which is not as sensitive as cogging torque. The results show the similar phenomenon no matter under open-circuit or on-load condition. Therefore, the section number is chosen as the twice of the slot number in the following analysis for this machine to guarantee both the accuracy and computation efficiency. Besides this kind of rotating asymmetric machine, the rotating symmetrical machine will also generate the UMF under rotor eccentricity condition, which is hardly noticed. The influence of section number on UMF for this kind of machine also needs investigation. Therefore, the waveforms of 12S/10P PM machine are shown in Fig. 2.14 similar to those of 9S/8P PM machine.



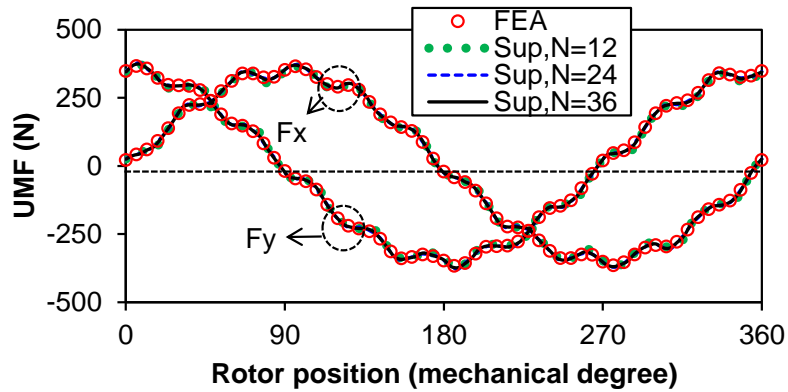
(a) Static eccentricity with 0.5 eccentricity ratio (Open-circuit)



(b) Static eccentricity with 0.5 eccentricity ratio (On-load)



(c) Rotating eccentricity with 0.5 eccentricity ratio (Open-circuit)



(d) Rotating eccentricity with 0.5 eccentricity ratio (On-load)

Fig. 2.14. Influence of section number on UMF waveforms (12-slot/10-pole PM machine).

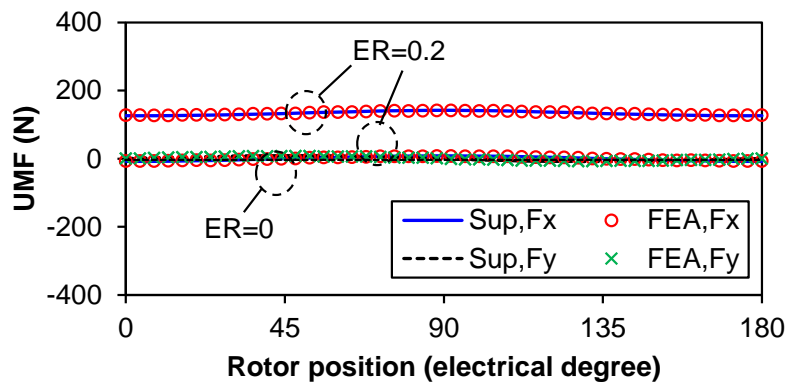
The phenomenon observed in Fig. 2.14 again shows that the section number does not have apparent effect on results. Thus, the section number is chosen to be twice of the slot number for this machine as well. According to the examples in this subsection,

it can be concluded that twice of the slot number is enough to obtain accurate UMF results. The detailed explanation of UMF waveforms will be shown later.

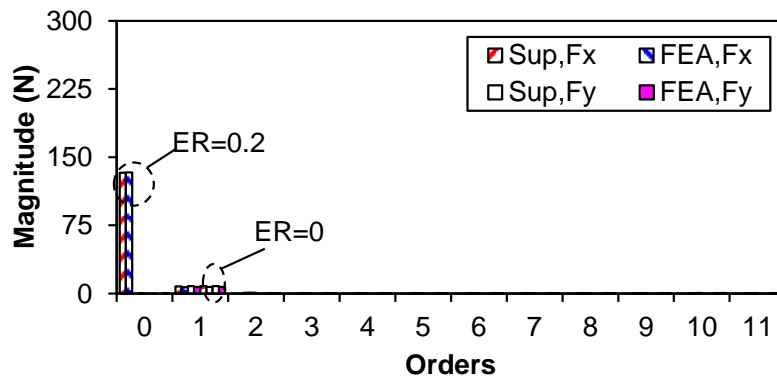
### 2.4.2 Finite Element Validation

In order to verify the effectiveness of the method, direct FEA is adopted. Since the case with 0.5  $ER$  has been used to investigate the influence of the section number and the waveforms obtained by two methods can match well, it will not be repeated again. In real applications, the 20% eccentricity is a normal case [CRO02]; therefore this conventional  $ER$  is chosen as example.

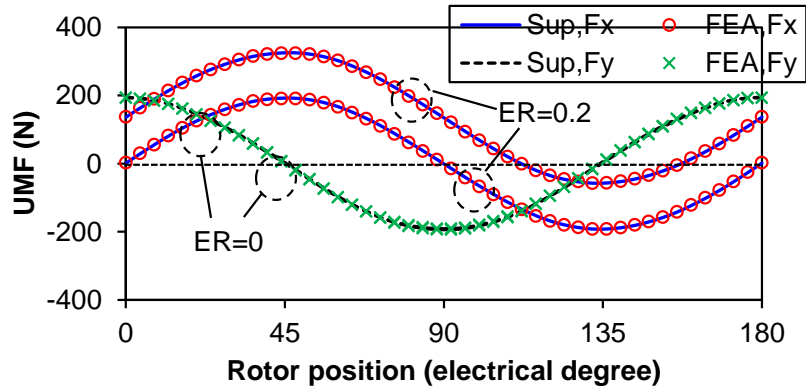
The waveforms and harmonics of the UMF of 9S/8P PM machine with 0.2  $ER$  are shown in Fig. 2.15 and 2.16 for static and dynamic eccentricity, respectively. As has been stated above, this machine possesses the intrinsic UMF even though it has no rotor eccentricity; therefore the results of concentric case are also presented. For more convincing comparison, both open-circuit and on-load situations are considered.



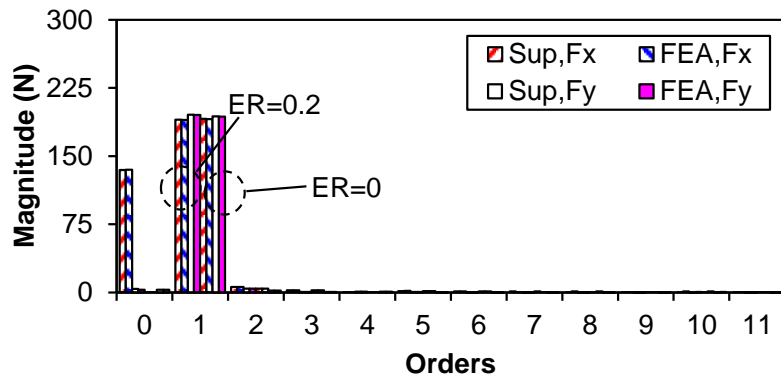
(a) Waveforms with 0.2 eccentricity ratio (Open-circuit)



(b) Harmonics with 0.2 eccentricity ratio (Open-circuit)

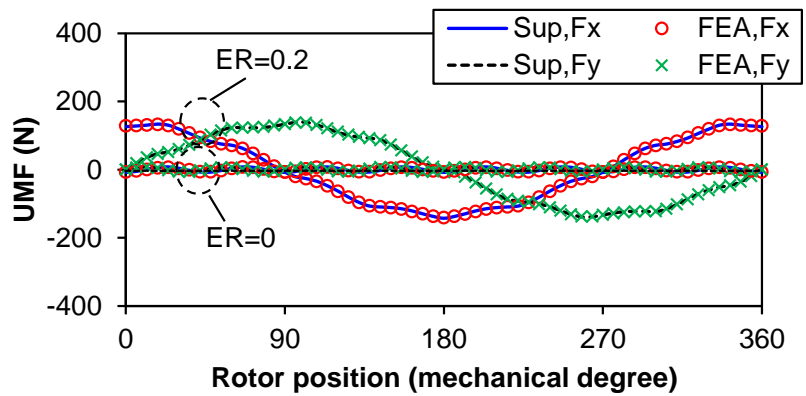


(c) Waveforms with 0.2 eccentricity ratio (On-load)

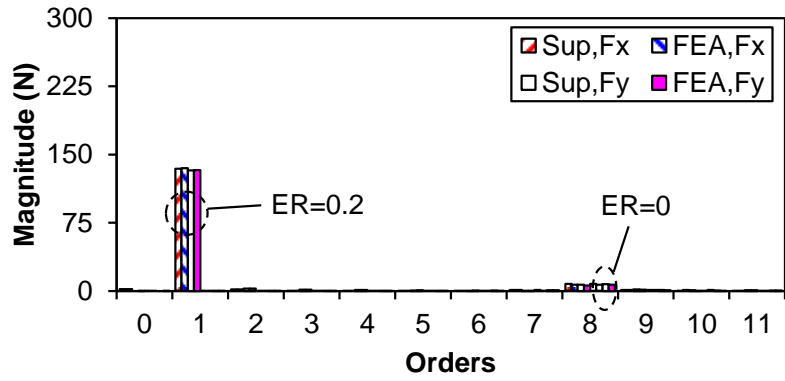


(d) Harmonics with 0.2 eccentricity ratio (On-load)

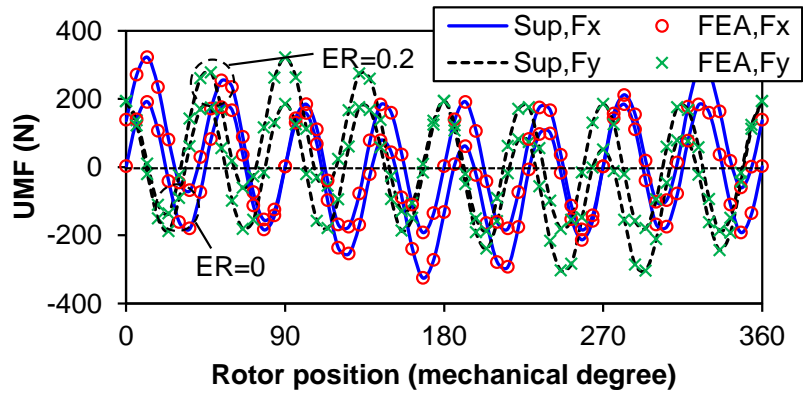
Fig. 2.15. UMF of 9-slot/8-pole PM machine (Static eccentricity).



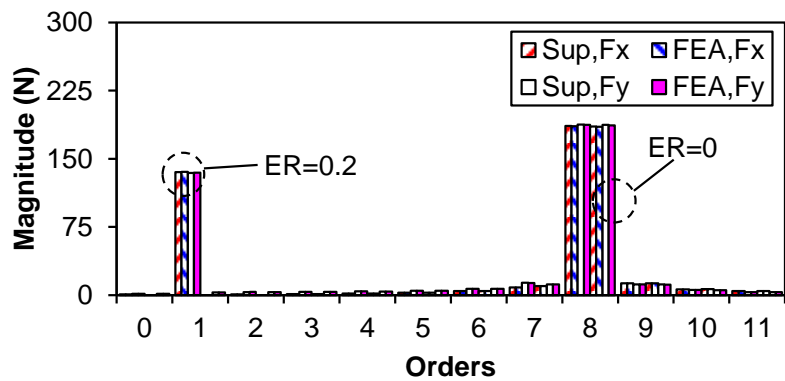
(a) Waveforms with 0.2 eccentricity ratio (Open-circuit)



(b) Harmonics with 0.2 eccentricity ratio (Open-circuit)



(c) Waveforms with 0.2 eccentricity ratio (On-load)



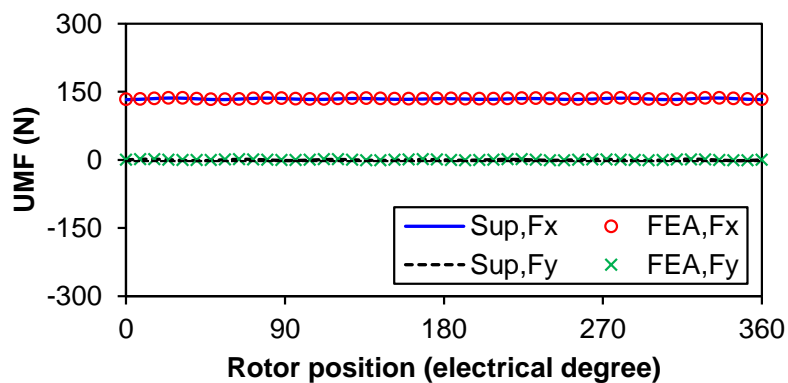
(d) Harmonics with 0.2 eccentricity ratio (On-load)

Fig. 2.16. UMF of 9-slot/8-pole PM machine (Rotating eccentricity).

All of the results obtained by two methods shown in Fig. 2.15 and 2.16 agree well, which verifies the effectiveness of the improved superposition method for the UMF prediction under rotor eccentricity conditions. Fig. 2.15(a) and (b) show that the UMF predominantly has a constant DC component towards the minimum air-gap direction under open-circuit condition if the machine has static eccentricity. Since the minimum

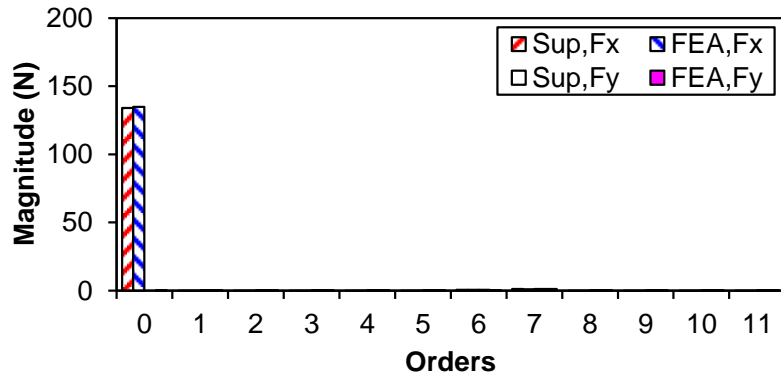
air-gap locates in the positive  $x$ -direction, that is why  $F_x$  is always maximum and  $F_y$  is negligible. In contrast, the UMF is much smaller for concentric case ( $ER=0$ ) under open-circuit condition, which means the slotting effect is small for this machine due to the small slot opening. When the machine runs under on-load condition, it can be found in Fig. 2.15(c) and (d) that the UMF contains more pulsating components, especially the 1<sup>st</sup> harmonic UMF. Apparently, the increase of these harmonic components comes from the armature field. For concentric situation, both  $F_x$  and  $F_y$  have the same magnitude and they are perpendicular to each other in terms of rotor position. Since the slotting effect is negligible, the appearance of UMF is owing to the armature field, which can be clearly seen by comparing open-circuit and on-load results. Fig. 2.16(a) and (b) show that the UMF mainly contains the 1<sup>st</sup> component under open-circuit condition for rotor dynamic eccentricity. However, the fluctuation of UMF under on-load condition (dominantly the 8<sup>th</sup> harmonic UMF) can be clearly seen in Fig. 2.16(c) and (d), which is from the armature field as well.

For this rotating symmetrical machine, it does not have the UMF without rotor eccentricity, which means the slotting effect will not lead to UMF for this machine as the 9S/8P PM machine. However, it will suffer the UMF under rotor eccentricity condition as well. Thus, the similar analysis is employed on the 12S/10P PM machine and the corresponding results are shown in Fig. 2.17 and 2.18. Since this machine does not have the intrinsic UMF, the results corresponding to zero  $ER$  will be zero and are not necessarily to be shown (coinciding with the horizontal axis labelled zero).

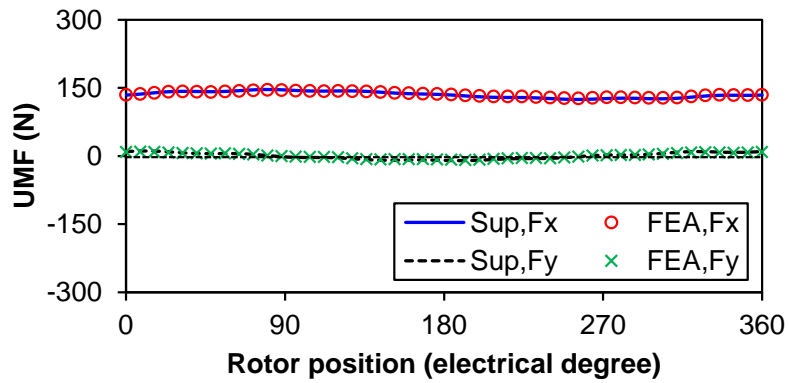


(a) Waveforms with 0.2 eccentricity ratio (Open-circuit)

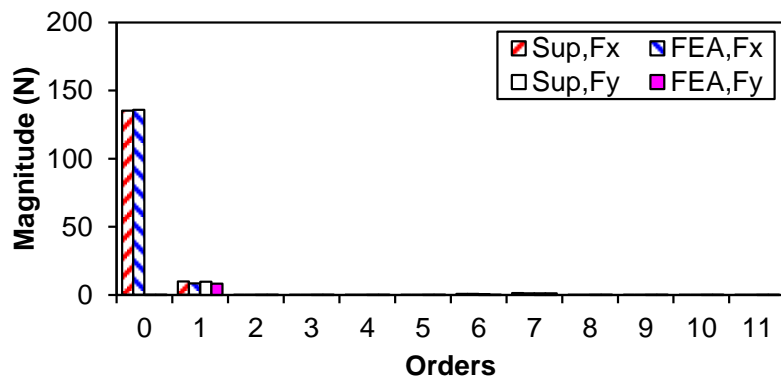




(b) Harmonics with 0.2 eccentricity ratio (Open-circuit)

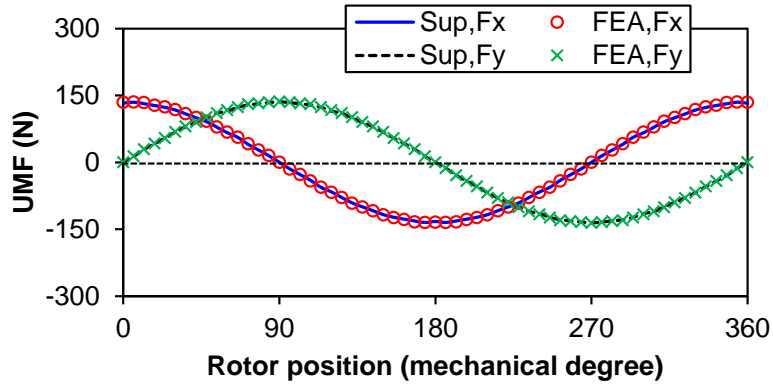


(c) Waveforms with 0.2 eccentricity ratio (On-load)

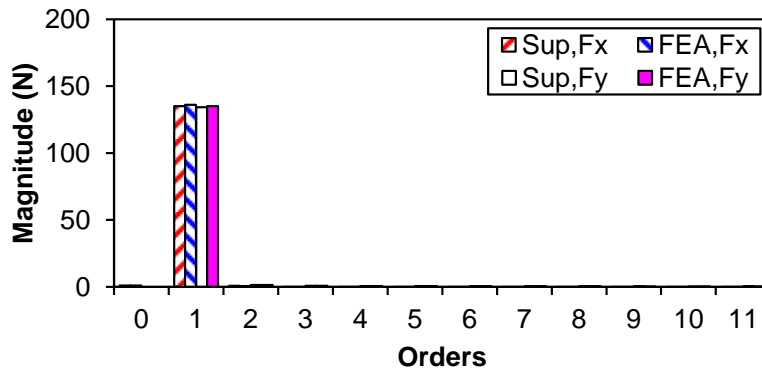


(d) Harmonics with 0.2 eccentricity ratio (On-load)

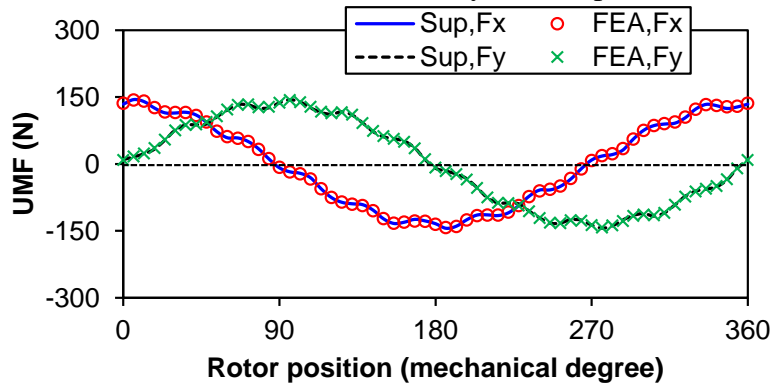
Fig. 2.17. UMF of 12-slot/10-pole PM machine (static eccentricity).



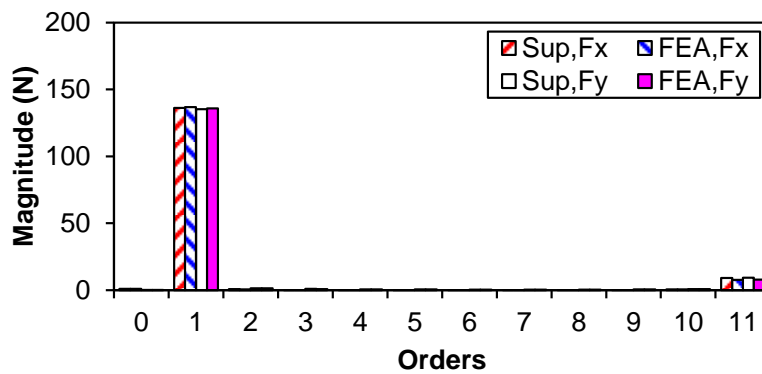
(a) Waveforms with 0.2 eccentricity ratio (Open-circuit)



(b) Harmonics with 0.2 eccentricity ratio (Open-circuit)



(c) Waveforms with 0.2 eccentricity ratio (On-load)

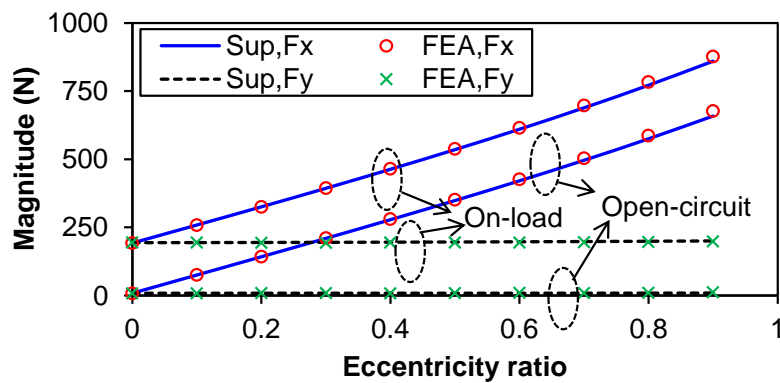


(d) Harmonics with 0.2 eccentricity ratio (On-load)

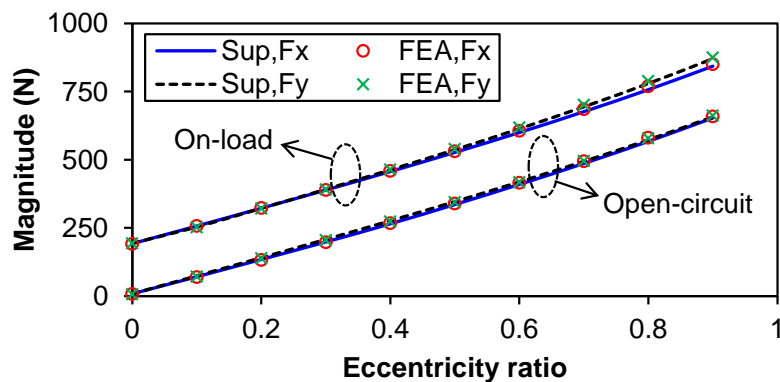
Fig. 2.18. UMF of 12-slot/10-pole PM machine (rotating eccentricity).

Fig. 2.17 and 2.18 demonstrate that the proposed method is applicable to rotating symmetrical machine as well. Fig. 2.17(a) and (b) show that  $F_x$  is still dominant, which is due to the unbalance of the PM magnetic field under static eccentricity situation.  $F_y$  is perpendicular to the minimum air-gap length direction, thus its value is nearly zero. For this machine, the armature field does not affect the UMF as obviously as the 9S/8P PM machine, which can be seen from Fig. 2.17(c) and (d). Although the 1<sup>st</sup> harmonic component appears, it is much smaller than the DC component. Fig. 2.18 shows the results under dynamic eccentricity situation. Comparing Fig. 2.18(b) and (d), it can conclude that the appearance of the 11<sup>th</sup> component of UMF also comes from the armature field.

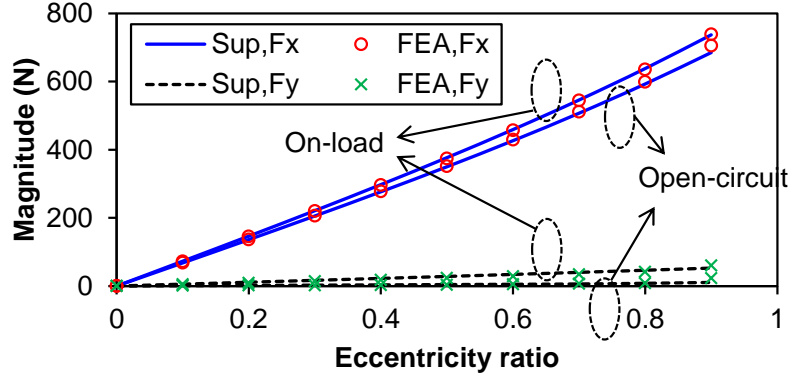
Finally, the variation of UMF magnitude with different  $ERs$  is shown in Fig. 2.19 for both machines.



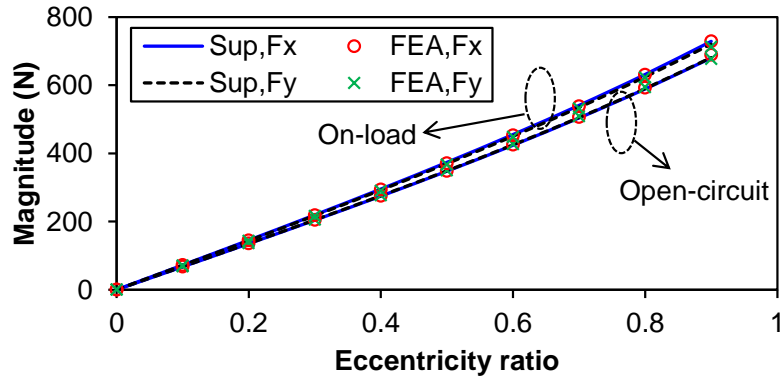
(a) Static eccentricity (9-sot/8-pole)



(b) Rotating eccentricity (9-sot/8-pole)



(c) Static eccentricity (12-sot/10-pole)



(d) Rotating eccentricity (12-sot/10-pole)

Fig. 2.19. Variation of UMF magnitude with  $ER$ .

The influence of slotting effect can be observed in Fig. 2.19 for concentric cases under open-circuit and on-load conditions, respectively. Fig. 2.19(a) shows that the proposed method is valid for all of the  $ER$ s under static eccentricity condition. Both  $F_x$  and  $F_y$  will almost linearly increase with the  $ER$ . It also shows that the machine can generate the UMF without rotor eccentricity, which explains its intrinsic rotating asymmetric property. The increase of  $F_x$  is more evident than that of  $F_y$ , which is due to the fact that the major contribution happens in the  $x$ -direction. If the machine has dynamic eccentricity, Fig. 2.19(b) again validates that the effectiveness of the method for all of the  $ER$ s under dynamic eccentricity. It can be found that the magnitudes of  $F_x$  and  $F_y$  are practically the same under dynamic condition, which is owing to the feature that the minimum air-gap position will instantly change with the rotor position. Therefore, it can be concluded that  $F_x$  and  $F_y$  have the same importance under such circumstance. The interesting phenomena can be observed for rotating symmetrical machine. Fig. 2.19(c) shows that the UMF of 12S/10P PM machine occurs due to the existence of rotor eccentricity and roughly linearly increases with the  $ER$  as well. It

also shows that the influence of armature field will gradually increase with the  $ER$  for this machine, which is quite different from the intrinsic rotating asymmetric machine. This phenomenon can be explained by comparing the winding arrangement of the two example machines. The 9S/8P PM machine has asymmetric winding, which will contribute to the generation of UMF. In contrast, the winding configuration of the 12S/10P PM machine is rotating symmetrical along the circumference. Therefore, armature field influence is weak under low  $ER$  and will become increasingly evident with the increase of the  $ER$ . However, such influence of armature field on UMF generation is still much lower. Fig. 2.19(d) again shows that the influence of the armature field will be more obvious with a larger  $ER$ .

Overall, the improved superposition method is proved to be effective for the UMF prediction under rotor eccentricity conditions.

## 2.5 Extension of the Method to Axial-varying Eccentricity

Most investigations of rotor eccentricity focus on axial-even type and the corresponding analysis can be degraded from 3-dimensional (3D) to 2-dimensional (2D). In fact, axial-varying eccentricity is more common, which means the problem is intrinsically 3D [DOR11a]. The view of such kind of eccentricity is shown in Fig. 2.20, where the right and left end of the rotor have different inclination magnitudes ( $\varepsilon_r$  and  $\varepsilon_l$ , respectively). For this kind of eccentricity, 3D FEA can be adopted to predict the performances. However, the requirement for computation is quite high, since no symmetry may be utilized and the whole machine should be modelled. Besides, if the machine has an inherent low cogging torque, it requires a large amount of mesh elements for accurate calculation, which further increases the burden of computation. In order to ease the prediction, the analytical method was used in [WAN15a]. It simplifies the 3D axial-varying eccentricity into 2D problem by projecting the slotless stator into the eccentric surface which is parallel to the rotor cross-section. Then, the perturbation method can be employed to obtain the air-gap magnetic field. However, this method cannot account for slotting effect which is the source of cogging torque. Even if the Subdomain model is used [FU12], the projection of slotted stator is too complicated due to the existing of slots.

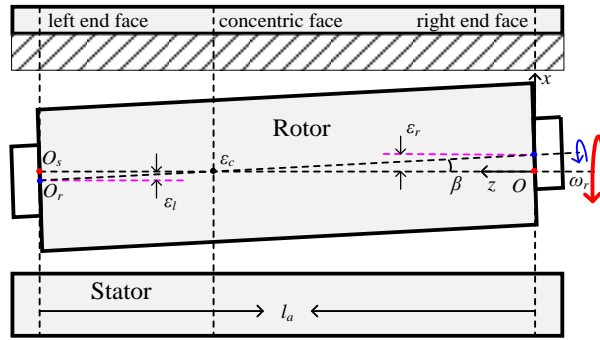
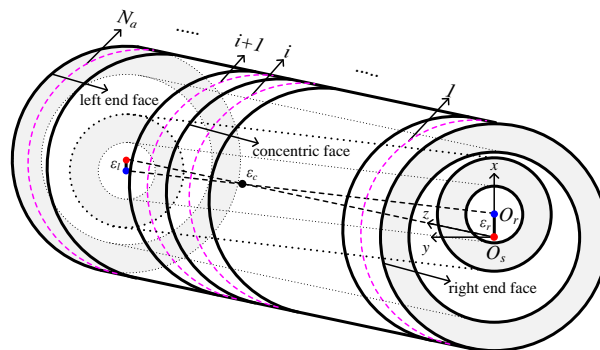
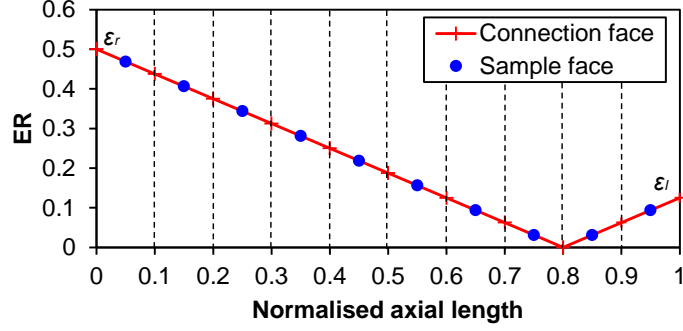


Fig. 2.20. Illustration of axial-varying eccentricity.

The proposed method consists of two important parts, viz. axial and circumferential superposition processes. The axial superposition process [MOH14] cuts the original axial-varying eccentric machine into  $N_a$  uniform slices along the axial direction in the first place, as shown in Fig. 2.21(a).  $N_a$  should be as small as possible, while the effect of axial-varying eccentricity is also accurately taken into account. Although each slice is still axial-varying eccentric, it is approximately considered to be axial-even by choosing the cross-section of its middle part (dashed line in Fig. 2.21) as a representation. Since the eccentricity is axial-varying, each slice will have different eccentricity magnitude. One general situation is considered for the prototype machine, where the two ends of the rotor have the different eccentricity magnitudes in opposite directions, as shown in Figs. 2.20 and 2.22. Along the positive direction of  $z$ -axis, there are three important faces (right end, concentric and left end). In this paper, the  $ER$  of them ( $\epsilon_r$ ,  $\epsilon_c$  and  $\epsilon_l$ , respectively) satisfies the following constraints:  $\epsilon_r=0.5$ ;  $\epsilon_c=0$ ;  $\epsilon_r:\epsilon_l=4:1$ . Here, the slice number of two parts satisfies this ratio as well ( $N_{ar}:N_{al}=4:1$ ). For the sake of clarity, the variation of  $ER$  along the axial direction is shown in Fig. 2.21(b), where the machine is cut in the connection face and the sample face is used to represent each slice.



(a) Axial division



(b) Variation of  $ER$  with the axial length

Fig. 2.21. Illustration of axial superposition.

After obtaining  $N_a$  axial-even slices with different  $ERs$ , the circumferential superposition method can be used to predict the air-gap flux density of each slice, as shown in section 2.2. The eccentric machine model is divided into  $N_e$  segments along the circumferential direction. Each eccentric segment is replaced by the same portion of its corresponding concentric machine model. The air-gap of this concentric machine model is picked at the position of each eccentric segment centre. For the sake of accurately accounting for slotting effect,  $N_e$  should be the integer times of the slot number (three times used here).

The air-gap flux densities of the original axial-varying eccentric machine can be synthesised as follows:

$$\begin{aligned} B_{rg} &= B_{rgij}, & \alpha \in (\alpha_{sij}, \alpha_{eij}) \\ B_{\alpha g} &= B_{\alpha gij}, & \alpha \in (\alpha_{sij}, \alpha_{eij}) \end{aligned} \quad (2.46)$$

where  $B_{rg}$ ,  $B_{\alpha g}$ ,  $B_{rgij}$  and  $B_{\alpha gij}$  are the radial and circumferential air-gap flux densities of the original eccentric machine and each concentric machine model corresponding to the  $i^{\text{th}}$  axial slice and  $j^{\text{th}}$  circumferential segment, respectively;  $\alpha_{sij}$ ,  $\alpha_{eij}$  are the start and end angles of the  $i^{\text{th}}$  axial slice and  $j^{\text{th}}$  circumferential segment, respectively;  $\alpha$  is the angular position.

Finally, the electromagnetic performance of the original axial-varying eccentric machine can be calculated. Taking cogging torque and UMF as example, the results will be described as follows. Since the Subdomain method can precisely consider the slotting effect, PM and armature field, the cogging torque and UMF results should be quite accurate. Full 3D model is modelled by JMAG package and linear direct FEA

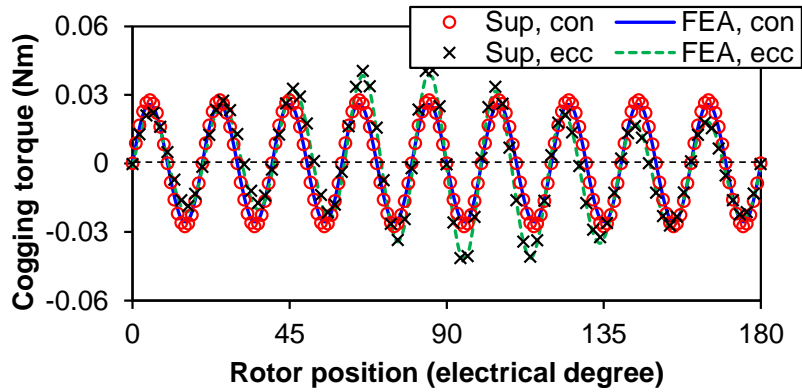
(legend “FEA”) is used to verify the effectiveness of the proposed method (legend “Sup”).

The cogging torque ( $T_{cog}$ ) under open-circuit condition can be predicted according to the following equation:

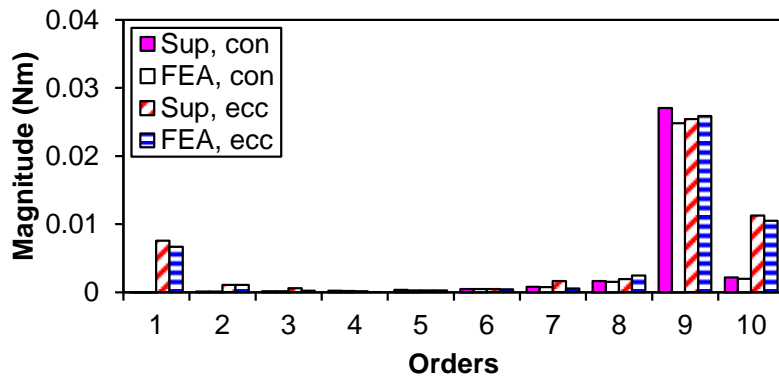
$$T_{cog} = \frac{l_a}{\mu_0} r_g^2 \int_0^{2\pi} B_{rg} B_{\alpha g} d\alpha = \frac{l_a}{\mu_0 N_a} r_g^2 \sum_{i=1}^{N_a} \sum_{j=1}^{N_e} \int_{\alpha_{sij}}^{\alpha_{eij}} B_{rgij} B_{\alpha gij} d\alpha \quad (2.47)$$

where  $l_a$  is the machine axial length;  $r_g$  is the radius of the minimal air-gap centre and  $\mu_0$  is the air-gap permeability. It shows the cogging torque is synthesized from the air-gap flux density of the  $i^{\text{th}}$  axial slice and the  $j^{\text{th}}$  circumferential segment.

To show the influence of eccentricity, the cogging torque of the machines with/without eccentricity (legend “ecc” and “con”, respectively) are compared, as shown in Fig. 2.22. Both waveforms and spectra obtained by Fast Fourier Transform (FFT) are given for clear illustration.

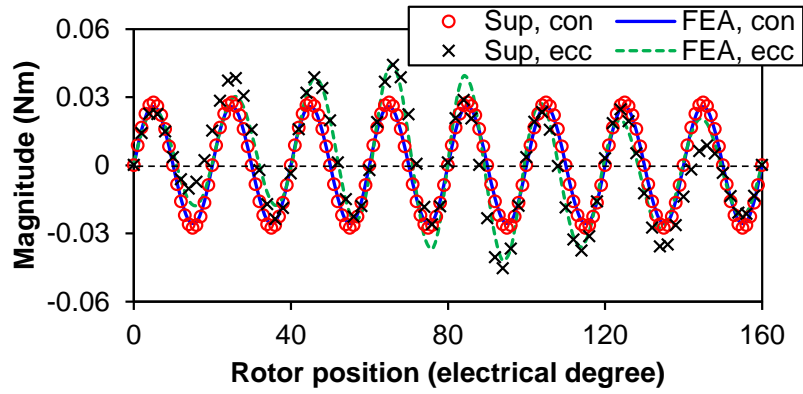


(a) Waveforms (Axial-varying static eccentricity)

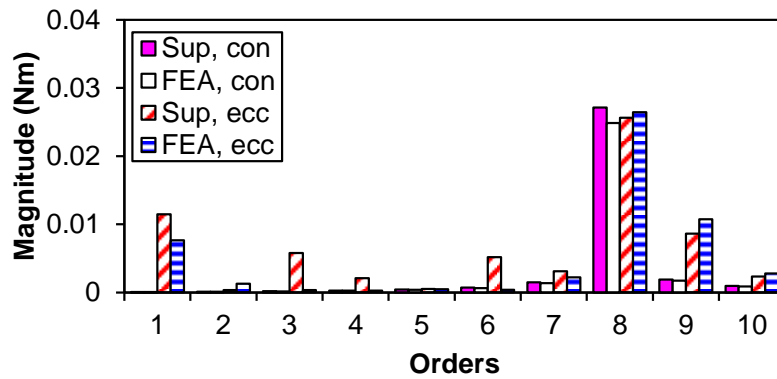


(b) Spectra (Axial-varying static eccentricity)





(c) Waveforms (Axial-varying rotating eccentricity)



(d) Spectra (Axial-varying rotating eccentricity)

Fig. 2.22. Cogging torque waveforms and spectra.

It can be seen that the results obtained by two methods match well, although there are some discrepancies due to computation errors. Based on the results over one cogging torque period (PM pole pitch and stator slot pitch for static and rotating eccentricities, respectively), it shows that the major harmonic orders for static and rotating eccentricities are 9 and 8, respectively. This coincides with the concentric situation. The appearance of the 1st component is due to the eccentric air-gap and will reach peak value when the inter-pole region of PMs is close to the slot opening. The reduction of cogging torque period number over one revolution causes the increase of cogging torque. Since the most apparent influence of the axis-varying eccentricity will happen at the two ends of the machine and will decrease from the end face to the concentric face, this average effect will decrease the influence of the axial-varying eccentricity compared with the axial-even eccentricity case. Another advantage of the proposed method is the high computation efficiency. The proposed method cost only around 10 minutes for each result, which is much less than about 90 hours used by 3D

FEA. Therefore, it is useful for axial-varying eccentricity investigation, especially the machines having large slot and pole numbers.

The  $x$ - and  $y$ - components of UMF ( $F_x$  and  $F_y$ ) can be predicted based on the following expressions:

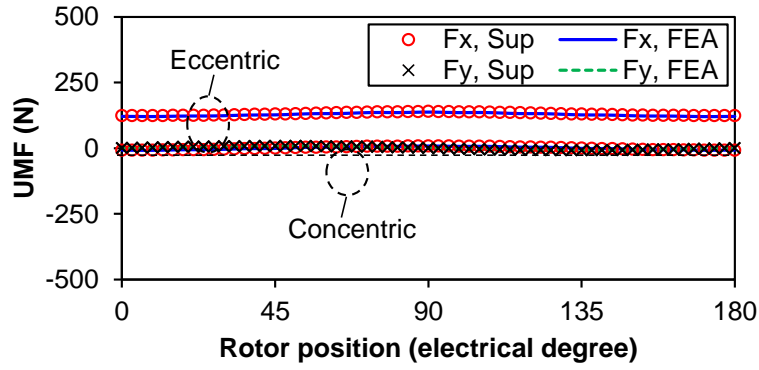
$$F_x = l_a r_g \int_0^{2\pi} (\sigma \cos \alpha - \tau \sin \alpha) d\alpha = \frac{l_a}{N_a} r_g \sum_{i=1}^{N_a} \sum_{j=1}^{N_e} \int_{\alpha_{sij}}^{\alpha_{eij}} (\sigma_{ij} \cos \alpha - \tau_{ij} \sin \alpha) d\alpha$$

$$F_y = l_a r_g \int_0^{2\pi} (\sigma \sin \alpha + \tau \cos \alpha) d\alpha = \frac{l_a}{N_a} r_g \sum_{i=1}^{N_a} \sum_{j=1}^{N_e} \int_{\alpha_{sij}}^{\alpha_{eij}} (\sigma_{ij} \sin \alpha + \tau_{ij} \cos \alpha) d\alpha \quad (2.48)$$

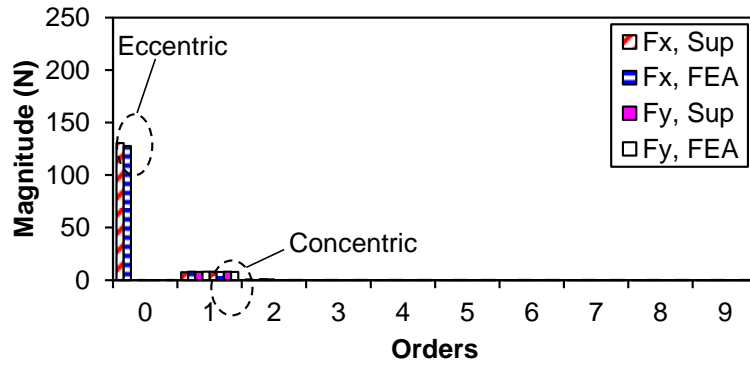
$$\sigma = (B_{rg}^2 - B_{\alpha g}^2) / 2\mu_0, \quad \tau = B_{rg} B_{\alpha g} / \mu_0$$

$$\sigma_{ij} = (B_{rgij}^2 - B_{\alpha gij}^2) / 2\mu_0, \quad \tau_{ij} = B_{rgij} B_{\alpha gij} / \mu_0$$

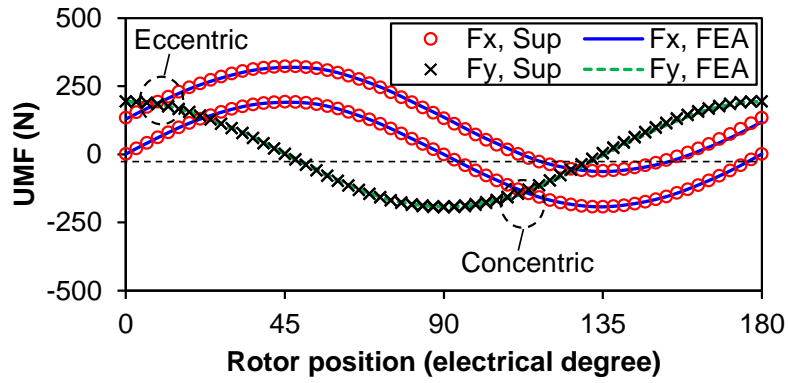
Based on the flux density, the normal and tangential force density ( $\sigma_{ij}$  and  $\tau_{ij}$ ) of the discretized  $i^{\text{th}}$  axial slice and the  $j^{\text{th}}$  circumferential segment are used to predict UMF. Since the UMF is closely related to the load condition, both the results under open-circuit and rated load conditions are predicted, as shown in Figs. 2.23 and 2.24. The results over one period are shown and the period for static and rotating eccentricity are one pole pitch and one revolution for UMF, respectively.



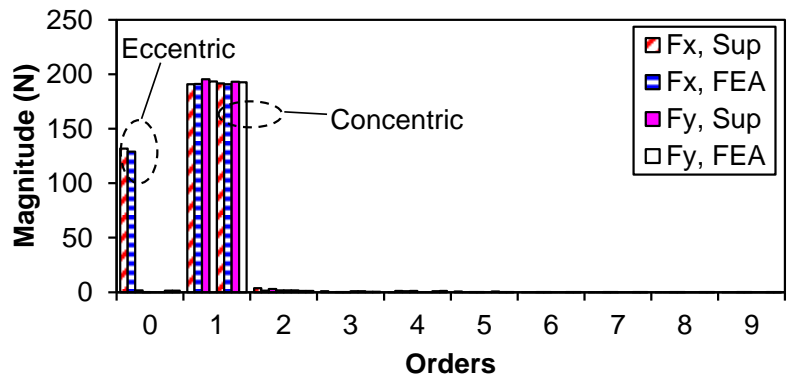
(a) Waveforms (Open-circuit)



(b) Spectra (Open-circuit)

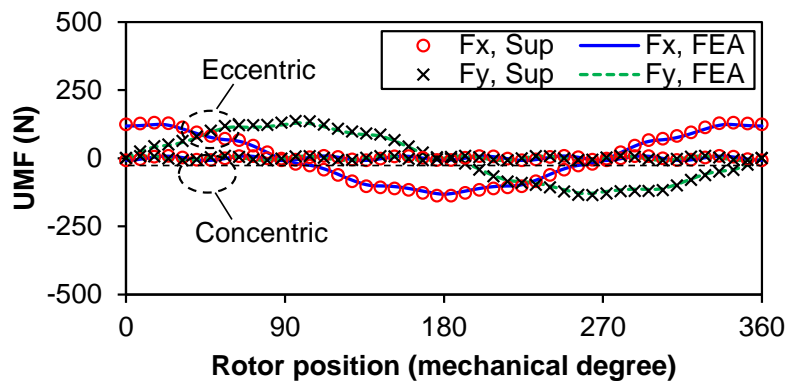


(c) Waveforms (On-load)

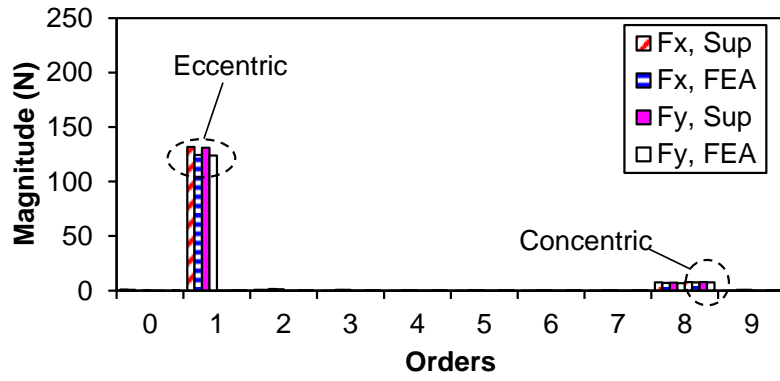


(d) Spectra (On-load)

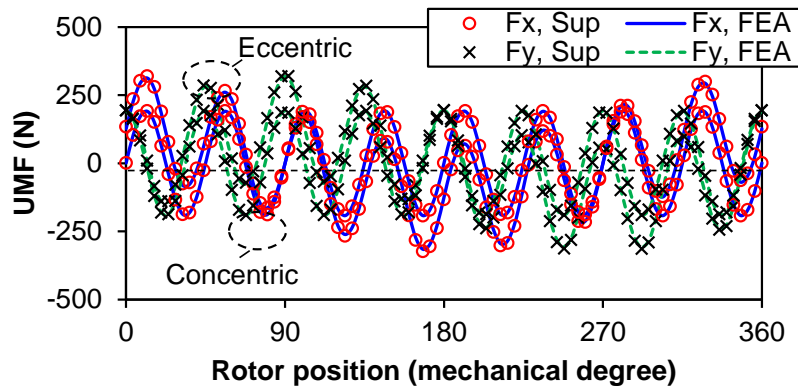
Fig. 2.23. UMF with axial-varying static eccentricity.



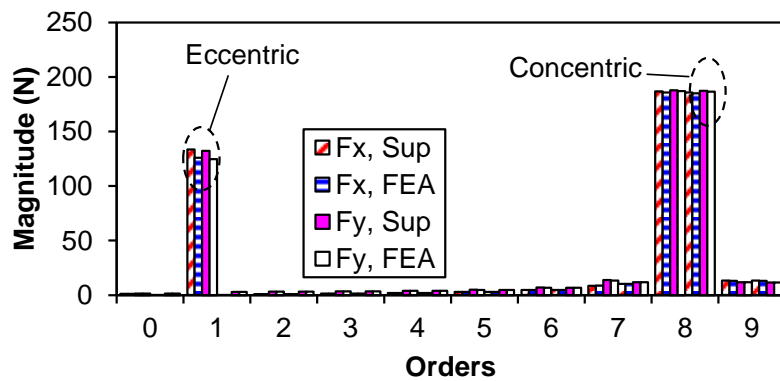
(a) Waveforms (Open-circuit)



(b) Spectra (Open-circuit)



(c) Waveforms (On-load)



(d) Spectra (On-load)

Fig. 2.24. UMF with axial-varying rotating eccentricity.

Figs. 2.23 and 2.24 demonstrate that the proposed method is also effective for UMF prediction under different load conditions no matter there are eccentricities or not. For static eccentricity, there is DC component in  $x$ -component due to the fixed minimal air-gap position. The most obvious phenomenon is the increase of the 1<sup>st</sup> component. This component is quite small under open-circuit condition, since the

slotting effect is not strong because of small slot opening. However, the armature field will obviously enlarge this component, which is consistent with the concentric situation. The appearance of the 1<sup>st</sup> component is the major influence of rotating eccentricity, while the increase of the 8<sup>th</sup> component also comes from the existence of armature field. The 3D FEA for UMF prediction needs less time than cogging torque calculation but still takes 30 hours, whereas the proposed method only cost 5 minutes.

## **2.6 Conclusion**

An analytical method, which combines the superposition and the subdomain methods, has been developed in this paper for fast and accurately predicting machine performance with rotor eccentricity. The accuracy of the proposed method has been validated by comparing the air-gap field, the phase flux linkage and back-EMF obtained by the proposed method and the direct FEA. Due to its demonstrated advantages, the proposed superposition method can also be employed to investigate the influence of rotor eccentricity on electromagnetic performance of machines with large slot/pole number in the future. The validation of the proposed method has been done on the prototyped PM machines analysed in this chapter and they can be found in published paper listed in Major Contribution part of Chapter 1 ([J1]-[J4]). For simplicity, they will not be repeated here.

## **Chapter 3 Development of Modular Double-layer Dual 3-phase PM Machine Topologies with Redundant Teeth**

In order to ease the manufacture process of very large permanent magnet (PM) machines, such as direct drive wind power generators, modularity technique is usually adopted. Although conventional dual 3-phase fractional-slot PM machines with double layer windings show good performance, the coils located at the end parts of each segment may be easily damaged as they are exposed to air. Thus, a modular machine with redundant teeth is proposed in this chapter, while more protection can be provided for coils located in these regions. The construction of the proposed modular machine having 42-slots/32-poles (42S/32P) is described as an example in detail, which can be treated as the combination of one conventional modular machine (36S/30P) and another redundant one (6S/2P). The reason for choosing 6S/2P electrical machine is to get rid of unbalanced magnetic force (UMF) which usually exists in rotational asymmetric electrical machines. If 3S/2P electrical machine is adopted, the UMF will appear and it is harmful for the stability of electrical machine operation.

Several reasonable requirements are listed before constructing a new modular machine:

- (1) Double layer wound dual 3-phase windings;
- (2) Balanced three phases within each set of windings;
- (3) End coils of each segment protected by unwound teeth;
- (4) No unbalanced magnetic force (UMF) under both open-circuit and on-load conditions should exist.

After obtaining the novel modular machine, its electromagnetic performances are compared with those of the conventional counterpart modular machine by finite element analysis (FEA). The reason for different performances is elaborated. Since the angle between two sets of windings will affect the dual 3-phase winding arrangement and the corresponding electrical machine performance will also be different, the proposed electrical machines with two types of dual 3-phase winding are compared. Finally, the proposed modular machine is prototyped and the corresponding experiments are executed to validate the analysis in this chapter.

### 3.1 Construction of Proposed Modular Machines

Among the available slot/pole number combinations for constructing the balanced dual 3-phase machines with non-overlapping windings, the 12S/10P structure is the simplest one [BAR09]. It consists of two 6S/5P complementary units and the winding arrangement of each unit is also balanced among phases. Thus, the minimal unit for constructing the modular machine has this combination. In order to construct a modular machine with 6 stator segments, an external rotor conventional fractional-slot PM machine with six 6S/5P electrical machine units, viz. 36S/30P, is adopted. The specifications of this novel electrical machine is the same as the existing 3kW PM generators which are obtained by downsizing megawatt (MW) electrical machines. Due to the commercial confidential requirement, the analyses on real MW generators are not allowed by the project sponsor; therefore all of the following analyses are based on the 3kW prototype machine. The cross-section of the original 3kW generator is shown in Fig. 3.1. The major structure parameters are listed in TABLE 3.1.

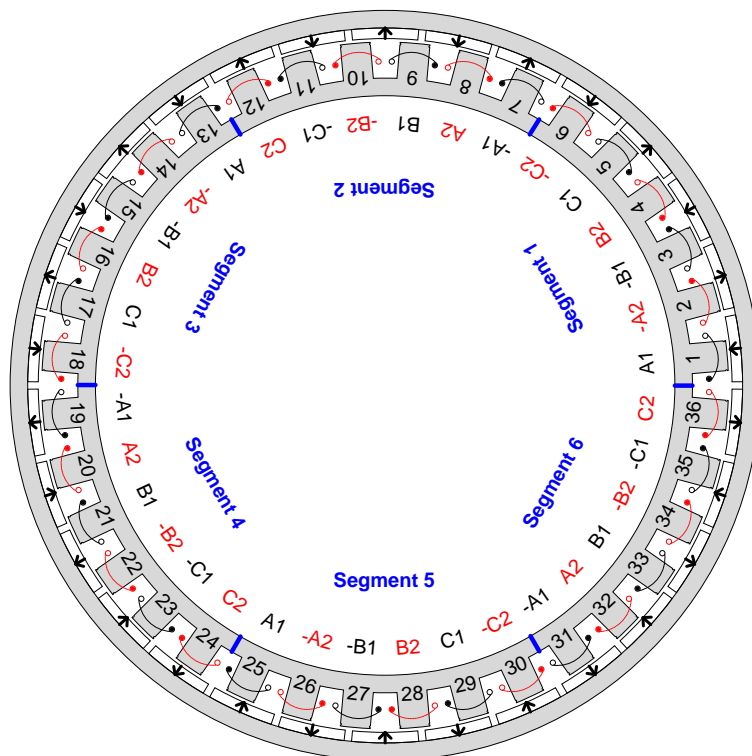


Fig. 3.1. Cross-section of the conventional modular machine (36S/30P).

TABLE 3.1 MAJOR PARAMETERS OF PROTOTYPE MACHINES (APPENDIX C)

Item	Conventional modular machine (36S/30P)	Proposed modular machine (42S/32P)
Stator inner diameter (mm)		319.4
Stator outer diameter (mm)		390.4
Stator yoke thickness (mm)	14.2	13.2
Stator tooth width (mm)	19.03	17.52 <sup>a</sup> and 7.9 <sup>b</sup>
Air-gap length (mm)		2
PM thickness (mm)		6
PM pole arc to pole pitch ratio		0.9
Rotor yoke thickness (mm)		10
Axial length (mm)		110
Turns per phase		408
Rated current (A)		3
Rated speed (rpm)		170

<sup>a</sup> the teeth from the conventional modular machine.

<sup>b</sup> the redundant teeth.

The rotor structure of this electrical machine is quite simple. 30 arc-shaped parallel magnetised PMs are glued to the inner surface of the uniformed cylindrical rotor yoke. For stator core, fully open slots are applied to ease the winding accommodation, which is widely used in large electrical machines with preformed winding coils. This stator core is made of 6 segments with balanced dual 3-phase winding layout for each segment as stated above. However, the conjunction positions between adjacent stator segments (highlighted by the bold solid lines in Fig. 3.1) cannot be set in the tooth centre, which makes the end coils of each segment exposed to the air. These end coils could be damaged during the transportation and the assembly of the electrical machine will be hard as well. Since this conventional machine has 3 repeated 12S/10P electrical machine units along the circumference, segments 1, 3 and 5 have exactly the same winding layouts. Segments 2, 4 and 6 have the corresponding complementary ones.

Starting from this conventional modular machine, a new modular machine with 6 redundant teeth for stator segment connection is proposed, while each stator segment still has balanced dual 3-phase windings. In order to obtain this proposed modular machine, another electrical machine unit having 6S/2P combination is adopted to construct the redundant teeth for each stator segment. The detailed construction



process for the proposed modular machine is shown as follows.

### 3.1.1. Rotor of Proposed Machine

Since the proposed modular machine is deduced from the conventional modular machine, both have the similar structures. The rotor outer diameter, rotor yoke thickness, PM magnetisation pattern, PM thickness and PM pole arc to pole pitch ratio are kept the same. The rotor pole number of the proposed modular machine ( $N_{pp}$ ) simply equals the addition of the conventional and redundant machine pole numbers ( $N_{pc}$  and  $N_{pr}$ , respectively), which is the only difference:

$$N_{pp} = N_{pc} + N_{pr} \quad (3.1)$$

In terms of the electrical machines analysed in this paper,  $N_{pp}$ ,  $N_{pc}$  and  $N_{pr}$  are 32, 30 and 2, respectively. In order to more clearly see the difference, the rotor cross-sections of two electrical machines are shown in Figs. 3.2(a) and (b), respectively. The first and the last rotor pole numbers are also highlighted for clarity.

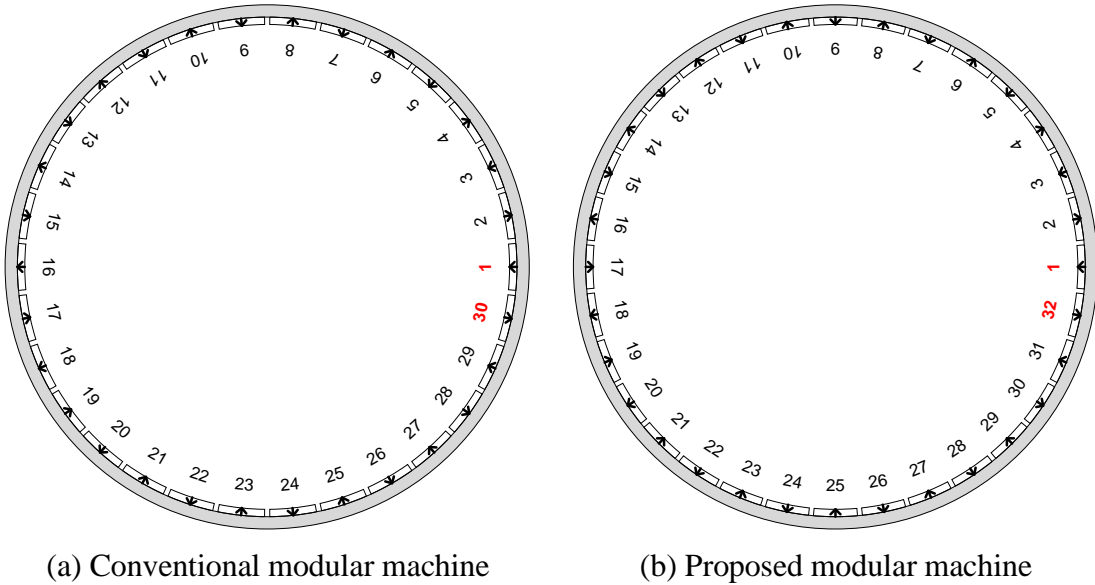


Fig. 3.2. Rotor construction of the conventional and proposed modular machines.

Since the proposed modular machine contains the redundant part for modularity purpose, the increased pole number due to the redundant machine unit does not contribute to the average torque production, which is the cost for using this kind of modular machine. This means 1/16 of the proposed modular machine is not used for torque generation compared with the conventional modular machine. However, this

side effect will be increasingly weak if the conventional modular machine has larger pole number by adopting the 2-pole redundant machine unit.

### 3.1.2. Stator Core of Proposed Machine

In order to obtain the stator of the proposed modular machine, the stator core of the conventional machine is firstly separated into 6 segments in the connection positions as can be seen in Fig. 3.3(a). Each stator segment possesses 6 teeth. Then, the stator core of redundant machine unit with 6 teeth is also cut into 6 segments in the same approach, while no coils will be wound on these 6 teeth for redundant purpose (named as ‘RT’ for simplicity). Combining the stator core segments of the conventional and the redundant machines alternately in the stator yoke, the stator core of the proposed modular machine is obtained, as shown in Fig. 3.3(b). Similar to the rotor pole number, the stator slot number/tooth number of the proposed modular machine can be obtained as follows:

$$N_{sp} = N_{sc} + N_{sr} \quad (3.2)$$

where  $N_{sp}$ ,  $N_{sc}$  and  $N_{sr}$  are the stator slot number of the proposed modular machine, the conventional modular machine and the redundant machine, respectively. Here, they are 42, 36 and 6, respectively.

Since the rotor pole number has changed, the tooth pitch of the teeth in the conventional machine (named as ‘effective teeth’ for simplicity) must be inversely proportional to the rotor pole number to keep the phase shift between adjacent effective teeth unchanged.

$$\tau_{sp} = \frac{N_{pc}}{N_{pp}} \tau_{sc} \quad (3.3)$$

where  $\tau_{sp}$  is the tooth pitch of the proposed modular machine between adjacent effective teeth and  $\tau_{sc}$  is the tooth pitch of the conventional modular machine. The illustration of two parameters can be seen in Fig. 3.3.

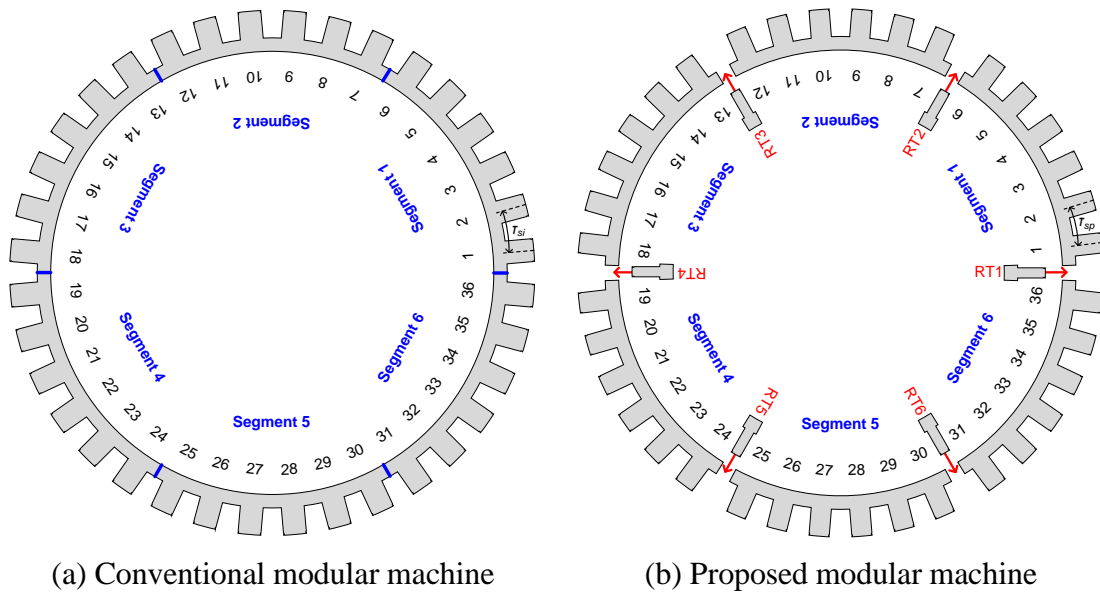


Fig. 3.3. Stator core construction of the conventional and proposed modular machines.

In theory, the dimensions of the proposed modular machine will be changed referring to the conventional modular machine, since it is equivalent to the reconstruction of two stators. However, some changes are made to ensure the two stators have the same outer diameter, inner diameter, slot area for windings and similar stator core saturation level. The effective teeth become thinner, while the width of the RT without coils for connecting stator segments are optimised to minimise the on-load torque ripple under rated operation condition and it almost equals the half width of the effective teeth. During the process of adjusting the tooth width of effective teeth, the stator yoke thickness is also accordingly changed to keep the saturation of the proposed modular machine similar to that of the conventional modular machine. What should be emphasised is that the slot area for winding accommodation is fixed. Therefore, when the turns per phase and the wire are unchanged, the slot filling factors of two electrical machines are the same. Under such condition, the following performance comparison between two electrical machines could be reasonable.

From the stator core structures shown in Fig. 3.3, it can also be seen that the physical repetition number of the proposed machine reduces. For the conventional modular machine, the repetition number is the same as the slot number, while this number equals to the RT number for the proposed modular machine. The reason for such difference is the unequal tooth pitches and tooth widths caused by effective and

redundant teeth in the proposed modular machine. The influence of such change on electrical machine performance will be shown and analysed later.

### 3.1.3. Stator Winding of Proposed Machine

The winding layout is the last but not least step for constructing the proposed modular machine. The star of slots technique is used to explain the winding layout of two electrical machines [BIA06a]. For both electrical machines, there are 36 teeth being wound with coils and each of them is numbered to represent a coil, as shown in Fig. 3.3. The phase shift between any two adjacent coils ( $\alpha_i$ ) is the same in the conventional modular machine and can be obtained according to the following equation:

$$\alpha_i = \frac{N_{pc}}{2} \cdot \frac{360}{N_{sc}} \quad (3.4)$$

The star of slots of this electrical machine is shown in Fig. 3.4(a). It can be seen that there are 12 uniformly distributed vectors along the circumference and each vector repeats 3 times. This is due to the 3 times repetition of 12S/10P electrical machine unit in the conventional modular machine. Based on the star of slots, 12 phase belts with 30 degrees can be obtained and every two anti-phase belts construct one phase. Thus, the coil wound direction for these two phase belts should be opposite to make sure the resultant back-EMF additive. According to this, the corresponding winding arrangement is given in Fig. 3.4(c). Finally, the real winding layout of the conventional modular machine shown in Fig. 3.1 is obtained. The first coils of 6 segments are all phase-A1 except the alternate 180 degree difference.

For the proposed modular machine, the phase shift between two adjacent effective teeth ( $\alpha_{pe}$ ) equals that of the conventional modular machine, viz.  $\alpha_{pe}=\alpha_i$ . However, the phase shift between the last and the first effective tooth of two adjacent stator segments ( $\alpha_{pr}$ ) is different. The insert of a redundant tooth between two segments will introduce additional phase shift:

$$\alpha_{pr} = \alpha_{pe} + \frac{360}{N_{sr}} \quad (3.5)$$

In the same method, the star of slots of the proposed modular machine is plotted in Fig. 3.4(b). Comparing the star of slots of two electrical machines, it can be found

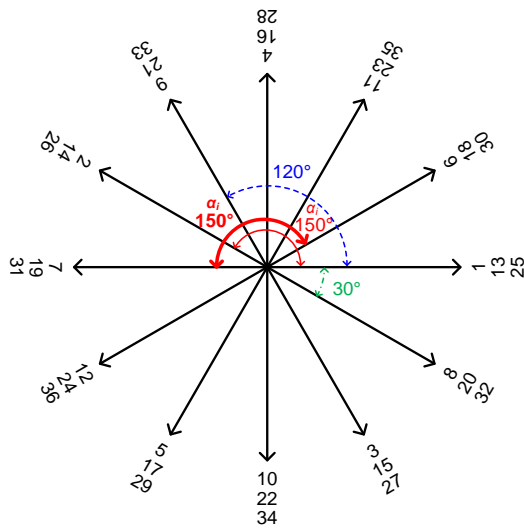
that:

(1) The phase shift between two effective adjacent coils ( $150^\circ$ ), the phase shift between two phases belonging to the same set winding ( $120^\circ$ ) and the phase shift between two sets of windings ( $30^\circ$ ), are the same for two electrical machines.

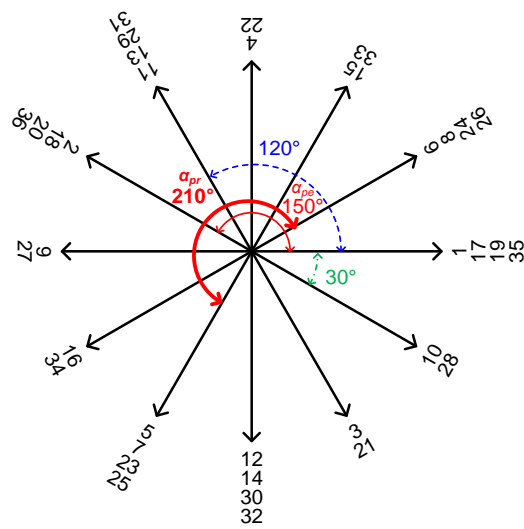
(2) There is an extra 60 electrical degree phase shift being added for the  $\alpha_{pr}$  compared with  $\alpha_{pe}$  for the proposed modular machine and  $\alpha_i$  for the conventional modular machine.

(3) Due to the additional phase shift caused by the redundant teeth, half of the vectors contain more numbers than the other half, while the total coil number of each phase is still the same.

Similar to the winding arrangement process of the conventional modular machine, the winding arrangement of the proposed machine is obtained and shown in Fig. 3.4(d).



(a) Star of slots of the conventional modular machine



(b) Star of slots of the proposed modular machine

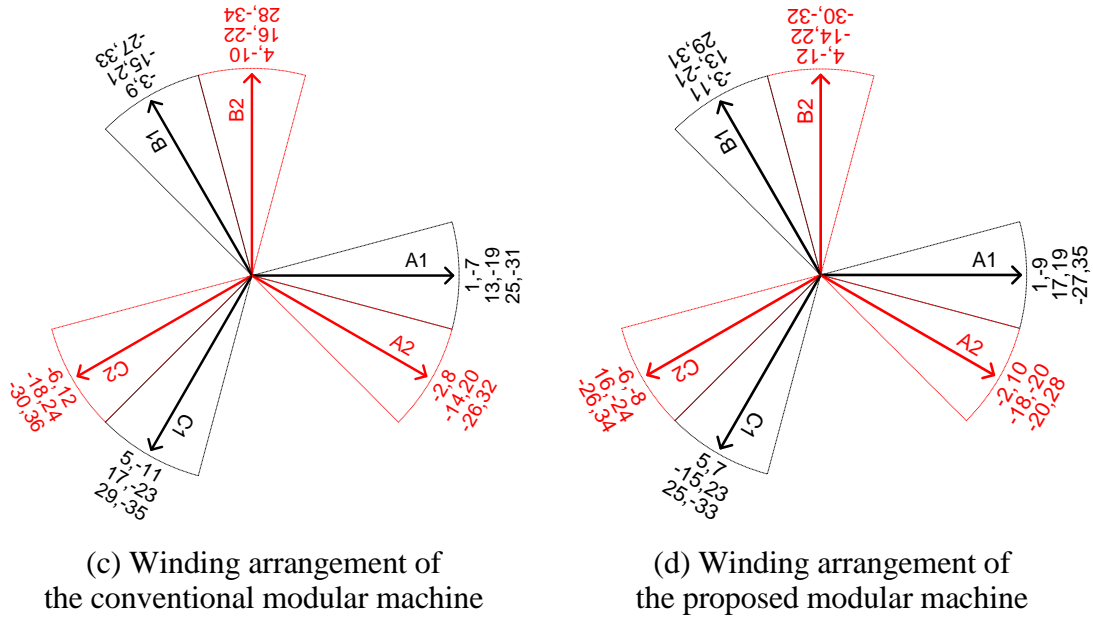


Fig. 3.4. Stator winding construction of the conventional and proposed modular machines.

The real winding layout can be obtained based on the winding arrangement shown in Fig. 3.4(d). When the segment 1 accommodates its winding like the conventional modular machine, the starting coil of the segment 2 should be  $180+60$  degrees lag behind that of the segment 1, resulting in phase-C1. When the starting coil of the segment 2 is found, the corresponding winding arrangement is determined as well. Similarly, the remaining four segments are treated in the same way (the starting coil belonging to phase-B1, A1, C1 and B1, respectively).

Finally, the proposed modular machine is obtained by combining the rotor, stator core and stator winding together and its cross-section is shown in Fig. 3.5.

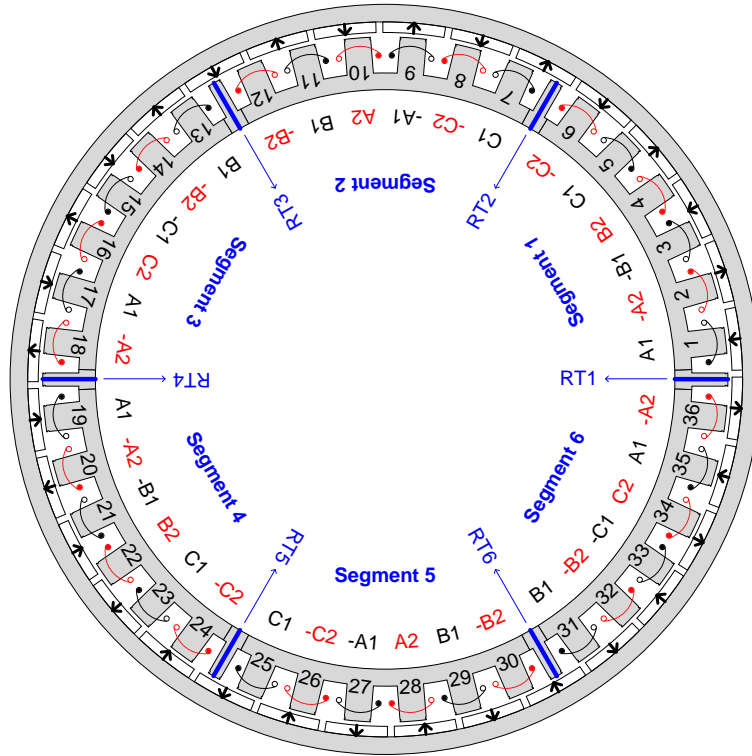


Fig. 3.5. Cross-section of the proposed modular machine (42S/32P).

Fig. 3.5 shows that the proposed modular machine contains redundant teeth between each segment; therefore the end coils of each segment can be protected. In order to fulfil this objective, quite a few changes have been made. Since the proposed modular machine is closely related to the conventional modular machine, the comparative study of electromagnetic performances between these two electrical machines will be shown in the following analysis. The major parameters of the proposed modular machine are also listed in TABLE 3.1 for easily comparing with the conventional one.

## 3.2 Electromagnetic Performance Analysis

### 3.2.1 Field Distribution

The equal potential line distributions of two electrical machines due to PMs are shown in Fig. 3.6, together with the flux density distributions. The rotor locates at the initial position where the rotor  $d$ -axis coincides with the winding phase-A1 axis. Fig. 3.6(a) shows that there are two repetitions along the circumference for the proposed 42S/32P modular machine. Therefore, no UMF exists. Although there are no coils

being wound around six redundant teeth, the flux passing through these teeth will affect electrical machine performances. In contrast, the conventional 36S/30P modular machine shows six repetitive field distributions, as shown in Fig. 3.6(b). For the sake of clarity, one repetition unit is highlighted. It can be expected that the orders of air-gap flux density having the highest amplitude should be 16 and 15 for two electrical machines, respectively. This is the same as the rotor pole pair number. Since the effective teeth of the proposed modular machine are thinner than those of the conventional modular machine, the flux density is a bit higher for the later because of the slight lower saturation. For the redundant teeth, the high saturation can be clearly seen. The influence of such difference will be reflected on the performances.

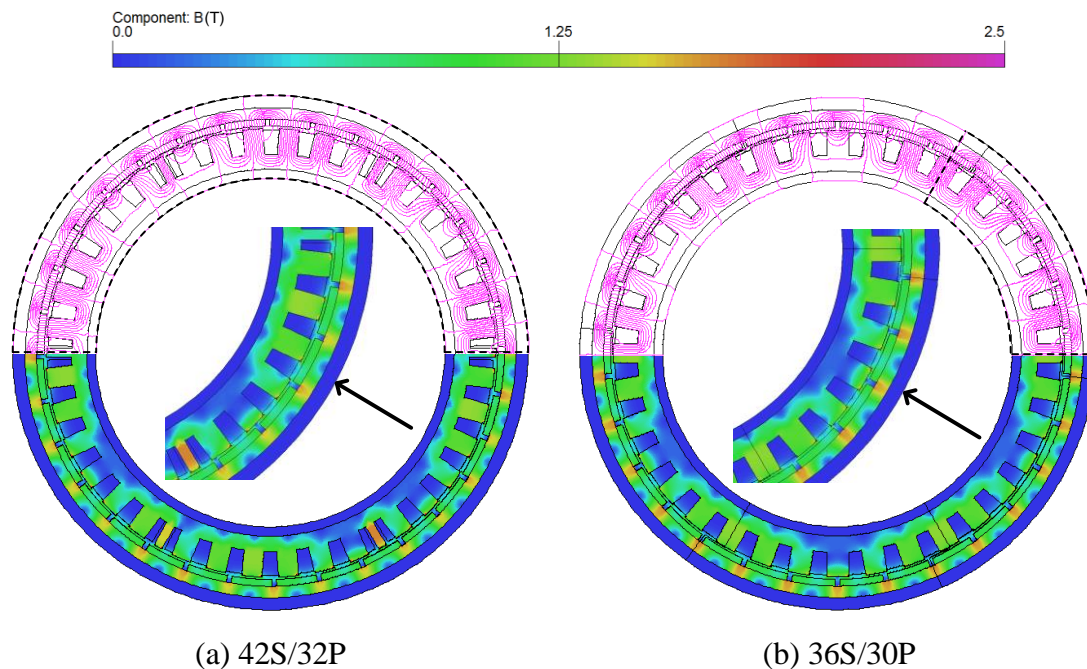
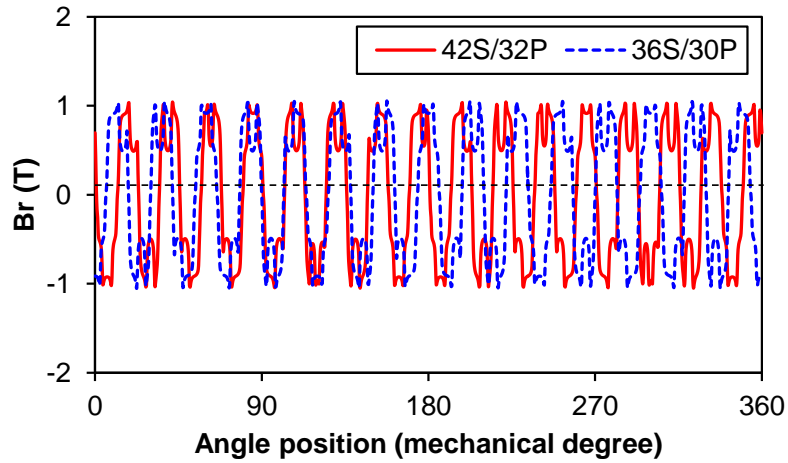


Fig. 3.6. Field distributions due to PMs.

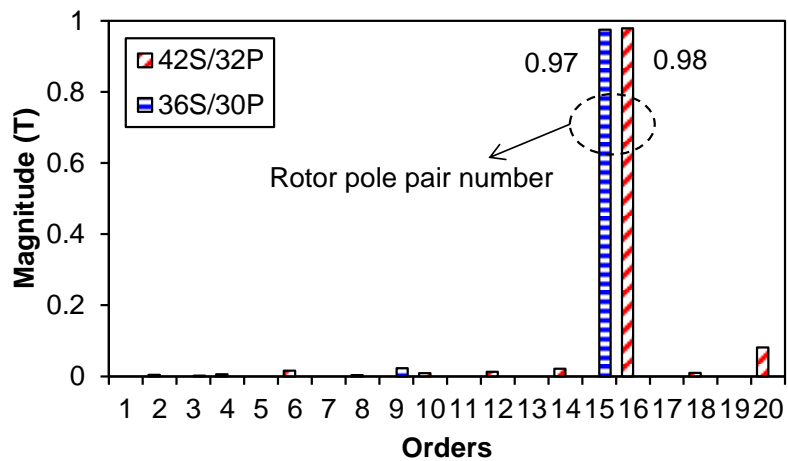
The radial components of air-gap flux density are plotted and compared in Fig. 3.7. For the waveforms shown in Fig. 3.7(a), two electrical machines show obvious pole pair number order along the circumference, which is verified by the spectra shown in Fig. 3.7(b). Due to the fully open slots, the original PM field is distorted. The slotting effect will also be reflected in the spectra. The original harmonic orders of the proposed machine are  $16k$  ( $k=1,3,5\dots$ ), while they are  $15k$  for the conventional modular machine. Therefore, the largest  $16^{\text{th}}$  and  $15^{\text{th}}$  magnitude can be seen for the two electrical machines, respectively. The additional harmonics caused by permeance variation due to slotting effect are  $|16k \pm 6n|$  and  $|15k \pm 36n|$  ( $n=1,2,3\dots$ ) for the proposed



and conventional modular machines, respectively. Within the harmonic range shown in Fig. 3.7(b), there are more additional harmonics for the proposed machine. This is the penalty of adopting modular structure.



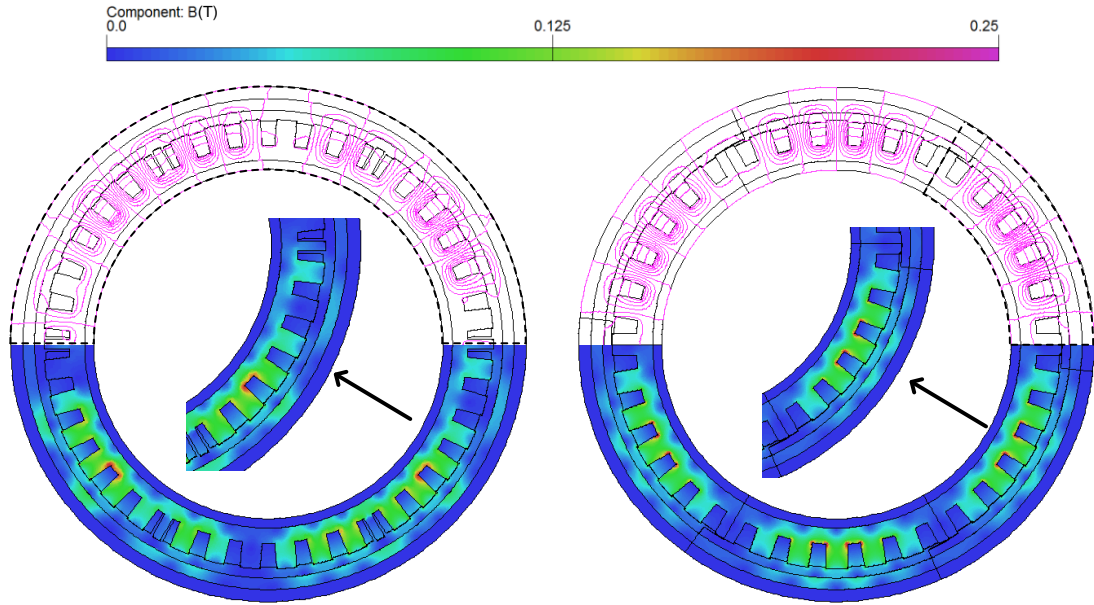
(a)



(b) Spectra

Fig. 3.7. Air-gap flux density due to PMs.

For the magnetic field generated by rated armature current, the corresponding equal potential line distribution and the flux density are shown in Fig. 3.8. The magnetic field repetition numbers along the circumference for the two electrical machines are still 2 and 6, respectively. Since the armature field generated by rated current is much smaller than the PM field due to surface-mounted PM (SPM) rotor, the flux density is much lower. However, the saturation of the proposed modular machine is still a bit heavier than that of the conventional modular machine because of narrower effective teeth.

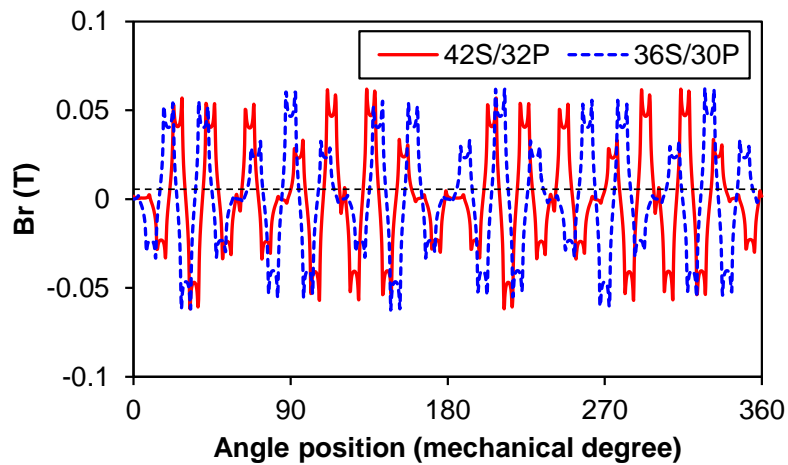


(a) 42S/32P

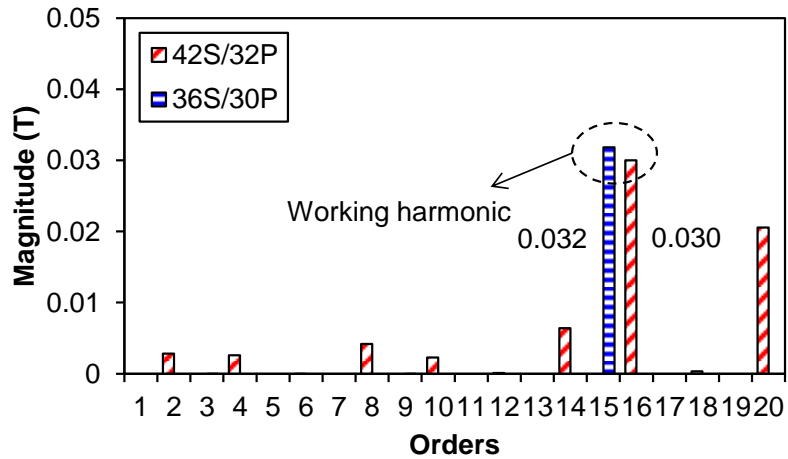
(b) 36S/30P

Fig. 3.8. Field distributions due to rated armature current.

Since the adoption of fractional-slot winding will generate abundant harmonics, the air-gap flux densities of two electrical machines are compared in Fig. 3.9. Referring to the spectra of two electrical machines, it can be clearly seen that the working harmonics have the highest magnitude. Similar to the PM field, the proposed modular machine contains more harmonics than the conventional modular machine. For the armature field, these additional harmonics are more obvious for the proposed modular machine. The influence of these harmonics can be seen in the following analysis.



(a) Waveforms

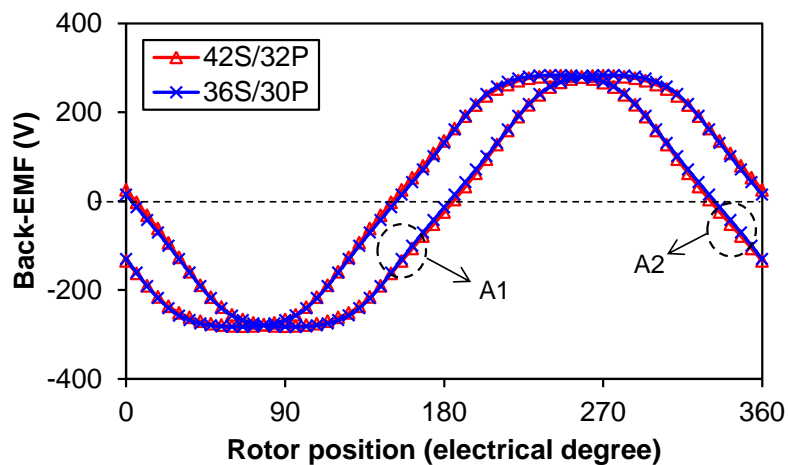


(b) Spectra

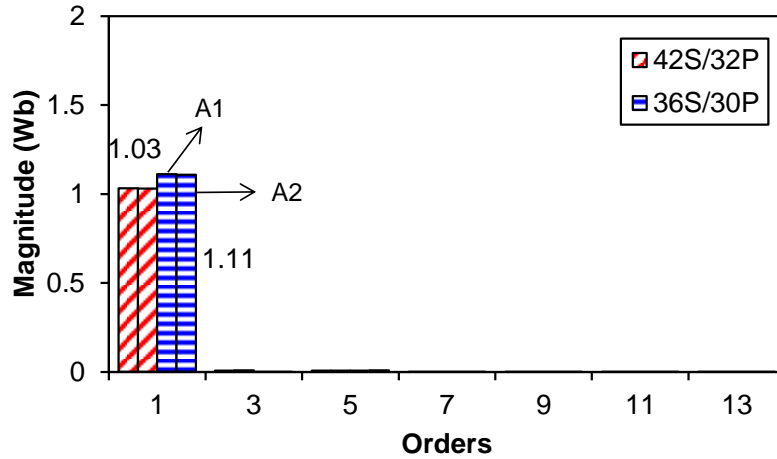
Fig. 3.9. Air-gap flux density due to armature current.

### 3.2.2 Open-circuit Flux-linkage and Back-EMF

Open-circuit flux-linkages of the two electrical machines are shown in Fig. 3.10. Since each set of winding is balanced, only phase-A1 and A2 are chosen as representatives to show the results. Fig. 3.10(a) shows that two sets of windings have 30 degree phase shift between each other and both phases have exactly the same waveforms except 30 degrees ahead for phase-A2 compared with phase-A1. Fig. 3.10(b) further enhances the explanation of this phenomenon. Furthermore, the magnitude of the proposed machine is lower than that of the conventional machine, which is caused by the reduced effective flux passing cross-section area due to narrow teeth. The reason for small harmonics in flux-linkages is the low harmonic winding factors and the optimised pole arc to pole pitch ratio.



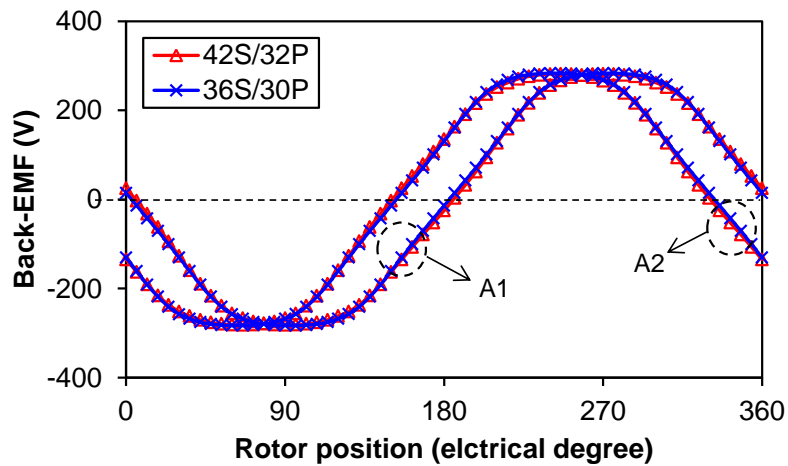
(a) Waveforms



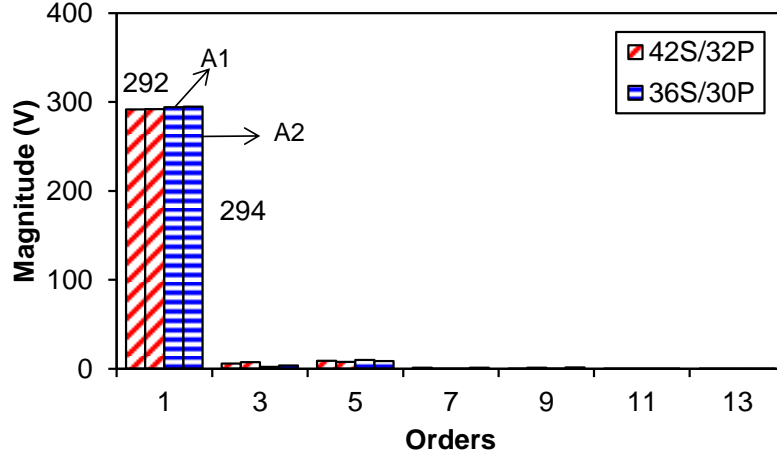
(b) Spectra

Fig. 3.10. Open-circuit phase flux-linkage.

The derivation of flux-linkage is the back electromotive force (EMF), as shown in Fig. 3.11. The similar phenomenon can be seen in open-circuit back-EMF. The obvious difference is the waveform shape. Both electrical machines do not have pure sinusoidal back-EMF and the spectra clearly show it. Due to the amplification effect of derivation operation, the magnitudes of the 3<sup>rd</sup> and 5<sup>th</sup> harmonics are enlarged. Although the proposed modular machine has lower flux-linkage magnitude, the increase of pole number can compensate the loss in back-EMF under the same rotor speed condition. Consequently, both electrical machines have similar fundamental components. However, this value of the conventional modular machine is slightly larger due to its wider tooth width which can capture more effective flux.



(a) Waveforms



(b) Spectra

Fig. 3.11. Open-circuit phase back-EMF (170 rpm).

### 3.2.3 Torque Characteristics

Under open-circuit condition, the interaction between PM field and slot openings will generate cogging torque, which is undesirable for smooth operation. The cogging torque of two electrical machines over one electrical period is shown in Fig. 3.12. Fig. 3.12(a) shows that the proposed modular machine has larger peak-to-peak (PP) value, since more harmonics are introduced due to the variation of the open-circuit field distribution, as shown in Fig. 3.7. Besides the predominant 12<sup>th</sup> harmonic, more cogging torque harmonics can be observed for the proposed modular machine, as shown in Fig. 3.12(b). Because of the modification of slot distribution along the circumference in the proposed modular machine, the 6<sup>th</sup> harmonic cogging torque appears, though its component is quite small. This undesirable component is reduced by using the specific tooth width of redundant teeth. In summary, the cogging torque periods within one pole pair range ( $N_{cogpp}$ ) can be predicted as follows:

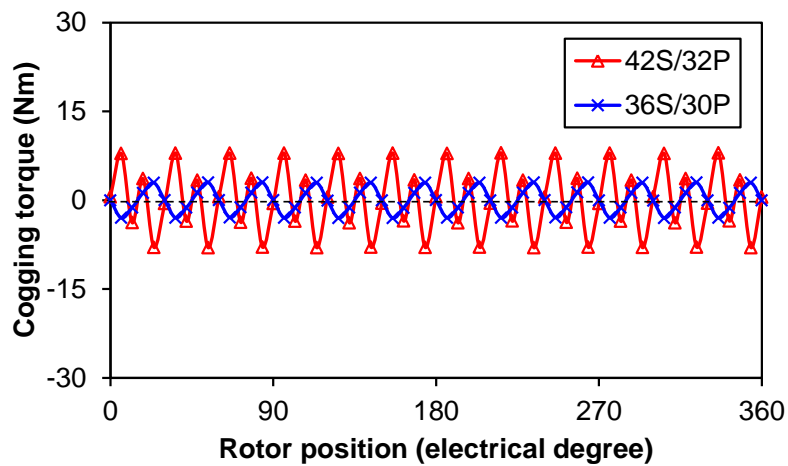
$$N_{cogpp} = \begin{cases} \frac{LCM(N_{sr}, N_{pp})}{N_{pp}/2}, & \text{for the proposed machine} \\ \frac{LCM(N_{sc}, N_{pc})}{N_{pc}/2}, & \text{for the conventional machine} \end{cases} \quad (3.6)$$

where  $LCM$  means the least common multiple of two numbers.

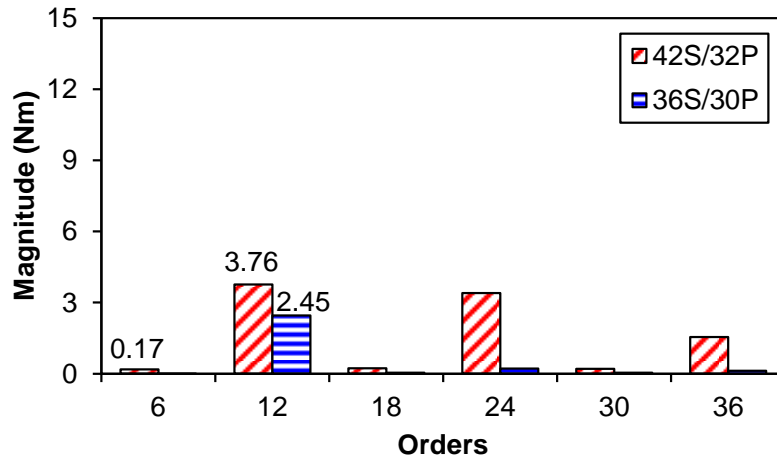
Analysing the equation (3.6), it can be found that the cogging torque period of the proposed modular machine is related with the redundant tooth number. Since the

stator contains 6 segments for 42S/32P modular machine, it can be considered that the stator tooth number is degraded into the redundant tooth number to some extent. That is why more harmonics appear and a higher cogging torque is obtained. In contrast, the cogging torque period of the conventional machine is quite easily determined by the slot and pole numbers.

The on-load torque under rated condition is shown in Fig. 3.13. Figs. 3.13(a) and 12(a) show that the torque waveforms are quite similar to cogging torque except a constant DC component, viz. average torque. According to the spectra shown in Fig. 3.13(b), the average torque of two electrical machines is quite similar, though the conventional machine is relatively a bit larger in terms of fundamental phase back-EMF. Comparing the torque ripples shown in Fig. 3.13(b) and cogging torque shown in Fig. 3.12(b), it can be found that they are almost the same, which means the open-circuit cogging torque is the major torque ripple source under rated condition and the armature reaction of two electrical machines is not strong compared with the PM field.

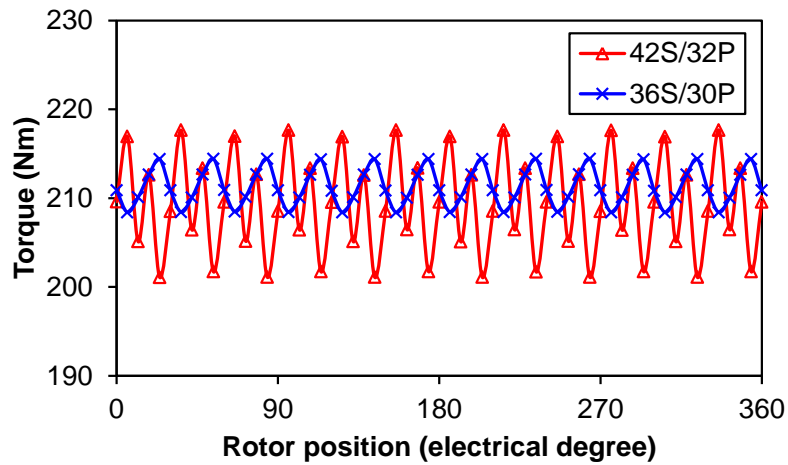


(a) Waveforms

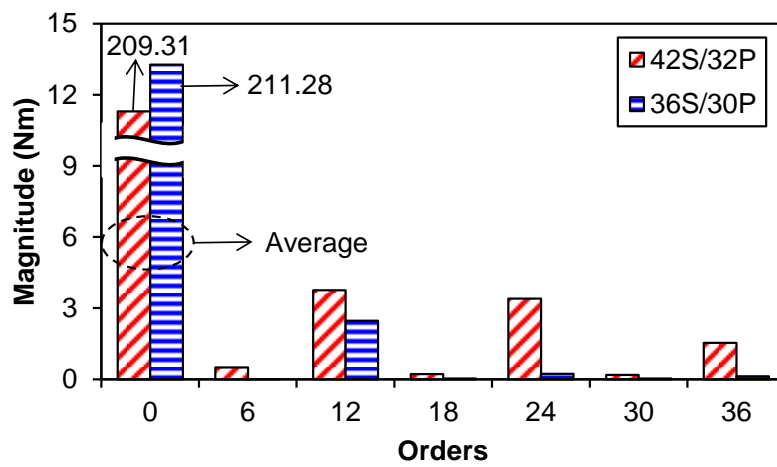


(b) Spectra

Fig. 3.12. Open-circuit cogging torque.



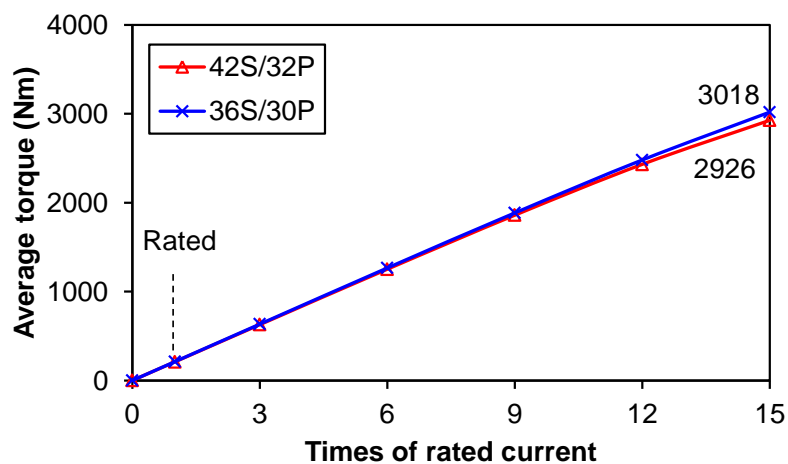
(a) Waveforms



(b) Spectra

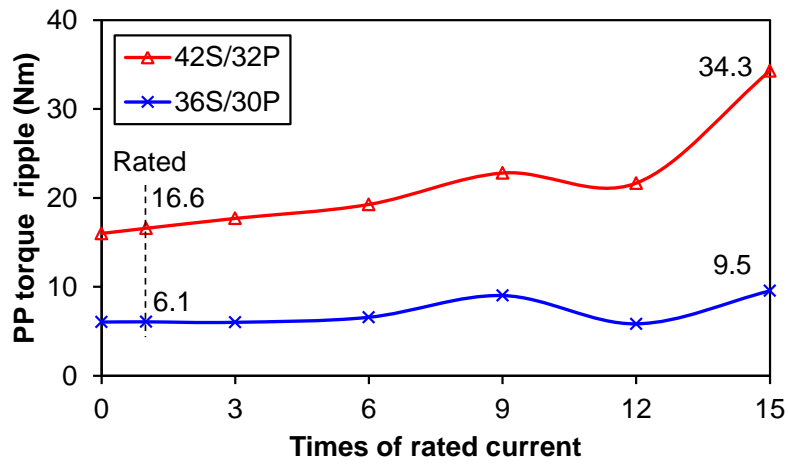
Fig. 3.13. On-load torque (Rated).

Since the armature reaction will be larger with higher current, the torque performances of two electrical machines will show different phenomena, as shown in Fig. 3.14. For average torque-current characteristic, Fig. 3.14(a) shows that both electrical machines have almost the same average torque with a lower current. This has been explained above as the weak armature reaction effect. However, the conventional modular machine will generate larger torque under high current condition, which is due to lower saturated level compared with the proposed modular machine. For the sake of clear explanation, the flux density and stator relative permeability distributions of two electrical machines are compared in Fig. 3.15 under both rated and overload conditions (15 times of rated current-explained in Appendix A). Comparing Fig. 3.15(a) and (b), the saturation level of two electrical machines is similar and the over-saturated redundant teeth in the proposed modular machine lead to some extra flux leakages, which contributes to the average torque reduction. In contrast, much more saturated stator can be seen for the proposed modular machine under overload condition. This is the reason for higher average torque reduction. The stator core relative permeability distributions shown in Figs. 3.15(c) and (d) further verify the saturation differences. When it comes to the PP torque ripple-current characteristic shown in Fig. 3.14(b), it shows that PP torque ripple will overall increase with the current as well. The cogging torque is predominant for lower current, while the higher current means the higher contribution to torque ripple from armature field. Since the increase of PP torque ripple is much smaller than that of average torque, the ratio of two quantities, viz. torque ripple, will decrease.



(a) Average torque





(b) PP torque ripple

Fig. 3.14. Influence of current on torque performance.

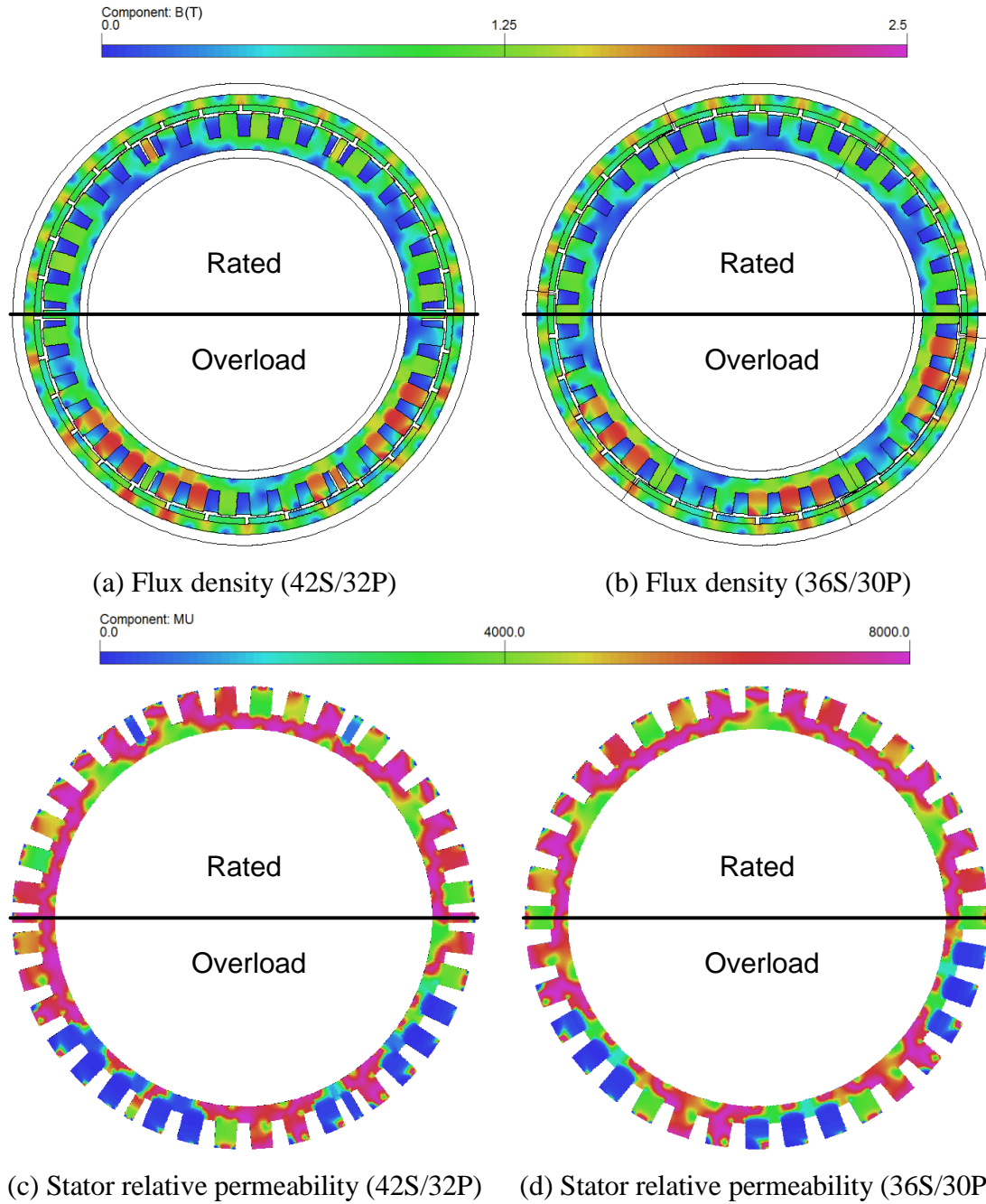


Fig. 3.15. Flux density and stator relative permeability distributions under different conditions.

### 3.2.4 Iron Losses

Due to the change of electrical machine topology, the iron losses of two electrical machines will show different performances. Laminated stator core iron loss ( $P_{Fe}$ ), solid PM and rotor yoke eddy current losses ( $P_{PM}$  and  $P_{ry}$ , respectively) are three major components to be concerned. They can be predicted by the following equations:

$$P_{Fe} = k_h B_m^\alpha f + k_e B_m^2 f^2 \quad (3.6)$$

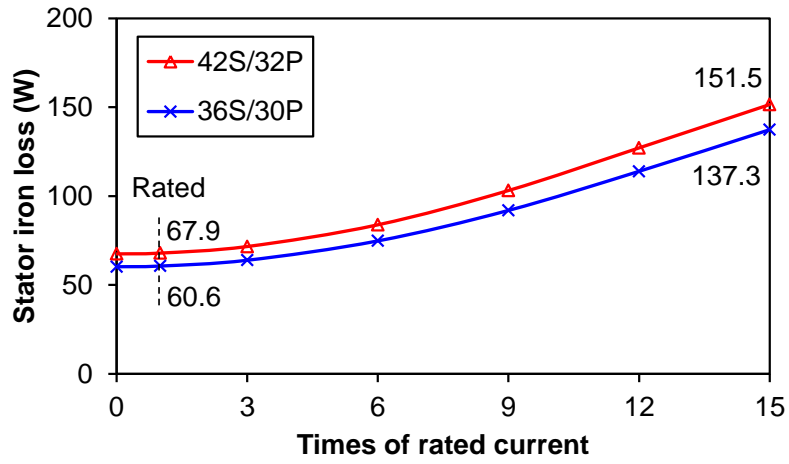
$$\alpha = K_{f1} f^2 + K_{f2} f + K_{f3}$$

$$P_{PM} = \frac{\omega_e}{2\pi} \int_0^{\frac{2\pi}{\omega_e}} \left( \sum_{i=1}^{N_p} \iint_{S_{PMi}} \frac{J_{PMi}^2(t)}{\sigma_{PM}} \cdot dS \right) dt \quad (3.7)$$

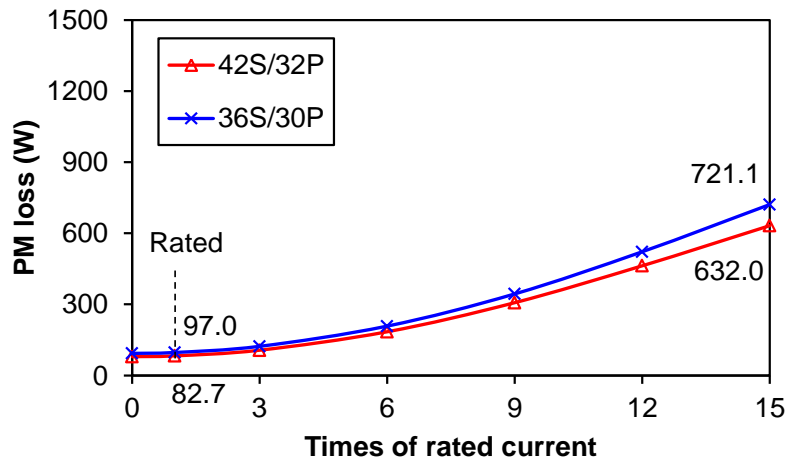
$$P_{ry} = \frac{\omega_e}{2\pi} \int_0^{\frac{2\pi}{\omega_e}} \left( \iint_{S_{ry}} \frac{J_{ry}^2(t)}{\sigma_{ry}} \cdot dS \right) dt \quad (3.8)$$

where  $k_h$  and  $k_e$  are the hysteresis and eddy current loss coefficients of stator lamination;  $B_m$  is the magnitude of flux density;  $f$  is the frequency;  $K_{f1}$ ,  $K_{f2}$  and  $K_{f3}$  are determined by the material property;  $\omega_e$  is the angular frequency in rad/s;  $S_{PMi}$  and  $S_{ry}$  are the area of the  $i^{\text{th}}$  PM and rotor yoke;  $J_{PMi}$  and  $J_{ry}$  are the current density of PM and rotor yoke;  $\sigma_{PM}$  and  $\sigma_{ry}$  (7.4e5 and 6e6 S/m for PMs and rotor cores of the machines in this thesis) are the rotor yoke conductivity of PM and rotor yoke.

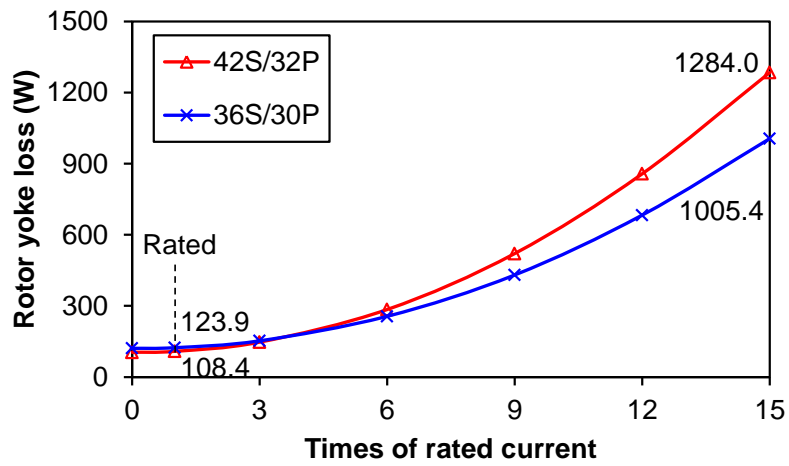
Since all of them are also closely related to the armature field, the variations of these losses with current are shown in Fig. 3.16. The stator iron loss shown in Fig. 3.16(a) occupies a small portion compared with other two components. For the fixed speed operation, this component is mainly related to the peak flux density. The electrical machine has some saturation under open-circuit condition due to PM magnetisation. Though the armature current will further saturate the stator, the increment of magnitude is limited by the material saturation property. The proposed modular machine always has larger stator iron loss owing to the heavier saturation, as stated before. PM eddy current loss obviously increases since it is almost proportional to the square of eddy current density, as shown in Fig. 3.16(b). The proposed modular machine has lower PM eddy current loss compared with the conventional modular machine. Since the total PM volumes of two electrical machines are the same, the higher pole number will contain more PM segments. The more isolated PMs can more effectively impede lower order harmonics inducing eddy current, which is beneficial to lower eddy current loss. Furthermore, this reduction effect can be more obviously observed under high current condition. Fig. 3.16(c) shows that the rotor yoke eddy current loss is larger for the proposed modular machine with the increase of current. The effect of abundant harmonics will be increasingly strong for the high current situations and the rotor yoke is non-segmented. Therefore, these additional harmonics will induce large eddy current. Consequently, the proposed machine has higher loss in the rotor yoke.



(a) Stator iron loss



(b) PM eddy current loss



(c) Rotor yoke eddy current loss

Fig. 3.16. Influence of current on iron losses (170rpm).

Besides these three major iron loss components, the stator copper loss ( $P_{cop}$ ) is one of the major losses in PM machines, which can be predicted based on the following equation:

$$P_{cop} = mI_{ph}^2 R_{ph} \quad (3.9)$$

where  $I_{ph}$  is the phase current in root mean square (RMS) value. For the proposed machine analysed in this chapter, the phase resistance is  $3.32\Omega$ . Thus, the corresponding copper loss is obtained.

For other losses, such as mechanical friction loss, winding loss, stray load loss, etc. They are much less than above four types of losses and are not considered for simplicity. Finally, the efficiency ( $\eta$ ) can be calculated by:

$$\eta = \frac{P_{em}}{P_{em} + P_{Fe} + P_{PM} + P_{ry} + P_{cop}} \times 100\% \quad (3.10)$$

where  $P_{em}$  is the electromagnetic power. The efficiency of the proposed machine is 90%.

### 3.2.5 Demagnetisation

When the electrical machine continuously operates, the losses will lead to the temperature rise of the whole electrical machine. For PMs, the demagnetisation property will be deteriorated with the increase of temperature, as shown in Fig. 3.17.

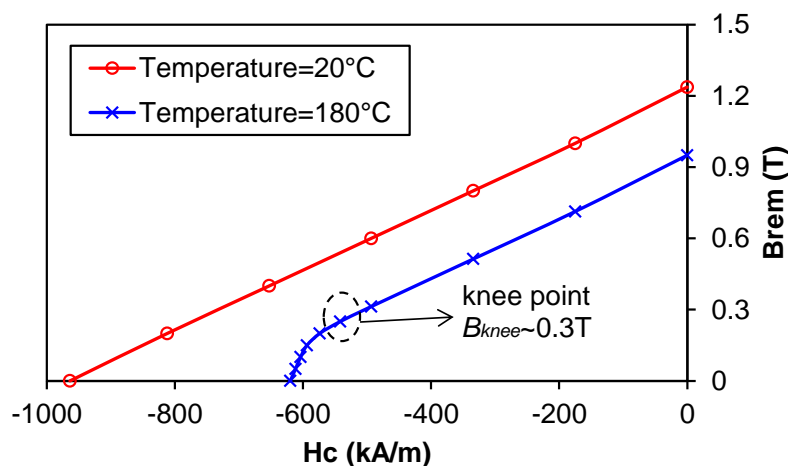


Fig. 3.17. Demagnetisation property of PM (N35UH) under different temperatures.

According to Fig. 3.17, the demagnetisation curve is practically linear under the normal room temperature (20 °C). However, the temperature rise will decrease both the remanence and coercive force. More seriously, the demagnetisation curve becomes more nonlinear. The knee point ( $B_{knee}$ ) is around 0.3T for 180 °C situation and the PM flux density will not move back along this curve if the external demagnetisation excitation is strong. This means the irreversible demagnetisation happens, which will deteriorate electrical machine performances and is undesirable for real applications. When the real demagnetisation property is considered, the performance prediction will be quite complicated [NAI16], which is not the main purpose of this chapter. Thus, only the posterior analysis is executed for 180 °C situation to simply evaluate the partial irreversible demagnetisation of PMs.

The criteria of judging the existence of irreversible demagnetisation is as follows [WAN08]:

$$B_{PMi//} < B_{knee} \quad (3.11)$$

where  $B_{PMi//}$  is the  $i^{\text{th}}$  PM flux density in magnetisation parallel direction.

In order to obtain this parallel component, some necessary derivations for PM flux density components are needed and they are summarised below:

$$B_{PMi//} = B_{PMix//} + B_{PMiy//} = B_{PMix} \cos(\alpha_{PMi}) + B_{PMiy} \sin(\alpha_{PMi}) \quad (3.12)$$

$$B_{PMi\perp} = B_{PMix\perp} + B_{PMiy\perp} = -B_{PMix} \sin(\alpha_{PMi}) + B_{PMiy} \cos(\alpha_{PMi}) \quad (3.13)$$

$$\alpha_{PMi} = \alpha_{PMi0} + \Omega_r t = \alpha_{PMi0} + (i-1) \cdot 2\pi / N_p + \Omega_r t \quad (2.14)$$

where  $B_{PMix}$  and  $B_{PMiy}$  are the  $x$ - and  $y$ -components of the  $i^{\text{th}}$  PM flux densities, respectively;  $B_{PMix//}$ ,  $B_{PMiy//}$  and  $B_{PMix\perp}$ ,  $B_{PMiy\perp}$  are the  $B_{PMix}$  and  $B_{PMiy}$  projections of the  $i^{\text{th}}$  PM flux densities in magnetisation parallel and vertical directions, respectively;  $B_{PMi\perp}$  is the PM flux density in magnetisation vertical direction;  $\alpha_{PMi}$  and  $\alpha_{PMi0}$  are the  $i^{\text{th}}$  PM instant and initial position, respectively;  $N_p$  is the rotor pole number and  $\Omega_r$  is the rotor mechanical speed in rad/s.

Taking the rotor of the proposed modular machine as example, the illustration of the quantities in (3.11)~(3.14) is more directly shown in Fig. 3.18, where the 1<sup>st</sup> PM is used to show the relationship of those flux densities.

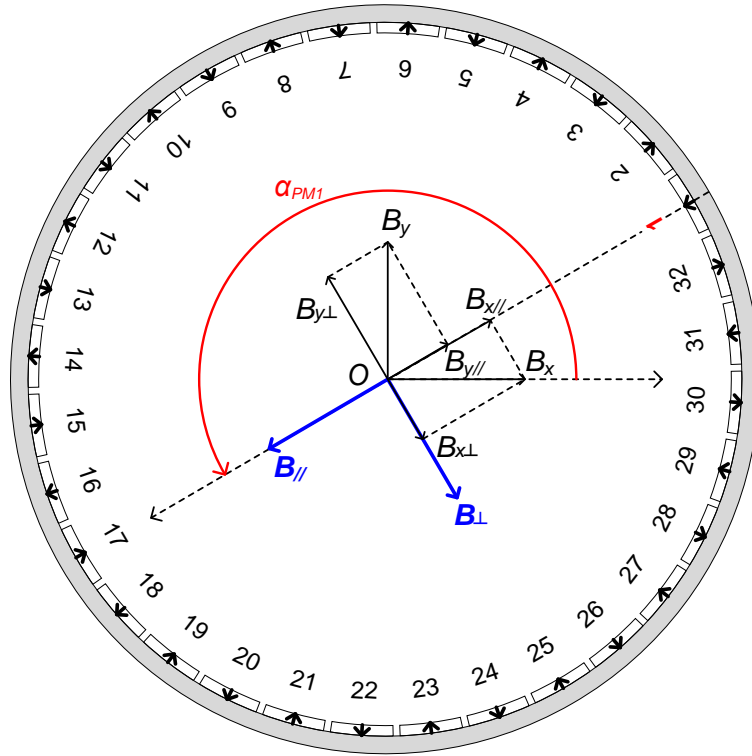


Fig. 3.18. Illustration of different flux densities in PMs.

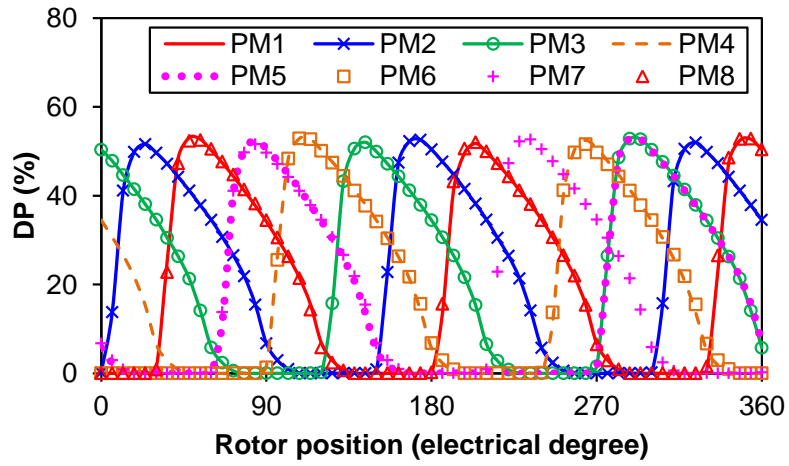
In order to describe the level of irreversible demagnetisation in PMs, the concept of demagnetisation percent (DP) is used. It is defined as follows:

$$DP = \frac{A_{DP}}{A_{PM}} \times 100\% \quad (3.15)$$

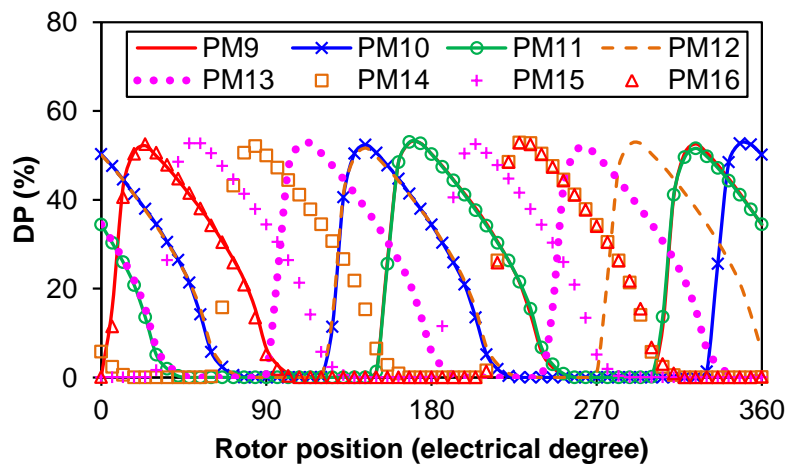
where  $A_{DP}$  is the area of PM with irreversible demagnetisation and  $A_{PM}$  is the PM area.

As has been claimed above, there are 2 and 6 basic units for the proposed and conventional modular machines, respectively. Therefore, only the PMs of each basic unit are concerned, since the irreversible demagnetisation phenomenon on other PMs is just the simple repetition. There are 16 and 5 PMs in each basic unit for the proposed and conventional modular machines, respectively.

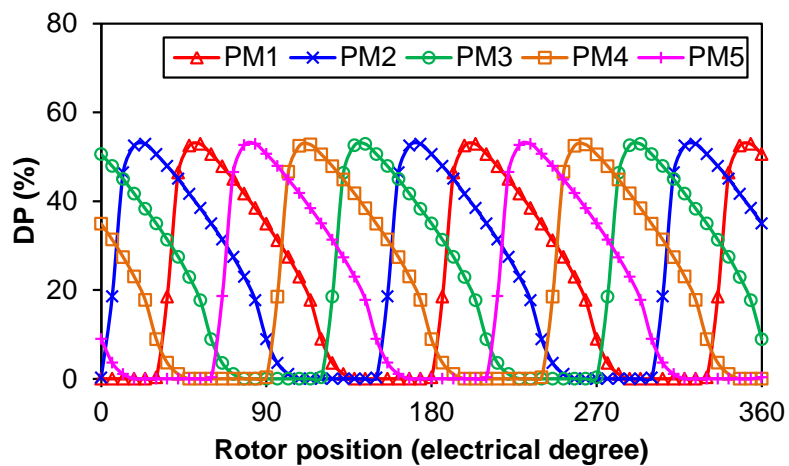
The detailed analysis of irreversible demagnetisation can be based on the DP variation under overload condition for clarity, as shown in Fig. 3.19.



(a) 42S/32P (PM1~PM8)



(b) 42S/32P (PM9~PM16)



(c) 36S/30P (PM1~PM5)

Fig. 3.19. Variation of irreversible DP (Overload).

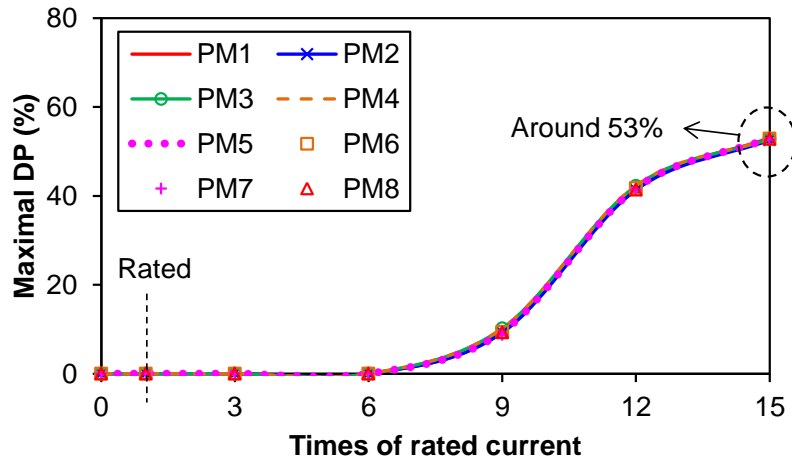
Fig. 3.19 shows that both electrical machines will have 12 times for PMs reaching the maximal DP over one electrical period. The variation pattern for the conventional



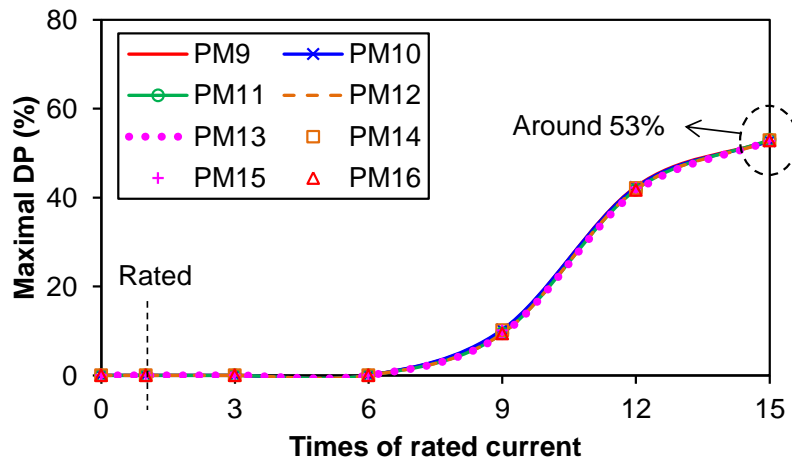
modular machine shown in Fig. 3.19(c) is more easily to be identified. During the rotation of the rotor, each phase coil within the basic unit will reach its absolute maximal value twice, which results in the 12 times appearance of maximal DP for PMs. What is more, the phase shift between two maximal DPs of each PM is fixed. This is due to the same winding layout of each basic electrical machine unit except the alternate anti-phase for adjacent segment. However, Figs. 3.19(a) and (b) show that the phase shift between adjacent maximal DPs for the proposed modular machine is different, although there are still 12 maximal DPs over one electrical period due to the adoption of dual 3-phase windings. The reason for the phase shift difference is the winding layout variation due to the additional phase shift caused by the redundant machine unit. When the rotor rotates, the PMs which pass the effective teeth only will still keep the same phase shift between adjacent maximal DPs (PM 1~4, 6~9, 11~15), while the additional phase shift due to redundant teeth will be added if the PMs move across them (PM 5, 10, 16). With the continuous operation, the phase shift variation will be observed for other PMs, since there will be different PMs alternately moving across redundant teeth. Therefore, the irreversible demagnetisation of each PM is similar.

Since the demagnetisation is related with the armature field, the influence of current on maximal DP over one electrical period is shown in Fig. 3.19.

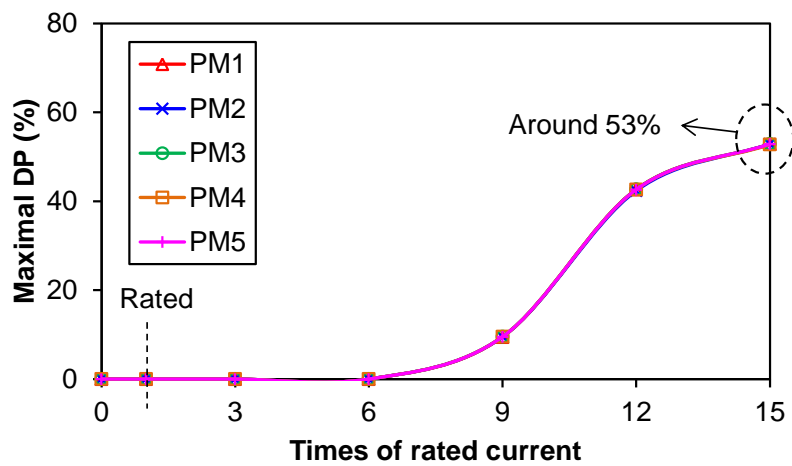
Figs. 3.20(a) and (b) show that 16 magnets have almost the same maximal DP over one electrical period, which is different from the phenomena shown in [PAT15]. The reason for no difference among these PMs is the advantage of adopting dual 3-phase windings with 30 degree phase shift between two sets of windings. Since the influence of subharmonics is restrained, each PM will experience similar electromagnetic field variation over one electrical period. It can be observed that the irreversible demagnetisation only happens when the current is high enough. Furthermore, the maximal DP will be gradually saturated with the increase of armature current, since the armature current is located in rotor  $q$ -axis and it will have opposite effect on the adjacent PMs. When it comes to the conventional modular machine, 5 PMs also show the same maximal DP within one electrical period because of the same reason. It can also be seen that the maximal DP is similar for two electrical machines, which means the structure of the proposed modular machine will not deteriorate irreversible demagnetisation characteristic.



(a) 42S/32P (PM1~PM8)



(b) 42S/32P (PM9~PM16)



(c) 36S/30P (PM1~PM5)

Fig. 3.20. Influence of armature current on maximal irreversible DP.

### 3.3 Influence of Angle between Two Sets of Windings

#### 3.3.1 Winding Connection

Besides the 30 degree phase shift between two sets of windings, zero phase shift type is another kind of dual 3-phase windings, which is also named as split phase winding [VIZ06]. The merit of such kind of winding is high fault-tolerant capability, since two sets of windings are physically separated. For the proposed modular machine, this kind of winding can be adopted as well and only the performances under normal operation will be compared. The faulty operation will be shown later. The star of slots shown in Fig. 3.4(c) is used to determine winding layout. The dual 3-phase windings are shown in Fig. 3.21 and they are named as “Thirty type” and “Zero type” for simplicity.

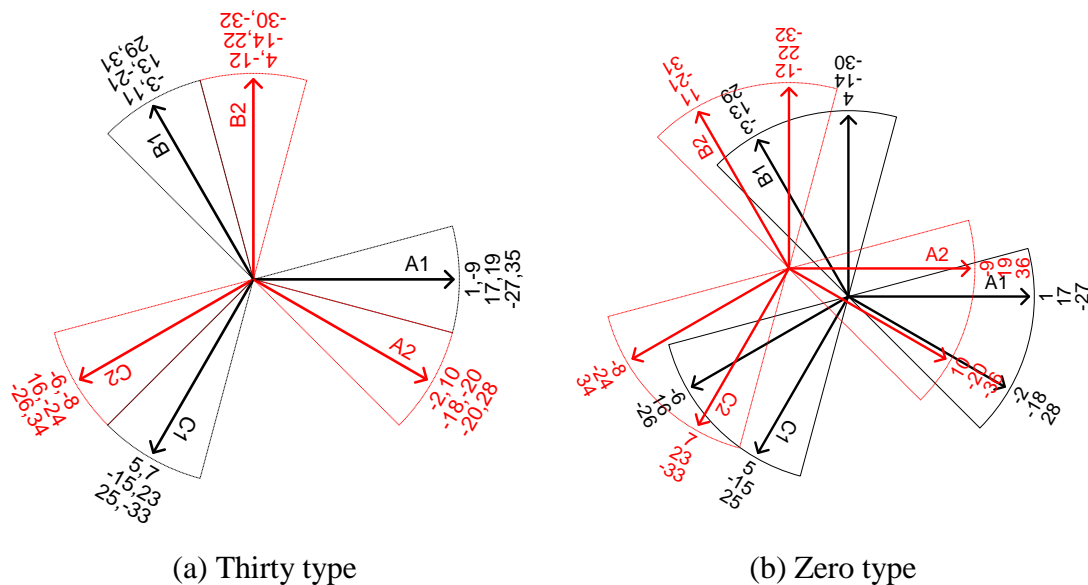


Fig. 3.21. Winding arrangements for two kinds of dual 3-phase windings.

For the Zero type shown in Fig. 3.21(b), there are some differences being observed compared with the Thirty type shown in Fig. 3.21(a):

- (1) The phase belt numbers are 6 and 12 for the Zero and the Thirty type, respectively. Thus, the coils of each phase are concentrated for the Thirty type and distributed for the Zero type in this example.
- (2) Since the winding arrangement has been changed, the coils constructing each phase are different for two kinds of windings as well.

(3) Each segment contains the coils of two sets of windings for the Thirty type, while only one set of winding exists in one segment for the Zero type.

Based on the winding arrangement shown above, the cross-sections of the same electrical machine with different dual 3-phase windings are plotted in Fig. 3.22.

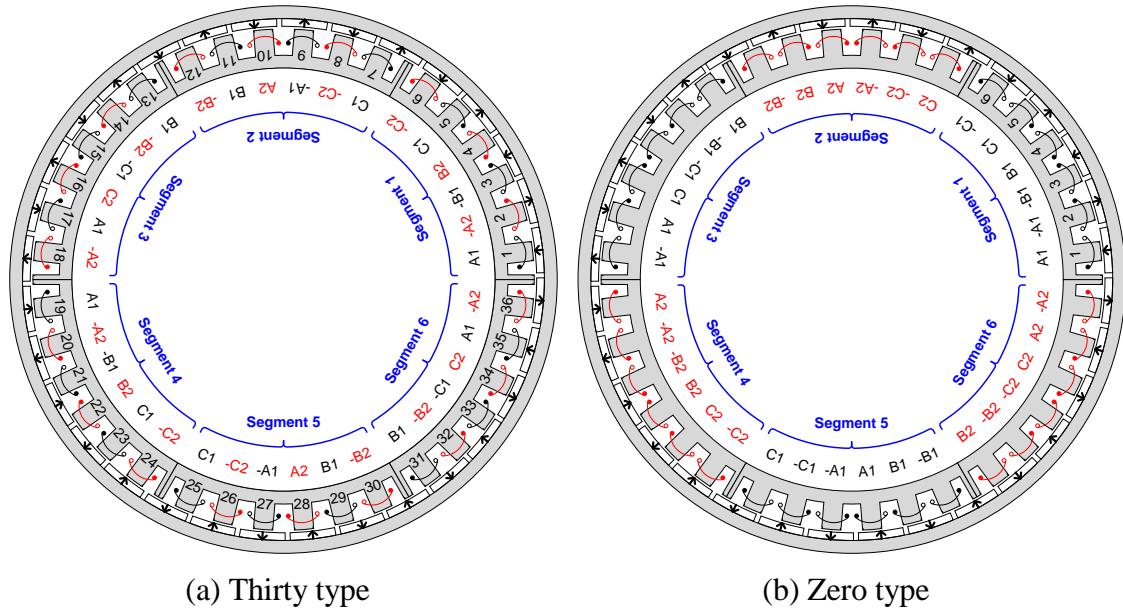


Fig. 3.22. Cross-sections of the proposed modular machine with different dual 3-phase windings.

Fig. 3.22 shows that the first coil of each segment is different due to the adoption of different phase shift between two sets of windings. If only one set of winding exists, it can be found that all slots are still occupied for the Thirty type. In contrast, the slots of some segments will be vacant if there is only one set of winding for the Zero type. The performance comparison will be shown for these two electrical machines following the above analysis procedure.

### 3.3.2 Field Distribution

Due to the change of winding type, the rotor initial positions of two electrical machines will be different. The phase-A1 axis coincides with the positive direction of vector 1 shown in Fig. 3.21(a), whereas the direction of phase-A1 axis should be 15 electrical degrees ahead referring to vector 1 shown in Fig. 3.21(b). When the rotor locates at this position, the equal potential line and flux density distribution are shown in Fig. 3.23.

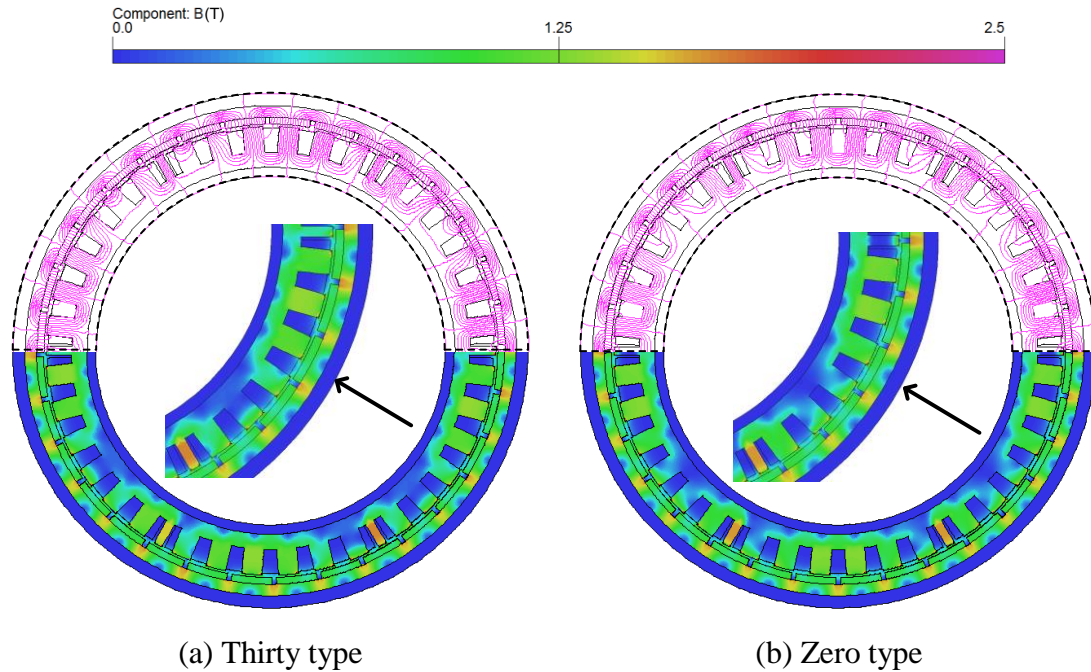
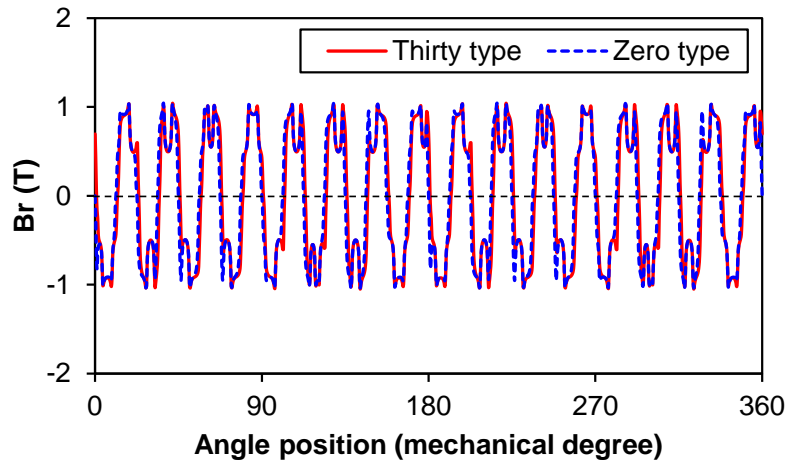
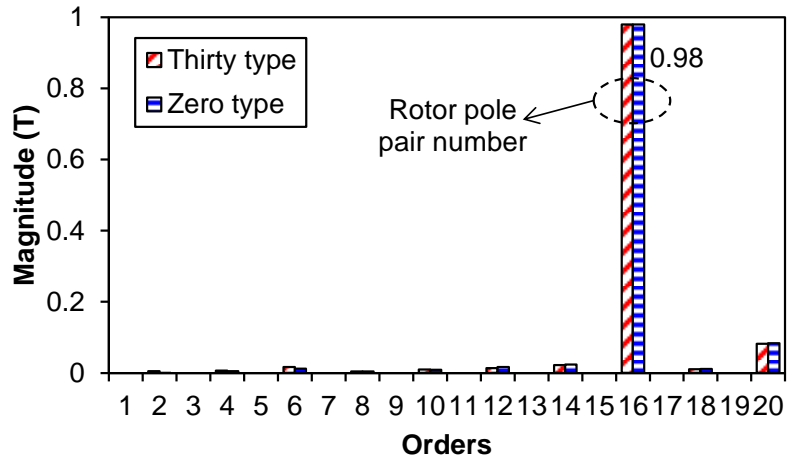


Fig. 3.23. Field distributions due to PMs.

Fig. 3.23 demonstrates that the difference is quite small for two electrical machines, since they can be treated as the results of two different instants for the same electrical machine. The clearer influence of different rotor initial positions can be seen from the air-gap flux density, as shown in Fig. 3.24. Since the rotor initial position of the Zero type is ahead, its waveform will be shifted to the left a bit as well compared with that of the Thirty type. Since the shift angle needs to be transferred into mechanical degree, the difference is negligible in Fig. 3.24(a). The more detailed difference can be found in Fig. 3.24(b). The harmonic orders are the same for two electrical machines as expected. In theory, the magnitude of each harmonic component of two electrical machines should be the same, while the unavoidable computation error results in minor difference.



(a) Waveforms



(b) Spectra

Fig. 3.24. Air-gap flux density due to PMs.

For the armature field, the field distribution is shown in Fig. 3.25 when only the rated current is fed into two sets of windings.

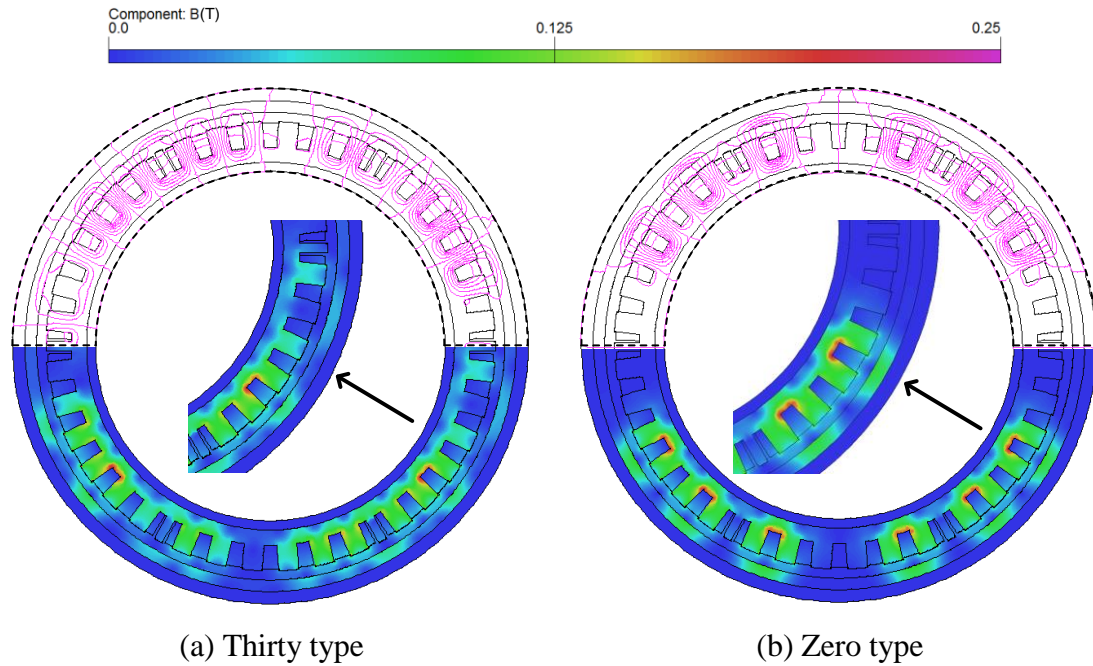
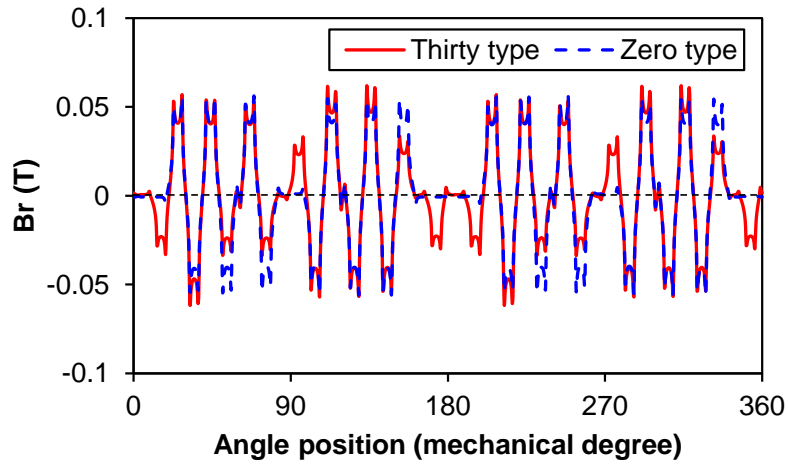
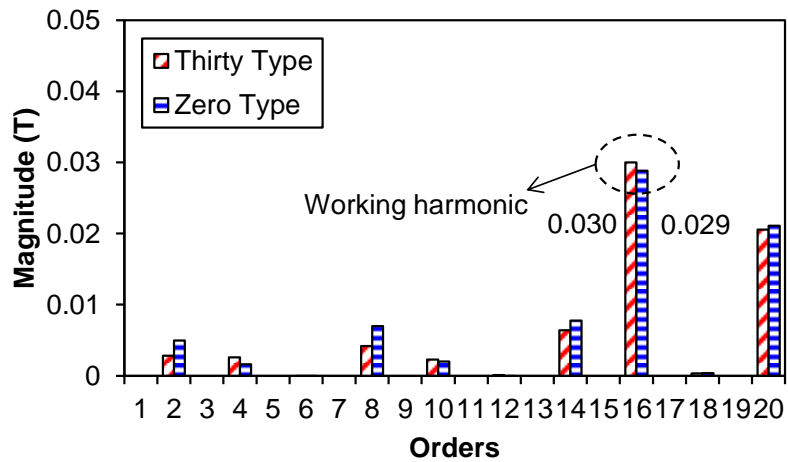


Fig. 3.25. Field distributions due to rated armature current only.

The more obvious difference can be clearly seen for two electrical machines in Fig. 3.25. Since the coils of each phase are more distributed for the Thirty type, the flux lines and flux densities are more uniformly distributed in this electrical machine. For the Zero type, the phase winding is more concentrated, which leads to the flux focusing in some parts of the electrical machine. This will make the electrical machine locally saturated. This difference will more clearly reflect in air-gap flux density, as shown in Fig. 3.26. Fig. 3.26(a) shows that the air-gap flux density waveform of the Zero type will be more distorted compared with that of the Thirty type. The waveforms of two electrical machines coincide with the equal potential line distributions. For the spectra shown in Fig. 3.26(b), more information can be acquired. The highest magnitude will be the 16<sup>th</sup> harmonic, viz. working harmonic. However, it will be a bit lower for the Zero type, which is due to the winding distribution effect. The winding arrangement shown in Fig. 3.21 can easily explain this difference. The harmonic orders of two electrical machines are the same and there are no odd orders because of the existence of 2 basic units in both electrical machines. The difference of harmonic magnitude comes from the properties of different dual 3-phase windings. The higher magnitude for harmonics will jeopardise the electrical machine performance. From this point of view, the Thirty type could be better.



(a) Waveforms



(b) Spectra

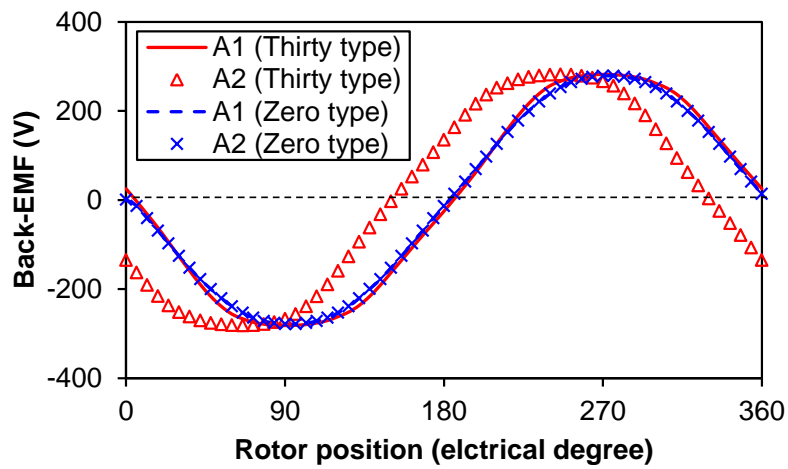
Fig. 3.26. Air-gap flux densities due to armature current (Rated).

### 3.3.3 Open-circuit Back-EMF and Cogging Torque

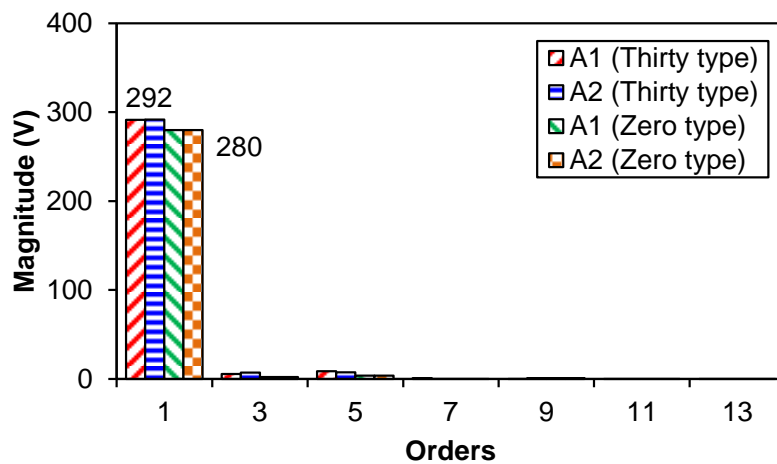
The phase-A1 and A2 are chosen as representatives to show the open-circuit phase back-EMF when the rotor rotates at rated speed, as shown in Fig. 3.27. The 30 degrees and zero degree phase shift between phase-A1 and A2 can be seen for two electrical machines in Fig. 3.27(a), respectively. Besides, the waveforms of two phases are balanced as well. Comparing the phase-A1 waveforms of two electrical machines, some differences can be seen and they will be more apparently observed in Fig. 3.27(b). The reduction of fundamental component for the Zero type is owing to the distribution factor as well. Since the winding of the Thirty type is concentrated, the 3<sup>rd</sup> and 5<sup>th</sup> harmonics have higher magnitude than the Zero type. However, the 3<sup>rd</sup> harmonic will disappear in the line back-EMF for the star connection winding and the



influence of the 5<sup>th</sup> harmonic will be reduced in the Thirty type; therefore the on-load torque is larger.



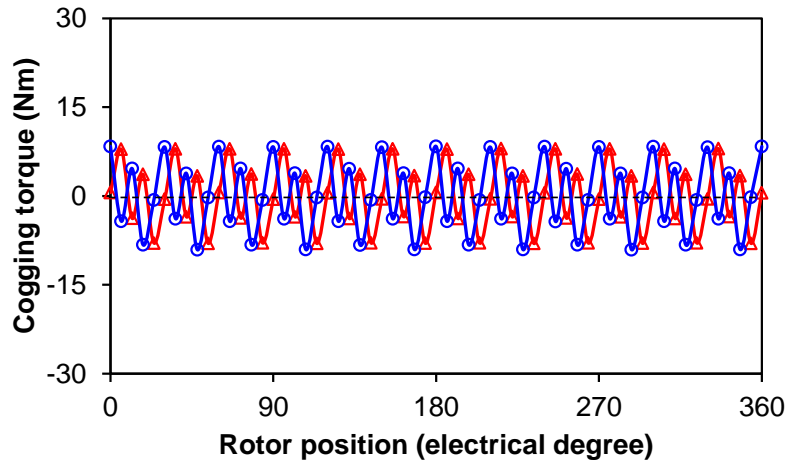
(a) Waveforms



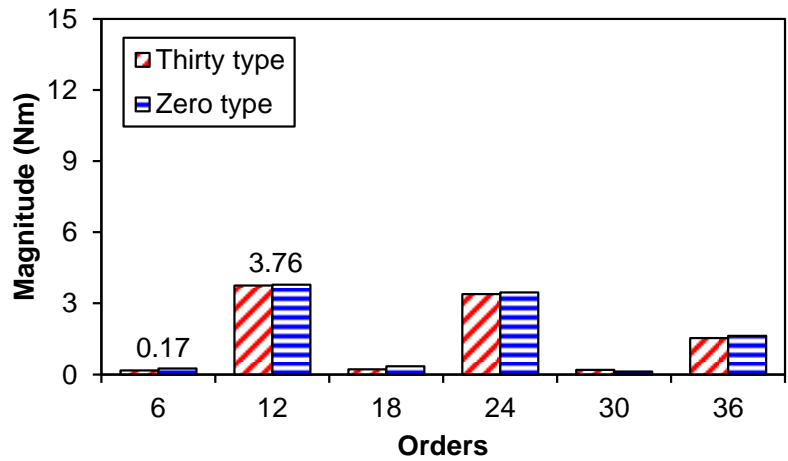
(b) Spectra

Fig. 3.27. Open-circuit phase back-EMFs (170 rpm).

The open-circuit cogging torque of two electrical machines is drawn in Fig. 3.28. As expected, the waveforms shown in Fig. 3.28(a) are practically the same in shape except the phase shift. This phase shift is the same as the rotor initial position phase shift, viz. 15 electrical degrees. Fig. 3.28(b) shows that the torque ripples (harmonics) have the same orders with some negligible differences in magnitude. Theoretically, they should be exactly the same. The reason for this is the unavoidable computation error as stated above.



(a) Waveforms



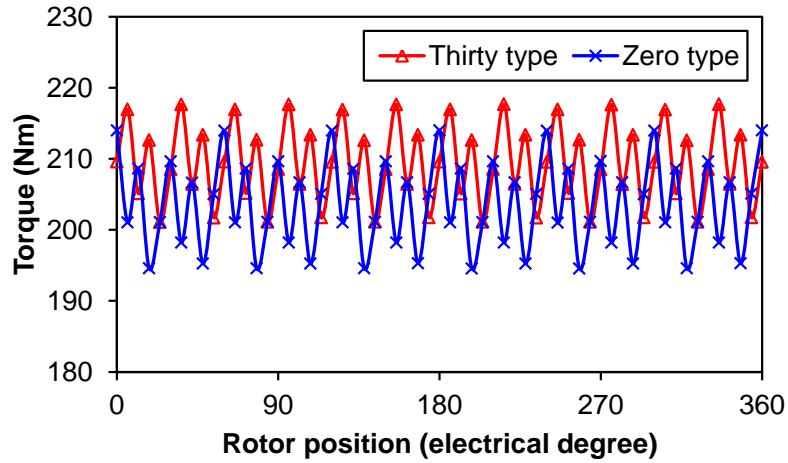
(b) Spectra

Fig. 3.28. Cogging torque.

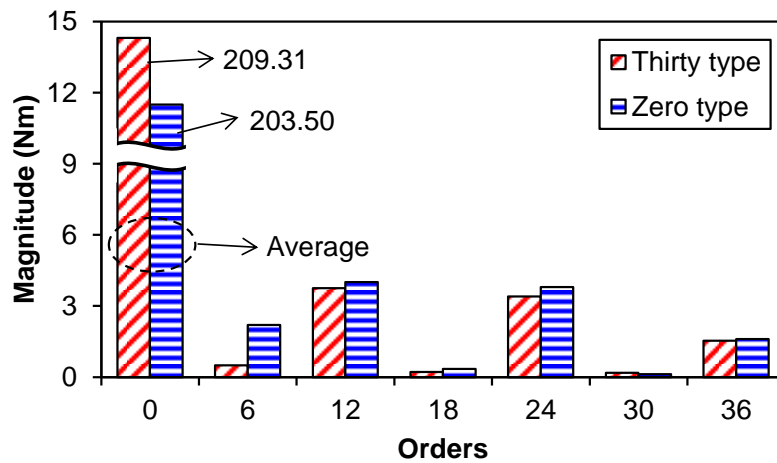
### 3.3.4 On-load Torque

When the two electrical machines operate under rated condition, the electromagnetic torque is shown in Fig. 3.29. It can be seen from Fig. 3.29(a) that average torque is lower for the Zero type. Since the armature field is much weaker compared with the PM field, the saturation is hardly changed under rated condition. Thus, the average torque can be considered to be determined by the fundamental phase back-EMF. Besides, the fluctuations of two electrical machines are different and more details are displayed in spectra shown in Fig. 3.29(b). The most obvious change of harmonic torques is the increase of the 6<sup>th</sup> component, especially for the Zero type. For the Thirty type, the phase shift between two sets of windings will prevent the amplitude of the 6<sup>th</sup> component and this is one of the advantages. For the

Zero type, the electrical machine is similar to a single 3-phase electrical machine. The existence of the 5<sup>th</sup> and 7<sup>th</sup> phase back-EMF harmonics will lead to this 6<sup>th</sup> harmonic torque.



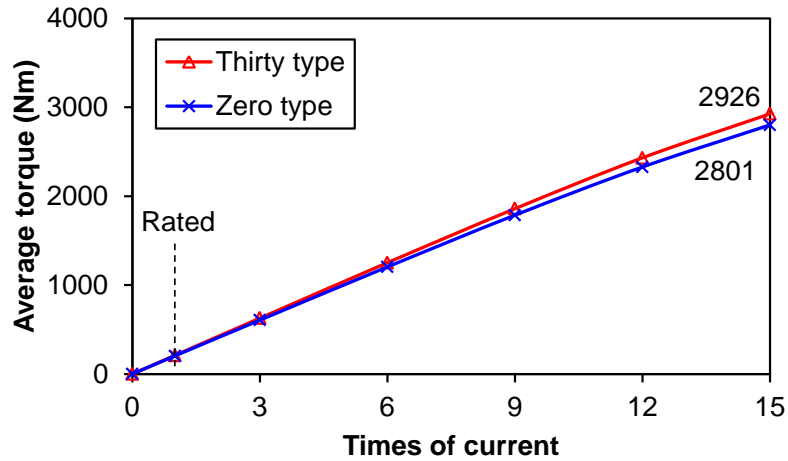
(a) Waveforms



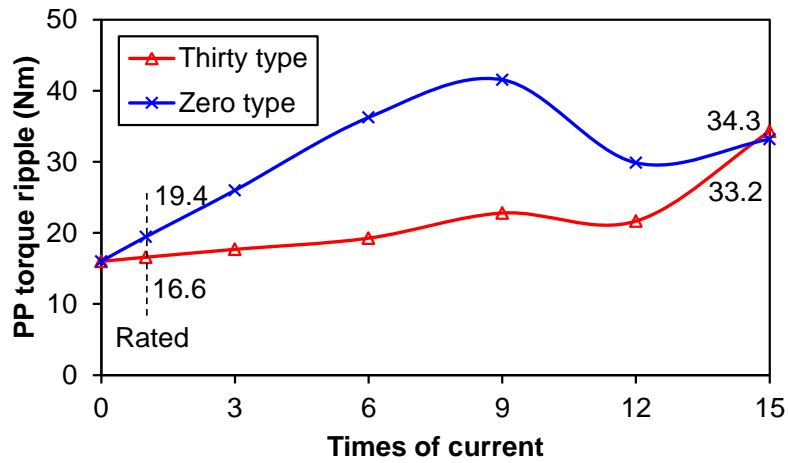
(b) Spectra

Fig. 3.29. On-load torque (Rated).

When the current varies, the on-load torque will accordingly show different performances in both average torque and PP torque ripple, as shown in Fig. 3.30. With the increase of current, the difference between two electrical machines will be enlarged for average torque. This is due to the increase of local saturation for the Zero type.



(a) Average torque



(b) PP torque ripple

Fig. 3.30. Influence of current on torque performance.

The flux density and stator core relative permeability distributions of two electrical machines are given in Fig. 3.31 for clarity. When the current equals to its rated value, the local saturation is not strong for the Zero type comparing the flux density distributions shown in Figs. 3.31(a) and (b). Although there is torque reduction compared with the Thirty type, the reduction in percent is minor. When the current reaches the 15 times of the rated value (Overload), the local saturation is much severer for the Zero type. Therefore, the average torque will be more reduced compared with the low current situation. Such difference can be more clearly observed for stator relative permeability distributions shown in Figs. 3.31(c) and (d). The variation of PP torque ripple with current is more complicated. When the current is low, the cogging torque is predominant and the armature influence is more obvious

for the Zero type. With the current increase, the torque ripple due to armature field will grow faster for the Zero type as well. However, the torque ripple will reduce if the current achieves specific value, since the torque component could cancel each other due to phase change caused by the local saturation. That is why the PP torque ripple more fiercely varies for the Zero type. The PP torque ripple of the Thirty type will not vary so obviously since the local saturation is not so heavy, whereas the trend of fast increase will be also expected when the current is much higher. In terms of torque performances, the Thirty type again shows better.

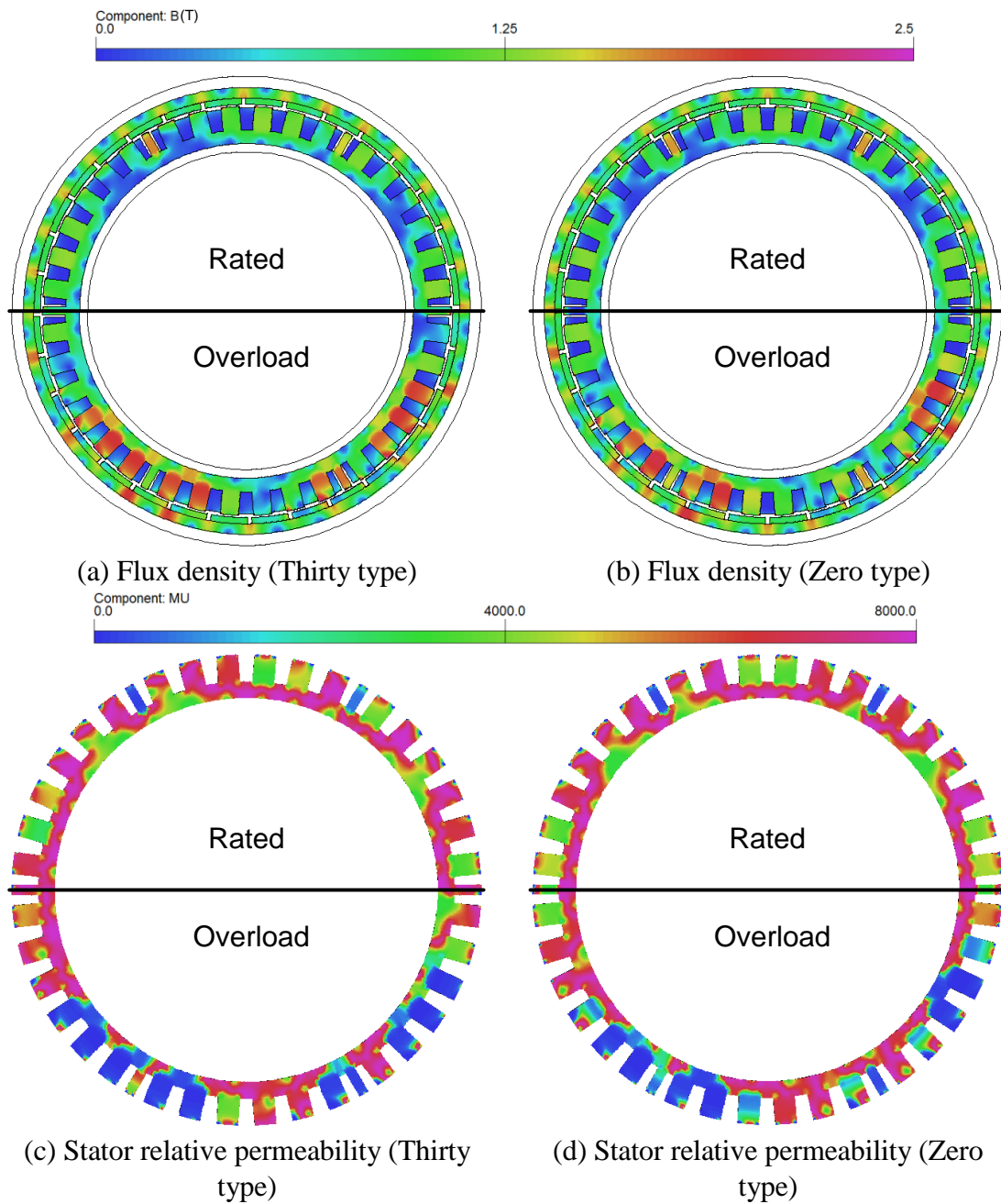
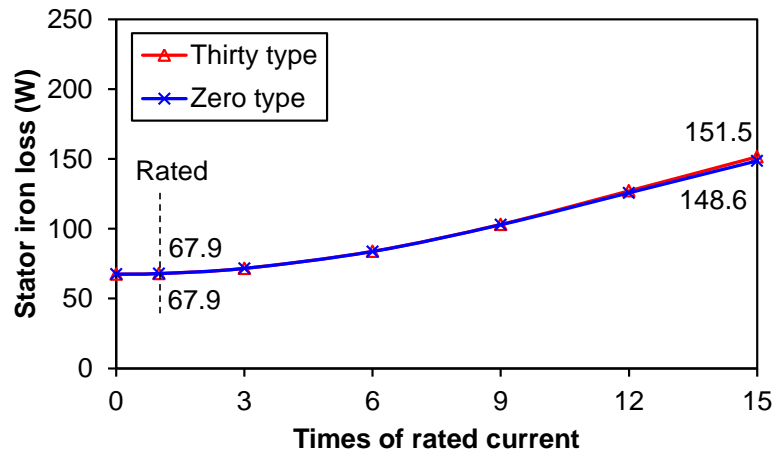


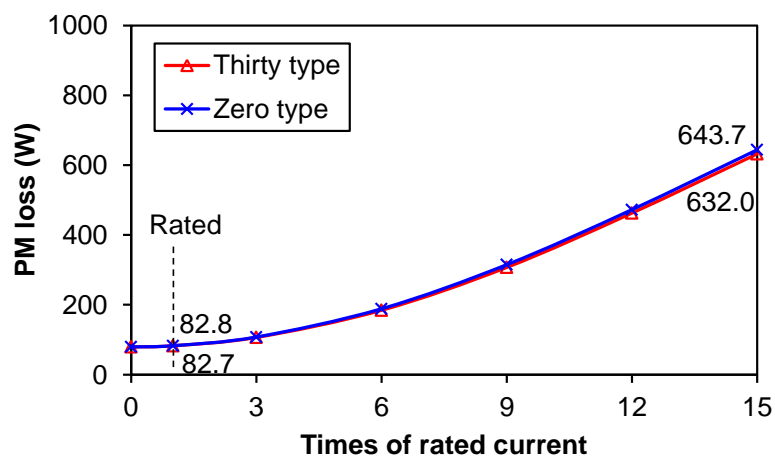
Fig. 3.31. Flux density distribution and stator relative permeability.

### 3.3.5 Iron Losses

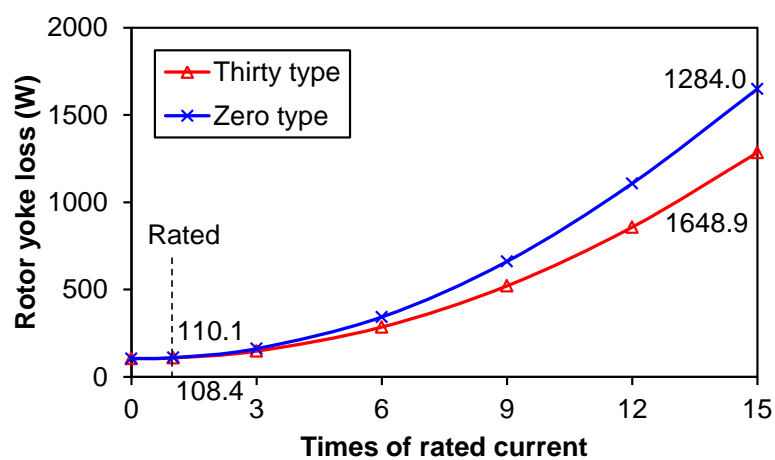
The stator iron loss, PM and rotor yoke eddy current loss are still concerned here. The influence of current on them is shown in Fig. 3.32.



(a) Stator iron loss



(b) PM eddy current loss



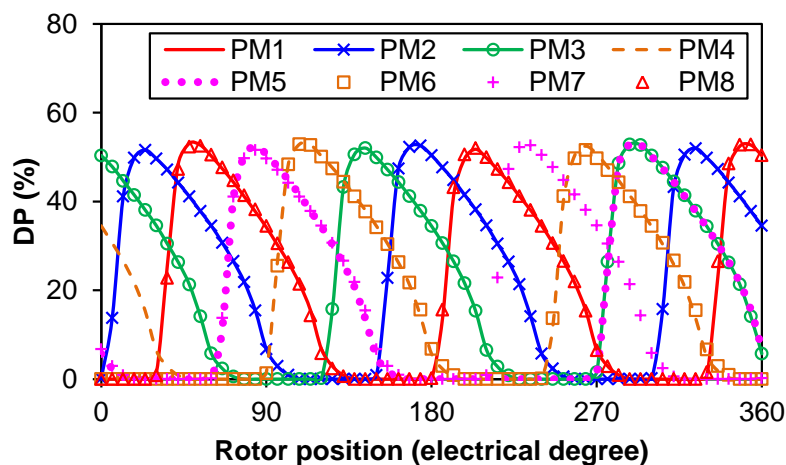
(c) Rotor yoke eddy current loss

Fig. 3.32. Influence of current on iron losses (170rpm).

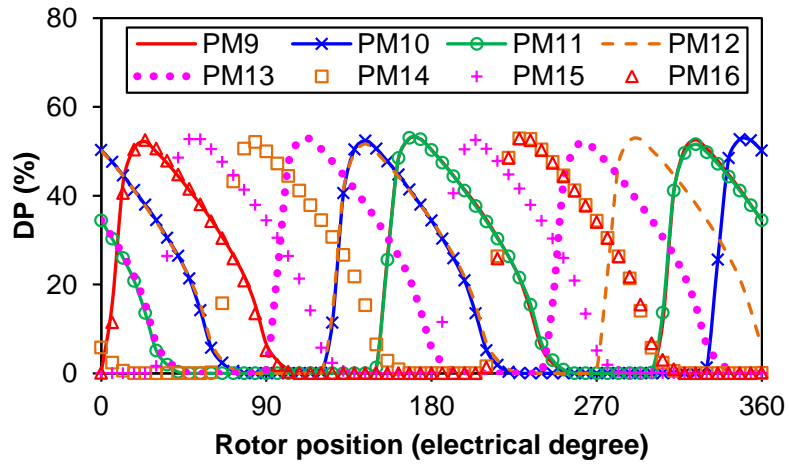
The difference of stator iron loss and PM eddy current loss is quite small for two electrical machines no matter the value of current. For the stator iron loss, the stator core saturation variation with current is not very obvious. Thus, only the negligible difference can be seen for two electrical machines even if the current is high in Fig. 3.32(a). Due to the isolation between adjacent PMs, the generation of induced current from those lower order harmonics will be prevented. That is why the PM eddy current loss is also quite similar for two electrical machines even though the current is high, as shown in Fig. 3.32(b). However, it can still be found that the PM eddy current loss of the Zero type is slightly larger than that of the Thirty type. After all, the side effect of subharmonics cannot be fully prohibited. The most obvious difference can be seen for the rotor yoke eddy current loss. It is not made of laminations as the stator core or does not consist of several segments. Thus, all of the harmonics asynchronous to the rotor speed will induce eddy current in solid body. Under such circumstance, the difference caused by two kinds of windings will be evidently observed. With the increase of current, the influence of harmonics will increase, as shown in Fig. 3.32(c). Since the rotor yoke eddy current loss will grow faster than that of induced eddy current, the difference is increasingly large.

### 3.3.6 Demagnetisation

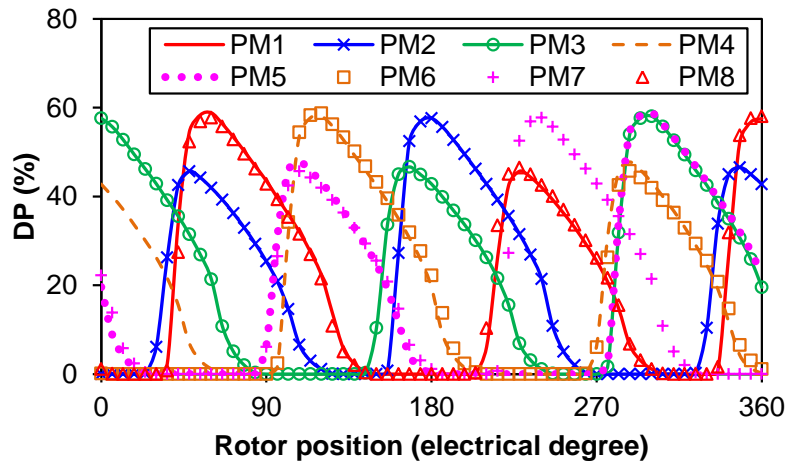
The same process is applied to compare the irreversible demagnetisation characteristics of two electrical machines. The detailed DP variations of each PM are shown in Fig. 3.33 for the sake of elaboration.



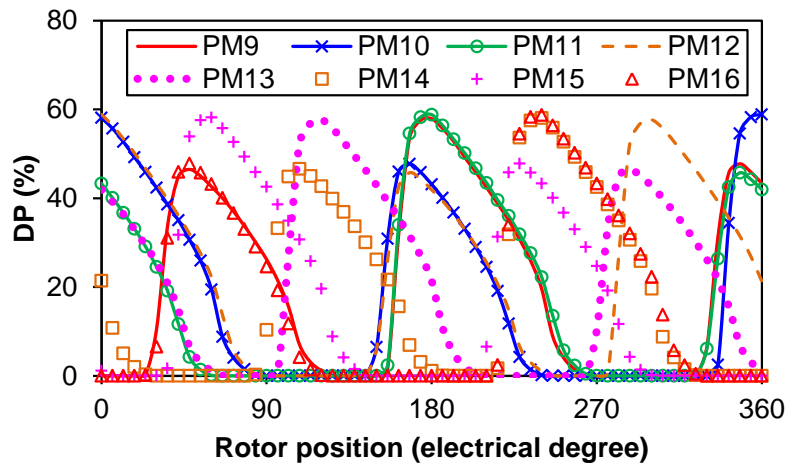
(a) Thirty type (PM1~PM8)



(b) Thirty type (PM9~PM16)



(c) Zero type (PM1~PM8)



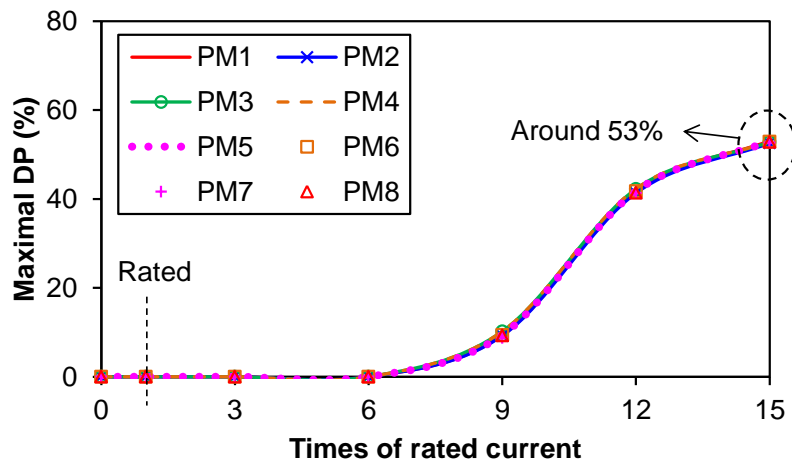
(d) Zero type (PM9~PM16)

Fig. 3.33. Variation of irreversible demagnetisation percent (Overload).

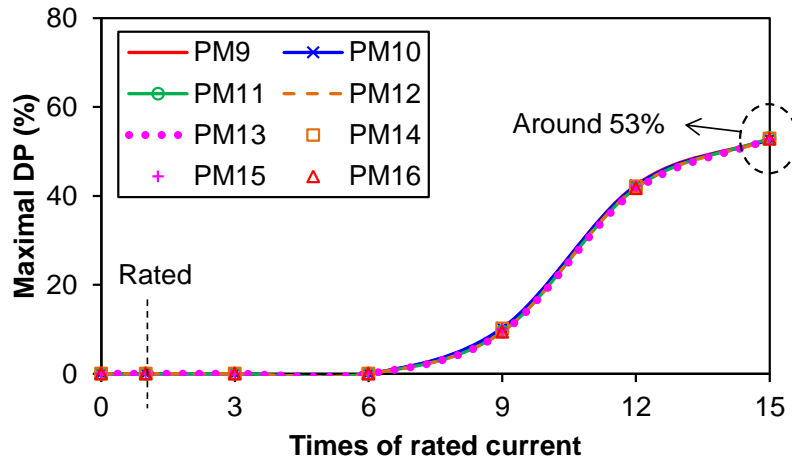


Fig. 3.33 clearly shows that the PM DP of the Zero type will be quite different from that of the Thirty type, which is the consequence of lower order harmonic influence. The 1<sup>st</sup> PM is taken as an example to explain the reason. For PM 1, the DP will shift a bit for the Zero type because of the shift of rotor initial position, while the most obvious difference is the adjacent peak values. They are the same for the Thirty type and different for the Zero type. Such difference is caused by the interaction between PM and armature field. The larger lower order harmonics of the Zero type will contribute to this. Furthermore, the positions having the maximal DP are also not uniformly distributed for the Zero type compared with the Thirty type, which is owing to the winding arrangement difference of two electrical machines. Other PMs can be analysed in the same way and the influence of redundant teeth on phase shift between DP peak values is the same for two electrical machines.

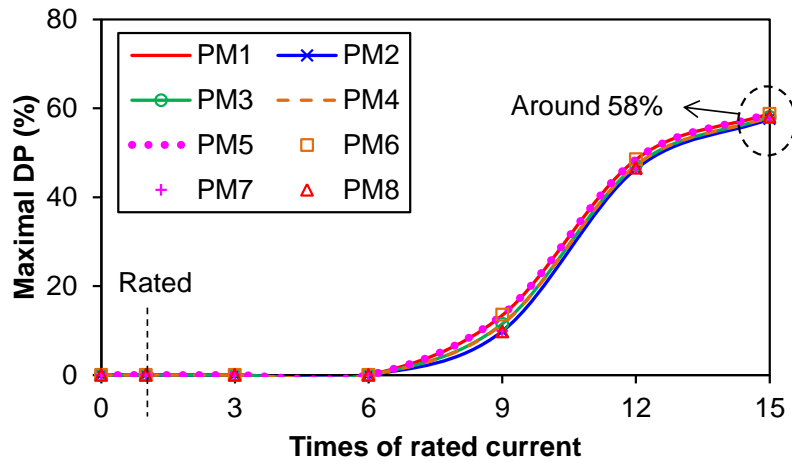
The influence of current on maximal DP is shown in Fig. 3.34 for 16 PMs within one basic unit.



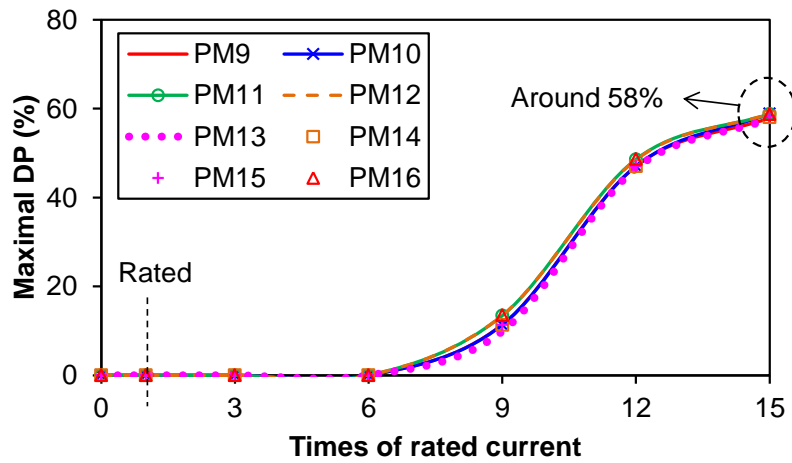
(a) Thirty type (PM1~PM8)



(b) Thirty type (PM9~PM16)



(c) Zero type (PM1~PM8)



(d) Zero type (PM9~PM16)

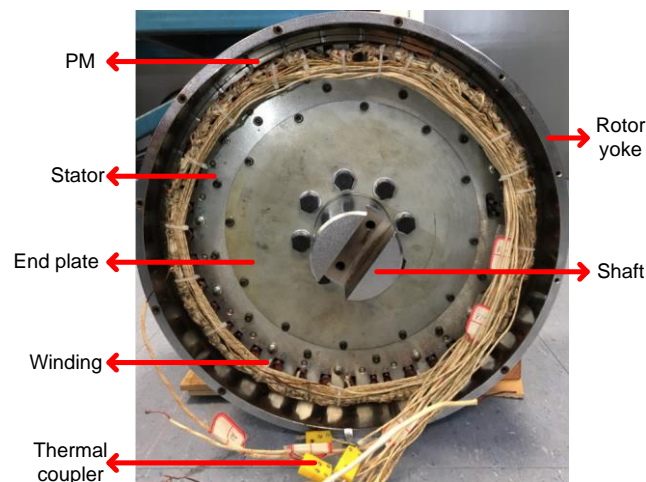
Fig. 3.34. Influence of current on maximal irreversible DP.

The trend of maximal DP variation is similar for two electrical machines, whereas the partial irreversible demagnetisation is heavier for the Zero type, which is again caused by the local saturation. Besides, the maximal DP shows more difference for the Zero type than the Thirty type, especially under low current situation. The reason for such difference is also the parasitic effect of lower order harmonics. Since the magnitude of these harmonics is higher for the Zero type, this results in the different irreversible demagnetisation over one electrical period for different PMs. However, the difference will become increasingly low with the increase of current, since the available demagnetisation has practically achieved its limit.

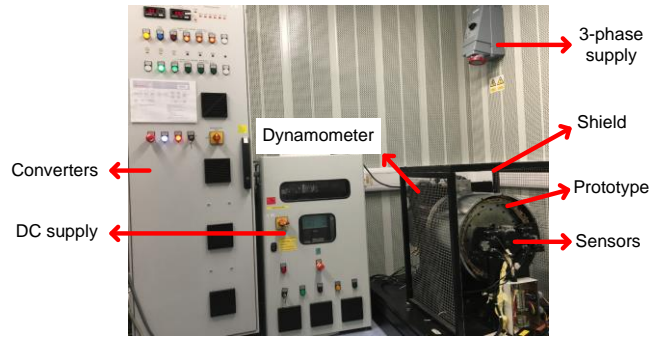
According to the results shown here, the Thirty type has more irreversible demagnetisation withstand capability.

### 3.4 Experimental Validation

The proposed modular machine has been prototyped to validate the analyses above and the detailed specifications are drawn in Appendix C. Because of the segmented stator core, the mechanical assembly is pretty hard. The additional air-gaps between each segment are unavoidable. Thus, special end ring is used to fix the stator segments. The side effects due to segmentation can be observed in the following test results. The picture of the electrical machine and the test rig are shown in Fig. 3.35. The winding is connected in the Thirty type here because of its advantages compared with the Zero type.



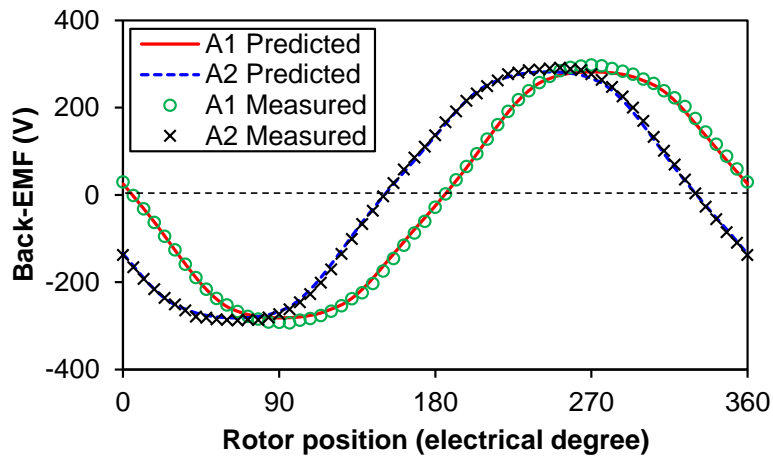
(a) Prototyped electrical machine



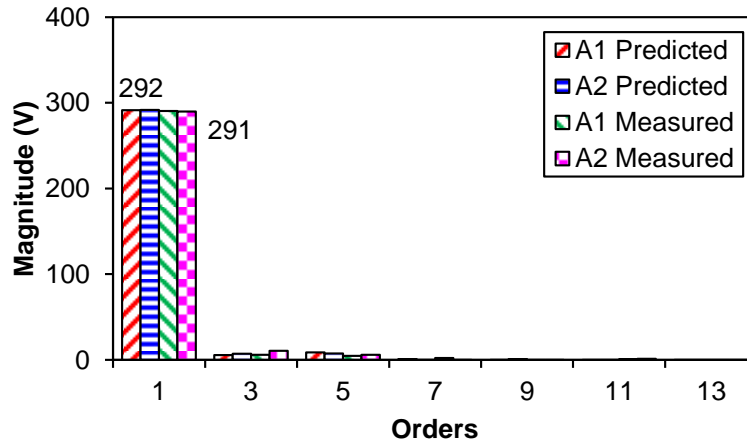
(b) Test rig

Fig. 3.35. Prototyped electrical machine and test rig.

The open-circuit back-EMFs of phase-A1 and -A2 are measured and compared in Fig. 3.36 under the rated speed. In term of waveforms shown in Fig. 3.36(a), the measured results for 42S/32P modular machine match those predicted by FEA quite well. The phase-A2 is 30 degrees ahead compared with the phase-A1, which means the winding arrangement is correct. The more details can be seen from spectra shown in Fig. 3.36(b). As expected, the fundamental components of measured results are a bit smaller than those of predicted ones. Although some differences can be seen in higher order harmonics, they are quite minor. The reason for these differences is the unavoidable manufacture tolerance.



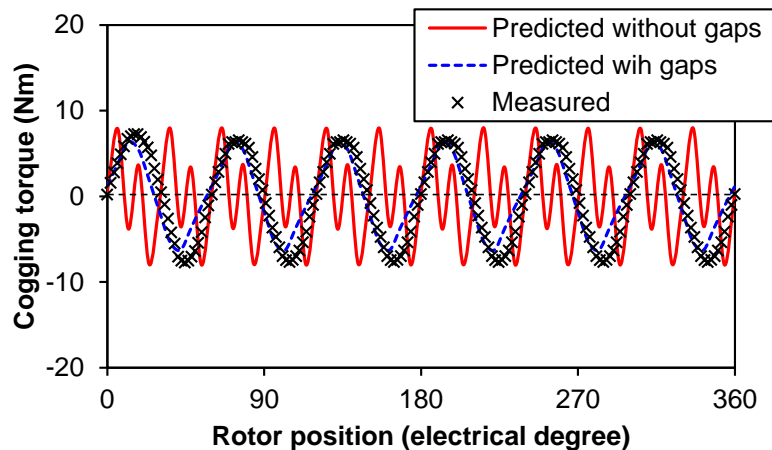
(a) Waveforms



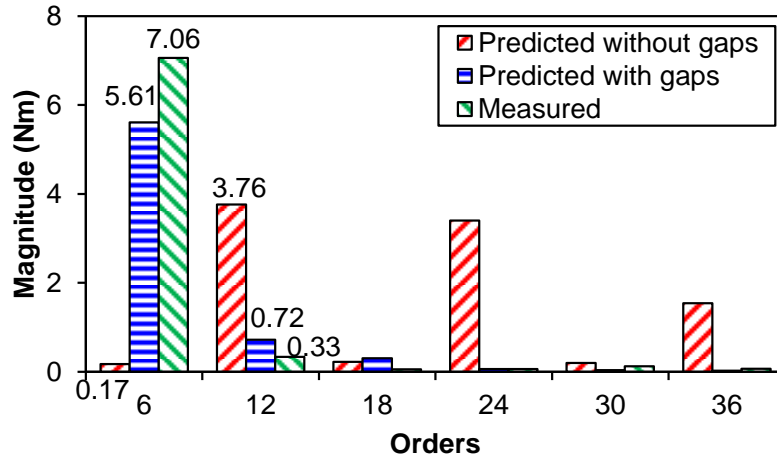
(b) Spectra

Fig. 3.36. Comparison of predicted and measured open-circuit back-EMFs for phase-A1 and -A2 (170rpm).

Under open-circuit, the cogging torque is measured as well and the results are plotted in Fig. 3.37. It can be seen that the difference between measured result and FE predicted ideal one are different in periodic number. This is also owing to the manufacture tolerance. Since the cogging torque is quite sensitive to air-gap flux density harmonics, the additional components resulted from manufacture tolerance will affect the cogging torque. According to the waveforms and spectra shown in Fig. 3.37, it can be estimated that the additional gaps between six stator segments could be the reason for such difference. When these additional gaps exist, the stator is equivalent to being consisted of six large teeth. Then, the cogging torque period will be six over one electrical period. The predicted results with 1mm additional gaps between segments are also shown in Fig. 3.37 to validate this.



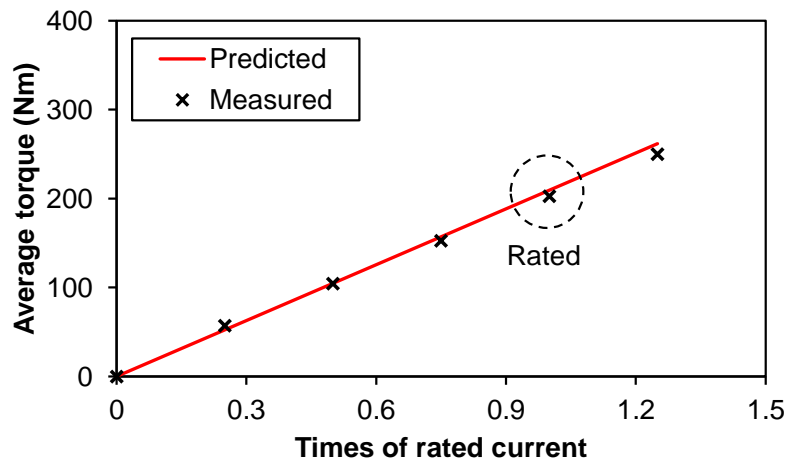
(a) Waveforms



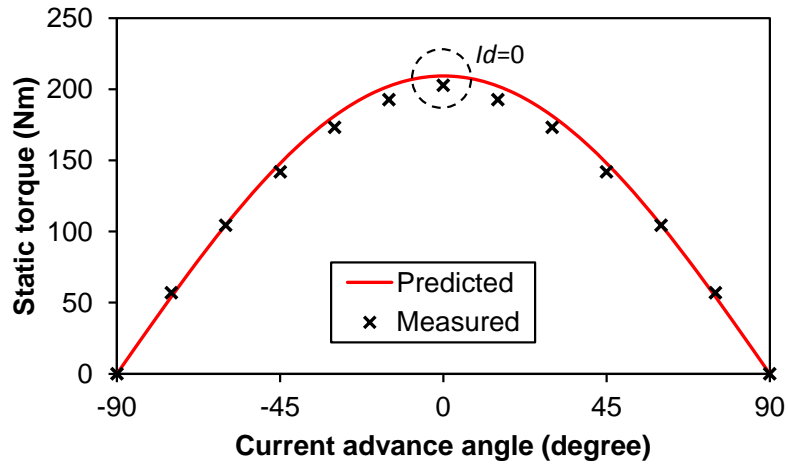
(b) Spectra

Fig. 3.37. Comparison of predicted and measured cogging torques.

When the currents are fed into two sets of windings, the proposed modular machine operates under normal operation. When the current value varies from zero to the overload value, the measured average torque results are shown in Fig. 3.38(a). Similarly, torque value versus the different current advance angle is compared in Fig. 3.38(b). For both characteristics, the results predicted by FEA are also given. The results shown in Fig. 3.38 again agree with the FE results quite well, except a bit reduction for higher current value, which is due to the saturation variation caused by armature field. From Fig. 3.38(b), it can also be seen that the optimal current advance for this kind of PM machine should be zero, which means there is practically no reluctance torque, which is different from the high electric loading situation shown in [CHU13a], [CHU13b].



(a) Torque-current



(b) Static torque (Rated current)

Fig. 3.38. Comparison of predicted and measured torque-current and static torque characteristics.

Overall, the FE predicted and measured results can validate the correctness of the proposed modular machine.

### 3.5 Conclusion

By comparing and analysing basic electromagnetic performances of the proposed modular machine with the conventional machine, it can be seen that the proposed modular machine shows comparable electromagnetic performances as its counterpart conventional modular machine. Although there are some space waste and more harmonics in the proposed modular machine, its stator core can be easily segmented and provides better protection for end coils of each segment. Besides, the balanced dual 3-phase winding can be obtained as well. The comparison between two kinds of dual 3-phase windings applied to the same electrical machine further shows the advantage of adopting the one with 30 degree phase shift between two sets of windings. The experiments on the prototyped machines validate the correctness of the analysis in this chapter. The proposed modularity technique can be further applied to other fractional-slot PM machines with different slot and pole number combinations.

## **Chapter 4 Investigation of Slot and Pole Number Combinations in Novel Modular Machines**

In order to provide a more general guidance in constructing the proposed modular machines with redundant teeth between segments, the balanced conditions for available slot and pole number combinations are summarised in this chapter. Based on the available slot and pole number combinations, the prototype machines analysed in this chapter are determined. Furthermore, the influence of slot and pole number combinations on prototype machine performances will be shown in detail by finite element analysis. The advantages and disadvantages of these different slot and pole number combinations are identified. Finally, the conclusions are drawn based on the analyses of this chapter.

### **4.1 Summary of Available Slot and Pole Number Combinations**

#### **4.1.1 Structure of Proposed Modular Machines**

The proposed modular machine with redundant teeth can be considered as the combination of a conventional modular machine for torque production and a redundant machine for modularity. In Chapter 3, the detailed process of constructing the proposed modular machine has been elaborated by taking the example of a 42-slots/32-poles (42S/32P) external rotor PM machine. This 42S/32P proposed modular machine combines a 36S/30P conventional modular machine and a 6S/2P redundant one. The stator of the proposed modular machine can be cut into 6 segments since the redundant machine provides 6 redundant teeth. In fact, the 3S/2P electrical machine can also be used as the redundant part for modularity if the constraint of UMF is neglected. Under such circumstance, another proposed modular machine with 39S/32P combination can be obtained based on the similar process. Under such condition, both the proposed 39S/32P and the conventional 36S/30P modular machines only have 3 segments. The constraints on the dimensions of these two modular machines are: fixed rotor outer diameter, rotor yoke thickness, PM thickness, PM pole arc to pole pitch ratio, air-gap length, effective slot area, stator inner diameter and turns per phase. In order to clearly show the differences, the cross-sections of two modular machines are shown in Fig. 4.1, together with the emphasis on the segmentation of stator cores.



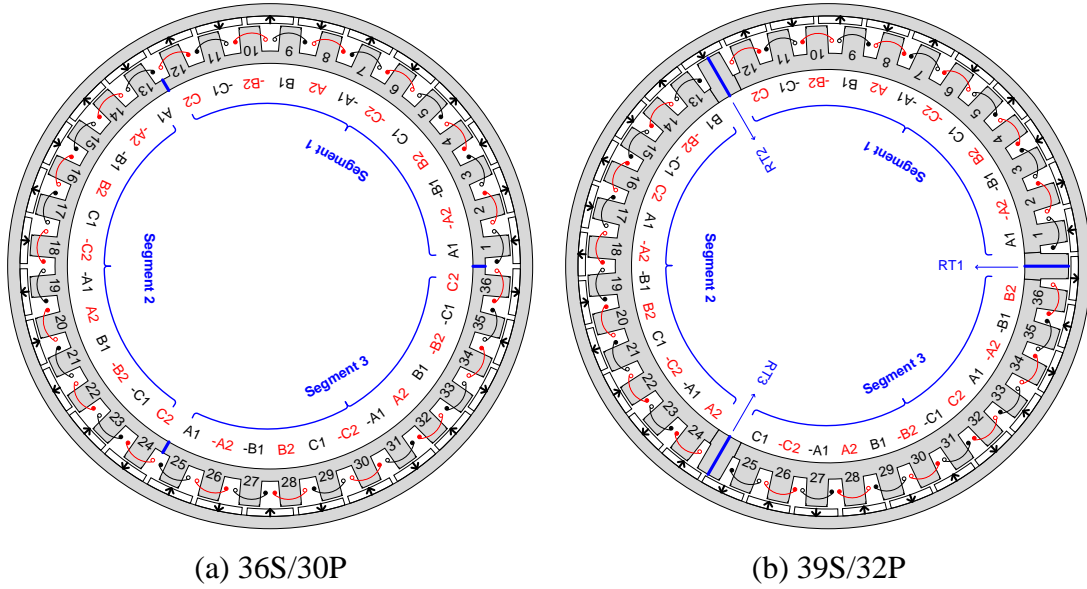


Fig. 4.1. Cross-sections of the conventional and proposed modular machines with 3 segments.

In terms of the structures shown in Fig. 4.1, the major differences of two electrical machines can be identified:

(1) The rotor pole number of the proposed modular machine and that of the conventional modular machine is differed by 2. However, the total PM volumes of two electrical machines are fixed.

(2) The stator core of the proposed modular machine can be cut in the position of redundant tooth centre, which provides protection for the coils located at the end parts of each segment. In contrast, the stator core segment of the conventional modular machine is connected in the stator yoke; therefore these coils will be exposed to the air, and more vulnerable to be damaged. This is the major advantage of the proposed modular machine.

(3) The winding configuration of the conventional modular machine is exactly the same for each segment, whereas there are additional phase shift for the windings of each segment in the proposed modular machine. Consequently, periodicities do not exist anymore.

#### 4.1.2 Conditions for Balanced Two Sets of Windings

In order to construct the balanced proposed modular machines, the limitations on slot and pole number combinations must be addressed in the first place. Because of the adoption of fractional-slot non-overlapping windings, the balance among each phase must be satisfied.

$$\begin{aligned} N_{sc0} &= N_{sc}/t_c = 3k, \quad k = 1, 2, 3... \\ N_{pc0} &= N_{pc}/t_c \\ t_c &= GCD(N_{sc}, N_{pc}/2) \end{aligned} \quad (4.1)$$

where  $N_{sc}$  and  $N_{pc}$  are the slot and pole number of the conventional modular machines, respectively;  $N_{sc0}$  and  $N_{pc0}$  are the slot and pole number corresponding to the minimal electrical machine unit of the conventional modular machines, respectively;  $t_c$  is the number of minimal electrical machine unit which equals the greatest common divisor ( $GCD$ ) of slot number and pole pair number.

Furthermore, the coil pitch must be within the certain range to make sure the winding factor large enough.

$$\left. \begin{aligned} (2/3)\tau_{pc} &\leq y_c \leq (4/3)\tau_{pc} \\ \tau_{pc} &= 2\pi/N_{pc} \\ y_c &= 2\pi/N_{sc} \end{aligned} \right\} \Rightarrow 2/3 \leq N_{pc}/N_{sc} \leq 4/3 \quad (4.2)$$

where  $y_c$  and  $\tau_{pc}$  are the coil pitch and pole pitch of the conventional modular machine, respectively.

Based on these two basic conditions, some available slot and pole number combinations are listed in TABLE 4.1. Each combination is further checked to find out whether it is suitable for the proposed modular machines.

TABLE 4.1 SLOT/POLE NUMBER COMBINATIONS FOR PROPOSED MODULAR MACHINES

$N_{pc}/3n$	$N_{sc}/3n$	$K_{wc}$ -S 3p	$t_c/3n$	$N_{sc}/t_c$	$N_{sr}$ ( $N_{seg}$ )	$N_{pp}$	$N_{sp}$	Winding
2	3	0.866	1	3	3	8	12	S 3p
4	3	0.866	1	3	3	14	12	S 3p
	6	0.866	2	3	3,6		21,24	S 3p
6	9	0.866	3	3	3,9	20	30,36	S 3p
8	6	0.866	2	3	3,6	26	21,24	S 3p
	9	0.945	1	9	3		30	S 3p
10	12	0.866	4	3	3,6,12	32	39,42,48	S 3p
	9	0.945	1	9	3		30	S 3p
10	<b>12▲</b>	<b>0.933</b>	<b>1</b>	<b>12</b>	<b>3,6</b>	32	<b>39,42</b>	<b>S 3p D 3p</b>
	15	0.866	5	3	3,15		48,60	S 3p
12	9	0.866	3	3	3,9	38	30,36	S 3p
	18	0.866	6	3	3,6,9,12		57,60,63,66	S 3p
14	<b>12▲</b>	<b>0.933</b>	<b>1</b>	<b>12</b>	<b>3,6</b>	44	<b>39,42</b>	<b>S 3p D 3p</b>
	15	0.951	1	15	3		48	S 3p
	18	0.902	1	18	3,6		57,60	S 3p
	21	0.866	7	3	3,21		66,84	S 3p
16	12	0.866	4	3	3,6,12	50	39,42,48	S 3p
	15	0.951	1	15	3		48	S 3p
	18	0.945	2	9	3,6		57,60	S 3p
	21	0.890	1	21	3		66	S 3p
	24	0.866	8	3	3,6,12,24		75,78,84,96	S 3p
18	27	0.866	9	3	3,9,27	56	87,93,111	S 3p
20	15	0.866	5	3	3,15	62	48,60	S 3p
	18	0.945	2	9	3,6		57,60	S 3p
	21	0.953	1	21	3		66	S 3p
	<b>24</b>	<b>0.933</b>	<b>2</b>	<b>12</b>	<b>3,6,12</b>		<b>75,78</b>	<b>S 3p D 3p</b>
	27	0.877	1	27	3		84	S 3p
	30	0.866	10	3	3,6,15		93,96,105	S 3p
22	18	0.899	1	18	3,6	68	57,60	S 3p
	21	0.953	1	21	3		66	S 3p
	<b>24</b>	<b>0.949</b>	<b>1</b>	<b>24</b>	<b>3,6</b>		<b>75,78</b>	<b>S 3p D 3p</b>
	27	0.915	1	27	3		84	S 3p
	30	0.874	1	30	3,6		93,96	S 3p
	33	0.866	11	3	3,33		96,126	S 3p
24	18	0.866	6	3	3,6,18	74	57,60,72	S 3p
	27	0.945	3	9	3,9		84,90	S 3p
	36	0.866	12	3	3,6,9,12,18,24		111,114,117,120,126,132	S 3p
26	21	0.890	1	21	3	80	66	S 3p
	<b>24</b>	<b>0.949</b>	<b>1</b>	<b>24</b>	<b>3,6</b>		<b>75,78</b>	<b>S 3p D 3p</b>
	27	0.954	1	27	3		84	S 3p
	30	0.936	1	30	3,6		93,96	S 3p
	33	0.903	1	33	3		102	S 3p
	36	0.867	1	36	3,6		111,114	S 3p
39	0.866	13	3	3,39	120,156	S 3p		

The meaning of each column can be explained as follows. Columns 1~5 in TABLE 4.1 are corresponding to the necessary conditions given by (4.1) and (4.2). To make sure each segment having balanced winding layout in the proposed modular machine, the conventional modular machines should contain integer times of 3 repetition electrical machine units.

$$t_c/3n = k, \quad n, k = 1, 2, 3... \quad (4.3)$$

That is why all of the  $N_{pc}$ ,  $N_{sc}$  and  $t_c$  are normalized to  $1/3n$ , whereas the minimal number of  $t_c$  is used in the chapter to construct the proposed modular machine for simplicity. For other numbers of electrical machine units, the similar results can be obtained as shown in TABLE 4.1.  $K_{wc}$ -S 3p column means the winding factor of the single 3-phase winding. This winding factor verifies the constraint on the selection range of the slot and pole number combinations for the conventional modular machines. In terms of the redundant machine, the pole number ( $N_{pr}$ ) is fixed to 2 for reducing the waste of PM and it is no need to show in TABLE 4.1. The slot number of the redundant machine ( $N_{sr}$ ) coincides with the stator segment number ( $N_{seg}$ ), as shown in the corresponding column of TABLE 4.1. This value should be an integer of 3 to guarantee balanced winding for the modular machine. All of the possible segment numbers for the stator of the proposed modular machine are:

$$N_{sr} = 3F_{ed}[t_c/3n], \quad n = 1, 2, 3... \quad (4.4)$$

where  $F_{ed}$  represents any exact divisor of a number.

The slot and pole number of the proposed modular machine ( $N_{sp}$  and  $N_{pp}$  columns in TABLE 4.1) can be obtained based on the following equations:

$$\begin{aligned} N_{sp} &= N_{sc} + N_{sr} = N_{sc} + N_{seg} \\ N_{pp} &= N_{pc} + N_{pr} = N_{pc} + 2 \end{aligned} \quad (4.5)$$

Finally, the available winding configurations can be seen in the last column of TABLE 4.1. Based on the information shown in the table, several key points can be observed:

(a) If the slot number of the minimal electrical machine unit is even, the available slot number of the redundant machine can be extended to include the following extra value:

$$N_{seg} = 6F_{ed}[t_c/3n], \quad n = 1, 2, 3... \quad (4.6)$$

(4.5) means the minimal electrical machine unit of the conventional modular machine is rotating symmetrical. Therefore, each electrical machine unit can be further separated into two parts to construct more stator segments. This point was applied to obtain the 42S/32P proposed modular machine. All of these extra values are underlined in  $N_{sr}$  ( $N_{seg}$ ) column of TABLE 4.1.

(b) For some slot and pole number combinations, there will be UMF in the proposed modular machines. This is closely related with the redundant machine. If  $N_{sr}$  is odd, the proposed modular machine will be rotating asymmetric, which means UMF will appear and vice versa. Observing the  $N_{sr}$  ( $N_{seg}$ ) column of TABLE 4.1, it shows that some electrical machines can avoid UMF by choosing the redundant machine having even slot number. For instance, 3 segments 39S/32P electrical machine has UMF, while 6 segments 42S/32P does not have.

(c) All of the slot and pole number combinations shown in TABLE 4.1 can construct the proposed modular machine with single 3-phase winding configuration. However, only the specific ones can adopt dual 3-phase winding. For these specific slot and pole number combinations, they can guarantee two balanced 3-phase systems with 30 degree phase shift between each other. In order to fulfil this compulsory condition, the conventional modular machine should construct balanced dual 3-phase structure. Thus, the constraint on  $N_{sc}$  must be further strengthened based on (4.1):

$$\begin{aligned} N_{sc0} &= N_{sc}/t_c = 12k, \quad k = 1, 2, 3... \\ N_{pc0} &= N_{pc}/t_c \\ t_c &= GCD(N_{sc}, N_{pc}/2) \end{aligned} \quad (4.7)$$

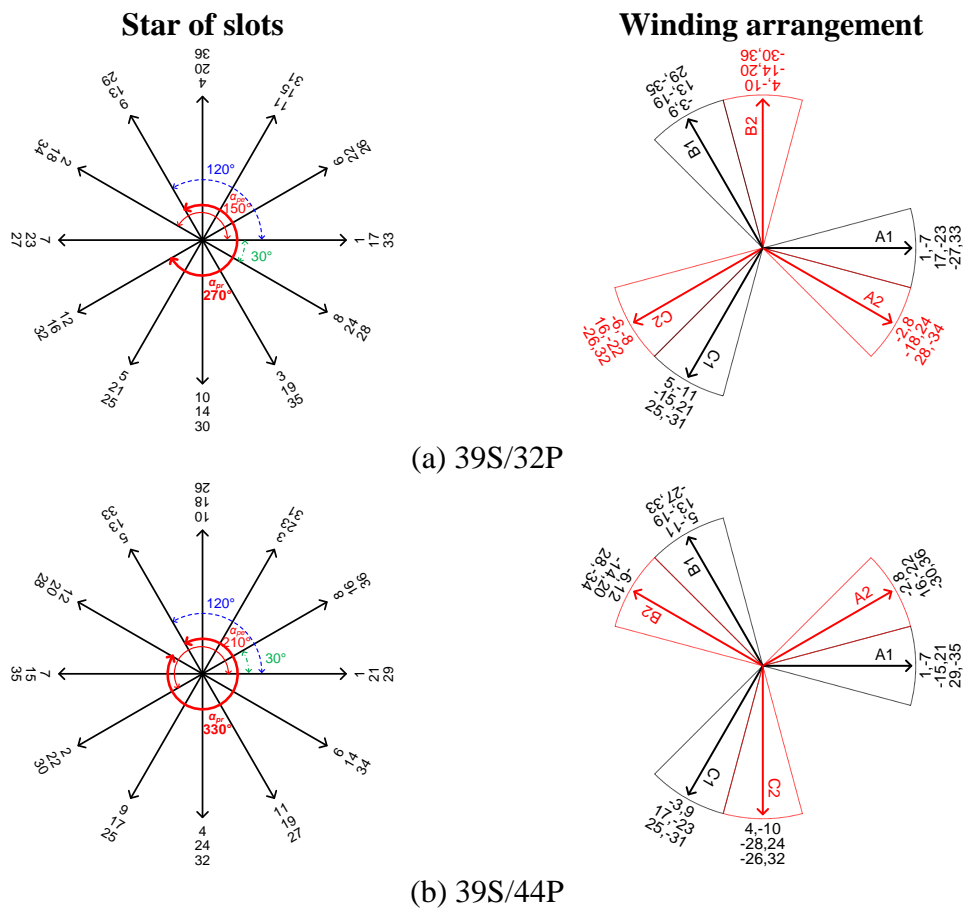
In summary, (4.1)-(4.7) give the conditions of constructing the balanced dual 3-phase non-overlapping windings for the proposed modular machines. All of the slot and pole number combinations satisfy these conditions are highlighted in the table by bold characters. The process can be described in brief. Firstly, the conventional modular machine used to construct the proposed modular machine needs to have integer times of 3 repetitive electrical machine units. This electrical machine unit should construct as a dual 3-phase type. Then, a redundant machine unit providing the redundant teeth for modularity is necessary. This redundant one only has one pole pair to make sure the minimal space and magnet waste. The slot number of this redundant machine is determined by the greatest common divisor of the slot and pole pair

numbers of the electrical machine unit. Finally, the combination of the conventional modular machine and the redundant one generates the proposed modular machine.

In order to more clearly illustrate the influence of slot and pole number combinations, four proposed modular machines with 39S/32P, 39S/44P, 42S/32P, 42S/44P combinations are selected to comparatively analyse the basic electromagnetic performances, as marked with ▲ in TABLE 4.1.

## 4.2 Prototype Machines

Employing the star of slots method, the corresponding star of slots and winding arrangements are obtained and shown in Fig. 4.2.



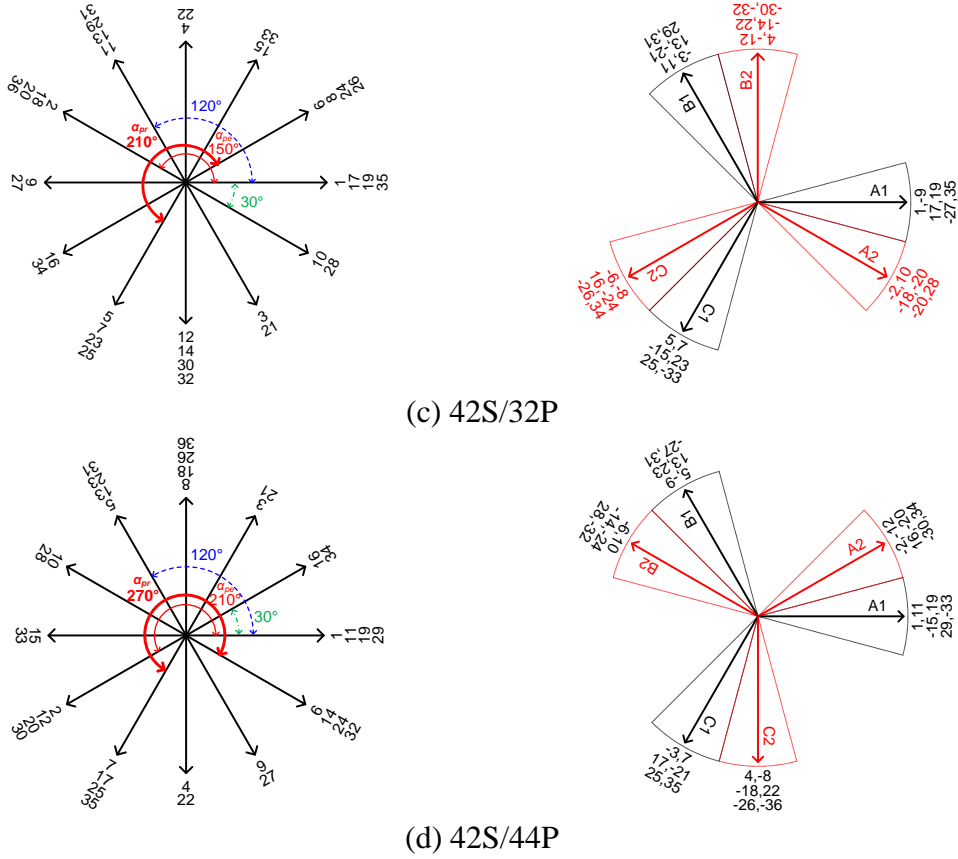


Fig. 4.2. Winding layouts of the proposed modular PM machines with different slot and pole number combinations.

For each star of slots, four significant angles are marked. The left column of Fig. 4.2 shows that the adjacent vectors have 30 electrical degrees and the phases within each set of winding have 120 electrical degrees. The largest differences among these four machines are the phase shift between effective teeth within each segment ( $\alpha_{pe}$ ) and the phase shift between two adjacent end teeth ( $\alpha_{pr}$ ). These two values are determined by the pole number of conventional machines and the slot number of redundant machines as follows:

$$\begin{aligned}\alpha_{pe} &= \pi N_{pc} / N_{sc} \\ \alpha_{pr} &= \alpha_{pe} + 2\pi / N_{sr}\end{aligned}\quad (4.8)$$

After drawing the star of slots for the prototype machines, the winding arrangement can be easily obtained according to the requirement of dual 3-phase winding. The right column of Fig. 4.2 shows that each phase belt contains 6 coils. The coils with/without minus marks have the opposite wound direction. For the electrical machines having a higher slot number than the pole number, the winding set 2 lags 30

electrical degrees to winding set 1 in space, while the opposite phenomenon can be seen for the electrical machines with the higher pole number than the slot number.

Accounting for the dimension constraints as the previous process of obtaining the proposed modular machines, the structures of four prototype machines are obtained. The cross-sections of four prototype machines are shown in Fig. 4.3, together with the illustration of the segmentation positions and the windings within each segment.

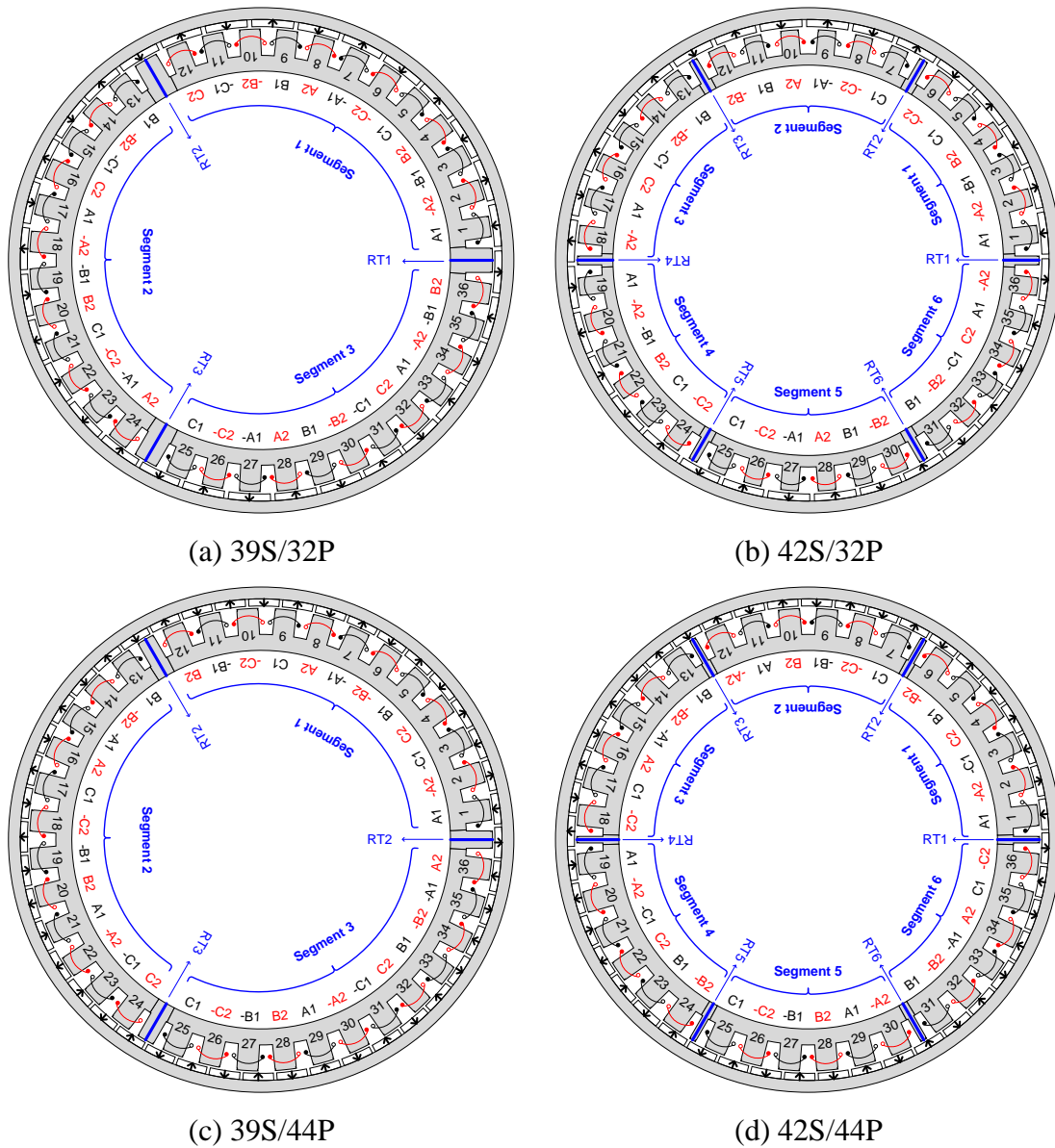
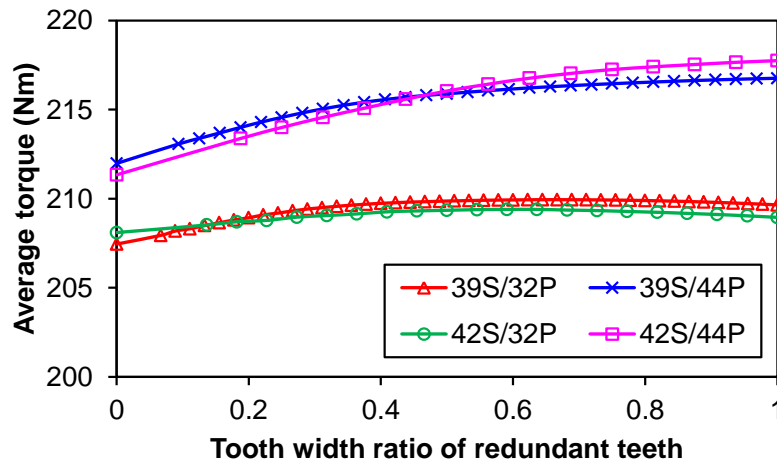


Fig. 4.3. Cross-sections of prototype modular PM machines with different slot and pole number combinations.

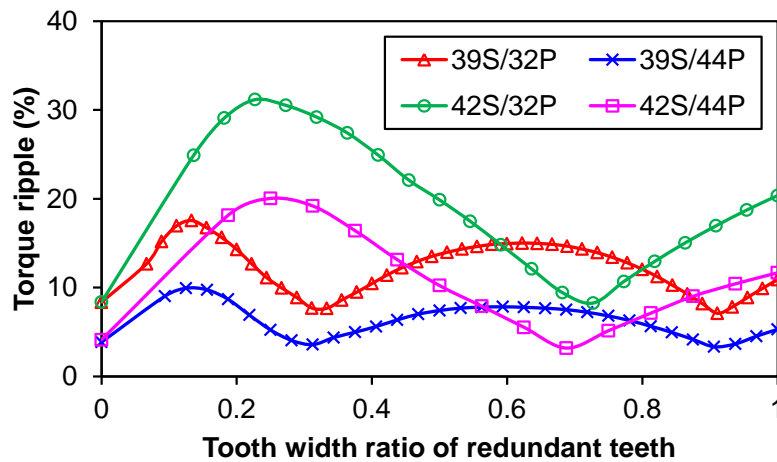
Since the electrical machines shown in the left column of Fig. 4.3 have odd number of segments, they will have undesirable effect of UMF. The electrical



machines in the right column of Fig. 4.3 do not suffer from UMF. For these machines, the tooth width of redundant teeth is thinner, which reduces the mechanical strength. The influence of this parameter on on-load average torque and torque ripple defined as the peak-to-peak (PP) torque ripple to the average torque are plotted in Fig. 4.4. To ease comparison, the variation of the parameter is normalized to its slot pitch.



(a) Average torque



(b) Torque ripple

Fig. 4.4. Influence of the tooth width of redundant teeth.

In terms of average torque, Fig. 4.4(a) shows that the electrical machines with the same pole number defer the influence of the tooth width of redundant tooth. When the redundant teeth do not exist, the average torque is minimal due to more leakage in the end part of each segment. With the increase of the tooth width ratio of redundant teeth, the average torque also increases because of more flux passing through the main flux path. However, when this ratio is larger than 0.5, the average value does not obviously

change any more. The curves in Fig. 4.4(b) demonstrate that the tooth width of redundant teeth has an important influence on torque ripple. The reason for the existence of these minimal torque ripple points is the effect of slotting effect. Since the cogging torque is the major torque ripple component in these fully open slot machines, the equation in [ZHU09a] can be used to explain this. The electrical machines with different slot and pole number combinations will have different optimal slot opening ratios for minimising cogging torque. For the redundant machines having 3S/2P combination, there are more optimal slot openings than the 6S/2P redundant one. Taking both average torque and torque ripple into account, the optimal tooth width of redundant teeth can be obtained. Finally, the major parameters of four prototype machines are listed in TABLE 4.2. It should be emphasised that the 42S/32P modular machine analysed in this thesis adopts the optimised redundant teeth.

TABLE 4.2 MAJOR PARAMETERS

Item	$N_{sp}/N_{pp}$			
	39S/32P	39S/44P	42S/32P	42S/44P
Stator inner diameter (mm)	319.4			
Stator outer diameter (mm)	390.4			
Stator yoke thickness (mm)	13.2	13.5	13.2	13.5
Stator tooth width (mm)	17.52 <sup>a</sup>	17.92 <sup>a</sup>	17.52 <sup>a</sup>	17.92 <sup>a</sup>
	20.5 <sup>b</sup>	14.7 <sup>b</sup>	7.9 <sup>b</sup>	5.5 <sup>b</sup>
Air-gap length (mm)	2			
PM thickness (mm)	6			
PM pole arc to pole pitch ratio	0.9			
Rotor yoke thickness (mm)	10			
Axial length (mm)	110			
Turns per phase	408			
Rated current (A)	3			
Rated speed (rpm)	170			

<sup>a</sup> the teeth corresponding to the initial modular machine.

<sup>b</sup> the redundant teeth.

### 4.3 Electromagnetic Performance Comparison of Prototype Machines

#### 4.3.1 Field Distribution

When the rotor  $d$ -axis coincides with the axis of phase-A1, the corresponding open-circuit equal potential line distributions are shown in Fig. 4.5. Under such condition, PMs are the only excitation source.

**3 segments**

**6 segments**

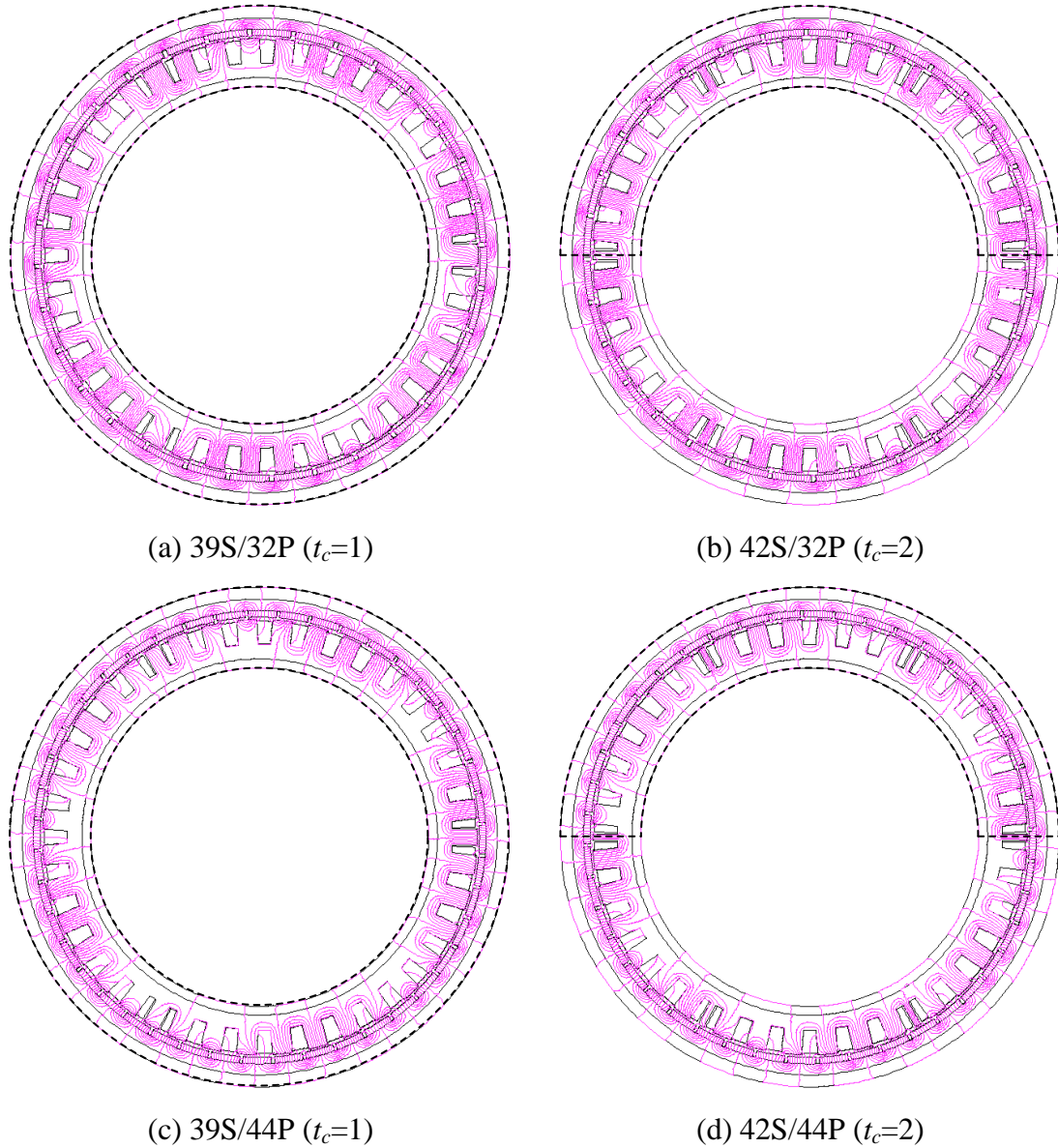
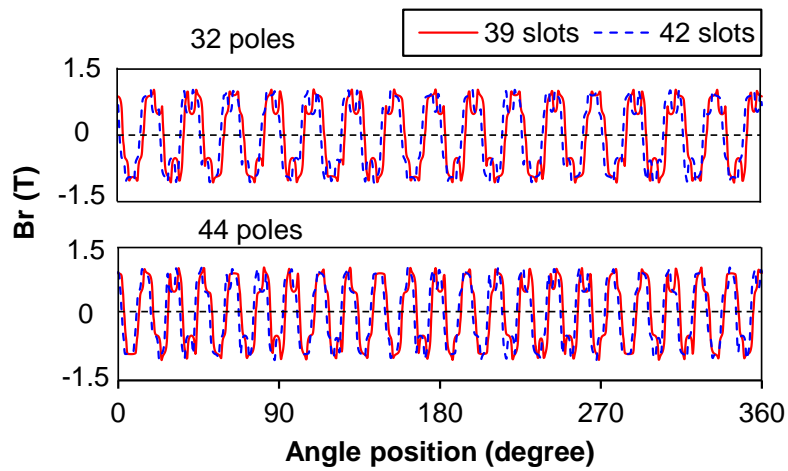
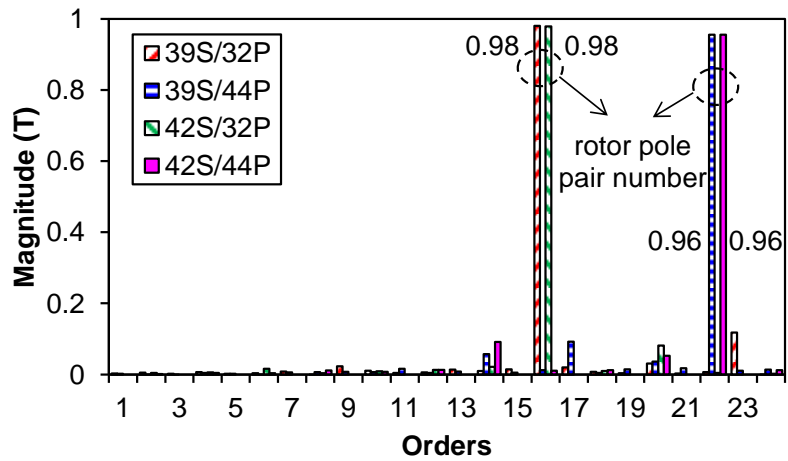


Fig. 4.5. Equal potential line distributions under open-circuit with the minimal repetition unit number highlighted.

For 39S/32P and 39S/44P proposed modular machines, neither even nor odd periodic condition can be applied, which means the electrical machine is rotating asymmetric as stated above. Comparing the two columns of Fig. 4.5, it shows that the proposed modular machines with 6 segments (42S/32P and 42S/44P) have two repetitions along the circumference. Thus, these two electrical machines are rotating symmetrical type. The minimal repetition unit is highlighted in Fig. 3.5 with dashed lines. The extracted radial air-gap flux densities under open-circuit condition are plotted in Fig. 4.6 for further explanation.



(a) Waveforms



(b) Spectra

Fig. 4.6. Air-gap flux density.

The waveforms in Fig. 4.6(a) show that all of the electrical machines have similar maximal value of air-gap flux density because of the dimension constraints. However, fully open slots lead to obvious distortions. The spectra in Fig. 4.6(b) can more clearly show the influence of slot openings. The harmonics with highest value are corresponding to the rotor pole pair number, viz. the working harmonic order. It can be seen that the magnitude of the air-gap flux density is a bit smaller for the electrical machines with higher pole number than the slot number. This is due to higher leakage in inter-pole region. Besides, there are other orders of harmonics being observed as well. All of these additional harmonics come from the interaction between PMs and slot openings. They will generate adverse effects on electrical machine performances.

Since the winding layouts of four electrical machines are also different and they will also play significant roles in determining electrical machine performances under on-load condition, the field distributions with only rated armature current are also compared in Fig. 4.7 at the rotor initial position.

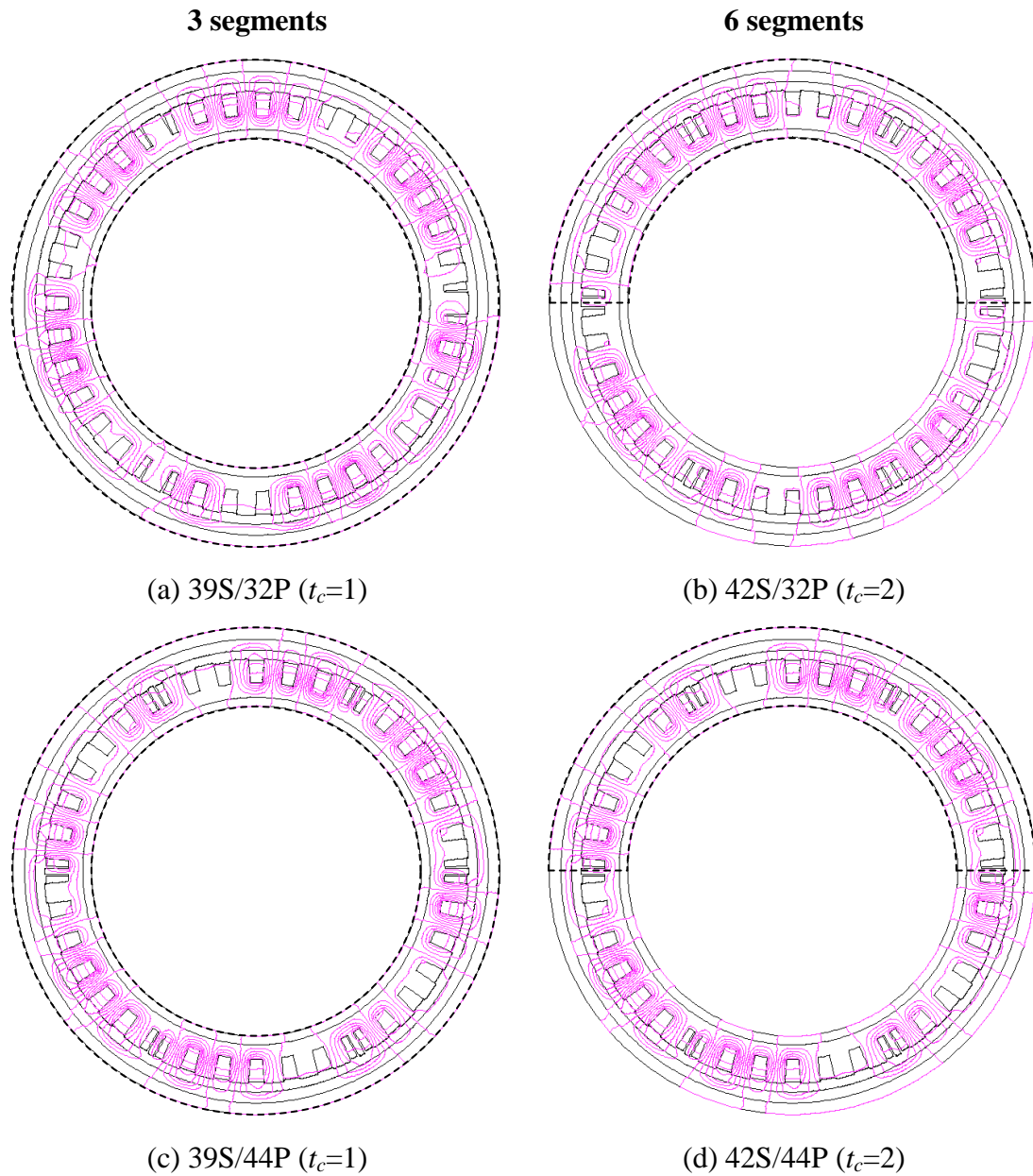
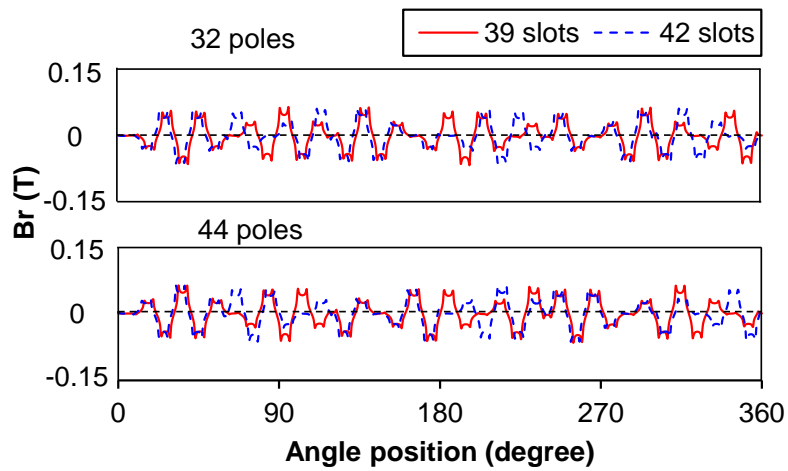
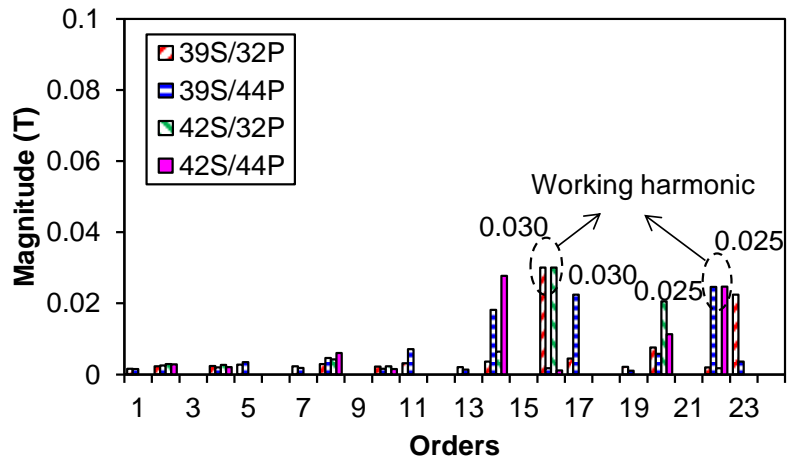


Fig. 4.7. Equal potential line distributions due to rated armature current.

Fig. 4.7 clearly shows the minimal repetition number of the proposed modular machines. The flux line distributions of four electrical machines are quite far away from the rotor pole pair number, viz. working harmonic. Abundant harmonics are expected and the air-gap flux densities are plotted in Fig. 4.8 for clarity.



(a) Waveforms



(b) Spectra

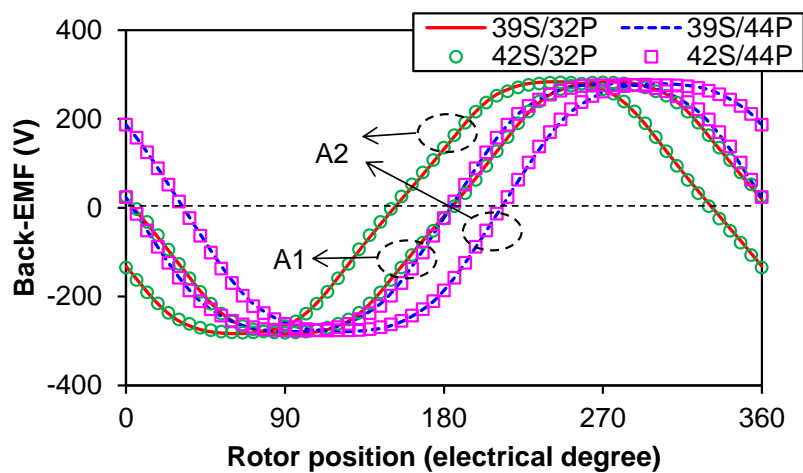
Fig. 4.8. Air-gap flux density.

Comparing Fig. 4.8(a) and 4.6(a), it can be found that the armature field is much weaker than PM field. More specific, the ratio of working harmonic magnitudes in armature field to those in PM field is around 3%. This means the saturation will not be evidently changed under rated condition. The waveforms shown in Fig. 4.8(a) are much distorted due to the special winding arrangement and this will be observed in Fig. 4.8(b). The spectra show that all of the proposed modular machines contain quite a few harmonics. For the electrical machines with higher slot number than pole number, there will be higher order harmonics. What is more, the magnitude of those lower order harmonics could even exceed that of the working harmonic, which could lead to some performances heavily exacerbated. Comparing the electrical machines with 3 and 6 segments, the former will have more harmonics and those differed by

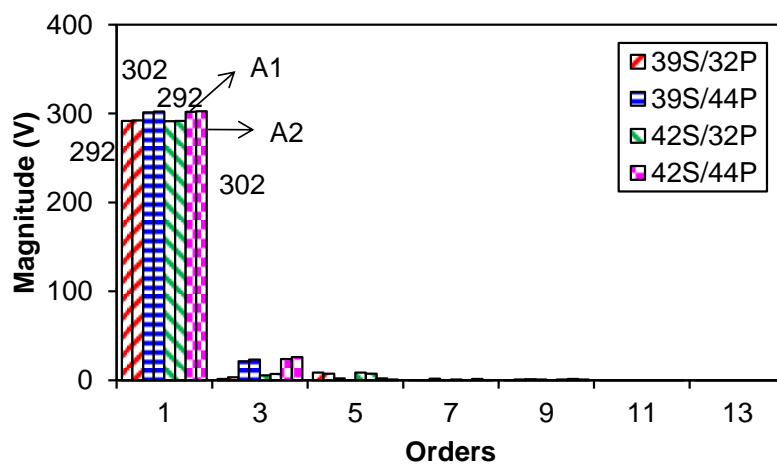
one will generated undesirable UMF. From this point of view, the 6 segments are more preferable. The more obvious influence of these harmonics can be seen in the following performance comparative analysis.

### 4.3.2 Open-circuit Performance

The open-circuit back electromotive force (EMF) is closely related to the on-load torque production; therefore the results of phase-A1 and A2 under the rated speed are compared in Fig. 4.9.



(a) Waveforms



(b) Spectra

Fig. 3.9. Open-circuit back-EMF (170rpm).

Fig. 4.9(a) shows that the back-EMF of phase-A1 lags 30 electrical degrees referring to that of phase-A2 for 39S/32P and 42S/32P modular machines in time and

vice versa for 39S/44P and 42S/44P modular machines. This verifies the previous conclusion on winding arrangement. The detailed harmonic spectra in Fig. 4.9(b) show that two sets of windings have balanced open-circuit back-EMF. The higher magnitude fundamental back-EMFs ( $E_{1m}$ ) can be seen in 39S/44P and 42S/44P modular machines. This can be explained based on the following equation:

$$E_{1m} = \omega_r \Psi_{1m} \propto N_{pp} n_r k_w N_{ph} \Phi_{1m} \quad (4.9)$$

where  $\omega_r$  and  $n_r$  are the rotor electrical speed in rad/s and rpm, respectively;  $\Psi_{1m}$  is the fundamental phase flux-linkage;  $k_w$  is the winding factor for fundamental component;  $N_{ph}$  is the turns per phase and  $\Phi_{1m}$  is the magnitude of fundamental flux.

According to (4.9),  $N_{pp}$  and  $\Phi_{1m}$  play the dominant roles in determining the fundamental back-EMF. The influence of the higher rotor pole number is more obvious than the lower fundamental flux for 39S/44P and 42S/44P modular machines. Furthermore, the waveforms of 39S/32P and 42S/32P modular machines are more sinusoidal because of lower 3<sup>rd</sup> harmonic, as shown in Fig. 4.9(b). When it comes to the 5<sup>th</sup> harmonic, higher magnitude for 39S/32P and 42S/32P modular machines will result in higher torque ripple.

Under open-circuit condition, the cogging torque will be generated due to the interaction between PMs and stator slots, as shown in Fig. 4.10. For the waveforms, it can be seen that the electrical machines with the same rotor pole number have practically the same cogging torque. The proposed modular machines with 44 poles always have smaller cogging torque. All of these can be observed based on the cogging torque periodicity number over one mechanical revolution ( $N_{cog}$ ):

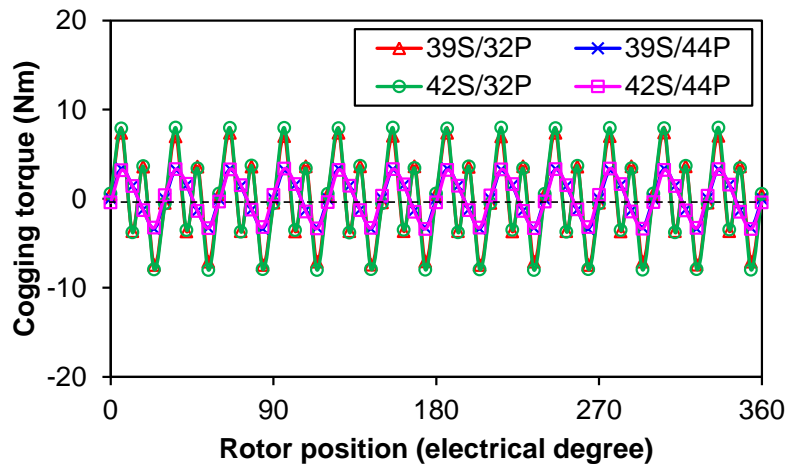
$$N_{cog} = LCM(N_{sr}, N_{pp}) \quad (4.10)$$

where  $LCM$  means the least common multiple of two numbers.

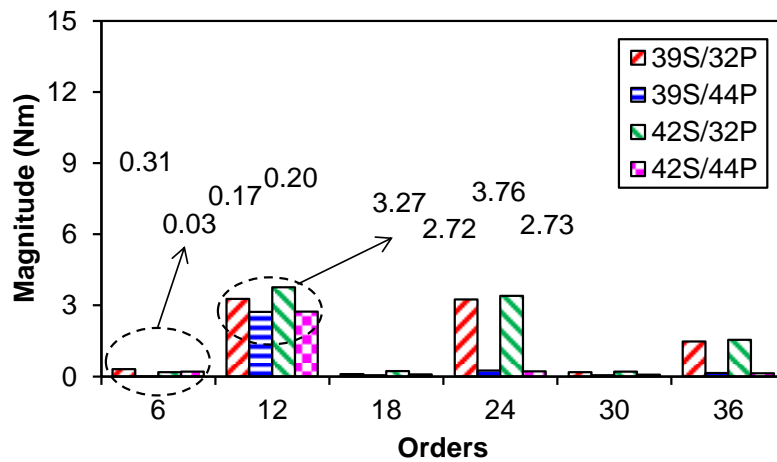
According to (4.10), prototype machines with 39 slots and 42 poles have the same  $N_{cog}$  if the pole number is the same. The higher  $N_{cog}$  for 39S/44P and 42S/44P modular machines gives rise to the lower cogging torque. In fact, the cogging torque periodicity number over one electrical revolution should be 6 for these prototype machines. However, the optimal tooth width of redundant teeth minimises the lowest cogging torque component. Thus, the spectra in Fig. 4.10(b) show the most predominant cogging torque harmonic is 12, 24, 36, etc. It also demonstrates that the modular machines with 32 poles have much more abundant cogging torque harmonics,



which is worse than the electrical machines with 44 poles. During the simulation process, there are more steps, such as 128 intervals over one electrical period, which can be used to obtain the harmonics more accurately. However, the waveforms shown here do not use so many points for clarity. All of the following figures containing several lines and much data are dealt with the same approach.



(a) Waveforms



(b) Spectra

Fig. 4.10. Cogging torque.

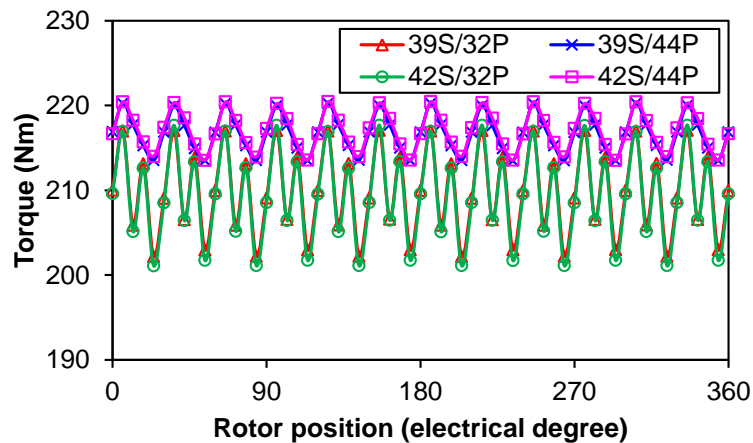
### 4.3.3 On-load Performance

When two sets of windings are fed with rated current by  $I_d=0$  control strategy, the effective torque will be generated, as shown in Fig. 4.11. The waveforms show that the fluctuations of these prototype machines are almost the same as the open-circuit cogging torque waveforms. The PM field is still predominant. The modular machines

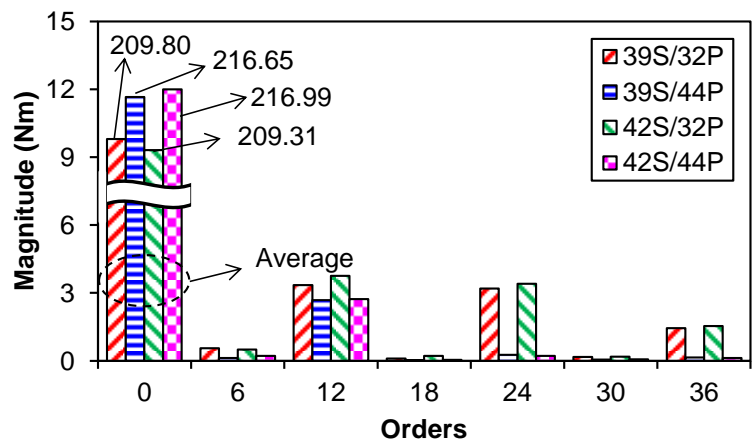
with the same rotor pole numbers exhibit similar torque waveforms. However, the average torque which can be seen in the waveforms confirms that the electrical machines with the higher rotor pole numbers generate larger average torque. This can be qualitatively explained by torque equation.

$$T_{avg} = \frac{6 E_{1m} \sqrt{2} I_{rat}}{2 \Omega_r} \propto N_{pp} k_w N_{ph} \Phi_{1m} I_{rat} \quad (4.11)$$

where  $T_{avg}$  is the average torque;  $I_{rat}$  is the rated phase current and  $\Omega_r$  is the rotor mechanical speed in rad/s. Since 39S/44P and 42S/44P modular machines have larger fundamental open-circuit back-EMF, the corresponding average torque will be larger as well. The clearer components of on-load torque can be seen in Fig. 4.11(b). The DC component is the average torque, which is zero under open-circuit condition. For the other torque harmonics, they show the similar orders and magnitudes as the open-circuit cogging torque as stated above.



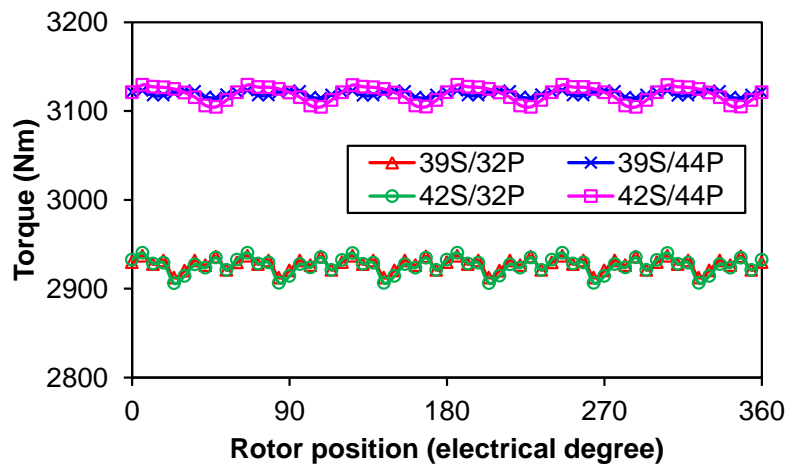
(a) Waveforms



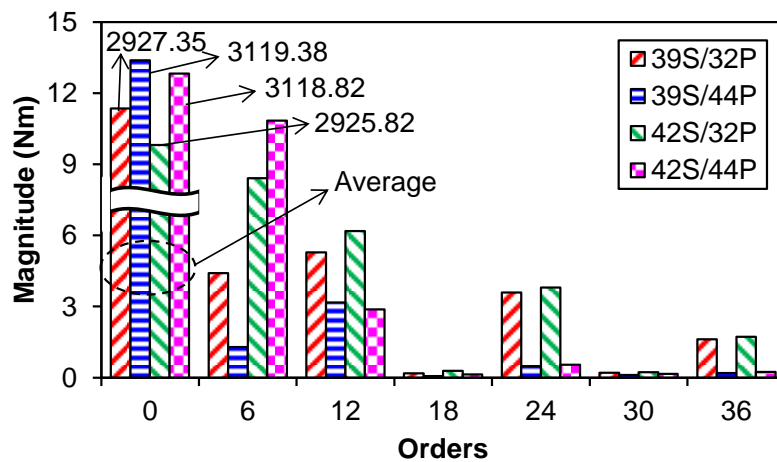
(b) Spectra

Fig. 4.11. On-load torque under rated condition.

When the electrical machines operate under overload condition, the torque will show quite different phenomena because of the obvious armature field influence. In order to make the influence clearer, the current is enlarged to the 15 times of rated value and the results are given in Fig. 4.12. The waveforms are quite different from those results with rated current. The much larger average torque for the electrical machines with 44 poles can be observed. Besides, the lower torque ripple is 6 for all of the prototype machines. The spectra in Fig. 4.12(b) mean that the high current makes the lower order torque ripples more apparent, especially the 6<sup>th</sup> harmonic torque. The saturation of the prototype machines has been evidently changed under such kind of overload condition, which is the reason for the differences.



(a) Waveforms



(b) Spectra

Fig. 4.12. On-load torque under overload condition.

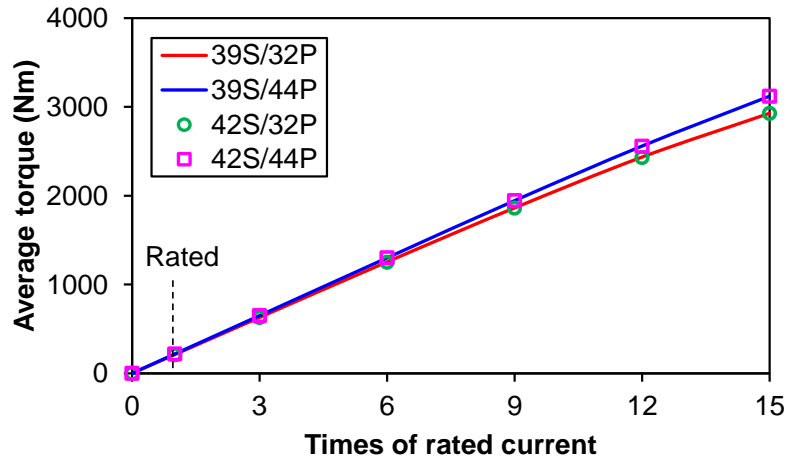
For the sake of clarity, the major values of torque performances under open-circuit, rated and overload conditions are summarised in TABLE 4.3, respectively.

TABLE 4.3 SUMMARY OF TORQUE PERFORMANCES

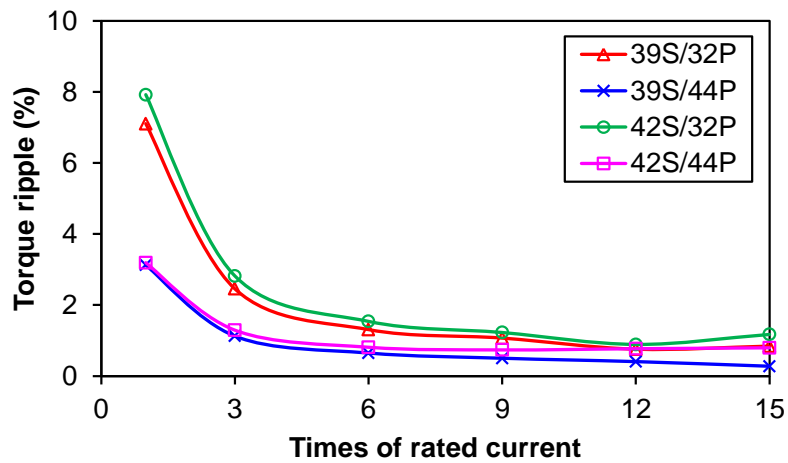
$N_s/N_p$	Load condition	Average torque (Nm)	PP torque (Nm)	Torque ripple (%)
39S/32P	Open	0	14.85	x
	Rated	209.76	14.90	7.10
	Overload	2927.37	24.68	0.84
39S/44P	Open	0	6.76	x
	Rated	216.65	6.78	3.13
	Overload	3119.39	8.63	0.28
42S/32P	Open	0	16.00	x
	Rated	209.31	16.58	7.92
	Overload	2925.88	34.28	1.17
42S/44P	Open	0	6.79	x
	Rated	217.00	6.93	3.19
	Overload	3118.84	24.80	0.80

Compared with the electrical machines operating under rated condition, the PP torques for the overload situation obviously increase. The torque ripple is always lower for the electrical machines with lower pole number. This coincides with the open-circuit back-EMF analysis.

The complete torque performance variations with the current are given in Fig. 4.13. As expected, the saturation curve can be seen for the average torque-current characteristics. With the increase of current, the modular machines with 44 poles have larger value due to less severe saturation level. For the torque ripple-current characteristics, the increase of average torque is much faster than that of PP torque; and therefore the torque ripple reduces. The 42S/32P and 42S/44P modular machines always show slightly larger torque ripple than the electrical machines with the same rotor pole number but lower slot number. This is also due to the influence of heavier armature effect on saturation.



(a) Average torque

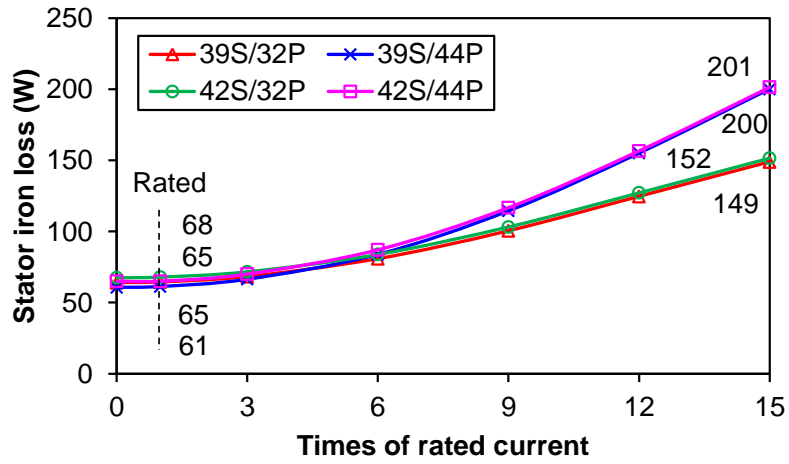


(b) Torque ripple

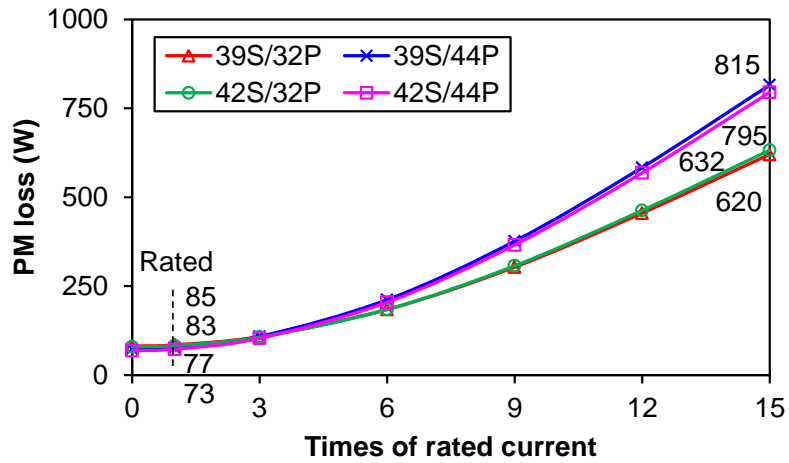
Fig. 4.13. Influence of current on torque performances.

#### 4.3.4 Iron Losses

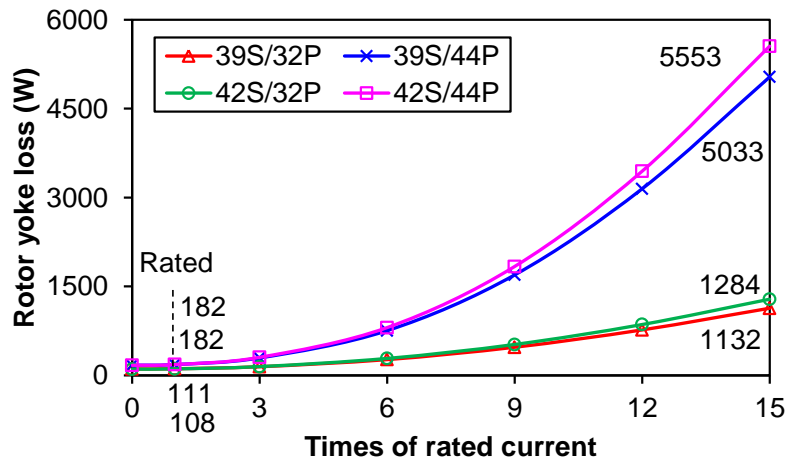
The iron loss mainly consists of three important components, viz. stator iron loss, PM eddy current loss and rotor yoke eddy current loss. Since all of them are related to the electrical machine operation condition, their variations with the current are shown in Figs. 4.14(a), (b) and (c), respectively.



(a) Stator iron loss



(b) PM eddy current loss



(c) Rotor yoke eddy current loss

Fig. 4.14. Influence of current on losses (170rpm).

Several phenomena can be observed from Fig. 4.14.

(1) All of the losses will increase with the increase of current. This is obvious since the higher current will enhance the influence of armature reaction, especially for the rotor yoke eddy current loss.

(2) When the current is low, all of the losses have negligible increase. Under such situation, the interaction between PMs and stator slot openings are the predominant source for the losses [WU12]. The electrical machines with the same rotor pole number have the same variation frequency and similar saturation level. That is why they have practically the same value. For the electrical machines with different pole numbers, the losses are also similar because of the cancellation effect of variation frequency and electrical machine flux density in iron parts.

(3) When the current is higher, the electrical machines with the same rotor pole number still have similar losses. The slightly larger value is seen for the electrical machines with the higher slot number but the same pole number. This is also owing to the stronger armature reaction. It is clear that 39S/44P and 42S/44P modular machines have increasingly larger losses than 39S/32P and 42S/32P modular machines for the higher current. This is the major drawback for the electrical machines with higher pole number than slot number.

(4) The influence of armature reaction on stator iron loss, PM eddy current loss and rotor yoke eddy current loss is more and more evident in sequence. For the stator iron loss, the high current will increase the flux density magnitude of the stator core, while the influence of variation frequency will be increasingly apparent. Therefore, 39S/44P and 42S/44P modular machines have larger stator iron loss. In terms of PM eddy current loss, the influence of current is more obvious. 39S/32P and 42S/32P modular machines have lower loss value under high current condition. The abundant armature field harmonics contribute to this loss. Due to the isolation between each PM, some harmonics cannot circulate in PMs. Thus, the increase of PM loss is not as heavy as that of rotor yoke loss. For the rotor yoke loss, there are no barriers cutting the flux path off. Therefore, the loss value of the modular machine with higher pole number than slot number will increase faster.

#### **4.3.5 Unbalanced Magnetic Force**

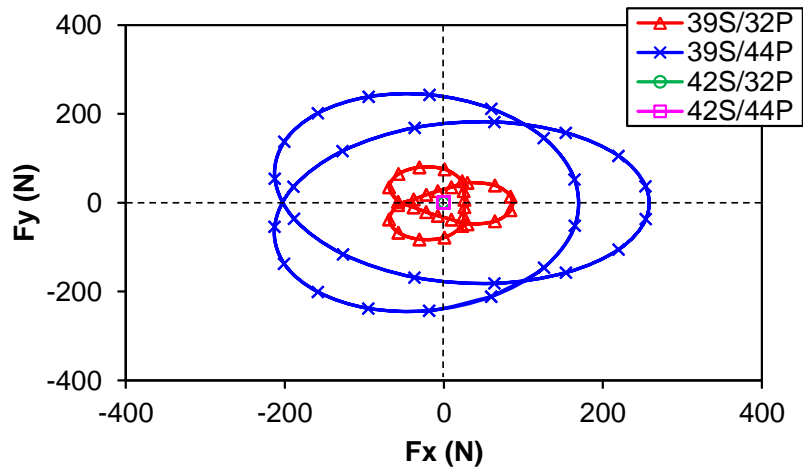
As mentioned above, another issue for adopting the proposed modular machines with 3 segments is the existence of UMF. The principle of UMF generation can be seen as follows:

$$\begin{aligned} F_x &= \frac{1}{2\mu_0} \oint_{gap} [(B_r^2 - B_\alpha^2) \cos \alpha - 2B_r B_\alpha \sin \alpha] r_{gap} d\alpha \\ F_y &= \frac{1}{2\mu_0} \oint_{gap} [(B_r^2 - B_\alpha^2) \sin \alpha + 2B_r B_\alpha \cos \alpha] r_{gap} d\alpha \end{aligned} \quad (4.12)$$

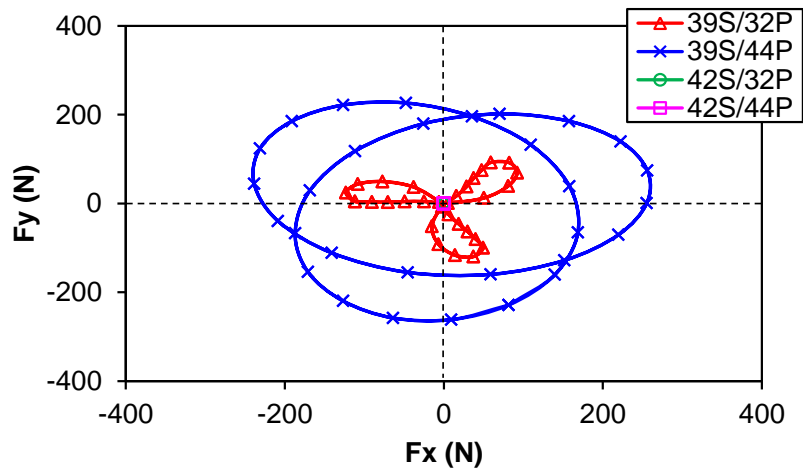
where  $F_x$  and  $F_y$  are the  $x$ - and  $y$ -components of UMF;  $B_r$  and  $B_\alpha$  are the radial and circumferential components of air-gap flux density;  $r_{gap}$  is the radius corresponding to air-gap centre;  $\mu_0$  is the air permeability and  $\alpha$  is the stator angular position position.

According to (4.12), the UMF is caused by the interaction between two harmonics differed by one. This condition is satisfied by 39S/32P and 39S/44P modular machines and the load condition will affect the UMF. To ease comparison, the UMFs under open-circuit, rated and overload condition are plotted in Fig. 4.15. For all of the results shown in Fig. 4.15, 42S/32P and 42S/44P modular machines do not have UMF, since they do not satisfy the condition given by (4.12). Thus, they all locate in the original point in  $F_y$ - $F_x$  diagram. Fig. 4.15 shows that the shape of UMF will be larger with the higher current. The difference between the result of open-circuit and rated situation is quite small, which is due to the weak armature field as well. The quite different UMF can be observed in Fig. 4.15(c) under overload condition. In a clearer view, the variation of UMF magnitude with the current is given in Fig. 4.16. When the modular machines operate under light load condition, the slotting effect is more important for UMF. However, the influence of armature field on UMF will be more and more obvious. The UMF of 39S/32P modular machine will gradually surpass that of 39S/44P modular machine with the increase of current, which is the property of the electrical machines with higher slot number than pole number. This coincides with the analysis in [ZHU13].

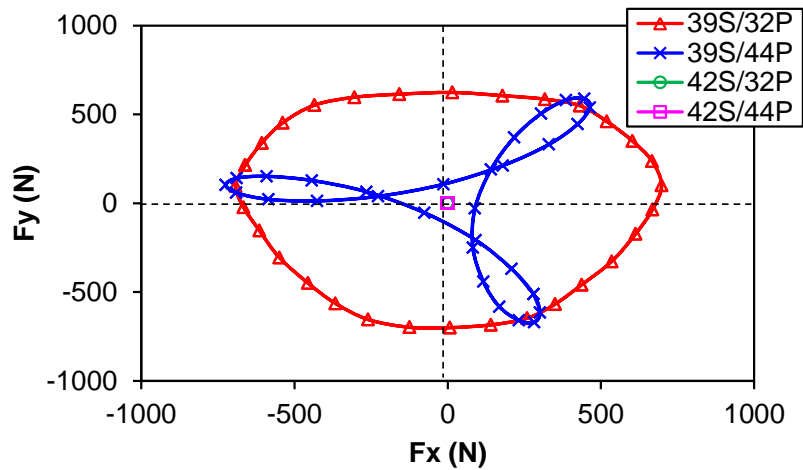




(a) Open-circuit



(b) Rated



(c) Overload

Fig. 4.15. UMF waveforms.

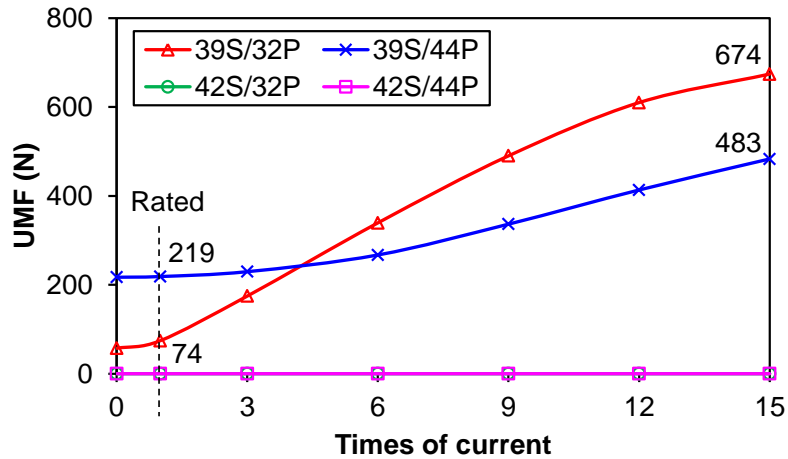
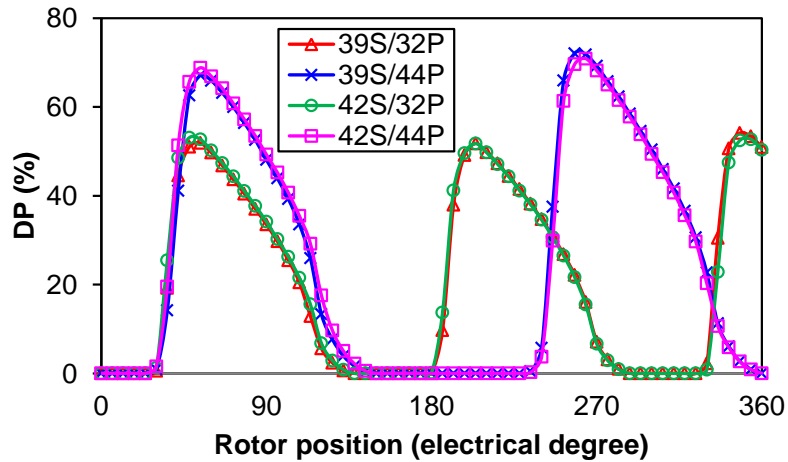


Fig. 4.16. Influence of current on UMF.

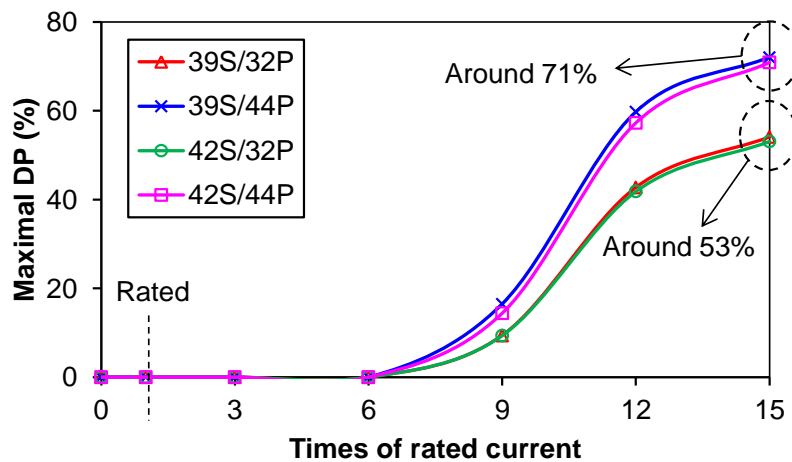
### 4.3.6 Demagnetisation

Theoretically, each PM of the minimal unit must be separately analysed in terms of irreversible demagnetisation. However, it can be found that they will have the same maximal demagnetisation percent (DP) when the electrical machine continuously operates, although the positions corresponding to maximal DP is different. Therefore, only the analysis of some sample PMs is enough to qualify the irreversible demagnetisation. For simplicity, two representatives (the first and the last PM of the segment 1) are chosen for each proposed modular machine. For four prototype machines, the first PM of segment 1 is the same, while the last PM of segment 1 is different, as shown in Fig. 3.3. PMs 10, 14, 5 and 7 are corresponding to the last PM for 39S/32P, 39S/44P, 42S/32P and 42S/44P modular machine, respectively. The first PM of segment 1 is analysed firstly, as shown in Fig. 4.17. Fig. 4.17(a) shows that this PM will experience the same irreversible demagnetisation process over one electrical period for the electrical machines with the same pole number. This is due to the similar winding layout for the region where the first PM passing across during the rotation. Besides, it can be seen that the electrical machines with higher pole number than slot number will have more DP, which is due to the influence of more harmonics. The positions of peak DP are also different for electrical machines with different poles. Since the slot pitch is smaller for the electrical machines having higher slot number than pole number, the distance between two adjacent maximal DPs is shorter as well. For the influence of current on maximal DP shown in Fig. 4.17(b), it can be seen that the irreversible demagnetisation happens when the current is high enough.

The electrical machines with the same pole number show the similar maximal DP variation with the current and the electrical machines having lower pole number are less demagnetised. The slight difference can be seen for the 39S/44P and 42S/44P modular machines. This is owing to the difference of lower order harmonics, as have been shown in [PAT15].



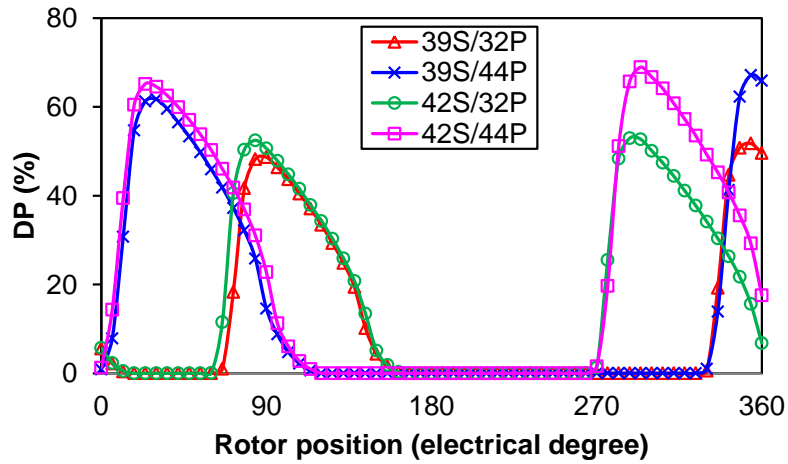
(a) DP variation



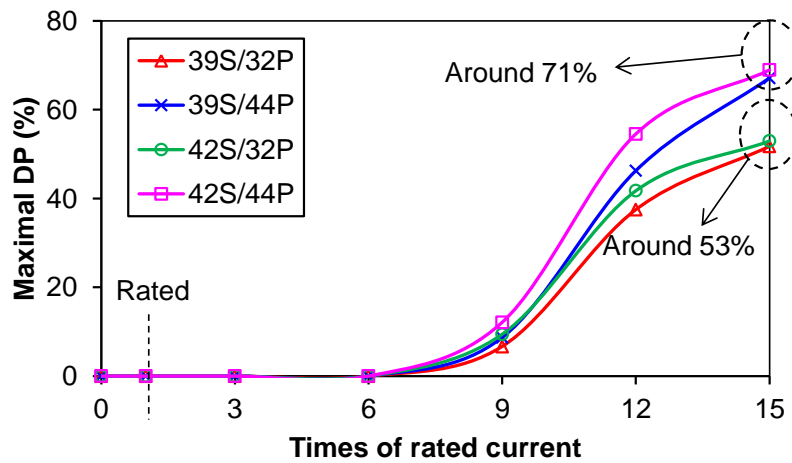
(b) Influence of current

Fig. 4.17. DP comparison of the first PM of segment 1.

The results of the last PM of segment 1 are shown in Fig. 4.18. The quite different phenomenon can be observed, although the electrical machines with higher pole number than slot number still have larger DP.



(a) DP variation



(b) Influence of current

Fig. 4.18. DP comparison of the last PM of segment 1.

Fig. 4.18(a) demonstrates that the distance between adjacent maximal DPs will be different for electrical machines with the same pole number. This is caused by the additional phase shift difference between two segments. The electrical machine with small segments will have larger additional phase shift; and therefore the distance is longer. Besides, it can also be found that the relative position of the first maximal DP will be different for electrical machines with the different pole number. This can also be explained according to the winding layout shown in Fig. 4.3. The larger slot pitch angle for electrical machines with the higher pole number leads to such difference for the last PM of segment 1. Fig. 4.18(b) exhibits that the maximal DP varies with current differently. Although the electrical machines with higher pole number than slot number are more demagnetised, the one with small segment number has lower

maximal DP. This can also be explained based on the electrical machine structure. The more additional phase shift will exist for the electrical machines with small segments and the last PM of segment 1 will be less affected by the armature field within this electrical period. However, it should be expected that all of the PMs will eventually have the same maximal DP over the whole mechanical revolution, since each of them will experience the same field variation.

#### **4.4 Conclusion**

Based on the conditions on the slot and pole number combinations, the proposed modular machines with dual 3-phase windings can be constructed. By analysing the performances of four representative prototype machines, the major conclusions can be drawn as follows:

(1) The conventional modular machines used to construct the proposed modular machines should contain the integer times of 3 basic electrical machine units, while the basic electrical machine unit should be able to accommodate balanced dual 3-phase winding.

(2) For electrical machines with higher pole number than slot number, the open-circuit back-EMF is larger, which means the on-load torque could be larger. This will be more obvious when the current is high. Besides, the torque ripple will be lower as well.

(3) In terms of iron losses, the electrical machines with lower pole number than slot number will be lower because of the less influence of armature reaction. The abundant harmonics will lead to a fast increase of iron losses for the electrical machines with higher pole number than slot number.

(4) The UMF will exist in the rotating asymmetric machines which can generate fields differed by one in orders no matter in open-circuit or on-load situation; therefore the redundant machine with odd number may be problematic in some applications.

(5) The electrical machines having lower pole number than slot number will have better irreversible demagnetisation withstand capability due to less high magnitude lower order harmonics.

Overall, none of the slot and pole number combination shows the best performance in all of the aspects. They should be determined from the requirements of specific application.

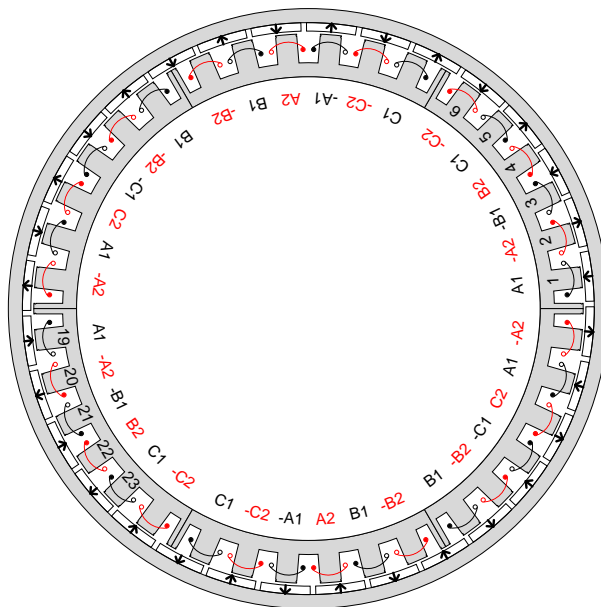
## **Chapter 5 Comparative Study of Modular Dual 3-phase PM Machines with Overlapping/Non-overlapping Windings**

Since the non-overlapping (NOLP) fractional slot windings have been proposed for PM machines [KEN85], [CRO02], the investigation of dual 3-phase electrical machines with this kind of windings is increasingly popular and was also extended to overlapping (OLP) fractional-slot windings [BAR10], [BAR11a], [BAR11b], [ZHE12], [ZHE13], [ABD16b], [PAT14]. A specific dual 3-phase electrical machine with 12-slot/10-pole (12S/10P) combination was fully investigated in terms of the torque performance [BAR10]. The faulty operation with only one set of winding in operation was further analysed and the fault-tolerant capability was identified [BAR11a]. In a more general point of view, the available slot and pole number combinations for constructing dual 3-phase windings were summarised in [BAR11b], which provides a quite clear guidance. Authors in [ZHA95], [ZHE12] elaborated the reason for harmonic reduction by using “Thirty type” dual 3-phase winding. Since the machines with such kind of winding are inherently semi twelve phase ones, more phase number gives rise to less harmonics and consequently better torque performance. The 24S/14P and 24S/10P machines with OLP fractional slot winding were separately analysed in [ZHE13] and [ABD16b] to further show the advantages. When the phase shift between two sets of windings is different from thirty and zero, more possible configurations can be proposed, as the one shown in [PAT14]. Moreover, when the suitable harmonic currents are injected into dual 3-phase windings, the torque performances will be better because of the more flexible current waveform selection [WAN15b], [HU17].

For more in-depth understanding, the comparison between “Thirty type” dual 3-phase modular electrical machines with OLP/NOLP windings and redundant teeth needs to be done, which is the main focus of this chapter. Two specific slot and pole number combinations are chosen as example. The structures of two machines are shown and the corresponding differences are emphasised in the first place. Then, the electromagnetic performances, especially the torque performance, are compared under three different conditions (normal, open-circuit and short-circuit faulty operation, respectively). Finally, the experiments are executed to validate the conclusions based on the analysis in the chapter.

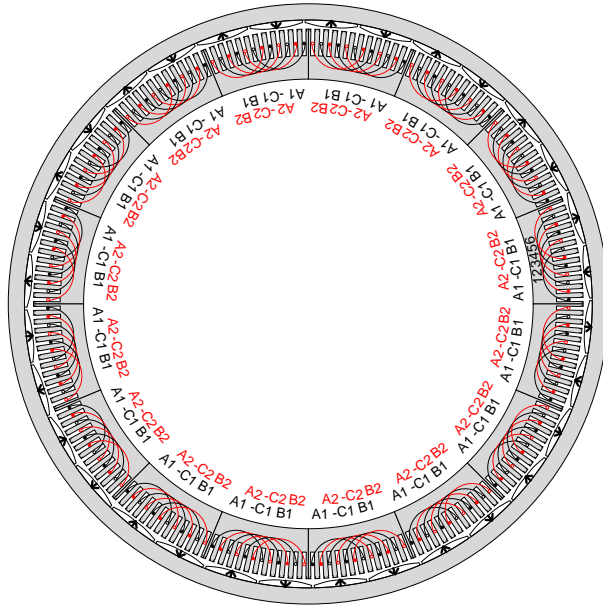
## 5.1 Prototype Machines

The two prototype machines to be analysed have the same rotor pole number, while the stator numbers are different to allow the accommodation of OLP/NOLP windings. The cross-sections are shown in Fig. 5.1. From Fig. 5.1, it can be seen that the modular machines with OLP/NOLP windings have 42-slots/32-poles (42S/32P) and 192S/32P combinations, respectively. Both of their stators can be cut into segments at the tooth centre, which will provide protection for coil sides located at the end parts of each segment during transportation and assembly process. Although the rotor pole number is the same for the two machines, conventional arc and surface shaped PMs are adopted for 42S/32P and 192S/32P modular machines, respectively. The reason for such difference is to reduce huge torque ripple for 192S/32P machine. For 42S/32P modular machine, it is fractional slot type; and therefore its torque ripple is inherently much lower compared with the integer slot 192S/32P one. However, the total PM volumes of two machines do not have too much difference since the pole arc to pole pitch ratio is adjusted accordingly. In terms of stator part, the maximum stator segment number is different for two machines, viz. 6 and 16 for 42S/32P and 192S/32P modular machines, respectively.

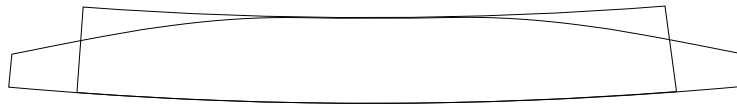


(a) 42S/32P (NOLP)





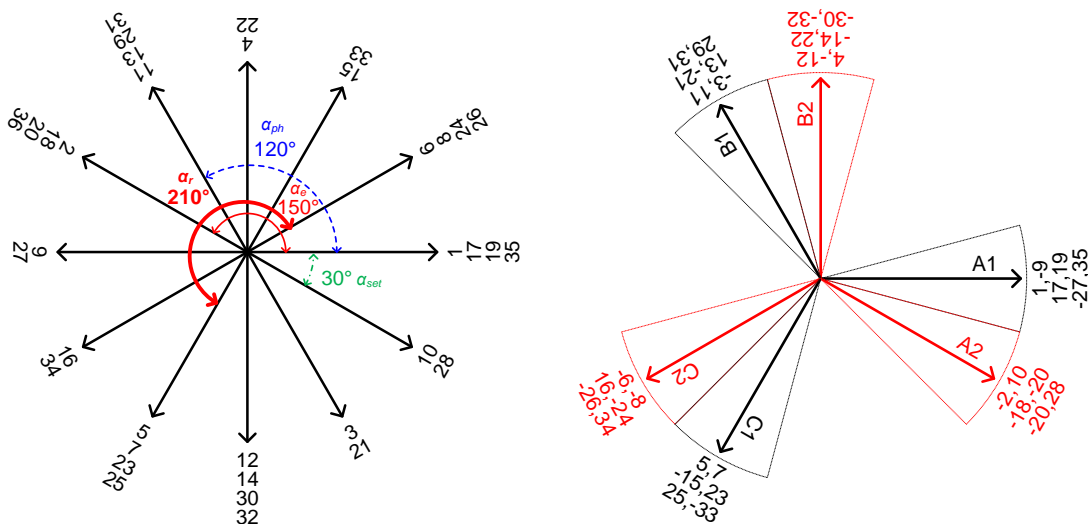
(b) 192S/32P (OLP)



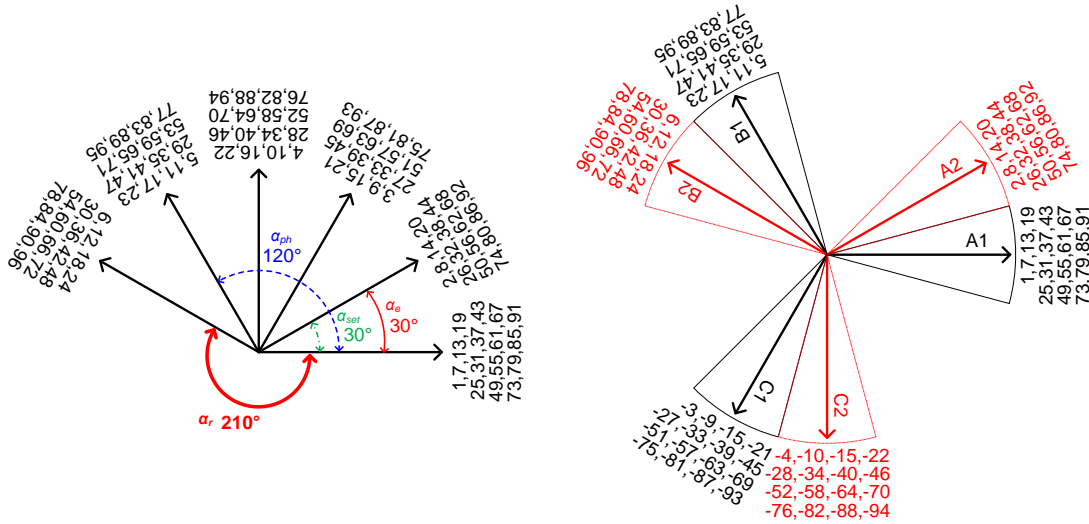
(c) PM shape comparison

Fig. 5.1. Cross-sections of the modular machines with OLP/NOLP windings.

In order to arrange the 36 and 96 coils for the two machines to construct the windings, the conventional star of slots method is used [BIA06a], as shown in Fig. 5.2.



(a) 42S/32P



(b) 192S/32P

Fig. 5.2. Winding arrangements of two modular machines.

The left column of Fig. 5.2 shows that the phase shift between adjacent coils within each segment ( $\alpha_e$ ) are 150 and 30 degrees for the two modular machines, respectively. The phase shift between two adjacent end coils ( $\alpha_r$ ) is the same for two machines, viz. 210 degrees. Three phases among one set of winding have 120 degree shift between each other ( $\alpha_{ph}$ ) and two sets of windings differ 30 degrees in space ( $\alpha_{set}$ ). However, the winding set 2 is 30 degrees ahead for the 42S/32P modular machine and vice versa for the 192S/32P one, as shown in the right column of Fig. 5.2. The minus symbol before the coil number means the wound direction is opposite. Although the coil numbers are different for two machines, the turns per phase and rated current are kept the same to guarantee the similar armature excitation.

Before the detailed analysis of the two machines, there are some limitations on structures for the sake of reasonable comparison. Both machines have the same stator inner diameter, stator outer diameter, effective slot area, air-gap length, PM thickness, rotor yoke thickness and axial length. Since the PMs have been shaped for the 192S/32P modular machine, the air-gap length means the minimal value and the PM thickness represents the maximum. The major parameters are listed in TABLE 5.1.

TABLE 5.1 MAJOR STRUCTURE PARAMETERS

Item	Slot number/Pole number	
	42S/32P	192S/32P
Stator inner diameter (mm)		319.4
Stator outer diameter (mm)		390.4
Stator yoke thickness (mm)	13.2	16.6
Stator tooth width (mm)	17.52 <sup>a</sup> and 7.9 <sup>b</sup>	
Stator slot width (mm)		18.87
Air-gap length (mm)	2	2 (minimum)
PM thickness (mm)	6	6 (maximum)
PM pole arc to pole pitch ratio	0.9	0.95
Rotor yoke thickness (mm)		10
Axial length (mm)		110
Turns per phase		408
Rated current (A)		3
Rated speed (rpm)		170

<sup>a</sup> the teeth with coils.

<sup>b</sup> the teeth without coils.

## 5.2 Performance Comparison under Normal Operation

In this section, there are no faults in the windings. Under such normal operation, two machines still show some differences in terms of electromagnetic performances.

### 5.2.1 Field Distribution

When the rotor  $d$ -axes of two machines coincide with the phase-A1 winding positive direction, this position is defined as the rotor initial position. The corresponding flux line and flux density distributions are shown in Fig. 5.3.

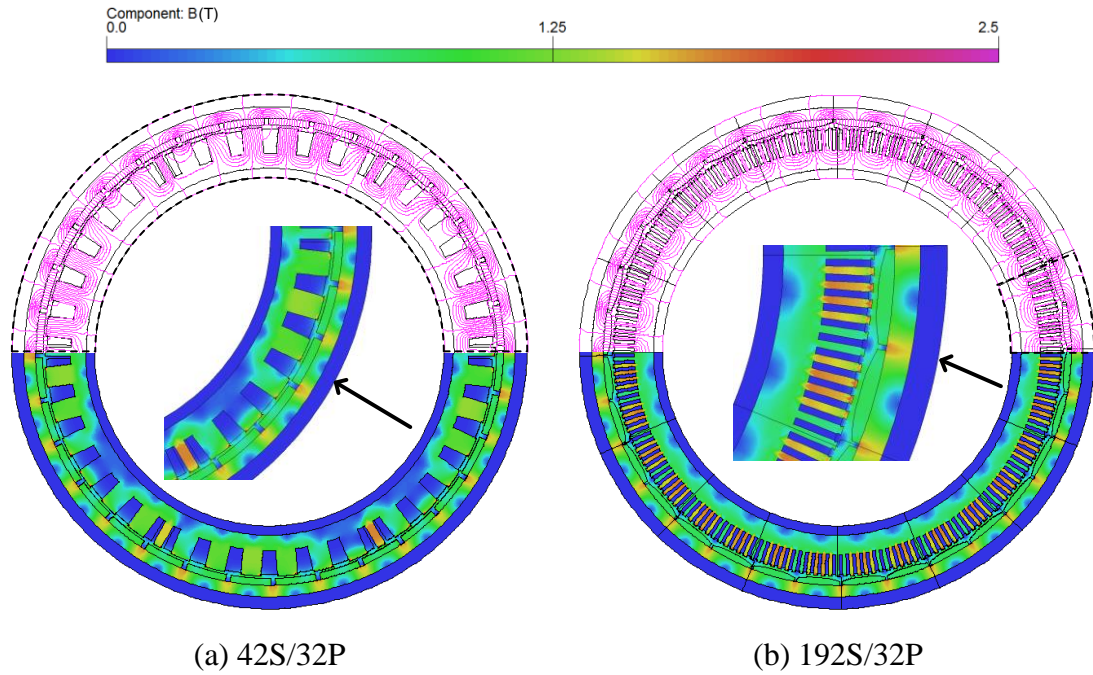
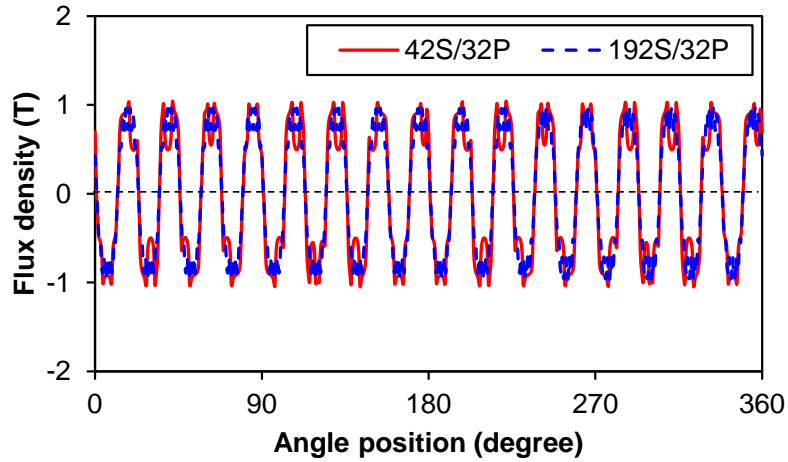
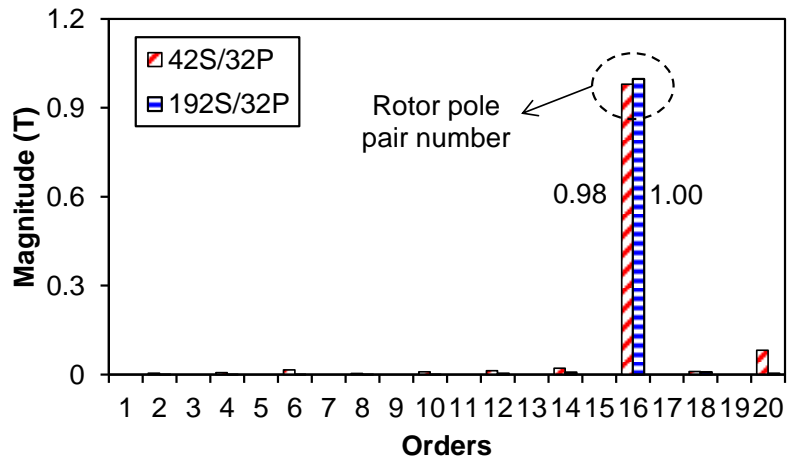


Fig. 5.3. Open-circuit PM field distribution.

In Fig. 5.3, the minimal repetition unit is highlighted with the dashed lines. As has been stated above, there are 2 and 16 repetition units for 42S/32P and 192S/32P modular machines, respectively. Since the minimal repetition unit is lower than the rotor pole pair number, the 42S/32P modular machine contains much more abundant harmonics than the 192S/32P one. From this point of view, the 192S/32P modular machine is better. However, the saturation is severer for this machine as well. Fig. 5.3 shows that quite a few number of stator teeth are more saturated for the 192S/32P modular machine compared with the 42S/32P one. Although the redundant teeth of 42S/32P modular machine are more saturated than effective teeth within each segment, they will not obviously affect performances. The air-gap flux density of the air-gap centre is compared in Fig. 5.4.



(a) Waveforms



(b) Spectra

Fig. 5.4. Air-gap flux density for PM field only.

Fig. 5.4(a) shows that the two machines have non-sinusoidal waveforms but similar peak values in airgap flux density. In order to clearly see the influence of slot opening, Fig. 5.4(b) compares their spectra. There is only one working harmonic component for the 192S/32P modular machine within 20 orders. In contrast, all of the even order harmonics exist in the 42S/32P machine. Due to larger slot openings in the 42S/32P modular machine, a slightly higher working harmonic magnitude can be seen for the 192S/32P one.

When the dual 3-phase winding is fed with the rated current, the armature field will be generated. The interaction between PM and armature fields can produce output torque. The field distribution of armature field only is shown in Fig. 5.5.

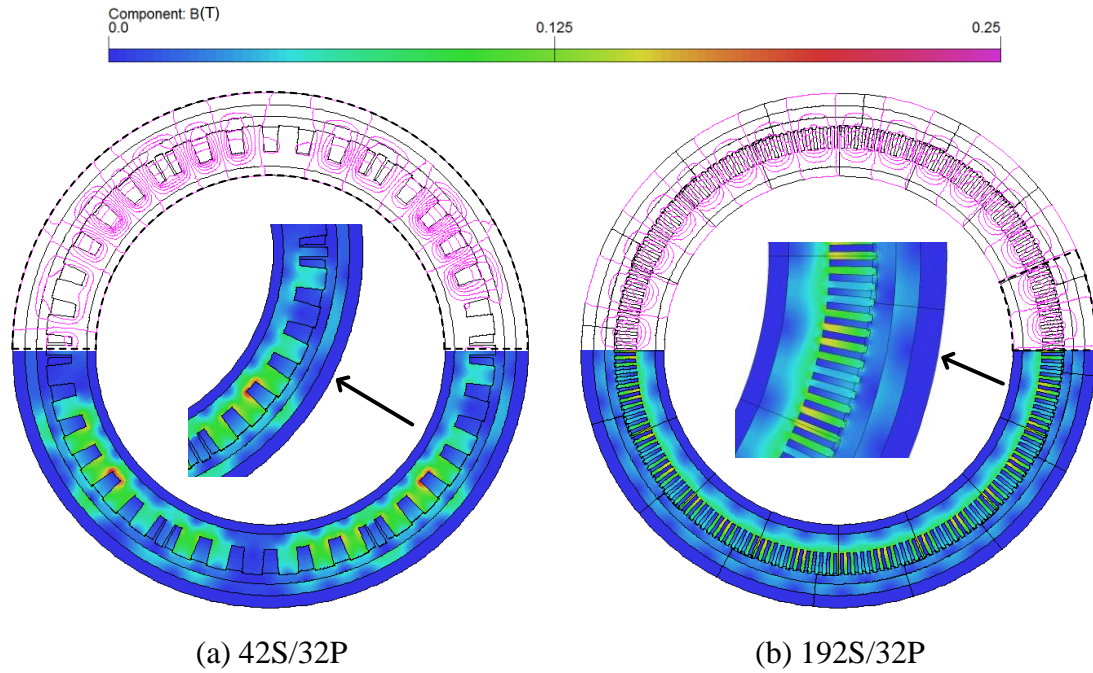
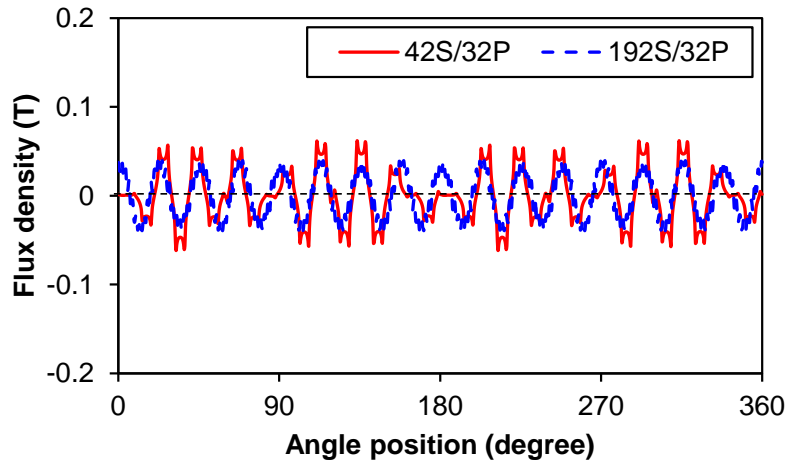


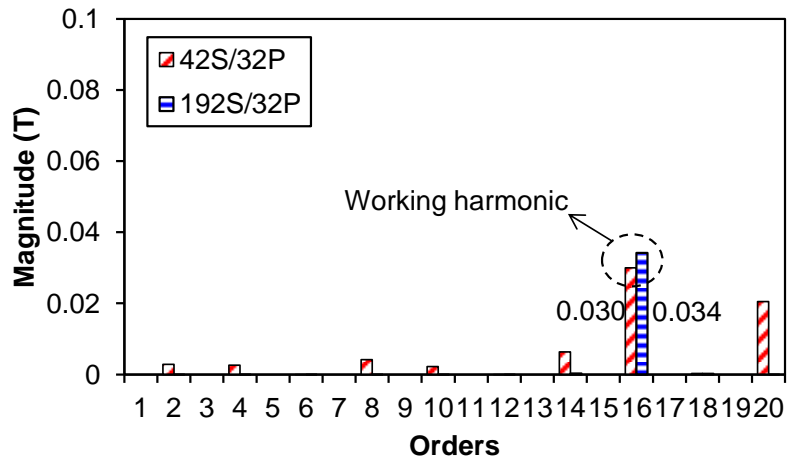
Fig. 5.5. Armature field distribution.

Since the currents of two machines are relatively low, the armature field is much weaker compared with the PM field. However, the repetition units of armature field are still the same as the PM field. Comparing Figs. 5.5 and 5.3, it can also be found that the saturation under armature field only condition is much lower than that under PM field only situation. Thus, the saturation of two machines is still mainly determined by the PM field under rated operation. Similar to PM field, the air-gap flux density of armature field only is plotted in Fig. 5.6.

Fig. 5.6(a) shows that the pole pair number of armature field of the 42S/32P modular machine is far from the rotor pole pair number. This is owing to the adoption of fractional slot dual 3-phase windings. The 192S/32P modular machine still keeps 16 repetition units, which is the property of integer slot winding. From the detailed spectra shown in Fig. 5.6(b), the existence of more harmonics in the 42S/32P modular machine verifies the distortion of its waveform. Instead, the 192S/32P modular machine has only one component with the same order as the rotor pole pair number. Besides, its magnitude is higher than that of the 42S/32P one. The higher winding factor for working harmonic (0.9659 and 1 for the 42S/32P and 192S/32P machines, respectively) and lower slot opening effect contributes to this phenomenon.



(a) Waveforms

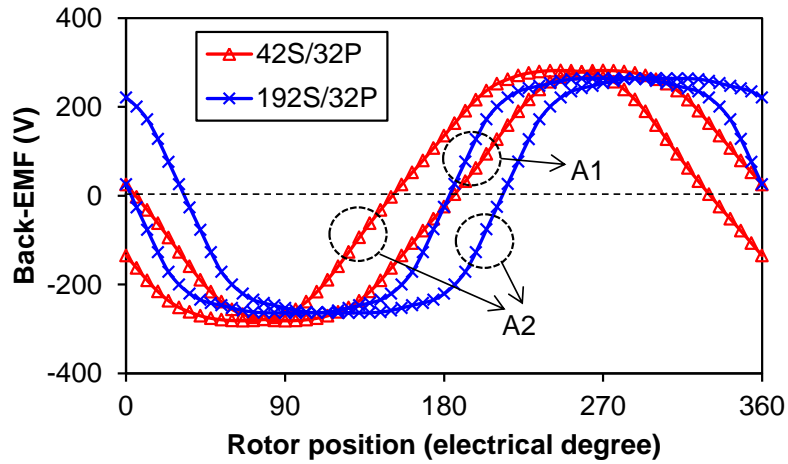


(b) Spectra

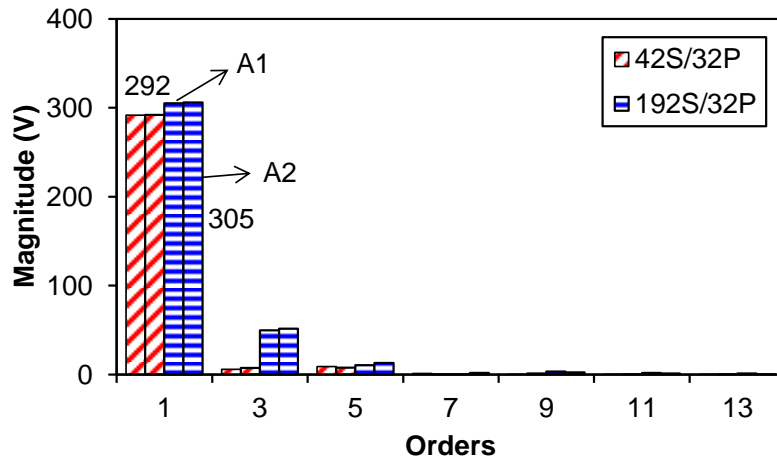
Fig. 5.6. Air-gap flux density for armature field only.

### 5.2.2 Open-circuit Performance

When the rotors of two machines rotate under open-circuit condition, the back electromotive force (EMF) will be induced in windings and the cogging torque will also appear. Since the three phases within each set of winding are balanced, only phase-A1 and A2 are chosen as representatives. Their phase back-EMFs are shown in Fig. 5.7.



(a) Waveforms



(b) Spectra

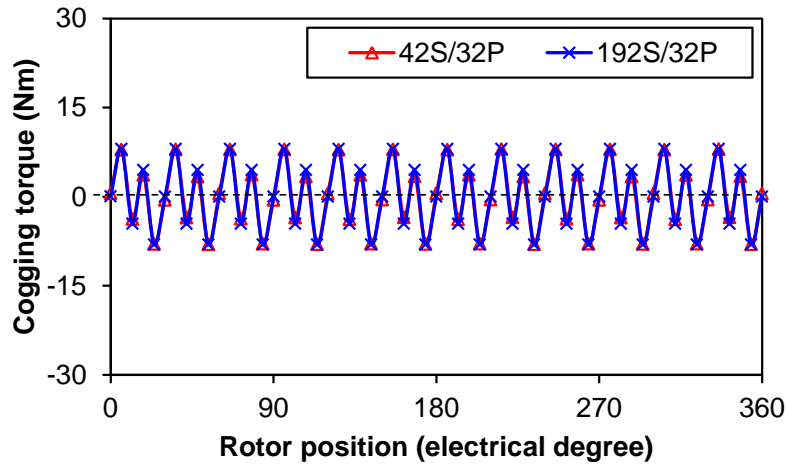
Fig. 5.7. Open-circuit phase back-EMF (170 rpm).

According to the waveforms shown in Fig. 5.7(a), the only difference between phase-A1 and A2 back-EMFs is the phase shift. Phase-A1 is 30 electrical degrees lag compared with phase-A2 in time for the 42S/32P modular machine and vice versa for the 192S/32P one. This coincides with the phase shift shown in Fig. 4.2 where the phase shift is in space. Comparing the waveforms of two machines, the 192S/32P modular machine has more trapezoidal back-EMF, which can be more clearly observed in Fig. 5.7(b). Since all of the harmonics have the same magnitude for phase-A1 and A2, this again verifies that two sets of windings are balanced. The higher fundamental component of the 192S/32P modular machine will contribute to a higher average torque under on-load condition neglecting saturation, while the reason

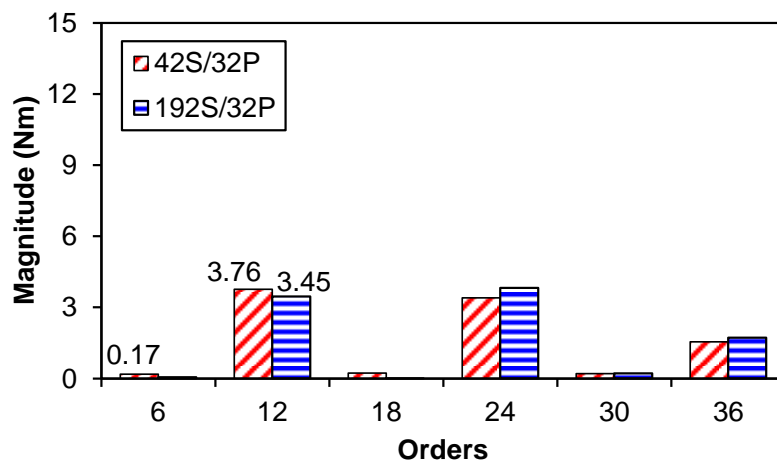


for more sinusoidal back-EMF is due to the lower 3<sup>rd</sup> harmonic in the 42S/32P modular machine.

Because of the fully open slots, the non-uniformed air-gap permeance results in the variation of the machine stored energy, which generates cogging torque under open-circuit condition. The results of two machines are shown in Fig. 5.8.



(a) Waveforms



(b) Spectra

Fig. 5.8. Cogging torque.

It is quite occasional that the two machines have the similar open-circuit cogging torque. The difference in waveforms is hardly to be identified in Fig. 5.8(a), while the 12<sup>th</sup> harmonic component can be obviously observed. Based on the spectra in Fig. 5.8(b), the major harmonics are the integer times of 12 for both machines. Although the magnitudes of each harmonic are different for two machines, such minor

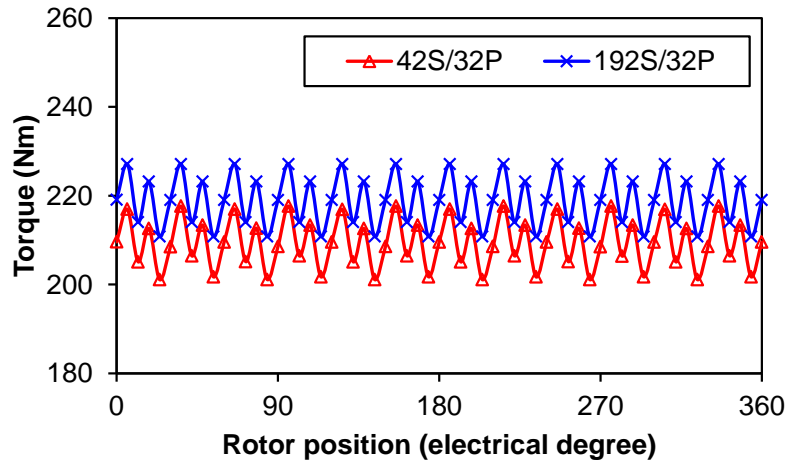
difference does not lead to quite different waveforms. Fig. 5.8(b) also exhibits another phenomenon that there is a tiny 6<sup>th</sup> harmonic component for 42S/32P modular machine. In fact, this component is minimised by optimising the tooth width of redundant teeth, as stated in Chapters 3 and 4. Due to the difference in structures, the minimal cogging torque periods over one electrical period ( $N_{cogpp}$ ) of the two kinds of machines are different and can be obtained as follows:

$$N_{cogpp} = \begin{cases} LCM(N_{trNOLP}, 2p)/p, & \text{for NOLP windings} \\ LCM(N_{sOLP}, 2p)/p, & \text{for OLP windings} \end{cases} \quad (5.1)$$

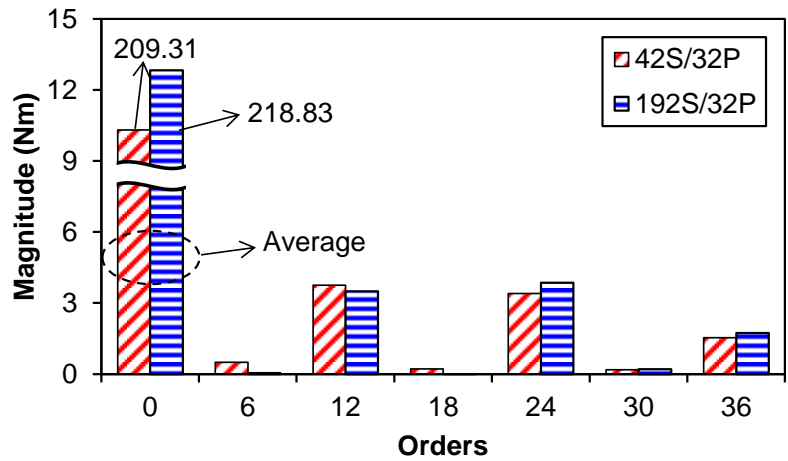
where  $LCM$  means the least common multiple of two numbers;  $N_{trNOLP}$  is the redundant tooth number for modular machines with NOLP windings;  $p$  is the rotor pole pair number and  $N_{sLOP}$  is the stator slot number for the modular machines with OLP windings. For the two machines analysed here,  $N_{cogpp}$  is 6 and 12, respectively. These are the same as the results shown in Fig. 5.8.

### 5.2.3 On-load Performance

When two sets of winding are fed with rated current, the average torque will be generated, as shown in Fig. 5.9. As expected, the average torque of the 192S/32P modular machine is higher than that of the 42S/32P one, which is the same as the magnitude of phase back-EMF fundamental component. The torque fluctuation under rated condition shown in Fig. 5.9(a) seems quite similar to cogging torques and the corresponding spectra shown in Fig. 5.9(b) can more clearly demonstrate this. The appearance of the DC component means the average torque and the other harmonic orders are the same as the cogging torque. However, the magnitudes of harmonics have changed, although the increase of magnitude is small. This can be explained by the PM and armature field flux density distribution in Figs. 5.3 and 5.5, where the armature field is much weaker than the PM field. That is why the armature field has such negligible influence on torque ripple under rated condition. Since the armature field is related with the current value, the influence of armature field on torque ripple can be seen when the current is high enough.



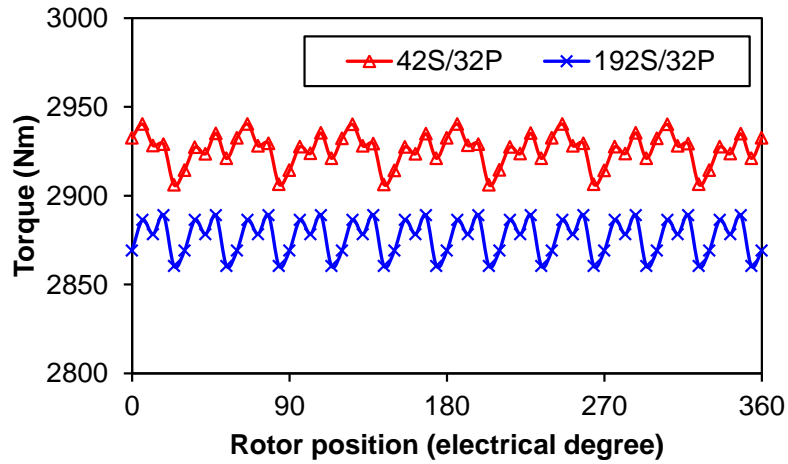
(a) Waveforms



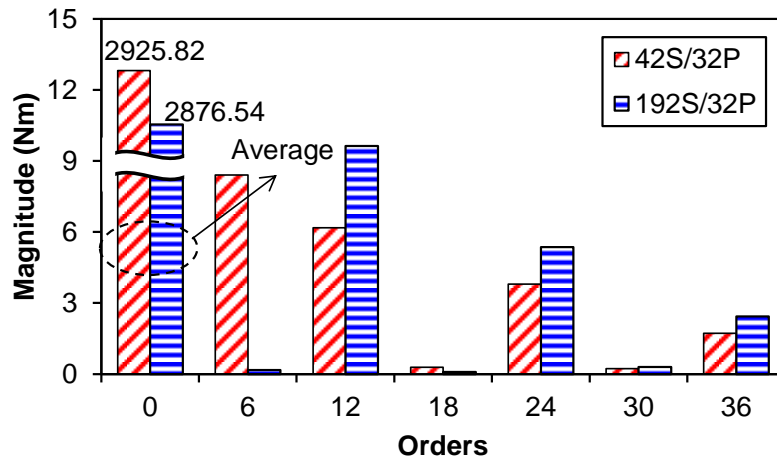
(b) Harmonics

Fig. 5.9. On-load torque under rated condition.

Under overload condition, the current is enlarged to 15 times of rated value and the torque performances are compared in Fig. 5.10. The average torque of the 42S/32P modular machine has exceeded that of the 192S/32P one, since the stator teeth are more saturated for the later. Due to the strong armature field, the torque waveforms are different from the torque under rated condition. The magnitudes of harmonic torque have apparently changed. For the 42S/32P modular machine, the 6<sup>th</sup> harmonic is now the major harmonic component, while it is the 12<sup>th</sup> harmonic for the 192S/32P one.



(a) Waveforms



(b) Harmonics

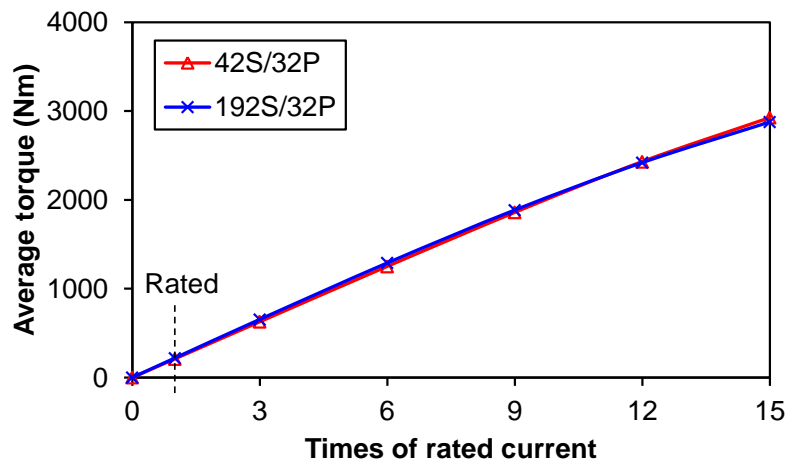
Fig. 5.10. On-load torque under overload condition.

The major values reflecting the torque performances are summarised in TABLE 5.2 for clarity (label as ‘Normal’), where the torque ripple is defined as the ratio of peak to peak (PP) torque ripple to average torque.

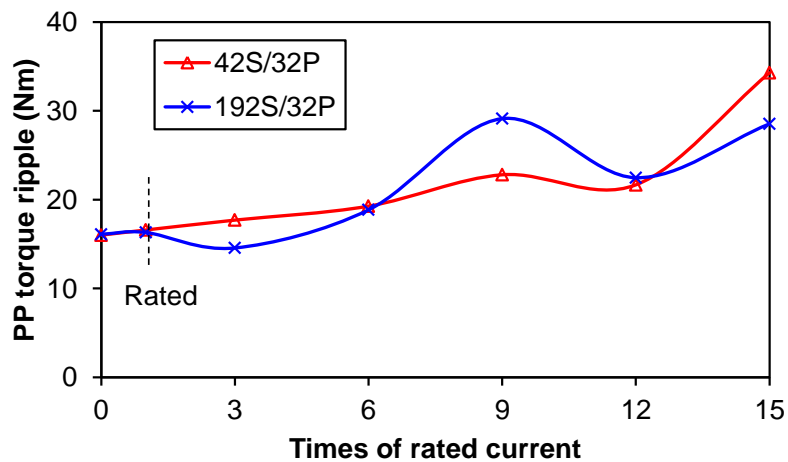
TABLE 5.2 MAJOR VALUES FOR TORQUE PERFORMANCES

	Load condition	Average torque (Nm)		PP torque (Nm)		Torque ripple (%)	
		42S/32P	192S/32P	42S/32P	192S/32P	42S/32P	192S/32P
Normal	Open	0	0	16	16	N/A	N/A
	Rated	209	219	17	16	7.9	7.5
	Overload	2926	2876	34	29	1.17	1
OC fault	Open	0	0	16	16	N/A	N/A
	Rated	105	109	20	23	19.3	20.8
	Overload	1528	1577	65	130	4.2	8.2
SC fault	Open	-778	-1178	54	84	6.9	7.2
	Rated	-706	-1089	49	93	6.9	8.6
	Overload	249	138	96	230	38.7	166.3

The complete average and PP torque-current characteristics are shown in Fig. 5.11. It shows that the average torques of both machines gradually increase with the current and show the saturation phenomenon. When the current surpasses a specific value, the average torque of the 42S/32P modular machine will be gradually larger than that of the 192S/32P one. For PP torque ripple, the overall trend is the increase, while the fluctuations can also be observed, especially for the 192S/32P modular machine. With the higher current, the interaction between PM and armature fields will accordingly change. Thus, the PP torque will show the fluctuation. Since the saturation of the 192S/32P modular machine is more sensitive than that of the 42S/32P one, the PP torque fluctuation is more obvious for this machine.



(a) Average torque



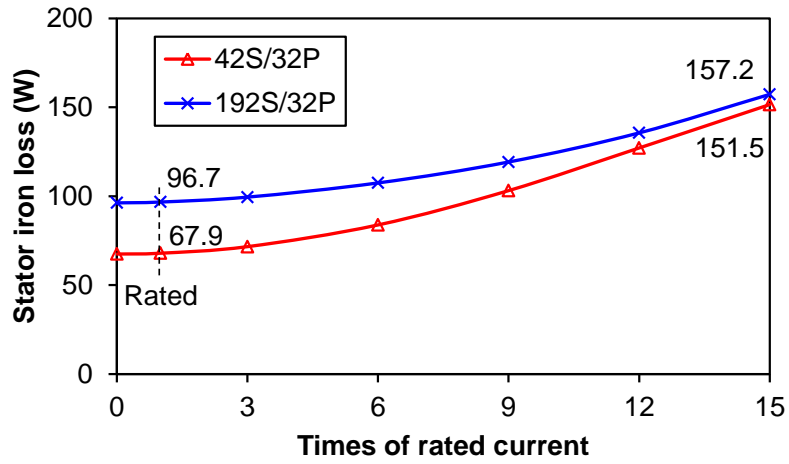
(b) PP torque ripple

Fig. 5.11. Influence of current on torque performances.

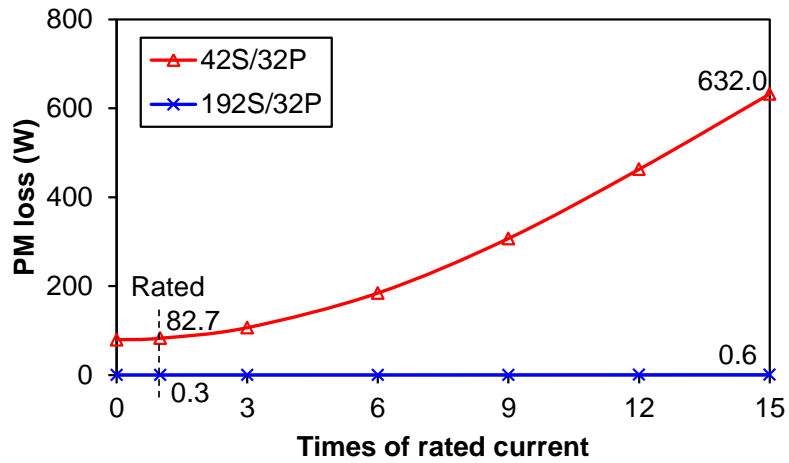
### 5.2.4 Iron Losses

In terms of iron losses, three major components (stator iron loss, PM and rotor yoke eddy current loss) are still concerned, especially the variation of their average values with the current. The principle of predicting these performances has been introduced in chapter 2 and the results for these two specific modular machines are shown in Fig. 5.12.

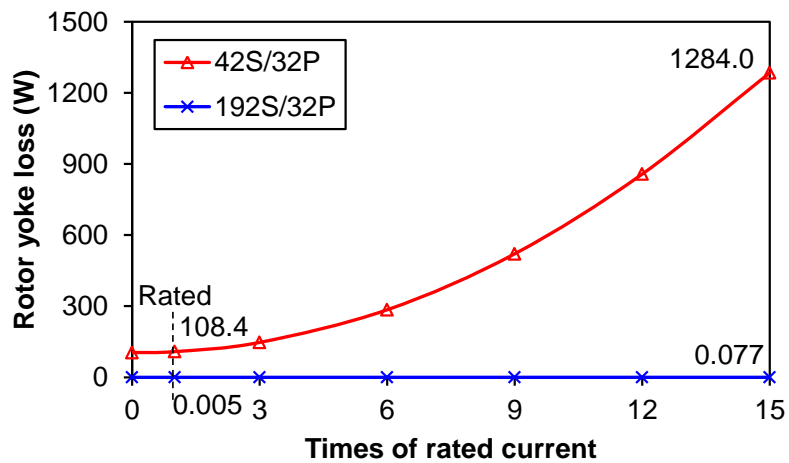
Fig. 5.12(a) shows that the dual 3-phase modular machine with NOLP winding has lower stator iron loss compared with the one with OLP winding. This comes from the lower stator core saturation, although the difference between two machines will increasingly low with the increase of current. Figs. 5.12(b) and (c) demonstrate that the other two iron losses are almost negligible for the 192S/32P machine compared with the relative huge value for the 42S/32P one. As has been clearly observed in Figs. 5.4 and 5.6, the harmonics are really more abundant for the 42S/32P modular machine no matter for the PM or armature field. Because of extremely low harmonic contents, the PM and rotor yoke eddy current losses are pretty small for the dual 3-phase machine with OLP winding, even if the current is high. However, the difference of two loss components can be found in the 42S/32P modular machine. Since the PMs are separated with each other, some lower order harmonics having longer wavelength will be suppressed. For the rotor yoke, there are no interruptions in the yoke body; and therefore all of the harmonics except the synchronous one will generate eddy current loss. That is why this component will be larger than the PM eddy current loss and the difference will become larger and larger with the increase of current. For the real applications, other measures must be adopted to reduce these two losses. It should be mentioned that the skin effect of flux density with high frequency variation is hard to be accurately considered; therefore the accuracy of the eddy current loss for integer slot machine needs more mesh elements and the step number must be high enough to account for higher order harmonics.



(a) Stator iron loss



(b) PM eddy current loss

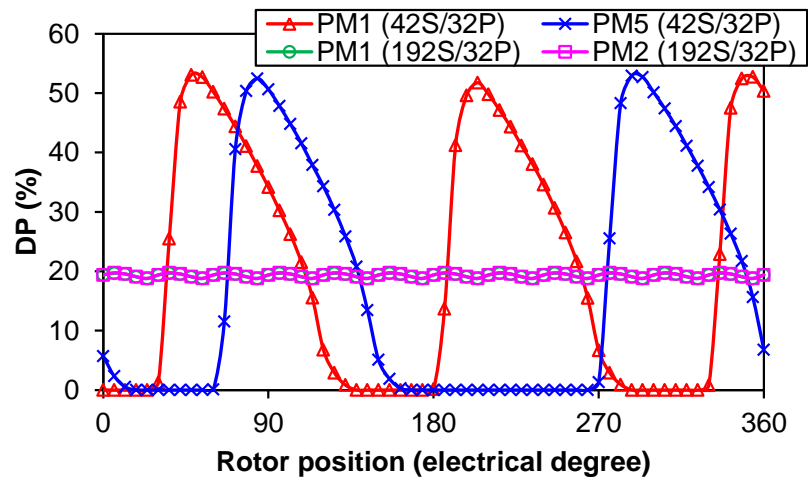


(c) Rotor yoke eddy current loss

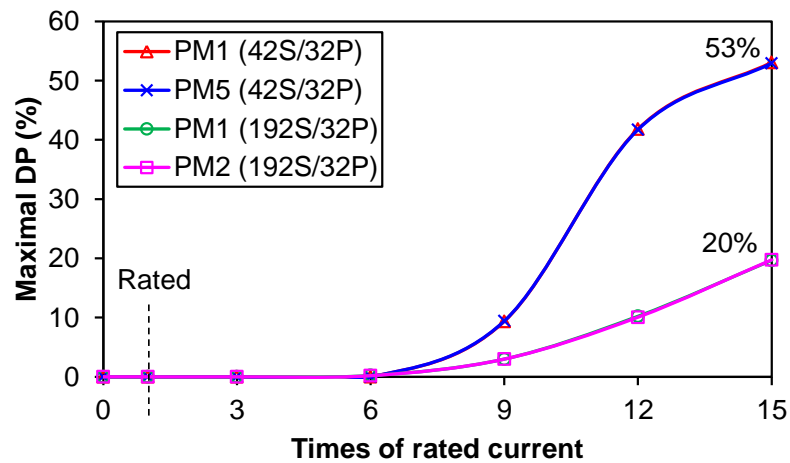
Fig. 5.12. Influence of current on iron losses (170rpm).

### 5.2.5 Demagnetisation

The irreversible demagnetisation is the same for each PM in integer slot machine [SHE13], while the two PMs within one segment are still analysed. For the 42S/32P machine, its irreversible demagnetisation characteristic has been analysed in chapter 2. Thus, only the corresponding first and last PMs of segment 1 are used as the reference. The results of two machines are shown in Fig. 5.13 with overload current.



(a) DP variation with the rotor position



(b) Influence of current on maximal DP

Fig. 5.13. Demagnetisation of the first and last PMs of segment 1.

Fig. 5.13(a) shows that both PMs of the 192S/32P modular machine have the same irreversible demagnetisation level during the operation and there is a constant component. The fluctuation of DP is 12, which is the same as the stator tooth number over one segment. Since each phase will exhibit maximum 12 times over one



electrical period, that is why they will vary 12 times. When it comes to the 42S/32P modular machine, the fluctuation is much larger and is caused by the influence of abundant harmonics. Moreover, the distance between two adjacent maximal DP will be different for two PMs because of the influence of redundant tooth on the last PM of segment 1. The variation of maximal DP in Fig. 5.13(b) exhibits that the dual 3-phase modular machine with OLP winding has stronger irreversible demagnetisation withstand capability. The lower harmonics contribute to this advantage and it will be more obvious under high current condition. The results shown in Fig. 5.13 validate the demagnetisation characteristic of integer slot machines, viz. each magnet having the same DP variation.

### 5.3 Performance Comparison under Faulty Operation

The comparison between two machines under normal operation shows that two machines have comparable electromagnetic performances in terms of open-circuit back-EMF and torque performances. However, the difference should be checked for faulty operation. When there is only one set of winding normally operates (A1, B1 and C1), the armature field will change and the corresponding field distribution is shown in Fig. 5.14.

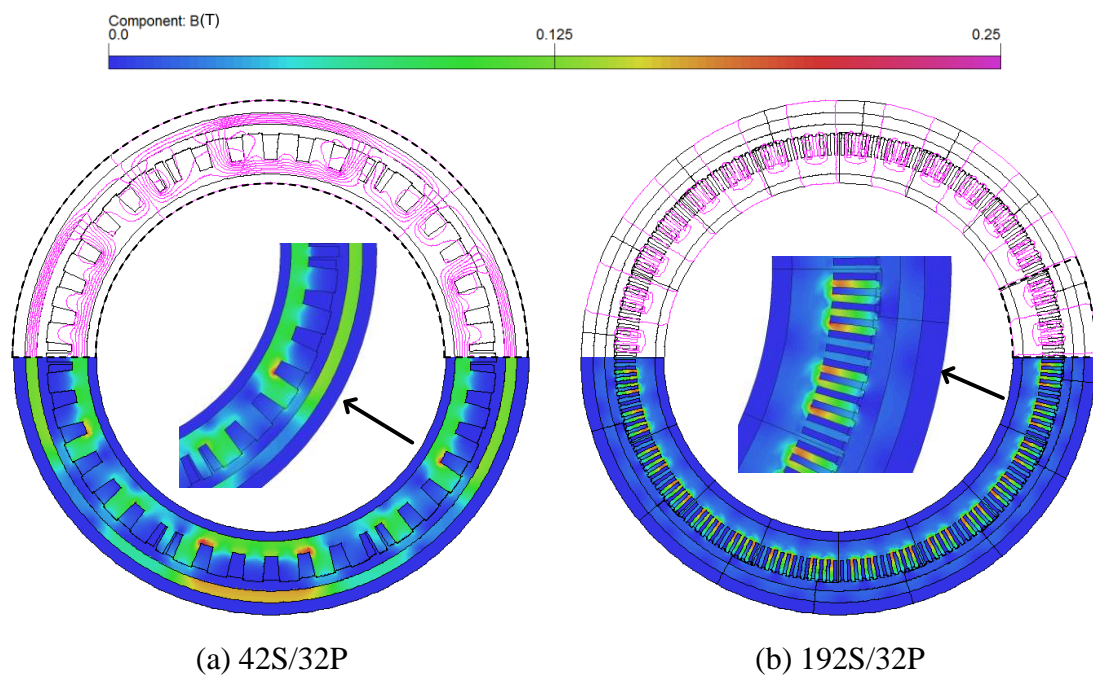
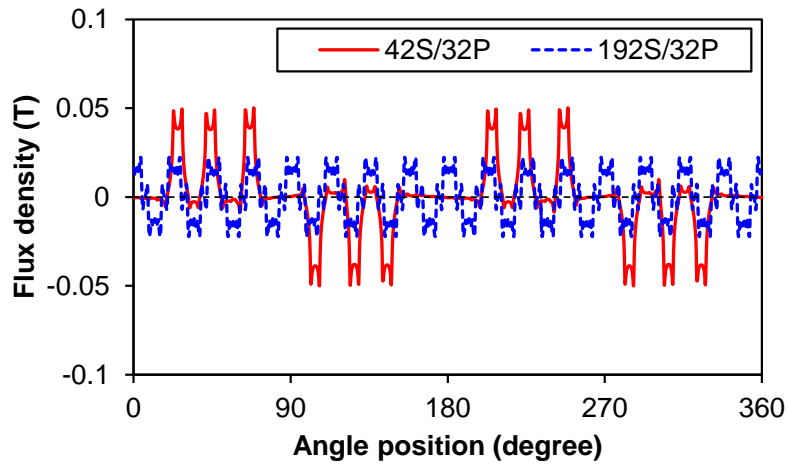
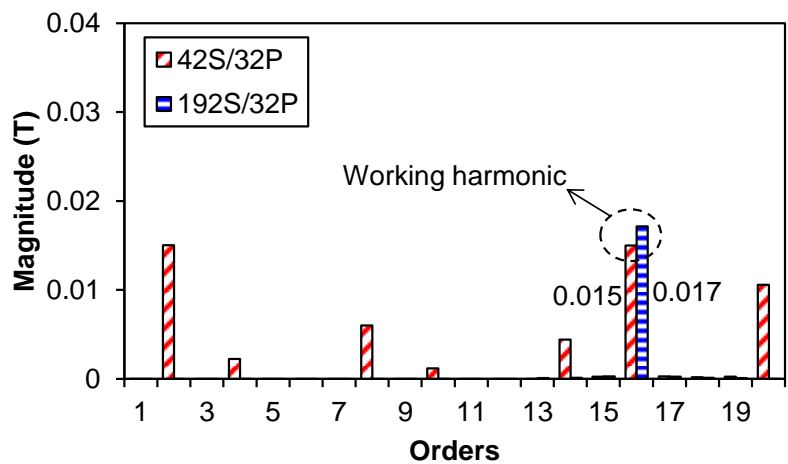


Fig. 5.14. Armature field distribution for only one set of winding.

Comparing with the field distribution in Fig. 5.5, the flux line and flux density distribution for one set of winding operation is quite different, though the periodic repetition number is still the same. As expected, the overall saturation decreases due to the lack of one set of winding. However, the saturation of some parts has changed due to the modification of armature field as well. The air-gap flux density shown in Fig. 5.15 can further explain this.



(a) Waveforms



(b) Spectra

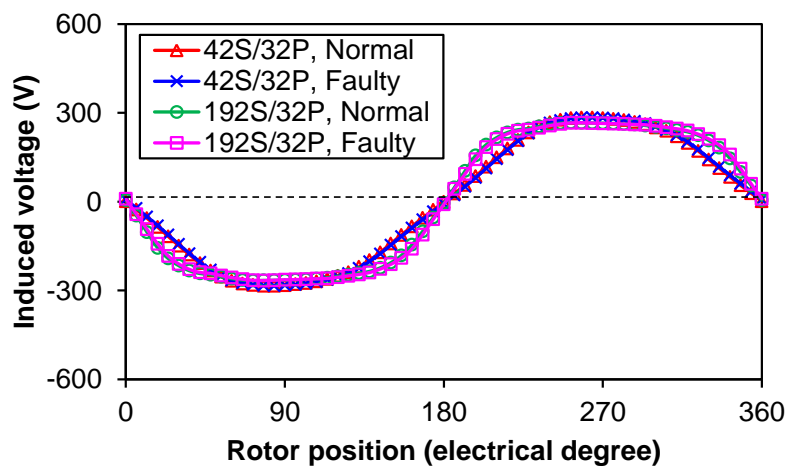
Fig. 5.15. Air-gap flux density for armature field only with one set of winding.

Fig. 5.15 shows that the air-gap flux density waveform of the 42S/32P modular machine changes more than that of the 192S/32P one. Comparing with Fig. 5.6, the 192S/32P modular machine still has only one fundamental component within 20 harmonic orders and the variation can only be seen when higher order harmonics are checked. In contrast, the harmonic variation of the 42S/32P machine is much more

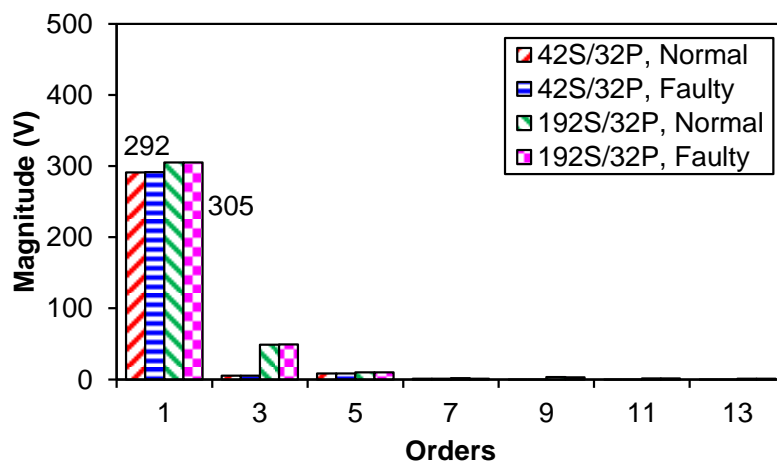
obvious. Although the harmonic orders are the same for both two set and one set winding operation, the magnitudes have apparently increased, especially for harmful lower order harmonics.

### 5.3.1 Open-circuit Fault

When the second set of winding (A2, B2 and C2) is open-circuit, the normal operation set of winding will be affected in theory. Moreover, the influence is also closely related to the current. For the induced voltage with rated current fed in the first set of winding, the results are shown in Fig. 5.16.



(a) Waveforms



(b) Spectra

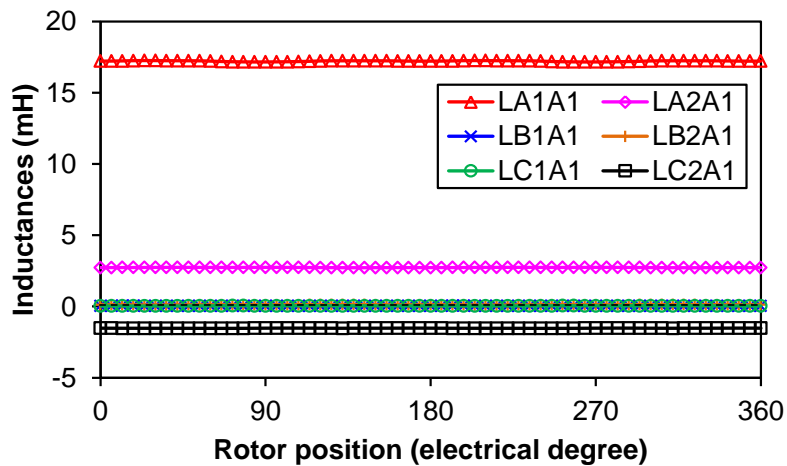
Fig. 5.16. Induced voltage of phase A1 under normal and faulty conditions (170rpm).

It can be seen that the lack of one set of winding has negligible influence on the induced voltages of the normal operation set of winding. The induced voltage of phase-A1 ( $v_{indA1}$ ) can be expressed as follows:

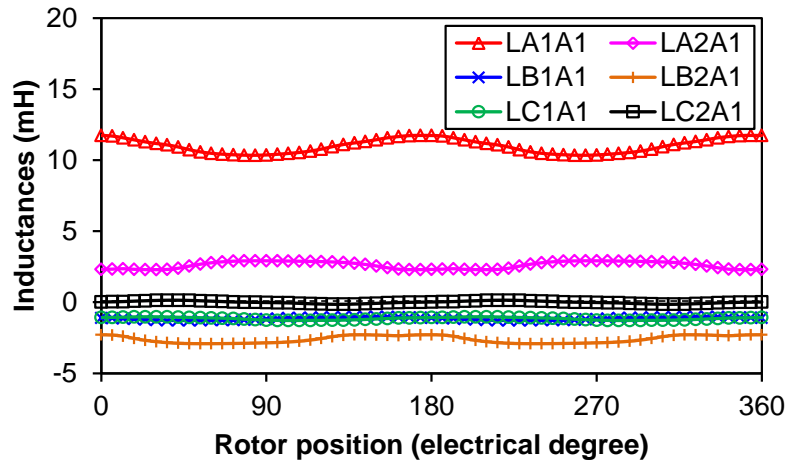
$$\begin{aligned}
 v_{indA1} &= \frac{d\psi_{A1}}{dt} \\
 &= \frac{d}{dt} (\psi_{PMA1} + \sum_{j1=A1,B1,C1} L_{A1j1} i_{j1} + \sum_{j2=A2,B2,C2} L_{A1j2} i_{j2})
 \end{aligned} \tag{5.2}$$

where  $\psi_{A1}$  and  $\psi_{PMA1}$  are the phase flux-linkage and its PM component;  $i_{j1}$  and  $i_{j2}$  are the currents;  $L_{A1j1}$  are the self and mutual inductances within the same set of winding and  $L_{A1j2}$  are the mutual inductance between two sets of windings.

Taking phase-A1 as example, the corresponding self and mutual inductances for the rated current are predicted with the help of frozen permeability (Appendix B) [HU03], as shown in Fig. 5.17. For the 42S/32P modular machine, phase-A2 and C2 have some coupling with phase-A1, which can be explained by the winding configuration shown in Fig. 5.1(a). When it comes to the 192S/32P modular machine, phase-A2 and B2 are coupled with phase-A1, which can also be illustrated based on winding layout given in Fig. 5.1(b). Due to the end OLP windings, the 192S/32P modular machine could be more affected under faulty operation. Since the armature field is much weaker compared with PM field for rated current, the induced voltage of phase-A1 is practically determined by the PM flux-linkage component. That is why the difference between normal and faulty operations is hardly to be observed.



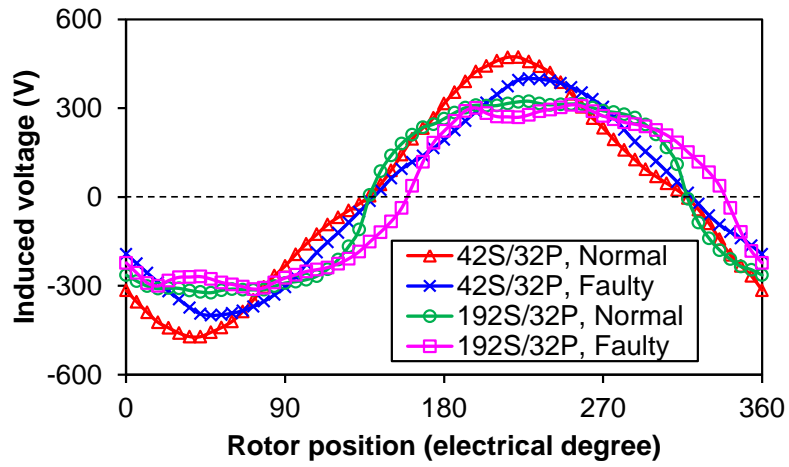
(a) 42S/32P



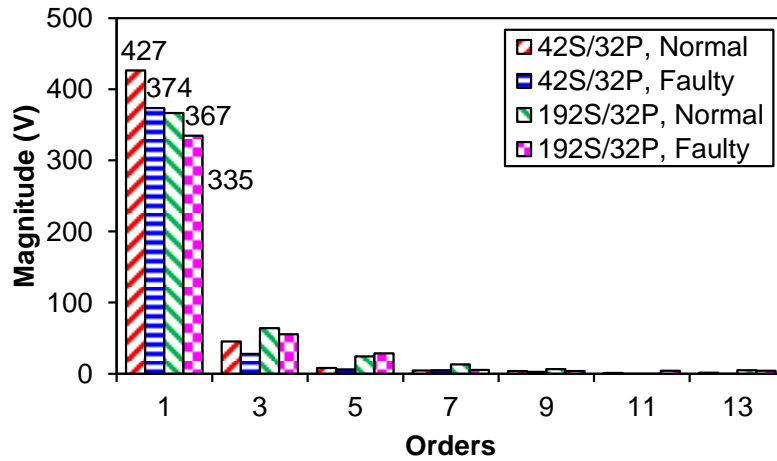
(b) 192S/32P

Fig. 5.17. Phase inductances of phase A1 for rated current.

For the sake of showing the difference between normal and faulty operations, the 15 times of rated current is fed into the first set of winding. The waveforms and spectra are compared in Fig. 5.18.



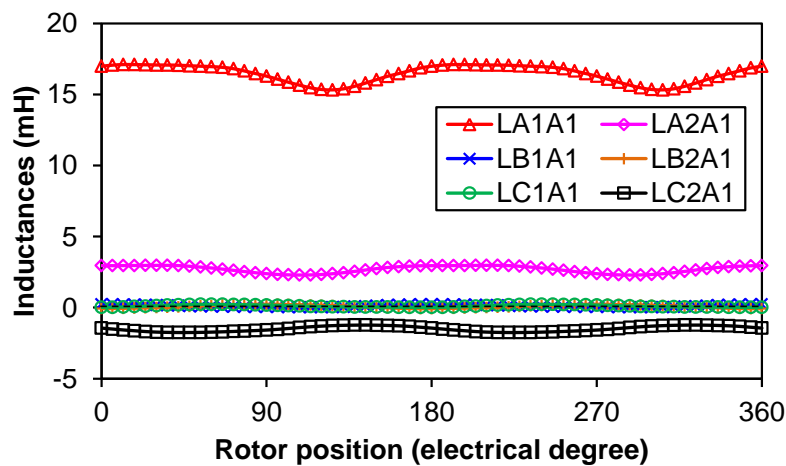
(a) Waveforms



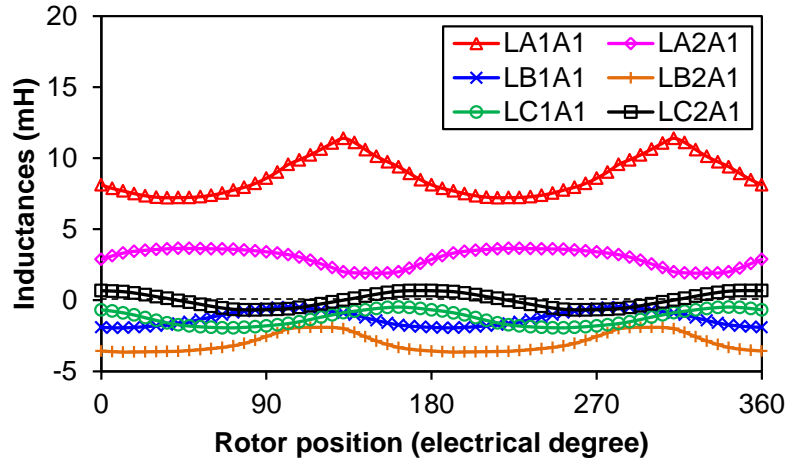
(b) Spectra

Fig. 5.18. Induced voltage of phase A1 under overload (15 times of rated current) normal and faulty conditions (170rpm).

Both machines show relative huge difference between normal and faulty operations now. The reduction of fundamental component is obvious. However, the distortion of waveforms is enlarged because of the influence of higher order harmonics. For the 192S/32P modular machine, the influence is severer because of more coupling between phases. (5.2) can be used to explain the difference as well. Since the inductances are related with the armature field strength, their values for 15 times of rated current are plotted in Fig. 5.19.



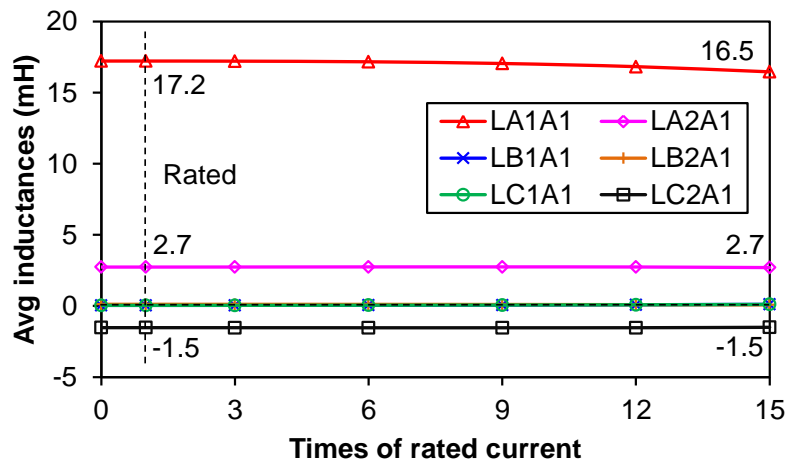
(a) 42S/32P



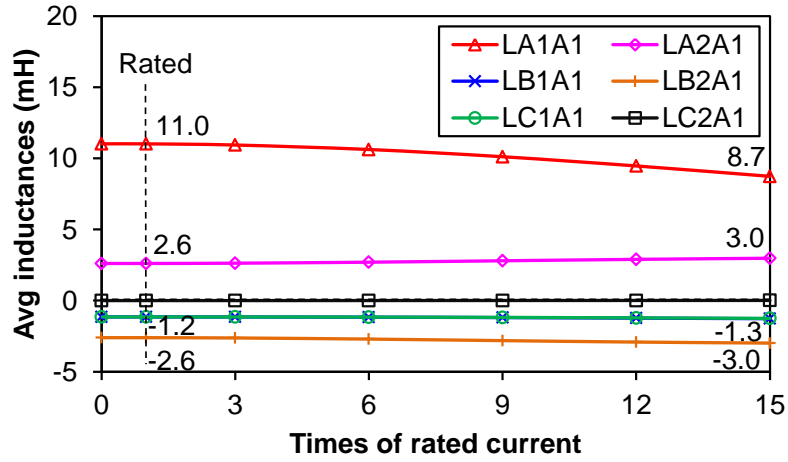
(b) 192S/32P

Fig. 5.19. Phase inductances of phase A1 for 15 times of rated current.

Fig. 5.19 shows that most of inductances fluctuate more obviously when the saturation is high, whereas the influence of current on the 42S/32P modular machine is weaker. Compared with Fig. 5.17, the reduction of self-inductance can be clearly observed, which is the result of severe saturation with the increase of current. On the other hand, the mutual inductances between other phases with phase-A1 are larger for the 192S/32P modular machine as well. This explains the reason for lower reduction of each harmonic in induced voltage. For clarity, the variation of average inductances with current is shown in Fig. 5.20.



(a) 42S/32P

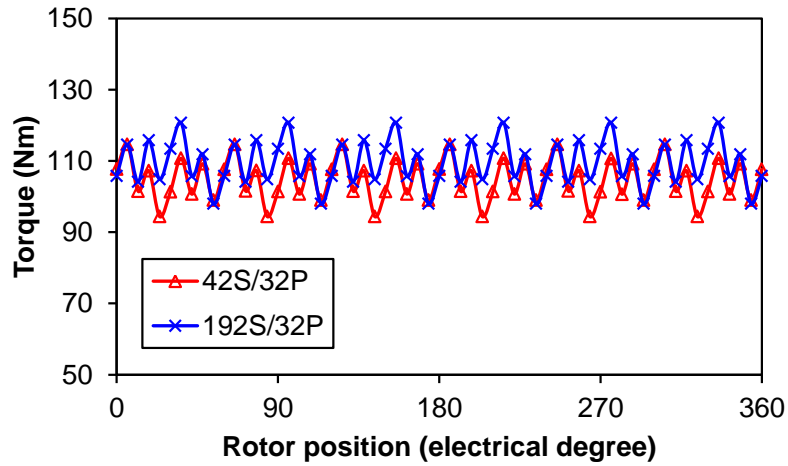


(b) 192S/32P

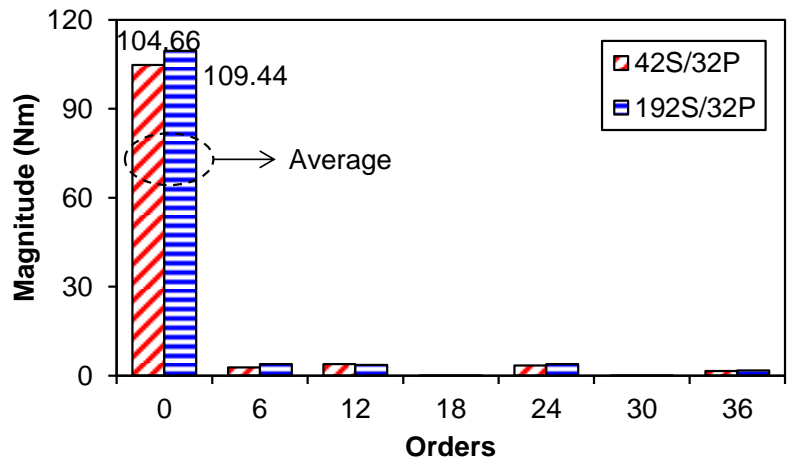
Fig. 5.20. Variation of phase-A1 inductances with current.

The torque performance is another important aspect should be investigated under faulty operation. Theoretically, the average torque under open-circuit fault is ought to provide half of its normal operation value. The results for one set of winding with rated current are shown in Fig. 5.21. Similar to the normal operation, the 192S/32P modular machine still has larger average torque compared with the 42S/32P one. Since the saturation level does not obviously change, the output torque could actually achieve half of its normal value. However, the torque ripple is different from the normal operation again. The lowest harmonic torque for both machines is 6 under open-circuit fault, since the merit of adopting dual 3-phase windings has disappeared. Furthermore, the 192S/32P modular machine shows higher torque ripple than the 42S/32P one because of its higher 5<sup>th</sup> and 7<sup>th</sup> harmonic components of open-circuit back-EMF, as shown in Fig. 5.7. Despite of the weak armature field, its influence on torque performance can be seen, which is different from normal operation.





(a) Waveforms

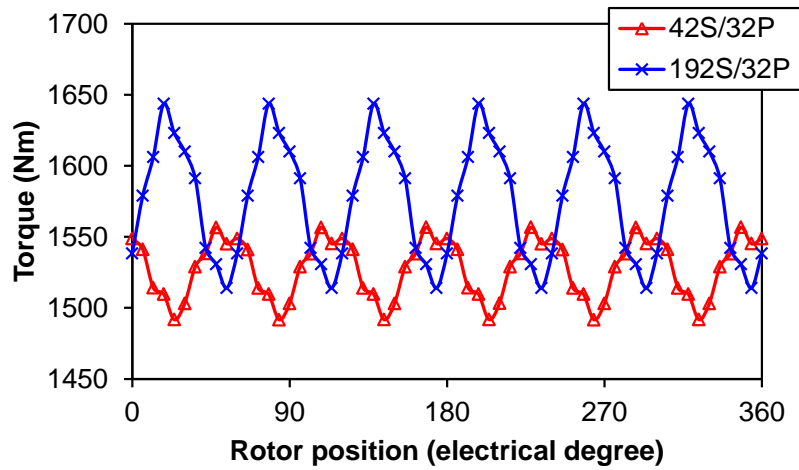


(b) Spectra

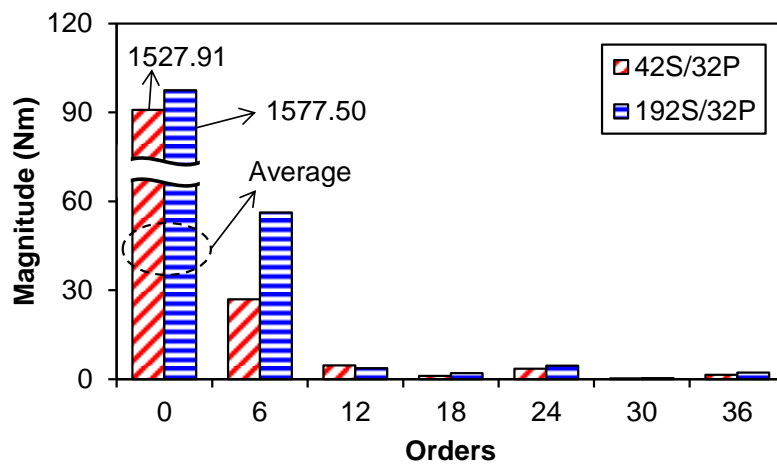
Fig. 5.21. On-load torque for one set of winding with rated current.

When the current fed into the first set of winding is increased to 15 times of rated value, the torque performance will accordingly change, as shown in Fig. 5.22. Fig. 5.22(a) shows that the average torque of the 192S/32P modular machine is still larger than that of the 42S/32P one, which is different from the normal operation. This can be explained by the winding configuration. For the 42S/32P modular machine, the lack of one set of winding does not affect the magnetic circuit of the other set of winding. However, there are more unsaturated teeth being provided for the 192S/32P modular machine under the condition of one set of winding operation. Therefore, such advantage will be more obvious at high current. In terms of torque ripple, the increase of the 6<sup>th</sup> harmonic torque can also be expected. The dual 3-phase machine is degraded into a single 3-phase machine and the integer slot machine suffers from higher

torque ripple, as shown in Fig. 5.22(b). Similar to normal operation, major characteristic values of torque are also summarised in TABLE 5.2 (labelled as ‘OC fault’).



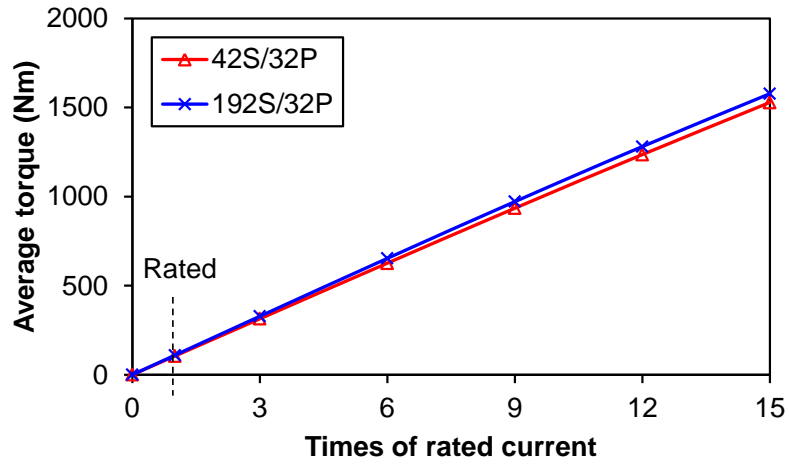
(a) Waveforms



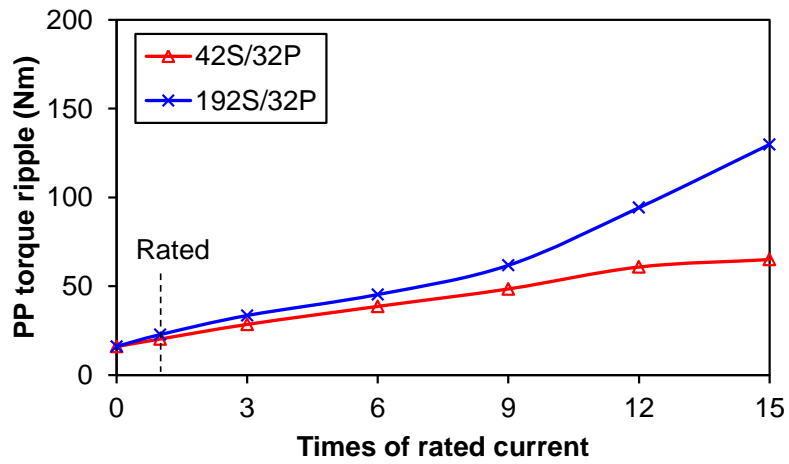
(b) Spectra

Fig. 5.22. On-load torque for one set of winding with 15 times of rated current.

The complete average and PP torque variation with the current are given in Fig. 5.23. The increasingly difference for both characteristics can be seen.



(a) Average torque

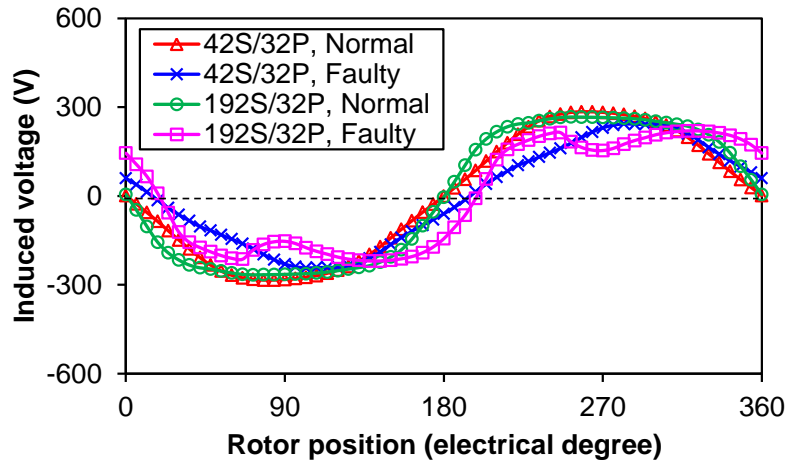


(b) PP torque ripple

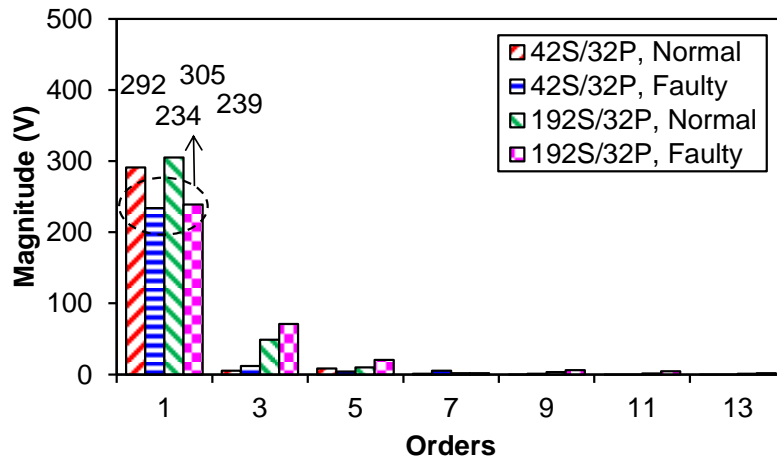
Fig. 5.23. Influence of current on torque performances for one set of winding.

### 5.3.2 Short-circuit Fault

When the second set of winding suffers symmetrical 3-phase short-circuit fault, the machine performances will be far from the normal and open-circuit faulty operations. Under the steady short-circuit situation, the induced voltages of phase-A1 are compared in Fig. 5.24.



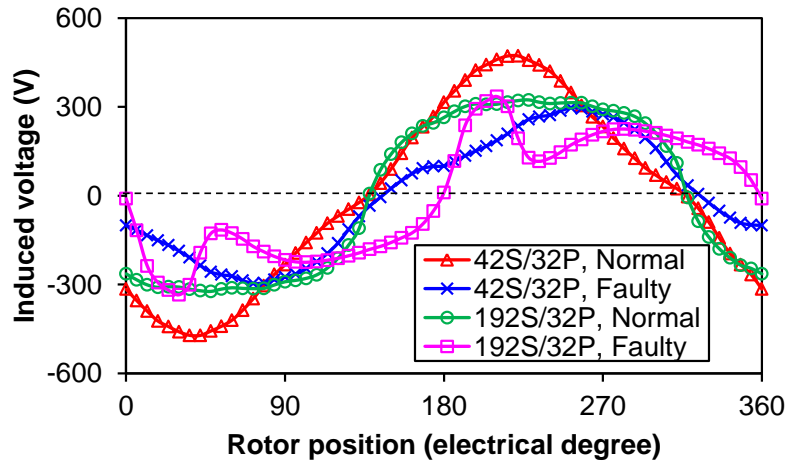
(a) Waveforms



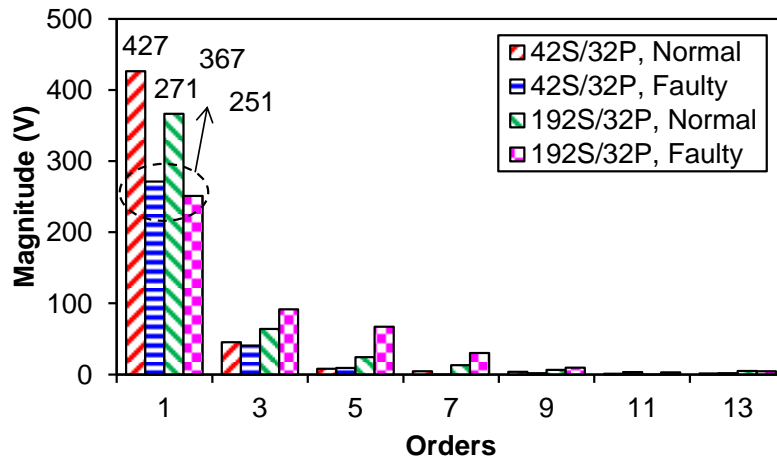
(b) Spectra

Fig. 5.24. Induced voltage of phase A1 for 3-phase short-circuit fault with rated current (170rpm).

Fig. 5.24 demonstrates that the induced voltage will be evidently distorted under short-circuit condition. Referring to (5.2), the first and second terms of flux-linkage should be not far from its normal and open-circuit fault situations, which means the third term plays the significant role. Short-circuit currents will be quite large and then the induced voltage will be obviously affected. Since the mutual coupling between two sets of windings is closer for 192S/32P modular machine, more demagnetisation effect will reflect on voltage reduction. However, the fluctuation of inductances will contribute to higher magnitudes due to higher order harmonics. For the 15 times of current situation, the results are compared in Fig. 5.25.



(a) Waveforms

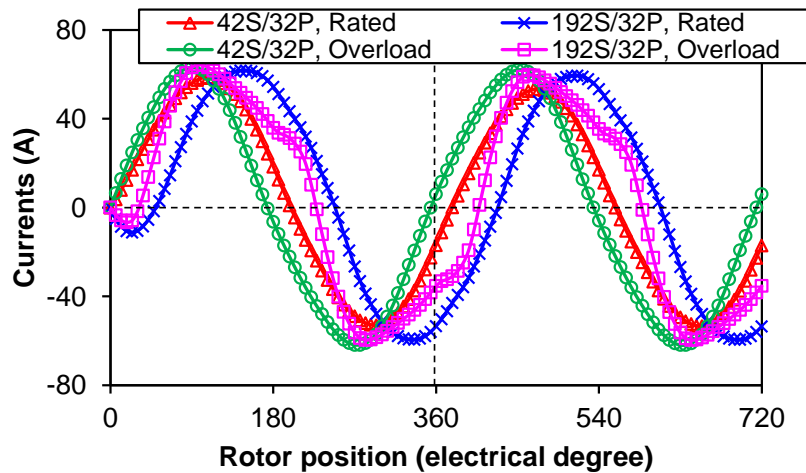


(b) Spectra

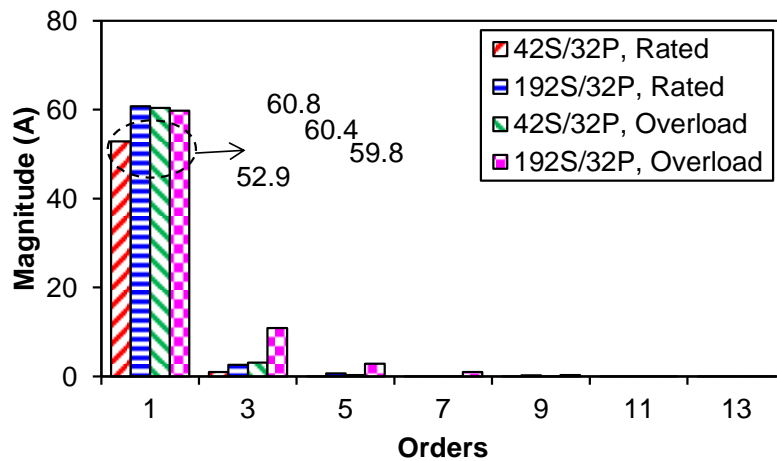
Fig. 5.25. Induced voltage of phase A1 for 3-phase short-circuit fault with 15 times of rated current (170rpm).

The strong demagnetisation effect due to the saturation caused by overload current and the mutual influence affected by short-circuit current of the second set of windings will lead to the reduction of fundamental component. The strong coupling effect results in a heavier distorted induced voltage for the 192S/32P modular machine. Besides, the peak value is larger for this machine as well. Since all of these coupling effect is related with the current, the short-circuit current of phase-A2 is chosen as the example, as shown in Fig. 5.26. After one period, the short-circuit current will be steady. As seen in Fig. 5.26(b), the fundamental component of the 42S/32P modular machine has evident increase, since the contribution of other phases to induced voltage will result in such phenomenon. In contrast, the demagnetisation

effect for the 192S/32P modular machine is stronger. The higher order harmonic currents instead of the fundamental component will increase. Due to more harmonic currents in the 192S/32P modular machine, the heat dissipation could be harder compared with the 42S/32P one.



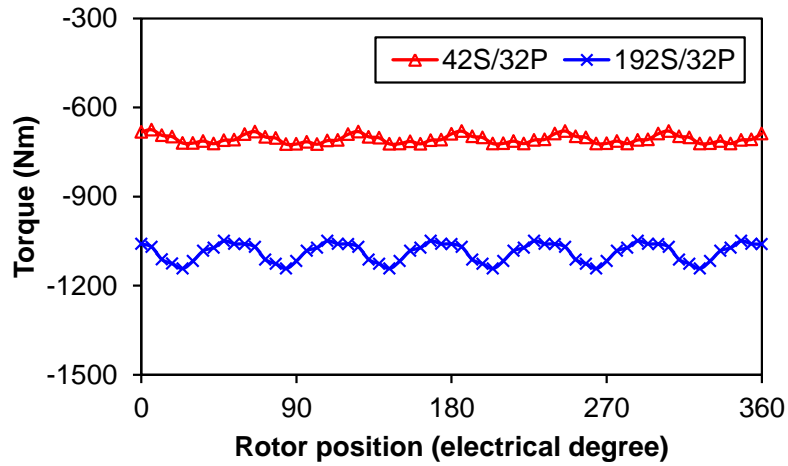
(a) Waveforms of the initial two periods



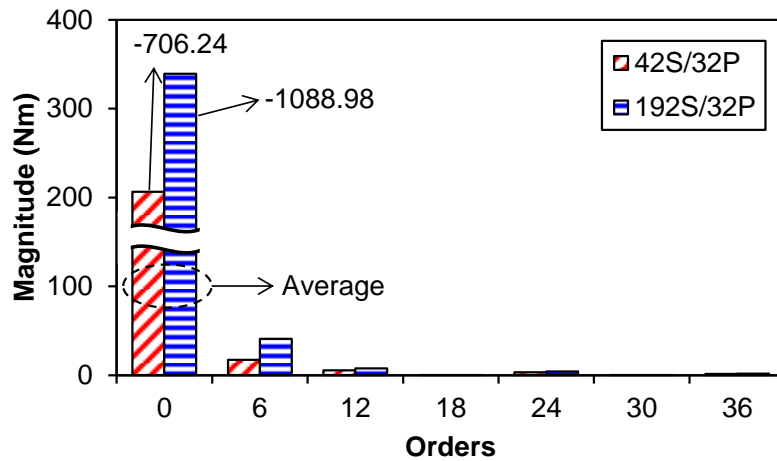
(b) Spectra at steady state

Fig. 5.26. Short-circuit current of phase A2 (170rpm).

The torque performance will show pretty special phenomenon under short-circuit faulty operation. Since short-circuit is much larger than that of rated current, the output torque is braking type when the rated current is fed into the first set of winding, as shown in Fig. 5.27. The larger short-circuit leads to a larger braking torque. Furthermore, the torque ripple is also higher for the 192S/32P modular machine because of the single 3-phase supply.



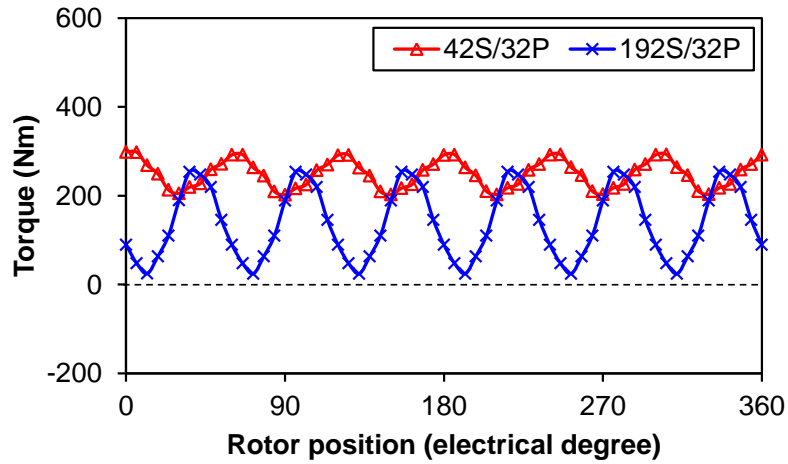
(a) Waveforms



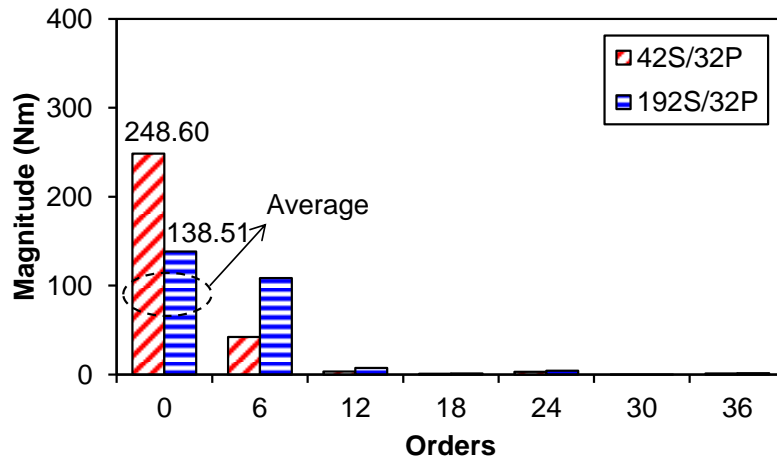
(b) Spectra

Fig. 5.27. On-load torque under one set winding short-circuit faulty operation with rated current.

With the increase of current fed into the first set of winding, the effective torque generated by this set of winding should increase. When the current reaches the 15 times of rated current value, there will be some active torque being produced, as exhibited in Fig. 5.28. However, the 42S/32P modular machine still generates larger average torque and the torque ripple of the 192S/32P one becomes much larger than that of the 42S/32P one. The strong armature reaction gives rise to this. TABLE 5.2 listed the characteristics torque values for this operation condition as well (Labelled as ‘SC fault’).



(a) Waveforms

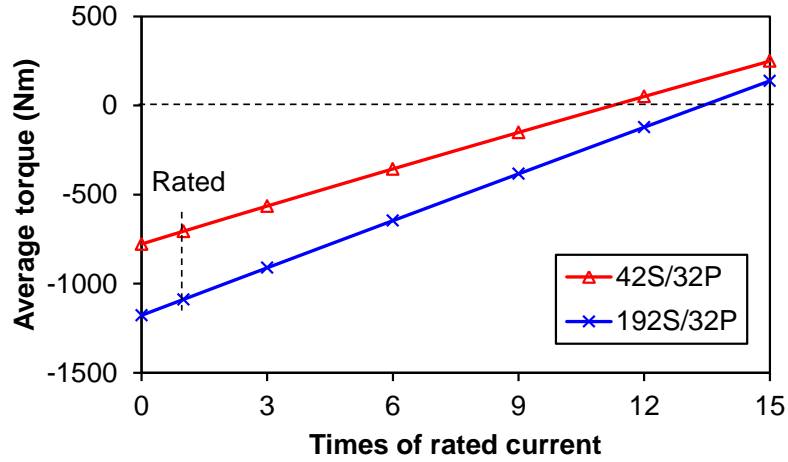


(b) Spectra

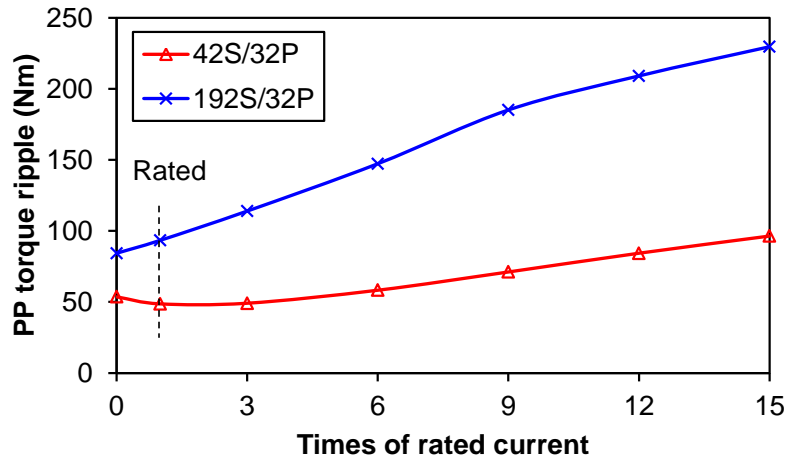
Fig. 5.28. On-load torque under one set winding short-circuit faulty operation with 15 times of rated current.

The average and PP torque variation with the current are compared in Fig. 5.29. Due to the demagnetisation effect of short-circuit current, the average torque is practically proportional to the supplied current. The difference between two machines is smaller, which is due to the reduction of braking torque for the 192S/32P modular machine. For PP torque-current characteristic, the 42S/32P modular machine performs much better than the 192S/32P one, though the value is larger compared with the normal and open-circuit faulty operations.





(a) Average torque

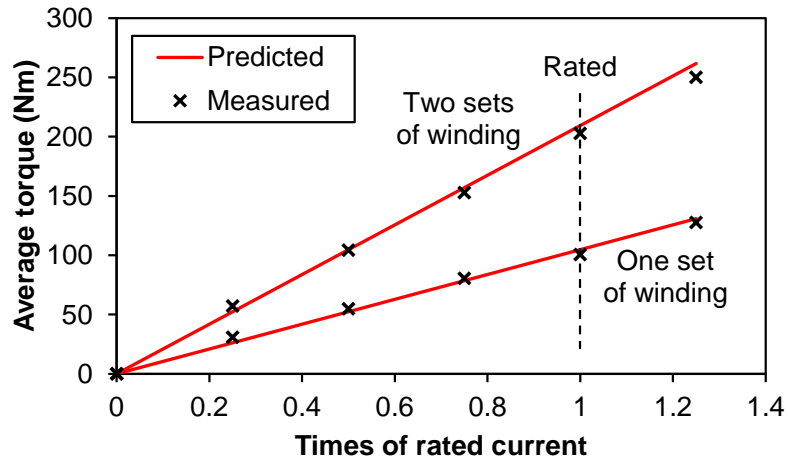


(b) PP torque ripple

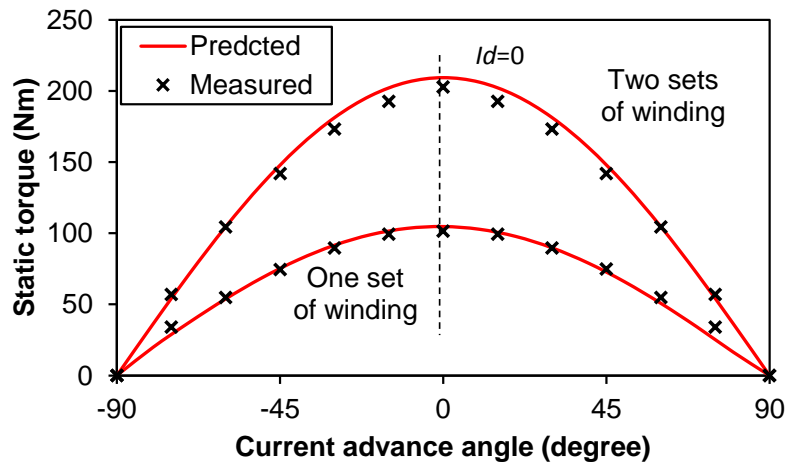
Fig. 5.29. Influence of current on torque performances under one set winding short-circuit faulty operation.

#### 5.4 Experimental Validation

The photos of 42S/32P prototyped machine and the test rig are shown in Fig. 4.35. The open-circuit back-EMFs of phase-A1 and -A2, open-circuit cogging torque, torque-current characteristic and static torque have been validated by comparing the results predicted by FEA and measured from experiments. Therefore, they will not be repeated here. Since the proposed modular machine can also operate with only one set of winding, the corresponding torque-current and static torque characteristics are shown in Fig. 5.30. In order to clearly observe the differences, the results of two sets winding operation are given as well.



(a) Torque-current



(b) Static torque (Rated current)

Fig. 5.30. Comparison of FE predicted and measured torque-current and static torque characteristics.

Fig. 5.30 demonstrates that the measured results agree well with those obtained from FEA even for the one set operation. However, the slight difference is owing to the manufacture tolerances and measurement errors. Within the current range shown in Fig. 5.30, the average torque will almost linearly increase with the current, since the saturation is hardly changed. The average torque under one set of winding operation is about half of those under two sets of windings operation, which is consistent with the theory analysis as well.

Due to the limit of test, only the nominal operation is validated and the faulty operation with obvious mutual influence is hardly measured. In order to validate the fault tolerant operation, a small size prototype could be manufactured and the faulty

operation can be tested on it. Besides, the inductances will be measured to validate the good fault tolerant capability as well.

## 5.5 Conclusion

By comparing the performances of two specific modular machines with OLP and NOLP windings, several conclusions can be drawn as follows:

(1) When the machines operate under normal condition, two machines have quite similar torque performances for rated current supply in terms of open-circuit back-EMF and on-load torque. When the current increases, the 42S/32P modular machine shows a larger average torque but a little higher torque ripple. The overall variation of PP torque is increasing with the current, while its fluctuation with current is more obvious for the 192S/32P modular machine. The OLP machine performs better in aspect of rotor iron losses and irreversible demagnetisation.

(2) If one set of winding is open-circuit, the other set of winding can provide almost half of the torque for both machines. However, the 192S/32P modular machine can provide higher torque compared with the 42S/32P one, especially for the higher current situation. This is due to the reduction of saturation on magnetic circuit for the former. Since the dual 3-phase operation degrades to single 3-phase type, the PP torque ripple for the 192S/32P modular machine becomes increasingly larger.

(3) If the second set of winding suffers from 3-phase symmetrical short-circuit, the output torque becomes braking type when the current is low. The much higher short-circuit current contributes to this. With the increase of current in normal operation set of winding, the effective torque will be obtained for large enough value. The strong coupling between phases for the 192S/32P modular machine will lead to more distorted induced voltage in normal winding and short-circuit in faulty winding.

Overall, modular machines with OLP and NOLP windings have the comparable torque performances under normal operation. In contrast, the modular machines with NOLP winding show better performances compared with those having OLP windings under faulty operation. The weaker mutual coupling between two sets of windings is the reason for the benefit of adopting NOLP windings. The future work on faulty operation can be done on a small size prototype, while the fault tolerance can be validated.

## **Chapter 6 Investigation of Fault-tolerant Modular Dual 3-phase PM machines with Different Winding Topologies**

Fault-tolerant permanent magnet (PM) machines have gained increasing attention with the higher requirement in safety-critical applications, for instance more electric aircraft [CAO12b]. From quite a few available electrical machine topologies, the multi-phase type was thought of as the most promising candidate [ELR11].

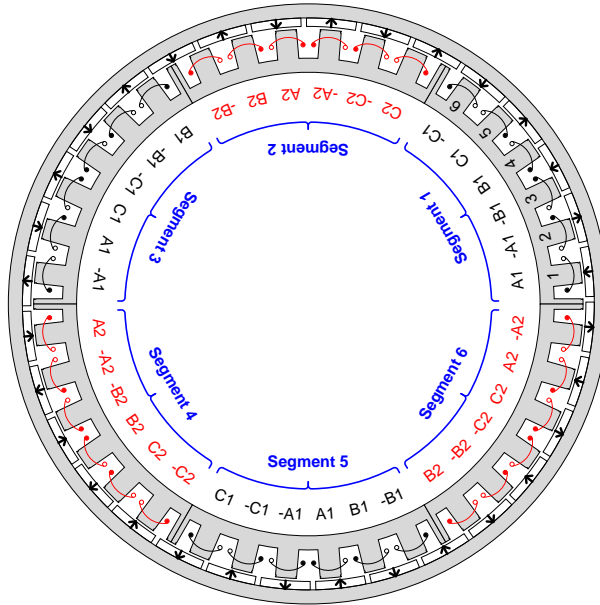
The merit of adopting independent inverter unit for multi-phase electrical machines was described in [JAH80], which shows that the phase-redundancy is a useful technique for high reliability. The accurate definition of phase number was discussed in [KLI83a], where the harmonic cancellation effect was addressed by using multiple 3-phase units. For validating the conclusion, the experiments on six and nine phase electrical machines were executed [KLI83b]. When it comes to PM machines, the fault-tolerant capability becomes more and more linked with the development of PM materials. The post faulty operation was investigated in [MEC96] to show the pretty good open-circuit and short-circuit fault withstand capability. The systematic summary of the available slot and pole number combinations for fault-tolerant machines was given in [BIA06a], where the star of slots method was used to identify how to achieve the requirement of negligible mutual coupling between two adjacent phases. Besides, the fault-tolerant operation also needs the support of drive technology. The research in this area is another important aspect [LEV08]. A series of research outcomes on fractional-slot dual 3-phase electrical machines provide good guidance in the research of fault-tolerant multi-phase electrical machines [BAR09], [ALB10], [BAR11a], [BAR11b], [ALB12]. Taking a 12-slot/10-pole (12S/10P) electrical machine as an example, the construction of dual 3-phase windings with thirty degree phase shift parallel converters was introduced in [BAR09]. The arrangement of two sets of windings was investigated and the most appropriate layout was identified in [ALB10]. Extending the slot and pole number combinations to other numbers was the major contribution in [BAR11a]. It can be seen that the constraints on obtaining a dual 3-phase winding with thirty degree phase shift is much stricter. When there is a fault in one set of winding, the electrical machine performance with only one set of winding was investigated in [BAR11b]. In terms of torque performance, the dual 3-phase winding with zero degree phase shift was not as good as its counterpart. Experimental validations were executed in an induction machine

[ALB12]. In fact, the dual 3-phase winding with zero degree phase shift (named as “Zero type”) have its own advantages in fault-tolerant operation as well and this chapter will focus on this.

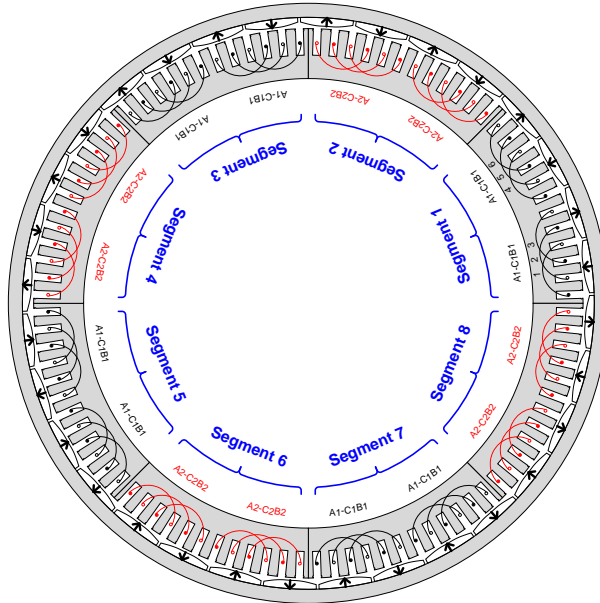
Two dual 3-phase modular permanent magnet (PM) machines with non-overlapping/overlapping windings are analysed and compared in this chapter. They have 42-slots/32-poles (42S/32P) and 96S/32P combinations, respectively. Besides, two sets of windings have zero degree phase shift between each other. The characteristics of the two electrical machines are described firstly and some necessary constraints are set in order to make a reasonable comparison. Since the two sets of windings are fed by independent inverters, operations with one set and two sets of windings are analysed and compared, especially in terms of terminal voltage and torque performance.

## **6.1 Prototype Machines**

Both prototype machines analysed in this chapter have dual 3-phase winding topology and there is zero degree phase shift between two sets of windings. However, they all have their own specialties because of the different winding configurations. For the proposed fractional-slot 42S/32P modular PM machine with redundant teeth, although its construction process has been introduced in Chapter 2, the winding connection is changed to make the phase shift between two sets of windings from thirty degree to zero. Comparing this modular machine with the one having overlapping winding and the same rotor pole number (96S/32P combination), performance difference can be expected. This integer slot modular PM machine is assembled with single layer, full-pitched winding. The cross-sections of two modular machines are shown in Fig. 6.1.



(a) 42S/32P



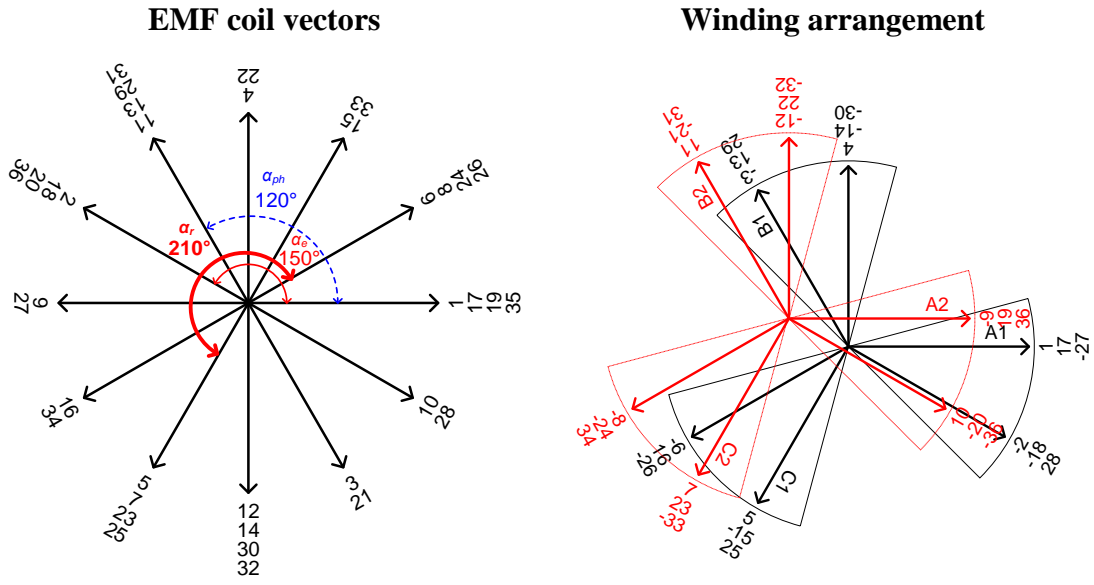
(b) 96S/32P

Fig. 6.1. Cross-sections of prototype machines with Zero type dual 3-phase windings.

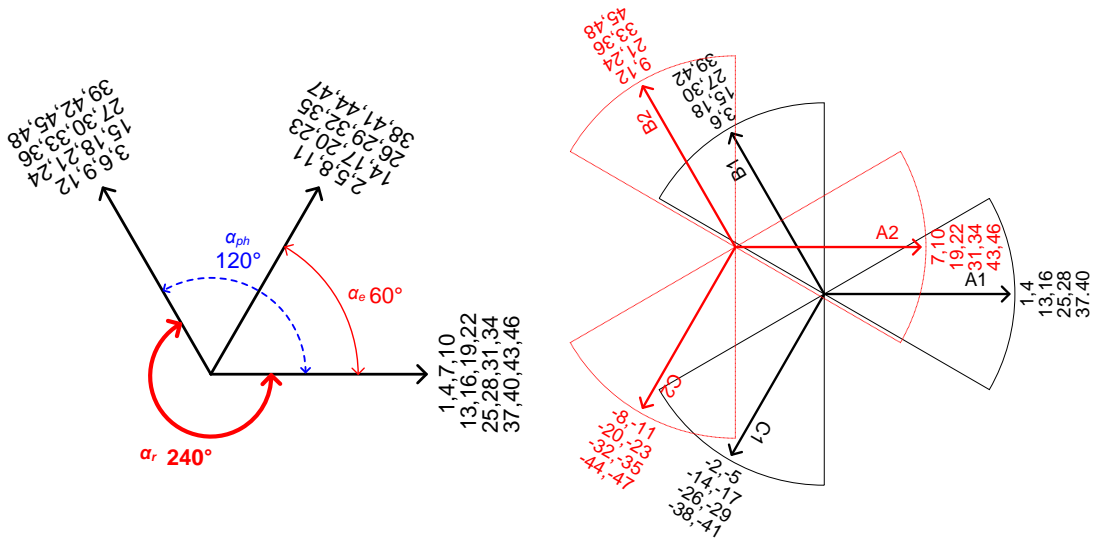
From Fig. 6.1, several characters of each electrical machine can be clearly seen. The stator of the 42S/32P modular machine shown in Fig. 6.1(a) consists of six segments and each segment is a half 12S/10P electrical machine unit. Six redundant teeth (without coils wound) are adopted to join the six segments together and protect the coils located at the end parts of each segment in spite of some stator space waste. Due to the additional phase shift between the two end coils of adjacent segments, the first coil of each segment does not belong to the same phase. In contrast, the

overlapped end parts of windings can be obviously seen in Fig. 6.1(b). The prototype machine is separated into eight segments here and each segment has two 6S/2P electrical machine units. Although this modular machine has the same rotor pole number as the 42S/32P one, all of its PMs are shaped to minimise the torque ripple, which is quite large in integer slot PM machines. Arc-shaped PMs are used in the 42S/32P modular machine, whereas two of them are wasted owing to constructing the proposed modular structure with redundant teeth. Even though there is a bit less PM volume for 96S/32P modular machine compared with 42S/32P one, the winding factor of the working harmonic, viz. rotor pole pair number, is smaller for the later because of the short pitched winding. Overall, two electrical machines will generate similar torque under normal rated operation condition. Therefore, the comparison is reasonable.

Since the different winding configurations of two modular machines are crucial to their performance difference, the corresponding process of obtaining the winding layout is shown in Fig. 6.2 by the star of slots method [BIA 06a]. According to the coil EMF vectors shown in the left column of Fig. 6.2, the slot pitch angle for the effective teeth within each segment ( $\alpha_e$ ) is 150 and 60 degrees for two electrical machines, respectively. The phase shift between two adjacent coils belonging to different segments ( $\alpha_r$ ) is also different for two electrical machines. They are 210 and 240 degrees for 42S/32P and 96S/32P modular machines, respectively. The phase shift between two phases among the same set of winding ( $\alpha_{ph}$ ) is 120 degrees for both of them. Based on the coil EMF phasors, the winding arrangement can be obtained, as shown in the right column of Fig. 6.2. Each phase belt spans 60 degrees in space and each phase contains the same coil numbers. Two sets of windings are in the same phase in terms of space, while the whole electrical machine is split into two equal parts. The final winding layout can be seen in Fig. 6.1.



(a) 42S/32



(b) 96S/32P

Fig. 6.2. Winding layouts of two prototype machines.

Before the comparative study, some constraints on structure must be satisfied. Two electrical machines have the same stator inner and outer radius, air-gap length, PM thickness, axial length, series turns per phase, rated current and rotor speed. The specific structure parameters are given in TABLE 6.1.



TABLE 6.1 MAJOR PARAMETERS

Item	$N_s/N_p$	
	42S/32P	96S/32P
Stator inner radius (mm)		159.7
Stator outer radius (mm)		195.2
Stator yoke thickness (mm)	13.3	16.6
Stator tooth width (mm)	17.52 <sup>a</sup> and 7.9 <sup>b</sup>	
Stator slot width (mm)		18.87
Air-gap length (mm)	2	2 (minimum)
PM thickness (mm)	6	6 (maximum)
PM pole arc to pole pitch ratio	0.9	0.95
Rotor yoke thickness (mm)		10
Axial length (mm)		110
Turns per coil	68	51
Rated current (A)		3
Rated speed (rpm)		170

<sup>a</sup> the teeth with coils.

<sup>b</sup> the teeth without coils.

## 6.2 Performance Comparison with Two Sets of Winding Operation

### 6.2.1 Field Distribution

When there is not fault in windings, the electrical machine runs under normal condition. Since the electrical machine on-load performance is the interaction between PM and armature field, the individual field distribution of two modular machines is firstly shown in Fig. 6.3. The rotor  $d$ -axis aligns with the axis of phase-A1, which is defined as the rotor initial position.

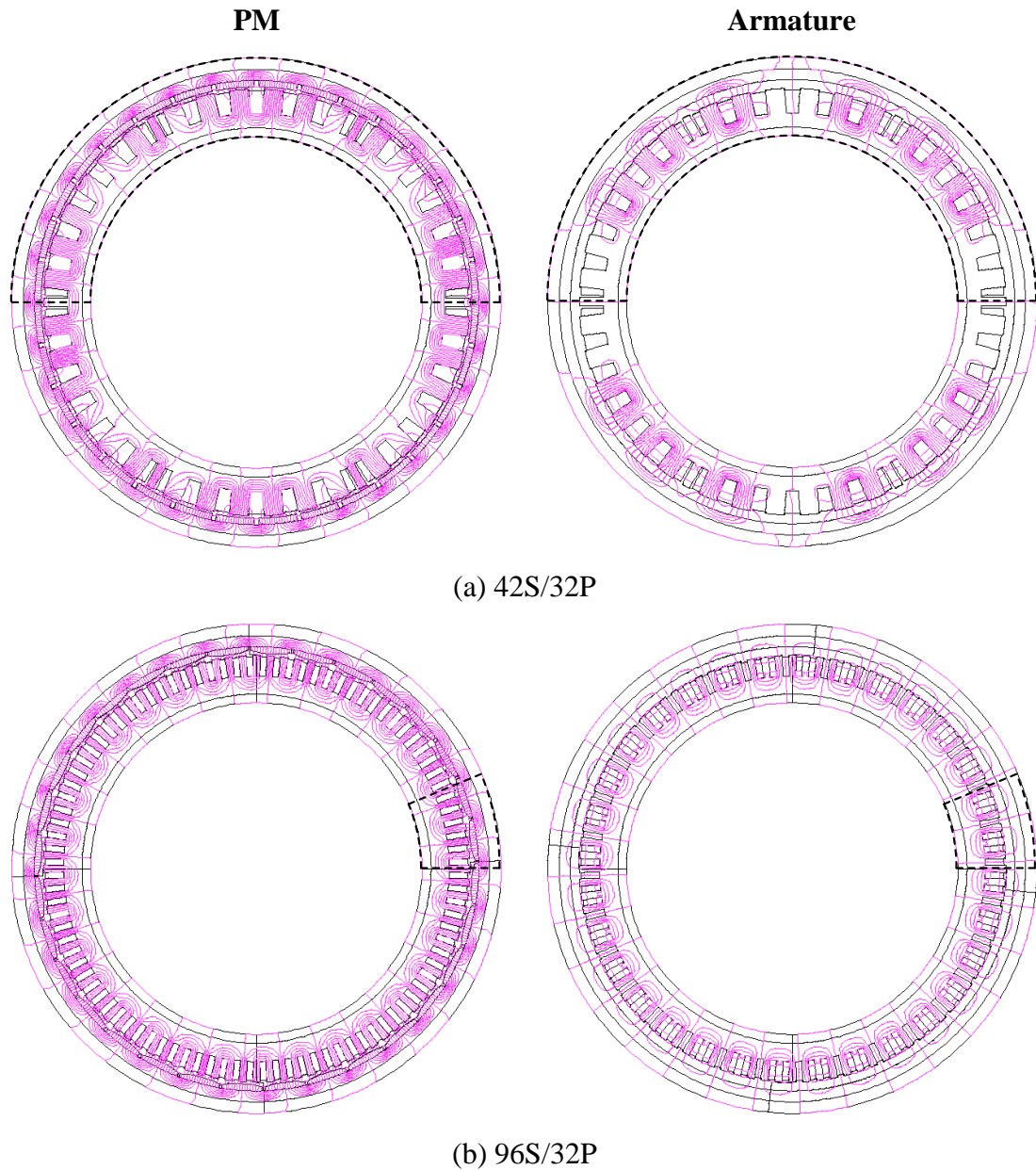
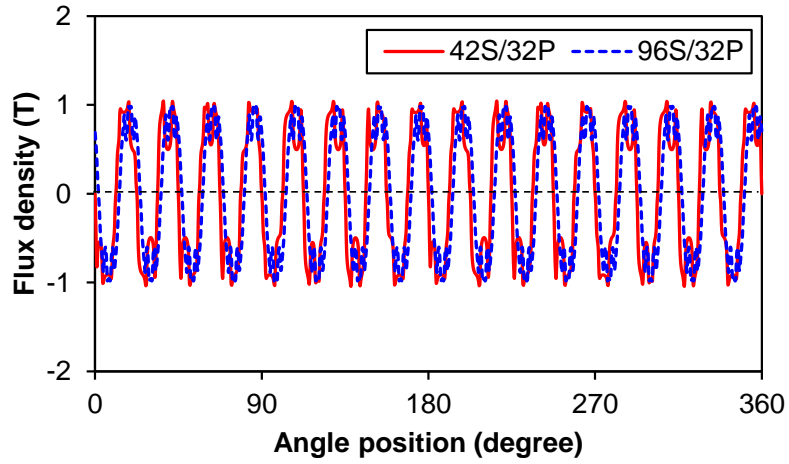
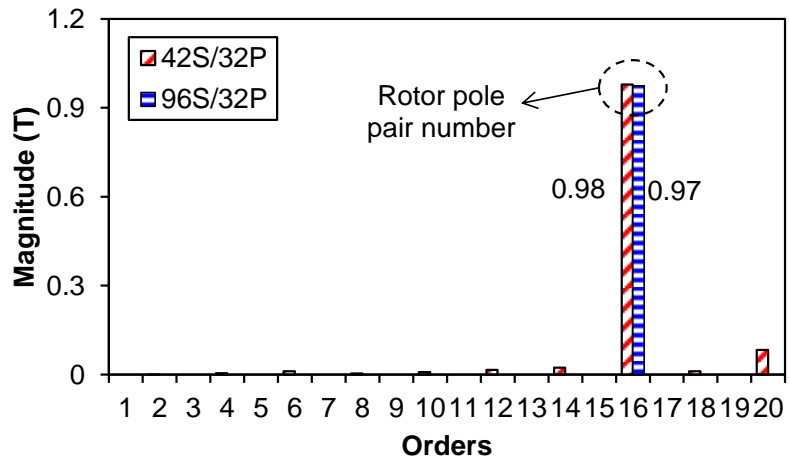


Fig. 6.3. Field distribution due to PM and rated armature current.

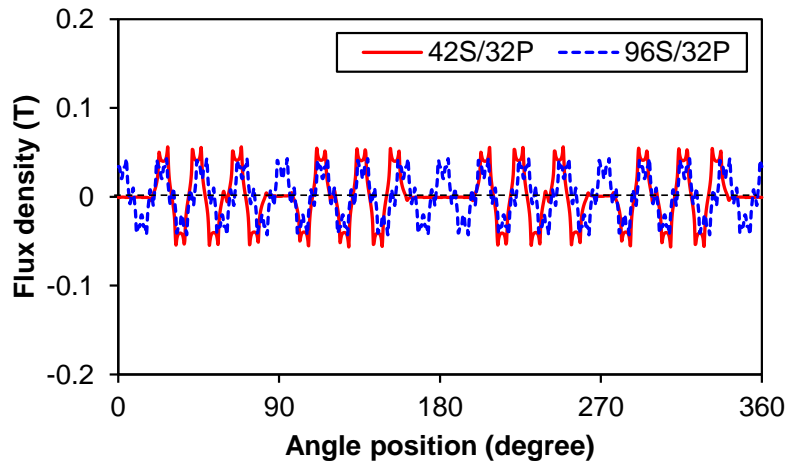
According to Fig. 6.3, the minimal repetition unit numbers of two electrical machines (addressed by the dashed line) are 2 and 16, respectively. Compared the field distribution due to PM and rated armature current, it can be seen that the PM and armature fields of the 42S/32P modular machine are more distorted due to the slotting effect and fraction-slot winding arrangement. Therefore, the abundant harmonics will be generated in air-gap flux densities, as shown in Fig. 6.4.



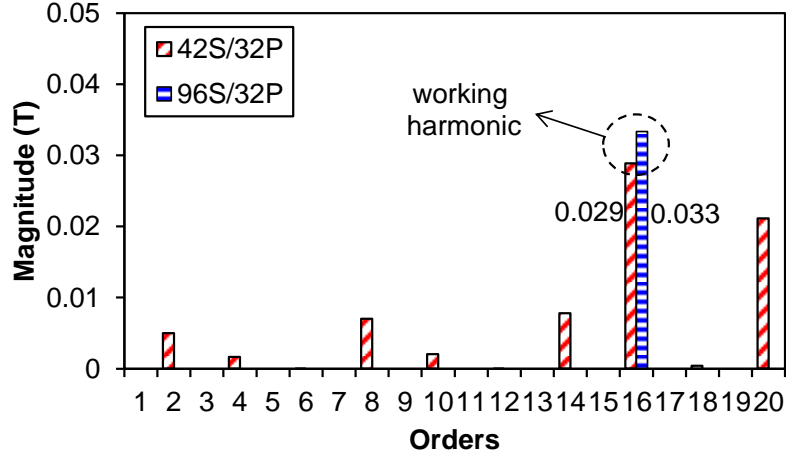
(a) Waveforms for PM field only



(b) Spectra for PM field only



(c) Waveforms for rated armature field only



(d) Spectra for rated armature field only

Fig. 6.4. Air-gap flux density.

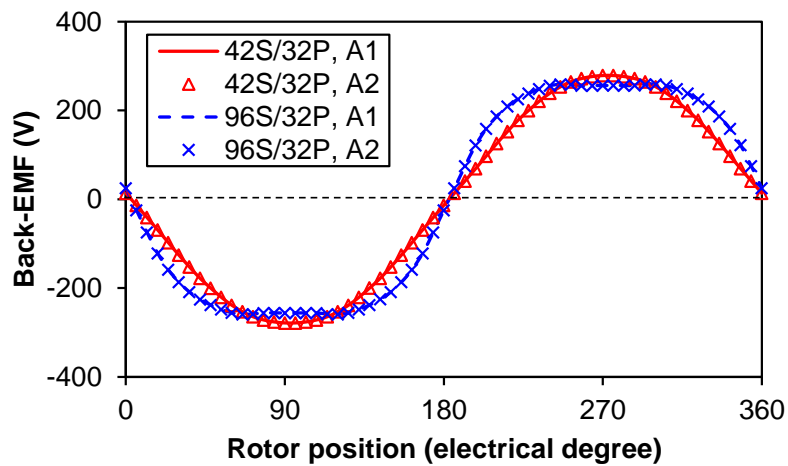
According to the waveforms shown in Fig. 6.4(a), the peak value of two electrical machines due to PM field only is almost the same, which is due to the constraints on machine structures. The distortion of waveforms comes from the stator slotting effect and can be clearly seen in Fig. 6.4(b). Almost the same maximal magnitude is corresponding to the rotor pole pair number, viz. working harmonic. There are abundant harmonics for the 42S/32P modular machine owing to the non-uniformed stator slot distribution. The harmonic orders are:  $|pn \pm N_{sr}v|$ ,  $n=1,3,5,\dots$ ,  $v=0,1,2,\dots$ , where  $p$  is the rotor pole pair number and  $N_{sr}$  is the stator redundant teeth number. The existence of these harmonics will cause local saturation which affects electrical machine performances. In contrast, the harmonic components are fairly low in the 96S/32P modular machine and the orders are:  $|pn \pm N_s v|$ , where  $N_s$  is the stator tooth number. This is the major merit of integer slot winding.

Different from the PM field, the air-gap flux density due to armature field only shows quite large difference between two electrical machines, as shown in Fig. 6.4(c). The waveform of 42S/32P modular machine is far from its working harmonic. The detailed spectra shown in Fig. 6.4(d) can explicitly elaborate the difference. The harmonic orders for this situation are  $t|3k \pm 1|$  and  $t|6k \pm 1|$  ( $k=0,1,2,\dots$ ) for the 42S/32P and 96S/32P modular machines, respectively, where  $t$  is the greatest common divisor of stator slot and rotor pole pair numbers. Comparing Figs. 6.4(b) and (d), it can be seen that the magnitude of working harmonic due to rated armature current is much lower than that from PM field. This means magnetic saturation will not show much

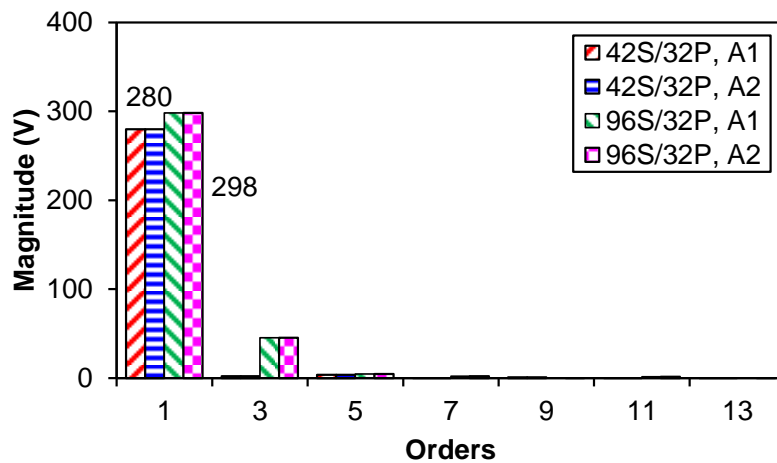
difference under open-circuit and rated conditions. In summary, the 96S/32P modular machine performs better in respect of air-gap flux density harmonics.

### 6.2.2 Open-circuit Performance

Because of the symmetrical distribution of three phases among each set of winding, only phase-A1 and -A2 are chosen as example to show the back-EMFs. The results are plotted in Fig. 6.5.



(a) Waveforms



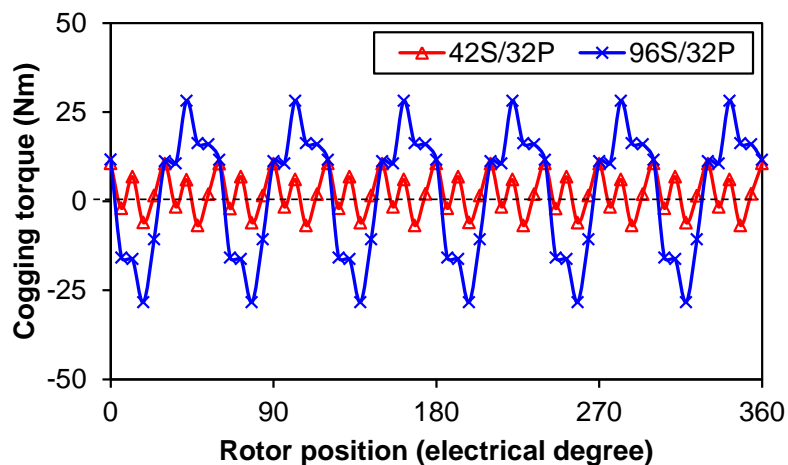
(b) Spectra

Fig. 6.5. Open-circuit phase back-EMFs (170 rpm).

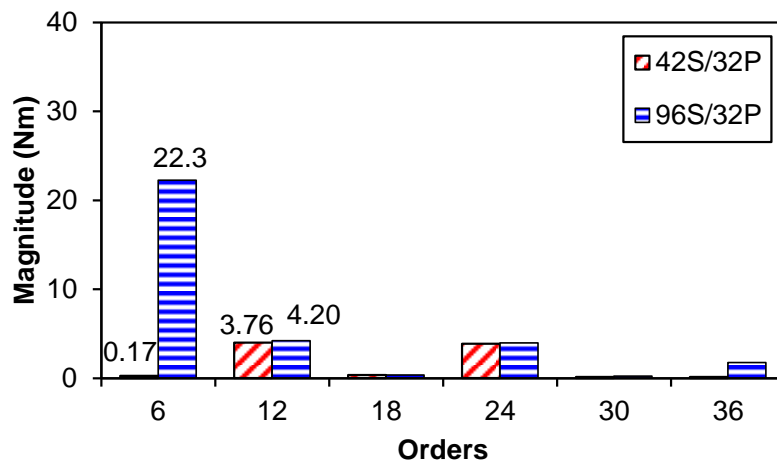
Fig. 6.5(a) shows that the waveforms of phase-A1 and -A2 are exactly the same, which is due to the same winding connection of two set windings and zero phase shift between each other. The difference of waveforms can be found based on the spectra

shown in Fig. 6.5(b). Since both phase-A1 and -A2 have the same harmonic orders and magnitudes, it again verifies the balance between two sets of windings. For torque production aspect, the fundamental component of phase back-EMF is crucial and it can be seen that the proposed 42S/32P modular machine has a lower value. This is the result of winding short-pitched and distribution factor. On the contrary, the winding factor is 1 for the 96S/32P one. Other higher order harmonics also affect electrical machine performance. The large component of the 3<sup>rd</sup> harmonic leads to the trapezoidal shape waveform of phase back-EMF for the 96S/32P modular machine. Furthermore, the larger 5<sup>th</sup> and 7<sup>th</sup> harmonics contribute to the more obvious on-load torque ripple.

When the rotor rotates without current fed into stator winding, there are still torque fluctuations. This torque ripple is cogging torque, as shown in Fig. 6.6.



(a) Waveforms



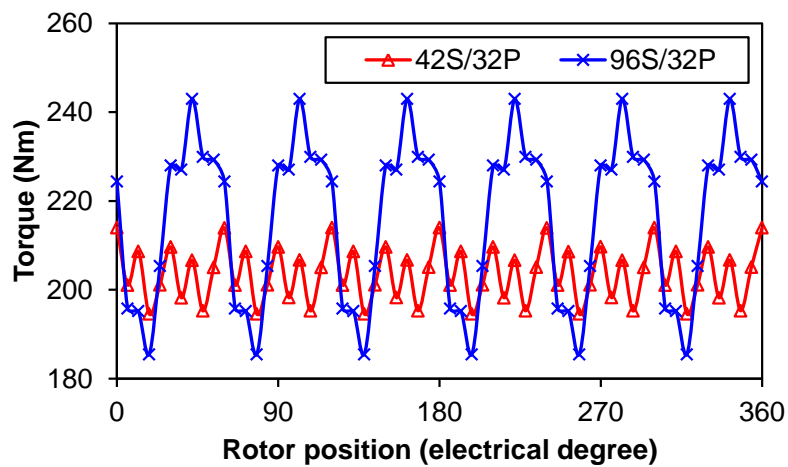
(b) Spectra

Fig. 6.6. Open-circuit cogging torque.

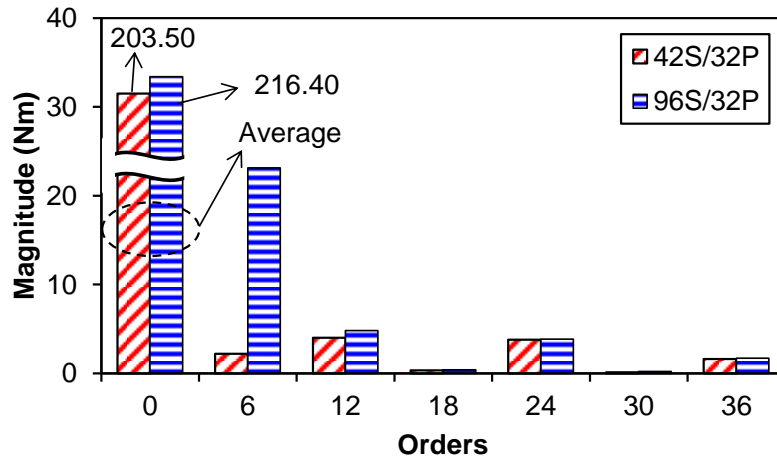
The merit of fractional-slot windings makes the cogging torque of the 42S/32P modular machine much lower than that of the integer slot 96S/32P one. That is why the PMs of the 96S/32P modular machine must be shaped. Based on the spectra shown in Fig 6.6(b), the lowest harmonic orders are all 6 for two electrical machines. The abundant harmonic orders and large magnitudes for the 96S/32P modular machine show the disadvantage of this electrical machine in terms of torque ripple. Although the optimised 42S/32P modular machine has negligible 6<sup>th</sup> cogging torque harmonic, the high order 12<sup>th</sup> and 24<sup>th</sup> harmonics still contribute to torque ripple.

### 6.2.3 On-load Performance

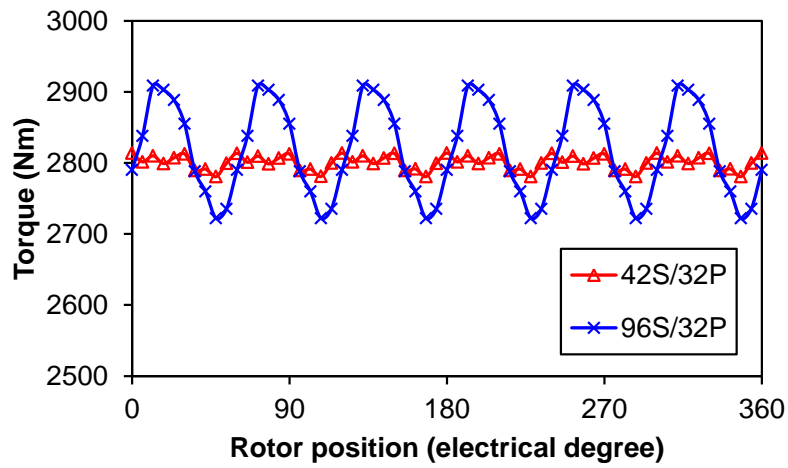
When two sets of winding are fed with current, the average torque is generated. Since the torque performance is related with current value, two situations are considered. One supplies rated current (rated condition), while the other enlarges the current to 15 times of its rated value (overload condition). The instantaneous torques of two situations are given in Fig. 6.7.



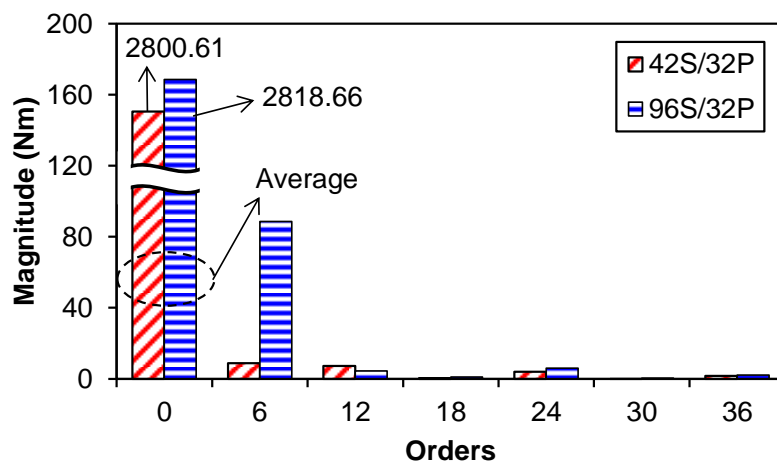
(a) Waveforms under rated condition



(b) Spectra under rated condition



(c) Waveforms under overload condition



(d) Spectra under overload condition

Fig. 6.7. On-load torque.



By comparing torque waveforms shown in Fig. 6.7(a), it can be found that the 96S/32P modular machine has a bit larger average torque with rated current. This is due to the larger fundamental phase back-EMF. As has been stated, the armature field is much weaker than PM field; therefore the torque fluctuations under rated condition is similar to the cogging torque shown in Fig. 6.6(a). Fig. 6.7(b) shows that the torque ripple is still lower for the 42S/32P modular machine, since the 6<sup>th</sup> harmonic torque is lower. This is due to the lower cogging torque by optimising the tooth width of redundant teeth. When the electrical machine runs under overload condition, the torque waveforms show quite different phenomenon, as shown in Fig. 6.7(c). The average torques of two electrical machines are practically the same, while the peak to peak (PP) torque ripple of the 96S/32P modular machine is much larger than that of the 42S/32P one. Fig. 6.7(d) exhibits that the 6<sup>th</sup> harmonic component of torque obviously increases for the integer slot machine, which is the major reason for such higher torque fluctuation. For the sake of clarity, some torque characteristic values under normal operation are listed in TABLE 6.2.

TABLE 6.2 TORQUE CHARACTERISTIC VALUES

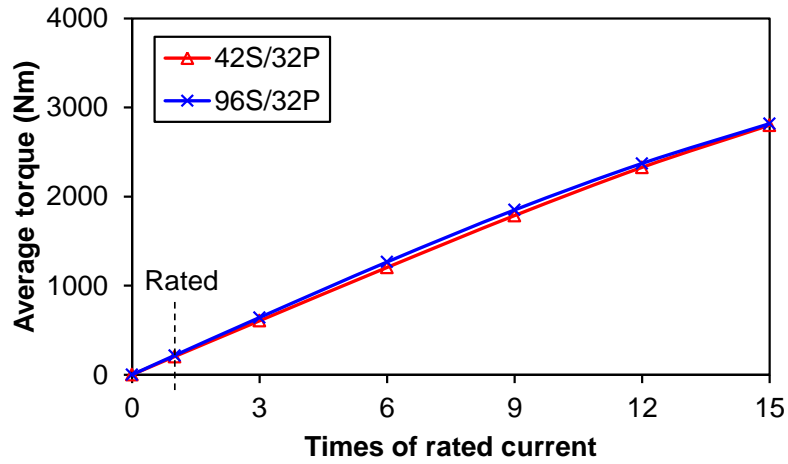
$N_s/N_p$	Load condition	Average torque (Nm)			PP torque ripple (Nm)		
		N <sup>a</sup>	OC <sup>b</sup>	SC <sup>c</sup>	N	OC	SC
42S/32P	Open	0	0	-473.70	17.45	17.45	41.75
	Rated	203.58	102.91	-372.84	19.44	18.10	41.82
	Overload	2800.71	1404.33	927.99	33.18	26.76	43.91
96S/32P	Open	0	0	-598.62	56.56	56.56	350.21
	Rated	216.45	109.42	-481.27	57.50	57.16	365.97
	Overload	2818.39	1389.41	898.99	186.85	90.02	654.75

<sup>a</sup> normal operation.

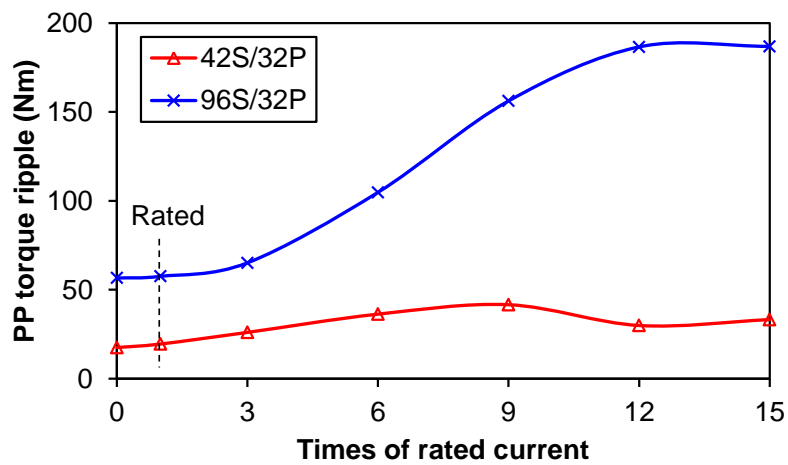
<sup>b</sup> open-circuit for one set of winding.

<sup>c</sup> short-circuit for one set of winding.

The complete variations of average torque and PP torque ripple with current are given in Fig. 6.8. With the increase of current, the difference of average torque between two electrical machines is increasingly small due to lower saturation level for the 42S/32P modular machine, as shown in Fig. 6.8(a). Besides, Fig. 6.8(b) demonstrates that the higher saturation will cause the faster increase of PP torque ripple for the 96S/32P modular machine, whereas the PP torque ripple of the 42S/32P modular machine is much smaller. In terms of torque performance, the modular machines with non-overlapping windings perform better.



(a) Average torque



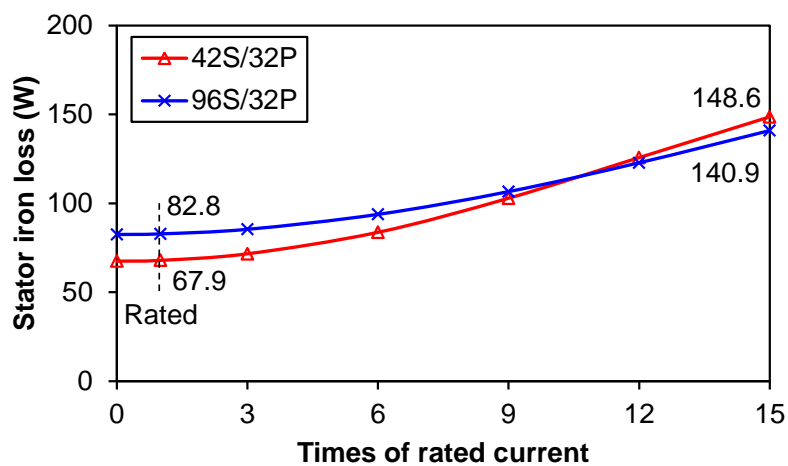
(b) PP torque ripple

Fig. 6.8. Influence of current on torque performances.

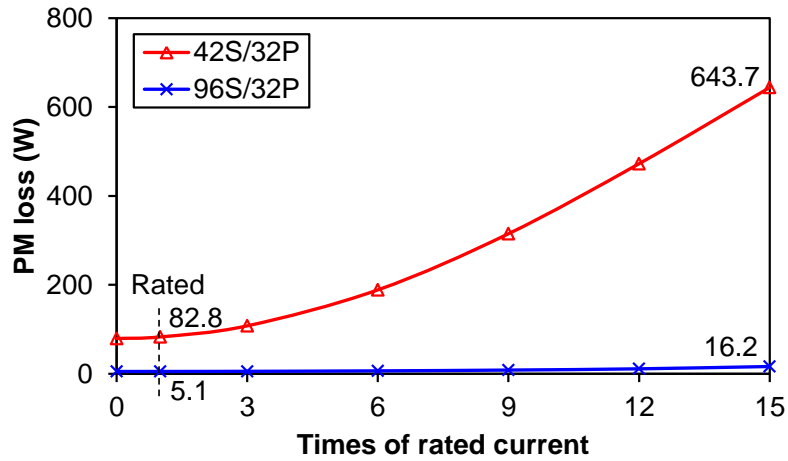
#### 6.2.4 Iron Losses

The variation of three major components of iron losses (stator iron loss, PM eddy current loss and rotor yoke eddy current loss) with current is shown in Fig. 6.9. Fig. 6.9(a) shows that the 96S/32P modular machine has larger stator iron loss when the current is low since the thinner stator teeth will make the stator core more saturated compared with the 42S/32P modular machine. However, the increase of stator iron loss is slower for the 96S/32P modular machine and the two electrical machines will have the same value for a specific current. If the current further increases, the stator iron loss of the 42S/32P modular machine will exceed that of the 96S/32P one. This is due to the existence of abundant harmonics, since the influence of harmonics on machine saturation will become more and more obvious with the increase of current. For PM and rotor yoke eddy current losses, Figs. 6.9(b) and (c) show that the 96S/32P

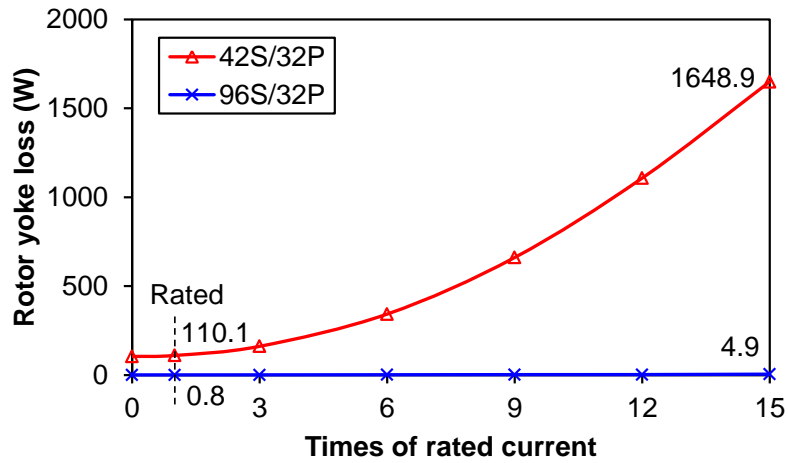
modular machine has practically negligible losses compared with the 42S/32P one. The reason for such huge difference is the difference of harmonics. No matter the electrical machine operates under open-circuit or overload condition, the harmonic components are much lower for the 96S/32P modular machine, as shown in Fig. 6.4. When the current is low, the slotting effect is the major cause of harmonics. According to Fig. 6.4(b), those harmonics have relatively small magnitudes compared with the working harmonic. In contrast, the harmonics shown in Fig. 6.4(d) have much larger magnitudes compared with the working harmonic for rated armature current field. With the increase of current, the influence of these harmonics coming from armature reaction will lead to much faster increase of both PM and rotor yoke eddy current losses. Since the PMs are isolated between each other, some harmonics are prevented from inducing eddy current in PMs, whereas the complete solid rotor yoke will generate much larger eddy current. For the 96S/32P modular machine, the rotor yoke eddy current loss is lower than PM eddy current loss, especially for high current value. Since the major contributions of these two losses are higher order harmonics in this electrical machine. It will be harder for these higher order harmonics to penetrate into the rotor yoke, which means the rotor yoke eddy current loss will be lower. From this point of view, the 96S/32P modular machine performs better.



(a) Stator iron loss



(b) PM eddy current loss

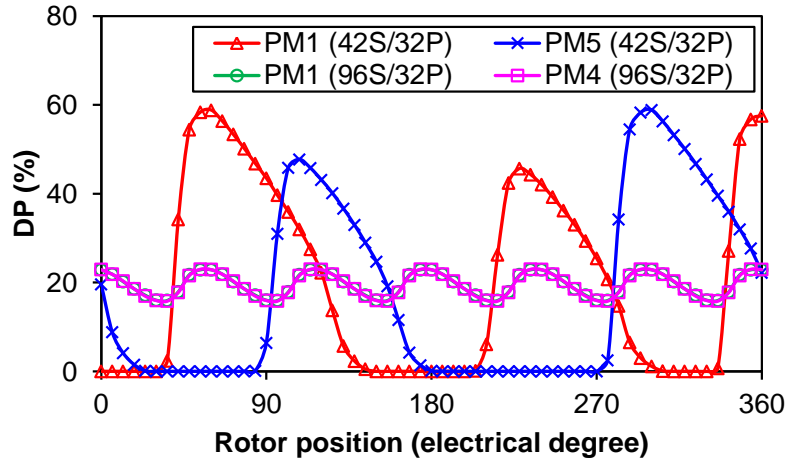


(c) Rotor yoke eddy current loss

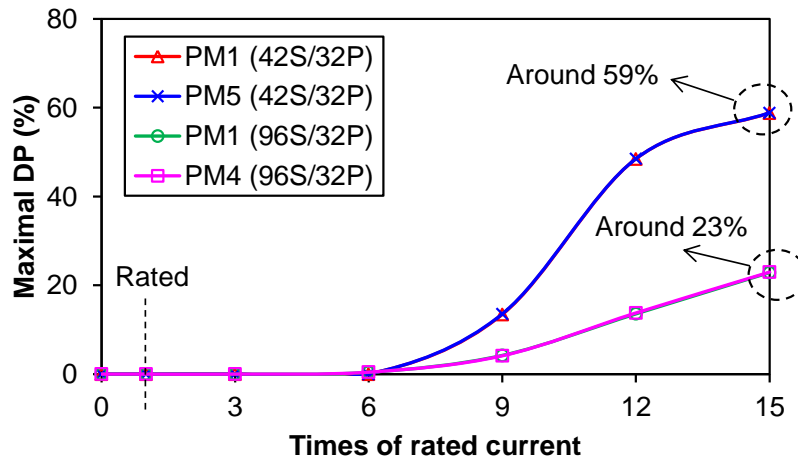
Fig. 6.9. Influence of current on iron losses (170 rpm).

### 6.2.5 Demagnetisation

As has been mentioned in the previous chapters, the first and the last PM of segment 1 can be used as the representatives to show the irreversible demagnetisation of modular machines. PMs 1 and 5 are the first and the last PM of segment 1 for the 42S/32P modular machine, while PMs 1 and 4 are corresponding to the 96S/32P one. The DP variations over one electrical period are shown in Fig. 6.10, together with the influence of current. It must be emphasised that the results of overload condition are used for the sake of clearly showing the difference.



(a) DP variations with the rotor position under overload condition



(b) Influence of current on maximal DP

Fig. 6.10. Demagnetisation of the first and the last PM of segment 1.

Fig. 6.10(a) shows that both PMs of the 96S/32P modular machine experience the same irreversible demagnetisation process. Since the working harmonic is dominant, there is an average DP during the operation. The fluctuation of DP comes from the variation of relative positions between PMs and stator teeth. Since each phase achieves its absolute value twice per electrical period, there are six ripples in total. However, the variation of DP is more complex for the 42S/32P modular machine. Due to the abundant harmonics, the fluctuations of DP are more obvious and the maximal DPs are higher. Both PMs have two peak DPs within this period, whereas the peak values are different, which is due to local saturation caused by lower order harmonics. Although each PM will achieve the same maximal DP, the distance between adjacent peak DPs are different. For PM 1, it will always moves in segment 1

within this period. Two peak values are 150 degrees shifted between each other, viz. slot pitch. For PM 5, it will pass through the redundant tooth during this period; and therefore the two peak values have another 60 degree phase shift. In fact, all of the PMs will alternately experience the same irreversible demagnetisation process in this fractional-slot machine over one mechanical revolution. Overall, the integer slot modular machine has better irreversible demagnetisation withstand capability under normal operation.

### 6.3 Performance Comparison with One Set of Winding Operation

Sometimes, the electrical machines run with only one set of winding. Under such condition, the armature field distribution will be quite different from that under normal operation. Similar to normal operation, the field distribution of armature field corresponding to one set of winding fed with rated current is shown in Fig. 6.11.

Fig. 6.11 shows that the minimal repetition units of the 42S/32P and 96S/32P modular machines are reduced from 2 and 16 to 1 and 4, respectively. This comes from the lack of the other set of winding and can be easily seen from winding topologies shown in Fig. 6.1.

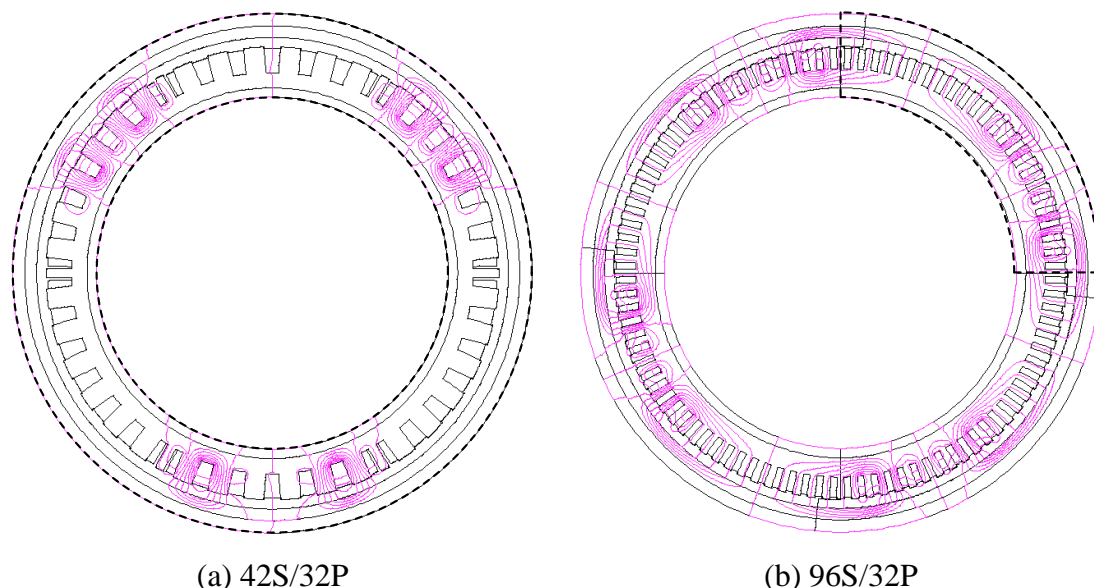
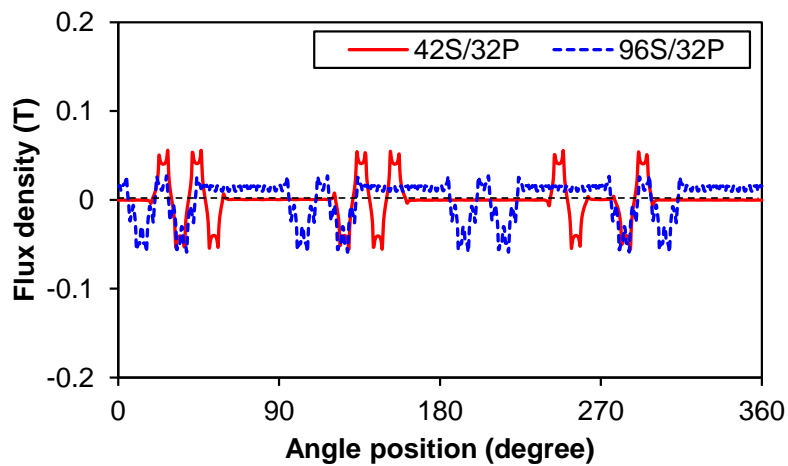
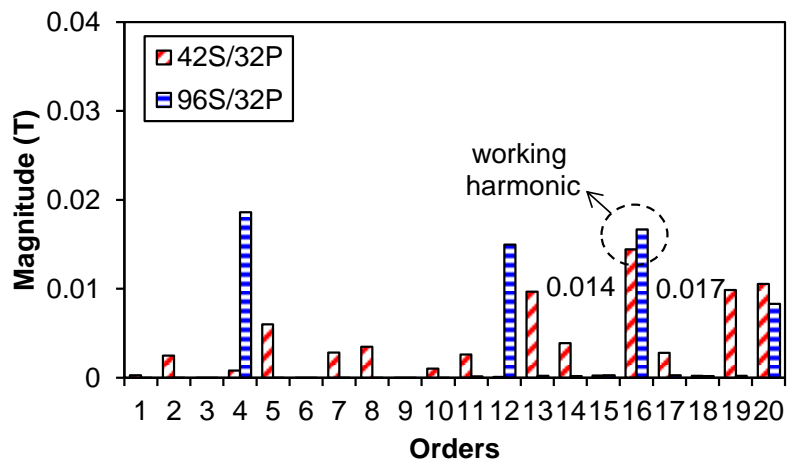


Fig. 6.11. Field distributions for armature field with only (Only one set of winding fed with rated current).

The air-gap flux density under such circumstance is plotted in Fig. 6.12. Comparing with the normal operation, the waveforms of air-gap flux density is more heavily distorted, especially for the 96S/32P modular machine, as shown in Fig. 6.12(a). For the spectra shown in Fig. 6.12(b), it demonstrates that there are other order harmonics appearing, while some new harmonics even have larger amplitude than the working harmonic in the 96S/32P modular machine. Thus, the performance should be evidently affected. Although the magnitudes of harmonics are not comparable to the working one for the 42S/32P modular machine, the existence of such abundant components will result in other side effect, such as unbalanced magnetic force.



(a) Waveforms

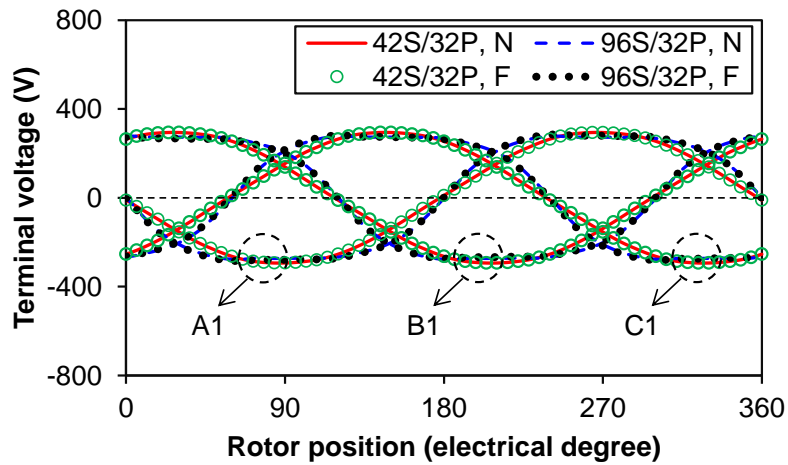


(b) Spectra

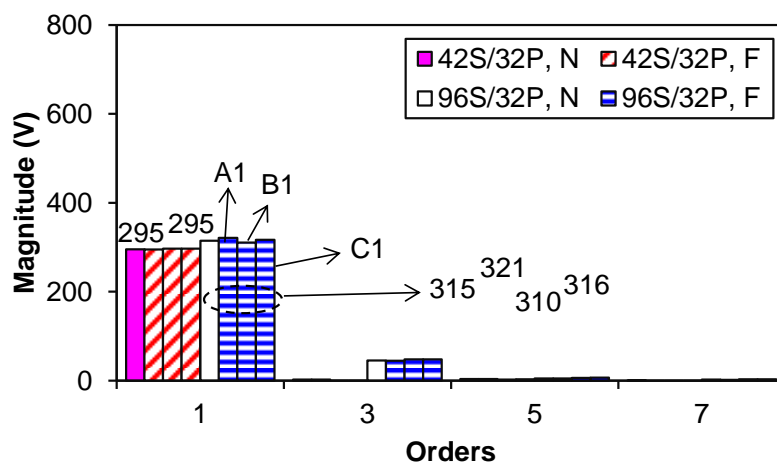
Fig. 6.12. Air-gap flux density for armature field only (Only one set of winding fed with rated current).

### 6.3.1 One Set of Winding Open-circuit

When the second set of winding is open-circuit, the terminal voltages of the first set of winding will show different phenomena for two machines. Since the current value still affects the armature field, both results with rated and overload current (15 times of rated value) are shown in Fig. 6.13.

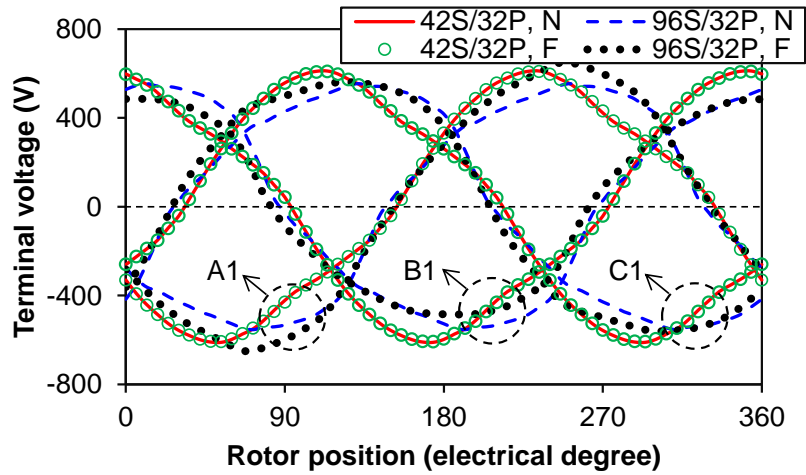


(a) Waveforms with rated current

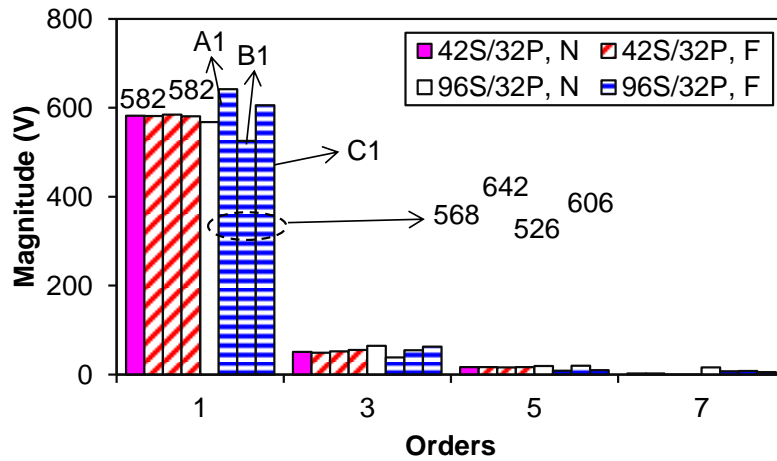


(b) Spectra with rated current





(c) Waveforms with overload current



(d) Spectra with overload current

Fig. 6.13. Terminal voltages of the first set of winding (170 rpm).

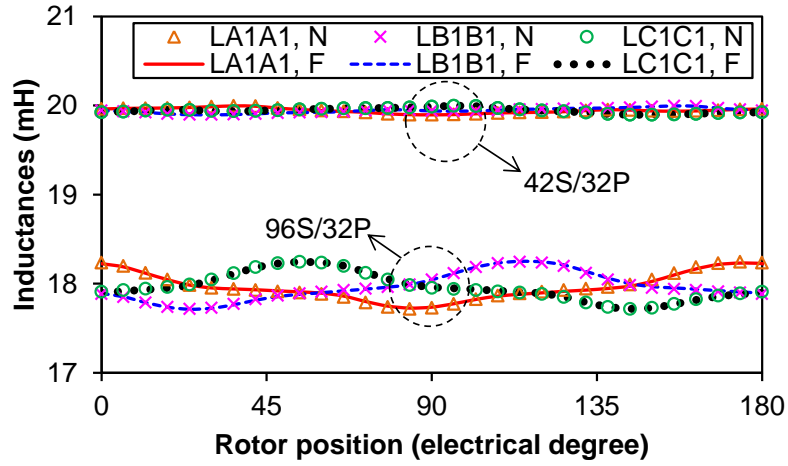
Due to the relative weak armature field for only one set of winding fed with rated current, the terminal voltages are practically unchanged compared with the open-circuit back-EMFs shown in Fig. 6.5. For the proposed 42S/32P modular machine, voltages of three phases keep symmetrical in space with 120 phase shift between each other. However, some differences can be observed for the 96S/32P modular machine according to Fig. 6.13(b). The magnitudes of voltages have different values although the difference is not very obvious. This can be explained by the winding configuration shown in Fig. 6.1. For the 42S/32P modular machine, the space arrangement of each phase is still symmetrical for only one set of winding operation and vice versa for the 96S/32P one. Due to the asymmetry in the 96S/32P modular machine, the magnitudes of some phases will exceed the values corresponding to normal operation. The results

shown in Figs. 6.13(c) and (d) can more clearly verify the statement above. Because of the overload current, the magnetic circuit becomes more saturated and the higher order harmonics appear in phase voltage. The terminal voltage waveforms of the 42S/32P modular machine with overload current fed into the first set of winding become flatter than those with rated current. Nevertheless, three phases are still symmetrical. In contrast, the voltage asymmetry becomes clear for the 96S/32P modular machine. Two phases have much larger fundamental components compared with the value under normal operation. For the sake of clearer, the terminal voltage expressions are:

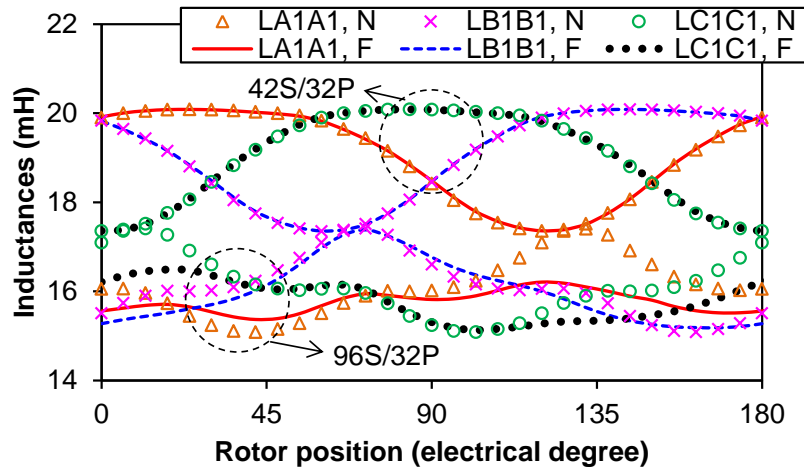
$$v_i = R_{ph}i_i + \frac{d\psi_i}{dt} = R_{ph}i_i + \frac{d}{dt}(\psi_{PMi} + \sum_j L_{ij}i_j) \quad i, j = A1, B1, C1, A2, B2, C2 \quad (6.1)$$

where  $v_i$ ,  $i_i$  and  $i_j$  are the terminal voltage and current of phases  $i$  and  $j$ , respectively.  $R_{ph}$  is the phase resistance;  $\psi_i$  and  $\psi_{PMi}$  are the phase flux-linkage and its PM portion.  $L_{ij}$  is the inductance between two phases and it is self- and mutual inductances for  $i=j$  and  $i \neq j$  situation, respectively.

According to (6.1), the terminal voltage contributed by resistance voltage drop is symmetrical for three phases and the second set of windings does not generate induced voltage due to open-circuit. It is PM flux-linkage component and the inductances of the first set of winding that lead to such unbalance. The self-inductances are used as example to explain the asymmetric phenomenon, as shown in Figs. 6.14(a) and (b) for results predicted with rated and overload currents. The frozen permeability method (Appendix B) is used to take the load condition into account [UGA08]. The characters 'N' and 'F' in legends represent the value under normal and faulty operations, respectively. The average value reduces with the increase of current due to the saturation. It is clear that the self-inductances are almost the same for the 42S/32P modular machine no matter the electrical machine runs under normal or faulty operation. Although the fluctuations become more obvious with overload current, the self-inductances of three phases are still symmetrical. On the contrary, the self-inductances of the 96S/32P modular machine are far from their value corresponding to normal operation, which is owing to the asymmetric magnetic circuit under faulty operation. Such distortion is aggravated with the increase of current, since the asymmetric armature field is increasingly strong.



(a) Rated current



(b) Overload current

Fig. 6.14. Self-inductances of the first set of winding.

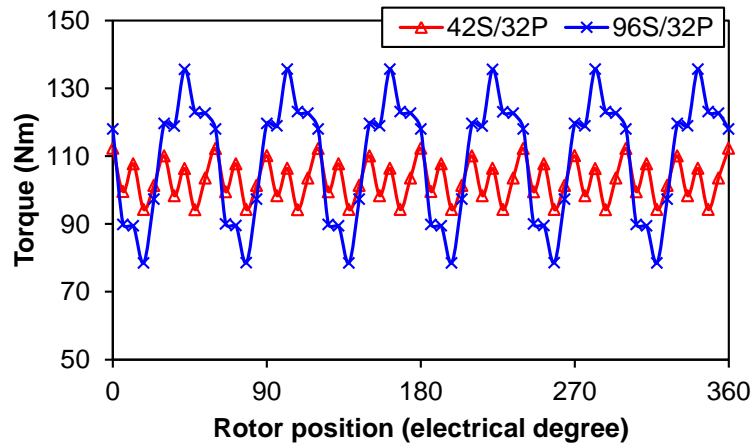
TABLE 6.3 lists average inductances related to phase-A1 for the sake of clarity.

TABLE 6.3 AVERAGE INDUCTANCES RELATED TO PHASE-A1

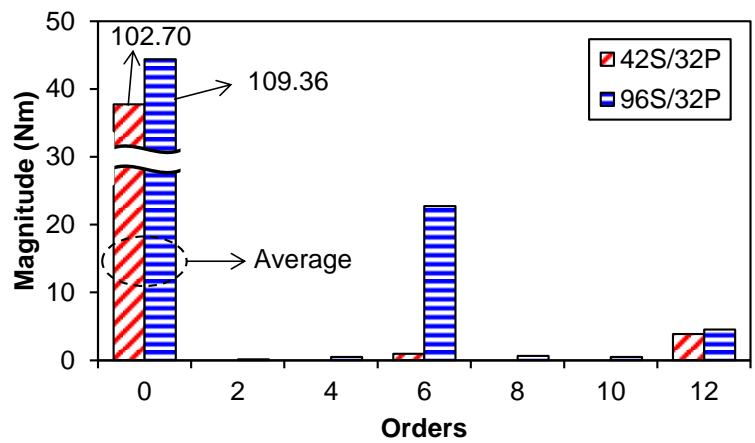
$N_s/N_p$	Load condition	Inductances (mH)					
		$L_{a1a1}$	$L_{b1a1}$	$L_{c1a1}$	$L_{a2a1}$	$L_{b2a1}$	$L_{c2a1}$
42S/32P	Rated	<b>19.94</b> (19.94) <sup>a</sup>	-0.67 (-0.67)	-0.67 (-0.67)	<b>0.0059</b> (0.0059)	0.0018 (0.0019)	0.0018 (0.0018)
	Overload	<b>19.01</b> (19.02)	-0.61 (-0.61)	-0.61 (-0.61)	<b>-0.0032</b> (0.0129)	0.0049 (0.0048)	0.0051 (0.0004)
96S/32P	Rated	<b>17.97</b> (17.96)	0.92 (0.92)	-5.45 (5.45)	<b>-3.16</b> (-3.16)	-3.21 (-3.19)	3.17 (3.16)
	Overload	<b>16.10</b> (15.76)	0.64 (0.43)	-5.56 (-5.22)	<b>-3.06</b> (-2.83)	-3.18 (-2.73)	3.07 (2.76)

<sup>a</sup> value in parenthesis corresponding to faulty operation.

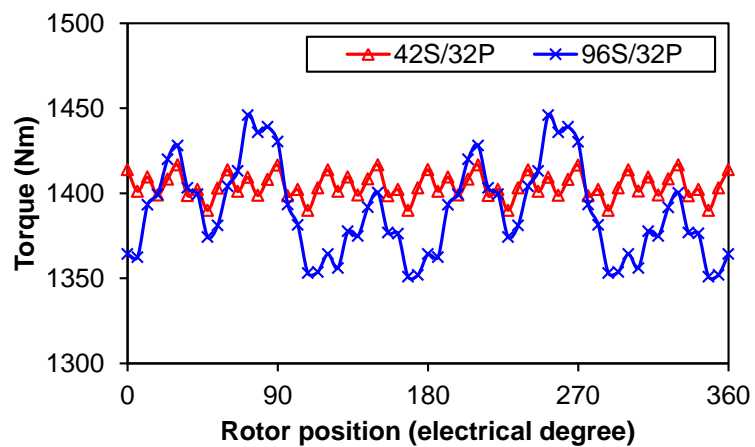
Similar to two sets of winding operation shown above, the instantaneous torque with only one set of winding operation and the other set of winding open-circuit are shown in Fig. 6.15.



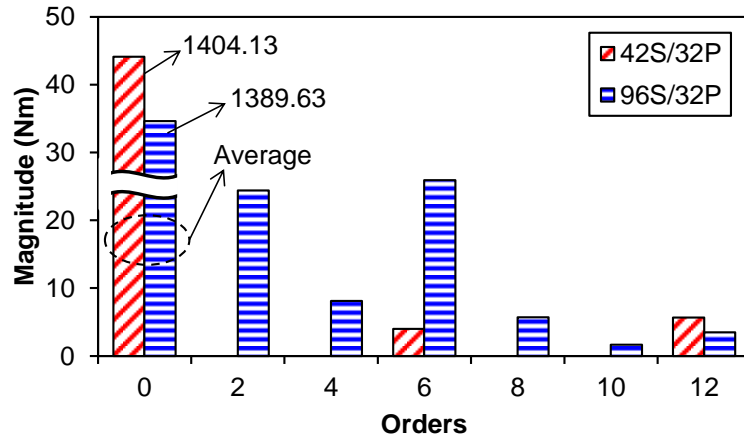
(a) Waveforms with rated current



(b) Spectra with rated current



(c) Waveforms with overload current



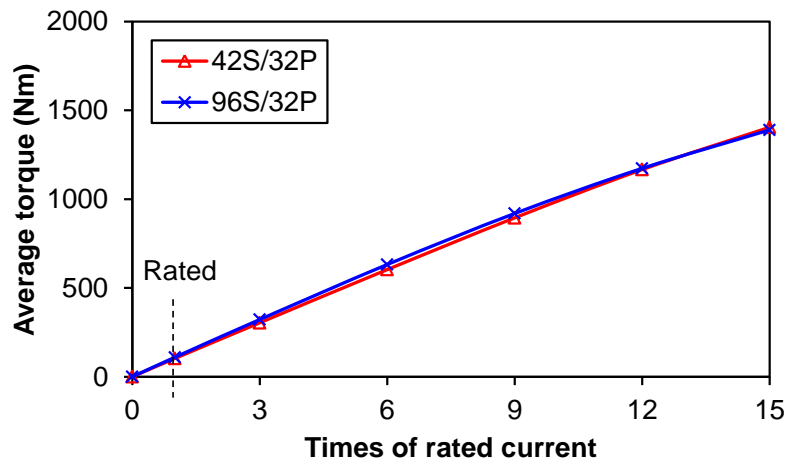
(d) Spectra with overload current

Fig. 6.15. On-load torque with one set of winding operation and the other set of winding open-circuit.

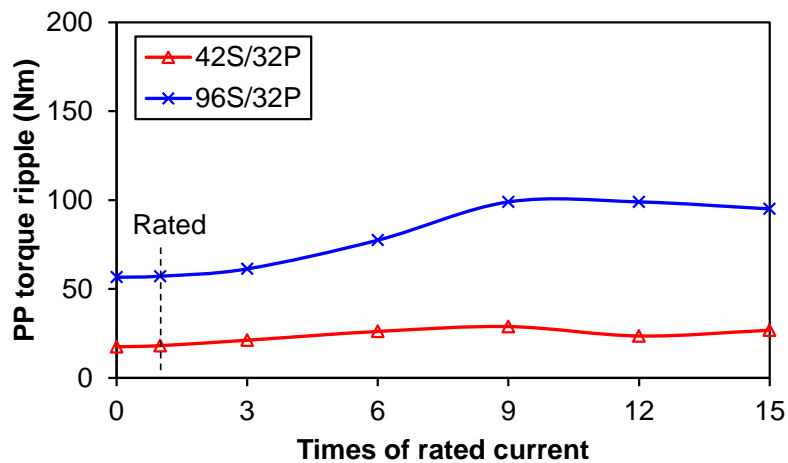
Comparing the results in Figs. 6.15 and 6.7, it can be seen that the average torque generated by only one set of winding is almost half of rated value no matter the rated or overload current is supplied. Similar to normal operation, the torque fluctuations are hardly changed with rated current fed into one set of winding, while huge difference can be seen if the overload current is fed. This is due to the variation of winding layout from dual 3-phase to single 3-phase type, which introduces more air-gap harmonics and the asymmetric magnetic circuit for the 96S/32P modular machine. The minimal torque harmonic order is still 6 for the 42S/32P modular machine because of the symmetrical three phases and it reduces to 2 for the 96S/32P one. According to the characteristic torque values listed in TABLE 6.3, it is clear that not only average torque but PP torque ripple reduces as well. However, the PP torque ripple of the 96S/32P modular machine is always much larger.

The influence of current on torque performance with one set of winding open-circuit fault is shown in Fig. 6.16. The average torque difference between two electrical machines is negligible, similar to those in Fig. 6.8. More specifically speaking, the 96S/32P modular machine becomes a bit easily saturated due to the local saturation caused by the new appeared harmonics. PP torque ripple is increasingly large within specific current value. When the current is larger than that specific value, the high saturation will lead to the phase variation of torque components. This could alleviate the fast increase of PP torque ripple. Overall the

torque performance of the proposed 42S/32P modular machine is better under this kind of faulty operation.



(a) Average torque

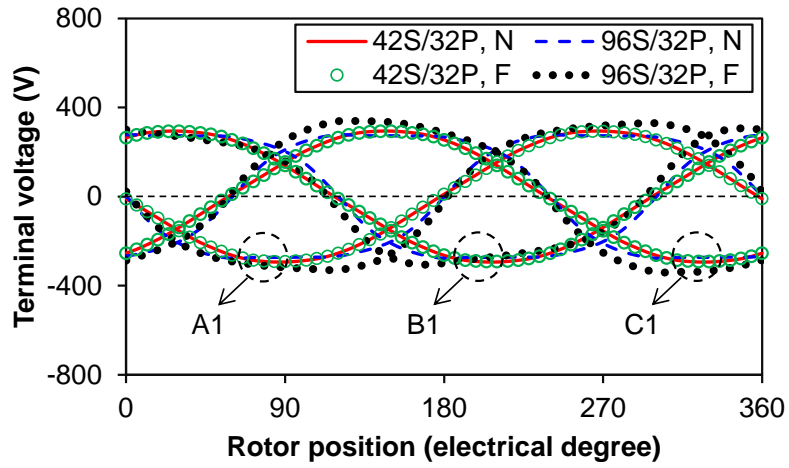


(b) PP torque ripple

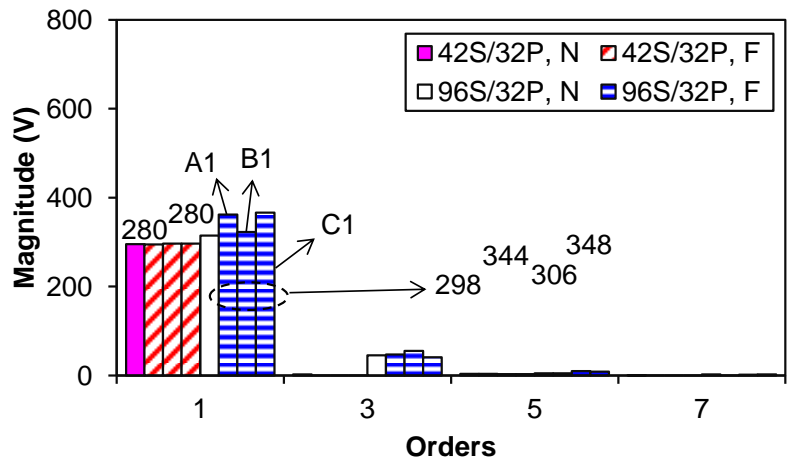
Fig. 6.16. Influence of current on torque performances with one set of winding open-circuit fault.

### 6.3.2 One Set of Winding Short-circuit

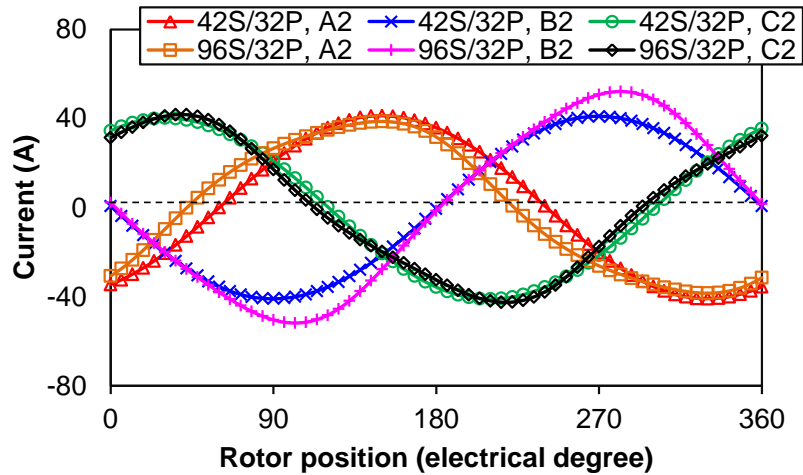
When the second set of winding is 3-phase symmetrical short-circuit, there will be short-circuit currents being generated when the electrical machine rotates. These short-circuit will affect the terminal voltages of the first set of winding by mutual inductances between two sets of windings. The three phase terminal voltages of the first set of winding and the short-circuit currents of the second set of winding are shown in Fig. 6.17, where the rated current is supplied in the first set of winding.



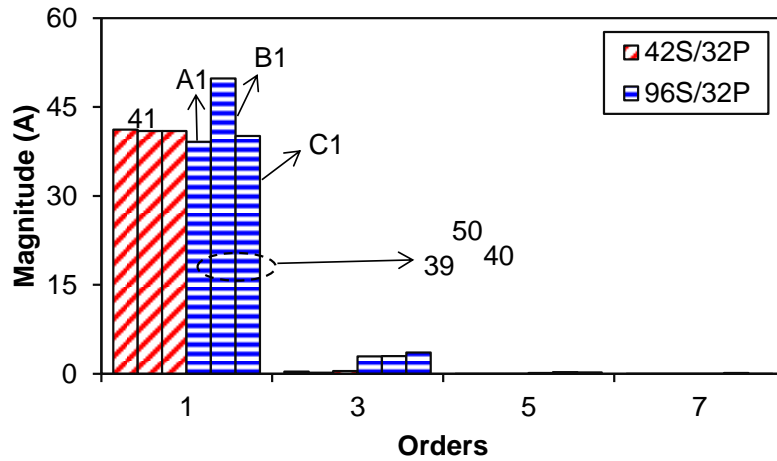
(a) Voltage waveforms



(b) Voltage spectra



(c) Current waveforms

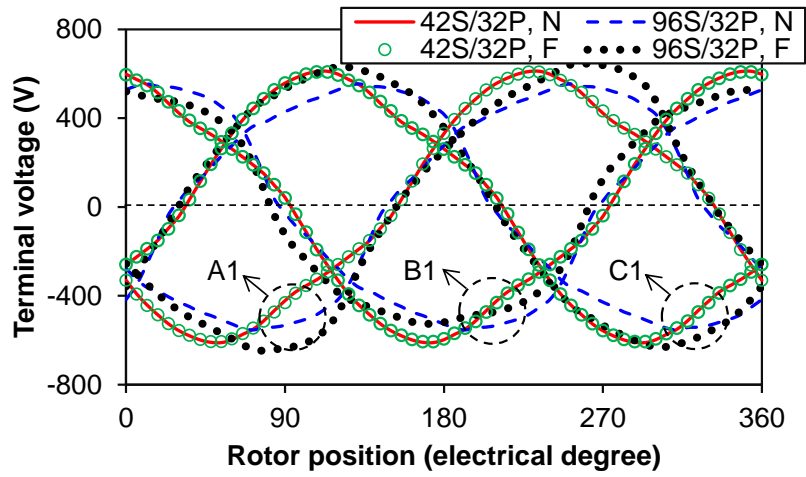


(d) Current spectra

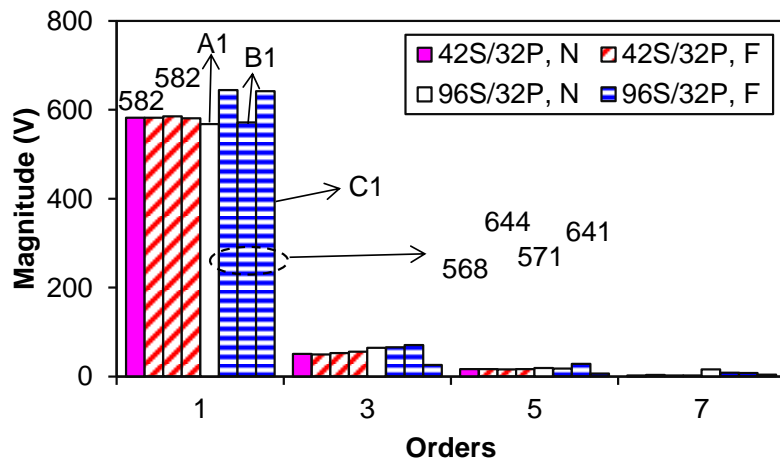
Fig. 6.17. Terminal voltage for the first set of winding with rated current and short-circuit current for the second set of winding (170 rpm).

Different from the open-circuit faulty operation, the terminal voltage waveform differences among three phases are apparent in the 96S/32P modular machine, as shown in Fig. 6.17(a). The corresponding spectra in Fig. 6.17(b) verify this phenomenon. According to (6.1), the short-circuit currents in the second set of winding will affect the terminal voltages of the first set of winding under such condition. Since both short-circuit currents and the mutual inductances between two sets of windings are all relative large, the asymmetric voltages can be seen. Besides, the short-circuit current is evidently asymmetric as well. For the 42S/32P modular machine, the short-circuit fault of the second set of winding still has negligible influence on terminal voltages of the normal operation set of winding. The symmetrical magnetic circuit for one set of winding operation and the negligible mutual inductances contribute to such results. When the overload current fed into the first set of winding, the corresponding results are shown in Fig. 6.18.

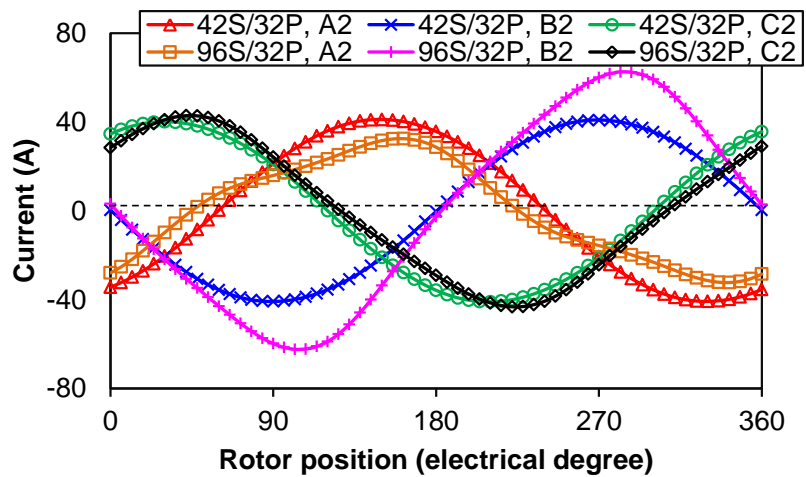




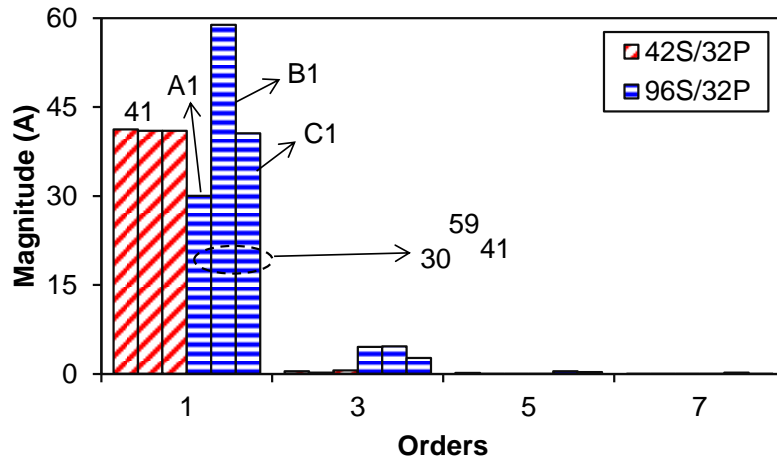
(a) Voltage waveforms



(b) Voltage spectra



(c) Current waveforms

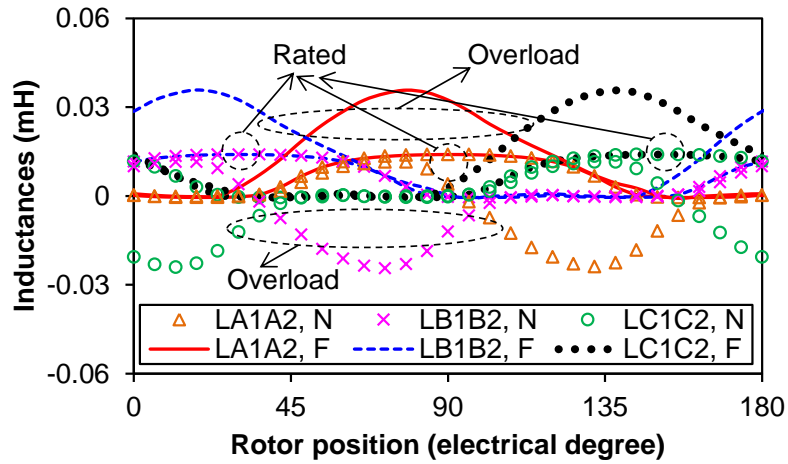


(d) Current spectra

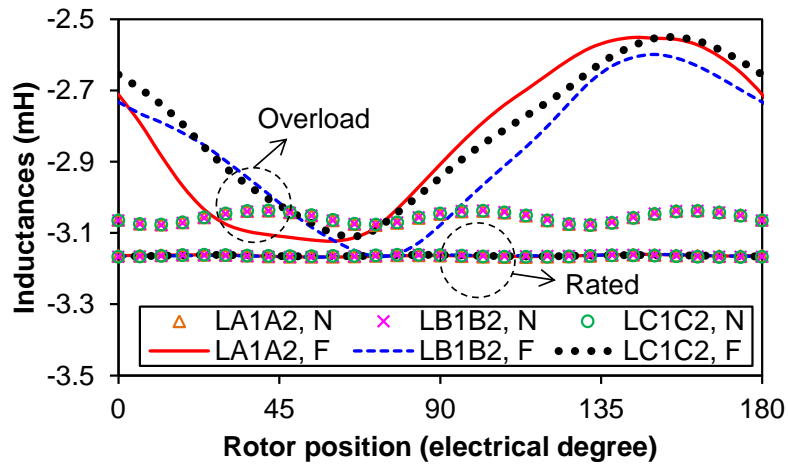
Fig. 6.18. Terminal voltage for the first set of winding with overload current and short-circuit current for the second set of winding (170 rpm).

Although the fundamental component of terminal voltage increases, the influence of short-circuit currents can still be ignored in the 42S/32P modular machine. The appearance of the 3<sup>rd</sup> harmonic is the consequence of saturation caused by higher current. The small mutual inductances make the short-circuit current hardly changed as well. When it comes to the 96S/32P modular machine, the differences among three phases become increasingly large for higher current. Some terminal voltages show larger peak value compared with the normal operation. The relative large mutual inductances will lead to larger short-circuit currents in the second set of winding as well. The three representative mutual inductances between two sets of windings ( $L_{A1A2}$ ,  $L_{B1B2}$  and  $L_{C1C2}$ ) are shown in Fig. 6.19.

The influence of current on mutual inductances can be clearly seen in both electrical machines, whereas three mutual inductances are still symmetrical for the 42S/32P modular machine. The small variation of average value hardly affects the terminal voltages of the first set of winding even if the short-circuit current is large in the second set of winding. The three mutual inductances of the 96S/32P modular machine are evidently changed. The fluctuation is more obvious and they will not coincide with each other anymore, which is different from the normal operation situation.



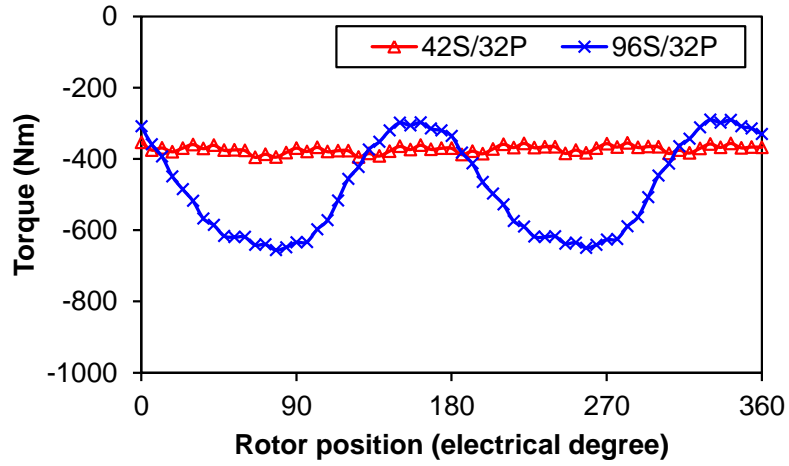
(a) 42S/32P



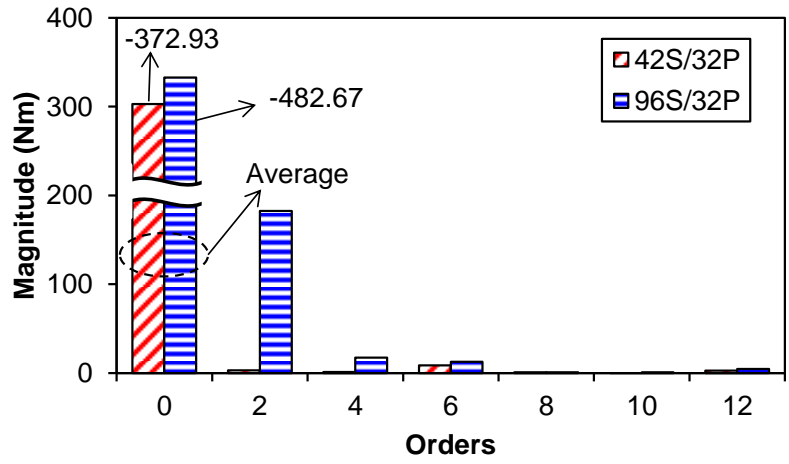
(b) 96S/32P

Fig. 6.19. Representative mutual inductances between two sets of windings.

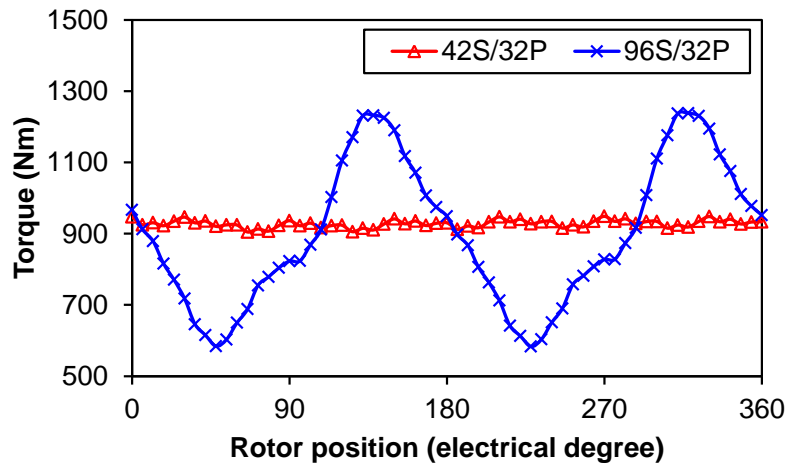
The torque results with rated and overload current fed into the first set of winding are shown in Fig. 6.20. When the rated current is supplied, the larger short-circuit current produces higher braking torque, as shown in Figs. 6.20(a) and (b). Since the short-circuit current of the 96S/32P modular machine is larger, the braking torque is also larger. Because of the asymmetric magnetic circuit in this electrical machine, the torque ripple is extremely huge and the torque fluctuation period reduced to 2. In contrast, the 42S/32P modular machine performs much better. A lower average braking torque and the much lower torque ripple can be seen. For the results corresponding to overload current situation, the effective output torque is generated. The fluctuation is still much more obvious for the 96S/32P modular machine, as shown in Figs. 6.20(c) and (d).



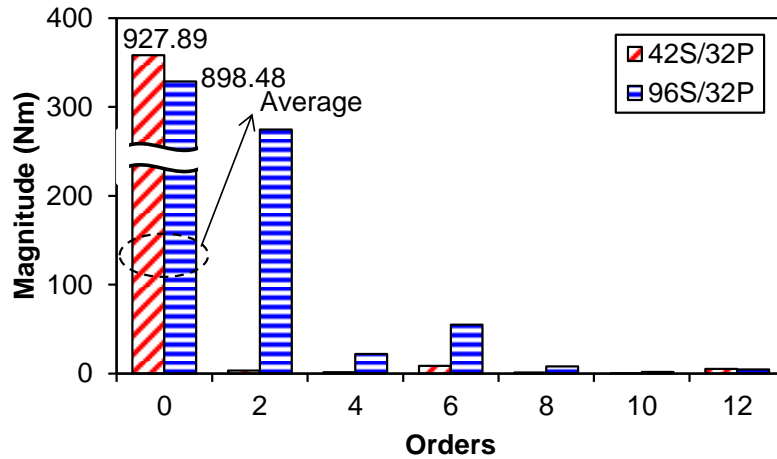
(a) Waveforms with rated current



(b) Spectra with rated current



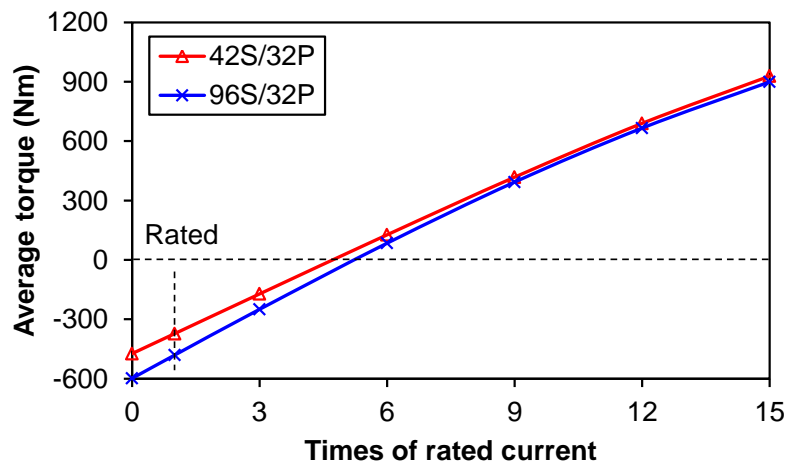
(c) Waveforms with overload current



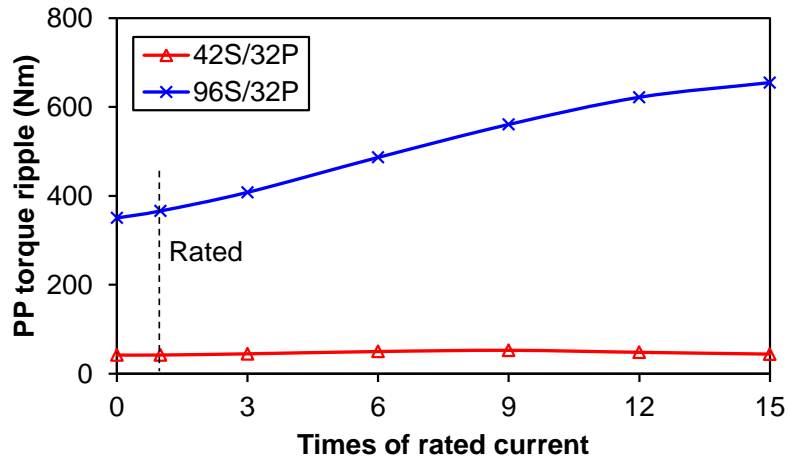
(d) Spectra with overload current

Fig. 6.20. On-load torque with one set of winding.

The average and PP torque ripple-current characteristics are shown in Fig. 6.21. It can be seen that the average torque differences between two electrical machines becomes increasingly small, which is due to the larger winding factor for the working harmonic in the 96S/32P modular machine. Furthermore, the short-circuit currents of the second set of winding alleviates the fast increase of saturation. For PP torque ripple, it will always increase with the current under such faulty operation in the 96S/32P modular machine and it is larger than 10 times than the value in the 42S/32P one.



(a) Average torque

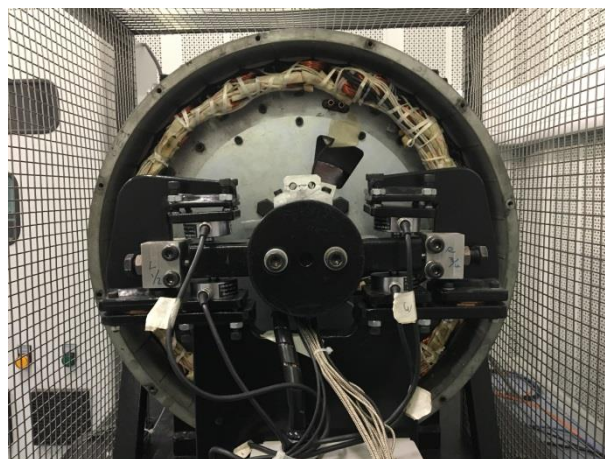


(b) PP torque ripple

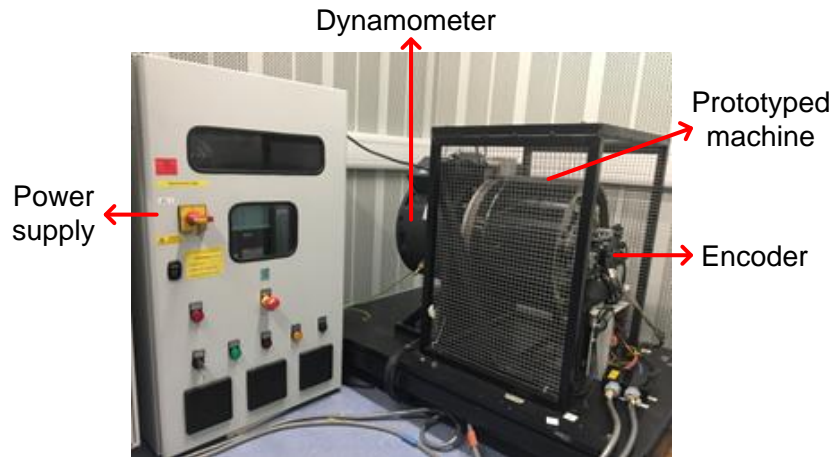
Fig. 6.21. Influence of current on torque performances with one set of winding short-circuit fault.

#### 6.4 Experimental Validation

A dual 3-phase 96S/32P modular machine with overlapping winding is prototyped with some small modifications in dimensions, where the maximum PM thickness is 4.5mm and the rotor yoke thickness increases to 11.5mm. The prototyped machine and the test rig are shown in Fig. 6.22. Although this prototype machine can be made with segmented stators, this is not done in real manufacture for easing mechanical assembly. The non-segmented stator will eliminate the influence of additional air-gaps on electromagnetic performance, which can be seen on cogging torque test result.



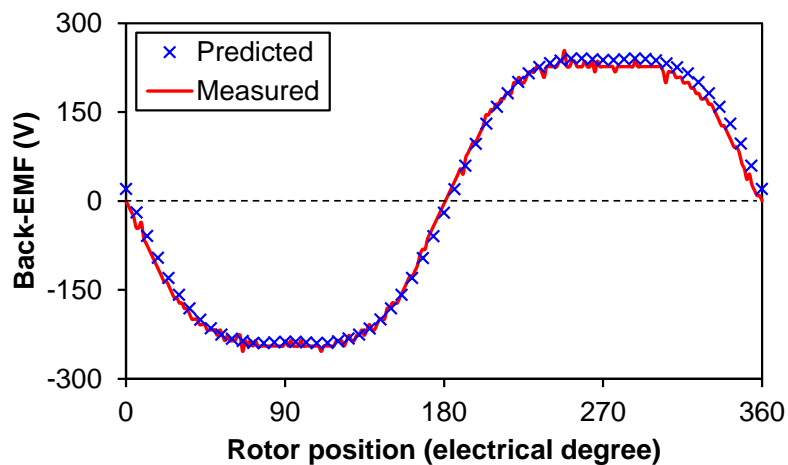
(a) Prototyped machine



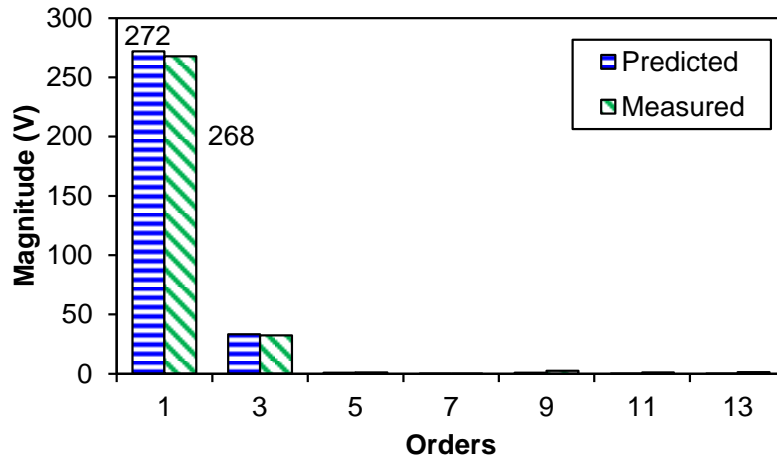
(b) Test rig

Fig. 6.22. Experiment rig.

The open-circuit back-EMF of phase-A1 is measured first of all and the result is compared with the finite element (FE) predicted ones, as shown in Fig. 6.23. The predicted and measured waveforms of the 96S/32P machine overall match well, although there are some glitches for the measured result due to sample errors. The fundamental component of phase back-EMF is a bit lower for the measured result shown in Fig. 6.23(b) could be owing to the end effect or measure error.



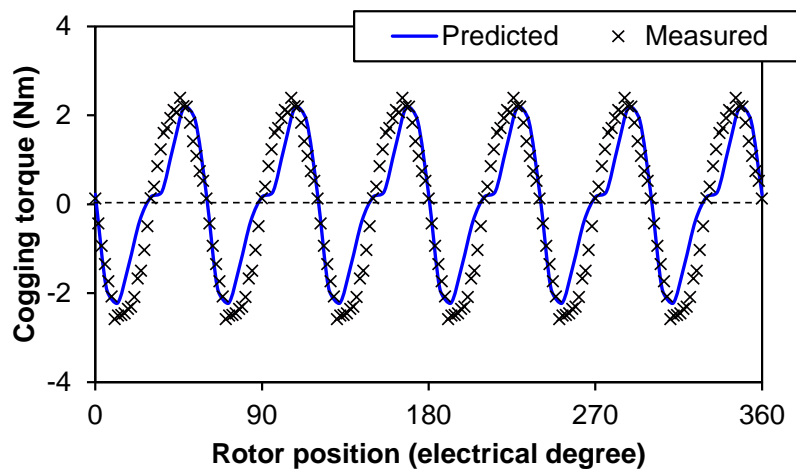
(a) Waveforms



(b) Spectra

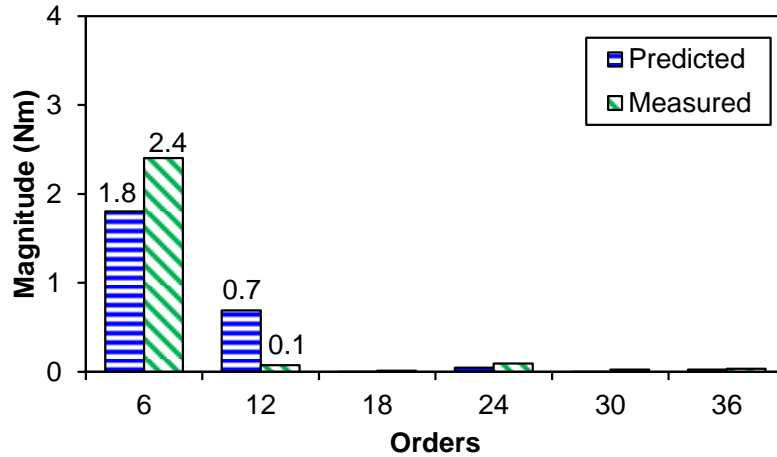
Fig. 6.23. Comparison of open-circuit back-EMFs for phase-A1 (170 rpm).

The open-circuit cogging torque is also measured. The predicted and measured results are compared in Fig. 6.24. As expected, the waveform of measured cogging torque basically agrees with the predicted one for the 96S/32P modular machine. However, the relative larger errors can be seen, since the cogging torque is quite sensitive and hard to be accurately measured. This is clearly shown in Fig. 6.24(b).



(a) Waveforms

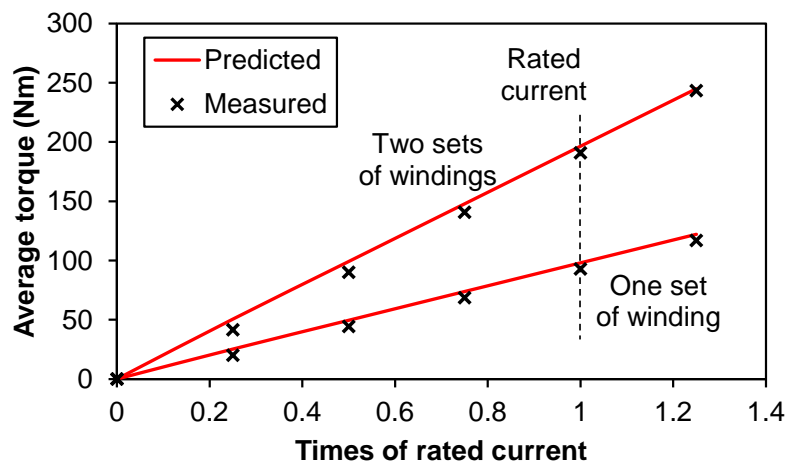




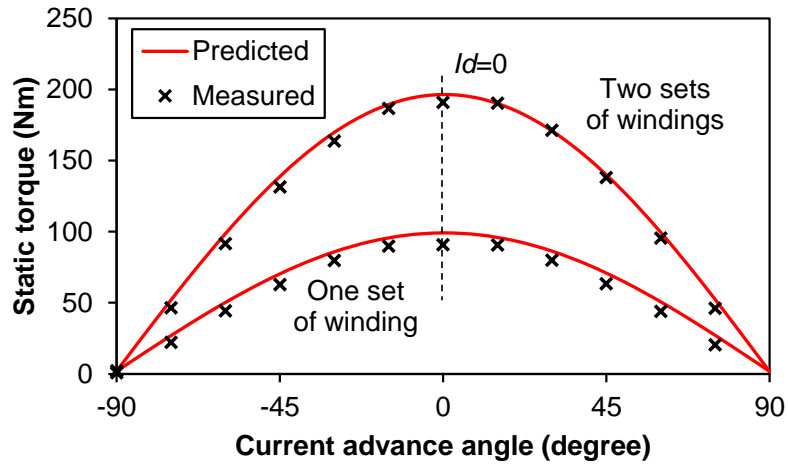
(b) Spectra

Fig. 6.24. Comparison of open-circuit cogging torques.

When the current is fed into two sets of winding or only one set of winding, the different torque will be generated. The former situation means the electrical machine runs under normal operation, while the later one is the open-circuit faulty operation. Due to the limit of experiment, the overload current cannot be as high as the theoretical analysis above, the allowable maximal current are supplied for normal and open-circuit faulty operations, respectively. The corresponding average torque variations with the current are given in Fig. 6.25(a). Since the average torque is also related with the current advance angle, the results of static torque are shown in Fig. 6.25(b).



(a) Torque-current



(b) Static torque (Rated current)

Fig. 6.25. Average torque-current and static torque characteristics under different conditions.

Fig. 6.25 shows that the average torque will linearly change with the current under both normal and faulty operations. The measured average torque always matches the predicted results quite well for the 96S/32P modular machine. When it comes to the static torque, quite good agreement between predicted and measured results is shown as well for both two set winding and one set winding operations, respectively. The slight difference for smaller current advance angle is owing to the saturation and end effect.

Overall, the experiments can validate the efficacy of the analysis in this chapter under nominal operation.

## 6.5 Conclusion

Two dual 3-phase modular PM machines with two sets of winding shifted zero degree are compared in this chapter. According to the comparative analysis, it can be found that the electrical machine with non-overlapping winding shows comparable average torque and lower PP torque ripple with two sets of winding operation than the electrical machine with overlapping winding. This is mainly due to the merit of lower harmonic torque even though the PMs of the later have been shaped. When there is only one set of winding operation in electrical machines with non-overlapping winding, the normal operation set of winding is hardly affected no matter the open-

circuit or short-circuit fault happens in the other set of winding. Besides, the three phases of the normal operation set of winding are still symmetrical, which means this electrical machine has really good fault-tolerant capability. However, when the electrical machine adopts overlapping winding, the magnetic circuit becomes asymmetric for one set of winding operation. This results in unbalance among three phases of the normal operation set of winding. Furthermore, such kind of asymmetry leads to a large torque ripple. Therefore, the proposed Zero type dual 3-phase modular machine with non-overlapping winding performs better in respect of torque performances under faulty operations.

## **Chapter 7 Influence of Magnetic Slot Wedges on Novel Dual 3-phase Modular Machines**

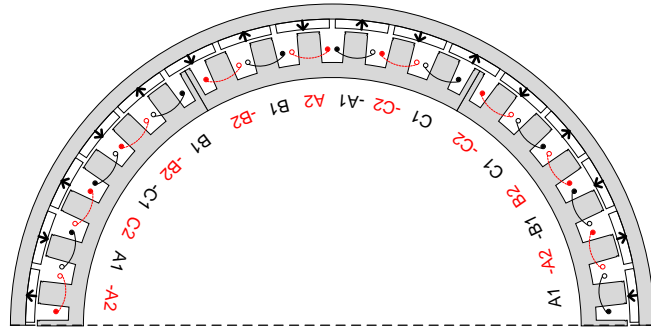
Most of small size electrical machines have tooth-tips for the sake of improving the back-EMF and minimising the torque ripple. However, the fully open slots which are usually used in large size megawatt (MW) electrical machines with preformed coils being accommodated cannot adopt tooth-tips. In order to solve this problem, the magnetic slot wedges can be used. They will be incorporated into the stator teeth after inserting the windings into slots even though the electrical machines have huge diameter, as shown in [SHI16]. Therefore, the influence of adopting magnetic slot wedges must be investigated. There are a multitude of publications investigating specific issues, such as stator iron loss [RED09], rotor eddy current loss [FOR12] and other electromagnetic performances [XUA13]. According to the results in these papers, the appropriate slot openings will maximise the back-EMF and the average torque while minimising the iron loss. When the extreme situation is considered, the fully closed slots will be used. The electrical machine performances will be quite different when operating in different conditions. The leakage plays an important role in determining electrical machine performances if the slots are fully closed [MOM09], [CHO10]. The reason for different torque performances was the local saturation in tooth-tip regions [WU15c].

The different kinds of magnetic slot wedges will also have their own influence on electrical machine performances. Five kinds of magnetic slot wedges are analysed to show their influence on electromagnetic performances of the proposed dual 3-phase modular machines with redundant teeth. For symmetrical magnetic slot wedges, each tooth is symmetrical about its own centre line. However, the magnetic slot wedges can also be accommodated in only one side of each tooth. Since both PM and armature field distributions are affected due to the existence of these magnetic slot wedges, the corresponding electrical machines will show different performances, such as back-EMF, on-load torque, iron losses, etc. It can be found that each kind of magnetic slot wedge has its own advantage. Therefore, the adoption of magnetic slot wedges needs to be determined according to the specific requirement.

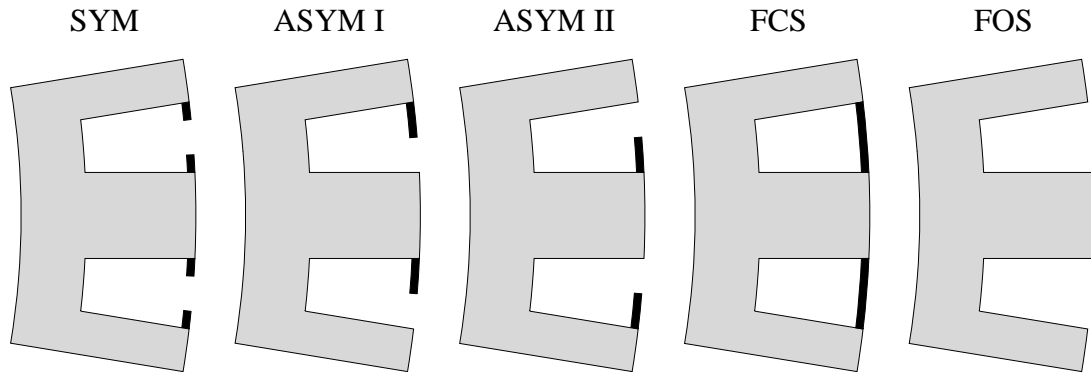
## 7.1 Prototype Machines

The construction process of the proposed modular machines with redundant teeth was systematically described in Chapter 3, while the dual 3-phase 42-slots/32-poles (42S/32P) combination is still adopted as the representative in this chapter. Five electrical machines with practically the same structure except different kinds of magnetic slot wedge shapes are considered, viz. symmetrical on both sides of teeth (SYM), asymmetric only on the front of teeth (ASYM I), asymmetric only on the back of teeth (ASYM II), fully . Here, the front and back of teeth are determined based on the rotor rotation direction. The tooth sides face the moving direction is defined as the front of teeth and vice versa for the back of teeth. The slot opening ratio (slot opening width to slot body width) is used to investigate the influence of magnetic slot wedge dimensions on electrical machine performances. The cross-section of the proposed modular machine is shown in Fig. 7.1. Since there are two repetition units for this electrical machine, only the half part of it is shown for simplicity. The different magnetic slot wedges are also given in Fig. 7.1 for intuitive illustration. Besides, two extreme cases, viz. fully closed slots (FCS) and fully open slots (FOS), are also drawn for clarity.

Fig. 7.1(a) shows that the specialty of this electrical machine is the stator core modularity. The existence of redundant teeth cuts the stator into 6 segments, while each segment contains the complete dual 3-phase winding. The unbalance due to the end effect is eliminated by alternating the winding arrangement of each segment. Consequently, the whole electrical machine is balanced for each phase and two sets of windings are shifted by 30 electrical degrees in space. The three magnetic slot wedges shown in Fig 7.1(b) (SYM, ASYM I and ASYM II) have 0.5 slot opening ratio. Since the rotor rotates counter clockwise by default, the ASYM I and ASYM II magnetic slot wedges are accordingly defined as shown in Fig. 7.1(b). It must be acknowledged that when the slot opening ratio is 0 or 1, SYM, ASYM I and ASYM II magnetic slot wedges will degrade to the same FCS or FOS cases. The proposed modular machines with five kinds of teeth-tips will be used as examples for the following comparative study.



(a) Cross-section of the prototype machine



(b) Illustration of different magnetic slot wedges

Fig. 7.1. Topology of the proposed modular machine and the definition of different magnetic slot wedges.

The major structure parameters of the proposed modular machine are listed in TABLE 7.1 with the magnetic slot wedge dimension. The magnetic slot wedge thickness is set to 1.5mm for all of the magnetic slot wedges and the material uses the same as the stator core lamination in order to easily make comparison.

TABLE 7.1 MAJOR PARAMETERS

Item	Value
Stator inner diameter (mm)	319.4
Stator outer diameter (mm)	390.4
Stator yoke thickness (mm)	13.2
Stator tooth body width (mm)	17.52 <sup>a</sup> and 7.9 <sup>b</sup>
<b>Stator magnetic slot wedge thickness (mm)</b>	<b>1.5</b>
Air-gap length (mm)	2
PM thickness (mm)	6
PM pole arc to pole pitch ratio	0.9
Rotor yoke thickness (mm)	10
Axial length (mm)	110
Turns per phase	408
Rated current (A)	3
Rated speed (rpm)	170

<sup>a</sup> the teeth with coils.

<sup>b</sup> the teeth without coils.

## **7.2 Influence of Magnetic Slot Wedges on Performances**

Since different magnetic slot wedges will affect the field distributions, the electrical machine performances will accordingly vary on both open-circuit and on-load conditions. The differences will be shown in this section.

### **7.2.1 Field Distribution**

The open-circuit flux line and flux density distributions of five electrical machines are shown in Fig. 7.2. The rotor locates at the initial position where the rotor  $d$ -axis coincides with the phase-A1 axis. Comparing these five electrical machines, it can be observed that the major flux path is almost the same, whereas there are still some flux lines changing their path. Furthermore, the flux density of each machine will also be different in magnetic slot wedge region, which will cause the variation of air-gap flux densities. Then, all of the electromagnetic performances will be affected.

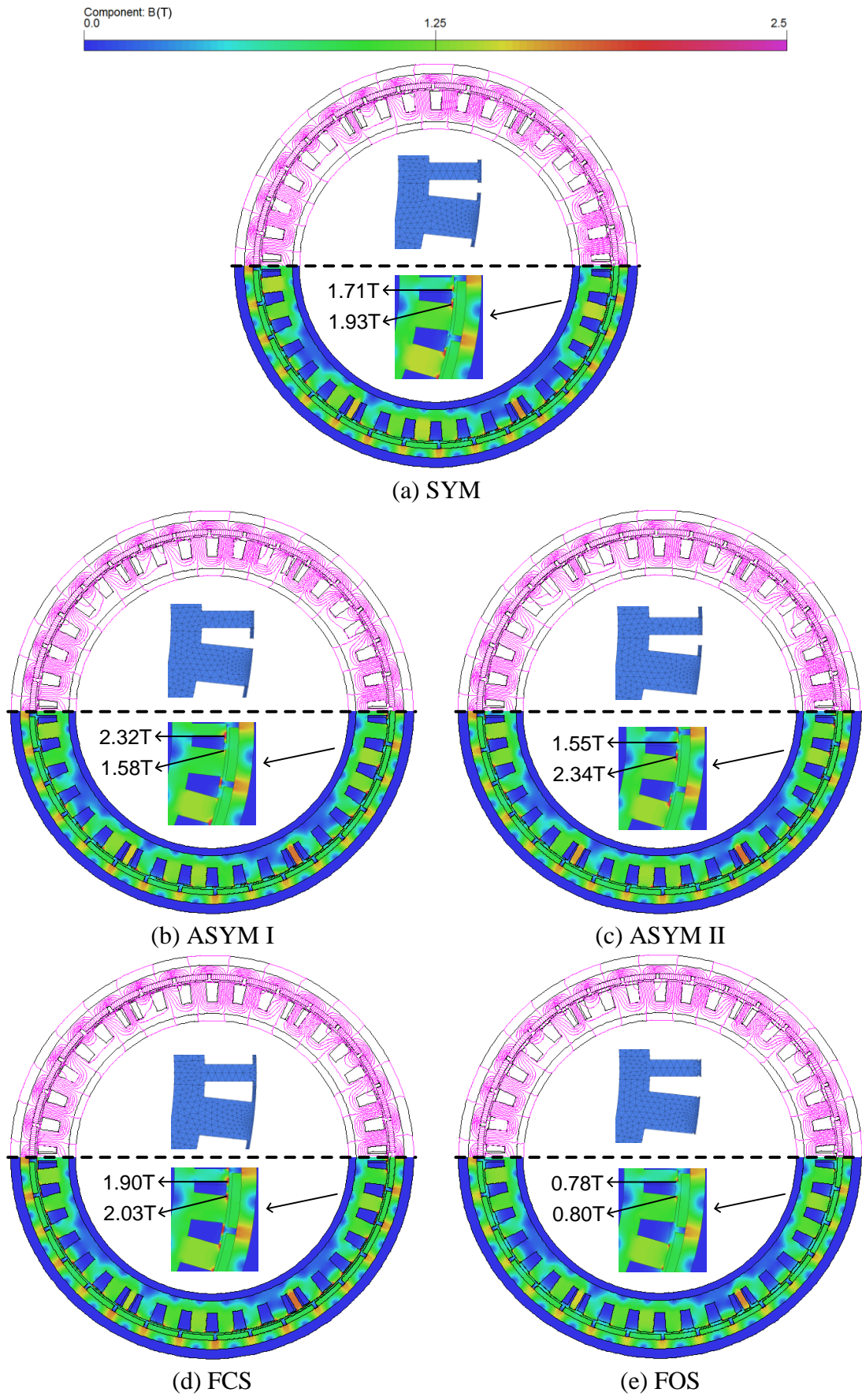
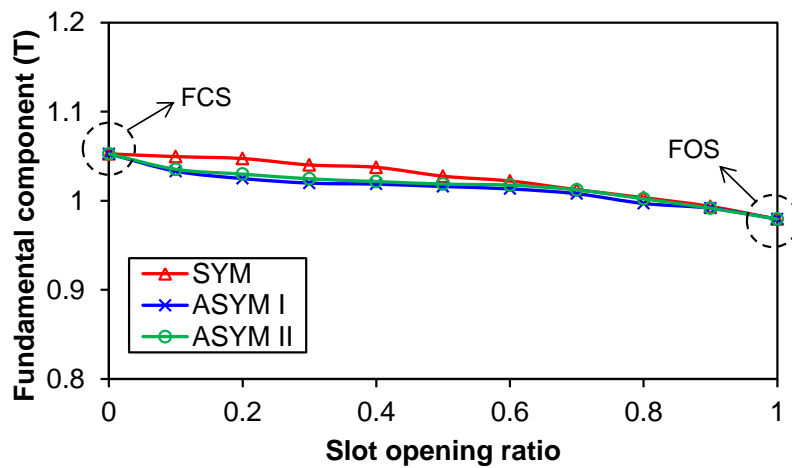


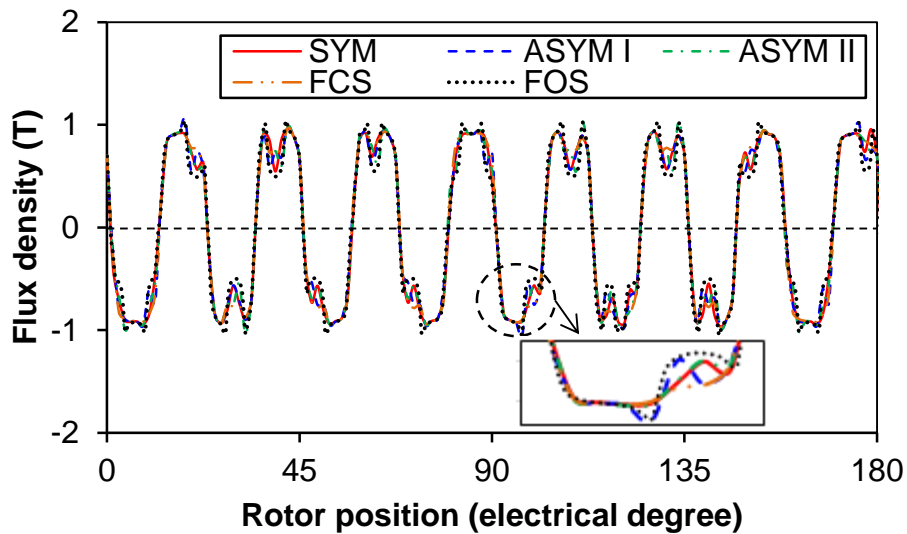
Fig. 7.2. Open-circuit flux distributions.



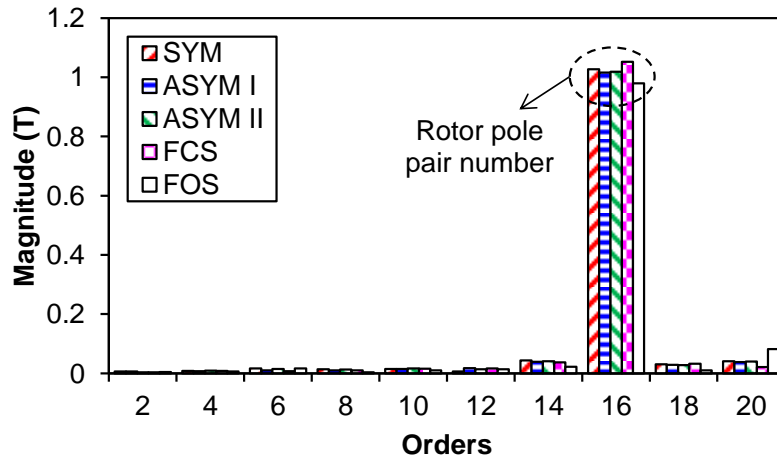
The air-gap flux densities are changed with the variation of the flux passing through the major magnetic circuit and flux leakages. Since the fundamental component of radial flux density ( $B_{r1m}$ ) is crucial to energy conversion, its variation with the slot opening ratio is plotted in Fig. 7.3(a). Besides the fundamental component, other harmonics are affected as well; and therefore the waveforms and the corresponding spectra of electrical machines with five different magnetic slot wedges are shown in Figs. 7.3(b) and (c). The slot opening ratio is still set to 0.5 for SYM, ASYM I and ASYM II magnetic slot wedges for all of the following waveforms when representing five kinds of magnetic slot wedges. The two special cases with FCS and FOS are compared at the same time as the references.



(a) Influence of magnetic slot wedges on fundamental component



(b) Waveforms



(c) Spectra

Fig. 7.3. Air-gap flux density.

According to Fig. 7.3(a), the fundamental component will decrease with the increase of slot opening for three electrical machines. This is due to the increase of equivalent air-gap length for a larger slot opening. The FCS machines have the minimal air-gap and the FOS machines have the maximal air-gap, which is coincided with the maximum and minimum for the fundamental component, respectively. Another phenomenon can be seen that the electrical machines with SYM magnetic slot wedges have larger fundamental air-gap flux density than other two kinds of electrical machines with ASYM I or ASYM II magnetic slot wedges. The difference of local saturation contributes to such difference. The electrical machines with SYM magnetic slot wedges can capture more flux since the saturation of two sides of magnetic slot wedges is similar. In contrast, the electrical machines with ASYM I or ASYM II magnetic slot wedges can provide only one side to further capture flux and the saturation will restrict the amount. However, the difference between symmetrical and asymmetric magnetic slot wedges becomes increasingly small with larger slot openings. The flux focusing effect is weak when the slot opening is large enough.

When it comes to the specific waveforms shown in Fig. 7.3(b), the major shape is almost the same for five electrical machines. The difference of these electrical machines can be seen in spectra. The fundamental component has the largest value and its order is 16 which is the rotor pole pair number. The difference in value is the same as the results shown in Fig. 7.3(a). For other harmonics, they are all from the modulation effect between PM poles and slot openings. Since the FOS machine has

the largest slot opening, such modulation is the strongest, vice versa for FCS machine. The harmonic orders ( $k$ ) can be obtained based on the following equation:

$$k = |p \pm \nu N_{sr}|, \quad \nu = 0, 1, 2, \dots \quad (7.1)$$

where  $p$  is the rotor pole pair number and  $N_{sr}$  is the number of redundant teeth. According to the above equation, only the even order harmonics exist. Because of the difference in these additional harmonics, the electrical machine performances should be different.

### 7.2.2 Open-circuit Performance

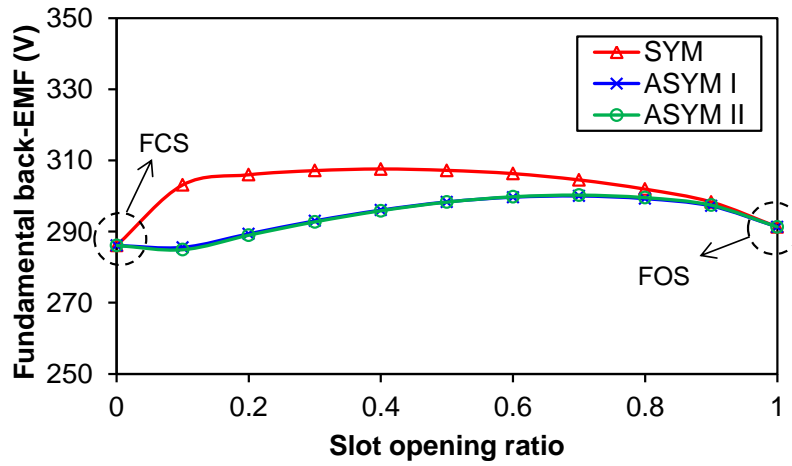
When the rotor rotates without current fed into windings, the back-EMF will be induced and the variation of magnetic field will also generate torque fluctuation with zero net output torque. The principle of induced phase back-EMF is based on the following equation:

$$e_{bi} = \frac{d\psi_i}{dt}, \quad i = A1, A2, B1, B2, C1, C2 \quad (7.2)$$

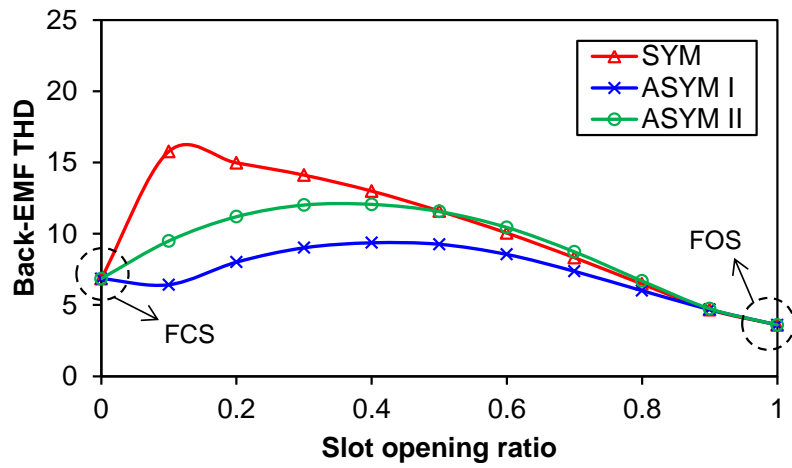
where  $e_{bi}$  is the induced phase back-EMF of phase  $i$  and  $\psi_i$  is the corresponding phase flux-linkage. Since only the fundamental component of back-EMF is related to average torque production, its variation with slot opening is shown in Fig. 7.4(a). For other higher order harmonics, they will affect torque ripple, thus it is necessary to show the variation of total harmonic distortion (THD) as well. This quantity is defined as follows:

$$THD = \frac{\sqrt{\sum_{i=3,5,7,\dots}^{\infty} E_{im}^2}}{E_{1m}} \quad (7.3)$$

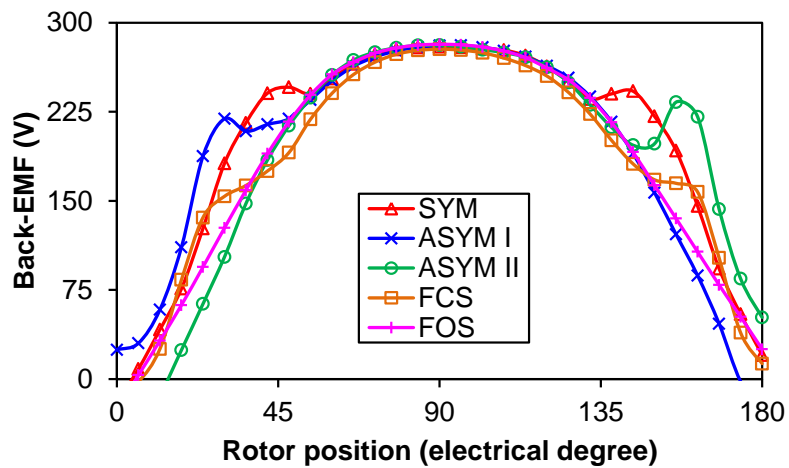
where  $E_{1m}$  is the amplitude of the fundamental phase back-EMF and  $E_{im}$  is corresponding to the magnitudes of other higher order harmonics. The results are shown in Fig. 7.4(b). The waveforms and spectra of five examples as the previous subsection are compared in Figs. 7.4(c) and (d) as well. Since six phases are symmetrical, only the results of phase-A1 are shown.



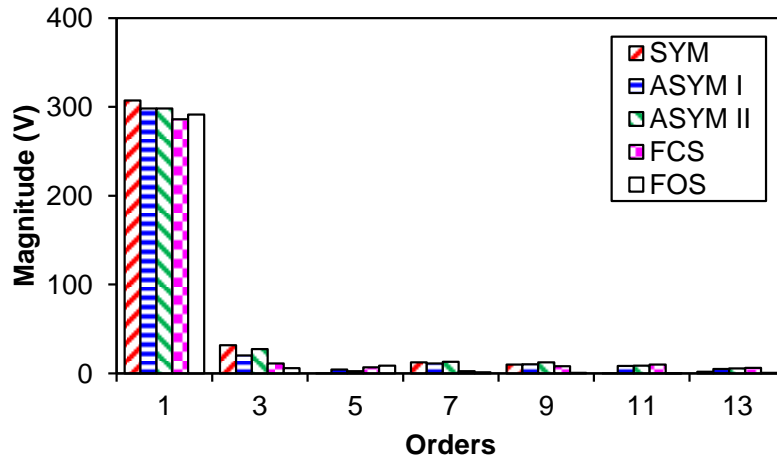
(a) Influence of magnetic slot wedges on fundamental component



(b) Influence of magnetic slot wedges on back-EMF THD



(c) Waveforms



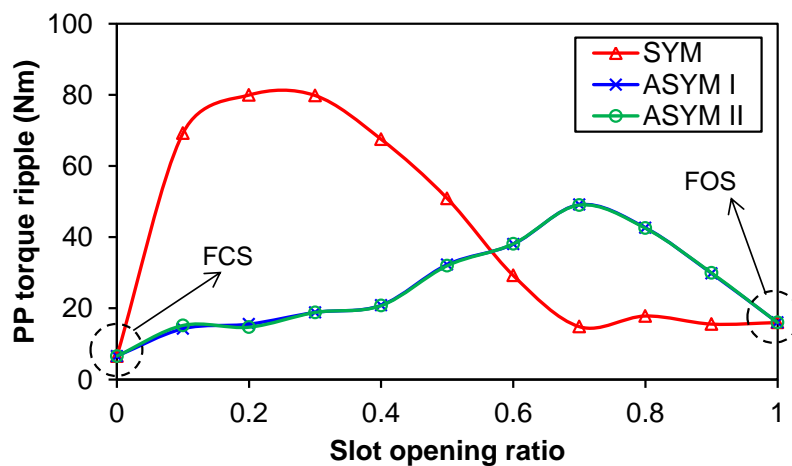
(d) Spectra

Fig. 7.4. Open-circuit phase back-EMF (170rpm).

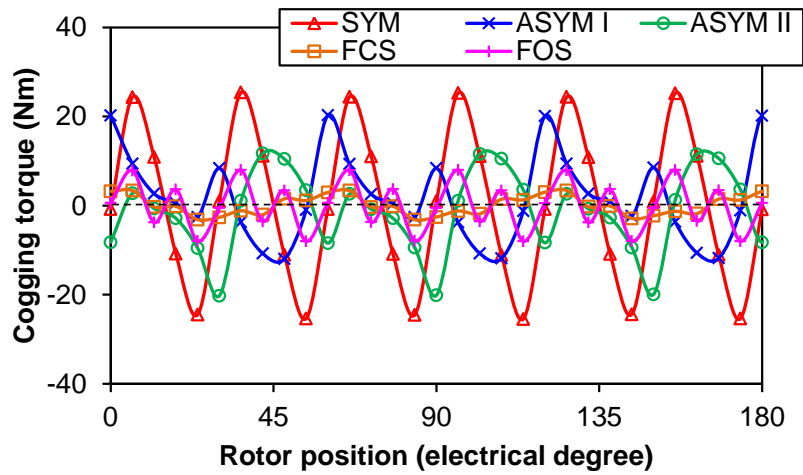
Fig. 7.4(a) demonstrates that there is a peak value for fundamental back-EMF with the increase of slot opening. When the slot opening is small, the leakage will reduce the flux linking the main magnetic flux path. If the slot opening is too large, the equivalent air-gap length will also be large, which decreases the main flux. The difference between symmetrical and asymmetric magnetic slot wedges can also be seen. Since the electrical machine with SYM magnetic slot wedges capture more flux than those with ASYM I or ASYM II magnetic slot wedges, it shows the largest fundamental value over the whole variation range. For electrical machines with asymmetric magnetic slot wedges, the small slot opening will result in local saturation, which prevents the increase of main flux; and therefore the obvious increase happens when the slot opening is large. The appropriate magnetic slot wedges can increase the fundamental value. Since the electrical machines with ASYM I and ASYM II magnetic slot wedges can be thought as complementary cases to some extent, the fundamental back-EMF variation is similar. However, the THD should be different. After all, the permeance due to slot opening is different. Fig. 7.4(b) shows that the electrical machines with ASYM I magnetic slot wedges have the minimal THD over the whole range. When the slot opening is small, the back-EMFs are more distorted due to the local saturation in magnetic slot wedges, especially for the electrical machines with SYM magnetic slot wedges. When the magnetic slot wedges become increasingly small, such side effect becomes weaker and weaker. For this 42S/32P modular machine, using FOS has the minimal THD.

The clearer illustration of magnetic slot wedges influence can be seen in Figs. 7.4(c) and (d). The waveform of the FOS machine is much less distorted compared with others. The electrical machine with SYM magnetic slot wedges is symmetrical distorted over half electrical period and severer than the FCS machine. The other two electrical machines with ASYM I and ASYM II magnetic slot wedges show the asymmetric waveforms within this range. According to Figs. 7.1(b) and (c), it can be seen that the sharp permeance variation will more early happen for electrical machines with ASYM I magnetic slot wedges when the rotor rotates counter clockwise. That is why the apparent distortion appears in the rise period, vice versa for electrical machines with ASYM II magnetic slot wedges. Fig. 7.4(d) can further reflect the difference in back-EMFs. The fundamental value coincides with the results shown in Fig. 7.4(a). The electrical machines with appropriate magnetic slot wedges can increase fundamental value, which is theoretically beneficial to larger output torque. In terms of torque ripple, the electrical machines with magnetic slot wedges will be worse, since the higher order harmonics are much more abundant than the FCS and FOS machines.

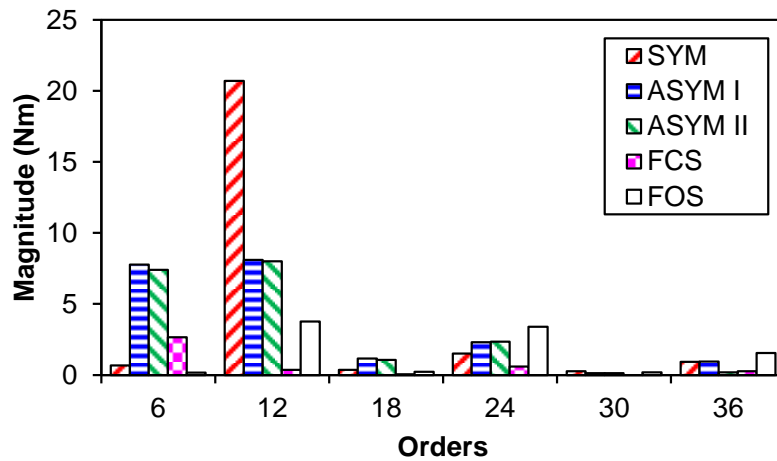
For cogging torque, its peak to peak (PP) value ( $T_{cogPP}$ ) is much more concerned. The smooth cogging torque is always preferable and the magnetic slot wedges will have significant influence on it. The variation of PP torque with slot opening is shown in Fig. 7.5(a). The detailed results of five examples are also given in Figs. 7.5(b) and (c).



(a) Influence of magnetic slot wedges on PP torque ripple



(b) Waveforms



(c) Spectra

Fig. 7.5. Open-circuit cogging torque.

For all of five electrical machines, the FCS one has the smallest cogging torque, since the variation of permeance is smoother than others with slot openings. There is a huge increase for the electrical machine with symmetrical magnetic slot wedges when the slot opening ratio is small, which is also owing to the sharp leakage variation in slot opening region. For electrical machines with asymmetric magnetic slot wedges, the larger slot opening could lead to the increase of harmonic air-gap flux density contributing to cogging torque. That is why the PP torque ripple is larger for large slot openings. The similar asymmetric influence due to magnetic slot wedges again leads to the similar PP torque ripple for electrical machines with either ASYM I or ASYM II magnetic slot wedges.

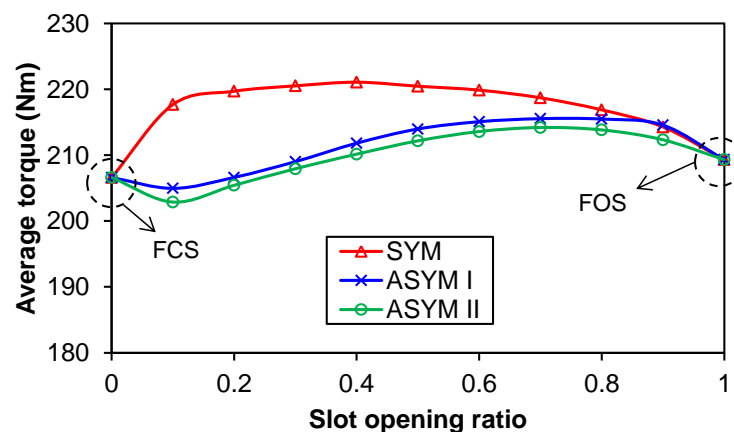
The results in Fig. 7.5(b) show that the cogging torque of the FCS machine is much smaller than others. This is the benefit for using this kind of slot, though it is very difficult to put the conductor in due to no slot openings and also higher losses. Since the redundant teeth have been optimised in the FOS machine to minimise torque ripple, it has smaller value as well compared with other three cases with SYM, ASYM I and ASYM II magnetic slot wedges. The electrical machines with ASYM I and ASYM II magnetic slot wedges show the complementary waveforms as expected. The largest cogging torque exists in the electrical machine with SYM magnetic slot wedges as a consequence of modifying the air-gap flux density by changing the permeance variation due to slots, thus this special slot opening ratio is inappropriate. The harmonic torques shown in Fig. 7.5(c) can more clearly explain the influence of magnetic slot wedges on cogging torque. The minimal cogging torque period over one electrical period ( $N_{cogpp}$ ) is determined as follows:

$$N_{cogpp} = \frac{LCM(N_{sr}, 2p)}{p} \quad (7.4)$$

where  $LCM$  represents the least common multiple of two numbers. For this 42S/32P modular machine, the cogging torque period is 6 over one electrical period.

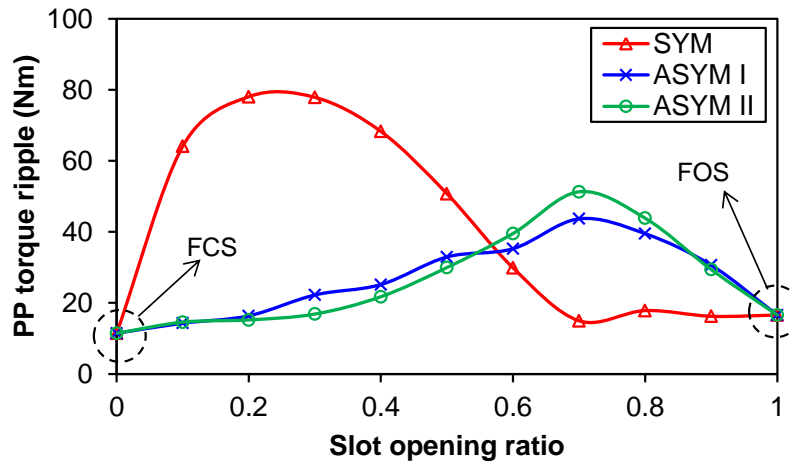
### 7.2.3 On-load Performance

When the rated current is fed into the winding, the effective torque will be produced. The influence of magnetic slot wedges on average torque and PP torque ripple is shown in Figs. 7.6(a) and (b), respectively. The detailed waveforms and spectra of five examples are plotted in Figs. 7.6(c) and (d) as a supplement.

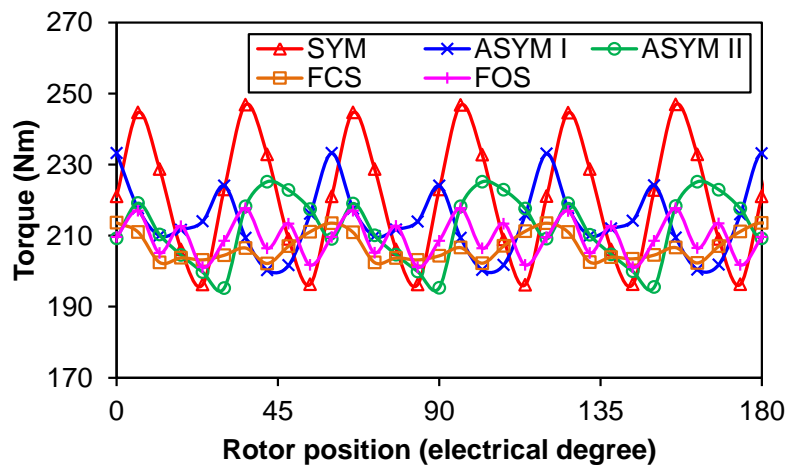




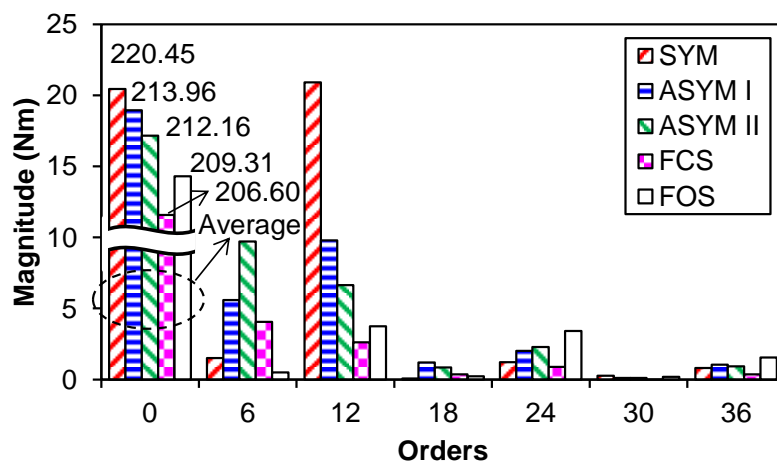
(a) Influence of magnetic slot wedges on average torque



(b) Influence of magnetic slot wedges on PP torque ripple



(c) Waveforms



(d) Spectra

Fig. 7.6. On-load torque under rated condition.

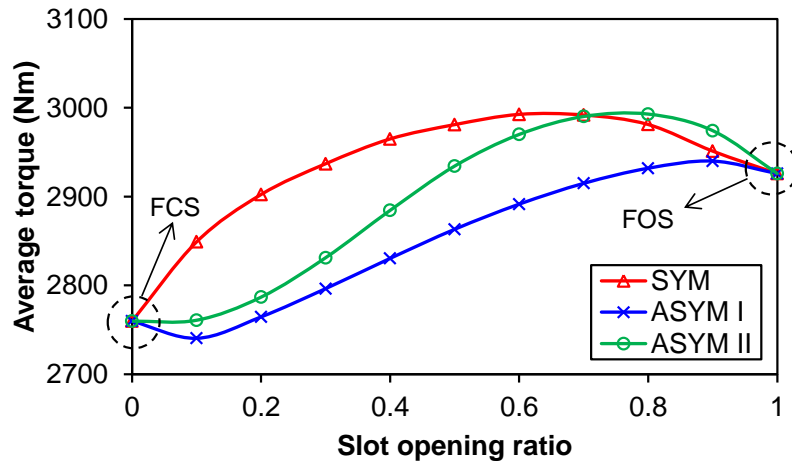
Fig 7.6(a) shows that the variation of average torque with magnetic slot wedges is very similar to that of fundamental back-EMF. This is due to the much weaker armature field compared with the PM field. There is still a quite minor difference among three electrical machines shown in Fig. 7.6(a), which comes from the slight saturation variation caused by the armature field. The machine with SYM magnetic slot wedges still has the largest average torque compared with other two because of the symmetrical saturation in magnetic slot wedge area. Besides, the average torques of electrical machines with ASYM I and ASYM II magnetic slot wedges are almost the same as well. The predominance of PM field is also observed in Fig. 7.6(b). The variation of PP torque ripple under rated condition is close to that of cogging torque, though there are still some small changes.

For the waveforms shown in Fig. 7.6(c), it can be found that the effective average torque of five electrical machines is generated and the torque ripple will be slightly different from cogging torque. In order to be clearer, the characteristic quantities representing the torque performance are listed in TABLE 7.2. Under open-circuit condition, each electrical machine cannot generate average torque, while the cogging torque exists. Even for the FCS machine, there is cogging torque because of the saturation. The average torque is consistent with the results shown in Fig. 7.6(a) and it can also verify that the on-load PP torque ripple is similar to cogging torque except for the FCS machine. Such relative huge difference comes from the local saturation due to the armature field. According to the characteristic values listed in TABLE 7.2, the average torque will be larger for electrical machines with magnetic slot wedges, especially symmetrical magnetic slot wedges. However, the torque ripples will be lower for electrical machines without magnetic slot wedges or fully closed slots in relative large size electrical machines.

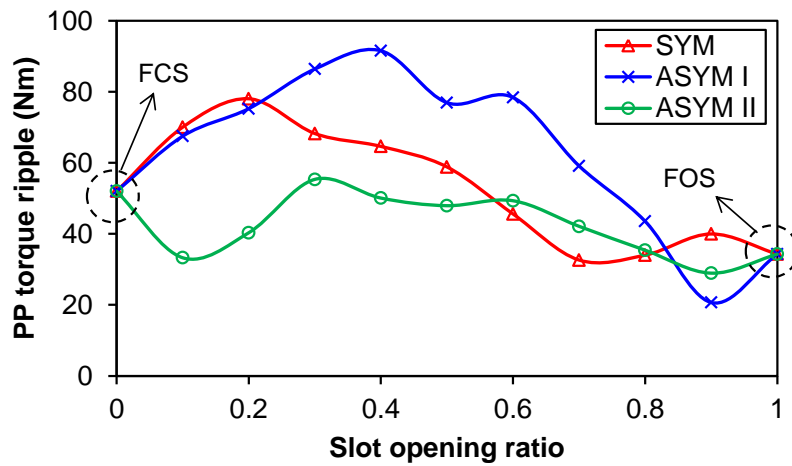
TABLE 7.2 CHARACTERISTIC QUANTITIES OF TORQUE

Item	Load condition	SYM	ASYM I	ASYM II	FCS	FOS
Average torque (Nm)	Open	0	0	0	0	0
	Rated	220.	214	212	207	209
	Overload	2981	2863	2934	2760	2926
PP torque ripple (Nm)	Open	51	32	32	7	16
	Rated	51	33	30	11	17
	Overload	59	77	48	52	34

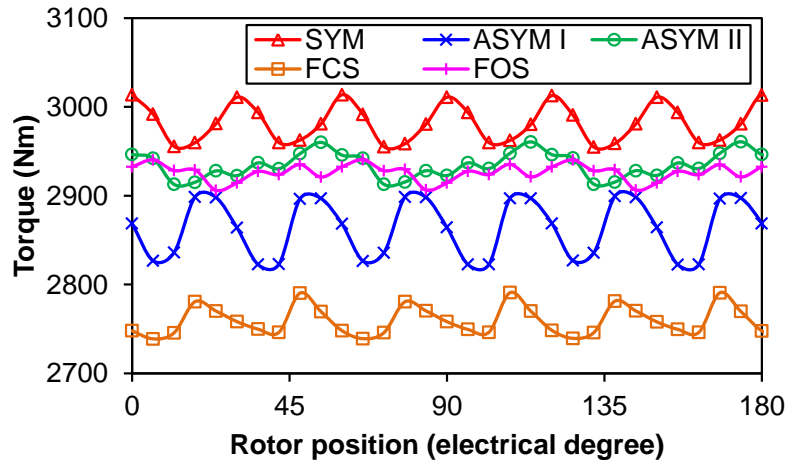
As has been stated above, the on-load torque performances is closely related with the armature field, the results under overload condition should be quite different and are shown in Fig. 7.7. The current is enlarged to 15 times of its rated value to emphasise this effect.



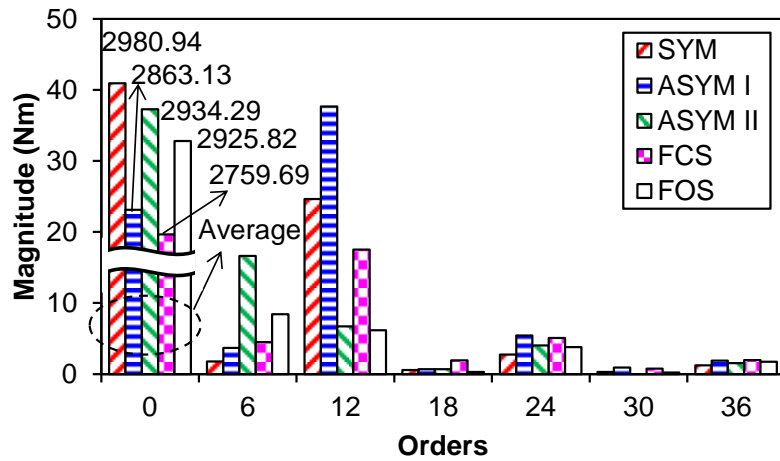
(a) Influence of magnetic slot wedges on average torque



(b) Influence of magnetic slot wedges on PP torque ripple



(c) Waveforms



(d) Spectra

Fig. 7.7. On-load torque under overload condition.

Comparing Figs. 7.7 and 7.6, it is clear that the torque performances are totally different when the current is high. Fig. 7.7(a) exhibits that the FCS machine practically has the smallest torque because of the heaviest local saturation in magnetic slot wedges. The machine with SYM magnetic slot wedges almost has the largest one over the whole range of slot opening ratio variation if compared with the electrical machines with ASYM I and ASYM II magnetic slot wedges. The reason for this is the different local saturation, as shown in Fig. 7.8. Since the B-H curve of stator lamination is provided below 1.8T usually by the supplier, the flux density surpasses this value is obtained based on different fitting method on magnetisation curve.

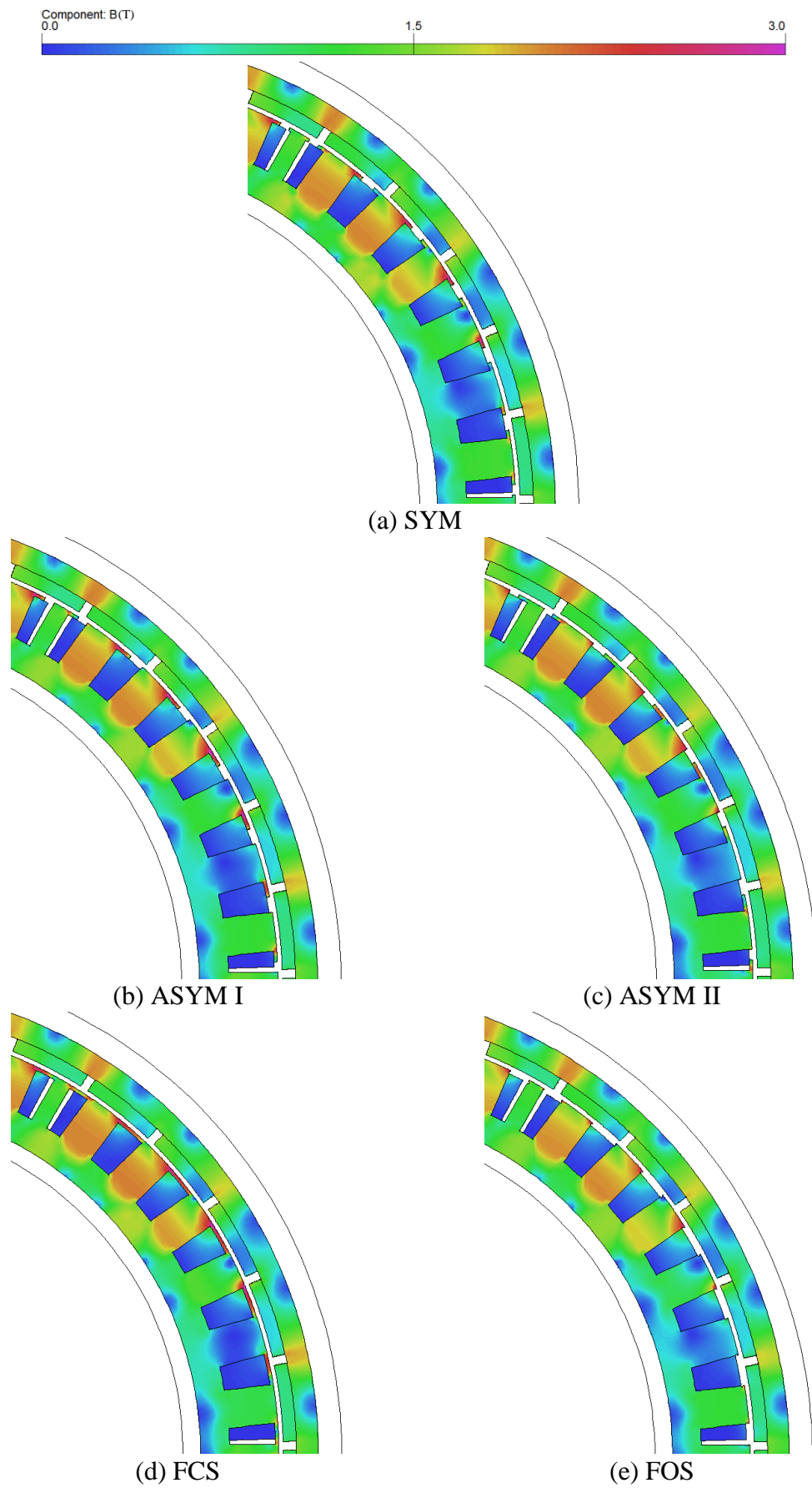
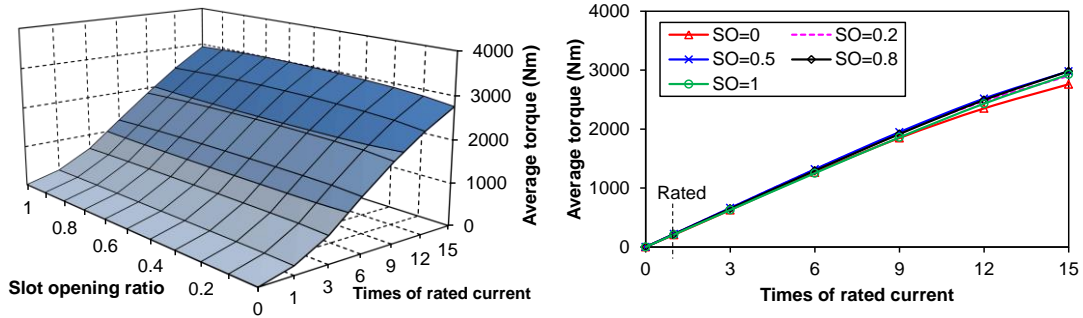


Fig. 7.8. Flux density distributions under overload conditions.

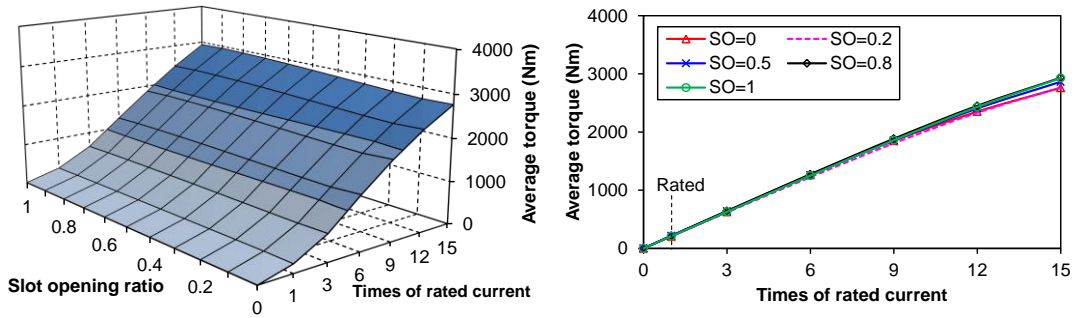
Different from the rated condition, the electrical machine with ASYM I magnetic slot wedges encounters much heavier local saturation in magnetic slot wedges with high current, which leads to the lower torque. In contrast, the electrical machine with ASYM II magnetic slot wedges can still capture more flux passing the main magnetic path; therefore it generates higher torque. For some specific magnetic slot wedge dimensions, this electrical machine can even generate the largest torque. For PP torque ripple shown in Fig. 7.7(b), the obvious influence of current and magnetic slot wedges can be seen. The electrical machine with ASYM I magnetic slot wedges has the largest torque ripple over the most range of slot opening variation, whereas the one with ASYM II magnetic slot wedges almost has the smallest value. One thing must be emphasised. The phenomena shown in Fig. 7.7 are related with the rotation direction. When the rotor rotates in clockwise direction opposite to the one adopted this chapter, the conclusions on these two kinds of magnetic slot wedges are opposite.

When it comes to the five examples, Fig. 7.7(c) shows that there is large difference on both average torque and PP torque ripple. The spectra shown in Fig. 7.7(d) can further demonstrate such difference. Comparing the harmonics under overload and rated conditions, it can be found that the major harmonic torques have evident increase due to the increase of armature field. Besides, it can be found that both the FCS machine and the electrical machine with ASYM I magnetic slot wedges largely increase on the 12<sup>th</sup> harmonic, while it is the 6<sup>th</sup> component for other three cases. This can also be explained according to the local saturation of magnetic slot wedges, as shown in Fig. 7.8. Similar to the rated situation, the characteristic values of torque are also listed in TABLE 7.2 as well. The electrical machines with magnetic slot wedges can still improve average torque, though the increase is quite minor for the electrical machine with ASYM I magnetic slot wedges due to local saturation. Since the armature field is quite strong under overload condition, the FCS machine loses the merit of having the smallest PP torque ripple. In contrast, the FOS machine performs the best in terms of the torque ripple, which is different from the rated condition.

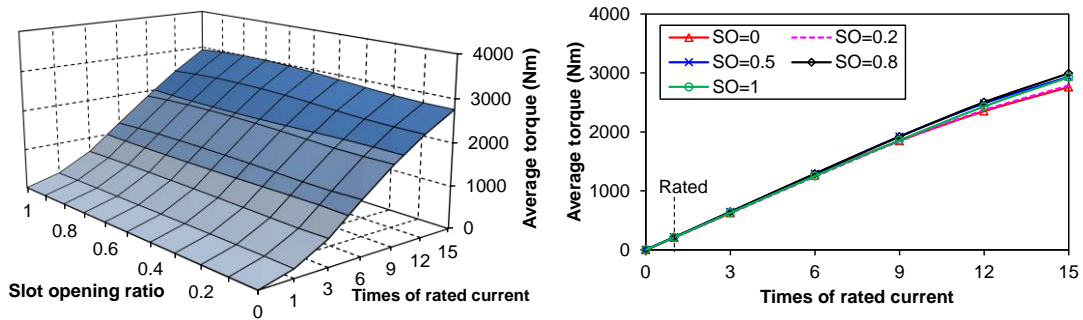
Since the current has a huge influence on torque performances [AZA12], the complete variation of average torque and PP torque ripple with current and slot opening ratio are shown in Figs. 7.9 and 7.10, respectively.



(a) SYM



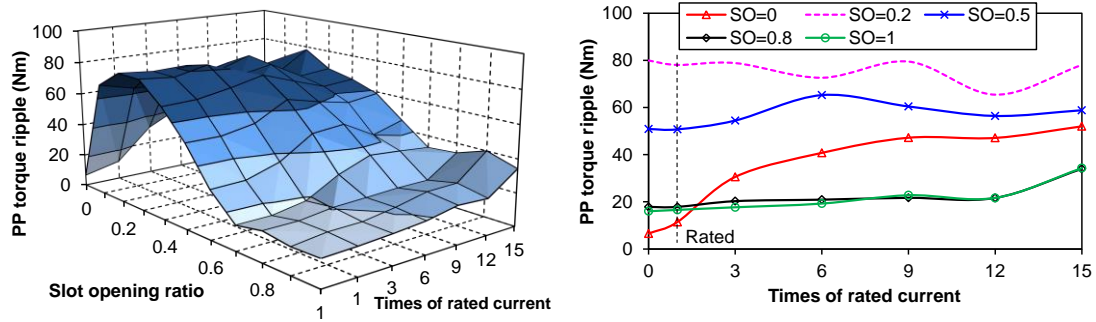
(b) ASYM I



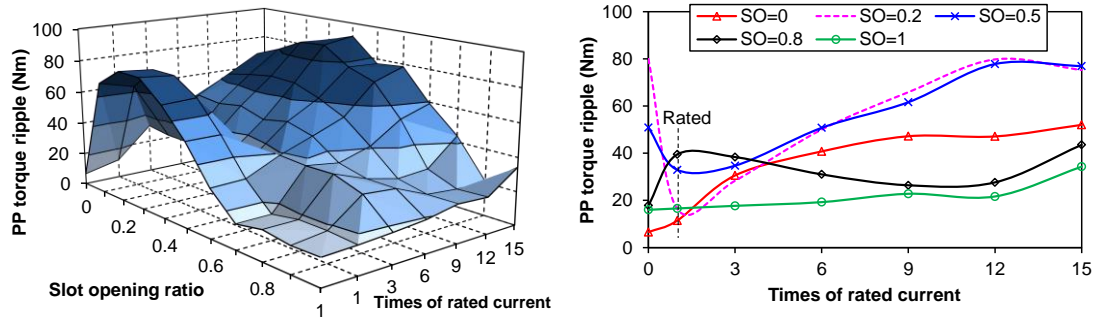
(c) ASYM II

Fig. 7.9. Influence of current on average torque.

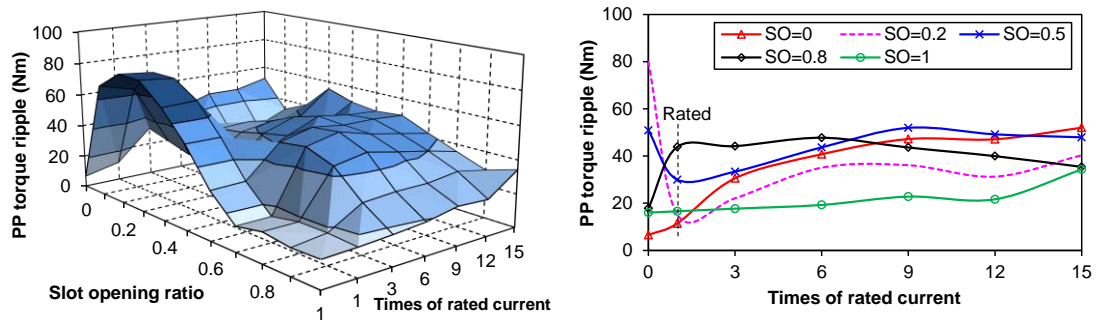
Fig. 7.9 shows that the electrical machine with SYM magnetic slot wedges almost keeps the largest average torque within the major slot opening ratio variation range. With the increase of current, the electrical machine with ASYM II magnetic slot wedges could exceed a bit if adopting small magnetic slot wedges. The electrical machine with ASYM I magnetic slot wedges produces the smallest torque with a higher current, which is the drawback for using this kind of magnetic slot wedges in terms of torque production.



(a) SYM



(b) ASYM I



(c) ASYM II

Fig. 7.10. Influence of current on PP torque ripple.

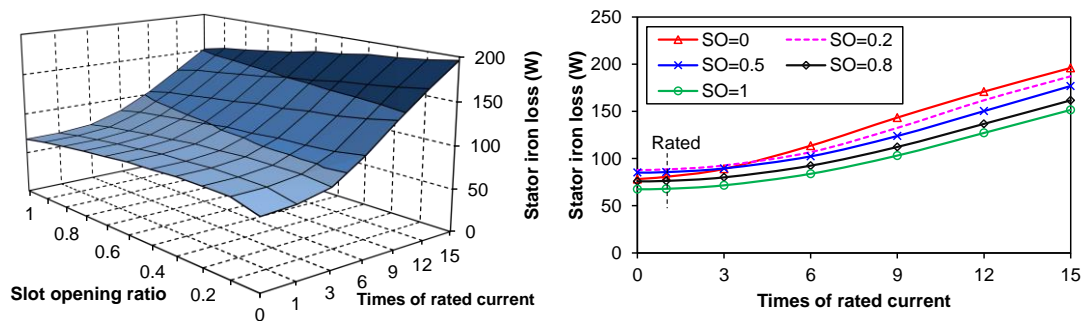
The variation of PP torque ripple is more obvious, as shown in Fig. 7.10. When the current is low, both the FCS and FOS machines have the smaller PP torque ripple due to smooth permeance variation and optimised redundant teeth, respectively. With the increase of current, it can be found that the adoption of small slot opening will enhance the local saturation caused by armature field. This makes the slot opening leakage change fast and consequently lead to large torque fluctuation. In contrast, the use of large slot opening avoids such kind of sharp change and the PP torque ripple will not obviously increase with the higher current. The reason for such huge difference on PP torque ripple performance is the saturation variation for the different combination of slot opening ratio and current. Overall, it can be seen that the larger



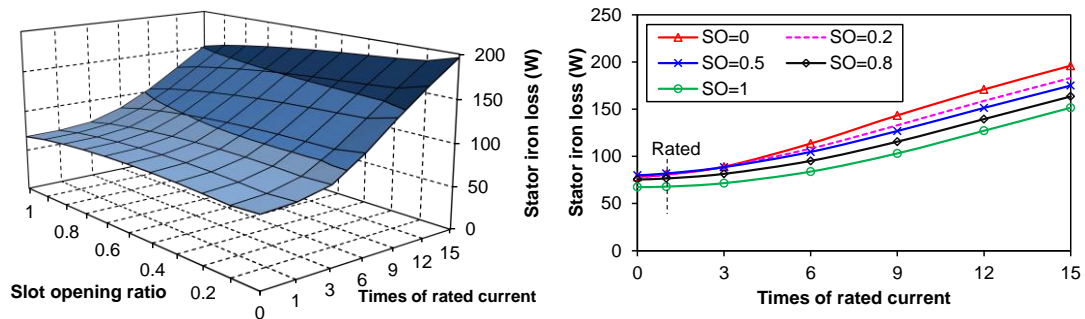
slot opening could keep the torque smoother within a relative large range of current variation.

### 7.2.4 Iron Losses

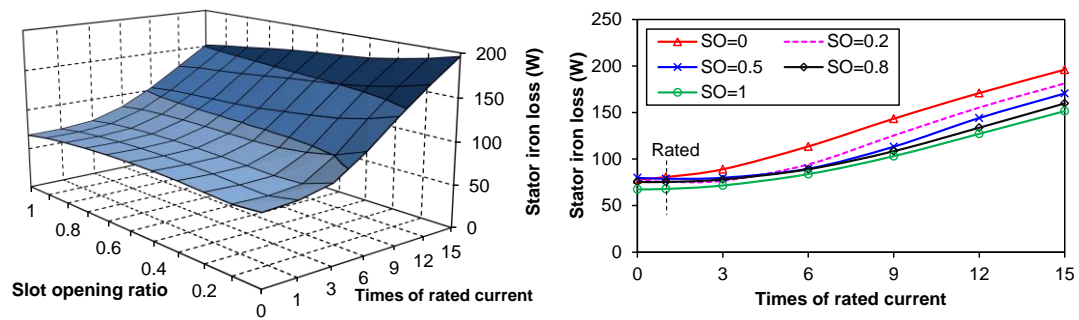
The influence of current on three major iron losses of the FOS machine, viz. stator iron loss, PM eddy current loss and rotor yoke eddy current loss, has been shown in Chapter 2. Since the different magnetic slot wedges will affect the field distribution, the variation of three kinds of losses will accordingly vary as well. The results are shown in Figs. 7.11, 7.12 and 7.13, respectively.



(a) SYM



(b) ASYM I



(c) ASYM II

Fig. 7.11. Influence of magnetic slot wedges on stator iron loss.

For the stator iron loss, the core saturation is predominant. It can be seen that the stator iron loss variation of three electrical machines are quite similar since the major part of the stator core has similar saturation level. However, the difference of local saturation in magnetic slot wedge part will affect this loss. As has been analysed above, the electrical machine with ASYM I magnetic slot wedges has the severest local saturation in magnetic slot wedges. Thus, its stator iron loss is slightly higher, especially for high current situation. When the symmetrical magnetic slot wedges are adopted, the stator core local saturation is reduced, which lead to a smaller iron loss. For the electrical machine with ASYM II magnetic slot wedges, the lowest stator iron loss is obtained because of the weakest local saturation. This advantage is the most obvious if the small slot opening is used.

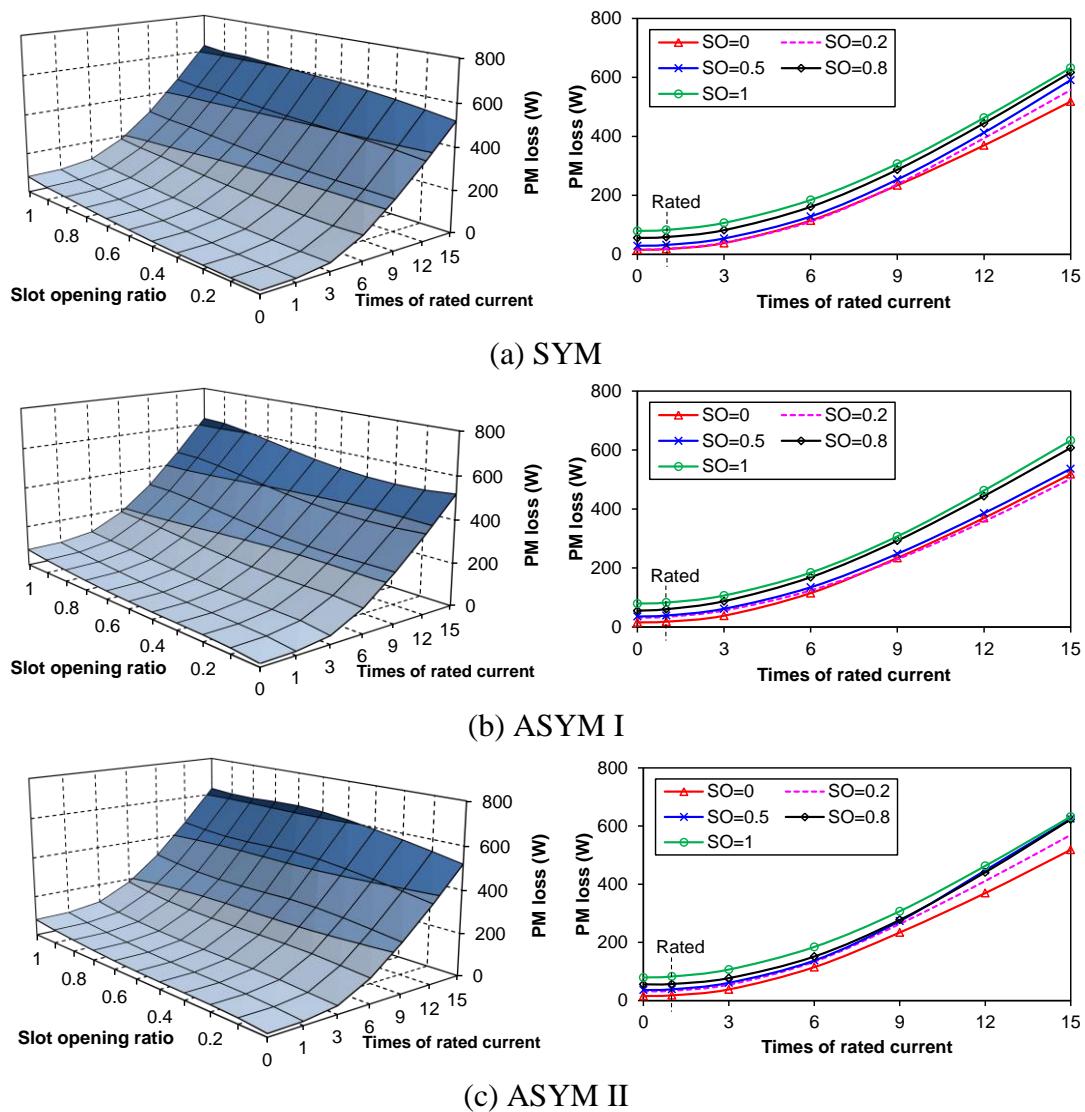
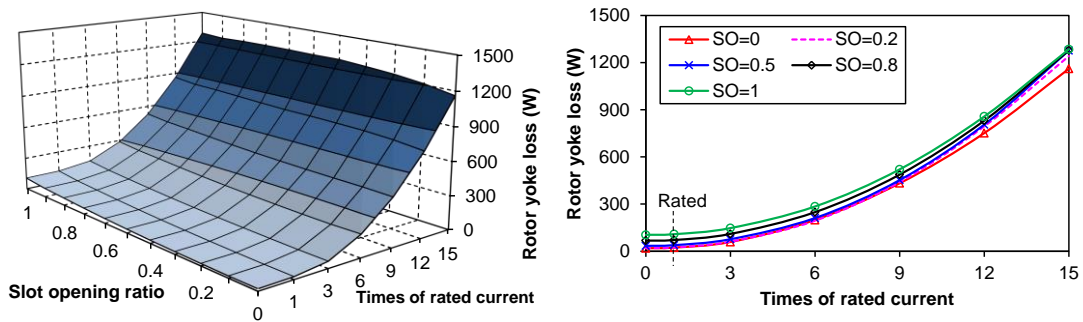
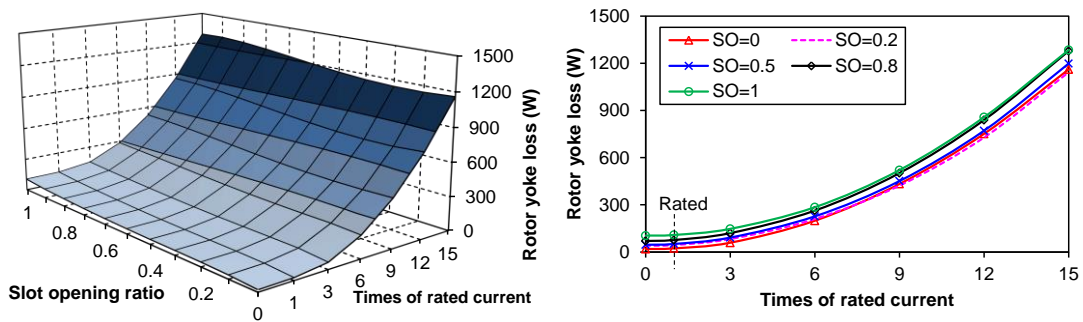


Fig. 7.12. Influence of magnetic slot wedges on PM eddy current loss.

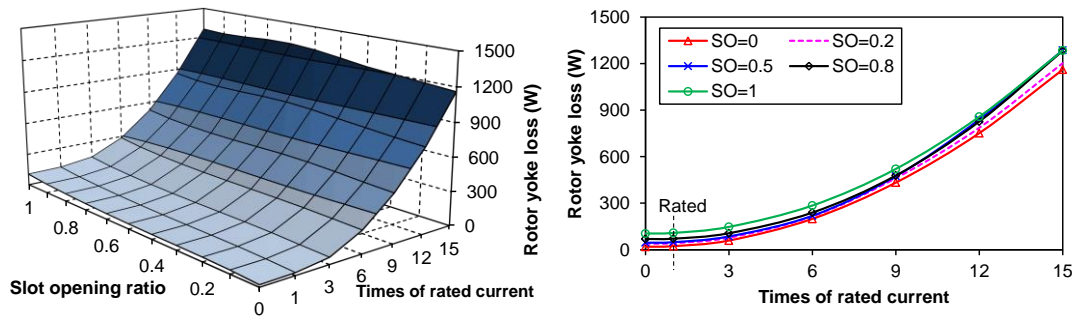
Fig. 7.12 shows that all of three electrical machines will have lower PM eddy current loss if the magnetic slot wedges are adopted. The smaller slot opening benefits the reduction of more harmonics penetrating to PMs, which gives rise to lower loss. Among three electrical machines, the one with ASYM I magnetic slot wedges has the lowest PM eddy current loss when the magnetic slot wedges are adopted, especially for high current situation. In contrast, the PM eddy current loss of the electrical machine with ASYM II magnetic slot wedges will be much higher. When the electrical machine adopts the ASYM I magnetic slot wedges, the heavier local saturation will filter some harmonics passing through the air-gap to the rotor. This is beneficial to a lower PM eddy current loss. For the electrical machine with ASYM II magnetic slot wedges, the local saturation is not such heavy; therefore the PM eddy current loss will be higher for high current situations. For the electrical machine adopting symmetrical magnetic slot wedges, the influence of local saturation is between two kinds of asymmetric magnetic slot wedges. That is why its loss value is between other two electrical machines.



(a) SYM



(b) ASYM I



(c) ASYM II

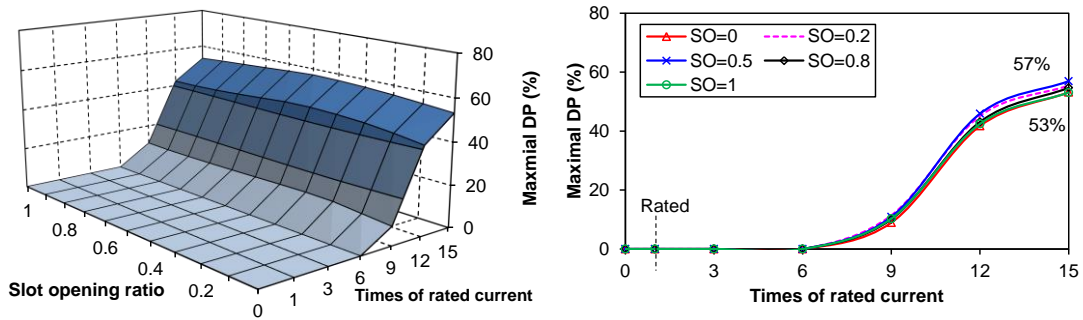
Fig. 7.13. Influence of magnetic slot wedges on rotor yoke eddy current loss.

The variation of rotor yoke eddy current loss shown in Fig. 7.14 is similar to that of PM eddy current loss, whereas there are still some differences. This is due to the influence of magnetic slot wedges on harmonics. All of PMs are isolated with each other, while there are no gaps in rotor yoke. Thus, the lower order harmonics will pass through the rotor yoke and the higher eddy current will be induced. However, the rotor yoke eddy current loss is still the smallest for the electrical machine with ASYM I magnetic slot wedges. The heavier local saturation prevents the harmonics inducing higher eddy current. For the electrical machine with ASYM II magnetic slot wedges, the small slot opening can also help filter some lower order harmonics, which contributes to a lower eddy current loss as well. The electrical machine with symmetrical magnetic slot wedges has the largest loss since most of harmonics will pass through the rotor yoke.

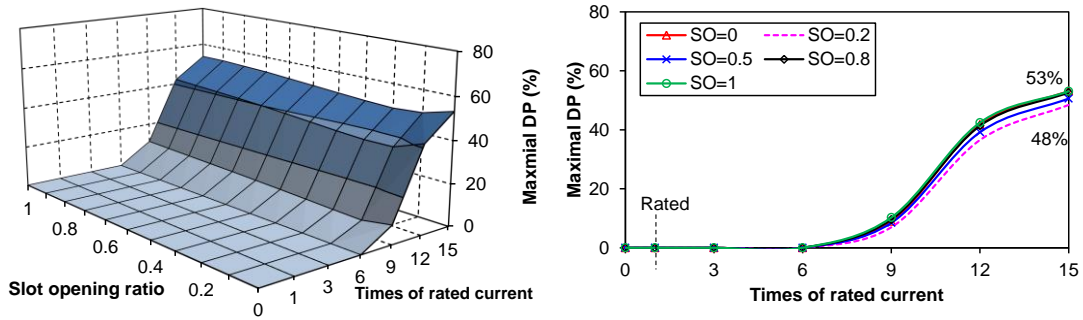
It must be addressed that the variation of iron losses in the electrical machines with ASYM I and ASYM II magnetic slot wedges will also be opposite if the rotor rotates in clockwise direction.

### 7.2.5 Demagnetisation

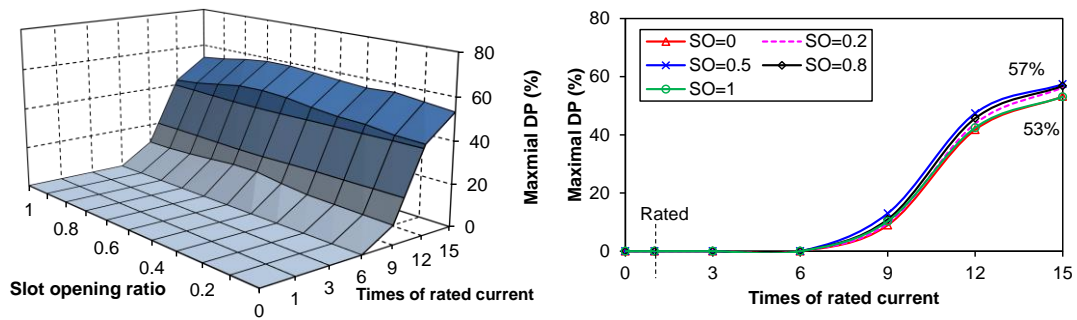
Since the magnetic slot wedges can affect the field distribution, the corresponding PM irreversible demagnetisation property will be changed as well. The analysis is also based on 180 °C situation, where the irreversible demagnetisation will happen if the parallel component of PM flux density is lower than knee point (around 0.3T) of PM demagnetisation curve. The influence of magnetic slot wedges and current on maximal DP is shown in Fig. 7.14.



(a) SYM



(b) ASYM I



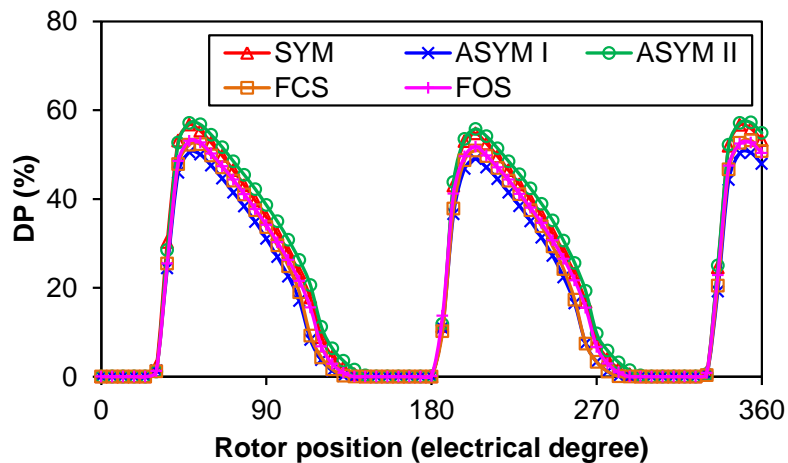
(c) ASYM II

Fig. 7.14. Influence of magnetic slot wedges on maximal DP.

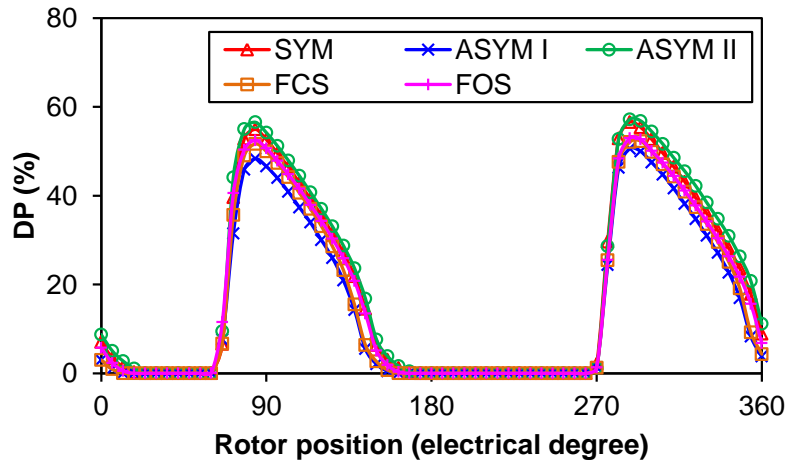
Fig. 7.14 shows that the modular machine with ASYM I magnetic slot wedges will enhance irreversible demagnetization withstand capability and this merit will be increasingly obvious with the increase of current. As has been stated above, the electrical machine with such kind of magnetic slot wedges will impede some harmonics penetrating to the PMs; and therefore the maximal DP will reduce as well. For the electrical machine using ASYM II magnetic slot wedges, the relatively large amount of harmonics will pass through the PMs and the PMs will be strongly demagnetised. If the SYM magnetic slot wedges are adopted, it combined the advantage and disadvantage of two kinds of asymmetric magnetic slot wedges. The

corresponding irreversible demagnetisation characteristic will be between other two cases as well.

The first and last PMs of segment 1 are chosen to show the DP variation with the rotor position, as shown in Fig. 7.15. It can be seen that the variation of DP will be a bit different for the electrical machines with different magnetic slot wedges. The difference of maximal DP has been clearly seen in Fig. 7.14, while the positions having these maximum are different for two sample PMs. For this electrical period, the first PM of segment 1 is always within the segments; and therefore the maximal DPs shift 150 electrical degrees, which is the same as the effective tooth-pitch. In contrast, the last PM of this segment will pass across the additional redundant tooth, which adds another 60 electrical degrees between two maximal DPs shown in Fig. 7.15(b). In fact, all of the PMs will experience such kind of DP variation when the machine operates. The saturation still plays the significant role in affecting irreversible demagnetisation.



(a) The first PM of segment 1



(b) The last PM of segment 1

Fig. 7.15. DP variation with the rotor position (Overload).

### 7.3 Conclusion

According to the results of electromagnetic performances shown in this chapter, some conclusions can be drawn as follows:

(1) The electrical machines with symmetrical magnetic slot wedges can have larger back-EMF than those with asymmetric magnetic slot wedges, since the saturation level in magnetic slot wedges is symmetrical. A smaller back-EMF THD is obtained if there are no magnetic slot wedges. This is due to the elimination of local saturation.

(2) Cogging torque is still minimal for fully closed slot machines, though it will obviously increase in large size electrical machines due to local saturation. For low current condition, the average torque variation is similar to open-circuit back-EMF variation and the cogging torque is predominant in torque fluctuation. If the current is increasingly high, the armature field will affect the variation of torque performance. The electrical machines with magnetic slot wedges still have higher output torque, whereas the PP torque ripple will be quite different for three kinds of magnetic slot wedges.

(3) The variation of the stator iron loss, PM eddy current loss and rotor yoke eddy current loss shows that the adoption of ASYM I magnetic slot wedges benefits to lower loss. This is different from the torque variation, where the electrical machines with ASYM II magnetic slot wedges have better performance. Since the interaction between PM and armature field is related with the rotation direction, the opposite

conclusion will be obtained for the ASYM I and ASYM II machines if the rotor reversely rotates.

Overall, the adoption of magnetic slot wedges will have both advantages and disadvantages and the different magnetic slot wedges show different effects. Its design must be determined according to the specific requirements.



## **Chapter 8 General Conclusions and Future Work**

### **8.1 General Conclusions**

Fractional-slot dual 3-phase modular PM machines with redundant teeth are investigated in this thesis. They mark a novel type of stator in the electrical machine research. The most significant advantage of this type of electrical machine is improving the manufacturability of large size electrical machines. Besides, other advantages can be summarised as follows.

#### **8.1.1 Novel Modular PM Machine Topologies**

The novel modular machine was put forward to solve the problem of easing the manufacture of large electrical machine stator core for electrical machines with all teeth wound non-overlapping windings. When electrical machines have large size stator core, such as the generators used in wind power and hydroelectric generation, they usually consist of several core segments for the sake of easy transportation and assembly. The modular stator cores of wind power generators have more stringent requirements. The stator windings and cores need to be assembled before transportation and the coils located at the end parts of each segment should be protected by adjacent stator teeth. Although the conventional all teeth wound dual 3-phase modular machines are the most promising electrical machines for this application, their stator cores cannot fulfil such requirements.

In order to solve this problem, the idea of combining the conventional all teeth wound dual 3-phase modular machine and a redundant electrical machine was put forward. The key process of obtaining such kind of novel modular machines has the following steps, as shown in Fig. 8.1 (Chapter 3).

It can be seen that the proposed modular machines have not only inherited the major structure properties of the conventional modular machines, but can be segmented in the centre of redundant teeth. This is beneficial to large size electrical machine stator core production. Based on the comparison with the counterpart modular machines, the proposed modular machines show comparable electromagnetic performances in most aspects. This means the proposed modular machines can be employed in real industry applications.

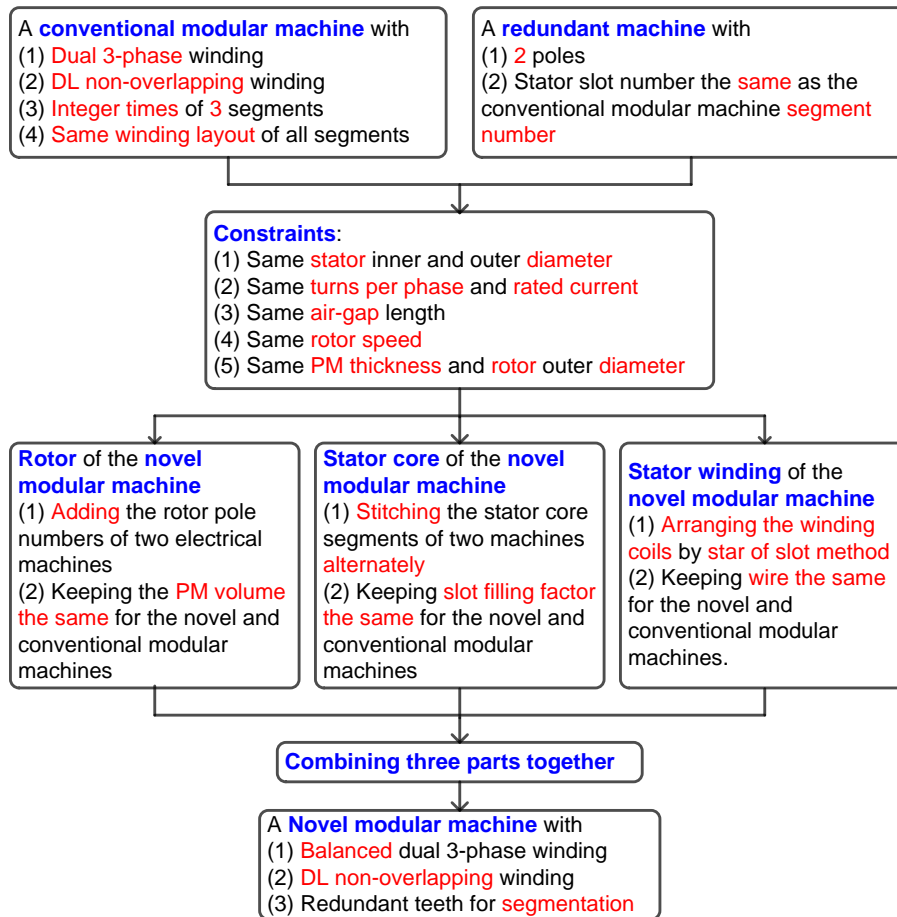


Fig. 8.1 Process of obtaining the novel modular machine.

### 8.1.2 Slot and Pole Number Combinations of Novel Modular Machines

In order to construct the novel dual 3-phase double layer modular machines with redundant teeth, some constraints on slot and pole number combinations must be satisfied, as discussed in Chapter 4:

(1) The slot and pole number combinations of the conventional modular machine ( $N_{sc}/N_{pc}$ ) should contain integer times of 3 basic electrical machine units.

(2) Each basic electrical machine unit can adopt dual 3-phase winding with 30 electrical degrees between two sets of windings.

(3) The slot number of the redundant machine ( $N_{sr}$ ) must guarantee that the EMF vectors of two coils are shifted 30 electrical degrees and it must be at least equal to 3.

(4) The pole number of the redundant machine ( $N_{pr}$ ) should be as small as possible to save space and its minimal value is limited to 2.

(5) The undesirable UMF can be eliminated when the stator segment number ( $N_{seg}$ ) is even and  $N_{seg}$  can be determined according to the minimal repetition number of the basic electrical machine unit ( $t_c$ ).

(6) The slot and pole numbers of the proposed modular machines equal the summation of the corresponding stator and pole numbers of the conventional modular machines and redundant machines.

According to the above conditions, the available slot and pole number combinations are listed in TABLE 8.1.

TABLE 8.1 SUMMARY OF SLOT AND POLE NUMBER COMBINATIONS FOR NOVEL MODULAR MACHINES

$N_{sc}/3n$	$N_{pc}/3n$	$K_{wc}$	$t_c/3n$	$N_{sc}/t_c$	$N_{sr} (N_{seg})$	$N_{pp}$	$N_{sp}$
<b>12</b>	<b>10</b>	<b>0.9659</b>	<b>1</b>	<b>12</b>	<b>3,6</b>	<b>32</b>	<b>39,42</b>
	<b>14</b>	<b>0.9659</b>	<b>1</b>	<b>12</b>	<b>3,6</b>	<b>44</b>	<b>39,42</b>
24	20	0.9659	2	12	3,6,12	62	75,78,84
	22	0.9830	1	24	3,6	68	75,78
	26	0.9830	1	24	3,6	80	75,78
	28	0.9659	2	12	3,6,12	86	75,78,84
36	30	0.9659	3	12	3,6	92	111,114
	34	0.9861	1	36	3,6	104	111,114
	38	0.9861	1	36	3,6	116	111,114
	42	0.9659	3	12	3,6	128	111,114
48	40	0.9659	4	12	3,6,12	122	147,150,156
	44	0.9830	2	24	3,6,12	134	147,150,156
	46	0.9872	1	48	3,6	140	147,150
	50	0.9872	1	48	3,6	152	147,150
	52	0.9830	2	24	3,6,12	158	147,150,156
	56	0.9659	4	12	3,6,12	170	147,150,156
60	50	0.9659	5	12	3,6	152	183,188
	58	0.9877	1	60	3,6	176	183,188
	62	0.9877	1	60	3,6	188	183,188
	70	0.9659	5	12	3,6	212	183,188

The four prototyped machines in red in TABLE 8.1 were analysed in Chapter 4. According to the electromagnetic performance comparison, some conclusions can be drawn:

(1) The fundamental components of phase back-EMF are higher for the proposed modular machines with higher pole number than slot number. Thus, the on-load average torque is also larger.

(2) Since the least common multiple is higher for the proposed modular machines with higher pole number than slot number, cogging torque is lower. The on-load torque ripple is lower for this kind of electrical machine as well.

(3) Stator iron loss, PM and rotor yoke eddy current losses are all lower for the proposed modular machines with lower pole number than slot number. For stator iron loss, the frequency is the major reason when all of the electrical machines have the same rotation speed. The more abundant harmonics contribute to the higher PM and rotor yoke eddy current losses for the proposed modular machines with higher pole number than slot number.

(4) Due to the less lower order harmonics, the proposed modular machines with lower pole number than slot number are more robust against irreversible demagnetisation.

(5) Since the proposed modular machines consisting from the same basic electrical machine unit show similar performances, the even segment number is preferable to get rid of UMF.

### **8.1.3 Comparison of Different Modular Machines**

In order to more clearly identify the advantages and disadvantages of the novel topology, the electromagnetic performances of different modular machines are compared, respectively.

Since the proposed modular machine is obtained from its counterpart conventional modular machine, the comparison between these two electrical machines is shown in TABLE 8.2 (Chapter 3) firstly. This table shows that the proposed modular machine has comparable performance with the conventional modular machine, although some spaces are wasted for accommodating redundant teeth to ease stator manufacture process. For the proposed modular machine itself, two kinds of dual 3-phase windings (Thirty and Zero types, respectively) can be adopted and the comparison of these two electrical machines is shown in TABLE 8.3 (Chapter 4). It is clearly seen that the adoption of the Thirty type performs better than the Zero type in almost all of electromagnetic performances. When the proposed modular machines are compared with the modular machines having overlapping windings, the Thirty and Zero types can be analysed separately, as shown in TABLEs 8.4 and 8.5. When the Thirty type is

considered, the electromagnetic performances are similar in terms of torque, while the investigated electrical machine with overlapping windings have much lower rotor eddy current loss and is less sensitive to be irreversibly demagnetised (Chapter 5). However, the proposed modular machines show better faulty operation performances no matter the other sets of winding is open-circuit (OC) or short-circuit (SC) in respect of induced voltage and torque. Similar conclusion can be drawn for the modular machines with overlapping/non-overlapping Zero type dual 3-phase windings (Chapter 6). Furthermore, the torque ripple is always lower for the proposed modular machines regardless of operating under normal or faulty situations.

Overall, the proposed modular machine has its own advantages and disadvantages and its employment must be determined according to the specific requirements.

TABLE 8.2 COMPARISON OF PROPOSED AND CONVENTIONAL MODULAR MACHINES

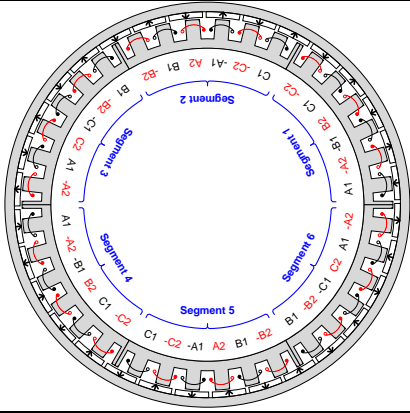
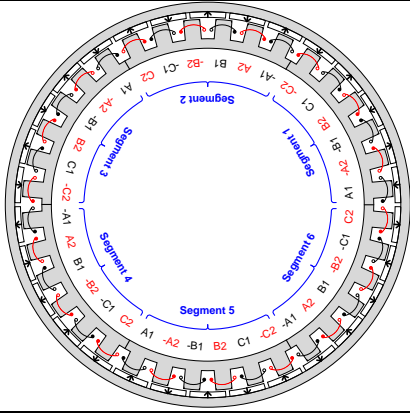
$N_s/N_p$	42S/32P	36S/30P
Cross-sections		
Windings	Dual 3-phase all teeth wound fractional-slot; 30 degree phase shift between two sets of windings; Set 1 30 degrees lag referring to Set 2 in space	
$K_w$	0.9659	
Segment number	6	
Air-gap flux density	Lower $B_{r1m}$ for PM field; More harmonics for PM field; Lower $B_{r1m}$ for armature field; More harmonics for armature field;	Higher $B_{r1m}$ for PM field; Less harmonics for PM field; Higher $B_{r1m}$ for armature field; Less harmonics for armature field;
Back-EMF	Sinusoidal waveforms; Balanced two sets of windings; Slightly lower $E_{1m}$ ; Slightly higher THD	Sinusoidal waveforms; Balanced two sets of windings; Slightly higher $E_{1m}$ ; Slightly lower THD
Cogging torque	6 fluctuations per period; Higher PP torque ripple	12 fluctuations per period; Lower PP torque ripple
Average torque	Slightly lower value for low current; Slightly faster saturated; A bit lower value for high current	Slightly higher value for low current; Slightly slower saturated; A bit higher value for high current
On-load torque ripple	High	Low
Iron losses	A bit higher $P_{si}$ ; Lower $P_{PM}$ ; Higher $P_{ry}$	A bit lower $P_{si}$ ; Higher $P_{PM}$ ; Lower $P_{ry}$
Demagnetisation	Same maximal DP; Different DP variation for each PM	Same maximal DP; Same DP variation for each PM

TABLE 8.3 COMPARISON OF PROPOSED MODULAR MACHINES WITH DIFFERENT SHIFTS

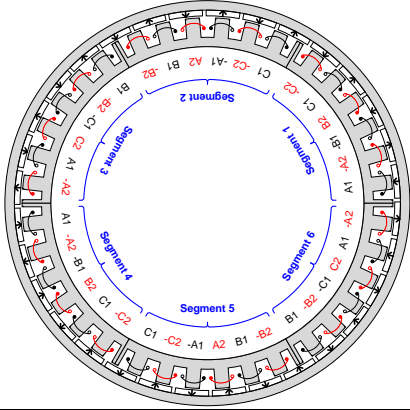
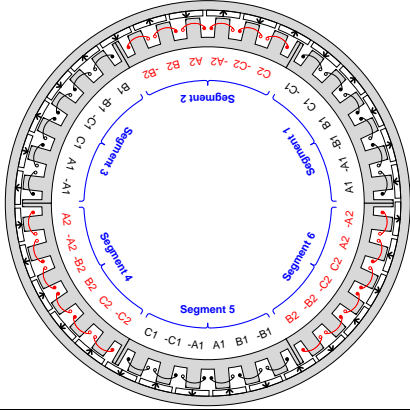
$N_s/N_p$	42S/32P	
Windings	Dual 3-phase; All teeth wound fractional-slot; 30 degree phase shift between two sets of windings; Set 2 30 degrees ahead in space	Dual 3-phase; All teeth wound fractional-slot; Zero degree phase shift between two sets of windings; Set 1 and 2 coinciding in space
Cross-sections		
$K_w$	0.9659	0.9330
Segment number	6	
Air-gap flux density	Same PM field; Higher $B_{r1m}$ for armature field; Lower magnitude harmonics for armature field	Same PM field; Lower $B_{r1m}$ for armature field; Higher magnitude harmonics for armature field
Back-EMF	Sinusoidal waveforms; Balanced two sets of windings; Higher $E_{1m}$ ; Higher THD	Sinusoidal waveforms; Balanced two sets of windings; Lower $E_{1m}$ ; Lower THD
Cogging torque	Same	
Average torque	Slightly higher value for low current; Slightly slower saturated; A bit higher value for high current	Slightly lower value for low current; Slightly faster saturated; A bit lower value for high current
On-load torque ripple	Low	High
Iron losses	Practically the same $P_{si}$ ; Practically the same $P_{PM}$ ; Lower $P_{ry}$	Practically the same $P_{si}$ ; Practically the same $P_{PM}$ ; Higher $P_{ry}$
Demagnetisation	Lower maximal DP; Different DP variation for each PM	Higher maximal DP; Different DP variation for each PM

TABLE 8.4 COMPARISON OF THIRTY TYPE MODULAR MACHINES

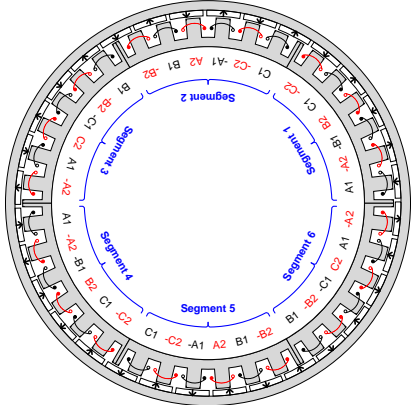
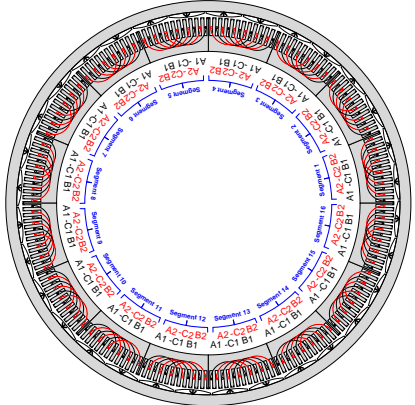
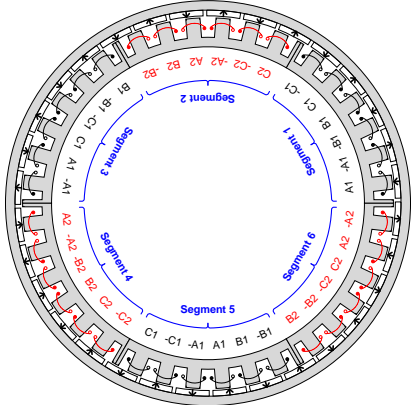
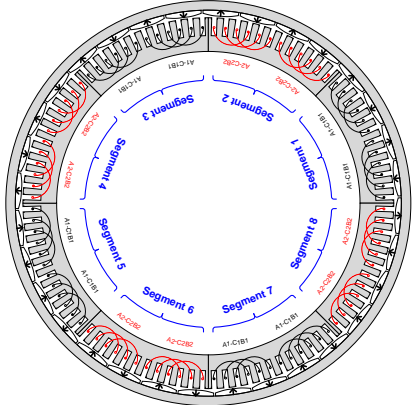
$N_s/N_p$	42S/32P	192S/32P
Windings	Dual 3-phase; All teeth wound fractional-slot; 30 degree phase shift between two sets of windings; Set 1 30 degrees lag in space	Dual 3-phase; Overlapping integer-slot; 30 degree phase shift between two sets of windings; Set 1 30 degrees ahead in space
Cross-sections		
$K_w$	0.9659	1
Segment number	6	16
Air-gap flux density	Slightly lower $B_{r1m}$ for PM field; More harmonics for PM field; Lower $B_{r1m}$ for armature field; Much more harmonics for armature field;	Slight higher $B_{r1m}$ for PM field; Less harmonics for PM field; Higher $B_{r1m}$ for armature field; Much less harmonics for armature field;
Back-EMF	Sinusoidal waveforms; Balanced two sets of windings; Lower $E_{1m}$ ; Lower THD	Trapezoidal waveforms; Balanced two sets of windings; Higher $E_{1m}$ ; Higher THD
Cogging torque	6 fluctuations per period; Similar PP torque ripple	12 fluctuations per period; Similar PP torque ripple
Average torque	A bit lower value for low current; Slightly faster saturated; Lower value for high current	A bit higher value for low current; Slightly slower saturated; Higher value for high current
On-load torque ripple	Similar	Similar
Iron losses	Lower $P_{si}$ ; Higher $P_{PM}$ ; Higher $P_{ry}$	Higher $P_{si}$ ; Negligible $P_{PM}$ ; Negligible $P_{ry}$
Demagnetisation	Larger maximal DP; Different DP variation for each PM	Lower maximal DP; Same DP variation for each PM
OC Fault for Set 2 winding	Less distorted terminal voltage A bit lower torque Lower PP torque ripple	More distorted terminal voltage A bit larger torque Higher PP torque ripple
SC Fault for Set 2 winding	Less distorted terminal voltage; Smaller short-circuit current; Smaller braking torque; Lower PP torque ripple	More distorted terminal voltage; Larger short-circuit current; Larger braking torque; Higher PP torque ripple



TABLE 8.5 COMPARISON OF ZERO TYPE MODULAR MACHINES

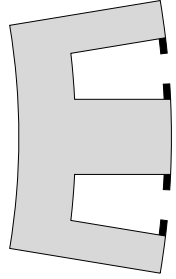
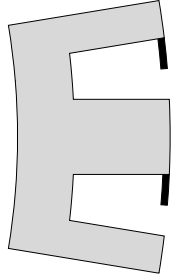
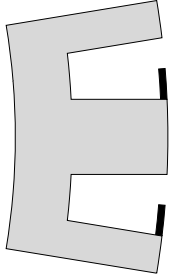
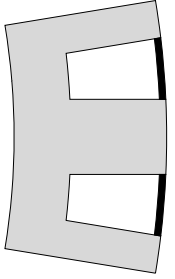
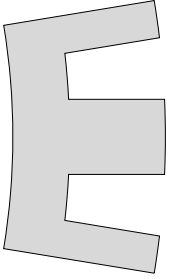
$N_s/N_p$	42S/32P	96S/32P
Windings	Dual 3-phase; All teeth wound fractional-slot; zero degree phase shift between two sets of windings; Set 1 and 2 coinciding in space	Dual 3-phase; Overlapping integer-slot; zero degree phase shift between two sets of windings; Set 1 and 2 coinciding in space
Cross-sections		
$K_w$	0.9330	1
Segment number	6	8
Air-gap flux density	Slightly higher $B_{r1m}$ for PM field; More harmonics for PM field; Lower $B_{r1m}$ for armature field; Much more harmonics for armature field;	Slight lower $B_{r1m}$ for PM field; Less harmonics for PM field; Higher $B_{r1m}$ for armature field; Much less harmonics for armature field;
Back-EMF	Sinusoidal waveforms; Balanced two sets of windings; Lower $E_{1m}$ ; Lower THD	Trapezoidal waveforms; Balanced two sets of windings; Higher $E_{1m}$ ; Higher THD
Cogging torque	6 fluctuations per period; Lower PP torque ripple	6 fluctuations per period; Higher PP torque ripple
Average torque	Lower value for low current; Slightly slower saturated; A bit lower value for high current	Higher value for low current; Slightly faster saturated; A bit higher value for high current
On-load torque ripple	Lower	Higher
Iron losses	Lower $P_{si}$ ; Higher $P_{PM}$ ; Higher $P_{ry}$	Higher $P_{si}$ ; Negligible $P_{PM}$ ; Negligible $P_{ry}$
Demagnetisation	Larger maximal DP; Different DP variation for each PM	Lower maximal DP; Same DP variation for each PM
OC Fault for Set 2 winding	Less distorted terminal voltage A bit lower torque Much lower PP torque ripple	More distorted terminal voltage A bit larger torque Much higher PP torque ripple
SC Fault for Set 2 winding	Balanced voltage among phases; Less distorted terminal voltage; Smaller short-circuit current; Smaller braking torque; Much lower PP torque ripple	Unbalanced voltage among phases; More distorted terminal voltage; Larger short-circuit current; Larger braking torque; Much higher PP torque ripple

#### **8.1.4 Influence of Magnetic Slot Wedges**

Although fully open slots are used in large size electrical machines for simplifying the stator manufacture, magnetic slot wedges can be used for improving electromagnetic performances. Five typical magnetic slot wedges were compared in Chapter 7 with the Thirty type 42S/32P machine. The major influence on performances is summarised in TABLE 8.6.

The level of each quantity is graded for easily making comparison. It is clear that the adoption of SYM magnetic slot wedges can obtain the highest average torque. Besides, it also has the lowest PM and rotor yoke eddy current loss with low current. The ASYNM I magnetic slot wedges are beneficial to lower PP torque ripple, PM and rotor yoke eddy current losses under high current condition. Although there are no benefits being observed by using ASYM II magnetic slot wedges, the conclusion between two kinds of asymmetric magnetic slot wedges will be exchanged if the rotation direction or operation mode is changed. When the fully closed slots are used, the maximal fundamental air-gap flux density can be obtained. The lowest cogging torque and PP torque ripple under low current condition come from the smooth permeance variation. In contrast, the fully open slots can reduce back-EMF harmonics and have the lowest stator iron loss.

TABLE 8.6 COMPARISON OF DIFFERENT MAGNETIC SLOT WEDGES

Type	SYM	ASYM I	ASYM II	FCS	FOS
Shape					
$B_{r1m}$	2	4	3	<b>1<sup>a</sup></b>	<b>5<sup>a</sup></b>
$E_{1m}$	<b>1</b>	3	2	5	4
THD	4	3	2	1	<b>5</b>
$T_{cogPP}$	2	3	4	<b>5</b>	1
$T_{avg}$	$R^b$	<b>1</b>	2	3	4
	$O^b$	<b>1</b>	3	2	4
$T_{PP}$	$R$	2	3	4	<b>5</b>
	$O$	3	<b>5</b>	4	1
$P_{Fe}$	$R$	3	2	4	1
	$O$	3	2	4	1
$P_{PM}$	$R$	<b>5</b>	2	3	4
	$O$	3	<b>5</b>	2	4
$P_{ry}$	$R$	<b>5</b>	2	3	4
	$O$	2	<b>5</b>	3	4
$DP$	1	<b>5</b>	1	3	4

<sup>a</sup> 1 and 5 represent the largest and smallest values, respectively

<sup>b</sup>  $R$  and  $O$  represent the rated and overload conditions, respectively

## 8.2 Future Work

Based on the content of this thesis, some future work is listed:

(1) More detailed work can be done. Firstly, irreversible demagnetisation of PMs under various kinds of faulty operations should be investigated, together with the experimental verifications. Then, the scalability between small size 3kW machine and 3MW large size machine can be investigated, which is useful for large machine investigation. Furthermore, there are unavoidable manufacture tolerances during the production process since the stator consists of several segments. The influence of these imperfections on electrical machine performance may be significant for real applications. Last but not least, more systematic investigation on faulty operations under different faults is useful for evaluating the machine fault-tolerant performance.

(2) Because of the surfaced-mounted PM rotor, the analytical model can be established by using the precise Subdomain method. With the help of the analytical model, the optimisation will be much easier. As the superposition method has been proposed for rotor eccentricity analysis and its efficacy is validated in small size PM machines, this method can be also employed to the proposed modular machines.

(3) Only dual 3-phase is considered in this thesis. In fact, this idea of constructing modular machines with redundant teeth can be used for different phase numbers. Then, the corresponding slot and pole number combinations can be extended as well.

## References

- [ABB84] M. A. Abbas, R. Christen, and T. M. Jahns, "Six-phase voltage source inverter driven induction motor," *IEEE Trans. Ind. Appl.*, vol. 16, no. 3, pp. 1251-1259, May/June 1984.
- [ABD16a] A. S. Abdel-Khalik, S. Ahmed, and A. M. Massoud, "Effect of multilayer windings with different stator winding connections on interior PM machines for EV applications," *IEEE Trans. Magn.*, vol. 52, no. 2, pp. 1-7, Feb. 2016.
- [ABD16b] A. S. Abdel-Khalik, S. Ahmed, and A. M. Massoud, "A six-phase 24-slot/10-pole permanent-magnet machine with low space harmonics for electric vehicle applications," *IEEE Trans. Magn.*, vol. 52, no. 6, pp. 1-10, June 2016.
- [ACK92] B. Ackermann, J. H. H. Janssen, R. Sottek, and R. I. van Steen, "New technique for reducing cogging torque in a class of brushless DC motors," *Proc. Inst. Elect. Eng. B*, vol. 139, no. 4, pp. 315-320, 1992.
- [AKI03] H. Akita, Y. Nakahara, N. Miyake, and T. Oikawa, "New core structure and manufacturing method for high efficiency of permanent magnet motors," in *Conf. Rec. IEEE IAS Annu. Meeting*, Oct. 12-16, 2003, pp. 367-372.
- [ALB10] L. Alberti, and N. Bianchi, "Impact of winding arrangement in dual 3-phase induction motor for fault tolerant applications," in *19th International Conference on Electrical Machines (ICEM 2010)*, Sept. 6-8, 2010, pp. 1-6.
- [ALB12] L. Alberti, and N. Bianchi, "Experimental tests of dual three-phase induction motor under faulty operating condition," *IEEE Trans. Ind. Electron.*, vol. 59, no. 5, pp. 2041-2048, May 2012.
- [ALB13] L. Alberti, and N. Bianchi, "Theory and design of fractional-slot multilayer windings," *IEEE Trans. Ind. Appl.*, vol. 49, no. 2, pp. 841-849, Mar./Apr. 2013.
- [ALG30] P. L. Alger, E. H. Freiburghouse, and D. D. Chase, "Double windings for turbine alternators," *AIEE Trans.*, vol. 49, no. 1, pp. 226-244, Jan. 1930.
- [AND09] M. Andriollo, G. Bettanini, G. Martinelli, A. Morini, and A. Tortella, "Analysis of double-star permanent-magnet synchronous generators by a general decoupled d-q model," *IEEE Trans. Ind. Appl.*, vol. 45, no. 4, pp. 1416-1424, July/Aug. 2009.
- [ATA03] K. Atallah, J. B. Wang, and D. Howe, "Torque-ripple minimization in modular permanent-magnet brushless machines," *IEEE Trans. Ind. Appl.*, vol. 39, no. 6, pp. 1689-1695, Nov./Dec. 2003.
- [ATK06] G. J. Atkinson, B. C. Mecrow, A. G. Jack, D. J. Atkinson, P. Sangha, and M. Benarous, "The analysis of losses in high-power fault-tolerant machines for aerospace applications," *IEEE Trans. Ind. Appl.*, vol. 42, no. 5, pp. 1162-1170, Sept./Oct. 2006.
- [BAK18] N. J. Baker, D. J. B. Smith, M. C. Kulan, and S. Turvey, "Design and performance of a segmented stator permanent magnet alternator for

- aerospace,” *IEEE Trans. Energy Convers.*, vol. 33, no. 1, pp. 40-48, Mar. 2018.
- [BAR09] M. Barcaro, N. Bianchi, and F. Magnussen, “Configurations of fractional-slot IPM motors with dual three-phase winding,” in *IEEE International Electric Machines and Drives Conference (IEMDC 2009)*, May 3-6, 2009, pp. 936-942.
- [BAR10] M. Barcaro, N. Bianchi, and F. Magnussen, “Analysis and tests of a dual three-phase 12-slot 10-pole permanent-magnet motor,” *IEEE Trans. Ind. Appl.*, vol. 46, no. 6, pp. 2355-2362, Nov./Dec. 2010.
- [BAR11a] M. Barcaro, N. Bianchi, and F. Magnussen, “Faulty operations of a PM fractional-slot machine with a dual three-phase winding,” *IEEE Trans. Ind. Electron.*, vol. 58, no. 9, pp. 3825-3832, Sept. 2011.
- [BAR11b] M. Barcaro, N. Bianchi, and F. Magnussen, “Six-phase supply feasibility using a PM fractional-slot dual winding machine,” *IEEE Trans. Ind. Appl.*, vol. 47, no. 5, pp. 2042-2050, Sept./Oct. 2011.
- [BAR12] M. Barcaro, A. Faggion, N. Bianchi, and S. Bolognani, “sensorless rotor position detection capability of a dual three-phase fractional-slot IPM machine,” *IEEE Trans. Ind. Appl.*, vol. 48, no. 6, pp. 2068-2078, Nov./Dec. 2012.
- [BAR13] O. d. I. Barriere, H. B. Ahmed, M. Gabsi, and M. LoBue, “Two-dimensional analytical airgap field model of an inset permanent magnet synchronous machine, taking into account the slotting effect,” *IEEE Trans. Magn.*, vol. 49, no. 4, pp. 1423-1435, Apr. 2013.
- [BAR16] F. Barrero, and M. J. Duran, “Recent advances in the design, modeling, and control of multiphase machines part I,” *IEEE Trans. Ind. Electron.*, vol. 63, no. 1, pp. 449-458, Jan. 2016.
- [BEK16] N. Bekka, M. E. H. Zaim, N. Bernard, and D. Trichet, “A novel methodology for optimal design of fractional slot with concentrated windings,” *IEEE Trans. Energy Convers.*, vol. 31, no. 3, pp. 1153-1160, Sept. 2016.
- [BI96] C. Bi, Z. J. Liu, and T. S. Low, “Analysis of unbalanced-magnetic-pulls in hard disk drive spindle motors using a hybrid method,” *IEEE Trans. Magn.*, vol. 32, no. 5, pp. 4308-4310, Sept. 1996.
- [BI97] C. Bi, Z. J. Liu, and T. S. Low, “Effects of unbalanced magnetic pull in spindle motors,” *IEEE Trans. Magn.*, vol. 33, no. 5, pp. 4080-4082, Sept. 1997.
- [BI09] C. Bi, H. N. Phyu, and Q. Jiang, “Unbalanced magnetic pull induced by leading wires of permanent magnet synchronous motor,” in *International Conference on Electrical Machines and Systems (ICEMS 2009)*, Nov. 15-18, 2009, pp. 1-5.
- [BIA98] N. Bianchi, and S. Bolognani, “Magnetic models of saturated interior permanent magnet motors based on finite element analysis,” in *Conf. Rec. IEEE IAS Annu. Meeting*, Oct. 12-15, 1998, pp. 27-34.

- [BIA05] N. Bianchi, Pre, x, M. D., G. Grezzani, and S. Bolognani, "Design considerations on fractional-slot fault-tolerant synchronous motors," in *IEEE International Conference on Electric Machines and Drives (IEMDC 2005)*, May 15, 2005, pp. 902-909.
- [BIA06a] N. Bianchi, and M. Dai Prè, "Use of the star of slots in designing fractional-slot single-layer synchronous motors," *IEE Proc.-Electr. Power Appl.*, vol. 153, no. 3, pp. 459-466, May 2006.
- [BIA06b] N. Bianchi, S. Bolognani, and P. Frare, "Design criteria for high-efficiency SPM synchronous motors," *IEEE Trans. Energy Convers.*, vol. 21, no. 2, pp. 396-404, June 2006.
- [BIA06c] N. Bianchi, M. D. Pre, and S. Bolognani, "Design of a fault-tolerant IPM motor for electric power steering," *IEEE Trans. Veh. Technol.*, vol. 55, no. 4, pp. 1102-1111, July 2006.
- [BIA06d] N. Bianchi, M. D. Prè G. Grezzani, and S. Bolognani, "Design considerations on fractional-slot fault-tolerant synchronous motors," *IEEE Trans. Ind. Appl.*, vol. 42, no. 4, pp. 997-1006, July/Aug. 2006.
- [BIA08] N. Bianchi, S. Bolognani, Pre, x, and M. D., "Magnetic loading of fractional-slot three-phase pm motors with nonoverlapped coils," *IEEE Trans. Ind. Appl.*, vol. 44, no. 5, pp. 1513-1521, Sept./Oct. 2008.
- [BIA09] N. Bianchi, and E. Fornasiero, "Impact of MMF space harmonic on rotor losses in fractional-slot permanent-magnet machines," *IEEE Trans. Energy Convers.*, vol. 24, no. 2, pp. 323-328, June 2009.
- [BIA10] N. Bianchi, S. Bolognani, and E. Fornasiero, "An overview of rotor losses determination in three-phase fractional-slot PM machines," *IEEE Trans. Ind. Appl.*, vol. 46, no. 6, pp. 2338-2345, Nov./Dec. 2010.
- [BOA14] B. Boazzo, G. Pellegrino, and A. Vagati, "Multipolar SPM machines for direct-drive application a general design approach," *IEEE Trans. Ind. Appl.*, vol. 50, no. 1, pp. 327-337, Jan./Feb. 2014.
- [BOL14] I. Boldea, L. Tutelea, and F. Blaabjerg, "High power wind generator designs with less or no PMs: An overview," in *International Conference on Electrical Machines and Systems (ICEMS2014)*, Oct. 22-25, 2014, pp. 1-14.
- [BOW75] B. Bowers, "The early history of electric motor," *Philips Technical Review*, vol. 35, no. 4, pp. 77-95, 1975.
- [BUR11] T. A. Burress, S. L. Campbell, C. L. Coomer, C. W. Ayers, A. A. Wereszczak, et al. "Evaluation of the 2010 Toyota Prius hybrid synergy drive system," *Oak Ridge National Laboratory (ORNL)*, Power Electronics and Electric Machinery Research Facility, 2011.
- [CAO12a] R. W. Cao, M. Cheng, C. Mi, W. Hua, W. Xin, and W. X. Zhao, "Modeling of a complementary and modular linear flux-switching permanent magnet motor for urban rail transit applications," *IEEE Trans. Energy Convers.*, vol. 27, no. 2, pp. 489-497, June 2012.
- [CAO12b] W. P. Cao, B. C. Mecrow, G. J. Atkinson, J. W. Bennett, and D. J. Atkinson, "Overview of electric motor technologies used for more electric

- aircraft (MEA),” *IEEE Trans. Ind. Electron.*, vol. 59, no. 9, pp. 3523-3531, Sept. 2012.
- [CHA04] T. F. Chan, L. L. Lai, and Y. Lie-Tong, “Performance of a three-phase AC generator with inset NdFeB permanent-magnet rotor,” *IEEE Trans. Energy Convers.*, vol. 19, no. 1, pp. 88-94, Mar. 2004.
- [CHA07] J. Chai, J. B. Wang, K. Atallah, and D. Howe, “Performance comparison and winding fault detection of duplex 2.phase and 3.phase fault-tolerant permanent magnet brushless machines,” in *Conf. Rec. IEEE IAS Annu. Meeting*, Sept. 23-27, 2007, pp. 566-572.
- [CHE95] Z. Chen, and E. Spooner, “A modular, permanent-magnet generator for variable speed wind turbines,” in *7th International Conference on Electrical Machines and Drives*, Sept. 11-24, 1995, pp. 453-457.
- [CHE00a] Y. S. Chen, “Motor Topologies and Control Strategies for Permanent Magnet Brushless AC Drives,” PhD thesis, the University of Sheffield, 2000.
- [CHE00b] J. Y. Chen, C. V. Nayar, and L. Y. Xu, “Design and finite-element analysis of an outer-rotor permanent-magnet generator for directly coupled wind turbines,” *IEEE Trans. Magn.*, vol. 36, no. 5, pp. 3802-3809, Sept. 2000.
- [CHE05] Y. C. Chen, P. Pillay, and A. Khan, “PM wind generator topologies,” *IEEE Trans. Ind. Appl.*, vol. 41, no. 6, pp. 1619-1626, Nov./Dec.2005.
- [CHE08] Y. G. Chen, Z. M. Du, W. G. Zhong, and L. B. Kong, “Modular stator structure permanent magnet synchronous machine,” in *World Automation Congress (WAC 2008)*, Sep. 28-Oct.2, 2008, pp. 1-5.
- [CHE09] Z. Chen, J. M. Guerrero, and F. Blaabjerg, “A review of the state of the art of power electronics for wind turbines,” *IEEE Trans. Power Electron.*, vol. 24, no. 8, pp. 1859-1875, Aug. 2009.
- [CHE10a] J. T. Chen, and Z. Q. Zhu, “Comparison of all- and alternate-poles-wound flux-switching PM machines having different stator and rotor pole numbers,” *IEEE Trans. Ind. Appl.*, vol. 46, no. 4, pp. 1406-1415, July/Aug. 2010.
- [CHE10b] J. T. Chen, and Z. Q. Zhu, “Winding configurations and optimal stator and rotor pole combination of flux-switching PM brushless AC machines,” *IEEE Trans. Energy Convers.*, vol. 25, no. 2, pp. 293-302, June 2010.
- [CHE11] M. Chen, W. Hua, J. Z. Zhang, and W. X. Zhao, “Overview of stator-permanent magnet brushless machines,” *IEEE Trans. Ind. Electron.*, vol. 58, no. 11, pp. 5087-5101, Nov. 2011.
- [CHE14a] X. Chen, J. B. Wang, and V. I. Patel, “A generic approach to reduction of magnetomotive force harmonics in permanent-magnet machines with concentrated multiple three-phase windings,” *IEEE Trans. Magn.*, vol. 50, no. 11, pp. 1-4, Nov. 2014.
- [CHE14b] M. Cheng, and Y. Zhu, “The state of the art of wind energy conversion systems and technologies: A review,” *Energy Conversion and Management*, vol. 88, pp. 332-347, 2014.



- [CHE16] X. Chen, J. B. Wang, V. I. Patel, and P. Lazari, "A nine-phase 18-slot 14-pole interior permanent magnet machine with low space harmonics for electric vehicle applications," *IEEE Trans. Energy Convers.*, vol. 31, no. 3, pp. 860-871, Sept. 2016.
- [CHE17] M. Cheng, P. Han, and W. Hua, "A general airgap field modulation theory for electrical machines," *IEEE Trans. Ind. Electron.*, vol. 64, no. 8, pp. 6063-6074, Aug. 2017.
- [CHO10] J. H. Choi et al., "Design of high power permanent magnet motor with segment rectangular copper wire and closed slot opening on electric vehicles," *IEEE Trans. Magn.*, vol. 46, no. 6, pp. 2070-2073, June 2010.
- [CHU12] T. Chun, W. L. Soong, G. S. Liew, and N. Ertugrul, "Effect of pole and slot number changes on the performance of a surface PM machine," in *20th International Conference on Electrical Machines (ICEM 2012)*, Sept. 2-5, 2012, pp. 220-227.
- [CHU13a] W. Q. Chu, and Z. Q. Zhu, "Average torque separation in permanent magnet synchronous machines using frozen permeability," *IEEE Trans. Magn.*, vol. 49, no.3, pp. 1202-1210, Mar. 2013.
- [CHU13b] W. Q. Chu, and Z. Q. Zhu, "Investigation of torque ripples in permanent magnet synchronous machines with skewing," *IEEE Trans. Magn.*, vol. 49, no.3, pp. 1211-1220, Mar. 2013.
- [CHU13c] W. Q. Chu, and Z. Q. Zhu, "Reduction of on-load torque ripples in permanent magnet synchronous machines by improved skewing," *IEEE Trans. Magn.*, vol. 49, no.7, pp. 3822-3825, July 2013.
- [CHU16] S. U. Chung, S. H. Moon, D. J. Kim, and J. M. Kim, "Development of a 20-pole-24-slot SPMSM with consequent pole rotor for in-wheel direct drive," *IEEE Trans. Ind. Electron.*, vol. 63, no. 1, pp. 302-309, Jan. 2016.
- [CIS10a] M. V. Cistelecan, F. J. T. E. Ferreira, and M. Popescu, "Three phase tooth-concentrated interspersed windings with low space harmonic content," in *19th International Conference on Electrical Machines (ICEM 2010)*, Sept. 6-8, 2010, pp. 1-6.
- [CIS10b] M. V. Cistelecan, F. J. T. E. Ferreira, and M. Popescu, "Three phase tooth-concentrated multiple-layer fractional windings with low space harmonic content," in *IEEE Energy Conversion Congress and Exposition (ECCE 2010)*, Sept. 12-16, 2010, pp. 1399-1405.
- [CRO02] J. Cros, and P. Viarouge, "Synthesis of high performance PM motors with concentrated windings," *IEEE Trans. Energy Convers.*, vol. 17, no. 2, pp. 248-253, June 2002.
- [DAJ11] G. Dajaku, and D. Gerling, "A novel 24-slots/10-poles winding topology for electric machines," in *IEEE International Electric Machines and Drives Conference (IEMDC 2011)*, May 15-18, 2011, pp. 65-70.
- [DAJ12a] G. Dajaku, and D. Gerling, "A novel 12-teeth/10-poles PM machine with flux barriers in stator yoke," in *20th International Conference on Electrical Machines (ICEM 2012)*, Sept. 2-5, 2012, pp. 36-40.

- [DAJ12b] G. Dajaku, and D. Gerling, “Low costs and high-efficiency electric machines,” in *2nd International Conference on Electric Drives Production, (EDPC 2012)*, Oct. 15-18, 2012, pp. 1-7.
- [DAJ13] G. Dajaku, “Elektrische Maschine,” German patent application No. DE 102011 011023.2.
- [DAJ14] G. Dajaku, W. Xie, and D. Gerling, “Reduction of low space harmonics for the fractional slot concentrated windings using a novel stator design,” *IEEE Trans. Magn.*, vol. 50, no. 5, pp. 1-12, May 2014.
- [DI15] C. Di, X. H. Bao, H. F. Wang, Q. Lv, and Y. G. He, “Modeling and analysis of unbalanced magnetic pull in cage induction motors with curved dynamic eccentricity,” *IEEE Trans. Magn.*, vol. PP, no. 99, pp. 1-7, Mar. 2015.
- [DOR96] D. G. Dorrell, “Calculation of unbalanced magnetic pull in small cage induction motors with skewed rotors and dynamic rotor eccentricity,” *IEEE Trans. Energy Convers.*, vol. 11, no. 3, pp. 483-488, Sept. 1996.
- [DOR97] D. G. Dorrell, W. T. Thomson, and S. Roach, “Analysis of airgap flux, current, and vibration signals as a function of the combination of static and dynamic airgap eccentricity in 3-phase induction motors,” *IEEE Trans. Ind. Appl.*, vol. 33, no. 1, pp. 24-34, Jan./Feb. 1997.
- [DOR10] D. G. Dorrell, M. Popescu, and D. M. Ionel, “Unbalanced magnetic pull due to asymmetry and low-level static rotor eccentricity in fractional-slot brushless permanent-magnet motors with surface-magnet and consequent-pole rotors,” *IEEE Trans. Magn.*, vol. 46, no. 7, pp. 2675-2685, July 2010.
- [DOR11a] D. G. Dorrell, “Sources and characteristics of unbalanced magnetic pull in three-phase cage induction motors with axial-varying rotor eccentricity,” *IEEE Trans. Ind. Appl.*, vol. 47, no. 1, pp. 12-24, Jan. /Feb. 2011.
- [DOR11b] D. G. Dorrell, M. Hsieh, M. Popescu, L. Evans, D. A. Staton, and V. Grout, “A review of the design issues and techniques for radial-flux brushless surface and internal rare-earth permanent-magnet motors,” *IEEE Trans. Ind. Electron.*, vol. 58, no. 9, pp. 3741-3757, Sept. 2011.
- [DOR12] D. G. Dorrell, A. M. Knight, L. Evans, and M. Popescu, “Analysis and design techniques applied to hybrid vehicle drive machines-assessment of alternative IPM and induction motor topologies,” *IEEE Trans. Ind. Electron.*, vol. 59, no. 10, pp. 3690-3699, Oct. 2012.
- [DUR16] M. J. Duran, and F. Barrero, “Recent advances in the design, modeling, and control of multiphase machines part II,” *IEEE Trans. Ind. Electron.*, vol. 63, no. 1, pp. 459-468, Jan. 2016.
- [DUT13] R. Dutta, L. Chong, and M. F. Rahman, “Design and experimental verification of an 18-slot/14-pole fractional-slot concentrated winding interior permanent magnet machine,” *IEEE Trans. Energy Convers.*, vol. 28, no. 1, pp. 181-190, Mar. 2013.
- [EBR09] B. M. Ebrahimi, J. Faiz, and M. J. Roshtkhari, “Static-, dynamic-, and mixed-eccentricity fault diagnoses in permanent-magnet synchronous motors,” *IEEE Trans. Ind. Electron.*, vol. 56, no. 11, pp. 4727-4739, Nov. 2009.

- [ELR05] A. M. El-Refaie, and T. M. Jahns, "Optimal flux weakening in surface PM machines using fractional-slot concentrated windings," *IEEE Trans. Ind. Appl.*, vol. 41, no. 3, pp. 790-800, May/June 2005.
- [ELR06a] A. M. El-Refaie, and T. M. Jahns, "Scalability of surface PM Machines with concentrated windings designed to achieve wide speed ranges of constant-power operation," *IEEE Trans. Energy Convers.*, vol. 21, no. 2, pp. 362-369, June 2006.
- [ELR06b] A. M. El-Refaie, T. M. Jahns, P. J. McCleer, and J. W. McKeever, "Experimental verification of optimal flux weakening in surface PM machines using concentrated windings," *IEEE Trans. Ind. Appl.*, vol. 42, no. 2, pp. 443-453, Mar./Apr. 2006.
- [ELR06c] A. M. El-Refaie, T. M. Jahns, and D. W. Novotny, "Analysis of surface permanent magnet machines with fractional-slot concentrated windings," *IEEE Trans. Energy Convers.*, vol. 21, no. 1, pp. 34-43, Mar. 2006.
- [ELR08a] A. M. El-Refaie, and T. M. Jahns, "Impact of winding layer number and magnet type on synchronous surface PM machines designed for wide constant-power speed range operation," *IEEE Trans. Energy Convers.*, vol. 23, no. 1, pp. 53-60, Mar. 2008.
- [ELR08b] A. M. El-Refaie, M. R. Shah, R. H. Qu, and J. M. Kern, "Effect of number of phases on losses in conducting sleeves of surface PM machine rotors equipped with fractional-slot concentrated windings," *IEEE Trans. Ind. Appl.*, vol. 44, no. 5, pp. 1522-1532, Sept./Oct.2008.
- [ELR10] A. M. El-Refaie, "Fractional-slot concentrated-windings synchronous permanent magnet machines: opportunities and challenges," *IEEE Trans. Ind. Electron.*, vol. 57, no. 1, pp. 107-121, Jan. 2010.
- [ELR11] A. M. El-Refaie, "Fault-tolerant permanent magnet machines: A review," *IET Proc. -Electr. Power Appl.*, vol. 5, no. 1, pp. 59-74, Jan. 2011.
- [FIT03] A. E. Fitzgerald, C. Kingsley, S. D. Umans, and B. James, *Electric Machinery*. New York: McGraw-Hill, 2003.
- [FOR12] E. Fornasiero, N. Bianchi, and S. Bolognani, "Slot harmonic impact on rotor losses in fractional-slot permanent-magnet machines," *IEEE Trans. Ind. Electron.*, vol. 59, no. 6, pp. 2557-2564, June 2012.
- [FOR13] E. Fornasiero, L. Alberti, N. Bianchi, and S. Bolognani, "Considerations on selecting fractional-slot nonoverlapped coil windings," *IEEE Trans. Ind. Appl.*, vol. 49, no. 3, pp. 1316-1324, May/June 2013.
- [FU12] J. J. Fu, and C. S. Zhu, "subdomain model for predicting magnetic field in slotted surface mounted permanent-magnet machines with rotor eccentricity," *IEEE Trans. Magn.*, vol. 48, no. 5, pp. 1906-1917, May 2012.
- [FUR01] E. P. Furlani, *Permanent Magnet and Electromechanical Devices: Materials, Analysis, and Applications*. Academic Press, 2001.
- [GAS09] L. Gasparin, A. Cernigoj, S. Markic, and R. Fiser, "Additional cogging torque components in permanent-magnet motors due to manufacturing

- imperfections,” *IEEE Trans, Magn.*, vol. 45, no. 3. pp. 1210-1213, Mar. 2009.
- [GAS13] L. Gasparin, and R. Fišer, “Cogging torque sensitivity to permanent magnet tolerance combinations,” *Archives of Electrical Engineering*, vol. 62, no. 3, pp. 449-461, 2013.
- [GER05] A. D. Gerlando, G. M. Foglia, R. Perini, and M. Ubaldini, “Design and operation aspects of field regulated PM synchronous machines with concentrated armature windings,” in *IEEE International Conference on Electric Machines and Drives (IEMDC 2005)*, May 15, 2005, pp. 1165-1172.
- [GIE08] J. F. Gieras, *Advancements in Electric Machines*. Springer Heidelberg, 2008.
- [GIE10] J. F. Gieras, *Permanent Magnet Motor Technology*. CRC Press Taylor and Francis, 2010.
- [GOP93] K. Gopakumar, V. T. Ranganthan, and S. R. Bhat, “Split-phase induction motor operation from PWM voltage source inverter,” *IEEE Trans. Ind. Appl.*, vol. 29, no. 5, pp. 927-932, Sept./Oct. 1993.
- [HAD04] D. Hadiouche, H. Razik, and A. Rezzoug, “On the modeling and design of dual-stator windings to minimize circulating harmonic currents for VSI fed AC machines,” *IEEE Trans. Ind. Appl.*, vol. 40, no. 2, pp. 506-515, Mar./Apr. 2004.
- [HAD06] D. Hadiouche, L. Baghli, and A. Rezzoug, “Space-vector PWM techniques for dual three-phase AC machine: analysis, performance evaluation, and DSP implementation,” *IEEE Trans. Ind. Appl.*, vol. 42, no. 4, pp. 1112-1122, July/Aug. 2006.
- [HAN02] L. H. Hansen, L. Helle, F. Blaabjerg, E. Ritchie, S. Munk-Nielsen, H. W. Bindner, *et al.*, *Conceptual Survey of Generators and Power Electronics for Wind Turbines*. DTU library, 2002.
- [HAN17] B. Hannon, P. Sergeant, and L. Dupré, “Computational-time reduction of Fourier-Based Analytical Models,” *IEEE Trans. Energy Convers.*, 2017, in press.
- [HAY99] J. A. Haylock, B. C. Mecrow, A. G. Jack, and D. J. Atkinson, “Operation of fault tolerant machines with winding failures,” *IEEE Trans. Energy Convers.*, vol. 14, no. 4, pp. 1490-1495, Dec. 1999.
- [HEI15] G. Heins, D. M. Ionel, and M. Thiele, “Winding factors and magnetic fields in permanent-magnet brushless machines with concentrated windings and modular stator cores,” *IEEE Trans. Ind. Appl.*, vol. 51, no. 4, pp. 2924-2932, July/Aug. 2015.
- [HEL77] B. Heller, and V. Hamata, *Harmonic Field Effects in Induction Machines*. Elsevier Science & Technology, 1977.
- [HEN10] J. R. Hendershot, and T. J. Miller, *Design of Brushless Permanent-Magnet Machines*. Motor Design Books, 2010.

- [HOL70] C. H. Holley, and D. M. Willyoung, "Stator winding systems with reduced vibratory forces for large turbine-generators," *IEEE Trans. Power App. Syst.*, vol. PAS-89, no. 8, pp. 1922-1934, Nov./Dec. 1970.
- [HOW92] D. Howe, and Z. Q. Zhu, "The influence of finite element discretisation on the prediction of cogging torque in permanent magnet excited motors," *IEEE Trans. Magn.*, vol. 28, no. 2, pp. 1080-1083, Mar. 1992.
- [HSI13] M. F. Hsieh, and Y. H. Yeh, "Rotor eccentricity effect on cogging torque of PM generators for small wind turbines," *IEEE Trans. Magn.*, vol. 49, no. 5, pp. 1897-1900, May 2013.
- [HU03] J. Hu, J. Zou, and W. Liang, "Finite element calculation of the saturation DQ-axes inductance for a direct drive PM synchronous motor considering cross-magnetization," in *5th International Conference on Power Electronics and Drive Systems (PEDS 2003)*, Nov. 17-20, 2003, pp. 677-681.
- [HU14] Y. S. Hu, Z. Q. Zhu, and K. Liu, "Current control for dual three-phase permanent magnet synchronous motors accounting for current unbalance and harmonics," *IEEE Journal of Emerging and Selected Topics in Power Electronics*, vol. 2, no. 2, pp. 272-284, June 2014.
- [HU17] Y. S. Hu, Z. Q. Zhu, and M. Odavic, "Torque capability enhancement of dual three-phase PMSM drive with fifth and seventh current harmonics injection," *IEEE Trans. Ind. Appl.*, vol. 53, no. 5, pp. 4526-4535, Nov./Dec. 2017.
- [HUS00] I. Husain, A. Radun, and J. Nairus, "Unbalanced force calculation in switched-reluctance machines," *IEEE Trans. Magn.*, vol. 36, no. 1, pp. 330-338, Jan. 2000.
- [HUT05] G. Huth, "Permanent-magnet-excited AC servo motors in tooth-coil technology," *IEEE Trans. Energy Convers.*, vol. 20, no. 2, pp. 300-307, June 2005.
- [HWA01] S. M. Hwang, K. T. Kim, W. B. Jeong, Y. H. Jung, and B. S. Kang, "Comparison of vibration sources between symmetric and asymmetric HDD spindle motors with rotor eccentricity," *IEEE Trans. Ind. Appl.*, vol. 37, no.6, pp. 1727-1731, Nov./Dec. 2001.
- [ISH05a] D. Ishak, "Low-speed High-torque Permanent Magnet Brushless Machines Having Fractional Number of Slots per Pole," PhD thesis, the University of Sheffield, 2005.
- [ISH05b] D. Ishak, Z. Q. Zhu, and D. Howe, "Eddy-current loss in the rotor magnets of permanent-magnet brushless machines having a fractional number of slots per pole," *IEEE Trans. Magn.*, vol. 41, no. 9, pp. 2462-2469, Sept. 2005.
- [ISH05c] D. Ishak, Z. Q. Zhu, and D. Howe, "Permanent-magnet brushless machines with unequal tooth widths and similar slot and pole numbers," *IEEE Trans. Ind. Appl.*, vol. 41, no. 2, pp. 584-590, Mar./Apr. 2005.
- [ISH06] D. Ishak, Z. Q. Zhu, and D. Howe, "Comparison of PM brushless motors, having either all teeth or alternate teeth wound," *IEEE Trans. Energy Convers.*, vol. 21, no. 1, pp. 95-103, Mar. 2006.

- [ISL04] M. S. Islam, S. Mir, and T. Sebastian, "Issues in reducing the cogging torque of mass-produced permanent-magnet brushless DC motor," *IEEE Trans. Ind. Appl.*, vol. 40, no. 3, pp. 813-820, May/June 2004.
- [JAC96] A. G. Jack, B. C. Mecrow, and J. A. Haylock, "A comparative study of permanent magnet and switched reluctance motors for high-performance fault-tolerant applications," *IEEE Trans. Ind. Appl.*, vol. 32, no.4, pp. 889-895, July/Aug.1996.
- [JAH80] T. M. Jahns, "Improved reliability in solid-state AC drives by means of multiple independent phase drive units," *IEEE Trans. Ind. Appl.*, vol. IA-16, no. 3, pp. 321-331, May/June 1980.
- [JAH 96] T. M. Jahns, and W. L. Soong, "Pulsating torque minimization techniques for permanent magnet AC motor drives-a review," *IEEE Trans. Ind. Electron.*, vol. 43, no. 2, pp. 321-330, Apr. 1996.
- [JAN96] G. H. Jang, J. W. Yoon, N. Y. Park, and S. M. Jang, "Torque and unbalanced magnetic force in a rotational unsymmetric brushless DC motors," *IEEE Trans. Magn.*, vol. 32, no. 5, pp. 5157-5159, Sept. 1996.
- [JAN03] S. K. Jang, S. H. Lee, H. W. Cho, and S. K. Cho, "Analysis of unbalanced force for high-speed slotless permanent magnet machine with Halbach array," *IEEE Trans. Magn.*, vol. 39, no. 5, pp. 3265-3267, Sept. 2003.
- [KAL13] S. Kallio, M. Andriollo, A. Tortella, and J. Karttunen, "Decoupled d-q model of double-star interior-permanent-magnet synchronous machines," *IEEE Trans. Ind. Electron.*, vol. 60, no. 6, pp. 2486-2494, June 2013.
- [KAT14] J. Karttunen, S. Kallio, P. Peltoniemi, P. Silventoinen, and O. Pyrhonen, "Decoupled vector control scheme for dual three-phase permanent magnet synchronous machines," *IEEE Trans. Ind. Electron.*, vol. 61, no. 5, pp. 2185-2196, May 2014.
- [KEN85] T. Kenjo, and S. Nagamori, *Permanent-magnet and Brushless DC Motors*. Oxford University Press, 1985.
- [KIM98a] U. Kim and D. K. Lieu, "Magnetic field calculation in permanent magnet motors with rotor eccentricity: without slotting effect," *IEEE Trans. Magn.*, vol. 34, no. 4, pp. 2243-2252, July 1998.
- [KIM98b] U. Kim and D. K. Lieu, "Magnetic field calculation in permanent magnet motors with rotor eccentricity: with slotting effect considered," *IEEE Trans. Magn.*, vol. 34, no. 4, pp. 2253-2266, July 1998.
- [KIM01] K. T. Kim, K. S. Kim, S. M. Hwang, T. J. Kim, and Y. H. Jung, "Comparison of magnetic forces for IPM and SPM motor with rotor eccentricity," *IEEE Trans. Magn.*, vol. 37, no. 5, pp. 3448-3451, Sept. 2001.
- [KIM05a] U. Kim, and D. K. Lieu, "Effects of magnetically induced vibration force in brushless permanent-magnet motors," *IEEE Trans. Magn.*, vol. 41, no. 6, pp. 2164-2172, June 2005.
- [KIM05b] T. H. Kim, S. H. Won, K. Bong, and J. Lee, "Reduction of cogging torque in flux-reversal machine by rotor teeth pairing," *IEEE Trans. Magn.*, vol. 41, no. 10, pp. 3964-3966, Oct. 2005.

- [KIM14] H. J. Kim, D. J. Kim, and J. P. Hong, "Characteristic analysis for concentrated multiple-layer winding machine with optimum turn ratio," *IEEE Trans. Magn.*, vol. 50, no. 2, pp. 1-4, Feb. 2014.
- [LEV07] E. Levi, R. Bojoi, F. Profumo, H. A. Toliyat, and S. Williamson, "Multiphase induction motor drives - a technology status review," *IET Proc. -Electr. Power Appl.*, vol. 1, no. 4, pp. 489-516, July 2007.
- [LEV08] E. Levi, "Multiphase electric machines for variable-speed applications," *IEEE Trans. Ind. Electron.*, vol. 55, no. 5, pp. 1893-1909, May 2008.
- [LI07] J. T. Li, Z. J. Liu, and L. H. A. Nay, "Effect of radial magnetic forces in permanent magnet motors with rotor eccentricity," *IEEE Trans. Magn.*, vol. 43, no. 6, pp. 2525-2527, June 2007.
- [LI08] H. Li and Z. Chen, "Overview of different wind generator systems and their comparisons," *IET Renew. Power Gener.*, vol. 2, no. 2, pp. 123-138, June 2008.
- [LI14a] Q. Li, T. Fan, X. H. Wen, X. Tai, and Y. Li, "A novel multi-layer winding design method for fractional-slot concentrated-windings permanent magnet machine," in *IEEE Conference and Expo Transportation Electrification Asia-Pacific (ITEC Asia-Pacific 2014)*, 31 Aug.-3 Sept. 2014, pp. 1-5.
- [LI14b] G. J. Li, Z. Q. Zhu, W. Q. Chu, M. P. Foster, and D. A. Stone, "Influence of flux gaps on electromagnetic performance of novel modular PM machines," *IEEE Trans. Energy Convers.*, vol. 29, no. 3, pp. 716-726, Sept. 2014.
- [LI14c] G. J. Li, Z. Q. Zhu, M. P. Foster, and D. A. Stone, "Comparative studies of modular and unequal tooth PM machines either with or without tooth tips," *IEEE Trans. Magn.*, vol. 50, no. 7, pp. 1-10, July 2014.
- [LI15a] G. J. Li and Z. Q. Zhu, "Analytical modelling of modular and unequal tooth width surface-mounted permanent magnet machines," *IEEE Trans. Magn.*, vol. 51, no. 9, pp. 1-9, Sept. 2015.
- [LI15b] G. J. Li, Z. Q. Zhu, M. P. Foster, D. A. Stone, and H. L. Zhan, "Modular permanent magnet machines with alternate teeth having tooth tips," *IEEE Trans. Ind. Electron.*, vol. 62, no. 10, pp. 6120-6130, Oct. 2015.
- [LI16] Y. X. Li, Z. Q. Zhu, and G. J. Li, "Torque investigation of fractional-slot permanent magnet machines with different winding topology and stator structures," in *Eleventh International Conference on Ecological Vehicles and Renewable Energies (EVER 2016)*, Apr. 6-8, 2016, pp. 1-8.
- [LIA95] Y. F. Liao, F. Liang, and T. A. Lipo, "A novel permanent magnet motor with doubly salient structure," *IEEE Trans. Ind. Appl.*, vol. 32, no. 5, pp. 1069-1078, Sept./Oct. 1995.
- [LIB04] F. Libert, and J. Souldard, "Investigation on pole-slot combinations for permanent-magnet machines with concentrated windings," in *16th International Conference on Electrical Machines (ICEM 2004)*, 2004, pp. 5-8.

- [LIB06] F. Libert, and J. Soulard, "Manufacturing methods of stator cores with concentrated windings," in *3rd IET International Conference on Power Electronics, Machines and Drives (PEMD 2006)*, Apr. 4-6, 2016, pp. 676-680.
- [LIS11] M. Liserre, R. Cardenas, M. Molinas, and J. Rodriguez, "Overview of multi-MW wind turbines and wind parks," *IEEE Trans. Ind. Electron.*, vol. 58, no. 4, pp. 1081-1095, Apr. 2011.
- [LIW43] M. M. Liwschitz, "Distribution factors and pitch factors of the harmonics of a fractional-slot winding," *AIEE Trans.*, vol. 62, no. 10, pp. 664-666, Oct. 1943.
- [LIW61] M. Liwschitz-Garik, and C. Whipple, *Alternating Current Machines*. New York: Van Nostrand, 1961.
- [MAG03] F. Magnussen, and C. Sadarangani, "Winding factors and Joule losses of permanent magnet machines with concentrated windings," in *IEEE International Conference on Electric Machines and Drives (IEMDC 2003)*, June 1-4, 2003, pp. 333-339.
- [MAG07] F. Magnussen, and H. Lendenmann, "Parasitic effects in PM machines with concentrated windings," *IEEE Trans. Ind. Appl.*, vol. 43, no. 5, pp. 1223-1232, Sept./Oct.2007.
- [MEC96] B. C. Mecrow, A. G. Jack, J. A. Haylock, and J. Coles, "Fault-tolerant permanent magnet machine drives," *IEE Proc.-Electr. Power Appl.*, vol. 143, no. 6, pp. 437-442, Nov. 1996.
- [MIC14] M. Michon, R. C. Holehouse, K. Atallah, and G. Johnstone, "Effect of rotor eccentricity in large synchronous machines," *IEEE Trans. Magn.*, vol. 50, no.11, pp. 1-4, Nov. 2014.
- [MIT04] A. Mitcham, G. Antonopoulos, and J. J. A. Cullen, "Favourable slot and pole number combinations for fault-tolerant PM machines," *IEE Proc.-Electr. Power Appl.*, vol. 151, no. 5, pp. 520-525, Sept. 2004.
- [MOH14] M. Mohr, O. Biro, and F. Diwoy, "Consideration of rotor eccentricity effects in a multi body dynamics simulation using a finite element based circuit model approach," in *21th International Conference on Electrical Machines (ICEM 2014)*, 2-5 Sept., 2014, pp. 1523-1528.
- [MOM09] M. F. Momen, and S. Datta, "Analysis of flux leakage in a segmented core brushless permanent magnet motor," *IEEE Trans. Energy Convers.*, vol. 24, no. 1, pp. 77-81, Mar. 2009.
- [MOR10] D. S. More, and B. G. Fernandes, "Power density improvement of three phase flux reversal machine with distributed winding," *IET Proc.-Electr. Power Appl.*, vol. 4, no. 2, pp. 109-120, Feb. 2010.
- [NAI16] S. S. Nair, V. I. Patel, and J. B. Wang, "Post-demagnetization performance assessment for interior permanent magnet AC machines," *IEEE Trans. Magn.*, vol. 52, no. 4, pp. 1-10, Apr. 2016.
- [NEL74] R. H. Nelson, and P. C. Krause, "Induction machine analysis for arbitrary displacement between multiple winding sets," *IEEE Trans. Power App. Syst.*, vol. PAS-93, no. 3, pp. 841-848, May 1974.



- [NOL14] A. Nollau, and D. Gerling, “Novel cooling methods using flux-barriers,” in *21th International Conference on Electrical Machines (ICEM 2014)*, Sept. 2-5, 2014, pp. 1328-1333.
- [OST03] V. Ostovic, “Memory motors,” *IEEE Magn. Ind. Appl.*, vol. 9, no. 1, pp. 52-61, Jan./Feb. 2003.
- [OWE10] R. L. Owen, Z. Q. Zhu, A. S. Thomas, G. W. Jewell, and D. Howe, “Alternate poles wound flux-switching permanent-magnet brushless AC machines,” *IEEE Trans. Ind. Appl.*, vol. 46, no. 4, pp. 790-797, July/Aug.2010.
- [PAT14] V. I. Patel, J. B. Wang, W. Y. Wang, and X. Chen, “Six-phase fractional-slot-per-pole-per-phase permanent-magnet machines with low space harmonics for electric vehicle application,” *IEEE Trans. Ind. Appl.*, vol. 50, no. 4, pp. 2554-2563, July/Aug. 2014.
- [PAT15] V. I. Patel, J. B. Wang, and S. S. Nair, “Demagnetization assessment of fractional-slot and distributed wound 6-phase permanent magnet machines,” *IEEE Trans. Magn.*, vol. 51, no. 6, pp. 1-11, June 2015.
- [PEL 16] G. Pellegrino, T. M. Jahns, N. Bianchi, W. L. Soong, and F. Cupertino, *The Rediscovery of Synchronous Reluctance and Ferrite Permanent Magnet Motors: Tutorial Course Notes*. Springer, 2016.
- [PON14] P. Ponomarev, I. Petrov, and J. Pyrhonen, “Torque ripple reduction in double-layer 18/16 TC-PMSMs by adjusting teeth widths to minimize local saturation,” in *21th International Conference on Electrical Machines (ICEM 2014)*, 2-5 Sept., 2014, pp. 1461-1467.
- [POP08] M. Popescu, D. G. Dorrell, D. Ionel, and C. Cossar, “Single and double layer windings in fractional slot-per-pole PM machines - effects on motor performance,” in *34th Annual Conference of IEEE Industrial Electronics, (IECON 2008)*, 10-13 Nov., 2008, pp. 2055-2060.
- [POP13] M. Popescu, D. G. Dorrell, L. Alberti, N. Bianchi, D. A. Staton, and D. Hawkins, “Thermal analysis of duplex three-phase induction motor under fault operating conditions,” *IEEE Trans. Ind. Appl.*, vol. 49, no. 4, pp. 1523-1530, July/Aug. 2013.
- [PRI15] B. Prieto, M. Martinez-Iturralde, L. Fontan, and I. Slosegui, “Fault-tolerant permanent magnet synchronous machine phase pole and slot number selection criterion based on inductance calculation,” *IET Proc. - Electr. Power Appl.*, vol. 9, no. 2, pp. 138-149, Feb. 2015.
- [PYR13] J. Pyrhonen, T. Jokinen, and V. Hrabovcova, *Design of Rotating Electrical Machines*. John Wiley & Sons, 2013.
- [RAZ17] S. M. Raziee, O. Misir, and B. Ponick, “Winding function approach for winding analysis,” *IEEE Trans. Magn.*, vol. 53, no. 10, pp. 1-9, Oct. 2017.
- [RED09] P. B. Reddy, and T. M. Jahns, “Modeling of stator teeth-tip iron losses in fractional-slot concentrated winding surface PM machines,” in *IEEE Energy Conversion Congress and Exposition (ECCE 2009)*, Sept. 20-24, 2009, pp. 1903-1910.

- [RED15] P. B. Reddy, A. M. El-Refaie, and H. Kum-Kang, "Effect of number of layers on performance of fractional-slot concentrated-windings interior permanent magnet machines," *IEEE Trans. Power Electron.*, vol. 30, no. 4, pp. 2205-2218, Apr. 2015.
- [REN16] W. Ren, Q. Xu, Q. Li, and L. Zhou, "Reduction of cogging torque and torque ripple in interior PM machines with asymmetrical V-type rotor design," *IEEE Trans. Magn.*, vol. 52, no. 7, pp. 1-5, July 2016.
- [ROK17] A. Røkke, and R. Nilssen, "Analytical calculation of yoke flux patterns in fractional-slot permanent magnet machines," *IEEE Trans. Magn.*, vol. 53, no. 4, pp. 1-9, Apr. 2017.
- [SAL04] P. Salminen, M. Niemela, J. Pyhonen, and J. Mantere, "Performance analysis of fractional slot wound PM-motors for low speed applications," in *Conf. Rec. IEEE IAS Annu. Meeting*, Oct. 3-7, 2004, pp. 1032-1037.
- [SEB87] T. Sebastian, and G. R. Slemon, "Operating limits of inverter-driven permanent magnet motor drives," *IEEE Trans. Ind. Appl.*, vol. IA-23, no. 2, pp. 327-333, Mar./Apr. 1987.
- [SHE11] J. X. Shen, C. F. Wang, D. M. Miao, M. J. Jin, D. Shi, and Y. C. Wang, "Analysis and optimization of a modular stator core with segmental teeth and solid back iron for pm electric machines," in *IEEE International Electric Machines and Drives Conference (IEMDC 2011)*, May 15-18, 2011, pp. 1270-1275.
- [SHE13] J. X. Shen, P. Li, M. J. Jin, and G. Yang, "Investigation and countermeasures for demagnetization in line start permanent magnet synchronous motors," *IEEE Trans. Magn.*, vol. 49, no. 7, pp. 4068-4071, July 2013.
- [SHE16] J. X. Shen, S. Cai, J. Yuan, S. Cao, and C. W. Shi, "Cogging torque in SPM machine with segmented stator," *COMPEL-The International Journal for Computation and Mathematics in Electrical and Electronic Engineering*, vol. 35, no. 2, pp. 641-654, 2016.
- [SHI16] U. Shipurkar, H. Polinder, and J. A. Ferreira, "Modularity in wind turbine generator systems Opportunities and challenges," in *18th European Conference on Power Electronics and Applications (EPE 2016)*, Sept. 5-9, 2016, pp. 1-10.
- [SKA06] S. Skaar, Ø. Krøvel, and R. Nilssen, "Distribution, coil-span and winding factors for PM machines with concentrated windings," *ICEM 2006*, pp. 2-5, 2006.
- [SMI16] S. P. Smith, "The theory of armature windings," *Journal of the Institution of Electrical Engineers*, vol. 55, no. 261, pp. 18-36, Dec. 1916.
- [SPO94] E. Spooner, and A. C. Williamson, "Modular electromagnetic machine," British Patent GB 2 278 738B.
- [SPO96] E. Spooner, A. C. Williamson, and G. Catto, "Modular design of permanent-magnet generators for wind turbines," *IEE Proc.-Electr. Power Appl.*, vol. 143, no. 5, pp. 388-395, Sept. 1996.

- [SPO98] E. Spooner, and A. C. Williamson, "Parasitic losses in modular permanent-magnet generators," *IEE Proc.-Electr. Power Appl.*, vol. 145, no. 6, pp. 485-496, Nov. 1998.
- [TAN12] C. Tang, W. L. Soong, G. S. Liew, and N. Ertugrul, "Effect of pole and slot number changes on the performance of a surface PM machine," in *20th International Conference on Electrical Machines (ICEM 2012)*, Sept. 2-5, 2012, pp. 220-227.
- [TES16] A. Tessarolo, M. Mezzarobba, and N. Barbini, "Improved four-layer winding design for a 12-slot 10-pole permanent magnet machine using unequal tooth coils," in *42th Annual Conference of IEEE Industrial Electronics Society (IECON 2016)*, 23-26 Nov., 2016, pp. 1686-1691.
- [TON14] C. D. Tong, F. Wu, P. Zhen, B. Yu, Y. Sui, and L. M. Cheng, "Investigation of magnetically isolated multiphase modular permanent-magnet synchronous machinery series for wheel-driving electric vehicles," *IEEE Trans. Magn.*, vol. 50, no. 3, pp. 1-4, June 2014.
- [UGA08] G. Ugalde, J. Poza, M. A. Rodriguez, and A. Gonzalez, "Space harmonic modeling of fractional permanent magnet machines from star of slots," in *18th International Conference on Electrical Machines (ICEM 2008)*, Sept. 6-9, 2008, pp. 1-6.
- [URR13] J. C. Urresty, J. R. Riba, and L. Romeral, "Influence of the stator windings configuration in the currents and zero-sequence voltage harmonics in permanent magnet synchronous motors with demagnetization faults," *IEEE Trans. Magn.*, vol. 49, no. 8, pp. 4885-4893, Aug. 2013.
- [VIL12] M. Villani, M. Tursini, G. Fabri, and L. Castellini, "High reliability permanent magnet brushless motor drive for aircraft application," *IEEE Trans. Ind. Electron.*, vol. 59, no. 5, pp. 2073-2081, May 2012.
- [VIZ06] D. Vizireanu, X. Kestelyn, S. Brisset, P. Brochet, Y. Milet, and D. Laloy, "Polyphased modular direct-drive wind turbine generator," in *2005 European Conference on Power Electronics and Applications (EPE 2005)*, Sept. 11-14, 2005, pp. 1-9.
- [WAL05] J. A. Walker, D. G. Dorrell, and C. Cossar, "Flux-linkage calculation in permanent-magnet motors using the frozen permeabilities method," *IEEE Trans. Magn.*, vol. 41, no. 10, pp. 3946-3948, Oct. 2005.
- [WAN99a] C. Wang, S. A. Nasar, and I. Boldea, "Three-phase flux reversal machine (FRM)," *IET Proc.-Electr. Power Appl.*, vol. 146, no. 2, pp. 139-146, Mar. 1999.
- [WAN99b] J. Wang, and D. K. Lieu, "Magnetic lumped parameter modeling of rotor eccentricity in brushless permanent-magnet motors," *IEEE Trans. Magn.*, vol. 35, no. 5, pp. 4226-4231, Sept. 1999.
- [WAN05] J. B. Wang, Z. P. Xia, and D. Howe, "Three-phase modular permanent magnet brushless machine for torque boosting on a downsized ICE vehicle," *IEEE Trans. Veh. Technol.*, vol. 54, no. 5, pp. 809-816, May 2005.

- [WAN06] J. B. Wang, Z. P. Xia, S. A. Long, and D. Howe, "Radial force density and vibration characteristics of modular permanent magnet brushless ac machine," *IEE Proc.-Electr. Power Appl.*, vol. 153, no. 6, pp. 793-801, Nov. 2006.
- [WAN08] J. B. Wang, W. W. Wang, K. Atallah, and D. Howe, "Demagnetization assessment for three-phase tubular brushless permanent-magnet machines," *IEEE Trans. Magn.*, vol. 44, no. 9, pp. 2195-2203, Sept. 2008.
- [WAN14] J. B. Wang, V. I. Patel, and W. Y. Wang, "Fractional-slot permanent magnet brushless machines with low space harmonic contents," *IEEE Trans. Magn.*, vol. 50, no. 1, pp. 1-9, Jan. 2014.
- [WAN15a] T. Wang, and Z. X. Zhou, "Analytical solution of magnetic field distribution in brushless permanent magnet machines with rotor axis deflection," *IEEE Trans. Magn.*, vol. 51, no. 4, pp. 1-6, Apr. 2015.
- [WAN15b] Y. W. Wang, R. H. Qu, and J. Li, "Multilayer windings effect on interior pm machines for EV applications," *IEEE Trans. Ind. Appl.*, vol. 51, no. 3, pp. 2208-2215, May/June 2015.
- [WAN15c] K. Wang, Z. Q. Zhu, Y. Ren, and G. Ombach, "Torque improvement of dual three-phase permanent magnet machine with 3rd harmonic current injection," *IEEE Trans. Ind. Electron.*, vol. 62, no. 11, pp. 6833-4844, Nov. 2015.
- [WRO10] R. Wrobel, P. H. Mellor, N. McNeill, and D. A. Staton, "Thermal performance of an open-slot modular-wound machine with external rotor," *IEEE Trans. Energy Convers.*, vol. 25, no. 2, pp. 403-411, June 2010.
- [WU11] L. J. Wu, Z. Q. Zhu, D. Staton, M. Popescu, and D. Hawkins, "Analytical prediction of electromagnetic performance of surface-mounted PM machines based on subdomain model accounting for tooth-tips," *IET Proc.-Electr. Power Appl.*, vol. 5, no. 7, pp. 597-609, 2011.
- [WU12] L. J. Wu, Z. Q. Zhu, D. Staton, M. Popescu, and D. Hawkins, "Analytical model for predicting magnet loss of surface-mounted permanent magnet machines accounting for slotting effect and load," *IEEE Trans. Magn.*, vol. 48, no. 1, pp. 107-117, Jan. 2012.
- [WU13] L. J. Wu, Z. Q. Zhu, and M. L. Mohd Jamil, "Unbalanced magnetic force in permanent magnet machines having asymmetric windings and static/rotating eccentricities," in *International Conference on Electrical Machines and Systems (ICEMS 2013)*, Oct. 26-29, 2013, pp. 937-942.
- [WU15a] D. Wu, "Effect of Magnetic Saturation in Fractional Slot PM Machines with Particular Reference to Terminal Voltage Distortion," PhD thesis, the University of Sheffield, 2015.
- [WU15b] Z. Z. Wu, Z. Q. Zhu, and J. T. Shi, "Novel doubly salient permanent magnet machines with partitioned stator and iron pieces rotor," *IEEE Trans. Magn.*, vol. 51, no. 5, pp. 1-12, May. 2015.
- [WU15c] D. Wu, and Z. Q. Zhu, "Design trade-off between cogging torque and torque ripple in fractional slot surface-mounted permanent magnet machines," *IEEE Trans. Magn.*, vol. 15, no. 11, pp. 1-4, Nov. 2015.

- [XU17] P. L. Xu, J. H. Feng, S. Y. Guo, S. Z. Feng, W. Q. Chu, Y. Ren, et al., "Analysis of dual three-phase permanent magnet synchronous machines with different angle displacements," *IEEE Trans. Ind. Electron.*, 2017, in press.
- [XUA13] H. V. Xuan, D. Lahaye, H. Polinder, and J. A. Ferreira, "Influence of stator slotting on the performance of permanent-magnet machines with concentrated windings," *IEEE Trans. Magn.*, vol. 49, no. 2, pp. 929-938, Feb. 2013.
- [YAN06] Y. Fan, K. T. Chau, and M. Chen, "A new three-phase doubly salient permanent magnet machine for wind power generation," *IEEE Trans. Ind. Appl.*, vol. 42, no. 1, pp. 53-60, Jan./Feb. 2006.
- [YAN14] H. D. Yang, and Y. S. Chen, "Influence of radial force harmonics with low mode number on electromagnetic vibration of PMSM," *IEEE Trans. Energy Convers.*, vol. 29, no. 1, pp. 38-45, Mar. 2014.
- [YAN17] Y. Y. Yang, S. M. Castano, R. Yang, M. Kasprzak, B. Bilgin, et al., "Design and comparison of interior permanent magnet motor topologies for traction applications," *IEEE Trans. Transport. Electrific.*, vol. 3, no. 1, pp. 86-97, Mar. 2017.
- [YOK16] Y. Yokoi, T. Higuchi, and Y. Miyamoto, "General formulation of winding factor for fractional-slot concentrated winding design," *IET Proc.-Electr. Power Appl.*, vol. 10, no. 4, pp. 231-239, Apr. 2016.
- [YOO05] T. Yoon, "Magnetically induced vibration in a permanent-magnet brushless DC motor with symmetric pole-slot configuration," *IEEE Trans. Magn.*, vol. 41, no. 6, pp. 2173-2179, June 2005.
- [YUA14] J. Yuan, C. W. Shi, and J. X. Shen, "Analysis of cogging torque in surface-mounted permanent magnet machines with segmented stators," in *International Conference on Electrical Machines and Systems (ICEMS 2014)*, Oct. 22-25, 2005, pp. 2513-2516.
- [ZHA95] Y. F. Zhao, and T. A. Lipo, "Space vector PWM control of dual three-phase induction machine using vector space decomposition," *IEEE Trans. Ind. Appl.*, vol. 31, no. 5, pp. 1100-1109, Sept./Oct. 1995.
- [ZHA13] M. Q. Zhang, A. Macdonald, K. Tseng, and G. M. Burt, "Magnetic equivalent circuit modeling for interior permanent magnet synchronous machine under eccentricity fault," in *48th International Universities Power Engineering Conference (UPEC2013)*, Sept. 2-5, 2013, pp. 1-6.
- [ZHA15] W. L. Zhao, T. A. Lipo, and B. Kwon, "Torque pulsation minimization in spoke-type interior permanent magnet motors with skewing and sinusoidal permanent magnet configurations," *IEEE Trans. Magn.*, vol. 51, no. 11, pp. 1-4, Nov. 2015.
- [ZHE12] P. Zheng, F. Wu, Y. Sui, P. F. Wang, Y. Lei, and H. P. Wang, "Harmonic analysis and fault-tolerant capability of a semi-12-phase permanent-magnet synchronous machine used for EVs," *Energies*, vol. 5, no. 9, pp. 3586-3607, Sept. 2012.
- [ZHE13] P. Zheng, F. Wu, Y. Lei, Y. Sui, and B. Yu, "Investigation of a novel 24-slot/14-pole six-phase fault-tolerant modular permanent-magnet in-wheel

- motor for electric vehicles,” *Energies*, vol. 6, no. 10, pp. 4980-5002, Sept. 2013.
- [ZHU02] Z. Q. Zhu, Y. S. Chen, and D. Howe, “Iron loss in permanent-magnet brushless AC machines under maximum torque per ampere and flux weakening control,” *IEEE Trans. Magn.*, vol. 38, no. 5, pp. 3285-3287, Sept. 2002.
- [ZHU07a] Z. Q. Zhu, and D. Howe, “Electrical machines and drives for electric, hybrid, and fuel cell vehicles,” *Proc. of the IEEE*, vol. 95, no. 4, pp. 746-765, Apr. 2007.
- [ZHU07b] Z. Q. Zhu, D. Ishak, D. Howe, and J. T. Chen, “Unbalanced magnetic forces in permanent-magnet brushless machines with diametrically asymmetric phase windings,” *IEEE Trans. Ind. Appl.*, vol. 43, no. 6, pp. 1544-1553, Nov./Dec. 2007.
- [ZHU09a] L. Zhu, S. Z. Jiang, Z. Q. Zhu, and C. C. Chan, “Analytical methods for minimizing cogging torque in permanent-magnet machines,” *IEEE Trans. Magn.*, vol. 45, no.4, pp. 2023-2031, Apr. 2009.
- [ZHU09b] Z. Q. Zhu, Z. P. Xia, L. J. Wu, and G. W. Jewell, “Influence of slot and pole number combination on radial force and vibration modes in fractional slot PM brushless machines having single- and double-layer windings,” in *IEEE Energy Conversion Congress and Exposition (ECCE 2009)*, Sept. 20-24, 2009, pp. 3443-3450.
- [ZHU10] Z. Q. Zhu, L. J. Wu, and Z. P. Xia, “An accurate subdomain model for magnetic field computation in slotted surface-mounted permanent-magnet machines,” *IEEE Trans. Magn.*, vol. 46, no. 4, pp. 1100-1115, Apr. 2010.
- [ZHU11] Z. Q. Zhu, “Switched flux permanent magnet machines innovation continues,” in *International Conference on Electrical Machines and Systems (ICEMS 2011)*, Aug. 20-23, 2011, pp. 1-10.
- [ZHU12a] Z. Q. Zhu, and J. B. Hu, “Electrical machines and power-electronic systems for high-power wind energy generation applications: part I-market penetration, current technology and advanced machine systems” *COMPEL: The international journal for computation and mathematics in electrical and electronic engineering*, vol. 32, no. 1, pp. 7-33, 2012.
- [ZHU12b] Z. Q. Zhu, and J. B. Hu, “Electrical machines and power-electronic systems for high-power wind energy generation applications: part II-power electronics and control systems” *COMPEL: The international journal for computation and mathematics in electrical and electronic engineering*, vol. 32, no. 1, pp. 34-71, 2012.
- [ZHU13] Z. Q. Zhu, M. L. Mohd Jamil, and L. J. Wu, “Influence of slot and pole number combinations on unbalanced magnetic force in PM machines with diametrically asymmetric windings,” *IEEE Trans. Ind. Appl.*, vol. 49, no. 1, pp. 19-30, Jan./Feb. 2013.
- [ZHU14a] Z. Q. Zhu, “Permanent magnet machines for traction applications,” in *Encyclopaedia of Automotive Engineering*, John Wiley & Sons, Ltd, 2014.
- [ZHU14b] Z. Q. Zhu, L. J. Wu, and M. L. Mohd Jamil, “Influence of pole and slot number combinations on cogging torque in permanent magnet machines

with static and rotating eccentricities,” *IEEE Trans. Ind. Appl.*, vol. 50, no. 5, pp. 3265-3277, Sept./Oct. 2014.

[ZHU14c] Z. Q. Zhu and D. Evans, “Overview of recent advances in innovative electrical machines-with particular reference to magnetically geared switched flux machines,” in *International Conference on Electrical Machines and Systems (ICEMS 2014)*, Oct. 22-25, 2014, pp. 1-10.

[ZHU15] Z. Q. Zhu, Z. Z. Wu, D. Evans, and W. Q. Chu, “Novel electrical machines having separate PM excitation stator,” *IEEE Trans. Magn.*, vol. 51, no. 4, pp. 1-9, Apr. 2015.

## Appendix A Determination of Overload Current Value

The electric loading of an electrical machine can be predicted as follows:

$$A_e = \frac{2mN_{ph}I_{rat}}{\pi D_{so}} \quad A.1$$

where  $m$  is the phase number;  $A_e$  is the electric loading and  $D_{so}$  is the stator outer diameter for an external rotor machine.

For the dual 3-phase prototype machines analysed in this thesis, the rated current, the turns per phase and the stator outer diameter are 3A, 408 and 390.4mm, respectively. Thus, the electric loading is 11.98kA/m, which is quite low and leads to much weaker armature field compared with PM field. That is why the saturation hardly changes under rated condition. In fact, the available electric loading for prototype machines can be estimated according to the method shown in [PYR13]. The limit of armature current should guarantee the half of PM is not demagnetised by armature field.

$$\Theta_{arm} \leq \Theta_{PM} \quad A.2$$

where  $\Theta_{arm}$  and  $\Theta_{PM}$  are the equivalent MMF of armature and PM fields, respectively. (A.2) can be re-written as follows:

$$\frac{1}{2} A_e \alpha_p \tau_p \leq \frac{B_{\delta 1}}{\mu_0} \delta k_c \Leftrightarrow A_e \leq \frac{2B_{\delta 1}}{\alpha_p \tau_p \mu_0} \delta k_c \quad A.3$$

where  $B_{\delta 1}$  is the peak value of fundamental open-circuit air-gap flux density;  $\alpha_p$  is the PM pole arc to pole pitch ratio;  $\tau_p$  is the pole pitch;  $\delta$  is the air-gap mechanical length;  $k_c$  is the Carter coefficient accounting for slotting effect and  $\mu_0$  is the air permeability.

For the proposed modular machine,  $B_{\delta 1}$  can be obtained from the FEA. Parameters  $\alpha_p$  and  $\delta$  are directly obtained from electrical machine dimensions, while the left two parameters,  $\tau_p$  and  $k_c$ , need to be predicted based on the following equations:

$$\tau_p = \frac{\pi(D_{so} + 2\delta)}{2p} \quad A.4$$

$$k_c = \frac{\tau_{se}}{\tau_{se} - \gamma b_{soe}} \quad A.5$$

$$\gamma = \frac{2}{\pi} \left( \arctan \frac{b_{soe}}{2\delta} - \frac{2\delta}{b_{soe}} \ln \sqrt{1 + \left( \frac{b_{soe}}{2\delta} \right)^2} \right)$$



where  $\tau_{se}$  is the stator tooth pitch of effective teeth and  $b_{soe}$  is the slot opening between effective teeth.

After substituting all of the parameters into (A.3), the limit of  $A_e$  is 112.37kA/m and the corresponding current is around 30A according to (A.1). It is about 10 times of rated value. In order to clearly see the influence of electric loading, the average torque-current characteristic of 42S/32P modular machine having dual 3-phase winding with 30 degree phase shift is plotted in Fig. A.1.

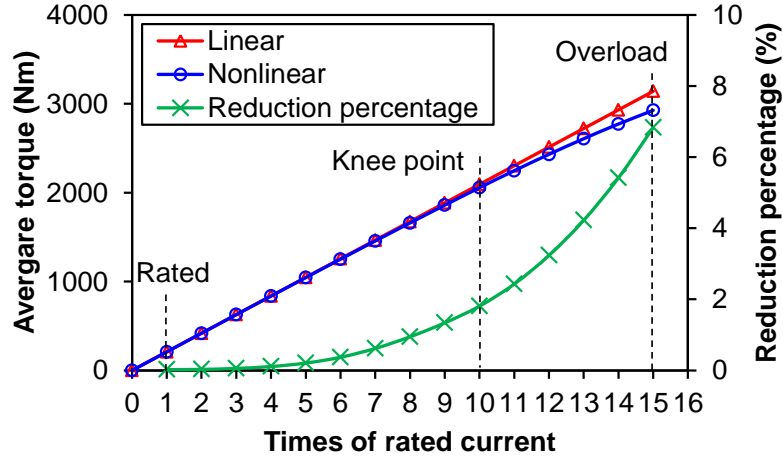


Fig. A.1. Comparison of linear and nonlinear average torque-current characteristics.

Another linear characteristic and the reduction percentage (RP) of average torque referring to this linear characteristic are also given to show the saturation. This corresponding is obtained as follows:

$$T_{eml} = \frac{m}{2} p \psi_{dPM}(OC) I_q \quad \text{A.6}$$

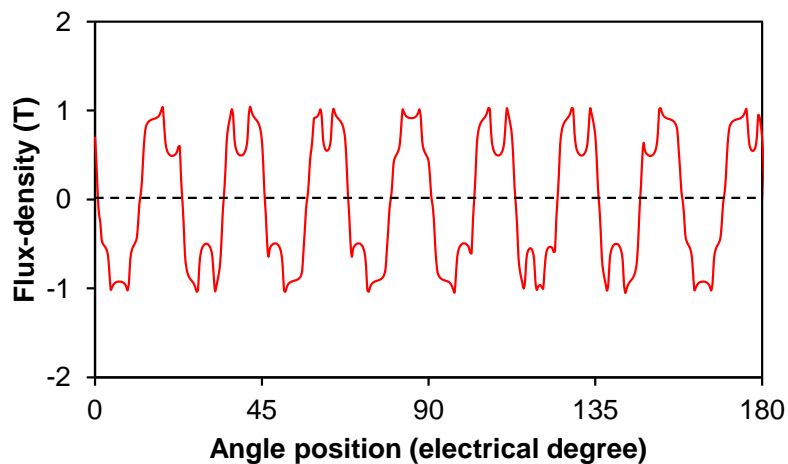
$$RP = (T_{eml} - T_{emnl}) / T_{eml} \times 100\%$$

where  $\psi_{dPM}(OC)$  is the  $d$ -axis PM flux-linkage under open-circuit condition;  $T_{eml}$  and  $T_{emnl}$  are the average torque of linear and nonlinear characteristics with the same current, respectively.

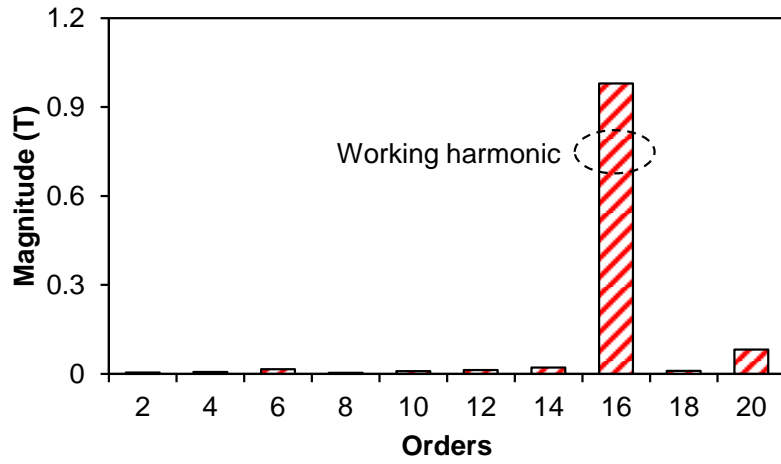
Since  $\psi_{dPM}$  is fixed for its open-circuit value, the average torque-current characteristic is linear. Fig. A.1 shows that the average torque will become saturated for real nonlinear situation when the current is beyond 10 times of rated value (Knee point). For the real large electrical machines, such saturation caused by armature field is important; and therefore the current value must be enlarged to such level in order to

see the different phenomena. Besides, it can also be seen that the saturation is still not quite obvious even though the current increases to 10 times of rated value. It is only about 2% reduction compared with the linear characteristic. If the 5% reduction percentage is expected accounting for fully utilising materials, the current should be larger than 14 times of rated value. Here, the 15 times of rated value is used for overload condition to more clearly show the saturation effect.

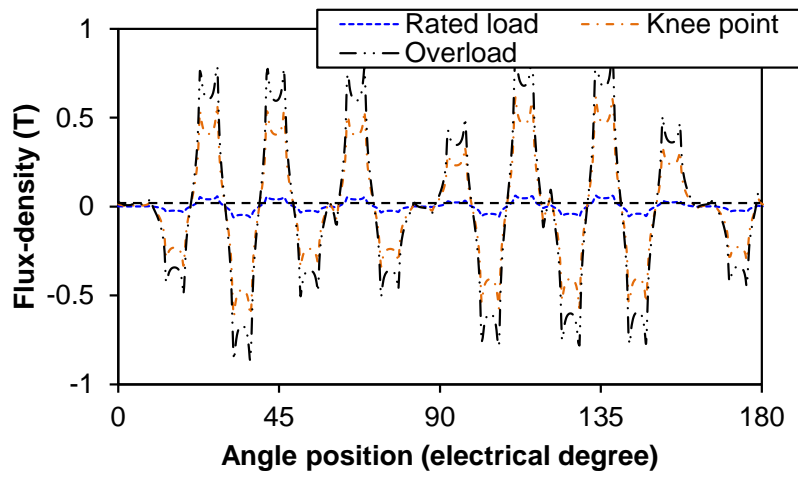
The influence of armature reaction on the resultant field can be observed according to air-gap flux densities and flux density distributions. The air-gap flux densities of the open-circuit PM and different armature currents are shown in Fig. A.2. For the open-circuit PM field, the modulation due to slotting effect is obvious, while the working harmonic is still predominant, as shown in Fig. A.2(a) and (b). However, the armature field due to current is much weaker if the current value is low. It is clear that the armature field is practically proportional to armature current value and the abundant harmonics exist. Besides, the magnitude of working harmonic is the largest. When the current is approaching the value corresponding to Knee point, the armature field is still a bit low compared with the PM field, as shown in Fig. A.2(c) and (d).



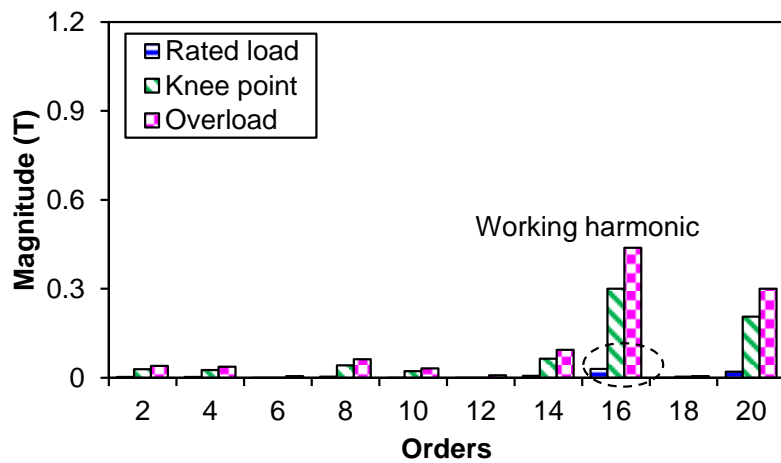
(a) Waveform for PM field



(b) Spectrum for PM field



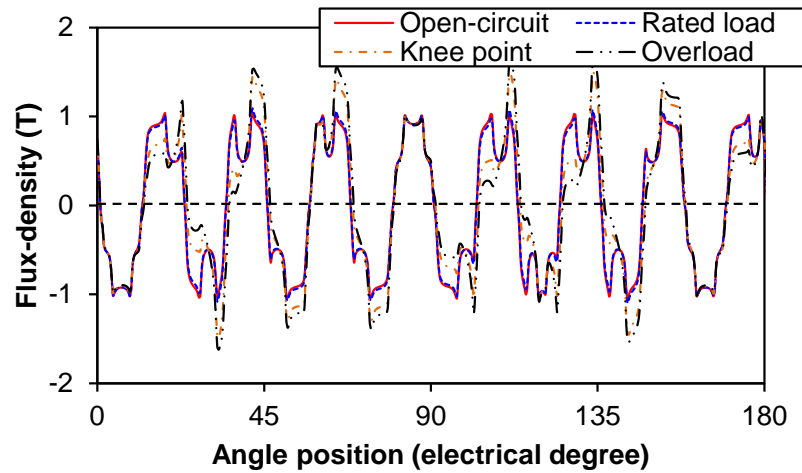
(c) Waveforms for armature field



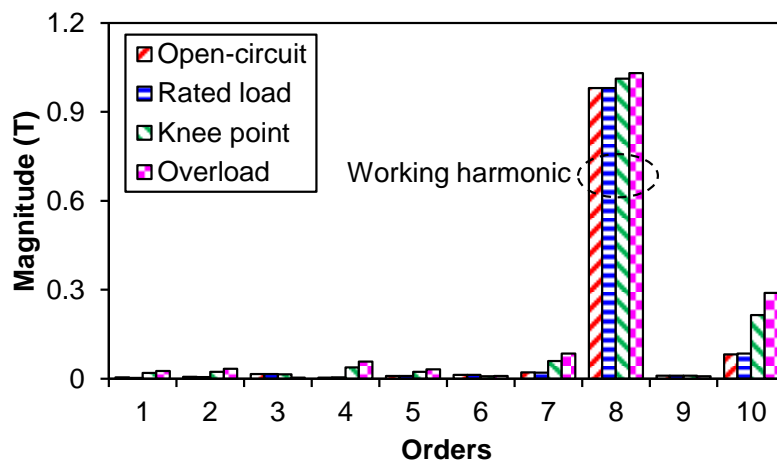
(d) Spectra for armature field

Fig. A.2. Air-gap flux densities for separate PMs and current.

When both PMs and armature current exist together, the resultant air-gap flux densities are shown in Fig. A.3



(a) Waveforms



(b) Spectra

Fig. A.3. Air-gap flux densities for resultant PMs and current.

Since the resultant field is not the simple addition of fields separately generated by PMs and armature currents, it has been obviously distorted. Both waveforms and harmonics show this distortion. In order to more clearly show the armature field influence, the occupation percentage (OP) of the fundamental armature field ( $B_{arm1m}$ ) to the fundamental PM field ( $B_{PM1m}$ ) is listed in TABLE A.1. From TABLE A.1, it can be seen that the armature field is about 50% of PM field under overload condition. The fundamental air-gap flux densities of resultant field ( $B_{res1m}$ ) are also shown in TABLE A.1. It shows that the armature reaction is really weak for rated current. The increase percentage (IP) is used to describe the level of armature field influence.

$$IP = (B_{res1m} - B_{PM1m}) / B_{PM1m} \times 100\%$$

A.7

TABLE A.1 PERCENTAGE OF ARMATURE FIELD TO PM FIELD

Load condition	$B_{PM1m}$	$B_{arm1m}$	OP (%)	$B_{res1m}$	IP (%)
Open-circuit		0	0	0.9794	0
Rated load	0.9794	0.0300	3.06	0.9799	0.05
Knee point		0.3003	30.66	1.0115	3.28
Overload		0.4387	44.79	1.0306	5.23

The flux densities of four situations for resultant fields are further shown in Fig. A.4 to demonstrate the saturation variation due to different armature reactions.

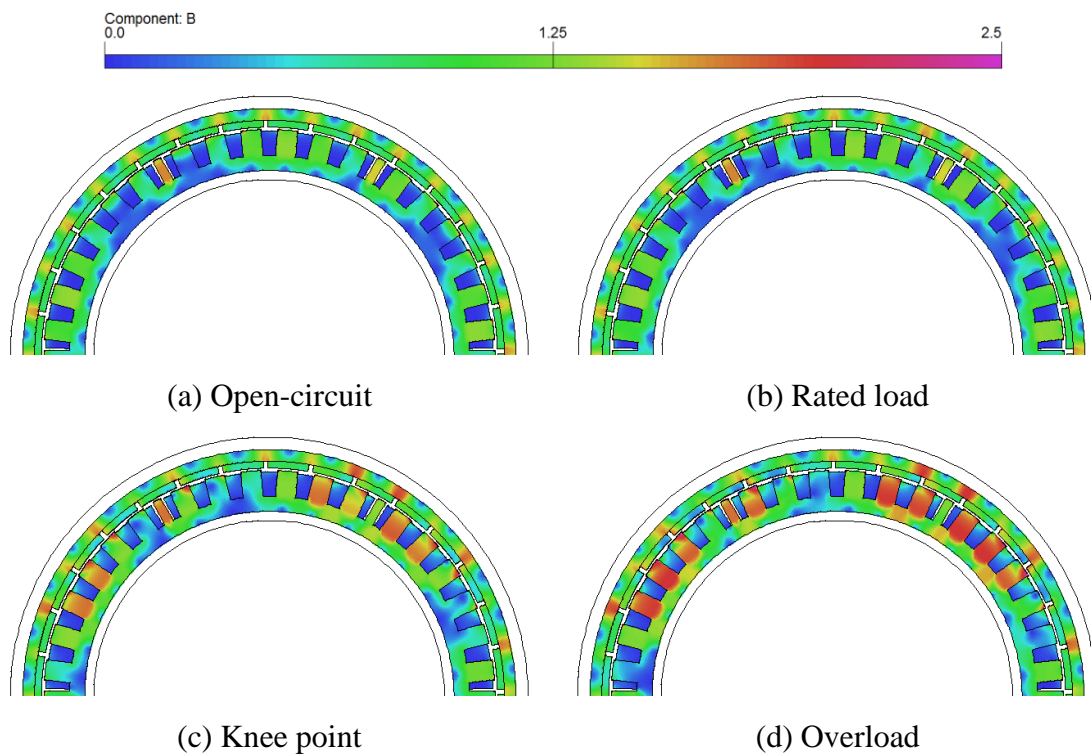


Fig. A.4. Flux density distributions.

The negligible difference between Fig. A.4(a) and (b) validate the statement of weak armature field. When it comes to Knee point situation, some parts of stator teeth become more saturated due to result field. This is expected since the materials should be fully utilised to generated effective torque. However, the 15 times of rated current is finally determined because of a more obvious influence of armature field can be seen, as shown in Fig. A.4(d).

One thing must be mentioned that the optimal current advance angle will not be zero any more for real large size SPM generators, since the high electric loading will

generated relatively strong armature field and the saturation will be much severer compared with small size electrical machines [CHU13b], [CHU13c]. By the way, the overload current used to mimic real large size electrical machine operation needs to be determined by the specific requirements as well.

## Appendix B Frozen Permeability Method

When PM machines operate under on-load condition, both PM and armature fields will exist. In order to separately investigate the influence of PM and armature fields on electrical machine performance, the frozen permeability (FP) method can be employed. This advanced technique was firstly put forward in [BIA98], where the on-load  $d$ - and  $q$ -axis inductances were predicted accounting for on-load saturation. Its principle can be simply explained as follows, as shown in Fig. B.1.

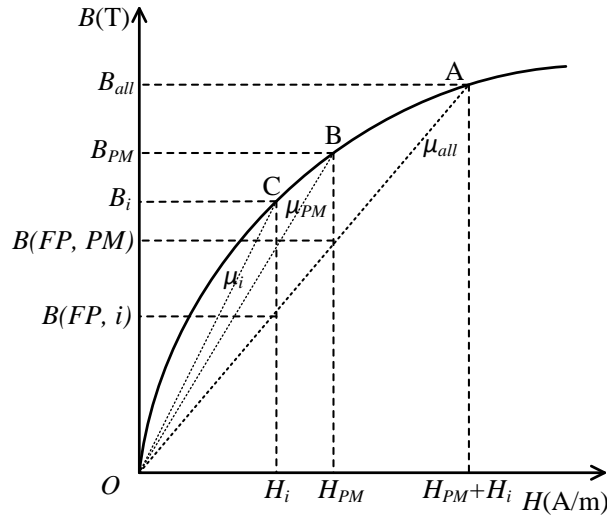


Fig. B.1. Principle of frozen permeability [CHU13].

For the nonlinear B-H curve of start lamination, the open-circuit flux density is  $B_{PM}$ , which is excited due to PM field intensity- $H_{PM}$ . The relative permeability will be  $\mu_{PM}$  under such condition. If only armature currents exist, the field intensity- $H_i$  will generate its corresponding flux density- $B_i$  as well. Under such situation, the relative permeability will be  $\mu_i$ . It is clear that the relative permeability of two cases will be different. When both sources work together, the resultant field intensity ( $H_{PM}+H_i$ ) will produce the on-load flux density- $B_{all}$ . Although the on-load field intensity can be simply added by open-circuit PM and armature only field intensity,  $B_{all}$  does not satisfy this relationship with  $B_{PM}$  and  $B_i$  due to the material nonlinear property. In order to solve this problem, the on-load field is predicted by finite element analysis (FEA) firstly. Then the relative permeability of each mesh element ( $\mu_{all}$ ) is frozen for the following analysis. After this, the nonlinear magnetic circuit is degraded into linear type. Then, the influence of PM and armature fields can be separated. The superposition principle will be effective again.

Under FP condition, flux density due to PM- $B(FP,PM)$  and armature current- $B(FP,i)$  can be added to obtain  $B_{all}$ . It can also be observed that the two flux densities predicted by FP method will be lower than their value corresponding to single excitation. This is due to the magnetic linearization by freezing permeability. For this method applied to self and mutual inductance prediction [WAL05], the next step is removing all of the initial excitation and only exciting the concerned phase with a constant current. After doing a linear FE calculation, the phase flux linkage of each phase can be predicted and the self- and mutual inductances can be obtained according, as summarised in Fig. B.2.

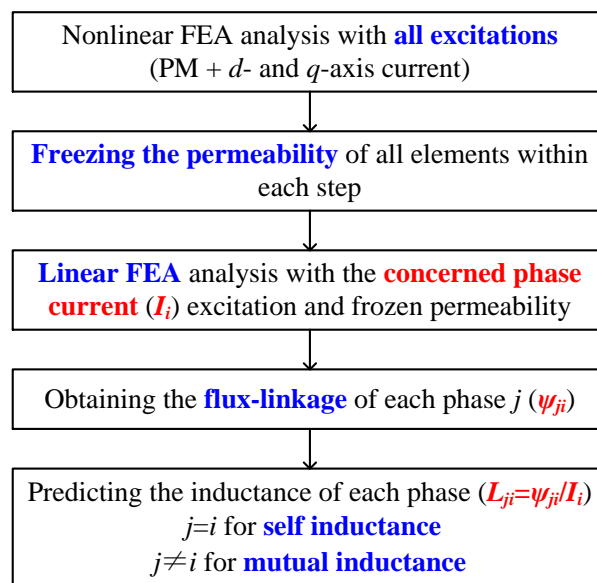


Fig. B.2. Phase inductance prediction process by employing FP method.



## Appendix C CAD Diagrams and Materials of Prototyped Machines

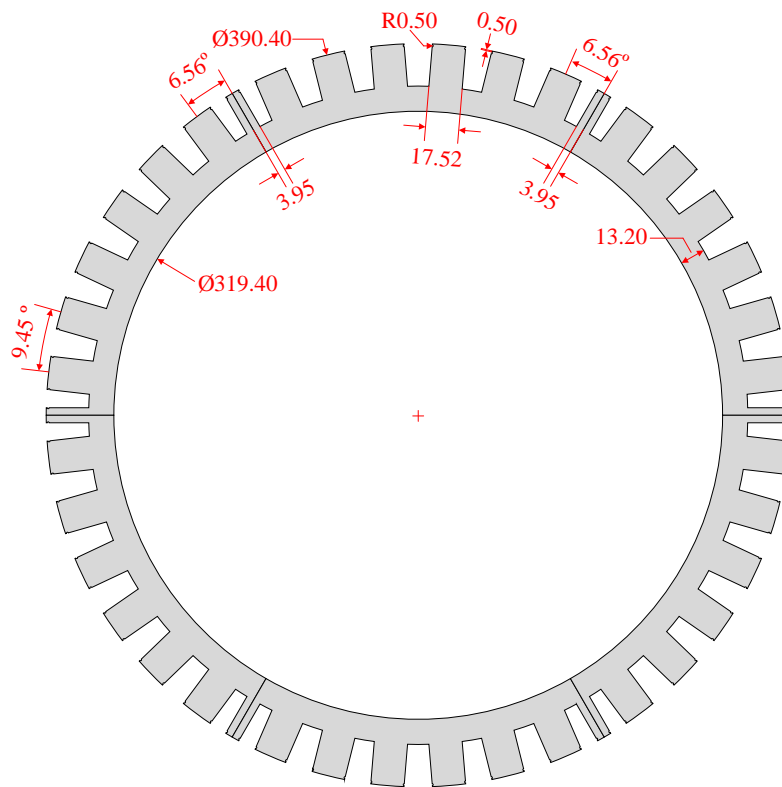


Fig. C.1. Stator of 42S/32P Prototyped Machine.

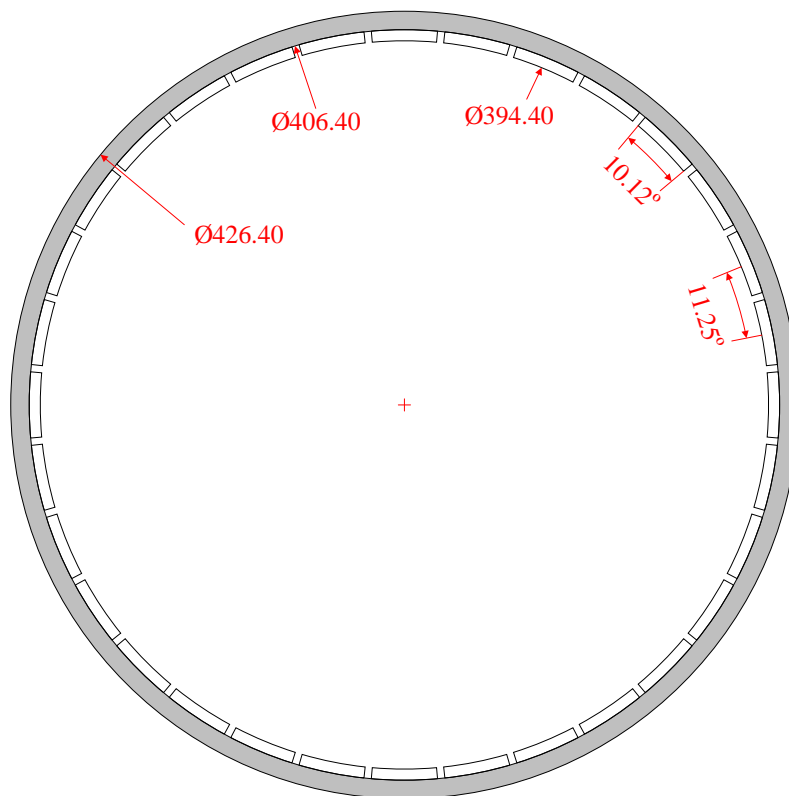


Fig. C.2. Rotor of 42S/32P Prototyped Machine.

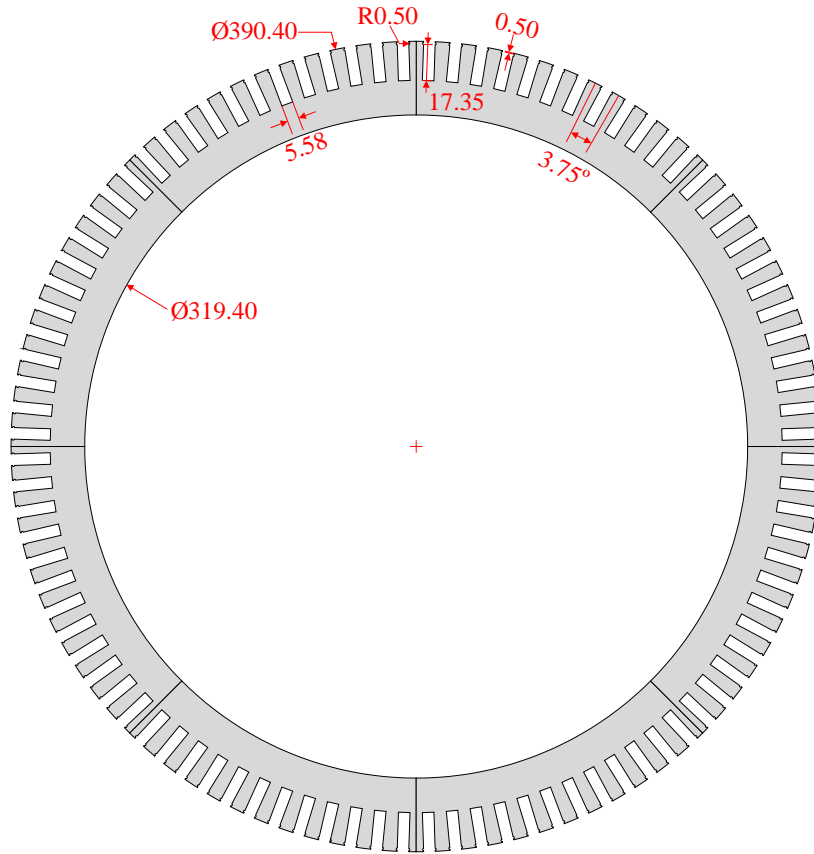


Fig. C.3. Stator of 96S/32P Prototyped Machine.

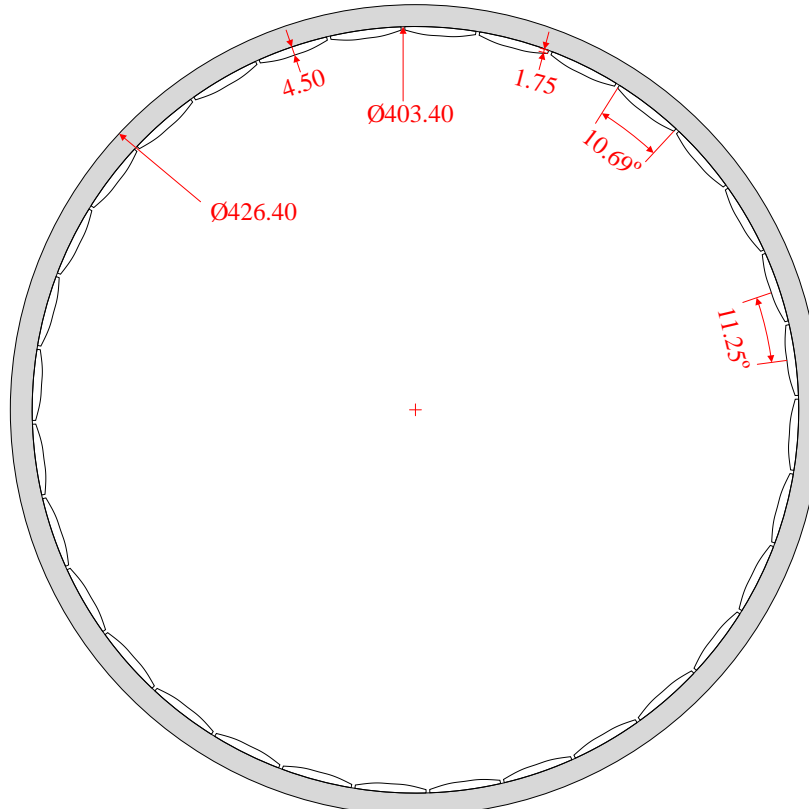


Fig. C.4. Rotor of 96S/32P Prototyped Machine.

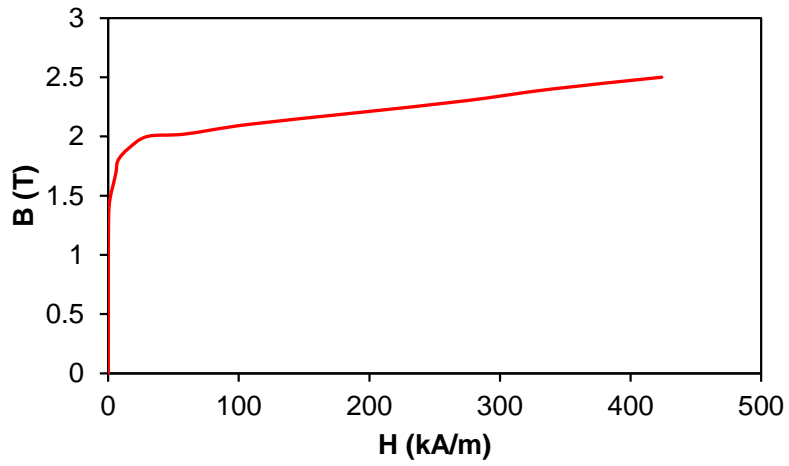


Fig. C.5. Stator lamination magnetisation curve (35DW250).

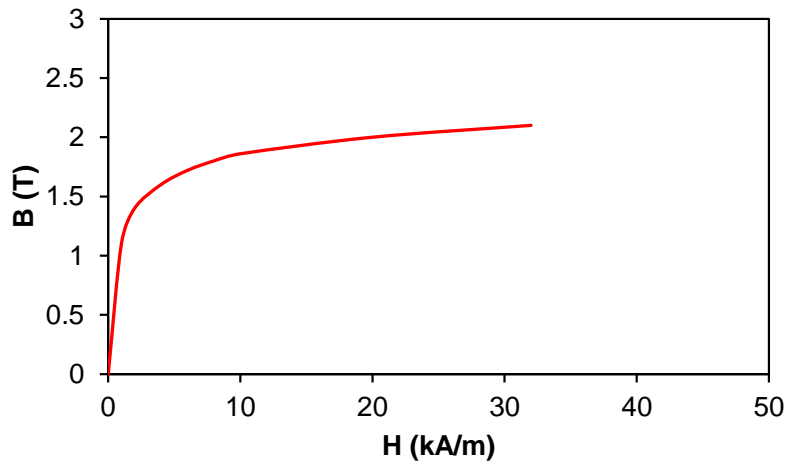


Fig. C.6. Rotor solid yoke magnetisation curve (S235 J0 with  $1.67 \times 10^{-7} \Omega \text{m}$ ).

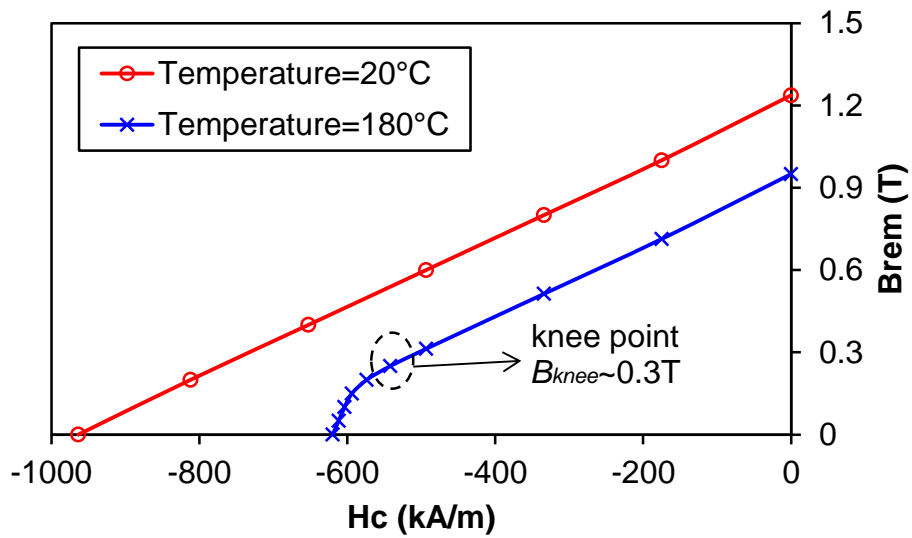


Fig. C.7. PM demagnetisation curve (N35UH with  $1.35 \times 10^{-6} \Omega \text{m}$ ).